Physics of the Solid State, Vol. 47, No. 8, 2005, pp. 1393–1399. From Fizika Tverdogo Tela, Vol. 47, No. 8, 2005, pp. 1348–1353.
Original English Text Copyright © 2005 by Yen.

PROCEEDINGS OF THE XII FEOFILOV WORKSHOP “SPECTROSCOPY OF CRYSTALS ACTIVATED BY RARE-EARTH AND TRANSITION-METAL IONS”

(Yekaterinburg, Russia, September 22–25, 2004)

General Factors Governing the Efficiency of Luminescent Devices[1]

W. M. Yen

Department of Physics and Astronomy, University of Georgia, Athens, GA, 30602 USA
e-mail: wyen@hal.physast.uga.edu; wyen@physics.wustl.edu

Abstract—Factors which determine the luminescence efficiency of activated wide band gap materials are discussed in general terms. These materials find usage in a large variety of luminescent devices. The factors affecting the efficiency can be classified into two broad categories. The first has been thoroughly studied and entails interactions which lead to nonradiative dissipation of optical energy at the specific active site. The second set concerns interactions leading to the delocalization and the transport of optical energy away from the originally excited state. Recent spectroscopic results from these studies have allowed the absolute placement of the ground state of the active centers with respect to the intrinsic bands of the host crystal and have allowed us to elucidate the systematics of such placement. These results are relevant to materials which evince the property of persistent phosphorescence and which are of our current interest. Developments in these materials, as well as a number of new applications, will be touched upon. © *2005 Pleiades Publishing, Inc.*

1. INTRODUCTION

In this article, factors which affect the luminescence efficiency of impurity activated insulators are discussed; though Professor Feofilov did not address this specific topic directly, his contributions to our understanding of the spectroscopy of impurity- and defect-activated systems necessarily provided the basis for our understanding of this subject. This article, then, is prepared as a tribute to his memory and to his influence on all who are engaged in this area of scientific inquiry. Much progress has already been made in delineating the physical processes governing luminescent efficiency of light emitting materials; we now believe that the interactions affecting efficiencies may be classified into two broad categories. The first set is localized and is specific to the active center or ion. The second category arises from interionic interactions and results in delocalization, transport, and/or energy trapping. By reclassifying in this manner, we have gained new insights with which to address the efficiency problem; as a bonus, we have developed the means with which to determine the absolute positioning of the impurity energy levels of the active centers within the host band gap. Some recent applications in which this better understanding can be exploited will be discussed.

2. LUMINESCENCE EFFICIENCIES

The static spectra of impurity-activated insulators can be understood in terms of the Coulomb interactions (crystalline field) produced by the neighboring host ions, which lead to the shifting and splitting of the ion wave functions and determine the nature of the radiative transitions within the active ion. For the most common activators, i.e., ions belonging to the $(3d)^n$ and $(4f)^n$ ion series, the majority of luminescent transitions arise between states belonging to the same atomic configuration and hence are LaPorte or parity forbidden. Nevertheless, radiative transitions occur because the crystalline field can admix high-lying allowed states into the interacting levels; the magnitude of this admixture is responsible to a large extent for the strength of the optical transition. Thus, because of the energy denominators, the energy placement of the atomically allowed states is one of the principal factors in determining the intrinsic light emission efficiency of a material and the determination of the energy of these states constitutes a predictor of efficiencies [1].

Further, the ion and the host lattice system are dynamically coupled and the intrinsic excitations of the lattice, such as phonons, can induce nonradiative relaxation processes in which optical excitation is dissipated through the creation of vibrational or other intrinsic excitations. These relaxation pathways, of course, have a deleterious effect on the radiative efficiencies; it is these processes, for example, which severely limit the number of metastable, emissive states in the systems of interest here. The radiative and nonradiative properties of impurity ions in solids have been a subject of intensive scrutiny over the past few decades, and we need not revisit the subject in detail here [2].

---

[1] This article was submitted by the author in English.

1063-7834/05/4708-1393$26.00 © 2005 Pleiades Publishing, Inc.

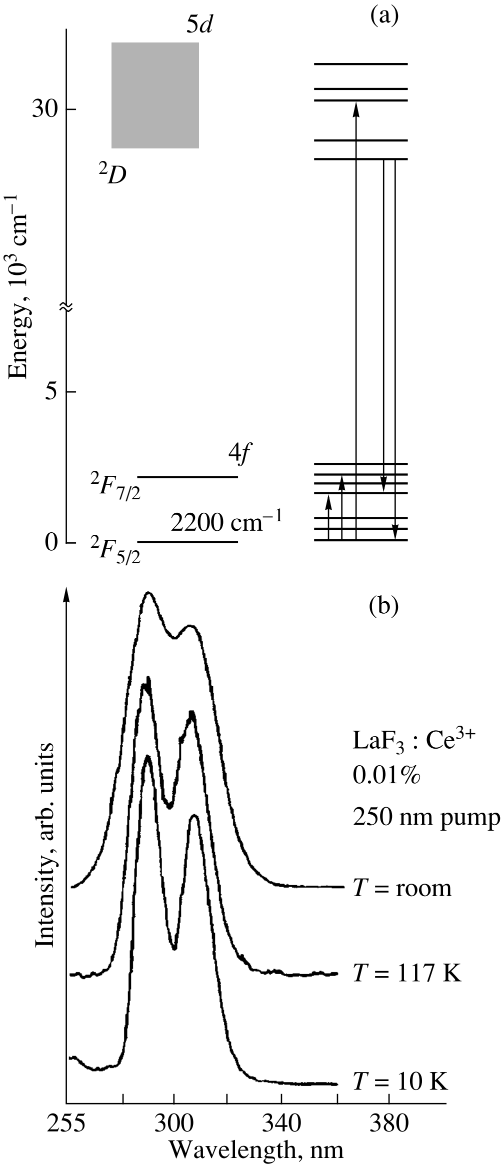

Fig. 1. (a) Schematic diagram of the energy levels of Ce^{3+}. The splitting of the ground state is approximately 2500 cm^{-1}; the 5d states are affected by the crystalline field, and emission is observed from the lowest d component. (b) The first observed Ce luminescence was in LaF_3 obtained through excitation using synchrotron radiation; the luminescence as a function of temperature is shown in part [3].

In our new reclassified picture, we consider these intraionic and ion–phonon interactions to be of a localized nature inasmuch as they are confined to an individual excited center.

3. DELOCALIZATION OF ENERGY

Recent work has led us to conclude that a second class of processes must also be considered and that this class plays an important and sometimes crucial role in determining the luminescence efficiency. These processes are ulterior to the individual centers and lead to the delocalization of optical energy through transfer or through transport. Interionic multipolar interactions, for example, lead to ion–ion transfer processes, which can cause cross relaxation and diffusion of the optical energy [2].

The importance of the second class of processes will become evident when we consider the luminescence behavior of a simple system, e.g., Ce^{3+} activated insulators. Ce^{3+} belongs to the $(4f)^1$ configuration and possesses a very simple energy level structure (shown in Fig. 1a) consisting of a ground-state doublet ($^2F_{5,\,7/2}$) separated by a few thousand wavenumbers and an allowed 5d state lying in the near UV region of the spectra. The 4f to 5d transition is allowed; a strong absorption band is observed which reflects the crystalline-field-induced effects on the 5d state. A strong luminescence originating from the lowest Ce^{3+} 5d component was first observed in LaF_3 and is also shown in Fig. 1b [3]. When excited, the energy structure of Ce is such that localized multiphonon nonradiative relaxation and transfer and cross relaxation quenching to other like ions are highly improbable; the expectation then is that 5d Ce luminescences will be invariably strong and highly efficient.

In a study of the properties of Ce^{3+} in a variety of host lattices, it came as a surprise that, though strong emissions were observed in some lattices, no 5d luminescences were observed in some others (see table). For our purposes, it is interesting to compare and contrast the behavior of Ce^{3+} in two lattices from the table, $LuSiO_5$ (LSO) and Lu_2O_3, where the band gaps of the hosts are about the same. In both cases, Ce^{3+} replaces Lu^{3+} and their local coordination is also roughly analogous. As the table shows, Ce^{3+} in LSO luminesces strongly whereas no 5d emission is observed in $Lu_2O_3 : Ce^{3+}$ [4].

The optical spectra of these two materials are shown in Figs. 2 and 3. The structure of the absorption and/or excitation spectra in both cases are identifiable as field components of the respective 5d states; the Stokes shifted luminescence of LSO : Ce^{3+} originates from the lowest d state of the manifold and reflects the ground-state structure of the cerium ion, also as expected. Since there is no emission at any temperature, Fig. 3 shows the absorption of pure as well as trivalent and tetravalent Ce-doped Lu_2O_3.

Photoconductivity (PC) measurements were conducted on these two compounds, which revealed the reason for their drastically different emission efficiencies. In PC spectroscopy, one measures the creation of mobile electronic charges into the conduction band from the valence band or from the photoionization of impurities. The measured PC spectrum for $Lu_2O_3 : Ce^{3+}$ is shown in Fig. 3 plotted against the 5d absorption; it can be seen from there that the PC spectra track the absorption faithfully; this implies that promotion of Ce electrons from the ground state to the 5*d* state is akin to promoting charges directly into the conduction band. It follows that in this case all the field components of the 5*d* configuration fall within the conduction band of the host and electrons promoted to these energies become undistinguishable from free conduction electrons. The fact that electrons in the conduction band are mobile then implies that the optical energy is no longer localized at a single ion site [5].

Figure 4 shows the PC observed in LSO : Ce^{3+}, which demonstrates that the PC signal is much smaller and that it is temperature-activated. The case for LSO can be understood in terms of the schematic shown in the inset. All 5*d* states, except the lowest level, lie within the conduction band, and optical energy can be stored in this lowest 5*d* level and radiated; the observed PC and its temperature dependence result simply from thermal activation from the radiative state to the conduction band [6]. Basically, the difference between the performance of these two materials lies in the placement of the 5*d* states relative to the conduction band; the absolute placement of the energy levels of the active center viz the intrinsic bands and the band gap of the host then can be seen to play a critical role in determining the emission efficiencies through the process of delocalization of the optical energy.

4. LOCALIZATION/DELOCALIZATION

In order to show that the interpretation of the contrast in behavior is correct, the behavior of $Lu_2O_3 : Ce^{3+}$ was investigated as a function of hydrostatic pressure. The rationale behind these experiments is shown in Fig. 5; hydrostatic pressure of the magnitudes attainable with a diamond anvil cell decreases the dimensions of the unit cell of the crystal and as a consequence increase the crystalline field strength. The splitting of the 5*d* manifold is then expected to increase with the lowest 5*d* component moving to lower energies while keeping the center of gravity of the 5*d* manifold unchanged. If the pressure is sufficiently high, a crossover of this 5*d* state with the conduction band edge will occur. Under these circumstances, the energy level scheme of $Lu_2O_3 : Ce^{3+}$ begins replicating that encountered in LSO; i.e., luminescence from the lowest 5*d* state will occur. Also in analogy to LSO, the pressure-

Emission of Ce^{3+} doped compounds

Efficient	Quenched
$Y_3Al_5O_{12}$(YAG)	Nitrates
$LuAlO_3$(LuAP)	Vanadates
$YAlO_3$(YALO)	Tungstates
Lu_2, $Y_2(SiO_4)O$	Lanthanum oxide
CaF_2, LaF_3	Gadolinium oxide

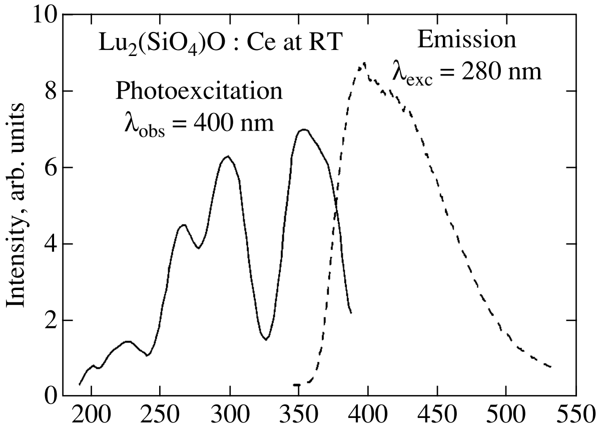

Fig. 2. Ce^{3+} luminescence observed in Lu_2SiO_5 (LSO); the excitation spectrum for the emission is also shown and reflects the crystalline field effects on the 5*d* manifold.

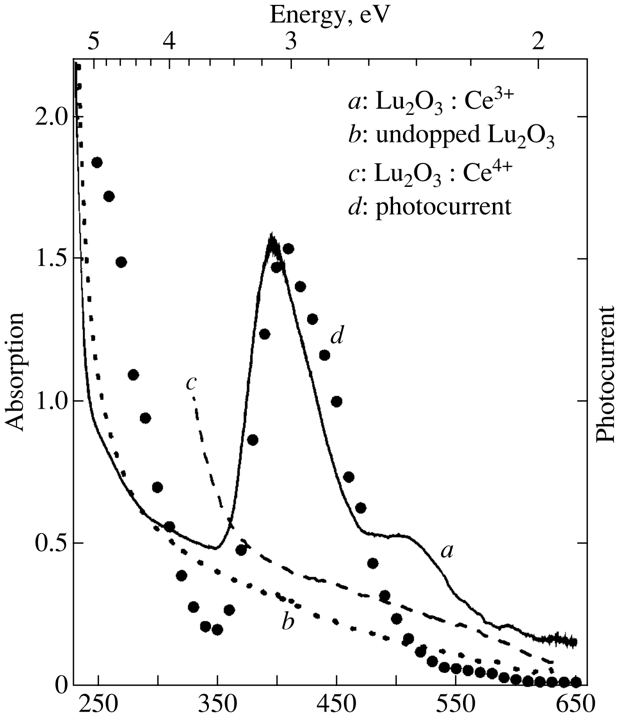

Fig. 3. Absorption and the PC spectra of $Lu_2O_3 : Ce^{3+}$. The absorption spectra of pure Lu_2O_3 and $Lu_2O_3 : Ce^{4+}$ are also shown. This system does not show any 5*d* luminescence. It is seen here that the PC spectrum closely follows the 5*d* absorption in the trivalent Ce compound. The energy shift observed in the PC spectrum can be ascribed to time constant effects.

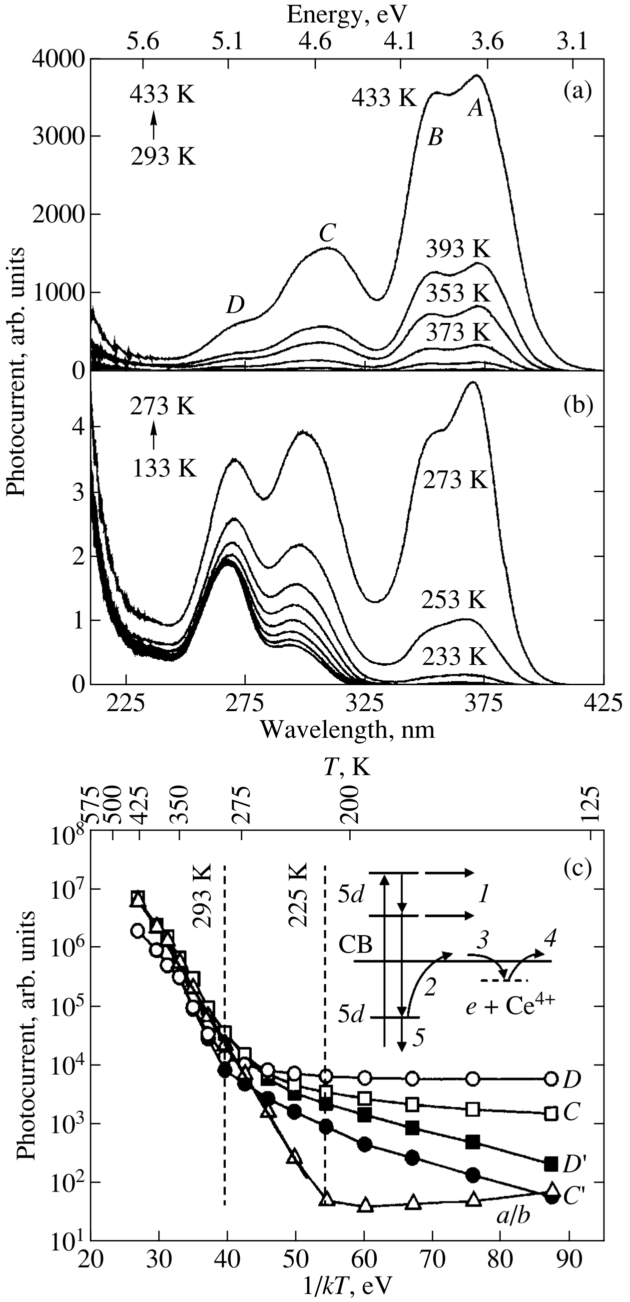

Fig. 4. (a, b) PC spectra observed from Ce in two different sites of LSO. The PC peaks labeled *A*, *B*, *C*, etc., represent the structure of the 5*d* band of the Ce in their respective sites. (c) The PC plotted against temperature clearly indicate a thermally activated behavior. These plots for various PC peaks allow us to determine the placement of the 5*d* components relative to the conduction band edge [6].

induced lowest 5*d* state in the oxide will be subject to quenching through thermal activation back into the conduction band [7].

Recalling that $Lu_2O_3 : Ce^{3+}$ shows no luminescence at ambient pressure, the result from the pressure studies

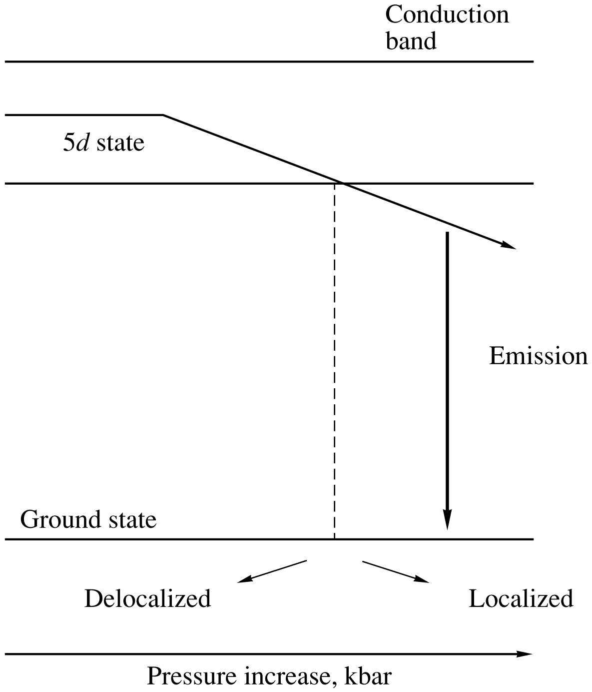

Fig. 5. Rationale behind the high pressure experiments on $Lu_2O_3 : Ce^{3+}$ showing the crossover of the lowest 5*d* state and the bottom of the conduction band. This crossover results in the emergence of 5*d* luminescence and signals the localization of the optical energy.

is shown in Fig. 6. Figure 6a shows the luminescence observed in the oxide material when a pressure of 71 kbar is applied at various temperatures. The behavior of the luminescence is seen to be similar to that observed in LSO, and with thermal quenching also apparent. Thermal activation curves such as those shown in Fig. 6b allow the determination of the position of the 5*d* level below the band edge.

As argued in an earlier section, the luminescence of the 5*d* state of Ce^{3+} signals the localization of the optical energy on a specific ion site, whereas the overlap of the 5*d* states with the conduction band results in the delocalization and transport of the energy through the conduction band. It follows that these experiments, in which a level crossing is induced between a 5*d* state and the conduction band edge, correspond to a transition between localized and delocalized states of the electronic excitations. This type of order-disorder transition has been considered previously in some detail and is related to the so-called Anderson transition; in other words, what our pressure experiments illustrate is an Anderson transition in the optical energy as affected by the transport properties of electronic carriers [8]. We would expect that the appearance of luminescence as a function of pressure will evince a sharp edge (the mobility edge); though our pressure control has not been sufficiently refined to allow the determination of such an edge, its observation is certainly a worthwhile goal to pursue.

5. PLACEMENT OF ENERGY LEVELS

It should be apparent that the placement of the high-lying energy levels of luminescent centers relative to the conduction band of the host plays an important role in determining the luminescence efficiencies of activated systems; hence, it is important to be able to locate the ground state of the active ions absolutely within the band gap of the host material. The placement of the levels may be accomplished by considering factors such as those represented in Fig. 3 for Lu_2O_3; the absorption of the undoped lattice, of course, corresponds to the band gap of the material. The tetravalent Ce ion has a closed shell structure similar to Xe and hence is expected to have absorptive transitions far into the UV. The absorption beginning at 350 nm for the Ce^{4+} material thus arises because of an acceptor-like charge transfer process from the valence band of the host to the tetravalent ion, converting it into a trivalent ion in the ground state. This fact coupled with the absorption due to the 5*d* states of Ce^{3+} allows us to make an absolute energy placement for the ground state [9]. Such a placement for the ground of Ce^{3+} is illustrated in Fig. 7a for $Y_2O_3 : Ce^{3+}$.

It has become clear that the absolute placement of the ground state of impurity ions in solids relative to the intrinsic bands of the host has been an often neglected but essential component in our understanding of the total behavior of emissive properties of impurity ion systems. These problems have only begun to be addressed recently, and several experimental techniques have been developed for their determination. PC has been shown to be useful in establishing the position of states from which conductivity may be induced; often, however, intrinsic bands and charge transfer processes complicate the interpretation of these results. In addition to PC studies, photoelectron spectroscopy has also been used to determine the position of the ground state of the 4*f* ion series in a number of lattices [10]; these studies have shown that in some of the rare-earth ions the ground states fall within the valence band of the host.

We recently developed a new PC-based technique which reduces the contributions from sources other than the center of interest. These two-step experiments are illustrated in Fig. 7a and entail the measurement of photoconductivity from selectively designated excited states of specific impurity centers, i.e., excited state PC [11]. This figure illustrates two-step PC measurements in $Y_2O_3 : Ce^{3+}$ (as noted above) and $Y_2O_3 : Er^{3+}$; in the latter, the first laser photon selectively excites the Er ion from its $^4I_{15/2}$ ground state to the metastable $^4S_{3/2}$ state. A second photon is then used to excite the ion to its 5*d* states or into the conduction band of the host to induce the photocurrent; comparison of the PC spectra under direct and two-step excitation provides sufficient information to allow the absolute placement of the ground state of the Er^{3+} ion relative to the intrinsic bands of the host, as is indicated in Fig. 7b. As can be seen from the figure, the Er^{3+} ground state actually falls within the valence band of the host Y_2O_3.

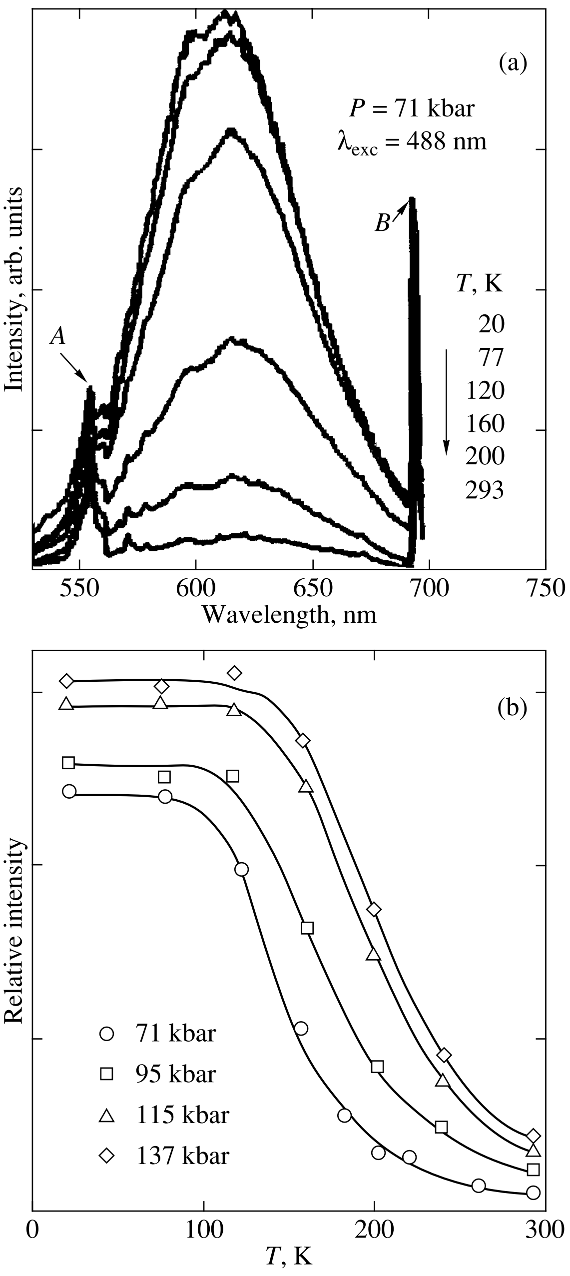

Fig. 6. (a) Temperature dependence of the pressure-induced luminescence in $Lu_2O_3 : Ce^{3+}$. The pressure is 71 kbars. The sharp lines shown in the figure arise from the anvil cell and from a ruby monitor. (b) Integrated emission intensities as a function of pressure. The transition edge allows the positioning of the 5*d* state as a function of pressure [7].

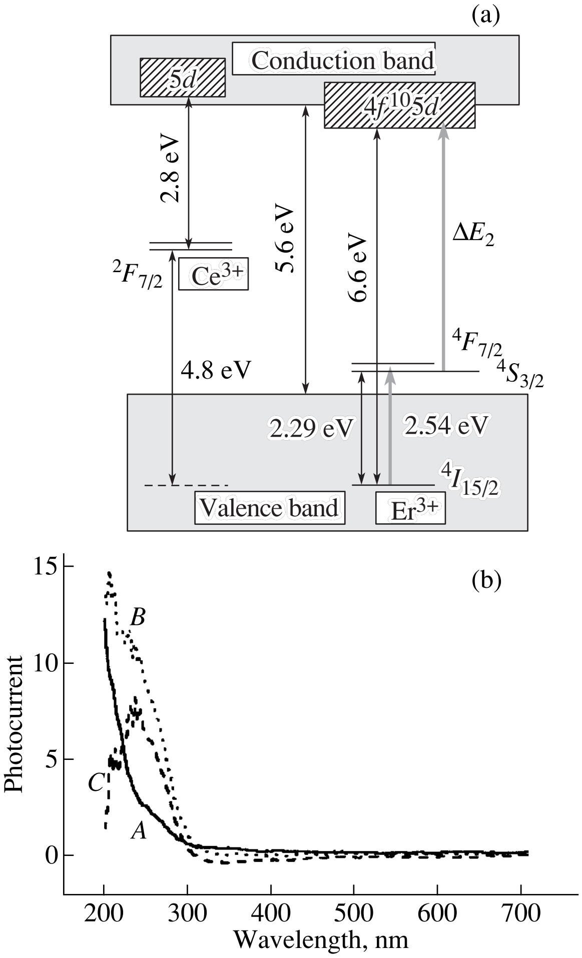

Fig. 7. (a) Placement of the ground state of Ce^{3+} and Er^{3+} in Y_2O_3 using two excitation photons and inducing photoconductivity from a metastable state [11]. (b) PC spectra of Er^{3+} in Y_2O_3. *A*—PC observed with a UV lamp only showing ground-state and intrinsically induced currents; *B* is the PC observed with lamp and laser excitation showing currents induced from the ground and metastable states, and *C* is the difference spectra showing contributions from the $^4S_{3/2}$ state only allowing the placement of the ground state as in part (a).

Recently, Dorenbos conducted an exhaustive survey of the systematics of the placement of the energy levels of the 4*f* ion series in large band gap solids [12]. He exploits trends observed in the ionization behavior of the ions in the series and focuses on the shared properties of certain common transitions of the ions in order to deduce the positioning of the ground states. He assumes, for example, that the energy necessary to ionize ions into a higher valence through charge transfer is roughly the same across the 4*f* ion series. Using these arguments, he has been successful in establishing the ground-state position of the 4*f* ion series in various insulating materials. His results generally agree with the experimental observations and signal that we are reaching a qualitative understanding of one of the last remaining problems in the spectral behavior of impurity-activated insulators.

6. APPLICATIONS AND CONCLUSIONS

As we gain a more detailed knowledge of the absolute placement of impurity ions within large band gap materials, we can better predict the behavior of these materials from different points of view; this includes the consideration of the overall performance efficiency of luminescent materials. For example, there has been considerable recent interest in phosphors which display phosphorescence persisting for tens of hours. One such material is $SrAl_2O_4 : Eu^{2+}, Dy^{3+}$, where a strong green emission arising from the *d* to *f* transition of Eu^{2+} is observed that persists for nearly twenty hours following excitation. The persistence has been ascribed to a mechanism in which the Dy^{3+} ions trap holes, thereby creating excess electrons, which can then transfer their energy to a Eu^{2+} emitter. The trapping behavior of various ions in the 4*f* series may be deduced from the energy trends derived from the energy systematics; the proximity of the Dy^{3+} ground state to the valence band, for example, favors hole trapping. Substitution of Tb^{3+} for Dy^{3+} in this aluminate destroys the persistence; Tb^{3+} is more likely to trap electrons [13]. We believe that the above developments will likely influence the way we look at electroluminescence behavior.

As a summary, we have classified two types of processes that affect the overall luminescent efficiency of luminescent materials, such as phosphors. Some factors, which have been ignored in these considerations, include interactions that lead to the delocalization of optical energy away from the active center or ion and lead to the diffusion and trapping of energy. The physical boundary between the maintenance of energy at a site and its delocalization constitutes an Anderson transition, which should display a mobility edge. Recently, we have also begun to understand the systematics that govern the placement of the impurity energy levels within the band gap of the host, which has made it possible to better predict the behavior and efficiency of phosphors.

ACKNOWLEDGMENTS

The contributions to this work from present and past members of my Georgia group are acknowledged with gratitude. The hospitality of Washington University at St. Louis during the preparation of this manuscript is acknowledged with thanks.

This work was supported by the National Science Foundation and by the University of Georgia Research Foundation.

REFERENCES

1. G. Blasse and B. C. Grabmaier, *Luminescent Materials* (Springer, Berlin, 1994).
2. B. Henderson and G. F. Imbusch, *Optical Spectroscopy of Inorganic Solids* (Science, Oxford, 1989).
3. L. R. Elias, W. S. Heaps, and W. M. Yen, Phys. Rev. B **8**, 4989 (1973).
4. M. Raukas, Doctoral Dissertation (Univ. of Georgia, 1997).
5. W. M. Yen *et al.*, J. Lumin. **69**, 287 (1996).
6. E. van der Kolk, S. A. Basun, G. F. Imbusch, and W. M. Yen, Appl. Phys. Lett. **83**, 1740 (2003).
7. Y. Shen *et al.*, Phys. Rev. B **65**, 212103 (2002).
8. P. W. Anderson, Phys. Rev. **109**, 1492 (1958).
9. W. M. Yen, J. Lumin. **83–84**, 399 (1999).
10. C. W. Thiel *et al.*, Phys. Rev. B **64**, 085107 (2001).
11. D. Jia, R. S. Meltzer, and W. M. Yen, Phys. Rev. B **65**, 235116 (2002).
12. P. Dorenbos, J. Lumin. **108**, 301 (2004).
13. T. Matsuzawa *et al.*, J. Electrochem. Soc. **143**, 2670 (1996).

Physics of the Solid State, Vol. 47, No. 8, 2005, pp. 1400–1405. Translated from Fizika Tverdogo Tela, Vol. 47, No. 8, 2005, pp. 1354–1358.
Original Russian Text Copyright © 2005 by Basiev.

PROCEEDINGS OF THE XII FEOFILOV WORKSHOP "SPECTROSCOPY OF CRYSTALS ACTIVATED BY RARE-EARTH AND TRANSITION-METAL IONS"

(Yekaterinburg, Russia, September 22–25, 2004)

New Crystals for Raman Lasers

T. T. Basiev

Laser Materials and Technology Research Center, Institute of General Physics, Russian Academy of Sciences,
ul. Vavilova 38, Moscow, 119991 Russia
e-mail: basiev@lst.gpi.ru

Abstract—Steady-state and transient stimulated Raman scattering (SRS) in crystals is analyzed. The basic laws of an increase in the SRS gain in crystals are revealed, and methods for searching and creating new SRS laser materials are developed. New crystals for picosecond and nanosecond SRS lasers are proposed, fabricated, and characterized. These materials have the highest SRS cross section, a low SRS threshold, and a wide spectral range of operation. *© 2005 Pleiades Publishing, Inc.*

Raman scattering (RS) was discovered almost 80 years ago (in 1928) simultaneously and independently by the outstanding Indian scientists C.V. Raman and K.S. Krishnan for liquids [1] and the outstanding Russian scientists L.I. Mandel'shtam and G.S. Landsberg for crystals (in quartz) [2]. This process is inelastic light scattering by molecular vibrations or phonons in a medium; so the scattered-light frequency is lower than that of the incident light by the molecular vibration frequency (e.g., by the vibration frequency of a SiO_4 tetrahedron in quartz), which usually ranges from 100 to 3000 cm^{-1} for condensed matter. The quantum yield of this two-photon process is very low (10^{-10}%). Therefore, it takes several tens of minutes for this radiation to be detected even now with the use of laser excitation, while it took several tens of hours to detect this radiation in the prelaser era.

Spontaneous Raman scattering is now widely used for the study and identification of the structures of new optical crystals and glasses.

When powerful laser light sources were created about 40 years ago, the situation with the low quantum yield of Raman scattering changed radically. It has been found that, when the pumping intensity increases to 10–100 MW/cm^2, the scattering yield increases exponentially (avalanchewise) and can be as high as 50–80%. This process of stimulated Raman scattering (SRS) was detected accidentally by E.J. Woodbury and W.K. Ng in 1962 [3] inside a ruby laser with a nitrobenzene-filled cell in the form of powerful coherent radiation at a frequency shifted toward the red spectral region.

Initially (in the 1960s), SRS was studied in natural diamond and calcite ($CaCO_3$) crystals and artificially grown crystals of calcium tungstate, lithium niobate, and lithium iodate. However, low optical quality and a large number of inclusions and bubbles led to rapid laser breakdown (damage of the crystal surface and bulk). After several tens of flashes, a crystal could not be radiant, and such studies were very expensive because of the high cost of the crystals (~$1000/crystal) [4–10].

Interest in crystalline Raman materials was rekindled in the 1980s, when synthetic $Ba(NO_3)_2$ and $KGd(WO_4)_2$ (KGW) crystals were grown. They had high purity and optical quality, low losses, a high threshold for laser damage, and high Raman gains for nanosecond (in $Ba(NO_3)_2$) and picosecond (in KGW) pulse durations [11–14].

The Raman laser is a sufficiently simple device in which an SRS crystal is placed between two parallel dielectric mirrors forming an optical cavity. The entrance mirror is transparent to pumping radiation with, e.g., $\lambda = 532$ nm and reflects Raman radiation. On the contrary, the exit mirror reflects pumping radiation and partly transmits Raman radiation. Thus, multiple reflection by the mirrors and multiple passages through the cavity and crystal make it possible to increase the length of interaction between the light and crystal and significantly decrease the threshold for SRS (photon avalanche). As a result, one, two, three, or more Stokes spectral components lying in different (yellow, orange, red) spectral regions, as well as (under certain phase matching conditions) anti-Stokes components (blue, violet), can be generated at the laser exit. The dominant color and the Raman gain are controlled by pumping and the reflection spectrum of the SRS laser mirrors.

When researchers sought crystals for wide-range laser spectrometers in the 1980s [15–18], they tried to understand why the materials mentioned above [$Ba(NO_3)_2$, KGW] were the best materials for Raman lasers and how they could create better crystals for such lasers. To this end, dozens of different single crystals have been studied and compared. We have investigated

1063-7834/05/4708-1400$26.00 © 2005 Pleiades Publishing, Inc.

the scattering spectra of crystals formed by the cations of alkali and rare-earth metals and by complex quasi-molecular anions like (CO_3), (NO_3), (PO_4), (ClO_3), (SiO_4), (NbO_3), (IO_3), (BrO_3), (SO_4), (WO_4), and (MoO_4) [19–27].

The most intense Raman lines are known to be caused by the internal fully symmetric vibrations of an oxygen triangle or tetrahedron in a complicated anion complex. In different crystals, the Raman line frequencies and widths can be different. Therefore, the challenge was to establish the factors that are responsible for the applicability of an optical material for SRS lasers and amplifiers, to understand why some crystals operate well at nanosecond pump pulse durations [e.g., $Ba(NO_3)_2$] and operate badly at picosecond pumping times [28] (and vice versa for $KGd(WO_4)_2$), and to find ways to increase the Raman gain of crystals.

To solve these problems, we need to consider two operating modes:

(1) A steady-state (long-pulse) mode, where the laser pump pulse duration t_{pump} is much longer than the time of loss of the coherency of molecular vibrations T_2 (dephasing time), which is proportional to the reciprocal width of the spontaneous RS spectrum, $t_{\text{pump}} \gg T_2$.

(2) A transient mode, where the pumping pulse is shorter than the dephasing time, $t_{\text{pump}} < T_2$.

In the first case, the increment of the exponential amplification of Raman scattering is proportional to the pumping intensity, the crystal length, and the peak Raman gain σ_R (one of the most important parameters of a nonlinear Raman medium). In the second case, this increment is proportional to the product of the square root of the parameters mentioned above by the square root of the pumping time and of the spontaneous RS spectral width $\Delta\nu$ (another important parameter).

The product of the peak SRS cross section σ_R by the gain spectral width $\Delta\nu_R$ is the integrated SRS cross section (a third important parameter).

We have determined and analyzed these most important parameters for several dozen crystals with ionic, covalent, and quasi-molecular bonds and found that the integrated RS intensity is maximum for crystals having the maximum size of a quasi-molecular complex (large thermochemical radius) and for crystals with the maximum internal covalence of the anion complex and the minimum complex–lattice coupling. These crystals include iodates, molybdates, and tungstates. Nitrates and carbonates have smaller sizes of quasi-molecular anions and, correspondingly, a lower integrated RS intensity. In turn, silicates and borates have a low degree of isolation of tetrahedral and triangle complexes, easily form skeleton or network structures (crystalline or glasslike), and have a low RS intensity.

As a result of this analysis, we have found that molybdates and tungstates are the most promising. Note also that they have high hardness, thermal conductivity, and moisture resistance as compared to iodates and nitrates [24–27]. However, it should be noted that the class of molybdates and tungstates includes several dozen compounds having different structures of the Raman scattering spectra. A comparison of the Raman spectra of crystals of sodium–lanthanum and potassium–lanthanum molybdates and strontium molybdate shows that all the spectra have a uniformly broadened low-frequency Raman line near 330 cm^{-1}. However, the high-frequency 880-cm^{-1} line of the totally symmetric vibration is uniformly broadened only in a $SrMoO_4$ crystal with a scheelite structure and the spectral disordering in the two other crystals is so high that it sharply decreases the peak SRS cross section.

To create a crystal with the best characteristics required for Raman lasers, we first chose the class of scheelite materials from among tungstates and molybdates, because in these materials the Raman lines are uniformly broadened at room temperature. Since the integrated SRS intensity in this class is approximately constant and the peak SRS cross section is inversely proportional to the uniform width of the SRS line, we tried to decrease the SRS line width by increasing the dephasing time of vibrational excitation.

One obvious method for solving this problem is to use heavier alkaline-earth cations, which decrease the lattice vibration frequencies. In this case, a larger number of lattice phonons is required to relax a high-frequency SRS-active vibration mode. Therefore, the phase relaxation rate decreases, which, in turn, decreases the spectral broadening.

Indeed, using the Sr^{2+} and Ba^{2+} cations (which are two and three times heavier than the Ca^{2+} ion, respectively) in scheelite crystals, we sharply decreased (by a factor of 3–4) the widths of the RS lines and simultaneously increased the peak SRS cross section by the same factor. A shift of an SRS-active vibration toward high frequencies due to an increase in the lattice parameter for cations with a larger radius also favors narrowing of the SRS spectrum and an increase in the peak SRS gain. Barium and strontium tungstates found using this approach have been patented as new highly efficient materials for Raman lasers [29].

Researchers at our research center have developed a process of synthesis and growth of large $BaWO_4$ and $SrWO_4$ crystals of high optical quality [29, 30]. This process is based on the Czochralski crystal growth technique, high-frequency heating in a platinum crucible, and crystal pulling with a seed. The pulling speed was 2–6 mm/h, the rate of rotation was 30 rpm, and the volume crystallization rate was less than 1 cm^3/h. We used a charge with excess 1.0–1.5 wt % WO_3. Oriented rectangular experimental samples having a Brewster cut were cut from crystalline boules.

Samples of the new $BaWO_4$ and $SrWO_4$ crystals [29–36] were subjected to laser tests under nanosecond and picosecond pumping along with well-known

Comparative SRS and thermomechanical properties of $Ba(NO_3)_2$, $KGd(WO_4)_2$, $SrWO_4$, and $BaWO_4$ crystals

Property	Crystal			
	$Ba(NO_3)_2$	$KGd(WO_4)_2$	$SrWO_4$	$BaWO_4$
RS vibration frequency ν_R, cm^{-1}	1047	901; 767	922	924
RS line width $\Delta\nu_R$, cm^{-1}	0.4	5.4; 6.4	2.74	1.6
Dephasing time T_R, ps	28	2.0	4	6.6
Gain g, cm/GW:				
g (0.53 μm) steady-state (ns)	47	11		36–40
g (0.53 μm) transient (20 ps)	4.7	11		14.4
g (1.06 μm) steady-state (ns)	11	4	5	8.5
g (1.06 μm) transient (30–50 ps)	1.1	3		3.8
g (1.3 μm) steady-state (ns)				5.8
Transmission band, μm	0.33–1.8	0.3–5	0.25–5	0.255–5
Moisture resistance	low	high	high	high
Thermal conductivity at 25°C, W/K m	1.17	2.5–3.4	3	3.0
Thermal expansion coefficient α, 1/K	13×10^{-6}	$(1.6–8.5) \times 10^{-6}$		6×10^{-6}
Hardness	19.2 ($NaNO_3$ Knoop)	4–4.5 (Mohs)	4 (Mohs)	4 (Mohs) 400 (Knoop)

$Ba(NO_3)_2$ and $KGd(WO_4)_2$ crystals. For nanosecond pumping, the threshold for the generation of powerful SRS radiation is lower even in shorter $BaWO_4$ and $SrWO_4$ crystals as compared to a KGW crystal and approaches the lowest threshold characteristic of a $Ba(NO_3)_2$ crystal. This behavior is related to the higher peak SRS gain cross sections as compared to that in KGW.

Picosecond tests also showed that the SRS gain in the $BaWO_4$ and $SrWO_4$ crystals was close to the record value (typical of KGW crystals), whereas the SRS gain of $Ba(NO_3)_2$ in the picosecond range decreased tenfold. Thus, we were the first to design new universal Raman crystals that can successfully operate in both the steady-state mode of nanosecond and longer pulses and the transient mode of picosecond pumping (see table).

As is seen from the table, apart from the unique properties given above, these crystals have a significantly wider range of optical transparency (0.25–5 μm), higher moisture resistance, higher thermal conductivity and hardness, and lower thermal expansion coefficients than $Ba(NO_3)_2$ crystals. All these properties specify the outstanding output parameters of solid-state SRS lasers.

The application of infrared nanosecond 1.34-μm pumping lasers allowed us for the first time to move deep into the IR spectral range using SRS in $BaWO_4$ crystals [37].

For example, we observed the generation of coherent first Stokes radiation with a wavelength λ_1 = 1.54 μm, second Stokes radiation with λ_2 = 1.78 μm, and third Stokes radiation with λ_3 = 2.13 μm. The output energy was several millijoules at an efficiency of 15–20%. It is interesting that, in terms of its spectral composition, one such Raman laser is equivalent to a combination of three different lasers based on Er^{3+} ions in glass and Tm^{3+} and HO^{3+} ions in crystals.

An important advantage of the new Raman crystals developed is the fact that they can be doped by laser-active rare-earth ions, such as Nd^{3+} ions, with a heterovalent substitution for Ba^{2+} and Sr^{2+} ions in the cation sublattice.

Such crystals can operate successively and accomplish two functions: first, they allow laser amplification and generation by Nd^{3+} ions (which is the function of a laser medium), and, second, they provide highly efficient SRS conversion of laser radiation with a frequency shift of ~920 cm^{-1} involving the vibrations of the $[WO_4]^{2-}$ complex (which is the function of an SRS medium). These new multifunctional Raman-laser media can generate powerful coherent radiation at many wavelengths and make it possible to tune the radiation frequency discretely.

Raman laser converters can be combined very well with continuously tunable solid-state laser complexes. For example, the best solid-state complexes based on crystals with color centers have a long-wavelength tuning-range limit of 1.3–1.4 μm, whereas Raman laser converters extend the tuning range to 1.5–1.7 μm for first and second Stokes radiation and to 2.2 μm for third Stokes radiation [15–18].

The new Raman crystals and Raman lasers can be combined perfectly with modern powerful solid-state neodymium pumping lasers that emit single-mode single-frequency radiation with a high peak and average power [38, 39]. The application of loop cavities with intersecting beams inside the active elements provides four-wave phase conjugation in the active medium of a neodymium laser and, thus, compensates for thermal and pumping-induced distortions. As a result, using single-mode single-frequency pumping with an average power of up to 34 W, an output power of about 5 W at a peak power above 1 MW has been attained for Raman radiation in a $BaWO_4$ crystal [38]. Using a pumping loop laser based on highly efficient large GGG : Nd crystals, a Raman laser based on a 6 × 8 × 95-mm $BaWO_4$ crystal has been realized for the first time with a train energy of 2 J and more than 50 pulses per train [39].

The last two types of solid-state Raman laser systems can serve as a good basis (prototype) for designing a “sodium star” project for applied astronomy and for controlling rapidly moving extraterrestrial objects. This ambitious project, which comes from the Star Wars program, consists in the creation of a powerful laser operating at a wavelength of 588.9 μm, which is in resonance with Na^+ ions. This laser should be installed on an adaptive telescope and move with it. At a height of 100 km above the surface of the earth, laser radiation with a wavelength $\lambda = 588.9$ nm resonantly excites Na^+ ions located in a 10-km-thick layer. The resonance fluorescence and scattering of the laser power by the Na^+ ions generates the image of an artificial star. The difference in the image of this star from a sphere indicates optical distortions of the laser beam in a 100-km-thick atmospheric layer. These distortions can then be compensated by the adaptive telescope, which increases the resolution of the system by several tens of times.

Our analysis has shown that the combination of highly efficient GGG : Nd laser crystals and $BaWO_4$ SRS crystals is the best for falling exactly in resonance with Na^+ ions [40, 41]. The 1062.1-nm SRS conversion of the GGG : Nd laser radiation gives radiation with a wavelength of 1177.9 nm, which can then be converted into yellow radiation with $\lambda = 588.9$ nm using frequency doubling in a nonlinear crystal (e.g., LBO). In [40], it was shown that the laser radiation spectrum corresponds well to the Na^+ resonance. A peak power of several tens or several hundred megawatts has been achieved with a prototype of this laser, and the optical conversion efficiency is many tens of percent.

Interesting SRS features have been detected in crystals of gadolinium and yttrium vanadates. For proper orientation of the crystals with respect to the directions of propagation of pumping light and of its polarization, the Raman gain in $GdVO_3$ and YVO_3 crystals was found to be extremely high (close to that of $BaWO_4$) [42]. The integrated RS cross section for these crystals is even higher than those for some tungstate crystals. A combination of the high Raman gain with the record large generation cross section of Nd^{3+} ions in tungstate crystals made it possible to realize a microlaser based on a $GdVO_4$: Nd laser with passive *Q*-switching on a LiF : F_2^- crystal, which generates self-SRS first Stokes radiation pulses ($\lambda_1 = 1174.4$ nm) shorter than 400 ps with a peak power of 10 kW at a repetition frequency of 20 kHz [43]. This method for generating single ultrashort pulses with a high repetition frequency in microlasers with a cavity several millimeters long without using complex, large, and expensive devices for mode locking and separating one spike from a pulse train seems to be very promising for many lidar applications.

The search for a proper SRS crystal for picosecond lasers with a minimum pulse duration required detailed investigation of the properties of several dozen crystals at pump pulse durations shorter than 10 ps. An analysis of the SRS threshold values reduced to the crystal unit length, of the vibration excitation dephasing times, and of the spectral line broadening in integrated and peak scattering cross sections for different crystal orientations has revealed a number of anomalies. The most pronounced anomaly detected by us was that crystals of lead molybdate and tungstate have SRS thresholds that are much lower than those for the other crystals of this class and that their integrated and peak SRS cross sections are much larger than those for the other crystals. The maximum SRS cross sections and the minimum SRS thresholds were detected in the case where the polarization and propagation vector of a pumping beam were orthogonal to those optimal for the other molybdates and tungstates [44]. This finding requires the development of a growth technique to produce crystals having orthogonal polarization with respect to the traditional polarization. Unfortunately, the unique properties of lead molybdates and tungstates cannot be used completely at the present time because of the low optical quality of the crystals and the low laser damage threshold, especially for nanosecond pulses.

The main results obtained in the series of studies are the following:

(1) Unique techniques have been developed for searching for and creating new Raman laser materials.

(2) The microscopic mechanisms of quasi-molecular vibration relaxation (dephasing, decay) responsible for the unique SRS properties of nitrate, tungstate, and molybdate crystals have been established.

(3) Based on an analysis of microscopic properties, new crystalline materials having a record SRS cross section, a low SRS threshold, and a wide spectral region of operation have been proposed.

(4) A process for growing SRS single crystals for the next generation of solid-state Raman lasers and optical amplifiers has been developed.

(5) New Raman laser devices have been designed for lidar applications, microelement control, laser range finding, adaptive optics, and medicine.

ACKNOWLEDGMENTS

This work was supported in part by the International Science and Technology Center (ISTC), project no. 2022r.

REFERENCES

1. C. V. Raman and K. S. Krishnan, Nature (London) **121**, 501 (1928).
2. S. G. Landsberg and L. I. Mandel'shtam, Zh. Russ. Fiz. Khem. Obshchestva **60**, 335 (1928).
3. E. J. Woodbury and W. K. Ng, IRE **50**, 2367 (1962).
4. V. A. Zubov, M. M. Sushchinskiĭ, and I. K. Shuvalov, Usp. Fiz. Nauk **83** (2), 197 (1964) [Sov. Phys. Usp. **7** (2), 419 (1964)].
5. G. Eckhart, IEEE J. Quantum Electron. QE-**2** (1), 1 (1966).
6. N. Bloembergen, Am. J. Phys. **35** (II), 989 (1967).
7. T. T. Basiev, Usp. Fiz. Nauk **169** (10), 1149 (1999) [Phys. Usp. **42** (10), 1051 (1999)].
8. R. C. Powell and T. T. Basiev, in *Advances in Laser Physics*, Ed. by V. S. Letokhov and P. Meystre (Harwood Academic, Amsterdam, Netherlands, 2000), p. 55.
9. T. T. Basiev, V. V. Osiko, A. M. Prokhorov, and E. M. Dianov, Top. Appl. Phys. **89**, 351 (2003).
10. T. T. Basiev and R. C. Powell, *Handbook of Laser Technology and Applications* (Institute of Physics Publishing, UK, 2003), Chap. B 1.7, pp. 1–29.
11. T. T. Basiev and R. C. Powell, Opt. Mater. **11** (4), 301 (1999).
12. P. G. Zverev, T. T. Basiev, and A. M. Prokhorov, Opt. Mater. **11** (4), 335 (1999).
13. P. G. Zverev, T. T. Basiev, V. V. Osiko, A. M. Kulkov, V. N. Voitsekhovskiĭ, and V. E. Yakobson, Opt. Mater. **11** (4), 315 (1999).
14. I. V. Mochalov, Opt. Zh. **11**, 4 (1995).
15. T. T. Basiev, V. V. Osiko, and S. B. Mirov, IEEE J. Quantum Electron. **24** (6), 1052 (1988).
16. T. T. Basiev and S. B. Mirov, *Room Temperature Tunable Color Center Lasers. Laser Science and Technology Books Series* (Gordon and Breach, New York, 1994), p. 33.
17. T. T. Basiev, V. N. Voĭtsekhovskiĭ, P. G. Zverev, F. V. Karpushko, A. V. Lyubimov, S. B. Mirov, V. P. Morozov, I. V. Mochalov, A. A. Pavlyuk, G. V. Sinitsyn, and V. É. Yakobson, Kvantovaya Élektron. **14** (12), 2452 (1987).
18. T. T. Basiev, P. G. Zverev, F. V. Karpushko, V. A. Konyushkin, S. M. Kulashchik, S. B. Mirov, V. P. Morozov, V. S. Motkin, A. G. Papashvili, N. A. Saskevich, G. V. Sinitsyn, and V. V. Fedorov, Izv. Akad. Nauk Resp. Kaz., Ser. Fiz.-Mat. **54** (8), 1450 (1990).
19. T. T. Basiev, E. M. Dianov, É. A. Zakhidov, A. Ya. Karasik, S. B. Mirov, and A. V. Prokhorov, Pis'ma Zh. Éksp. Teor. Fiz. **37** (4), 192 (1983) [JETP Lett. **37** (4), 229 (1983)].
20. P. G. Zverev and T. T. Basiev, in *Advanced Solid State Lasers*, Ed. by B. H. T. Chai and S. A. Pain (OSA Proc. Washington, DC: OSA, 1995), Vol. 24, p. 288.
21. P. G. Zverev, T. T. Basiev, V. Jia, and H. Liu, in *Advanced Solid State Lasers*, Ed. by S. A. Pain and C. Pollok (Oesterr. Akad. Wiss., Washington, 1996), Vol. 1, p. 554.
22. T. T. Basiev and P. G. Zverev, Kvantovaya Élektron. **22** (12), 1241 (1995) [Quantum Electron. **25** (12), 1204 (1995)].
23. P. G. Zverev, W. Jia, H. Liu, and T. T. Basiev, Opt. Lett. **20**, 2378 (1995).
24. T. T. Basiev, A. A. Sobol, P. G. Zverev, V. V. Osiko, and R. C. Powell, Appl. Opt. **38**, 594 (1999).
25. T. T. Basiev, A. A. Sobol, P. G. Zverev, L. I. Ivleva, V. V. Osiko, and R. C. Powell, Opt. Mater. **11** (4), 307 (1999).
26. T. T. Basiev, A. A. Sobol, Yu. K. Voron'ko, and P. G. Zverev, Opt. Mater. **15**, 205 (2000).
27. T. T. Basiev, P. G. Zverev, A. A. Sobol, and V. V. Osiko, *Advanced Solid State Lasers* (2002), MB10-1.
28. P. G. Zverev, J. T. Murray, R. C. Powell, R. J. Reeves, and T. T. Basiev, Opt. Commun. **97**, 59 (1993).
29. T. T. Basiev, A. A. Sobol, P. G. Zverev, L. I. Ivleva, and V. V. Osiko, RF Patent No. 2 178 938, Byull. Izobret., No. 3 (2002).
30. P. G. Zverev, T. T. Basiev, A. A. Sobol, V. V. Skornyakov, L. I. Ivleva, N. M. Polozkov, and V. V. Osiko, Kvantovaya Élektron. **30** (1), 55 (2000) [Quantum. Electron. **80** (1), 55 (2000)].
31. T. T. Basiev, A. A. Sobol, P. G. Zverev, V. V. Fedorov, M. E. Doroshenko, L. I. Ivleva, N. M. Polozkov, V. V. Osiko, A. M. Prokhorov, and G. Hager, in *Proceedings of International Conference, Laser-1998, Tucson, 1998*, Ed. by V. J. Corcoran and T. A. Goldman (SRS Press, Tuscon, 1999), p. 712.
32. P. Černý, H. Jelínková, T. T. Basiev, and P. G. Zverev, *Growth, Fabrication, Devices and Applications of Laser and Nonlinear Materials*; Proc. SPIE **4268**, 101 (2001).
33. P. Černý, H. Jelínková, J. Sulc, P. G. Zverev, and T. T. Basiev, *Advanced Solid State Lasers* (Oesterr. Akad. Wiss., Washington, 2001), Vol. 50.
34. P. Černý, P. G. Zverev, H. Jelínková, and T. T. Basiev, Opt. Commun. **177**, 397 (2000).
35. P. Černý, P. G. Zverev, H. Jelínková, T. T. Basiev, L. I. Ivleva, and V. V. Osiko, Proc. SPIE **3928**, 124, (2000).
36. P. Černý, H. Jelínková, J. Sulc, P. G. Zverev, and T. T. Basiev, Prog. Quantum Electron. **28** (2), 113 (2004).
37. T. T. Basiev, M. E. Doroshenko, V. V. Osiko, V. M. Pusikov, V. K. Komar, B. Grinyov, and M. B. Kosmyna, in *Proceedings of International Conference on Advanced Optoelectronics and Lasers, Alushta, Crimea, Ukraine, 2003* (Alushta, 2003), p. 122.
38. T. T. Basiev, A. V. Gavrilov, V. V. Osiko, S. N. Smetanin, and A. F. Fedin, Kvantovaya Élektron. **34** (7), 1 (2004) [Quantum Electron. **34** (7), 649 (2004)].

39. T. T. Basiev, Yu. K. Danilenko, M. E. Doroshenko, A. V. Fedin, A. V. Gavrilov, V. V. Osiko, and S. N. Smetanin, Proc. SPIE **5481**, 23 (2004).
40. P. G. Zverev, T. T. Basiev, M. E. Doroshenko, and V. V. Osiko, Opt. Soc. Am., Ser. Trends Opt. Photonics **34**, 348 (2000).
41. T. T. Basiev, N. E. Doroshenko, P. G. Zverev, and A. M. Prokhorov, RF Patent No. 2 178 938, Byull. Izobret., No. 3 (2002).
42. P. G. Zverev, A. Ya. Karasik, A. A. Sobol, D. S. Chunaev, T. T. Basiev, A. I. Zagumennyĭ, Yu. D. Zavartsev, S. A. Kutovoĭ, V. V. Osiko, and I. A. Shcherbakov, in *Proceedings of Advanced Solid State Photonics Conference on Technical Digest, Santa Fe, USA, 2004* (Santa Fe, 2004), TuB10, pp. 25–27.
43. T. T. Basiev, S. V. Vassiliev, V. A. Konyushkin, V. V. Osiko, A. I. Zagumennyĭ, Y. D. Zavartsev, S. A. Kutovoĭ, and L. A. Shcherbakov, Laser Phys. Lett. **1** (5), 237 (2004).
44. T. T. Basiev, P. G. Zverev, A. Ya. Karasik, V. V. Osiko, A. A. Sobol', and D. S. Chunaev, Zh. Éksp. Teor. Fiz. **126** (5), 11 (2004) [JETP **99** (5), 934 (2004)].

Translated by K. Shakhlevich

Physics of the Solid State, Vol. 47, No. 8, 2005, pp. 1406–1411. From Fizika Tverdogo Tela, Vol. 47, No. 8, 2005, pp. 1359–1363.
Original English Text Copyright © 2005 by Pédrini.

PROCEEDINGS OF THE XII FEOFILOV WORKSHOP "SPECTROSCOPY OF CRYSTALS ACTIVATED BY RARE-EARTH AND TRANSITION-METAL IONS"

(Yekaterinburg, Russia, September 22–25, 2004)

Scintillation Mechanisms and Limiting Factors on Each Step of Relaxation of Electronic Excitations[1]

C. Pédrini

Laboratoire de Physico-Chimie des Matériaux Luminescents, Unité Mixte de Recherche 5620,
Université Lyon 1, Villeurbanne cedex, 69622 France
e-mail: PEDRINI@PCML.UNIV-LYON1.FR

Abstract—Scintillation mechanisms in insulating materials are described in the general case of a simple electronic band structure and in special cases of most interest for applications: rare-earth-containing crystals and cross-luminescent materials with a more complicated electronic band structure. At each of the three main steps of the energy relaxation, namely, (i) the creation of electronic excitations, (ii) the transfer to luminescent centers, and (iii) the emission of luminescent centers, factors limiting the performance of the scintillators are identified and the related processes described. © *2005 Pleiades Publishing, Inc.*

1. INTRODUCTION

Scintillating materials are ideal devices for detecting elementary particles and for measuring their parameters. Therefore, they are playing a major role in the development of modern nuclear physics. Scintillators are also of great importance for other applications, in particular, in nuclear medical imaging. Depending on the particular requirement of a given application, different scintillators will be preferred. Among the desirable properties of a good scintillator, high efficiency, fast scintillation, and good energy resolution are of the most interest in a number of cases.

The optimization of scintillating materials will only come with a good understanding of the scintillation mechanism. In this paper, we propose to focus our attention on scintillation in inorganic crystalline media. Scintillation mechanisms will be described in the general case and in two other special interest cases: rare-earth-containing crystals and cross-luminescent materials. Limiting factors at each step of the energy relaxation will be identified and discussed.

2. SCINTILLATION MECHANISMS

The relaxation of electronic excitations involves complex mechanisms which can be simply described using schemes of the electronic band structure of the crystal [1]. In a general scheme (Fig. 1), a core level, the valence band, and the conduction band separated by the band gap are presented, with the time scale in abscissa and the energy in ordinate. After high energy excitation, for example by an x-ray or γ-ray photon, a deep core hole and a hot electron are produced. The first stage of relaxation of the electronic excitation occurs in a very short time through inelastic electron–electron (*e*–*e*) scattering and Auger processes, leading to the multiplication of electronic excitations. Multiplication is stopped when the energy of electrons and holes becomes lower than the threshold of *e*–*e* scattering and Auger relaxation. The second stage deals with the thermalization of electrons and holes with the production of phonons. At the end of this stage, all the electrons are at the bottom of the conduction band and all the holes are at the top of the valence band. Then, localization of the excitations may occur with the formation of self-trapped excitons and self-trapped holes, the capture of electrons and holes by traps, etc. As a result, these centers have localized states located in the band gap. After the interaction and recombination of localized excitations (fourth stage), centers may emit photons (luminescence final stage).

In many cases, strong luminescence is obtained by crystals containing luminescent ions like rare-earth (RE) ions. In this case (Fig. 2), the scheme must involve the 4*f* band of the RE located in general in the band gap. During the first stage of relaxation, excitation of the RE ions can be obtained through electron impact. The probability of such excitation is significant only when the electron has kinetic energy below the threshold of *e*–*e* scattering and, of course, above the threshold of *e*–RE scattering. So, rare-earth-excited centers can be obtained very early. An additional channel of excitation of RE ions is possible later on, after the thermalization stage, through sequential capture of holes and electrons by RE ions. The last stage involves radiative recombination of luminescent centers, in particular, of RE centers.

---

[1] This article was submitted by the author in English.

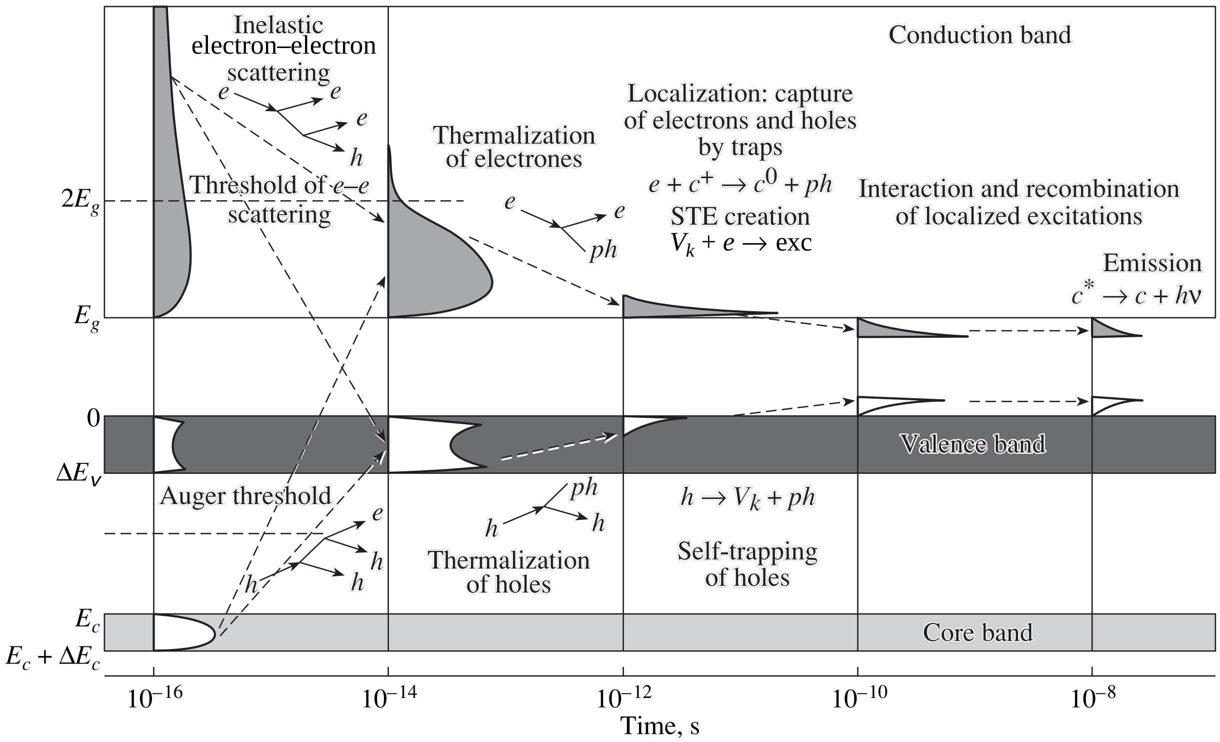

Fig. 1. General scheme of relaxation of electronic excitations in an insulating material.

Another interesting case is cross-luminescent crystals. Cross luminescence is due to a radiative electronic transition from the valence band to the uppermost core band; providing Auger relaxation of the uppermost core band hole is strictly forbidden. This situation occurs when the energy difference between the uppermost core level and the valence band is less than the band gap. The archetype of cross-luminescent crystals is BaF_2. Such crystals give rise to very short subnanosecond luminescence decays, which can be of interest for some applications. Unfortunately, the light yield is usually relatively weak because only a small number of excitations created in the crystal are useful for producing cross luminescence. To describe the relaxation of excitations, it is therefore necessary to involve the uppermost core band in the scheme [1].

3. LIMITING FACTORS AT EACH STEP OF THE ENERGY RELAXATION

It is well known that the scintillation efficiency η can be described as the product of three terms, each one representing a step in the energy relaxation:

$$\eta = N_{\mathrm{eh}} S Q, \qquad (1)$$

where N_{eh} is the conversion efficiency (number of electron–hole (*e*–*h*) pairs or excitons), S is the probability of transfer to emitting centers, and Q is the luminescence quantum yield.

3.1. First Step: Creation of Electronic Excitations

The number of *e*–*h* pairs can be written as

$$N_{\mathrm{eh}} = E_{\mathrm{inc}}/E_{\mathrm{eh}},$$

where E_{inc} is the energy deposited by an ionizing particle and E_{eh} is the average energy required for the creation of a thermalized *e*–*h* pair.

A general accepted estimation of E_{eh} is around (2–3)E_g (E_g is the forbidden energy band gap) for the simple case presented in Fig. 1 [2, 3]. So, E_g is a limiting factor for the production of *e*–*h* pairs and excitons.

However, N_{eh} is a relevant factor only in the case of a simple insulator for which thermalized electrons and holes are the only types of electronic excitations and E_g is the only parameter characterizing the conversion efficiency. We have seen that this is not the case for scintillators with a core-valence transition. For example, in BaF_2, the relevant factor is not N_{eh} but the number of uppermost Ba^{2+} 2*p* core holes. In the case of cerium compounds, for example CeF_3, two types of excitons coexist: Ce Frenkel and anion Wannier excitons. It was shown that cerium excitation is not efficient, either through energy transfer from an anion exciton [4, 5] or through sequential capture of holes [6]. Useful excitations can be produced efficiently only through impact excitation and, as indicated in Fig. 2, by electrons with kinetic energies in a narrow band between the two thresholds of *e*–*e* scattering and of *e*–RE scattering. As

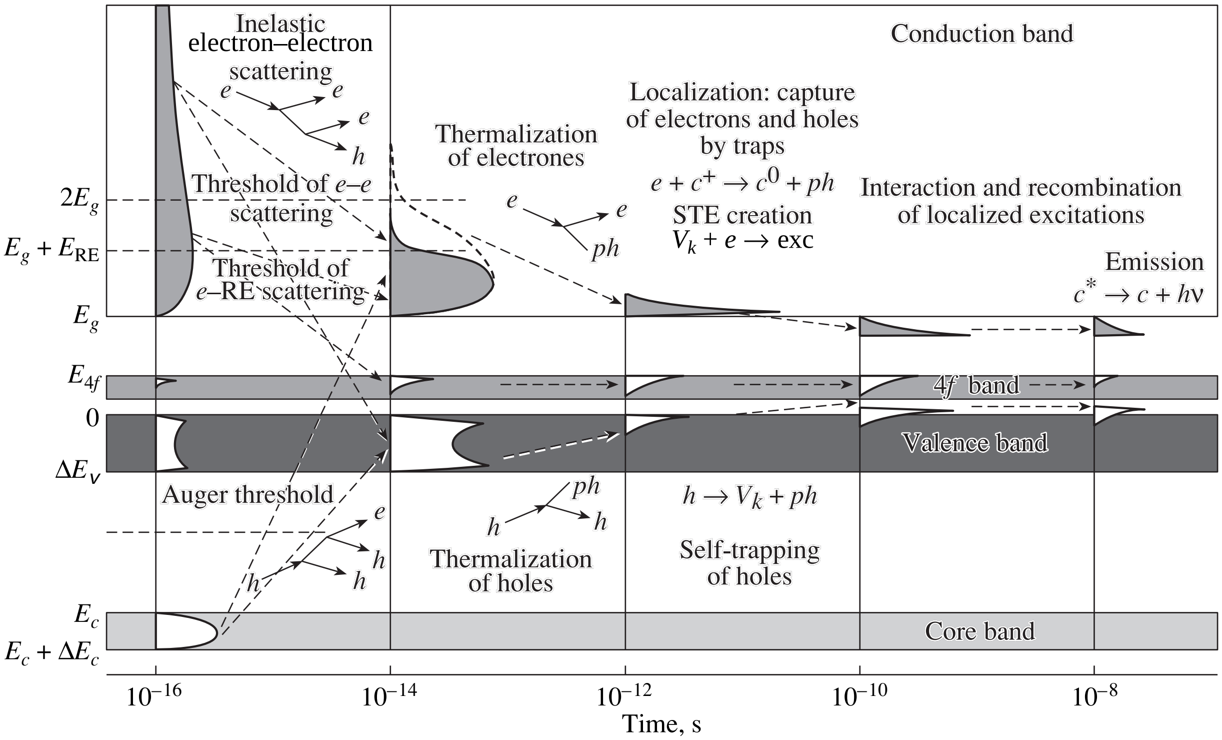

Fig. 2. Relaxation of electronic excitations in rare-earth-containing crystals.

a result, the number of useful excitations is reduced by a factor of around 5 in CeF_3, which explains its relatively low light yield.

3.2. Second Step: Transfer to Luminescence Centers

This is a very critical part of the scintillation mechanism.

For high light yield scintillators, the transfer to luminescence centers occurs essentially through the sequential capture of charge carriers. This is, for example, the case for Na- and Tl-doped CsI. In the case of Ce^{3+}-doped or -based crystals, a limiting factor is the energy difference ΔE between the Ce4*f* level in the forbidden bandgap and the top of the valence band. In oxides and halides, ΔE is weak and the cross section for hole capture may be high. In fluorides, ΔE is large and the hole capture probability is never high [6].

Impurity ions can compete with active ions for the capture of charge carriers and/or interact with them and can therefore induce severe limitations in the scintillation efficiency. For example, in cerium-doped or cerium-based crystals, in general, the presence of metal ions M^{n+} with two or more stable valence states is harmful. Charge transfer may occur between M^{n+} and Ce^{3+} according to the following process: $(Ce^{3+}, M^{n+}) \longrightarrow (Ce^{4+}, M^{(n-1)+})$. Furthermore, M^{n+} ions may act as traps for charge carriers. It is known that the presence, along with Ce^{3+}, of ions like Yb^{3+}, Eu^{3+}, W^{6+}, and V^{5+} most often kill the Ce^{3+} fluorescence. It was shown that the presence of Ir^{4+} in $Lu_2Si_2O_7 : Ce^{3+}$ strongly quenches the scintillation of this crystal [7]. The coexistence of Ce^{4+} with Ce^{3+} is harmful as well because Ce^{4+} is an efficient electron trap and does not lead to charge transfer luminescence.

Self-trapping can strongly influence the efficiency and the time-dependence of the scintillation, in particular, the creation of self-trapping holes (V_k centers) and self-trapped excitons (STE). Energy transfer is very fast through direct correlated *e*–*h* capture, while it is fast through binary *e*–*h* recombination $V_k + e^-$ on the scintillation center and much longer through STE diffusion.

Trapping effects on the scintillation may be very spectacular. This is the case in YAG : Yb^{3+}, in which the charge transfer luminescence is strongly quenched at low temperature where glow peaks arise reflecting the presence of traps. At the temperature of these peaks, a long component in the fluorescence decay profiles is observed due to detrapping and retrapping processes [8].

Closely spaced electronic excitations can be formed in an insulator after high-energy excitation [9, 10]. This is due to the fact that the mobility of holes is much smaller than the mobility of electrons. The formation of a cluster of electronic excitations is illustrated in Fig. 3. Interactions between closely spaced electronic excitations may lead to a substantial decrease in the number of correlated and noncorrelated *e*–*h* pairs and consequently of the light yield of the scintillator. For exam-

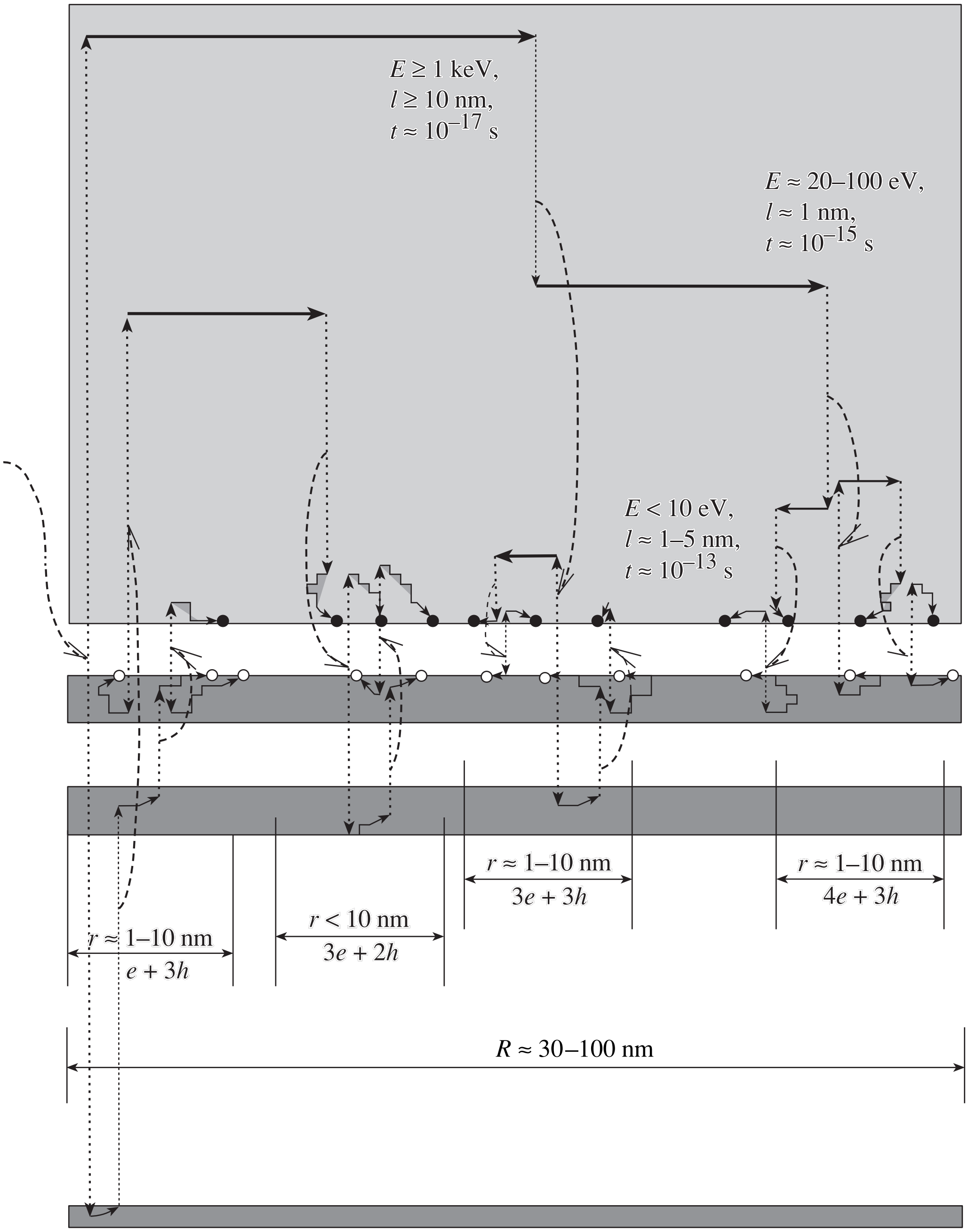

Fig. 3. Clusters of closely spaced electronic excitations created in an insulating crystal after excitation by a high energy particle.

ple, an exciton may disappear after interaction with a close low-energy electron or hole; a core hole may interact with a low energy electron or a valence band hole and no more excitations are created [10].

3.3. Third Step: Emission of Scintillation Centers

Many processes may limit the luminescence efficiency, and most of them are well known: (i) electron–phonon coupling resulting in competition between radiative and nonradiative transitions, (ii) concentration quenching due to interaction between luminescence centers, (iii) reabsorption process where the luminescence traveling through the scintillator can be reabsorbed either by identical or by unlike centers, and (iv) photo- and thermal-ionization quenching processes.

These latter processes can be illustrated through two examples.

3.3.1. Electron ionization in cerium-doped crystals. The location of the lowest 5d emitting state may be close or degenerated in the conduction band. It was

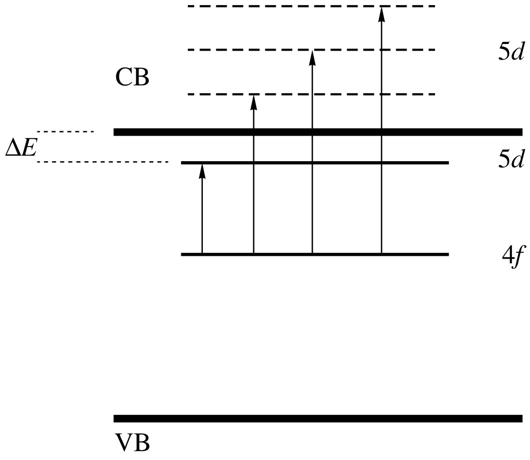

Fig. 4. Thermostimulated ionization process in cerium-doped crystals.

demonstrated that the autoionization rate from a 5*d* state is large in many cases [11–13] and the delocalization of the electron may lead to quenching of the luminescence. The photoionization process is an important limiting factor for the light yield.

When all the 5*d* states are degenerated in the conduction band (the case of Ce-doped sesquioxides La_2O_3, Y_2O_3, Lu_2O_3), the onset of the room-temperature and liquid-nitrogen-temperature photoconductivity coincides with the onset of the lowest absorption band and the cerium emission is totally quenched [14].

When the lowest 5*d* state is close to the conduction band, thermal quenching is governed mainly by thermostimulated ionization (Fig. 4). For a Ce-doped Lu_2SiO_5 scintillator, ΔE is a few tenths of an electron-volt and efficient emission is observed even at room temperature. However, the light yield strongly decreases for T above room temperature. For Ge-doped LaI_3, $\Delta E < 0.1$ eV and no emission is detected at room temperature; efficient emission is only detected at $T <$ 100 K [15].

Of course, when the lowest 5*d* state is well below the conduction band, the photoionization process does not occur. This is the case for most Ce-doped fluorides, chlorides, and oxides. Thermal quenching is then governed by nonradiative relaxation to the ground state. High luminescence efficiency can be exhibited at high temperature by some scintillators, such as $LuAlO_3 : Ce^{3+}$ and $Lu_2Si_2O_7 : Ce^{3+}$.

3.3.2. Hole ionization in ytterbium-doped crystals. The temperature dependence of the charge transfer and IR luminescence yield under excitation in the charge transfer (CT) band (Fig. 5a) shows that the feeding of $^2F_{5/2}$ and $^2F_{7/2}$ states through radiative and nonradiative transitions from the CT state (Fig. 5b) can explain both the CT and IR luminescences thermal dependence for $T > 150$ K, but not the behavior of the IR luminescence at lower temperature. Another quenching mechanism must be involved. After taking into account hole ionization with the formation of the CT state after thermal dissociation, a good simulation of the IR luminescence at low temperature is obtained. It seems that the dominant thermal quenching process of CT luminescence in most Yb^{3+}-doped oxide systems could be due to hole thermostimulated ionization from the charge transfer state [16].

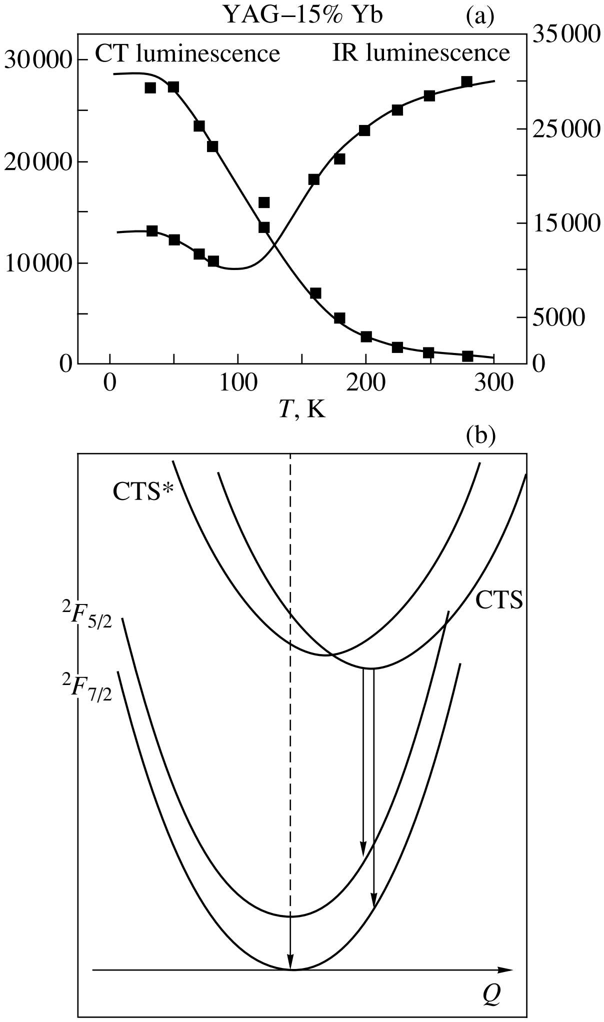

Fig. 5. (a) Temperature dependence of the charge transfer and IR luminescence yield under excitation in the CT state (6.2 eV). (b) CT states and emission transitions.

4. CONCLUSIONS

Scintillation mechanisms are described using simple schemes deduced from appropriate models. Multiplication of electronic excitations is described using kinetic equations. Modeling of energy relaxation is performed using the Monte Carlo technique describing the thermalization, separated diffusion, and spatial correlation of electronic excitations.

It has been shown that a good estimation of the light yield can be obtained provided some considerations are taken into account, such as the fact that created electronic excitations are not all useful excitations in systems with a complicated band structure and clusters of closely spaced electronic excitations can be formed.

Many limiting factors for the light yield and the time dependence of the scintillation must be considered at each stage of the energy relaxation.

REFERENCES

1. A. N. Vasil'ev, in *Proceedings of the 5th International Conference on Inorganic Scinetillators and Their Applications*, Ed. by V. V. Mikhailin (Moscow State Univ., Moscow, 2000), p. 43.
2. W. Shockley, Solid State Electron. **2**, 35 (1961).
3. C. A. Klein, J. Appl. Phys. **39**, 2029 (1968).
4. A. N. Belsky, R. A. Glukhov, P. Martin, V. V. Mikhailin, C. Pédrini, and A. N. Vasil'ev, J. Lumin. **72–74**, 96 (1997).
5. A. N. Belsky, I. A. Kamenskikh, V. V. Mikhailin, C. Pédrini, and A. N. Vasil'ev, Radiat. Eff. Defects Solids **150**, 1 (1999).
6. C. Pédrini, D. Bouttet, C. Dujardin, A. Belsky, and A. Vasil'ev, in *Proceedings of the International Conference on Inorganic Scintillators and Their Applications (SCINT-95)* (Delft Univ. Press, Delft, 1996).
7. L. Pidol, A. Kahn-Harari, B. Viana, F. Ferrand, P. Dorenbos, J. T. M. de Haas, C. W. E. van Eijk, and E. Virey, J. Phys.: Condens. Matter **15**, 2091 (2003).
8. N. Guerassimova, N. Garnier, C. Dujardin, A. G. Petrosyan, and C. Pédrini, Chem. Phys. Lett. **339**, 197 (2001).
9. C. Pédrini, A. N. Belsky, A. N. Vasil'ev, D. Bouttet, C. Dujardin, B. Moine, P. Martin, and M. J. Weber, Mater. Res. Soc. Symp. Proc. **348**, 225 (1994).
10. A. N. Belsky, R. A. Glukhov, I. A. Kamenskikh, P. Martin, V. V. Mikhailin, I. H. Munro, C. Pédrini, D. A. Shaw, I. N. Shpinkov, and A. N. Vasil'ev, J. Electron Spectrosc. Relat. Phenom. **79**, 147 (1996).
11. R. Fuller and D. S. McClure, J. Lumin. **38**, 193 (1987).
12. C. Dujardin, B. Moine, and C. Pédrini, J. Lumin. **53**, 444 (1992).
13. C. Dujardin, B. Moine, and C. Pédrini, J. Lumin. **54**, 259 (1993).
14. W. M. Yen, M. Raukas, S. A. Basun, W. van Schaik, and U. Happek, J. Lumin. **69**, 287 (1996).
15. Bessiére, P. Dorenbos, C. W. E. van Eijk, K. W. Krämer, H. U. Gädal, C. de Mello Donega, and A. Meijerink, Nucl. Instrum. Methods B (in press).
16. C. Pédrini, Phys. Status Solidi C (in press).

Physics of the Solid State, Vol. 47, No. 8, 2005, pp. 1412–1415. Translated from Fizika Tverdogo Tela, Vol. 47, No. 8, 2005, pp. 1364–1367.
Original Russian Text Copyright © 2005 by Shul'gin, Petrov, Pustovarov, Arbuzov, Raĭkov, Ivanovskikh, Ishchenko.

PROCEEDINGS OF THE XII FEOFILOV WORKSHOP "SPECTROSCOPY OF CRYSTALS ACTIVATED BY RARE-EARTH AND TRANSITION-METAL IONS"

(Yekaterinburg, Russia, September 22–25, 2004)

Scintillation Neutron Detectors Based on ^{6}Li-Silica Glass Doped with Cerium

B. V. Shul'gin*, V. L. Petrov*, V. A. Pustovarov*, V. I. Arbuzov, D. V. Raĭkov*, K. V. Ivanovskikh*, and A. V. Ishchenko***

**Ural State Technical University, ul. Mira 19, Yekaterinburg, 620002 Russia*
e-mail: rdv@dpt.ustu.ru
***Vavilov State Optical Institute, Birzhevaya liniya 12, St. Petersburg, 193171 Russia*

Abstract—The photoluminescence (PL), PL excitation, and PL decay kinetics of $^6Li_2O–MgO–SiO_2–Ce$ glasses were studied using time-resolved VUV spectroscopy. The Ce^{3+} ion PL excitation spectrum contains a known group of structural bands at 4.4–5.2 eV caused by $4f \longrightarrow 5d$ transitions. Moreover, features at 6.4–7.7 eV were detected and their nature is discussed. At an exciting photon energy $E_{exc} > 25$ eV, the photon multiplication effect manifests itself. Based on ^{6}Li-silica glasses, a scintillation neutron detector with improved parameters was developed and produced. *© 2005 Pleiades Publishing, Inc.*

1. INTRODUCTION

Neutron radiation detection remains an important problem in radiation monitoring. To solve this problem, there has been a search for low-cost glass-based scintillation detectors. While zirconium silicate– and beryllium phosphate–based glasses developed at the Ural State Technical University (USTU) [1, 2] exhibit increased radiation resistance and light yield, their manufacturability leaves much to be desired. Glasses that are more manufacturable have been developed at the Vavilov State Optical Institute [3] on the basis of cerium-doped lithium silica. These glasses have a better sensitivity to neutrons. At a Li_2O content of 22.5 mol %, the glass light yield has a radioluminescence spectrum maximum at 3.2 eV and exceeds that of NE-905 glasses (currently accepted as the most appropriate scintillators) by a factor of 1.8 [3]. Thermal neutrons are detected by the reaction $^6Li_3(n, \alpha)^3H_1$. The reaction products (alpha particles) cause 60-ns scintillations in glass. Despite the fact that certain spectral and kinetic performance parameters of cerium-doped lithium-silica glasses as scintillators have been studied previously [3], their basic properties in the expanded VUV spectral range have not yet been studied. It also seems expedient to study the neutron detection efficiency of these glasses and use them to develop scintillation neutron detectors with an increased efficiency.

2. EXPERIMENTAL

$Li_2O–MgO–SiO_2–Ce$ glasses prepared at the Vavilov Institute contain 0.8 mol % Ce (calculated for CeO_2) and 22.5 to 30 mol % Li (in the form of Li_2O). The glass melting point is 1500°C, the density is 2.52 g/cm^3, the refractive index is 1.55, and the ^{6}Li isotope concentration is as high as 1.15×10^{22} cm^{-3}. The samples under study were prepared as $10 \times 10 \times 1$ mm plates.

The Photoluminescence (PL) and PL excitation spectra were measured at temperatures of 295 and 9–10 K at the SUPERLUMI station (HASYLAB Laboratory, DESY, Hamburg) using synchrotron radiation (SR). A 2-m vacuum monochromator with replaceable Al or Pt gratings was used to excite PL in the range 3.7–33 eV. The PL excitation spectra were normalized to a fixed number of photons incident on a sample. The PL spectra were analyzed using a 0.3-m ARC Spectra Pro-308i monochromator and an R6358P photomultiplier tube. The PL and PL excitation spectra were measured for time-integrated luminescence and for luminescence that was detected in gated time windows (of width Δt) correlated with respect to an exciting SR pulse (the delay from the SR pulse start is δ_t). Reasoning from the decay kinetics, the parameters δ_t and Δt were set as 2.3 and 22 ns for the fast PL component and 72 and 104 ns for the slow PL component, respectively. The neutron detection efficiency was measured (at USTU) using a stand with a ^{252}Cf neutron source certified for measurements.

3. RESULTS AND DISCUSSION

Figure 1 shows the time-resolved PL spectra measured for an excitation energy $E_{exc} = 4.7$ eV at $T = 9$ K. The fast-component spectrum characterizing the Ce^{3+} ion luminescence is an asymmetric band (as is also the case at $T = 295$ K) with a maximum at $h\nu_{lum} = 3.2$ eV (FWHM = 0.5 eV) caused by interconfigurational transitions from the lowest level of the 5*d* shell to the 4*f*-configuration ground-state levels. The shape of the PL spectra is independent of the excitation photon energy in the range 3.7–33 eV, and the PL yield is almost independent of temperature. We note that the luminescence spectra of these glasses excited by 3-MeV He^+ ion beams or 150-keV electron beams are identical to the PL spectra.

Figure 2 shows time-resolved 3.2-eV PL excitation spectra. The fast PL component is efficiently excited in the glass transmission band, where a structured broad band at 3.7–8.5 eV is observed in the PL excitation spectrum. This band has a feature near 6.9 eV that is most pronounced at low temperatures. Almost no luminescence is excited in the range of interband transitions (E_{exc} = 9–22 eV). The cause of this is a significant nonradiative energy loss at the sample surface, as is the case for many dielectrics with mobile electronic excitations. Photon multiplication begins at energies exceeding 25 eV and manifests itself as an increase in the Ce^{3+} PL yield.

Figure 3 shows the 3.2-eV PL decay kinetics of glass at various values of E_{exc}. The PL was established to decay exponentially with a time constant $\tau = 37.5$ ns under excitation immediately in the impurity absorption band, i.e., at E_{exc} = 4–6 eV. Under excitation in the region of the fundamental absorption edge, the PL kinetics exhibits a microsecond-range component. Under excitation in the photon multiplication region (E_{exc} > 25–33 eV), the decay time decreases and the kinetics becomes noticeably nonexponential ($\Delta_{1/2}$ = 20.8 ns).

An analysis of the Ce^{3+} PL excitation spectra and a comparison with the data on the spectrum of the free Ce^{3+} ion show that there are two groups of structural bands: one at 3.7–5.2 eV and one at 6.4–7.7 eV. The former band is caused by interconfigurational 4*f* ⟶ 5*d* transitions, and the latter can be associated either with transitions to higher energy states of the 5*d* shell or with transitions to the states of the empty 6*s* shell. The band in the PL excitation spectra caused by 4*f* ⟶ 6*s* transitions in Ce^{3+} ions (in the LaF_3 lattice) was interpreted for the first time by Pedrini, Belsky, and coworkers [4–6]; this band was detected at ~7.7 eV. For the glass under study, this excitation band is observed in the range 6.4–7.7 eV, which does not contradict the data from [4–7].

In [5], a model of configuration curves of the Ce^{3+} ion in crystals was proposed (Fig. 4a). With a certain modification, this model can be used to explain the PL spectrum of Ce^{3+} ions in the glasses under study (Fig. 4b). This model takes into account the Ce^{3+} recharging effect [8], as well as the charge-transfer and photoionization effects in the crystals considered in [5].

Thus, the photo- and radioluminescence spectra of Li_2O–MgO–SiO_2–Ce glasses reveal a common luminescence center associated with the Ce^{3+} ion. In [8], it was shown that, in glasses with Ce^{3+} ions, ionizing radi-

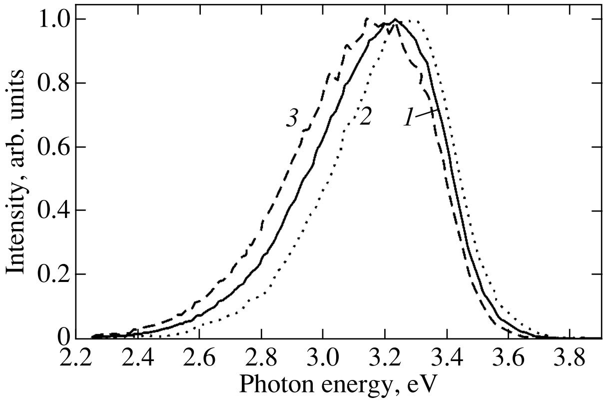

Fig. 1. PL spectra of a Li_2O–MgO–SiO_2–Ce glass at T = 9 K. (*1*) Time-integrated spectrum and (*2*) the fast and (*3*) slow components.

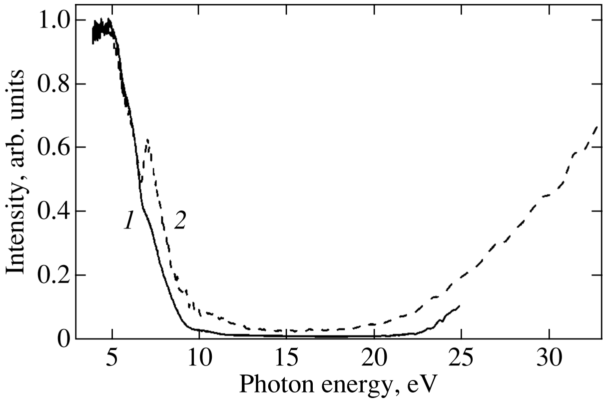

Fig. 2. Time-resolved excitation spectrum of the fast PL component (at 3.2 eV) of a Li_2O–MgO–SiO_2–Ce glass measured at (*1*) 295 and (*2*) 9 K.

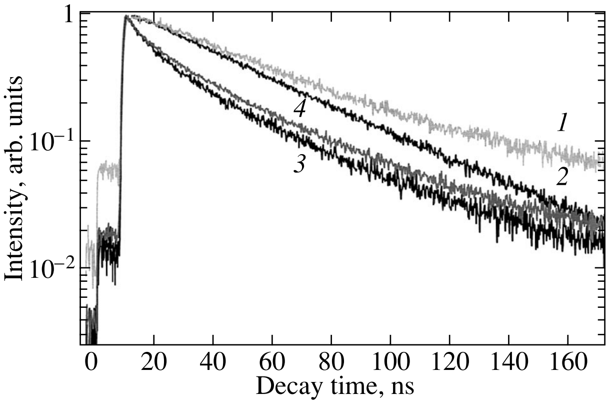

Fig. 3. Decay kinetics of 3.2-eV PL in a Li_2O–MgO–SiO_2–Ce glass at excitation photon energies of (*1*) 7.8, (*2*) 5.0, (*3*) 13.8, and (*4*) 31.0 eV; T = 9 K.

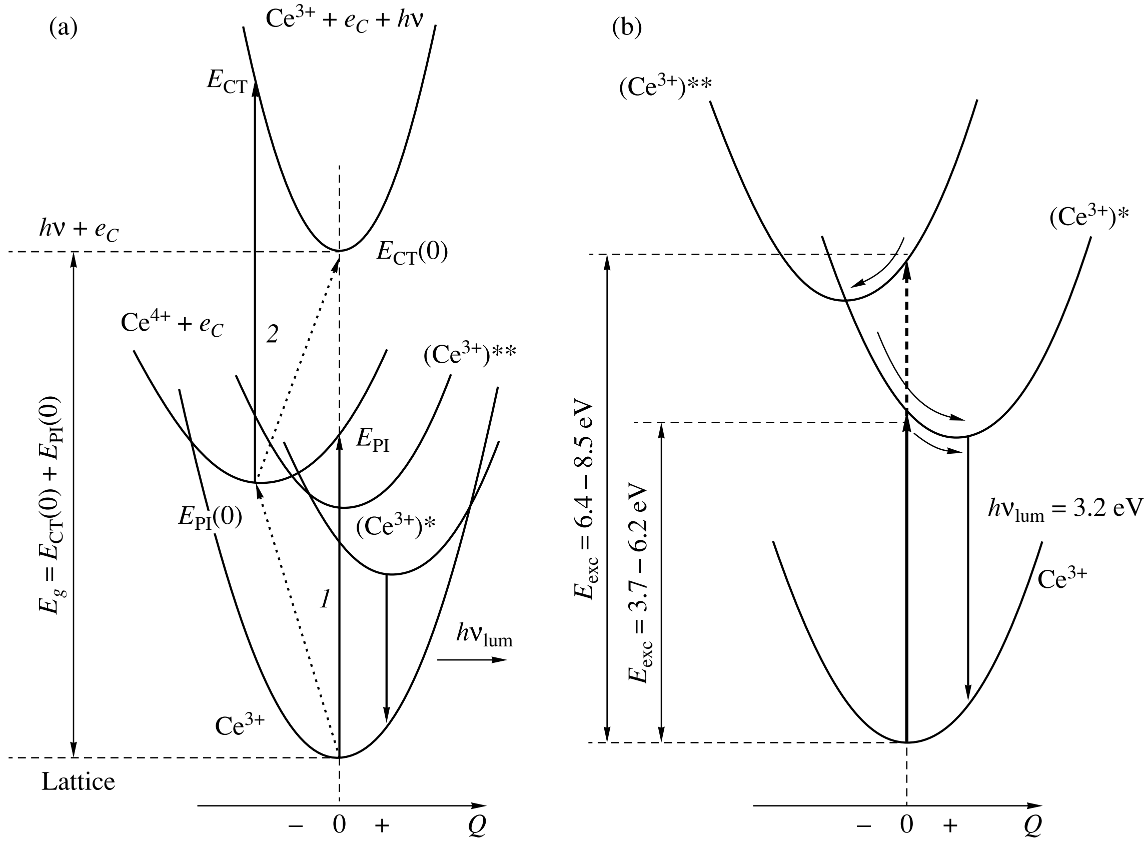

Fig. 4. Models of configuration curves of the Ce^{3+} ion (a) in crystals [5, 6] and (b) in a Li_2O–MgO–SiO_2–Ce glass.

ation causes recharging and the onset of recombination luminescence with a spectrum typical of the Ce^{3+} ion. Under ionizing radiation, which generates separate electron–hole pairs in glasses, the Ce^{3+} recharging can occur in the following sequence: $Ce^{3+} + h^+ \longrightarrow Ce^{4+}$, $Ce^{4+} + e^- \longrightarrow (Ce^{3+})^*$, and $(Ce^{3+})^* \longrightarrow Ce^{3+} + h\nu_{lum}$ [6]. The above data on the luminescence excitation spectra of the glasses under study in a wide energy range, as well as the data on ion-beam-induced and cathodoluminescence, show that only the kinetics of radiation-induced recharging of an activator and the recombination luminescence kinetics depend on the nature of the luminescence excitation. This finding explains the difference in duration between neutron scintillations (in fact, α scintillations, $\tau \cong 60$ ns) and scintillations caused, e.g., by an electron beam ($\tau \cong 108$ ns). The final step of intracenter luminescence is almost the same for any type of excitation. The decrease in the decay time observed both in α scintillations and under photoexcitation in the fundamental absorption range is caused by a high local excitation density. These effects have been observed and studied for some inorganic scintillators [9].

Studying the PL, PL decay kinetics, and radioluminescence made it possible to develop efficient scintillation media based on ^{6}Li silica glasses and create a neutron detector. The scintillation glass in the detector is 38 mm in diameter and 5-mm thick. The main performance parameter of the scintillation detector—the neutron detection efficiency (sensitivity)—was determined, using the technique proposed in [10], to be 12.3 cm^2/neutron. Testing of the device using a ^{252}Cf neutron source (fission neutrons) showed that the efficiency of the developed scintillation detector exceeds that of MKS-A02 commercial neutron detectors based on ^{3}He counters.

4. CONCLUSIONS

The luminescence properties of Ce^{3+}-doped ^{6}Li silica glasses have been studied using time-resolved VUV spectroscopy. An analysis of the results has demonstrated the crucial role of the intracenter transitions in the complex scintillation process. The strongest luminescence excitation band of cerium ions in the glasses under consideration in the range 3.7–6.2 eV is associated with the $4f \longrightarrow 5d$ transitions. The band observed at 6.4–7.7 eV can be associated with the transitions both to high-energy states of the 5*d* shell and to the 6*s* shell. This finding made it possible to improve the model of configuration curves for Ce^{3+} ions in glasses with inclusion of charge transfer and photoionization. By analyzing the PL excitation spectra in a wide energy range, the photon multiplication effect has been found to occur at $E_{\text{exc}} > 25$ eV. Therefore, these glasses can be applied as an efficient scintillation material. Based on the glasses under study and using their basic properties, a scintillation neutron detector with improved performance parameters has been developed and tested.

ACKNOWLEDGMENTS

This study was supported by the Russian Foundation for Basic Research (project no. 02-02-16322), the Ural Science and Education Center (program “Promising Materials”), and CRDF (grant REC-005 EK-005-X1).

REFERENCES

1. B. V. Shul’gin, A. L. Shalyapin, F. F. Gavrilov, V. G. Chukhlantsev, and N. I. Kordyukov, Zh. Prikl. Spektrosk. **14**, 89 (1971).
2. I. A. Dmitriev, A. F. Zatsepin, A. L. Shalyapin, and B. V. Shul’gin, Steklo SSSR, No. 463641 (1975).
3. V. I. Arbuzov, N. Z. Andreeva, V. A. Vitenko, and M. A. Milovidov, Radiat. Meas. **25** (1–4), 475 (1995).
4. C. Pedrini, C. Dujardin, J. C. Gacon, A. N. Belsky, A. N. Vasiliev, and A. G. Petrosyan, Radiat. Eff. Defects Solids **154**, 277 (2001).
5. C. Pedrini, C. Dujardin, and N. Garnier, in *Problems in Spectroscopy and Spectrometry* (Ukr. Gos. Tech. Univ., Yekaterinburg, 2002), Vol. 11, p. 3 [in Russian].
6. A. N. Belsky and J. C. Krupa, Displays **19**, 185 (1999).
7. P. A. Rodnyĭ and D. M. Seliverstov, Preprint No. 1886 (Peterb. Inst. Yad. Fiz., Gatchina, 1993).
8. B. I. Arbuzov and M. N. Tolstoĭ, Fiz. Khim. Stekla **14** (1), 3 (1988).
9. V. A. Pustovarov, A. L. Krymov, and E. I. Zinin, Nucl. Instrum. Methods Phys. Res. A **359**, 336 (1995).
10. *Neutron Radiometers: Methods and Control Facilities*, GOST (Standart) No. 8.355-79.

Translated by A. Kazantsev

Physics of the Solid State, Vol. 47, No. 8, 2005, pp. 1416–1424. From Fizika Tverdogo Tela, Vol. 47, No. 8, 2005, pp. 1368–1375.
Original English Text Copyright © 2005 by Kirm, Makhov, True, Vielhauer, Zimmerer.

PROCEEDINGS OF THE XII FEOFILOV WORKSHOP “SPECTROSCOPY OF CRYSTALS ACTIVATED BY RARE-EARTH AND TRANSITION-METAL IONS”

(Yekaterinburg, Russia, September 22–25, 2004)

VUV-Luminescence and Excitation Spectra of the Heavy Trivalent Rare-Earth Ions in Fluoride Matrices[1]

M. Kirm[1, 2], V. N. Makhov[3], M. True[1], S. Vielhauer[1], and G. Zimmerer[1]
[1] *Institut für Experimentalphysik, University of Hamburg, Hamburg, D-22761 Germany*
e-mail: georg.zimmerer@desy.de
[2] *Institute of Physics, University of Tartu, Tartu, 51014 Estonia*
[3] *Lebedev Physical Institute, Russian Academy of Sciences, Moscow, 119991 Russia*

Abstract—VUV $4f^n \longrightarrow 4f^{n-1}5d$ transitions of Gd^{3+}, Er^{3+}, Tm^{3+}, and Lu^{3+} in fluoride matrices have been analyzed with high-resolution luminescence and excitation spectroscopy. In trifluorides, strong electron–phonon coupling has been found. In the other matrices, the luminescence spectra clearly yield zero-phonon lines and phonon replica, indicating intermediate coupling. The energies of the zero-phonon lines observed are compared with theoretical predictions. Near the threshold of $f \longrightarrow d$ excitations, some of the excitation spectra yield sharp structures which cannot be explained with phonon replica but will be discussed in terms of the energy levels of the $4f^{n-1}5d$ configuration. *© 2005 Pleiades Publishing, Inc.*

1. INTRODUCTION

Already as of 1966, $4f^n \longrightarrow 4f^{n-1}5d$ transitions of trivalent rare-earth (RE^{3+}) ions in a CaF_2 matrix had been reported [1]. Except for Ce^{3+} and Pr^{3+}, the transition energies are in the vacuum ultraviolet (VUV) range. In the past, the VUV $4f^n \longrightarrow 4f^{n-1}5d$ transitions have not attract as much attention as the $4f^n \longrightarrow 4f^{n-1}4f^*$ transitions because no application was forseeable. In recent years, however, $4f^n \longrightarrow 4f^{n-1}5d$ transitions gained much interest, being an essential aspect of quantum cutting phosphors [2].

Concerning the experimental difficulties in VUV spectroscopy, the pioneering work of Yen *et al.* [3] demonstrated the potential of synchrotron radiation (SR) for luminescence experiments. It was applied for the first time to RE^{3+} $4f^n \longrightarrow 4f^{n-1}5d$ excitations by Elias *et al.* and Heaps *et al.* [4, 5]. The first $4f^{n-1}5d \longrightarrow 4f^n$ VUV luminescence spectra of Nd^{3+}, Er^{3+}, and Tm^{3+} were published by Yang and DeLuca [6]. For the first half of the lanthanide series, transitions from the lowest $4f^{n-1}5d$ level into the $4f^n$ ground state are spin-allowed with short lifetimes (up to ≈50 ns). In the second half, such transitions are spin-forbidden (lifetimes in the microsecond range). Depending on the ion and the host, spin-forbidden emission from the lowest high-spin and spin-allowed emission from the lowest low-spin $4f^{n-1}5d$ state coexist [2, 7]. In the past, VUV RE^{3+} emission has been detected only from Nd^{3+}, Er^{3+}, and Tm^{3+} [2, 7–10].

RE^{3+} $4f^{n-1}4f^*$ excitations couple weakly to the lattice because the $4f$ wave functions are shielded by the filled $5s$ and $5p$ shells. The $5d$ wave functions are more extended. Therefore, $4f^{n-1}5d$ excitations are expected to interact stronger with the lattice. The VUV $d \longrightarrow f$ emission bands observed in the past were broad, nearly Gaussian shaped, indicating at first sight strong coupling. However, already Schlesinger and Szczurek [11] observed zero-phonon lines (ZPLs) in $f \longrightarrow d$ absorption spectra. Wegh *et al.* [2] also found ZPLs in luminescence excitation spectra and pointed out that the smooth shape of the emission bands originates from a rather poor spectral resolution. SR-excited experiments recording high-resolution spectra were lacking until recently [12]. In the meantime, laser-excited spectra have also been reported [13, 14]. In the present paper, high-resolution spectra of $d \longrightarrow f$ luminescence of Er^{3+} [12] and Tm^{3+} [14] will be discussed. The first $d \longrightarrow f$ spectra of Gd^{3+} and Lu^{3+} [15] will also be presented. Gd^{3+} is of particular interest because Gd^{3+} $d \longrightarrow f$ emission was not expected at all for the reasons given below. The sample include RE^{3+} doped fluorides and stoichiometric fluorides. Strong and intermediate coupling was established. The results agree well with predictions based on papers by Dorenbos [16, 17].

2. EXPERIMENT

Most of the experiments were performed under selective SR excitation at the SUPERLUMI setup at HASYLAB (Hamburg) [18]. The resolution intervals in excitation $\Delta\lambda_{ex}$ were chosen between 3 and 0.5 Å. The

---

[1] This article was submitted by the authors in English.

time structure of SR with its short pulses (width 150 ps) at a repetition rate between 1 and 5 MHz is the basis of time-resolved spectroscopic methods [19]. High-resolution VUV-luminescence analysis was performed with a 1-m monochromator equipped with a position-sensitive channel-plate detector. Most spectra were recorded in first order with $\Delta\lambda_{em} \approx 1$ Å. In some cases, luminescence analysis was carried out in second order ($\Delta\lambda_{em} \approx 0.5$ Å). In most of the experiments, the temperature was near LHe temperature (7–10 K).

For excitation spectra of VUV luminescence, the Pouey-type VUV monochromator of SUPERLUMI was used to select the respective emission band. This monochromator has a large *f* number (2.8), at the expense, however, of spectral resolution ($\Delta\lambda_{em} = 10$–20 Å). Therefore, in the spectral range of ZPLs, scattered light from excitation falsifies the spectra. In the case of spin-forbidden $d \longrightarrow f$ emission with its long lifetime, the spectra can be measured in the time-resolved mode, with the emission recorded within a time window avoiding any contribution from the (prompt) scattered light of excitation. Spin-allowed emission, however, strongly overlaps in time with the scattered light. Therefore, discrimination between both contributions is difficult. Some experiments were performed under soft x-ray excitation at the undulator beamline BW3 of HASYLAB, where luminescence was analyzed with $\Delta\lambda_{em} = 6$ Å.

Tm^{3+} doped crystals have also been investigated under F_2-laser excitation (157.6 nm/63452 cm^{-1}) at the University of Utrecht [14]. The spectra yield an excellent signal-to-noise ratio. The spectral resolution of $f \longrightarrow f$ spectra under laser excitation exceeds the one available at the SUPERLUMI station at least by a factor of 2. In the VUV, a comparable resolution is achieved at both setups. Laser excitation is superior to SR excitation in those cases where the excitation wavelength fits the requirements. However, VUV-excitation spectra, which presently can be measured only with SR, are of similar importance. Both excitation sources are complementary and should be used in parallel for the spectroscopy of RE^{3+} VUV $d \longrightarrow f$ luminescence.

3. RESULTS AND DISCUSSION

3.1. Er^{3+} $d \longrightarrow f$ Luminescence

$LiYF_4 : Er^{3+}$ was chosen as a model for two reasons: (i) there exists only one site for the RE ion, and (ii) all kinds of Er^{3+} luminescence coexist. Moreover, the Stark splitting of the $4f^{11}$ $^4I_{15/2}$ ground state is known with high accuracy (8 Stark levels) [20, 21]. This is an essential condition for an analysis of the high-resolution spectra. In Fig. 1, the $d \longrightarrow f$ luminescence spectra of $LiYF_4 : Er^{3+}$ (1%) are shown. They yield narrow lines and broad sidebands. For comparison, the excitation spectrum of the spin-forbidden $d \longrightarrow f$ emission is plotted as well. The relative calibration in excitation and in emission is correct within ±0.2 Å (±8 cm^{-1} at 64000 cm^{-1}). The $d \longrightarrow f$ emission is compared with $LiYF_4 : Er^{3+}$ (1%) $^4S_{3/2} \longrightarrow {}^4I_{15/2}$ emission. The bars correspond to an assignment of the $^4S_{3/2}$ emission lines to the Stark levels of the ground state [20, 21]. $^4S_{3/2}$ emission was positioned with respect to the $d \longrightarrow f$ emissions in order to obtain the best agreement with the lines in the $d \longrightarrow f$ spectra.

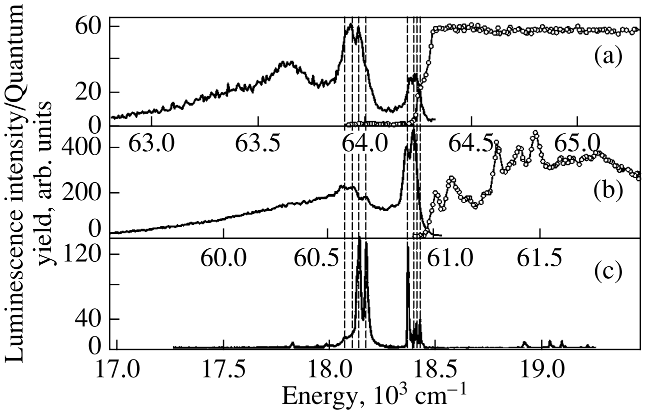

Fig. 1. Spin-allowed (a), spin-forbidden (b), and $^4S_{3/2} \longrightarrow {}^4I_{15/2}Er^{3+}$ $f \longrightarrow f$ luminescence (c) of $LiYF_4 : Er^{3+}$ (1%) at $T = 6$ K. The bars indicate the Stark levels of the $^4I_{15/2}$ ground state with $2|M_J| = 5, 15, 3, 1, 9, 7, 11, 13$ [21] (from right to left). The resolution intervals are $\Delta\lambda_{ex} = 0.6$ Å and $\Delta\lambda_{em} = 0.6$ Å.

As the emission and excitation spectra are in scale, we are able to compare the sharp structures with the bars. In the spin-allowed case, the Stark level $2|M_J| = 5$ (the only one being populated at liquid-helium temperature!) agrees with the shoulder at the low-energy onset of excitation (64 265 cm^{-1}). This shoulder is ascribed to the ZPL in excitation, being strongly suppressed by reabsorption. In emission, the respective ZPL is also indicated by a shoulder. The sharp structures at lower energy correspond to bars indicating the Stark levels of the ground state. They are ascribed to ZPLs as well. In the spin-forbidden case, the bar $2|M_J| = 5$ is energetically below the first maximum of the excitation spectrum at 61013 cm^{-1}. Provided this maximum arises from the ZPL in excitation, there is a shift of the order of 60 cm^{-1} between excitation and emission, indicating an emission originating from disturbed centers. In the spin-forbidden case, not all lines are resolved. This may indicate a variety of disturbed centers.

Phonon sidebands are not clearly resolved. As an estimate of the effective phonon energy, $\omega_{eff} = 330$ cm^{-1} measured by Renfro *et al.* [22] for the coupling of *f* levels to the $LiYF_4$ host may be considered. Then, the first sidebands of the ZPLs with $2|M_J| = 5, 15, 3, 1$ are expected to overlap with the second group of ZPLs. The second group of phonon sidebands of the ZPLs $2|M_J| =$

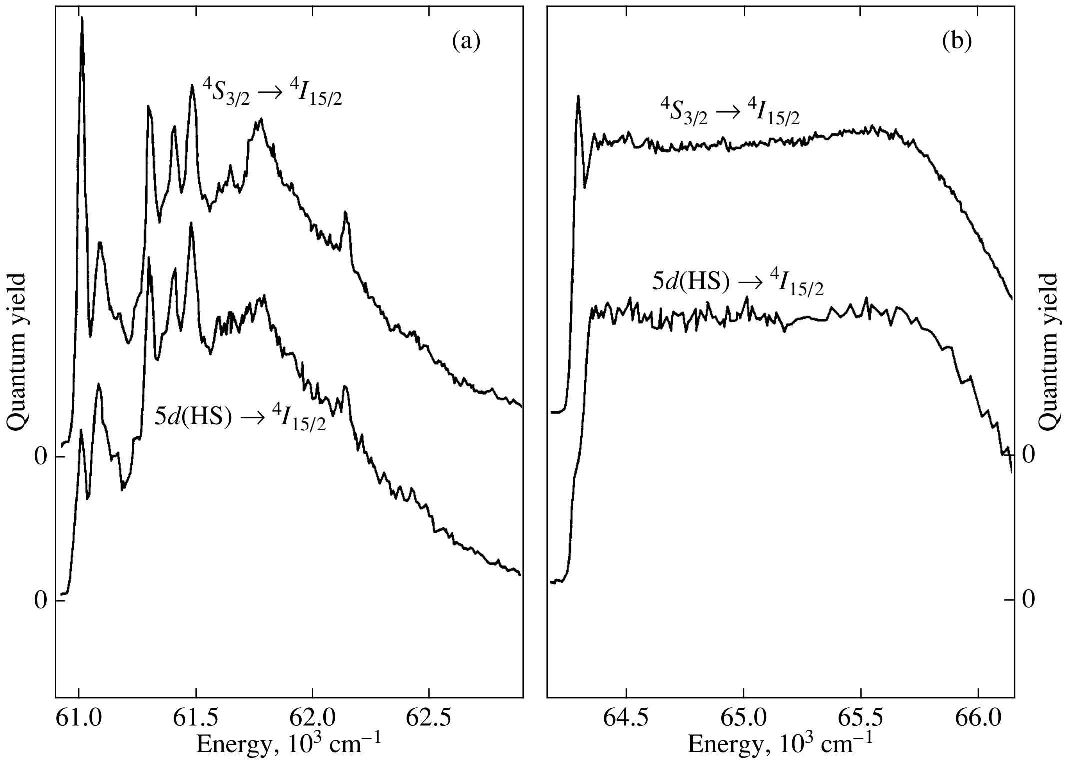

Fig. 2. Excitation spectra of the spin-forbidden LiYF$_4$: Er^{3+} (1%) $d \longrightarrow f$ and $^2S_{3/2} \longrightarrow {}^4I_{15/2}$ emission at the onset of (a) spin-forbidden and (b) spin-allowed $f \longrightarrow d$ excitation. T = 9 K, $\Delta\lambda_{ex}$ = 0.6 Å.

5, 15, 3, 1 would roughly coincide with the first group of sidebands of the ZPLs $2|M_J|$ = 9, 7, 11, 13. This may explain the maximum at 63650 cm^{-1} (spin-allowed) and the shoulder at 60350 cm^{-1} (spin-forbidden).

In Fig. 2, excitation spectra are presented in the range of the lowest spin-forbidden and spin-allowed $f \longrightarrow d$ excitations. An excitation spectrum of $^4S_{3/2} \longrightarrow {}^4I_{15/2}$ emission is included for comparison. In the spin-allowed case, the spectrum has a fast rise (with the shoulder discussed above) to a flat plateau. The plateau arises from total absorption (saturation). In the spin-forbidden case, saturation is not reached but a fine structure is observed. At first sight, it seems straightforward to ascribe the structures to vibronic sidebands. Note, however, that the maxima in the excitation spectrum have no counterpart in the spin-forbidden $d \longrightarrow f$ emission. Therefore, phonon replica cannot account for the fine structure; it originates from a coupling of the d excitations with the f^{10} core of the Er^{3+} ion. Pieterson *et al.* calculated the energy levels of the Er^{3+} $4f^{10}5d$ configuration [23]. In Fig. 2, the respective energy levels are indicated by bars. The height of a bar is a relative measure of the oscillator strength. The numerical values were communicated to us by Meijerink [24].

Concerning the peak positions, good agreement is found between the calculated levels and the maxima of the excitation spectrum. The peaks represent the ZPLs in excitation for the spin-forbidden $4f^{10}5d$ levels. The relative heights, however, are in disagreement with experiment. This is explained as follows. Like in luminescence, each ZPL is accompanied by phonon sidebands, merging together into a background in the excitation spectrum. The spin-forbidden $d \longrightarrow f$ emission of LiYF$_4$: Er^{3+} has also been measured by Peijzel [13] in good agreement with the results of [12].

3.2. *Tm^{3+} $d \longrightarrow f$ Luminescence*

Tm^{3+} $d \longrightarrow f$ emission has been investigated in LiCaAlF$_6$ (Li*CAF*). The choice of Li*CAF* was motivated by the fact that this matrix offers a divalent and a trivalent site, which makes it a promising candidate for codoping with a RE^{3+} and a divalent ion as in Mn^{2+} doped LiSrAlF$_6$ [25]. Figure 3 shows VUV-emission spectra of Li*CAF* : Tm^{3+} (0.04%) with a fine structure, merging into a smooth wide band. At first sight, it may be tempting to ascribe the fine structure to $f \longrightarrow f$ transitions. However, in the respective energy range, the Tm^{3+} ion has no f levels [26]. In particular, the $^1S_0$ level at ~75000 cm^{-1} [26, 27] cannot contribute to the spectra shown (note also that both excitation energies are well below the $^1S_0$ level). At *L*He*T*, the emission has a lifetime τ = 7 μs [14]. Therefore, it is ascribed to the spin-forbidden transition into the $^3H_6$ ground state. Only spin-forbidden $d \longrightarrow f$ emission was observed, whereas other systems also emit spin-allowed luminescence [7, 8]. In view of the low Tm^{3+} concentration, weak spin-allowed $d \longrightarrow f$ luminescence in Li*CAF* cannot be excluded.

Compared to $LiYF_4 : Er^{3+}$, the Tm^{3+} doped system is more complicated. Depending on the symmetry of the site, up to 13 Stark levels can exist for the $^3H_6$ ground state. In order to get more insight into the origin of the fine structure, a spectrum of the $^1G_4 \longrightarrow {}^3H_6$ luminescence around 21000 cm^{-1} was plotted in Fig. 3 for comparison. The scales were arranged such that the sharp lines with the highest energies coincided. True [14] tentatively assigned the sharp structures in the $^1G_4 \longrightarrow {}^3H_6$ spectrum to 12 Stark levels, covering a range of ~400 cm^{-1}. In the context of the present paper, this means that the peaks in the $d \longrightarrow f$ spectra below 61000 cm^{-1} cannot originate from ZPLs; they are ascribed to vibronic sidebands. Only the sharp maxima above ~61000 cm^{-1}, in particular, the one at 61 410 cm^{-1}, originate from ZPLs. The assignment of the peak at 61410 cm^{-1} is further supported by an analysis of the spin-forbidden $d \longrightarrow f$ emission terminating at $^3F_4$ (inset to Fig. 3). Two closely spaced peaks at 55797 and 55766 cm^{-1} were observed, having an energy difference to the first ZPL terminating at $^3H_6$ of 5613 cm^{-1} and 5644 cm^{-1}, respectively. These energies coincide well with the energy of the first excited f state in $LaF_3 : Tm^{3+}$ at 5615 cm^{-1} [26], a value that hardly changes in different matrices. Both peaks may be due to electronic transitions to closely spaced Stark levels of $^3F_4$; however, they can also be due to ZPLs of Tm^{3+} on different occupational sites.

3.3. Gd^{3+} $d \longrightarrow f$ *Luminescence*

The case of Gd^{3+} is of special interest because Gd^{3+} $d \longrightarrow f$ emission was not expected at all due to the fact that the $4f^7$ energy levels are very dense at higher energies [13, 28]. Such a dense level system is an ideal acceptor for energy transfer from d excitations and subsequent nonradiative relaxation into the emitting f levels of Gd^{3+}, thus quenching radiative $d \longrightarrow f$ transitions. Nevertheless, the final answer is given by an experiment. In Fig. 4, VUV-luminescence spectra of Gd^{3+} ions in $LiGdF_4$ and GdF_3 are presented [15]. At $T = 10$ K, the following lifetimes were measured: $\tau = 2.8$ ns ($LiGdF_4$) and $\tau = 0.97$ ns (GdF_3) [15]. The luminescence observed is ascribed to spin-allowed Gd^{3+} $d \longrightarrow f$ emission. The arguments are as follows.

(i) The emission is clearly correlated to Gd^{3+} $4f^7 \longrightarrow 4f^65d$ excitation (see below).

(ii) In the case of GdF_3, in spite of the high spectral resolution, only a broad band is observed which is typical for strong coupling to the lattice, excluding an

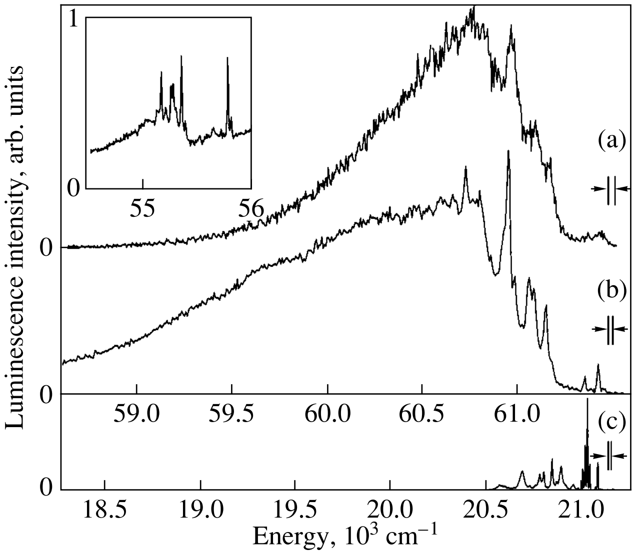

Fig. 3. Spin-forbidden $d \longrightarrow f$ luminescence of Tm^{3+} in $LiCaAlF_6$. (a) SR excitation at 67 659 cm^{-1}, $\Delta\lambda_{em} = 0.8$ Å, and $T = 7.4$ K; (b) laser excitation at 63 452 cm^{-1}, $\Delta\lambda_{em} = 0.3$ Å, and $T = 7.3$ K; and (c) $^1G_4 \longrightarrow {}^3H_6$ luminescence in $LiCaF_6 : Tm^{3+}, Mn^{2+}$; laser excitation like in (b), at $\Delta\lambda_{em} = 0.8$ Å and $T = 7.3$ K.

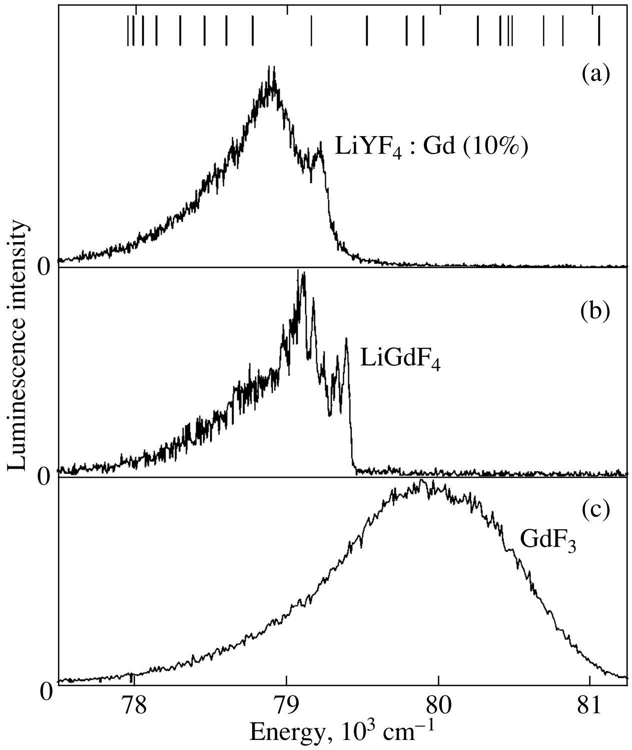

Fig. 4. Gd^{3+} $d \longrightarrow f$ emission of (a) $LiYF_4 : Gd^{3+}$ (10%), (b) $LiGdF_4$, and (c) GdF_3, excited by (a, b) 84 034 and (c) 85470 cm^{-1}. Resolution interval $\Delta\lambda_{em} = 0.8$ Å, $T = 10$ K. Energy levels of the Gd^{3+} $4f^7$ configuration in the range of the onset of $f \longrightarrow d$ excitation [24] are included as bars.

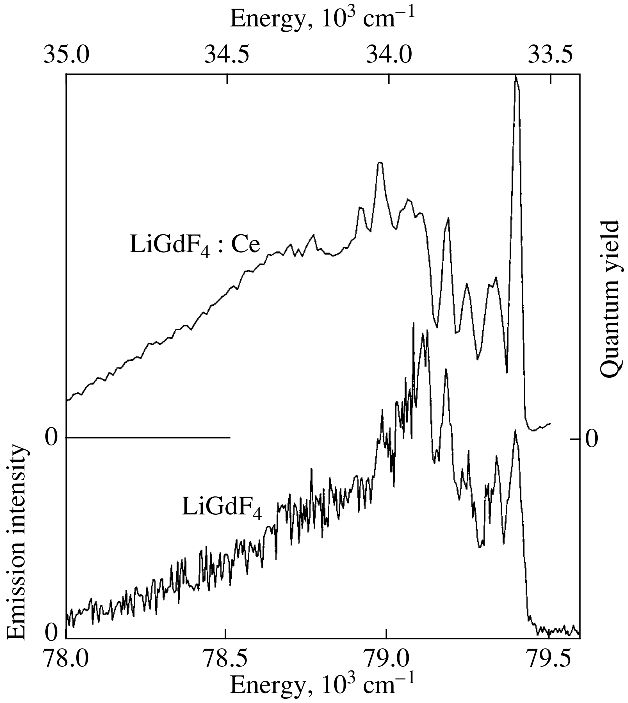

Fig. 5. Comparison of Gd^{3+} $d \longrightarrow f$ luminescence in $LiGdF_4$ (excited at 84034 cm^{-1}, $\Delta\lambda_{em} = 0.8$ Å) with a Ce^{3+} $f \longrightarrow d$ excitation spectrum in $LiGdF_4$: Ce^{3+} (0.05%) measured with $\Delta\lambda_{ex} = 2.9$ Å. For both spectra, $T = 10$ K.

$f \longrightarrow f$ nature of the emission. In the case of $LiGdF_4$, sharp lines and a broad sideband are observed. This is typical for intermediate coupling.

(iii) There is good agreement with an estimate of the transition energies according to the phenomenological approach by Dorenbos [16, 17].

As already mentioned, the Gd^{3+} results are really unexpected. In order to demonstrate why, we included in Fig. 4 recently calculated 4*f* energy levels of the Gd^{3+} ion in LaF_3 which should be a good approximation to the case of $LiYF_4$: Gd^{3+} [24]. The levels are all doublet or quartet levels, whereas the emitting *d* level is an octet level. Therefore, nonradiative transitions from the emitting *d* level to these high-lying *f* levels are highly spin-forbidden. This may qualitatively explain why the emitting *d* level is not quenched by the *f* levels. In this context, we would like to point out that the Gd^{3+} $d \longrightarrow f$ luminescence is thermally quenched, disappearing near 200 K.

We have to discuss now the fine structure of Gd^{3+} emission. Contrary to the case of Er^{3+}, the level structure of the Gd^{3+} $^8S_{7/2}$ ground state is simple (no Stark splitting in first order) and only one ZPL is expected. The fine structures may arise from (i) phonon sidebands, (ii) site effects, or (iii) a mixture of both. More insight could be obtained from excitation spectra. In the stoichiometric, as well as in $LiYF_4$: Gd^{3+} (10%), in the range of allowed excitations, the sample is optically thick, thus preventing an analysis of the spectral shape of absorption. What can be done, however, is doping of the crystal with another RE^{3+} ion as a test ion to probe electron–phonon interaction. Therefore, Ce^{3+} doped $LiGdF_4$ has been investigated. Due to the small Ce^{3+} concentration (0.05%), the excitation spectrum of the Ce^{3+} $d \longrightarrow f$ transitions in the transparency range of the host could be measured[2] without saturation effects. This yields a fine structure with a ZPL at 33615 cm^{-1}. In Fig. 5, the excitation spectrum of the Ce^{3+} $d \longrightarrow f$ emission is compared with the Gd^{3+} $d \longrightarrow f$ emission. The scale of the Ce^{3+} spectrum is opposite to the scale of the Gd^{3+} spectrum, and the scales are shifted such that the Ce^{3+} ZPL coincides with the first sharp line of the Gd^{3+} emission. The spectra agree well within the range of the pronounced lines. Therefore, the line at 79377 cm^{-1} is assigned to the ZPL of Gd^{3+} $d \longrightarrow f$ emission.

The sidebands in the Ce^{3+} $f \longrightarrow d$ excitation spectrum most probably originate from phonon replica. The fine structure is spread over ~500 cm^{-1}, which is in good agreement with the energy spread of phonon spectra of isostructural scheelite compounds Li*Ln*F_4 (*Ln* = Y, Ho, Er, Tm, Yb) [29]. (The energies are not in agreement with the phonon spectra; in particular, there are no phonons with such small energies. Data on $LiGdF_4$ are not available in the literature.) The close similarity between both spectra in Fig. 5 indicates that the fine structure of the Gd^{3+} $d \longrightarrow f$ emission mainly originates from vibronic modes. The smooth shape of the luminescence at longer wavelengths is assigned to a superposition of vibronic modes with more that one phonon involved. The general behavior is typical for intermediate electron–phonon coupling. A Huang–Rhys parameter $S \sim 1$ was estimated in [15].

GdF_3 emits a broad band centered at ~80 000 cm^{-1}. It is ascribed to spin-allowed Gd^{3+} $d \longrightarrow f$ emission as well. The same spectra were obtained from single crystals and powder samples. The spectral shape indicates much stronger electron–phonon coupling than in $LiGdF_4$. Similar observations were reported in [7], where stronger electron–lattice coupling was found for some REF_3 as compared to $LiYF_4$: RE^{3+}. In [15], an estimate of the Huang–Rhys parameter is given, $S > 5$. The shift of the Gd^{3+} $d \longrightarrow f$ emission of GdF_3 to higher energies as compared to $LiGdF_4$ is ascribed to the different coordination numbers for the Gd^{3+} ion (9 in

---

[2] To be more precise, in $LiGdF_4$: Ce^{3+}, Ce^{3+} $d \longrightarrow f$ emission is quenched by energy transfer to $4f^64f^*Gd^{3+}$ levels, leading to Gd^{3+} $^6P_{7/2} \longrightarrow {}^8S_{7/2}$ emission at 311 nm. This emission was monitored while measuring the Ce^{3+} $f \longrightarrow d$ excitation spectrum.

GdF_3, 8 in $LiGdF_4$), causing a smaller crystal field splitting of the *d* excitation in GdF_3.

In Fig. 6, the Gd^{3+} $d \longrightarrow f$ luminescence and excitation spectra are plotted together. For $LiGdF_4$, the ZPL in emission coincides with the steep onset of the excitation spectrum, which supports our assignment. In the stoichiometric material, the system is optically thick; therefore, no fine structure can be observed. In GdF_3, the excitation spectrum consists of a single band which is much broader than the luminescence band. At first sight, this seems to indicate linear-quadratic electron–phonon coupling (different phonons coupling in the excited and the ground state [30]). Nevertheless, we hesitate to draw this conclusion because, at higher energies, the system is optically thick, preventing a line-shape analysis. More than one electronic transition may be hidden in the maximum. The decrease in intensity towards higher energies may be ascribed to the onset of band-to-band transitions (it seems to be a general rule that RE^{3+} $d \longrightarrow f$ luminescence is hardly excited at the onset of band-to-band excitations). The smooth onset, however, originates from strong electron–phonon coupling.

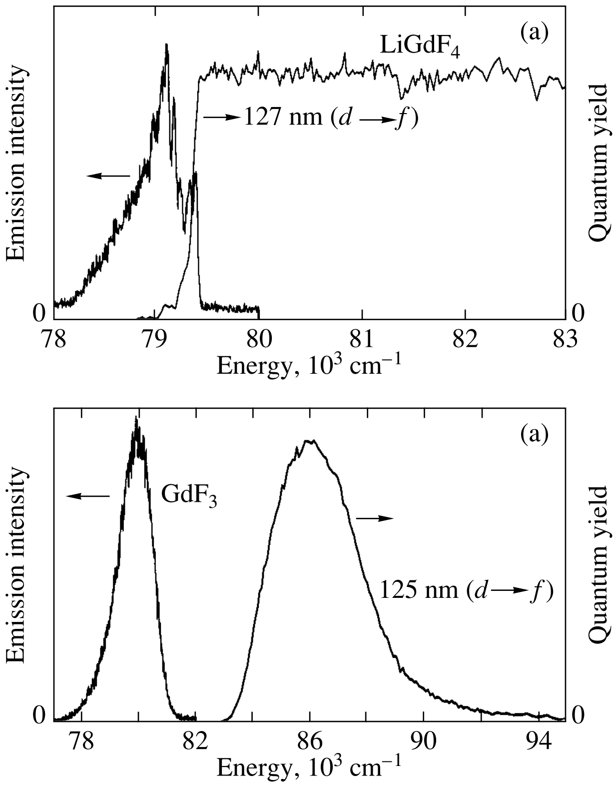

Fig. 6. Comparison of (a) Gd^{3+} $d \longrightarrow f$ luminescence ($\Delta\lambda_{em} = 0.8$ Å) and excitation ($\Delta\lambda_{ex} = 1.0$ Å) in $LiGdF_4$ and of (b) Gd^{3+} $d \longrightarrow f$ luminescence ($\Delta\lambda_{em} = 0.8$ Å) and excitation ($\Delta\lambda_{ex} = 2.9$ Å) in GdF_3. $T = 10$ K.

3.4. Lu^{3+} $d \longrightarrow f$ *Luminescence*

The electronic structure of Lu with its $4f^{14}$ configuration is simple. The filled *f* shell gives rise to only one energy level, $^1S_0$. At the onset of electronic excitation, an *f* electron is promoted to a *d* orbital. The lowest excited state is an $S = 1$ state (the spin of the electron changes its direction), and the next state is a singlet state (the spin keeps its direction). In other words, concerning the *d* excitations, we have a situation like that in all other RE^{3+} ions in the second half of the series. The important difference is that, in the range of $f \longrightarrow d$ excitations, there are no other energy levels of Lu^{3+} available for energy transfer and subsequent quenching of the Lu^{3+} $d \longrightarrow f$ emission.

The reason why Lu^{3+} $d \longrightarrow f$ emission has never been detected before may arise from the fact that the energy is the highest among all RE^{3+} ions (free ion value near 100 000 cm^{-1}) [16, 17]. In Fig. 7, VUV-luminescence spectra of a $LiLuF_4 : Ce^{3+}$ crystal, a $LuF_3 : Ce^{3+}$ crystal, and of LuF_3 powder are shown (see also [15]). As a consequence of the Ce^{3+} doping, the $LiLuF_4$ VUV luminescence was weak; therefore, the spectrum was measured at the BW3 beamline, providing high-intensity excitation by XUV photons (130 eV). $LiLuF_4$ emits two broad emission bands at 80200 and 82600 cm^{-1}. The band at 82 600 cm^{-1} has a lifetime in the nanosecond range and is ascribed to spin-allowed $4f^{13}5d \longrightarrow 4f^{14}$ emission. The band at 80 200 cm^{-1} has a considerably longer lifetime and is ascribed to spin-forbidden $4f^{13}5d \longrightarrow 4f^{14}$ emission. The different nature of both bands is demonstrated in Fig. 7. The open circles are time-integrated measurements, and the full circles were obtained within a time window of 0.8 ns after the excitation pulses. The assignments will be established in Subsection 3.5.

Due to the weak luminescence intensity, the excitation spectra around the threshold of Lu^{3+} $f \longrightarrow d$ excitation could not be measured in $LiLuF_4 : Ce^{3+}$. The moderate spectral resolution of 6 Å and the absence of excitation spectra prevent an analysis of the electron–phonon interaction. The VUV emission from the $LuF_3 : Ce^{3+}$ single crystal and from the undoped LuF_3 powder consists of a broad band (~80 500 cm^{-1}) with slow decay (longer than the accessible range). The emission was intense enough to measure high-resolution luminescence and excitation spectra at the SUPERLUMI station. No fine structure was found, indicating strong electron–phonon coupling. The results of the crystal and of the powder sample agree well. On the basis of the long lifetime, the emission is ascribed to spin-forbidden Lu^{3+} $4f^{13}5d \longrightarrow 4f^{14}$ emission.

Although electron–phonon interaction of the Lu^{3+} $4f^{13}5d$ excitation in $LiLuF_4$ was not analyzed for the reasons given above, information is obtained from Ce^{3+} emission in $LiLuF_4 : Ce^{3+}$ [31]. The Ce^{3+} luminescence

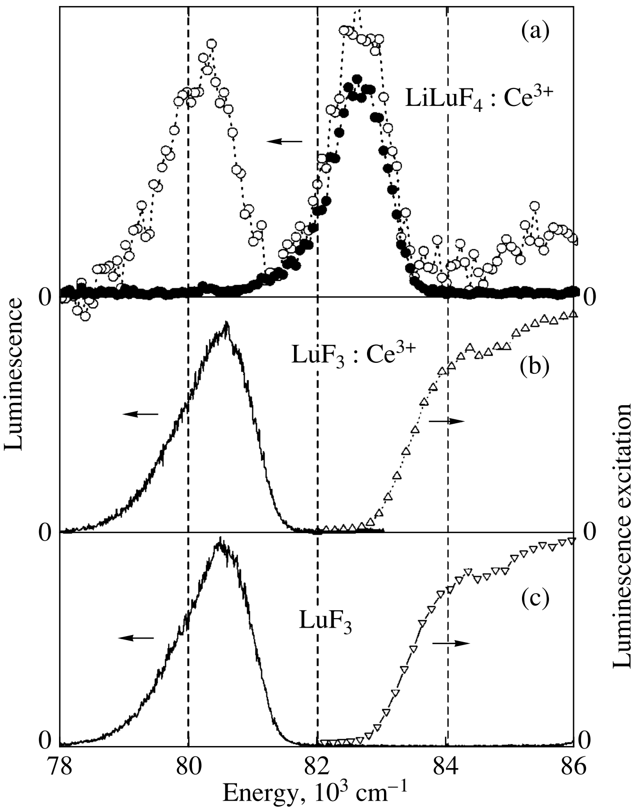

Fig. 7. (a) Lu^{3+} $d \longrightarrow f$ luminescence ($\Delta\lambda_{em}$ = 6 Å) from LiLuF$_4$: Ce^{3+} excited by 130-eV photons recorded within 0.8 ns after the excitation pulse (full circles) and time-integrated (open circles). High-resolution ($\Delta\lambda_{em}$ = 0.8 Å) luminescence excited at 86 210 cm^{-1}, and high-resolution excitation spectra ($\Delta\lambda_{ex}$ = 1.0 Å) of (b) LuF$_3$: Ce^{3+} crystal and (c) LuF$_3$ powder at T = 10 K.

clearly yields a ZPL with phonon replica and a smooth low-energy sideband, as is characteristic for intermediate coupling. Moreover, in the energy range corresponding to Lu^{3+} $4f^{14} \longrightarrow 4f^{13}5d$ excitation, the excitation spectra of the Ce^{3+} emission yield pronounced sharp lines, which were assigned by Kirikova *et al.* [31] to ZPLs of Lu^{3+} $4f^{14} \longrightarrow 4f^{13}5d$ transitions because their energies agree well with calculations based on the model of Dorenbos [16, 17].

3.5. Comparison with Theory

The energies of the lowest spin-allowed 5d states of RE^{3+} ions in a host crystal can be predicted if at least for one RE^{3+} ion in the particular crystal this value is known [16, 17]. Dorenbos collected spectroscopic data on $f \longrightarrow d$ transitions of RE^{3+} ions in various hosts and tabulated average values for each host. As a reference ion, Ce^{3+} has been chosen because this ion has been investigated extensively. The predicted energy for the spin-allowed transition of a RE^{3+} ion is given by

$$\Delta E^{\mathrm{RE},\,s-a} = 49\,340\ \mathrm{cm}^{-1} - D(A) + \Delta E^{\mathrm{RE,Ce}}, \qquad (1)$$

where 49 340 cm^{-1} is the energy of the first $f \longrightarrow d$ transition of the free Ce^{3+} ion, $D(A)$ is the crystal field depression of compound A, and $\Delta E^{\mathrm{RE,Ce}}$ is the energy difference between the first spin-allowed $f \longrightarrow d$ transition of the RE^{3+} ion and of Ce^{3+}. The basis of this approximation is the fact that the crystal field depression is not sensitive to the individual ion, $D(A)$ being an average of the $D(\mathrm{RE}^{3+}, A)$ values for different RE^{3+} ions. The quantity $\Delta E^{\mathrm{RE,Ce}}$ is in first approximation independent from the host and can be regarded as an intrinsic property of the respective ion. The values used by Dorenbos are average values over many compounds.

In the table, data for part of the crystals investigated are listed. Ce^{3+} $f \longrightarrow d$ excitation energies measured separately are given as well. The estimates according to Eq. (1) are then compared with the experimental results. For those cases where we measured the Ce^{3+} values, the transition energies were also calculated according to

$$\Delta E^{\mathrm{RE},\,s-a}_{\mathrm{direct}} = E^{\mathrm{Ce}} + \Delta E^{\mathrm{RE,Ce}}. \qquad (2)$$

The calculations can be extended to the spin-forbidden $f \longrightarrow d$ transitions. Dorenbos showed that the energy difference, $\Delta E^{sa,\,sf}_{\mathrm{RE}}$, between the spin-allowed and the spin-forbidden $f \longrightarrow d$ excitation energy is merely a property of the respective ion but is nearly independent from the host. The values for Er^{3+} and Tm^{3+} are 3050 and 2350 cm^{-1}, respectively. Subtracting these values from the results obtained from Eqs. (1) and (2) results in $\Delta E^{\mathrm{RE},\,s-f}$, which is also given in the table.

Dorenbos treated the data in the strong coupling limit, which means absorption and emission are approximated by Gaussian bands energetically separated by the Stokes shift $\Delta S(A)$. It turns out that $\Delta S(A)$ is characteristic for host A but nearly independent of the RE^{3+} ion. Consequently, the $\Delta E^{\mathrm{RE,Ce}}$ are energetical differences between such Gaussian-shaped peaks. The results from Eq. (1) should therefore not be compared with the energies of ZPLs without further correction. Dorenbos included in [17] averaged values of $S(A)$. For linear coupling to the lattice, the ZPL would be in the middle between the absorption (excitation) and the luminescence maximum. The corrected results are then given by

$$\Delta E^{\mathrm{RE},\,s-a}_{\mathrm{corr}} = \Delta E^{\mathrm{RE},\,s-a} - \frac{1}{2}\Delta S(A). \qquad (3)$$

Equation (2), however, should provide us with reliable results without any correction if E^{Ce} is the energy of the ZPL.

In most cases, the predictions agree within 600 cm^{-1} with the experimental results [16, 17]. Comparing the

Comparison between calculated and experimental values of the lowest spin-forbidden and spin-allowed $f \longrightarrow d$ excitation energies of Er^{3+}, Tm^{3+}, Gd^{3+}, and Lu^{3+} ions in various fluoride-type hosts (ZPLs)

Energy		$LiYF_4$ (Er^{3+})	$LiCaAlF_6$ (Tm^{3+})	$LiGdF_4$ (Gd^{3+})	$LiYF_4$ (Gd^{3+})	$LiLuF_4$ (Lu^{3+})
$D(A)$	[15]	15262	13344	15093	15262	15140
$\Delta E^{\mathrm{RE, Ce}}$	[14]	30000	29300	45800	45800	49170
$\Delta S(A)$	[15]	1597	1389		1597	1242
$\Delta E^{\mathrm{RE},\, s-a}$		64078	65296	80047	79878	83370
$\Delta E^{\mathrm{RE},\, s-a}_{\mathrm{corr}}$		**63279**	**64601**		**79079**	**82749**
$\Delta E^{\mathrm{RE},\, s-f}$		61028	62946			
$\Delta E^{\mathrm{RE},\, s-f}_{\mathrm{corr}}$		**60229**	**62251**			
E^{Ce}	(ZPLs)			33615	33450 [31]	33130 [31]
$\Delta E^{\mathrm{RE},\, s-a}_{\mathrm{direct}}$	(ZPLs)			**79415**	**79250**	**82300**
ΔE^{s-a}	(ZPLs)	**64265**	**63200**	**79377**	**79250**	**82900** [31]
ΔE^{s-f}	(ZPLs)	**61020**	**61410**			**81550** [31]

Note: Experiment: this paper and [31]. Energies are given in cm^{-1}. Numbers to be compared are given in bold type.

estimates according to Eq. (2) with the measured ZPLs ($LiGdF_4$, $LiYF_4 : Gd^{3+}$, $LiLuF_4$) yields agreement within this limit, which strongly supports our assignments. For $LiYF_4 : Gd^{3+}$ and $LiLuF_4(Lu^{3+})$, the agreement between the results of Eq. (3) and experiment is also very good. For $LiYF_4 : Er^{3+}$, the experimental values and the predictions differ by 800–1000 cm^{-1}. In the case of Li*CAF* : Tm^{3+}, the disagreement is somewhat larger. Concerning the ZPLs of the spin-forbidden $d \longrightarrow f$ luminescence of $LiYF_4 : Er^{3+}$ and Li*CAF* : Tm^{3+}, the agreement is better. Estimates have also been made for GdF_3 and LuF_3 [15]. Good agreement has been obtained.

4. CONCLUSIONS

High-resolution $4f^{n-1}5d \longrightarrow 4f^n$ VUV-luminescence spectra of fluorides doped with Gd^{3+}, Tm^{3+}, and Er^{3+} and of stoichiometric Gd^{3+} and Lu^{3+} fluorides have been presented. Only for GdF_3 and for LuF_3 has strong coupling of the $4f^{n-1}5d$ configuration to the lattice been established. In all other cases, ZPLs and vibronic sidebands have been observed, indicating intermediate coupling. In some cases, the coupling of RE^{3+} *d* levels to the lattice has been analyzed with a “test ion” (Ce^{3+}) doped into the respective matrix at a low doping level. This is a promising method that could be applied in other cases where the excitation spectra are saturated. The detailed comparison with the predictions of *d* excitation energies by the empirical method of Dorenbos [16, 17] underlines the potential power of the method, but in addition it seems to be a worthwhile goal to extend the method to ZPLs. The observation of Gd^{3+} $d \longrightarrow f$ emission requires revision of the stand point that a dense *f* level system behind the *d* excitations generally quenches *d* emission. A strong influence of spin selection rules on energy transfer has been established.

ACKNOWLEDGMENTS

The authors are indebted to A. Meijerink, who provided us with numerical values for the energy levels and who made accessible to us the laser setup at the Debye Institute, University of Utrecht. Thanks are due to P. Vergeer for assistance during the measurements in Utrecht and to J.Y. Gesland and T.V. Uvarova for growing the crystals.

This work was supported by the Minister of Science and Technology of Germany under contract nos. 05 KS1GUD/1 and 03N8019D. Support by the Graduiertenkolleg Felder und lokalisierte Atome–Atome und lokalisierte Felder of the Deutsche Forschungsgemeinschaft (GRK 403) is gratefully acknowledged.

REFERENCES

1. E. Loh, Phys. Rev. **147** (1), 332 (1966).
2. R. T. Wegh, H. Donker, and A. Meijerink, Phys. Rev. B **57** (4), R2025 (1998).
3. W. M. Yen, L. R. Elias, and D. L. Huber, Phys. Rev. Lett. **24** (18), 1011 (1970).
4. L. R. Elias, Wm. S. Heaps, and W. M. Yen, Phys. Rev. B **8** (11), 4989 (1973).
5. Wm. S. Heaps, L. R. Elias, and W. M. Yen, Phys. Rev. B **13** (1), 94 (1976).

6. K. H. Yang and J. A. DeLuca, Appl. Phys. Lett. **29** (8), 499 (1976).
7. R. T. Wegh and A. Meijerink, Phys. Rev. B **60** (15), 10820 (1999).
8. J. Becker, J. Y. Gesland, N. Yu. Kirikova, J. C. Krupa, V. N. Makhov, M. Runne, M. Queffelec, T. V. Uvarova, and G. Zimmerer, J. Lumin. **78** (2), 91 (1998).
9. N. M. Khaidukov, N. Yu. Kirikova, M. Kirm, J. C. Krupa, V. N. Makhov, E. Negodin, and G. Zimmerer, Proc. SPIE **4766**, 154 (2002).
10. J. Becker, J. Y. Gesland, N. Yu. Kirikova, J. C. Krupa, V. N. Makhov, M. Runne, M. Queffelec, T. V. Uvarova, and G. Zimmerer, J. Alloys Compd. **275–277**, 205 (1998).
11. M. Schlesinger and T. Szczurek, Phys. Rev. B **8** (5), 2367 (1973).
12. Y. Chen, M. Kirm, E. Negodin, M. True, S. Vielhauer, and G. Zimmerer, Phys. Status Solidi B **240** (1), R1 (2003).
13. P. Peijzel, Doctoral Dissertation (Univ. of Utrecht, 2004).
14. M. True, Doctoral Dissertation (Univ. of Hamburg, 2004).
15. M. Kirm, J. C. Krupa, V. N. Makhov, M. True, S. Vielhauer, and G. Zimmerer, Phys. Rev. B (in press).
16. P. Dorenbos, J. Lumin. **91** (1–2), 91 (2000).
17. P. Dorenbos, J. Lumin. **91** (3–4), 155 (2000).
18. G. Zimmerer, Nucl. Instrum. Methods Phys. Res. A **308** (1–2), 178 (1991).
19. T. Möller and G. Zimmerer, Phys. Scr. T **17**, 177 (1987).
20. C. K. Jayasankar, M. F. Reid, and F. S. Richardson, Phys. Status Solidi B **155** (2), 559 (1989).
21. M. A. Couto dos Santos, E. Antic-Fidancev, J. Y. Gesland, J. C. Krupa, M. Lemaître-Blaise, and P. Porcher, J. Alloys Compd. **275–277**, 435 (1998).
22. G. M. Renfro, J. C. Windscheif, W. A. Sibley, and R. F. Belt, J. Lumin. **22** (1), 51 (1980).
23. L. van Pieterson, M. F. Reid, G. W. Burdieck, and A. Meijerink, Phys. Rev. B **65** (4), 045114 (2002).
24. A. Meijerink, Private communication.
25. M. True, M. Kirm, E. Negodine, S. Vielhauer, and G. Zimmerer, J. Alloys Compd. **374** (1–2), 36 (2004).
26. W. T. Carnall, G. L. Goodman, K. Rajnak, and R. S. Rana, J. Chem. Phys. **90** (7), 3443 (1989).
27. J. Hölsä, R.-J. Lamminmaki, E. Antic-Fidancev, M. Lemaître-Blaise, and P. Porcher, J. Phys.: Condens. Matter **7** (26), 5127 (1995).
28. G. H. Dieke, in *Spectra and Energy Levels of Rare Earth Ions in Crystals*, Ed. by H. M. Crosswhite and H. Crosswhite (John Wiley and Sons, Chichester, 1968).
29. S. Salaün, M. T. Fornoni, A. Bulou, M. Rousseau, P. Simon, and J. Y. Gesland, J. Phys.: Condens. Matter **9** (32), 6941 (1997).
30. C. W. Struck and W. H. Fonger, *Understanding Luminescence Spectra and Efficience Using Wp and Related Functions* (Springer-Verlag, Berlin, 1991).
31. N. Yu. Kirikova, M. Kirm, J. C. Krupa, V. N. Makhov, E. Negodine, and J. Y. Gesland, J. Lumin. **110** (3), 135 (2004).

Physics of the Solid State, Vol. 47, No. 8, 2005, pp. 1425–1430. Translated from Fizika Tverdogo Tela, Vol. 47, No. 8, 2005, pp. 1376–1380.
Original Russian Text Copyright © 2005 by Klimin, Popova, Chukalina, Malkin, Zakirov, Antic-Fidancev, Goldner, Aschehoug, Dhalenne.

PROCEEDINGS OF THE XII FEOFILOV WORKSHOP “SPECTROSCOPY OF CRYSTALS ACTIVATED BY RARE-EARTH AND TRANSITION-METAL IONS”

(Yekaterinburg, Russia, September 22–25, 2004)

Stark Structure of the Yb^{3+} Ion Levels in $(Yb_xY_{1-x})_2Ti_2O_7$ and the Crystal Field in Rare-Earth Titanates with a Pyrochlore Structure

S. A. Klimin*, M. N. Popova*, E. P. Chukalina*, B. Z. Malkin, A. R. Zakirov**, E. Antic-Fidancev***, Ph. Goldner***, P. Aschehoug***, and G. Dhalenne******

**Institute of Spectroscopy, Russian Academy of Sciences, Troitsk, Moscow oblast, 142190 Russia*
e-mail: klimin@isan.troitsk.ru
***Kazan State University, ul. Kremlevskaya 18, Kazan, 420008 Tatarstan, Russia*
****Laboratoire de Chimie Appliquée de l’État Solide, CNRS UMR 7574, ENSCP, Paris, Cedex 05, F-75231 France*
***** Laboratoire de Physico-Chimie de l’État Solide, Université Paris-Sud, Orsay, F-91405 France*

Abstract—The absorption spectra of $Yb_2Ti_2O_7$ single crystals and the luminescence and luminescence excitation spectra of $Y_2Ti_2O_7$: Yb (1%) polycrystals were studied in the temperature range 4.2–300 K. The spectra were analyzed in terms of the crystal-field theory and the exchange-charge model. Based on the set of crystal-field parameters found for $Yb_2Ti_2O_7$, analogous sets of parameters were determined for other rare-earth titanates and proved to be in reasonable agreement with all available experimental data. *© 2005 Pleiades Publishing, Inc.*

1. INTRODUCTION

Rare-earth (RE) double oxides $R_2A_2O_7$ (where A = Ti, Sn, Zn, Hf; R is a rare-earth element or yttrium) have a pyrochlore structure [1]. In this fcc structure (space group $Fd\bar{3}m$), rare-earth R^{3+} ions form a sublattice of tetrahedra, which are linked together by shared vertices (Fig. 1a). Since the magnetic dipole–dipole interaction between R^{3+} ions does not favor a specific configuration of magnetic moments, the ground state is multiply degenerate. This situation is illustrated in Fig. 1b, which shows one of the six possible configurations of four spins situated at the vertices of a regular tetrahedron, with two spins pointing toward the center of the tetrahedron and with the other two pointing away from the center. As a result, in compounds $R_2A_2O_7$ (R = Ho, Dy, Tb, Yb) where R^{3+} ions are in the magnetic ground state, long-range magnetic order does not occur at temperatures down to 0.05 K and structures like a spin liquid or a spin ice with short-range order are observed [2–4]. In order to explain the low-temperature magnetic structure and spin dynamics, we need to know the energies of the low-lying RE ion states, which are dictated by the crystal field (CF). Available experimental data on the position of the RE ion energy levels in pyrochlore-structure compounds are scarce and have been obtained predominantly from neutron-scattering studies [5–8]. Two sets of CF parameters obtained for $Yb_2Ti_2O_7$ in [9, 10] agree well with the experimental data on magnetization, magnetic susceptibility, specific heat, and the electric-field gradient at the ^{172}Yb nucleus sites but differ strongly from each other. Furthermore, both sets of CF parameters differ dramatically from that obtained for $Ho_2Ti_2O_7$ [5], which is difficult to explain. When determining the CF parameters, it is important to use experimental data on the RE ion energy levels over the maximum possible energy range. These data can be derived from optical measurements.

In this work, we perform a spectroscopic study on $Yb_2Ti_2O_7$, determine the CF parameters for this compound, and analyze the variations in the CF parameters

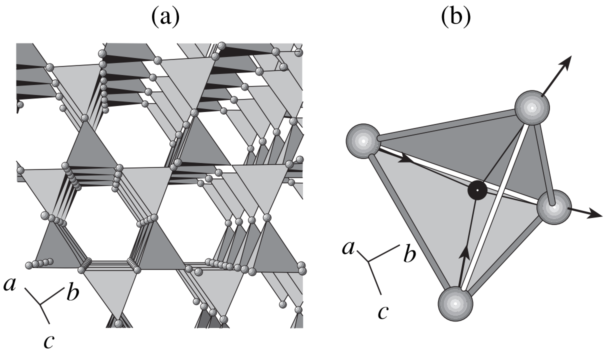

Fig. 1. (a) Sublattice of R_4 tetrahedra in $R_2Ti_2O_7$(Ti and O atoms are not shown). (b) Spin “frustration.”

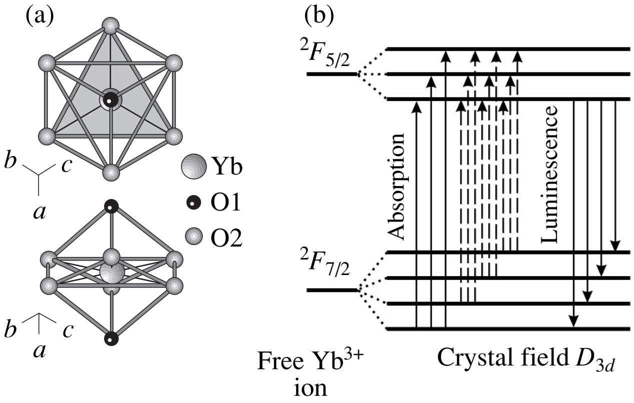

Fig. 2. (a) Nearest neighbors of the ytterbium ion in $Yb_2Ti_2O_7$ (symmetry D_{3d}); the contributions from O^{2-} ions in the two nonequivalent positions to the crystal field are different. (b) Stark sublevels of the Yb^{3+} ion in a D_{3d} symmetry crystal field. Solid arrows indicate transitions associated with absorption and luminescence at low temperatures. Dashed arrows indicate transitions associated with absorption at elevated temperatures, where the population of the excited Stark sublevels becomes noticeable.

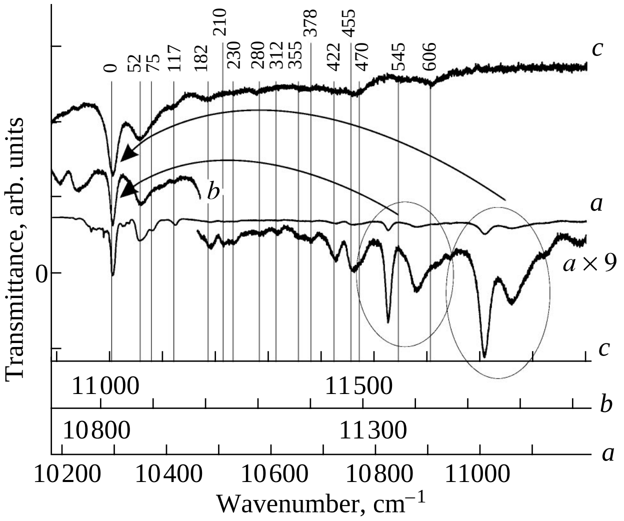

Fig. 3. Transmission spectrum of $Yb_2Ti_2O_7$ at 5 K. Numerals above the figure indicate the positions (cm^{-1}) of the peaks in phonon wings relative to the zero-phonon line.

as one goes from one pyrochlore-structure $R_2Ti_2O_7$ compound to another.

2. EXPERIMENTAL

Transparent, high optical quality $Yb_2Ti_2O_7$ single crystals typically ~10 mm in size were grown using the floating-zone technique. Absorption spectra were measured over a wide spectral range (9000–14000 cm^{-1}) and a wide temperature range (4.5–300 K) with a resolution of 0.15 cm^{-1} using a BOMEM DA3.002 Fourier spectrometer and an optical cryostat from a special construction department in Kiev. Three tailor-made plane-parallel plates with thicknesses of 1.55, 0.60, and 0.09 mm were employed in the experiment.

Luminescence spectra were measured on the $Y_2Ti_2O_7$: Yb (1%) compound, because concentration quenching of luminescence occurs at high dopant concentrations. Polycrystalline $(Y_{0.99}Yb_{0.01})_2Ti_2O_7$ samples were prepared using solid-state synthesis at 1400°C. X-ray analysis confirmed the pyrochlore structure; however, a small quantity of the Y_2O_3 impurity was also detected. Powders obtained were compressed into pellets, which were attached to the cold finger of a closed-cycle liquid-helium cryostat. Luminescence spectra were excited by a cw Coherent 890 (Ti : sapphire) laser, which was pumped by an argon laser, and were recorded with a cooled InGaAs photodiode.

3. EXPERIMENTAL RESULTS

The free Yb^{3+} ion has only two energy levels, $^2F_{5/2}$ and $^2F_{7/2}$, which correspond to the $4f^{13}$ electronic configuration. The energy spacing between these levels is ~10000 cm^{-1} [11]. In the pyrochlore structure, the ytterbium ion is in a D_{3d} symmetry position (Fig. 2a). In the crystal field, the $^2F_{7/2}$ ground level is split into four Kramers doublets, $3\Gamma_4 + \Gamma_{56}$, and the excited $^2F_{5/2}$ level is split into three Kramers doublets, $2\Gamma_4 + \Gamma_{56}$ (Fig. 2b). One might expect the absorption spectrum at low temperatures to have three lines corresponding to transitions from the ground Stark sublevel of the $^2F_{7/2}$ multiplet to the sublevels of the $^2F_{5/2}$ multiplet. Accordingly, the luminescence spectrum would have four lines. Zero-phonon transitions are allowed in the magnetic-dipole approximation only. Electronic–vibrational (vibronic) transitions are allowed in the electric-dipole approximation, and the intensity of these transitions can be high if the electron–phonon interaction is fairly strong. This is the case in the $Yb_2Ti_2O_7$ compound under study.

Figure 3 shows the absorption spectrum of an $Yb_2Ti_2O_7$ single crystal taken at 5 K (lower spectrum). Instead of the expected three spectral lines, the spectrum is seen to exhibit a complex structure. In this structure, the three narrowest lines are at 10297, 10821, and 11005 cm^{-1} and can be assigned to the transitions from the ground sublevel of the $^2F_{7/2}$ multiplet to the Stark sublevels of the $^2F_{5/2}$ multiplet. This interpretation is confirmed by the fact that these three lines have similar phonon wings. In Fig. 3, the portions of the spectrum corresponding to these narrowest lines are shifted along the wavenumber axis in such a way as to bring them into coincidence. The positions of the peaks in the phonon wings of these lines are seen to coincide.

The width of each phonon wing is about 600 $cm^{–1}$, which is approximately equal to the width of the phonon spectrum of $Yb_2Ti_2O_7$ [12]. The strongest peak in a phonon wing located at ~52 $cm^{–1}$ is observed for all three lines and also manifests itself on the anti-Stokes side, with the anti-Stokes component vanishing as the temperature decreases (Figs. 4a, 4b).

The positions of the two excited Stark sublevels of the $^2F_{7/2}$ ground state were determined from the temperature dependence of the anti-Stokes vibronic structure of the spectral line at 10297 $cm^{–1}$ (Fig. 4c). In Figs. 4a and 4c, other narrow lines are also seen (near 10297 $cm^{–1}$); these lines can be assigned to other Yb^{3+} centers present in the crystal under study.

Figure 5 shows the luminescence and luminescence excitation spectra of the Yb^{3+} ion in an $Y_2Ti_2O_7$ sample. Spectrum *a* is taken at an excitation wavelength of 920 nm and is seen to consist of more than four lines at low temperatures. Interpretation of the spectrum (separation of zero-phonon lines) is hampered both by the presence of the spectral lines of ytterbium embedded in the Y_2O_3 impurity matrix and by the fact that the zero-phonon lines are comparable in intensity to their phonon wings. The data on the positions of the energy levels of ytterbium embedded in Y_2O_3 taken from [13] are presented in Fig. 5 (*f*). The luminescence line at 9700 $cm^{–1}$ in spectrum *a* is related to Y_2O_3 : Yb [13]. The narrower line at 9630 $cm^{–1}$ can be assigned to the ytterbium ion in the $Y_2Ti_2O_7$ matrix under study. In order to verify this assignment, we studied the excitation spectra of the luminescence at frequencies of 9700 (Yb^{3+} in Y_2O_3; spectrum *b*) and 9630 $cm^{–1}$ (Yb^{3+} in $Y_2Ti_2O_7$; *c*). The lines at 10510 and 11030 $cm^{–1}$ in spectrum *b* correspond to the data from [13] and support the validity of our assignment. The other narrow lines in spectrum *b* can be associated with the luminescence at a frequency of 9700 $cm^{–1}$, which can belong to the phonon wing of the line at 9630 $cm^{–1}$ from Yb^{3+} in $Y_2Ti_2O_7$. Spectrum *c* can be considered to consist of three zero-phonon lines (indicated by arrows) each of which has phonon wings on both the Stokes and anti-Stokes sides, with the strongest peak in the phonon wing lying at 52 $cm^{–1}$, as is the case in the transmission spectra. Table 1 gives the positions of the $^2F_{5/2}$ multiplet Stark sublevels of the ytterbium ion in the titanate as determined from the spectrum *c*. In order to find the luminescence spectrum of ytterbium in $Y_2Ti_2O_7$, we measured luminescence spectra using selective excitation at wavelengths of 967 nm (spectrum *d*; excitation of the phonon wing with significant detuning from the level of ytterbium in Y_2O_3) and 972 nm (spectrum *e*; exact excitation of the level of Yb in $Y_2Ti_2O_7$ but with small detuning from the wide level of Yb in Y_2O_3). Spectra *d* and *e* do not differ significantly, and we can separate four lines corresponding to transitions to the four Stark sublevels of the ground multiplet (indicated by arrows). The energies of the Stark sublevels of the $^2F_{7/2}$ multiplet as calculated from the positions of these lines are listed in Table 1. Note that the strongest lines have clearly defined satellites at ±52 $cm^{–1}$.

Thus, based on the experimental transmission and luminescence spectra, we determined the energy levels of the ytterbium ion in $Yb_2Ti_2O_7$ and $Y_2Ti_2O_7$, respectively. Furthermore, we detected strong electron–phonon interaction, which should be taken into account when analyzing the spin dynamics in the frustrated $Yb_2Ti_2O_7$ magnet.

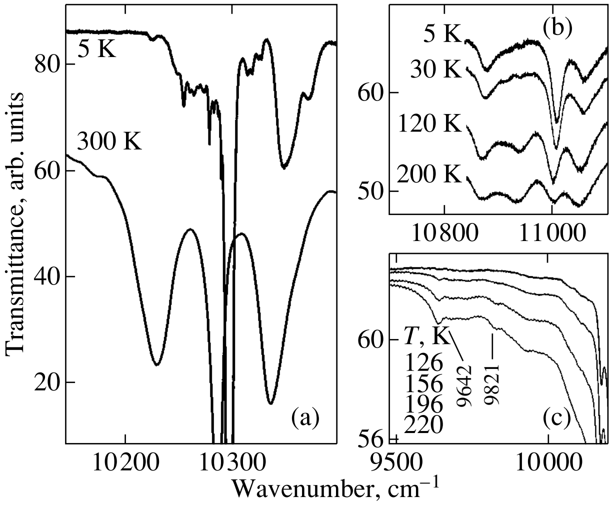

Fig. 4. Fragments of the transmission spectra of $Yb_2Ti_2O_7$ at various temperatures.

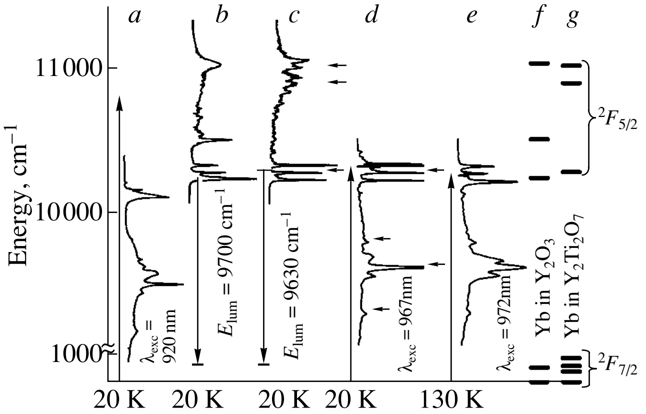

Fig. 5. (a) Luminescence spectrum of the Yb^{3+} ion in a $Y_2Ti_2O_7$ sample; (*b*, *c*) luminescence excitation spectra for luminescence measured at frequencies of 9700 and 9630 $cm^{–1}$, respectively; (*d*, *e*) selectively excited luminescence spectra; (f) Yb^{3+} levels in a Y_2O_3 sample [13]; and (*g*) Yb^{3+} levels in $Y_2Ti_2O_7$.

Table 1. Energies (cm^{-1}), symmetry (irreducible representations of the D_{3d} group), and g factors for the Stark sublevels of rare-earth ions in $R_2Ti_2O_7$

$Y_2Ti_2O_7$: Yb (1%)		$Yb_2Ti_2O_7$ ($^2F_{7/2}$, $^2F_{5/2}$)		$Er_2Ti_2O_7$ ($^4I_{15/2}$)		$Ho_2Ti_2O_7$ ($^5I_8$)		$Tb_2Ti_2O_7$ ($^7F_6$)	
experiment		experiment	calculation	experiment [8]	calculation	experiment [5, 21]	calculation	experiment [4, 6]	calculation
	0		$0(\Gamma_4)$	0	0	$0(E)$	$0(E)$	$0(E)$	$0(E)$
	$g_\parallel = 1.79$		$g_\parallel = 1.836$		(Γ_4)	$g_\parallel = 18.70$	$g_\parallel = 19.32$	$g_\parallel = 10.2 \pm 0.6$	$g_\parallel = 10.4$
	$g_\perp = 4.27$		$g_\perp = 4.282$		$g_\parallel = 2.32$	–	$166(A_2)$	$12.1 \pm 0.5(E)$	$12.1(E)$
$^2F_{7/2}$	[10]			$g_\perp > 6$	$g_\perp = 6.8$	$177.4(E)$	$177(E)$	$g_\parallel = 11.8 \pm 1.6$	$g_\parallel = 13.4$
	481	476	$528(\Gamma_4)$	51	$51.6(\Gamma_{56})$	$209.7(E)$	$213(E)$	83.5 ± 0.7	$76.4(A_2)$
	657	655	$649(\Gamma_{56})$	59	$58.8(\Gamma_4)$	–	$224(A_1)$	116.7	$120(A_1)$
	976	–	$972(\Gamma_4)$	–	$135(\Gamma_4)$	$475.8(E)$	$471(E)$		$284(E)$
	10291	10297	10293	–	$447(\Gamma_4)$	–	$545(A_1)$		$314(A_2)$
			(Γ_4)	–	$458(\Gamma_{56})$	–	$564(A_2)$		$318(A_1)$
$^2F_{5/2}$	10847	10821	10736	–	$490(\Gamma_4)$	$572.6(E)$	$565(E)$		$439(E)$
			(Γ_4)	–	$710(\Gamma_{56})$	$621(E)$	$617(E)$		$510(A_1)$
	11014	11005	11004			–	$647(A_1)$		
			(Γ_{56})			–			

4. CALCULATION OF THE ENERGY SPECTRUM USING THE CRYSTAL-FIELD THEORY

The effective Hamiltonian of a RE ion in a D_{3d} symmetry crystal field can be written as

$$H_{CF} = B_0^2 C_0^{(2)} + B_0^4 C_0^{(4)} + B_0^6 C_0^{(6)} + B_3^4 (C_3^{(4)} - C_{-3}^{(4)}) + B_3^6 (C_3^{(6)} - C_{-3}^{(6)}) + V_6^6 (C_6^{(6)} + C_6^{(6)}) \quad (1)$$

This Hamiltonian contains six independent nonzero parameters B_q^k ($C_q^{(k)}$ are spherical tensor operators). In order to estimate the CF parameters, we use the exchange-charge model (ECM) [14], in which

$$B_q^k = B_q^{(\mathrm{el})k} + B_q^{(\mathrm{ex})k}, \quad (2)$$

where $B_q^{(\mathrm{el})k}$ and $B_q^{(\mathrm{ex})k}$ are the contributions from the electrostatic field of the lattice and from exchange charges, respectively. When calculating $B_q^{(\mathrm{el})k}$, we take into account screening [15] and the spatial distribution of the ligand charges [16]. The potential produced by the exchange charges is found as a linear combination of the squares of the overlap integrals S_s, S_σ, and S_π of the RE-ion 4f orbitals and the 2s and 2p orbitals of the nearest neighbor oxygen ions, which determine the exchange effectiveness [14]:

$$S_k(R_L) = G_s[S_s(R_L)]^2 + G_\sigma[S_\sigma(R_L)]^2 + [2 - k(k+1)/12] G_\pi [S_\pi(R_L)]^2. \quad (3)$$

Here, R_L is the distance from the RE ion to a ligand and G_s, G_σ, and G_π are phenomenological ECM parameters. The overlap integrals are calculated using the radial wave functions taken from [17] (for the 4f orbitals of RE ions) and [18] (for O^{2-} ions). The ECM parameters are significantly different for the two nonequivalent oxygen-ion positions O1 and O2 (Fig. 2a): $G_\sigma = G_s = G_\pi = 13.5$ for O1, and $G_\sigma = G_s = G_\pi/0.8 = 20$ for O2. These values are obtained using relations between the parameters G_α found earlier [14, 19] and the data on the CF parameters for $Ho_2Ti_2O_7$ [5] and on the ECM parameters for Yb^{3+} in $Yb_3Al_5O_{12}$ [20].

The CF parameters found within the exchange-charge model are then varied to attain the best fit of the eigenvalues of Hamiltonian (1) to the experimental energy levels of Yb^{3+} in $Yb_2Ti_2O_7$. Based on the results of calculations for $Yb_2Ti_2O_7$, we also determined the CF parameters for $Tb_2Ti_2O_7$, $Er_2Ti_2O_7$, $Ho_2Ti_2O_7$, and $Tm_2Ti_2O_7$. The values of the CF parameters obtained using the variation procedure are listed in Table 2. Note that the dependence of the CF parameters on the ionic radius of a RE ion and on the distance to the nearest neighbor ligands is found to be almost monotonic. The energy levels and g factors calculated with these CF parameters are compared with experimental data in Table 1.

The calculated wave functions of the Yb^{3+} ion in a crystal field are used to determine the electric-field gradient at the ^{172}Yb nucleus sites in $Yb_2Ti_2O_7$ as a function of temperature. The results agree well with experi-

Table 2. Crystal-field parameters B_p^k (cm^{-1}) and the bond lengths (nm) between the rare-earth ion and the nearest neighbor oxygen ions [R(RE–O1) = R_1, R(RE–O2) = R_2] in rare-earth titanates $R_2Ti_2O_7$

		B_0^2	B_0^4	B_0^6	B_3^4	B_3^6	B_6^6	$R1$	$R2$
$Tb_2Ti_2O_7$		440	2535	850	735	–630	850	0.2194	0.2496
$Ho_2Ti_2O_7$	[5]	550 ± 18	2216 ± 14	701 ± 7	675 ± 9	–504 ± 5	819 ± 9		
	ECM	552	2476	782	700	–583	845	0.2187	0.2489
		532	2475	805	716	–596	838		
$Er_2Ti_2O_7$		534	2524	748	698	–521	755	0.2182	0.2488
$Tm_2Ti_2O_7$		540	2510	850	670	–505	775	0.2179	0.2474
$Yb_2Ti_2O_7$	[10]	539	569	1568	916	–510	790	0.2172	0.2454
	ECM	590	2186	822	611	–498	701	0.2187	0.2477
($Y_2Ti_2O_7 : Yb^{3+}$)		546	2540	840	602	–462	757		

mental data [10]. The calculated relative intensities of magnetic-dipole transitions in the transmission spectrum (1 : 0.171 : 0.298) are in reasonable agreement with the experimental integrated intensities of the zero-phonon lines (1 : 0.09 : 0.22; Fig. 3).

5. CONCLUSIONS

Thus, we have measured the absorption spectra of $Yb_2Ti_2O_7$ and the luminescence spectra of $Y_2Ti_2O_7 : Yb^{3+}$ (1%). The results have been used to find the energy levels of the $4f^{13}$ configuration of the Yb^{3+} ion in the pyrochlore-structure titanates. It has been found that, in the absorption and luminescence spectra, the zero-phonon lines are comparable in intensity to their phonon wings, which is evidence of strong electron–phonon coupling in $Yb_2Ti_2O_7$. The energy levels and g factors have been calculated for titanates $Yb_2Ti_2O_7$, $Y_2Ti_2O_7$: Yb, $Tb_2Ti_2O_7$, $Er_2Ti_2O_7$, $Ho_2Ti_2O_7$, and $Tm_2Ti_2O_7$ using a variation procedure for the CF parameters initially calculated within the exchange-charge model. The results agree with the experimental data obtained in this work and that available in the literature.

ACKNOWLEDGMENTS

This study was supported by the Russian Foundation for Basic Research (project nos. 04-02-17346, 03-02-16449), the Presidium of the Russian Academy of Sciences (program "Quantum Macroscopic Physics"), and the Department of Physical Sciences of the Russian Academy of Sciences (program "Strongly Correlated Electrons in Semiconductors, Metals, Superconductors, and Magnetic Materials").

REFERENCES

1. O. Knop, F. Brisse, and L. Castelliz, Can. J. Chem. **47**, 971 (1969).
2. S. T. Bramwell, M. J. Harris, B. C. Den Hertog, M. J. P. Gingras, J. S. Gardner, D. F. McMorrow, A. R. Wildes, A. L. O. Cornelius, J. D. M. Champion, R. G. Melko, and T. Fennell, Phys. Rev. Lett. **87** (4), 047205 (2001).
3. A. P. Ramirez, A. Hayashi, R. J. Cava, R. Siddharthan, and B. S. Shastry, Nature **399**, 333 (1999).
4. M. J. P. Gingras, B. C. Den Hertog, M. Faucher, J. S. Gardner, S. R. Dunsiger, L. J. Chang, B. D. Gaulin, N. P. Raju, and J. E. Greedan, Phys. Rev. B **62** (10), 6496 (2000).
5. S. Rosenkranz, A. P. Ramirez, A. Hayashi, R. J. Cava, R. Siddharthan, and B. S. Shastry, J. Appl. Phys. **87** (9), 5914 (2000).
6. J. S. Gardner, B. D. Gaulin, A. J. Berlinsky, P. Waldron, S. R. Dunsiger, N. P. Raju, and J. E. Greedan, Phys. Rev. B **64** (22), 224 416 (2001).
7. J. S. Gardner, S. R. Dunsiger, B. D. Gaulin, M. J. P. Gingras, J. E. Greedan, R. F. Kiefl, M. D. Lumsden, W. A. MacFarlane, N. P. Raju, J. E. Sonier, I. Swainson, and Z. Tun, Phys. Rev. Lett. **82** (5), 1012 (1999).
8. J. D. M. Champion, M. J. Harris, P. C. W. Holdsworth, A. S. Wills, G. Balakrishnan, S. T. Bramwell, E. Cizmar, T. Fennell, J. S. Gardner, J. Lago, D. F. McMorrow, M. Orendac, A. Orendacova, D. McK. Paul, R. I. Smith, M. T. F. Telling, and A. Wildes, Phys. Rev. B **68** (2), 020401 (2003).
9. A. Sengupta, J. Jana, and D. Ghosh, J. Phys. Chem. Solids **60**, 331 (1999).
10. J. A. Hodges, P. Bonville, A. Forget, M. Rams, K. Krolas, and G. Dhalenne, J. Phys.: Condens. Matter **13**, 9301 (2001).
11. G. H. Dieke, *Spectra and Energy Levels of Rare Earth Ions in Crystals* (Interscience, New York, 1968).
12. M. T. Vandemborre, E. Husson, J. P. Chatry, and D. Michel, J. Raman Spectrosc. **14** (2), 63 (1983).

13. E. Antic-Fidancev, J. Holsa, and M. Lastusaari, J. Phys.: Condens. Matter **15**, 863 (2003).
14. B. Z. Malkin, in *Spectroscopy of Solids Containing Rare Earth Ions*, Ed. by A. A. Kaplyanskiĭ and R. M. Macfarlane (North-Holland, Amsterdam, 1987), Chap. 2.
15. R. P. Gupta and S. K. Sen, Phys. Rev. A **7** (3), 850 (1973).
16. D. Garcia and M. Faucher, Phys. Rev. B **30** (4), 1703 (1984).
17. A. J. Freeman and R. E. Watson, Phys. Rev. **127** (6), 2058 (1962).
18. E. Clementi and A. D. McLean, Phys. Rev. **133** (2A), A419 (1964).
19. M. Faucher, D. Garcia, and C. K. Jørgensen, Chem. Phys. Lett. **129**, 387 (1986).
20. G. A. Bogomolova, L. A. Bumagina, A. A. Kaminskii, and B. Z. Malkin, Sov. Phys. Solid State **19**, 1428 (1977).
21. R. Siddharthan, B. S. Shastry, A. P. Ramirez, A. Hayashi, R. J. Cava, and S. Rosenkranz, Phys. Rev. Lett. **83** (9), 1854 (1999).

Translated by Yu. Epifanov

Physics of the Solid State, Vol. 47, No. 8, 2005, pp. 1431–1435. Translated from Fizika Tverdogo Tela, Vol. 47, No. 8, 2005, pp. 1381–1385.
Original Russian Text Copyright © 2005 by Nikiforov, Zakharov, Ugryumov, Kazanskiĭ, Ryskin, Shakurov.

PROCEEDINGS OF THE XII FEOFILOV WORKSHOP "SPECTROSCOPY OF CRYSTALS ACTIVATED BY RARE-EARTH AND TRANSITION-METAL IONS"

(Yekaterinburg, Russia, September 22–25, 2004)

Crystal Fields of Hexameric Rare-Earth Clusters in Fluorites

A. E. Nikiforov*, A. Yu. Zakharov*, M. Yu. Ugryumov*, S. A. Kazanskiĭ,**
A. I. Ryskin, and G. S. Shakurov*****
** Ural State University, pr. Lenina 51, Yekaterinburg, 620083 Russia*
e-mail: Anatoliy.Nikiforov@usu.ru
*** Vavilov State Optical Institute, St. Petersburg, 199034 Russia*
**** Zavoĭskiĭ Physicotechnical Institute, Kazan Scientific Center, Russian Academy of Sciences,*
Sibirskiĭ trakt 10/7, Kazan 29, 420029 Tatarstan, Russia

Abstract—In solid solutions of alkaline- and rare-earth fluorides with a fluorite structure, ions of most elements of the rare-earth (RE) row form hexameric clusters that assimilate the minor component of the solid solutions (fluorine) and build it into the cubic fluorite lattice without changing its shape. An analysis of the EPR spectra of paramagnetic RE ions (Er^{3+}, Tm^{3+}, Yb^{3+}) in clusters of diamagnetic ions (Lu^{3+}, Y^{3+}) confirms their hexagonal structure, which was established when studying the superstructures of the compounds under study. In such a cluster, a RE ion is in a nearly tetragonal crystal field, with the parameters of this field differing radically from those of single cubic and tetragonal RE centers in crystals with a fluorite structure. In particular, this field causes high (close to limiting) values of the $g_{\|}$ factors of the ground states of the paramagnetic RE ions. Computer simulation is used to determine the atomic structure of a hexameric cluster in MF_2 crystals (M = Ca, Sr, Ba). The crystal field and energy spectrum of Er^{3+}, Tm^{3+}, and Yb^{3+} ions in such clusters are calculated, and the spectroscopic parameters of the ground states of these ions are determined. The calculations confirm the earlier assumption that the unusual EPR spectra of nonstoichiometric fluorite phases are related to RE ions in hexameric clusters. *© 2005 Pleiades Publishing, Inc.*

1. INTRODUCTION

Crystals of alkaline-earth fluorides have a simple cubic fluorite lattice, which can be represented as an infinite sequence of fluorine cubes where half the central positions are occupied by cations. These crystals can easily be activated by trivalent rare-earth (RE) ions (lanthanides, Ln) and yttrium [1]. Ln (Y) ions occupy the normal cation position, and the excess charge (+1) of the impurity is compensated for by additional F^- ions situated in interstices of the anion sublattice. At low activator concentrations (~0.01 mol % or less), simple centers with local (Ln^{3+}–F^-, tetragonal and/or trigonal centers) and nonlocal (Ln^{3+}, cubic center) charge compensation form in the fluorite lattice. At a high concentration, clusters of Ln^{3+} and F^- ions form [1].

Based on neutron scattering [2, 3] and EXAFS [4, 5] data, researchers have proposed more than 20 models for clusters of several (two to six or more) Ln ions, vacancies, and interstitials. The possible realization of these models has been confirmed by calculations [3–5]. However, it should be noted that, in essence, most of these models are based on indirect experimental data.

The most reliable structural information has been obtained for hexameric clusters. With x-ray diffraction, Fedorov *et al.* [6] showed that, under special synthesis conditions, nonstoichiometric fluorite-like solid solutions exhibit superstructure ordering. The main statistical motif of these superstructures is an R_6F_{37} cluster, which is actually identical to the M_6F_{32} building block (M = Ca, Sr, Ba) of the fluorite lattice in terms of both volume and shape and, hence, can easily penetrate into the lattice.

Direct information on the structure of impurity centers in crystals can be obtained with electron paramagnetic resonance (EPR). However, RE ions in clusters were not detected earlier by traditional EPR methods [1]. Using optical detection to fix the circular dichroism of the optical absorption spectra of RE ions, the authors of [7–9] could observe unusual EPR spectra of Er^{3+}, Tm^{3+}, and Yb^{3+} ions in $M_{1-x}Ln_xF_{2+x}$ (Ln = Lu, Y; M = Ca, Sr, Ba) solid solutions. Studies have shown that, over the entire solid-solution range, the symmetry of the crystal field (CF) at a RE ion site is close to tetragonal. The paramagnetic ions under study have the highest principal value of the $g_{\|}$ tensor (which is comparable to the theoretical limit), and $g_{\perp} \approx 0$ for them. Moreover, the EPR spectrum of non-Kramers Tm^{3+} ions was detected in those studies for the first time. Based on the spectrum symmetry and an analysis of the structures of the ordered phases characteristic of solid solutions of ions from the second half of the RE row, the authors of [7–9] attributed the anomalous EPR spectra to para-

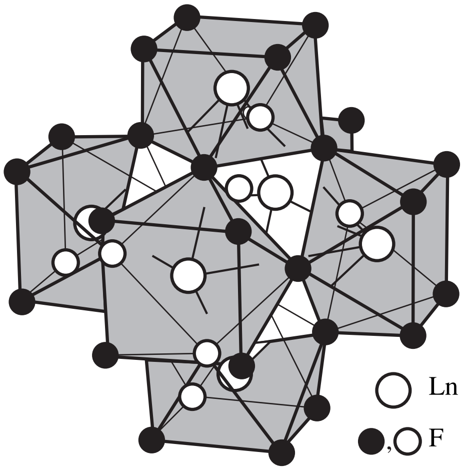

Fig. 1. R_6F_{37} hexameric cluster with an inner F_{12+1} cuboctahedron that substitutes for the M_6F_{32} building block (inner fluorine cube) of the fluorite lattice.

magnetic ions located in hexameric clusters formed by diamagnetic Ln^{3+} and Y^{3+} ions. These clusters contain an F^{12} cuboctahedron made of twelve F^- anions with one F^- ion inside. The cuboctahedron is surrounded by six square antiprisms, and the six Ln (Y) ions that form the octahedron are located at their centers (Fig. 1).

In this work, we study Tm^{3+} ions in these clusters using traditional EPR in the *Q* range and EPR at high frequencies (65–100 GHz). For this purpose, a spectrometer is used that has a quasi-optical channel for recording microwave radiation absorption. Moreover, we calculate the ground-state parameters for all three paramagnetic RE ions (Er^{3+}, Tm^{3+}, Yb^{3+}) in an R_6F_{37} cluster. The calculations confirm the assumption that the anomalous EPR spectra belong to the paramagnetic ions located in the cluster.

2. EPR SPECTRUM OF A Tm^{3+} ION IN HEXAMERIC CLUSTERS IN FLUORITE-TYPE CRYSTALS

The crystals to be studied were grown using the Bridgman–Stockbarger method in graphite crucibles in a setup with graphite heaters. To remove the traces of oxygen, the initial high-purity materials were calcined along with lead fluoride. The crystals grown did not exhibit absorption bands of oxygen or hydroxyl and did not have growth defects characteristic of oxygen contamination.

The EPR spectra of paramagnetic RE ions in diamagnetic-ion clusters were studied on an E-12 Varian spectrometer (*Q* band; microwave-field frequency, ~37 GHz) and on a spectrometer with a quasi-optical channel for recording microwave radiation absorption [10] in the frequency range 65–100 GHz.

We reliably detected EPR spectra from RE clusters only in thulium-containing samples. To measure spectra with a Varian spectrometer, we used the following crystals: CaF_2 : (1 mol % Y, 0.05 mol % Tm) and CaF_2 : (5 mol % Y 0.1 mol % Tm). The samples under study were 4 × 2 × 0.5 mm in size. The EPR signals were the most intense for parallel polarization of the static and microwave magnetic fields.

We measured the dependences of the resonance frequencies on magnetic field for the $\mathbf{B}_0 \parallel [001]$ orientation on a quasi-optical spectrometer for the following crystals: CaF_2 : (1 mol % Y, 0.05 mol % Tm) and SrF_2 : (3 mol % Lu, 0.1 mol % Tm). Since this spectrometer had no resonator, the samples must have large sizes for EPR to be recorded. The usual sample dimensions were 10 × 10 × 10 mm, which results in a substantially increased number of microblocks. However, the angular dependence of the EPR spectra is weak for the $\mathbf{B}_0 \parallel [001]$ orientation and spectra taken from different blocks merge to form one line.

The results obtained for crystals with Tm^{3+} are interpreted under the assumption that the ground-state non-Kramers doublet is sufficiently remote from the other excited levels. In this case, the behavior of the non-Kramers doublet in a magnetic field is described by only one factor $g_{\parallel}$ ($g_{\perp} = 0$) [11]. The effective spin Hamiltonian of a system consisting of one electron spin ($S = 1/2$) and one nuclear spin ($I = 1/2$) in a magnetic field has the form

$$H = \Delta S_x + g_{\parallel}\mu_B S_Z B_{0Z} + A S_Z I_Z, \qquad (1)$$

where Δ is the initial splitting and A is the hyperfine interaction constant of a Tm^{3+} ion ($A = 0.1550(\pm 0.002)$ cm^{-1}).

The resonance frequency is

$$\nu_M = [(g_{\parallel}\mu_B B_{0Z} + Am)^2 + \Delta^2]^{1/2}/h, \qquad (2)$$

where $m = \pm 1/2$ is the projection of the nuclear spin.

The EPR spectra of Tm^{3+} ions consist of relatively narrow lines forming characteristic doublets due to hyperfine interaction. The distance between doublet components is approximately constant and equal to the hyperfine interaction constant in units of the magnetic field $\mathbf{B}_0 \parallel C_4$ (Fig. 2). The EPR spectra of Tm^{3+} ions in clusters can contain both a single doublet and a few closely or widely spaced doublets, depending on the host cation of the fluorite crystal (Ca, Sr, or Ba), the type of diamagnetic ions forming the clusters (Ln or Y), and the conditions of crystal growth. The presence of a few doublets indicates a scatter of the initial splittings of the ground state of the non-Kramers Tm^{3+} ion in a zero magnetic field.

The spectroscopic parameters measured by optically detected EPR [7–9] and by traditional EPR are given in the table.

3. CRYSTAL FIELD AND SPECTROSCOPIC PARAMETERS OF THE GROUND STATES OF RE IONS IN HEXAMERIC CLUSTERS

When an R_6F_{37} cluster forms, the crystal structure changes substantially both inside the cluster and fairly far from it in the crystalline matrix. The ions in a cluster are in low-symmetry positions, which leads to the appearance of dipole moments. Thus, a preliminary stage of calculating the CF at a RE ion site is the self-consistent determination of the coordinates and dipole moments of ions in the large crystal region around the cluster. To calculate the atomic structure of hexameric clusters in MF_2 crystals (M = Ca, Sr, Ba), we used the embedded-cluster method within the shell model in the pair-potential approximation [12–14]. The center of the defect region was taken to be an interstice occupied by the central fluorine ion. The equilibrium positions of the ion cores and shells in the defect region were found by minimizing the crystal energy. In the shell model in the pair-potential approximation, the energy of the crystal lattice with an embedded cluster is

$$E = 1/2\sum_i \sum_{j(\neq i)} V_{ij} + 1/2\sum_i k_i l_i^2, \qquad (3)$$

where the first term takes into account the interaction of ion pairs and the second term is the interaction energy between the core and shell of an individual ion (l_i is the shell shift of the ith ion with respect to its core). The pair potential V_{ij} includes the Coulomb interaction, Born–Mayer repulsion, and van der Waals attraction between the ith and jth ions. The R–F potentials for all the RE ions under study were approximated by the Gd^{3+}–F^- potential. The pair-potential parameters were taken from [13].

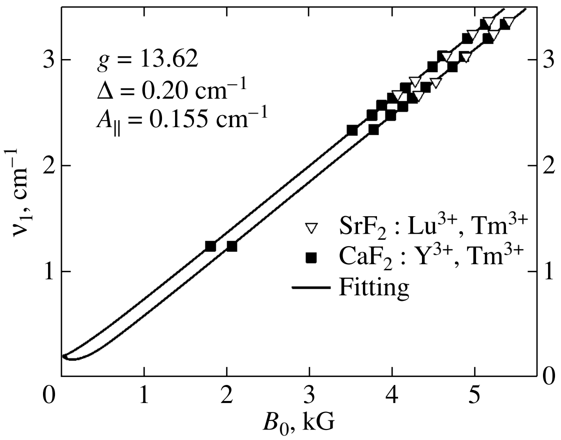

Fig. 2. Effect of an applied magnetic field B_0 on the resonance frequency of the Tm^{3+} doublet in crystals CaF_2 : (1 mol % Y, 0.05 mol % Tm) and SrF_2 : (3 mol % Lu, 0.1 mol % Tm).

Experimental values of the spectroscopic parameters of the ground states of paramagnetic Er^{3+}, Tm^{3+}, and Yb^{3+} ions in clusters of diamagnetic Lu^{3+} and Y^{3+} ions in fluorite-type crystals and the calculated values of these parameters for LnR_6F_{37} (Ln = Er^{3+}, Tm^{3+}, Yb^{3+}) clusters in these crystals

Ion	Crystal	Ground state	$g_\parallel^{lim}$	Experimental values		Calculated values	
				$g_\parallel$	δ, cm^{-1}	$g_\parallel$	δ, cm^{-1}
Er^{3+}	CaF_2	±15/2	18	15.5 ± 0.3*	–	17.9	–
	SrF_2			16 ± 0.5*	–	17.9	–
	BaF_2			17.2 ± 0.3*	–	18.0	–
Tm^{3+}	CaF_2	±6	14	13.62 ± 0.03**	δ_1 = 0.20 ± 0.07**	13.8	0.9
				13.8 ± 0.3*	δ_1 = 0.3 ± 0.1*		
					δ_2 = 2 ± 1*		
	SrF_2			13.62 ± 0.03**	δ_1 = 0.20 ± 0.07**	13.8	2.2
				13.8 ± 0.3*	δ_1 = 0.3 ± 0.2*		
					δ_2 ≥ 1*		
	BaF_2			13.8 ± 0.3*	0.2 ± 0.1*	13.8	1.9
Yb^{3+}	GaF_2			6.8 ± 0.2*	–	8.0	–
	SrF_2	±7/2	8	Experimentally undetected	–	7.9	–
	BaF_2			The same	–	7.9	–

*Optically detected EPR results (ν_1 = 36 GHz) for solid solutions over a wide range (y = 0.001–0.4) [9].

**EPR data (ν_1 = 37–100 GHz) for CaF_2 : (1 mol % Y, 0.05 mol % Tm).

***EPR data (ν_1 = 37–100 GHz) for SrF_2 : (3 mol % Lu, 0.1 mol % Tm).

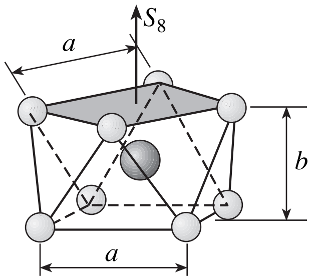

Fig. 3. Nearest symmetric environment of a RE ion in a hexameric cluster.

Our calculations show that it is sufficient to consider a defect region consisting of 12–14 coordination shells (~250 ions). In all MF_2 crystals (M = Ca, Sr, Ba), relaxation results in the formation of a stable configuration of the R_6F_{37} cluster and surrounding ions. As a result of relaxation, the F_{12} cuboctahedron increases in size and is attracted to R_6. Weak distortions in the structure are observed as far away as the defect-region boundary (~12 coordination shells of the center of the cluster), and the strongest dipole moments are induced on the fluorine ions.

For further analysis, the structure of the nearest environment of a RE ion in the hexameric cluster is particularly important. When the cluster forms, the fluorine cube surrounding an M ion in the fluorite structure transforms into a square antiprism with a different base area and with the C_{4v} local symmetry of the CF at the RE ion site (Fig. 1). The nearest symmetric environment is a regular antiprism with identical bases and a RE ion at its center. In this case, the symmetry of the local environment of the RE ion is D_{4d} with an eightfold reflection axis (Fig. 3). Therefore, the CF should have axial symmetry, which can only be violated by antiprism distortions. The antiprism local environment of a RE ion in the hexameric cluster gives rise to a substantial difference between the CFs in the cluster and in a simple tetragonal center (which also has C_{4v} symmetry), where the nearest neighbor symmetrical configuration is a fluorine cube. The Hamiltonian of the interaction between the RE ion and the CF has the form

$$H = \sum_{p = 2, 4, 6} \sum_{q} B_{pq} O_p^q = \sum_{p = 2, 4, 6} \alpha_p \sum_{q} B_p^q Q_p^q, \qquad (4)$$

where α_p are the Stevens parameters; O_p^q are equivalent operators, whose tabulated matrix elements can be found in [15]; and B_p^q are the CF parameters that determine the interaction between the 4f electrons of the RE ion and its crystalline environment.

In this work, we use the exchange charge model (ECM) [16–18], which includes the long-range contributions to the CF coming both from point charges and dipoles and from the nonorthogonality of the wave functions of the 4f electrons and ligands. The parameters B_p^q contain the electrostatic and exchange contributions. The ECM parameters for Er^{3+}, Tm^{3+}, and Yb^{3+} ions are taken from [17, 18].

Let us analyze in more detail the case where a Tm^{3+} ion is in CaF_2. The $^3H_6$ ground state is split in the axial field of the regular compressed antiprism (a = 3.07 Å, b = 2.07 Å; $b < a$) (B_2^0 = –561.27, B_4^0 = –69.01, B_6^0 = 27.17) to form Kramers doublets ($\pm M$) and one singlet (M = 0). The ground-state doublet $|\pm 6\rangle$ is 381.7 cm^{-1} from the next doublet; therefore, the criterion for applicability of the spin Hamiltonian (1) is well satisfied.

The ground-state doublet is then split by the tetragonal CF component (B_2^0 = –438.71, B_4^0 = –47.40, B_4^4 = 544.55, B_6^0 = 19.19, B_6^4 = –184.61) caused both by the distortion of the local environment (due to the different bases of the antiprism and a shift of the RE ion from the center) and by the CF contribution from the rest of the crystal. The ground level becomes a singlet with wave function $\psi_1 = 0.701(|-6\rangle - |6\rangle) + 0.072(|2\rangle - |-2\rangle)$, and the nearest excited state is a singlet with wave function $\psi_2 = 0.701(|6\rangle + |-6\rangle) - 0.072(|2\rangle + |-2\rangle)$ and energy $\Delta = 0.9$ cm^{-1}. Magnetic dipole transitions (which are detected with EPR) can occur between the singlets. Calculations of the g factors for the singlets with the wave functions ψ_1 and ψ_2 give $g_{\|} = 13.8$ and $g_{\perp} = 0$.

As follows from calculations of the Tm^{3+} spectrum, the ground level in either cubic or tetragonal simple centers is a singlet with an excited state spaced far away; therefore, we failed to detect EPR spectra from simple centers in the fluorites.

For the Er^{3+} and Yb^{3+} ions with an odd number of f electrons, the lower levels are found to be doublets with maximum projections, ±15/2 and ±7/2; for them, the principal value of the g factor is close to the maximum values of $g_{\|}$ (18 and 8, respectively) and $g_{\perp} = 0$. The calculated spectroscopic parameters for the Er^{3+}, Tm^{3+}, and Yb_{3+} ions in hexameric clusters in CaF_2, SrF_2, and BaF_2 crystals are given in the table.

4. CONCLUSIONS

We have discussed the experimental EPR spectra of ions of the elements from the second half of the rare-earth (RE) row (Er–Lu, Y). It has been shown that the study of the EPR spectra and their theoretical analysis can successfully be applied to determine the structures of random crystalline media, nonstoichiometric fluorite phases. The EPR lines of all RE ions except Tm^{3+} are found to be broad. Here, it is helpful to use an EPR method where a signal is optically detected using magnetic circular dichroism in the absorption bands of RE ions in solid solutions. It has been found that, over the entire range of solid solutions, the symmetry of the RE ions in clusters is nearly tetragonal and the crystal field is anomalous. This behavior results in the highest (comparable to the theoretical limit) principal values of the *g* tensor for the paramagnetic ions under study and in the appearance of the EPR spectrum from non-Kramers Tm$_{3+}$ ions, which was not detected earlier in fluorite-type crystals.

Using computer simulation, we have determined the atomic structure of an R_6F_{37} hexagonal cluster in crystals and calculated the crystal field and the energy spectrum of Er^{3+}, Tm^{3+}, and Yb^{3+} ions in such clusters. The calculations confirmed the earlier assumption that the unusual EPR spectra of nonstoichiometric fluorite phases are related to RE ions in hexameric clusters.

ACKNOWLEDGMENTS

This work was supported by the Russian Foundation for Basic Research (project no. 04-02-16427) and CRDF (grant REC-005 (EK-005-XI)).

REFERENCES

1. *Crystals with the Fluorite Structure*, Ed. by W. Hayes (Clarendon, Oxford, 1974).
2. J. P. Laval, A. Mikon, and B. Frit, Solid State Ionics **28–30**, 1300 (1988).
3. C. R. A. Catlow, A. V. Chadwick, and J. Corish, J. Solid State Chem. **48**, 65 (1983).
4. C. R. A. Catlow, A. V. Chadwick, J. Corish, L. M. Moroney, and A. N. O. Relly, Phys. Rev. B **39**, 1897 (1989).
5. C. R. A. Catlow, A. V. Chadwick, C. N. Jacobs, and S. H. Ong, Phys. Rev. B **25**, 6425 (1982).
6. P. P. Fedorov, O. E. Izotova, V. B. Alexandrov, and B. P. Sobolev, J. Solid State Chem. **9**, 368 (1974).
7. S. A. Kazanskiĭ, Pis'ma Zh. Éksp. Teor. Fiz. **38**, 430 (1983) [JETP Lett. **38**, 521 (1983)].
8. S. A. Kazanskiĭ, Zh. Eksp. Teor. Fiz. **89** (4), 1258 (1985) [Sov. Phys. JETP **62** (4), 727 (1985)].
9. S. A. Kazanskiĭ and A. I. Ryskin, Fiz. Tverd. Tela (St. Petersburg) **44** (8), 1356 (2002) [Phys. Solid State **44** (8), 1415 (2002)].
10. V. F. Tarasov and G. S. Shakurov, Appl. Magn. Reson. **2** (3), 571 (1991).
11. J. M. Griffith, Phys. Rev. **132**, 316 (1963).
12. C. R. A. Catlow, M. Dixon, and W. C. Mackrodt, *Computer Simulation of Solids*, Ed. by C. R. A. Catlow and W. C. Mackrodt (Springer, Berlin, 1982).
13. V. A. Chernyshev, A. D. Gorlov, A. A. Mekhonoshin, A. E. Nikiforov, A. I. Rokeakh, S. Yu. Shashkin, and A. Yu. Zaharov, Appl. Magn. Reson. **14** (1), 37 (1998).
14. A. E. Nikiforov, A. Yu. Zakharov, and V. A. Chernyshev, Fiz. Tverd. Tela (St. Petersburg) **46**, 9 (2004) [Phys. Solid State **46**, 1639 (2004)].
15. S. A. Al'tshuler and B. V. Kozyrev, *Electron Paramagnetic Resonance in Compounds of Transition Elements* (Nauka, Moscow, 1972) [in Russian].
16. B. Z. Malkin, in *Spectroskopy of Solids Containing Rare-Earth Ions*, Ed. by A. A. Kaplyanskiĭ and R. M. Macfarlane (North-Holland, Amsterdam, 1987), p. 13.
17. L. A. Bumagina, B. N. Kazakov, B. Z. Malkin, and A. L. Stolov, Fiz. Tverd. Tela (Leningrad) **19**, 1073 (1977) [Sov. Phys. Solid State **19**, 624 (1977)].
18. M. P. Davydova, B. N. Kazakov, and A. L. Stolov, Fiz. Tverd. Tela (Leningrad) **20**, 2391 (1978) [Sov. Phys. Solid State **20**, 1378 (1978)].

Translated by K. Shakhlevich

Physics of the Solid State, Vol. 47, No. 8, 2005, pp. 1436–1438. Translated from Fizika Tverdogo Tela, Vol. 47, No. 8, 2005, pp. 1386–1388.
Original Russian Text Copyright © 2005 by Potapov, Rodnyĭ, Mikhrin, Magunov.

PROCEEDINGS OF THE XII FEOFILOV WORKSHOP “SPECTROSCOPY OF CRYSTALS ACTIVATED BY RARE-EARTH AND TRANSITION-METAL IONS”

(Yekaterinburg, Russia, September 22–25, 2004)

Praseodymium Luminescence in Fluorides

A. S. Potapov*, P. A. Rodnyĭ*, S. B. Mikhrin*, and I. R. Magunov**
**St. Petersburg State Polytechnic University, ul. Politekhnicheskaya 25, St. Petersburg, 195251 Russia*
e-mail: potapov@tuexph.stu.neva.ru
***Physicochemical Institute, National Academy of Sciences of Ukraine, Odessa, 65080 Ukraine*

Abstract—This work is a continuation of studies of the Pr^{3+} cascade emission in various matrices. The effect of the environment of the luminescence center on the mutual position of the lowest 5*d* and the 4*f* level $^1S_0$ of Pr^{3+} is considered. PrF_3 clustering in BaF_2 is observed at a high praseodymium concentration. The promising potential of magnesium as a charge compensator for praseodymium in $SrAlF_5$ is demonstrated. *© 2005 Pleiades Publishing, Inc.*

1. INTRODUCTION

Considerable attention is currently being focused on ecological problems and energy-saving technologies, including the development of environmentally friendly materials and new approaches to reducing power consumption in domestic appliances. This accounts for the increasing interest in luminophors that exhibit cascade emission of photons (CPE). These luminophors are capable of producing one photon (ideally two photon) in the visible range for each absorbed VUV photon. In many present gas discharge devices (mercury-free luminescent lamps, plasma display panels), VUV light is generated in a Ne–Xe discharge plasma. The radiation intensity of this plasma is maximum at 170 nm. The excitation (and absorption) spectrum of the Pr^{3+} ion overlaps the emission spectrum of a Ne–Xe plasma [1], and the Pr^{3+} level diagram is convenient for producing CPE. The cascade emission in Pr^{3+} consists of two consecutive radiative transitions: $^1S_0 \longrightarrow {}^1I_0$ (the first stage of the cascade) and $^3P_0 \longrightarrow {}^3F_J$, ^3H_J (the second stage). About 20 luminophors capable of cascade emission have recently been discovered (see, e.g., [2–4]). To facilitate searching for new CPE luminophors, a system of requirements for matrices favoring the onset of cascade emission has been developed [5]. The main requirement set for matrices to produce $^1S_0$ luminescence is a weak crystal field that which would provide a higher position of the lower 5*d* level relative to the 4*f* level $^1S_0$ of the praseodymium ion. To meet this requirement, the matrix should possess the following properties: a large ionic radius of the substituted cation, a large Pr^{3+} anion distance, a high coordination number of the substituted cation, low anisotropy of the emitting center, high anion electronegativity, and a large charge and small ionic radius of a cation in the second coordination shell. These rules are actually not rigorous. For instance, the Ba^{2+} ion has a larger ionic radius than Sr^{2+}. However, strontium is preferable to barium for substitution by praseodymium, because the ionic radius of strontium is closer to that of Pr^{3+}. The second stage in CPE requires for its onset that two additional conditions be met, namely, a low phonon energy in the matrix as compared to the energy spacing between the 4*f* levels of the praseodymium ion and a relatively low activator concentration.

In this communication, we consider the influence of various factors on the CPE efficiency in the particular examples of BaF_2 : Pr and $SrAlF_5$: Pr.

2. EXPERIMENTAL CONDITIONS

BaF_2 : Pr crystals were grown using the Stockbarger method at the Vavilov State Optical Institute. We studied single crystals of undoped barium fluoride and of barium fluoride activated by 0.3 and 3% praseodymium.

$SrAlF_5$: Pr samples were obtained through solid-phase synthesis at the Physicochemical Institute, National Academy of Ukraine, by calcining carefully prepared mixtures of strontium and aluminum fluorides. The polycrystalline samples thus produced were subjected to x-ray structural analysis. The samples used in subsequent measurements were all single-phase.

Luminescence spectra were measured on a setup with cw x-ray excitation (U = 40 kV, I = 14 mA) [6]. The luminescence kinetics curves were measured on a setup with pulsed x-ray excitation (pulse duration $\tau \approx$ 1 ns, U = 30 kV) [7].

3. EXPERIMENTAL RESULTS

Figure 1 displays the luminescence spectra of barium fluoride, more specifically, of an undoped crystal

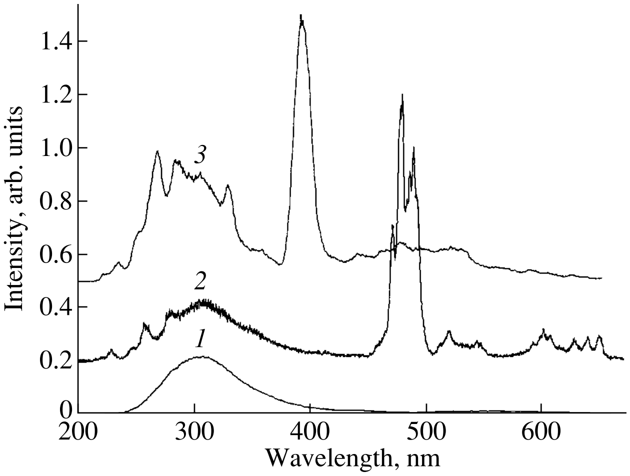

Fig. 1. Luminescence spectra of (*1*) undoped barium fluoride, (*2*) BaF_2 : Pr(0.3%), and (*3*) BaF_2 : Pr(3%).

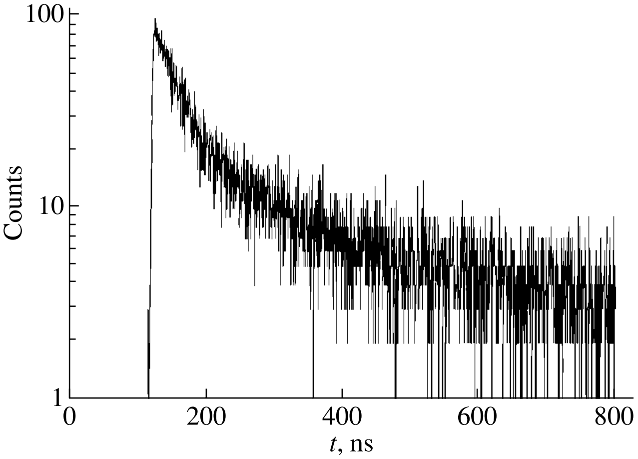

Fig. 2. Luminescence kinetics of BaF_2 : Pr(3%).

(curve *1*), a crystal doped with 0.3% praseodymium (curve *2*), and a crystal doped with 3% praseodymium (curve *3*). All spectra contain a broad band peaking at about 300 nm. In addition, the luminescence spectrum of BaF_2 : Pr(0.3%) features a strong line with a maximum at 480 nm and the luminescence spectrum of BaF_2 : Pr(3%) has a strong line peaking at 392 nm.

Figure 2 shows the luminescence kinetics of the BaF_2 : Pr(3%) sample obtained in a 800-ns time window. Two components can be isolated in the luminescence kinetics: a fast one with a decay constant of 39 ns and a slow one with a decay constant of 690 ns.

Shown in Fig. 3 are the luminescence spectra of $SrAlF_5$: Pr(0.5%) samples obtained with different charge compensators, namely, magnesium (Fig. 3a) and sodium (Fig. 3b). The emission line due to the $^3P_0 \longrightarrow {}^3H_4$ transition is seen to remain strong in both cases, while the efficiency of the first cascade stage turns out to be substantially higher in the case where magnesium is used as a charge compensator.

4. ANALYSIS OF THE EXPERIMENTAL DATA

A broad band peaking at about 300 nm is present in all three of the barium fluoride spectra (Fig. 1) and derives from intrinsic exciton luminescence. The decay constant of this luminescence is 680 ns (the slow component in Fig. 2), which fits the earlier data well [8].

Estimation of the mutual position of the lowest 5*d* and the 4*f* level $^1S_0$ of the Pr^{3+} ion in barium fluoride shows that the $^1S_0$ level overlaps with the 5*d* subband. Thus, the $^1S_0$ luminescence in praseodymium-doped barium fluoride should be quenched. This suggestion is strengthened by the shape of the BaF_2 : Pr(0.3%) luminescence spectrum (curve *2* in Fig. 1). A similar curve was obtained earlier [9]. To explain the presence of the line associated with $^1S_0 \longrightarrow {}^1I_0$ transitions in the BaF_2 : Pr(3%) spectrum (curve *2* in Fig. 1), we note that the luminescence of praseodymium in this material is similar to that in undoped PrF_3 [10].

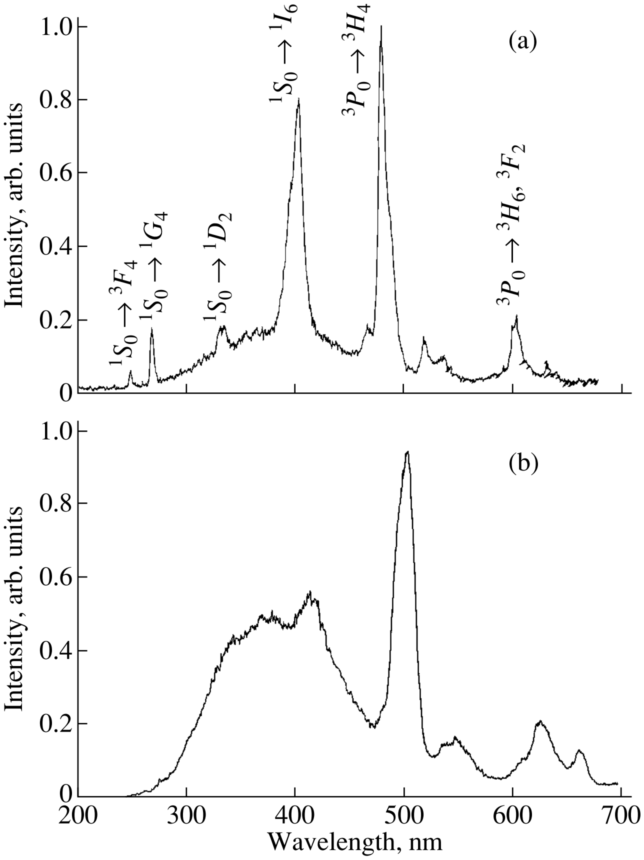

Fig. 3. Luminescence spectrum of $SrAlF_5$: Pr(0.5%) (a) with a Mg^{2+} charge compensator and (b) with a Na^+ charge compensator.

The praseodymium substituting for barium in barium fluoride is surrounded by eight fluorine ions. This small coordination number of praseodymium accounts for the CPE not being observed [5]. For CPE to be observed in fluorides, the coordination number of praseodymium should be no smaller than 9. Substitution of the trivalent praseodymium for the divalent barium requires charge compensation. Interstitial fluorine may act as such a charge compensator. In praseodymium fluoride, the cation is surrounded by nine anions. The similarity between the luminescence spectra of BaF_2 : Pr(3%) and PrF_3 gives us grounds to suggest that, in the presence of a high praseodymium concentration, barium fluoride undergoes local lattice rearrangement involving the formation of PrF_3 clusters. The formation of analogous clusters in $Me_{1-x}Ln_xF_{2+x}$ systems (Me = Ca, Sr, Ba; Ln is a lanthanide) was discussed in detail in [11]. This suggestion accounts for the absence of $^3P_0$ luminescence in BaF_2 : Pr(3%); namely, this luminescence in PrF_3 is quenched by cross relaxation. The presence of a fast component with τ = 39 ns in the luminescence kinetics of BaF_2 : Pr(3%) can be explained as being due to the partial admixture of 5*d* states to the $^1S_0$ state of the Pr^{3+} ion [12].

The luminescence lines of $SrAlF_5$: Pr turn out to be broader than those of other praseodymium-doped materials, which should be assigned to the fact that, in this material, there are four inequivalent positions for the praseodymium substituting for strontium [13]. In addition, the luminescence lines in the spectrum of $SrAlF_5$: Pr,Na (Fig. 3b) are broader than those of $SrAlF_5$: Pr,Mg (Fig. 3a) and the $^1S_0$ luminescence intensity becomes lower in the sample containing a sodium compensator. These features reflect the strong effect of the charge compensator on the shape of the luminescence spectrum. We believe that, in the case of magnesium, there occurs local charge compensation. The Na^+ ion possessing a large ionic radius (1.30 Å) substitutes for strontium (1.46 Å), whereas the Mg^{2+} ion with an ionic radius of 0.86 Å substitutes for aluminum (0.67 Å). In the $SrAlF_5$ lattice, the Sr–Al distance is smaller than the Sr–Sr distance. Thus, charge compensation with magnesium takes place at a smaller distance. The local charge compensation results in a smaller distortion of the luminescence center and, as a consequence, in favorable conditions for the onset of $^1S_0$ luminescence. In the presence of sodium, charge compensation takes place at a larger distance, thus giving rise to high anisotropy of the luminescence center. As a result, the intensity of the first cascade stage is low in the case of $SrAlF_5$: Pr,Na. The dipole moment of the compensator–emitting-center system in the case of magnesium is smaller than with sodium, which can entail larger line broadening in the $SrAlF_5$: Pr,Na case.

5. CONCLUSIONS

In most CPE luminophors, the energy spacing between the lowest level of the 5*d* configuration and the 4*f* level $^1S_0$ turns out to be very small (0.1–0.2 eV). As a result, a very small change in the environment of the luminescence center affects the efficiency of the first stage of the cascade (the $^1S_0 \longrightarrow {}^1I_0$ transition).

REFERENCES

1. I. deBoer, Stratech Rep., IRI-ISO-990035 (Delft, 1999).
2. E. Van derKolk, P. Dorenbos, C. W. E. van Eijk, A. P. Vink, C. Fouassier, and F. Cuillen, J. Lumin. **97**, 212 (2002).
3. P. A. Rodnyĭ, A. N. Mishin, and A. S. Potapov, Opt. Spektrosk. **93** (5), 775 (2002) [Opt. Spectrosc. **93** (5), 714 (2002)].
4. P. A. Rodnyĭ, S. B. Mikhrin, P. Dorenbos, E. var derKolk, C. W. E. van Eijk, A. P. Vink, and A. G. Avanesov, Opt. Commun. **204**, 237 (2002).
5. P. A. Rodnyĭ, Opt. Spektrosk. **89** (4), 609 (2000) [Opt. Spectrosc. **89** (4), 556 (2000)].
6. A. S. Potapov, P. A. Rodnyĭ, and S. B. Mikhrin, Radiat. Meas. **38**, 839 (2004).
7. P. A. Rodnyĭ, S. B. Mikhrin, and A. N. Mishin, Pis'ma Zh. Tekh. Fiz. **26** (8), 72 (2000) [Tech. Phys. Lett. **26** (8), 678 (2000)].
8. P. A. Rodnyĭ, A. N. Mishin, and A. S. Potapov, Nauchno-Tekh. Ved. St. Petersburg Tekh. Univ. **4**, 95 (2001).
9. W. Drozdowski and A. J. Wojtowicz, J. Alloys Compd. **300–301**, 261 (2000).
10. S. Kuck and I. Sokolska, Appl. Phys. A **77**, 469 (2003).
11. B. P. Sobolev, A. M. Golubev, and P. Herrero, Crystallogr. Rep. **48** (1), 141 (2003).
12. S. Huang, X.-J. Wang, R. S. Meltzer, and W. M. Yen, J. Lumin. **94–95**, 119 (2001).
13. F. Kubel, Z. Anorg. Allg. Chem. **624**, 1481 (1998).

Translated by G. Skrebtsov

Physics of the Solid State, Vol. 47, No. 8, 2005, pp. 1439–1442. Translated from Fizika Tverdogo Tela, Vol. 47, No. 8, 2005, pp. 1389–1391.
Original Russian Text Copyright © 2005 by Gorlov, Chernyshev, Ugryumov, Abrosimov.

PROCEEDINGS OF THE XII FEOFILOV WORKSHOP "SPECTROSCOPY OF CRYSTALS ACTIVATED BY RARE-EARTH AND TRANSITION-METAL IONS"

(Yekaterinburg, Russia, September 22–25, 2004)

Local Structure of Tm^{2+} and Yb^{3+} Impurity Centers in MeF_2 (Me = Ca, Sr, Ba) Fluoride Crystals

A. D. Gorlov, V. A. Chernyshev, M. Yu. Ugryumov, and A. V. Abrosimov
Ural State University, pr. Lenina 51, Yekaterinburg, 620083 Russia
e-mail: Vladimir.Chernyshev@usu.ru

Abstract—The local structure of Tm^{2+} and Yb^{3+} cubic impurity centers in $MeF_2 : Tm^{2+}$ and $MeF_2 : Yb^{3+}$ (Me = Ca, Sr, Ba) fluoride crystals, as well as Yb^{3+} trigonal and tetragonal impurity centers in $MeF_2 : Yb^{3+}$ crystals, is calculated within the shell model in the pair potential approximation. *© 2005 Pleiades Publishing, Inc.*

1. INTRODUCTION

The considerable interest expressed by researchers in rare-earth impurity centers in wide-band-gap dielectric crystals MeF_2 (Me = Ca, Sr, Ba) stems from the fact that these materials have been widely used as laser media, detectors of ionizing radiation, and scintillators. Upon doping of a fluoride crystal, a rare-earth ion (Tm^{2+}, Yb^{3+}) substitutes for an Me^{2+} cation to form a cubic impurity center in the crystal lattice [1–3]. Heterovalent substitution of Yb^{3+} ions for Me^{2+} cations leads to the formation of trigonal and tetragonal impurity centers [4–6], in which an excess charge is compensated for by an additional lattice defect. The role of an additional defect is played by a F^- ion located at the nearest interstice on the C_3 or C_4 crystallographic axis (Fig. 1). The local structure of Yb^{3+} and Tm^{2+} impurity centers in $MeF_2 : Yb^{3+}$ and $MeF_2 : Tm^{2+}$ crystals has been investigated using ligand electron–nuclear double resonance (ENDOR) spectroscopy [1–6]. However, the positions of F^- ions surrounding the impurity ion cannot be determined to sufficient accuracy by the ENDOR technique due to the covalence and overlapping effects. Moreover, it is impossible to determine the positions of cations with zero nuclear spin. Since other methods have also not provided reliable information on the local structure of rare-earth impurity centers in fluorides, it is expedient to calculate the local structure of these centers in the framework of the shell model. One of the first calculations of the local structure of rare-earth impurity centers in MeF_2 compounds was carried by Malkin and coworkers [7, 8]. In the present work, the local structure of impurity centers was determined in the framework of the shell model in the pair interaction approximation.

2. MODEL CALCULATION OF THE ENERGY OF A CRYSTAL

The equilibrium positions of ions in a crystal can be determined by minimizing the energy of the crystal lattice. Within the framework of the shell model in the pair

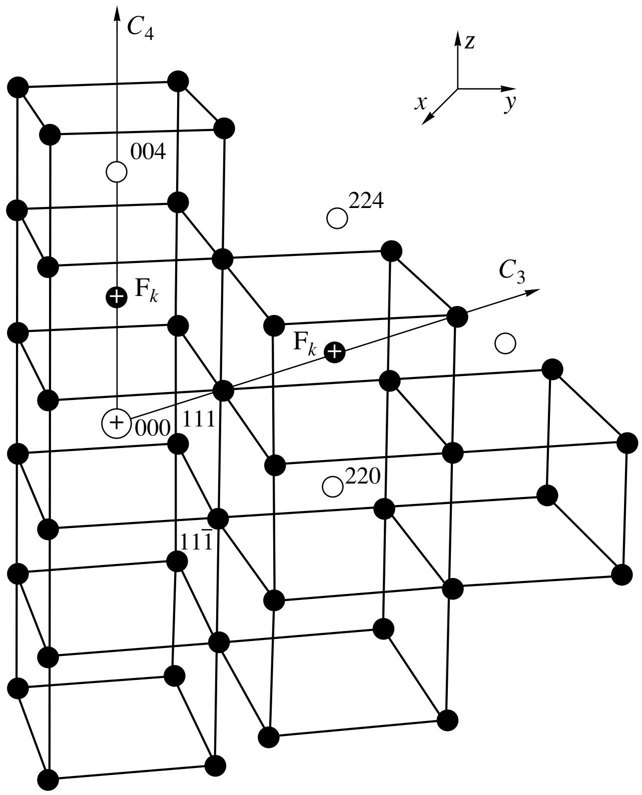

Fig. 1. Positions of F^- compensating ions in the fluoride structure. Closed and open circles indicate anions and cations, respectively.

Table 1. Radial coordinates of ions in the vicinity of the Tm^{2+} cubic impurity center in $MeF_2 : Tm^{2+}$ fluorides (pm)

Shell (ion type)	CaF_2			SrF_2			BaF_2	
	pure crystal	experiment [3]	calculation	pure crystal	experiment [3]	calculation	pure crystal	calculation
1 (F)	235.8		238.5	250.3		244.3	267.5	251.1
2 (*Me*)	385.1		386.0	408.8		407.1	436.9	434.0
3 (F)	451.6	452.4(6)	452.0	479.3	479.0(14)	479.3	512.3	514.2

Note: Numbers in parentheses denote the error in units of the last decimal place.

Table 2. Radial coordinates of ions in the vicinity of the Yb^{3+} cubic impurity center in $MeF_2 : Yb^{3+}$ fluorides (pm)

Shell (ion type)	CaF_2			SrF_2			BaF_2		
	pure crystal	experiment [1]	calculation	pure crystal	experiment [1]	calculation	pure crystal	experiment [1]	calculation
1 (F)	235.8		235.5	250.3		238.7	267.5		241.8
2 (*Me*)	385.1		391.6	408.8		412.6	436.9		439.7
3 (F)	451.6	448.7(7)	449.7	479.3	475.3(6)	476.8	512.3	506.5(18)	512.2

Note: Numbers in parentheses denote the error in units of the last decimal place.

potential approximation, the lattice energy can be represented in the form

$$U_{\text{lat}} = \frac{1}{2}\sum_i \sum_{k(\neq i)} V_{ik} + \frac{1}{2}\sum_i k_i \delta_i^2, \tag{1}$$

where $k_i\delta_i^2$ is the energy of the core–shell interaction of the *i*th ion, δ_i is the displacement of the shell with respect to the core of the ion, and V_{ik} is the energy of the interaction between the *i*th and *k*th ions. This energy can be written in the form

$$\begin{aligned} V_{ik} &= \frac{X_i X_k}{|\mathbf{r}_i - \mathbf{r}_k|} + \frac{Y_i X_k}{|\mathbf{r}_i - \mathbf{r}_k + \delta_i|} \\ &+ \frac{X_i Y_k}{|\mathbf{r}_i - \mathbf{r}_k - \delta_k|} + \frac{Y_i Y_k}{|\mathbf{r}_i - \mathbf{r}_k + \delta_i - \delta_k|} \\ &+ f_{ik}(|\mathbf{r}_i - \mathbf{r}_k|) + g_{ik}(|\mathbf{r}_i - \mathbf{r}_k + \delta_i - \delta_k|). \end{aligned} \tag{2}$$

Here, the function

$$f_{ik}(r) = -A_{ik}\exp(-B_{ik}r)/r \tag{3}$$

describes the short-range screening of the electrostatic interaction of the ion cores; the function

$$g_{ik}(r) = C_{ik}\exp(-D_{ik}r) - \lambda_{ik}/r^6$$

characterizes the short-range repulsion between the ion shells (which is written in the form of the Born–Mayer potential) and the van der Waals interaction; X_i and Y_i are the charges of the core and the shell of the *i*th ion, respectively; and $\mathbf{r}_i$ is the vector specifying the position of the core of the *i*th ion. In this work, we used the following values of the core charges: $X_F = +5$, $X_{Me} = +8$, $X_{Yb} = +11$, and $X_{Tm} = +10$. The shell charges were determined from the condition $Z_i = X_i + Y_i$, where Z_i is the charge of the ion in the compound. The energy of the Coulomb interaction between the ions was calculated using the Ewald method. The parameters of the short-range interaction for MeF_2 compounds are given in [9]. When calculating the Yb^{3+}–F^- and Tm^{2+}–F^- short-range interactions, the electrostatic screening was ignored and the parameters *C* and *D*, as well as the parameter k_i for the Yb^{3+} ion, were obtained from the best fitting of the results of calculations to the experimental data on the radial and angular displacements of the anions in the Yb^{3+} and Tm^{2+} impurity centers in $MeF_2 : Yb^{3+}$ and $MeF_2 : Tm^{2+}$ fluorides ($C_{\text{Yb, Tm–F}} = 262.594$, $D_{\text{Yb–F}} = 2.054$, $D_{\text{Tm–F}} = 2.181$; $k_{Yb} = 25.020$ au). The local structure of the impurity centers in the crystal was calculated by the embedded-cluster method, and the defect region included seven or more coordination shells.

3. CUBIC IMPURITY CENTERS IN $MeF_2 : Tm^{2+}$ CRYSTALS

For Tm^{2+} cubic impurity centers in the $MeF_2 : Tm^{2+}$ compounds (Table 1), the calculations predicted that, compared to pure crystals, the distance from the rare-earth ion to the ligands should increase by 3 pm in the CaF_2 compound and decrease by 6 and 10 pm in the SrF_2 and BaF_2 compounds, respectively. According to

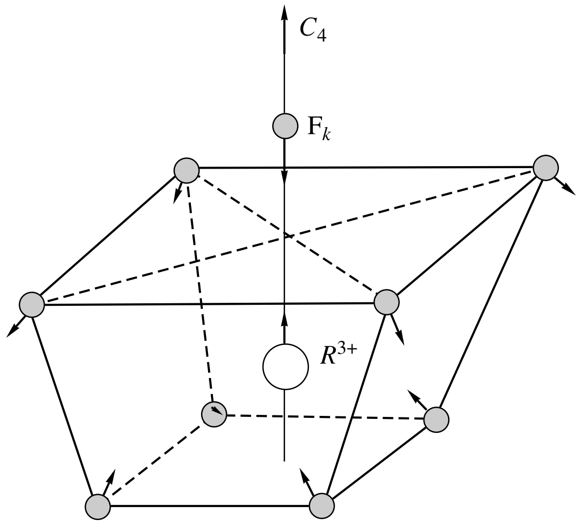

Fig. 2. Displacements of anions in the tetragonal impurity center.

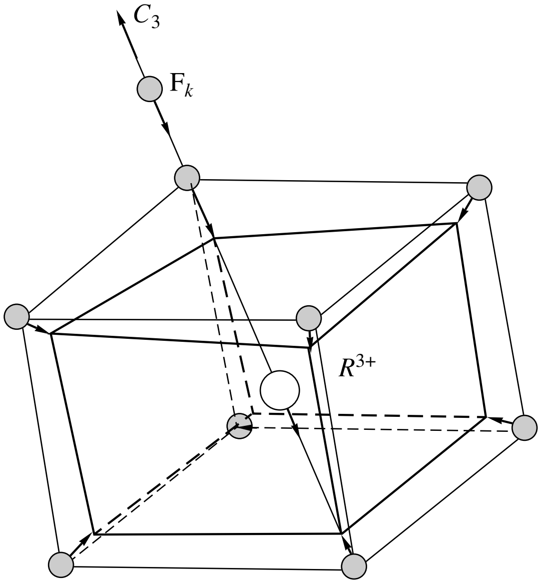

Fig. 3. Displacements of anions in the trigonal impurity center.

these calculations, the nearest cation environment of the Tm^{2+} ion expands in the CaF_2 crystal and contracts in the SrF_2 and BaF_2 crystals. The angular coordinates of the ions change only slightly (by no more than 0.02°) in the CaF_2 crystal and increase by 0.06° and 0.12° in the third coordination shell of the SrF_2 and BaF_2 compounds, respectively.

4. CUBIC, TETRAGONAL, AND TRIGONAL IMPURITY CENTERS IN MeF_2 : Yb^{3+} CRYSTALS

As follows from our calculations, the Yb^{3+}–ligand distance in the cubic impurity centers (Table 2) decreases in such a way that the change in this distance in the series of MeF_2 compounds increases with an increase in the difference between the ionic radii of the Yb^{3+} impurity ion and the substituted cation. The nearest cation environment of the impurity ion expands. The angular coordinates of the ions in the third coordination shell of the CsF_2, SrF_2, and BaF_2 compounds increase by 0.18°, 0.26°, and 0.33°, respectively.

For an Yb^{3+} tetragonal impurity center in the $CaF_2 : Yb^{3+}$ compound, the calculations demonstrated that the rare-earth ion is displaced by 23 pm toward the compensating fluorine ion (Fig. 2). In this case, the compensating ion is displaced by 11 pm toward the impurity ion and pushes apart the four ligands located between this compensating ion and the ytterbium ion. The angle between the C_4 axis and the straight line passing through the compensating fluorine ion and the ion of the four ligands increases. The cations surrounding the impurity ion are displaced in the following way. The tetragon formed by four ions of the 220 type (Fig. 1) expands in the plane perpendicular to the C_4 axis and is displaced downward along this axis. Tetragons of the 202 and $20\bar{2}$ type contract in the plane perpendicular to the C_4 axis and are displaced upward and downward along this axis, respectively.

For Yb^{3+} trigonal impurity centers in the $SrF_2 : Yb^{3+}$ and $BaF_2 : Yb^{3+}$ compounds, the calculations predicted similar displacements (Fig. 3). The Yb^{3+} impurity ion is displaced away from the compensating fluorine ion along the C_3 axis by 4.4 pm in the $SrF_2 : Yb^{3+}$ crystal and by 4.6 pm in the $BaF_2 : Yb^{3+}$ crystal. The compensating fluorine ion is displaced with respect to the interstice in the pure crystal toward the Yb^{3+} ion by 44 and 27 pm in the BaF_2 and SrF_2 crystals, respectively. The nearest environment of the impurity ion contracts so that the largest displacement is observed for the 111 ion (Fig. 1), which is displaced toward the Yb^{3+} ion by 45 and 31 pm in the BaF_2 and SrF_2 crystals, respectively. The angle between the C_3 axis and the straight line passing through the compensating fluorine ion and the

Table 3. Coordinates of anions in the vicinity of the Yb^{3+} tetragonal impurity center in the $CaF_2 : Yb^{3+}$ fluoride (the origin of the coordinates coincides with the impurity ion)

Shell, ion type (number of ions)	R, pm	θ, deg	φ, deg
1, 111 (4)	235.2	63.92	45
1, $11\bar{1}$ (4)	247.9	129.94	45
F_k	238.4	0	0

Table 4. Coordinates of anions in the vicinity of the Yb^{3+} trigonal impurity center in $SrF_2 : Yb^{3+}$ and $BaF_2 : Yb^{3+}$ fluorides (the origin of the coordinates coincides with the impurity ion)

Shell, ion type (number of ions)	$SrF_2 : Yb^{3+}$			$BaF_2 : Yb^{3+}$	
	R, pm	θ, deg		*R*, pm	θ, deg
	calculation	calculation	experiment [5]	calculation	calculation
1, 111 (1)	224.2	0	0	226.7	0
1, $\bar{1}\bar{1}\bar{1}$ (1)	239.4	180	180	243.3	180
1, $11\bar{1}$ (3)	241.9	70.57	71.0(1)	245.9	70.97
1, $\bar{1}\bar{1}1$ (3)	238.9	109.03	109.6(1)	241.4	109.14
F_k	478.8	0	0	499.9	0

ligand increases for a triad of the $11\bar{1}$ ligands and decreases for a triad of the $\bar{1}\bar{1}1$ ligands. The coordinates of the anions in the vicinity of the tetragonal and trigonal Yb^{3+} impurity centers are listed in Tables 3 and 4, respectively.

5. CONCLUSIONS

Thus, the structure of both cubic and low-symmetry impurity centers is described in the framework of the shell model using the same set of parameters for the Yb^{3+}–F and Tm^{2+}–F short-range interactions.

ACKNOWLEDGMENTS

This work was supported by the US Civilian Research and Development Foundation for the New Independent States of the Former Soviet Union (project no. REC 005, EK-005-XI) and the Russian Foundation for Basic Research (project no. 04-02-16427).

REFERENCES

1. C. A. Ramos, C. Fainstein, and M. Tovar, Phys. Rev. B **32** (1), 64 (1985).
2. D. Kiro and W. Low, Phys. Rev. Lett. **20** (18), 1010 (1968).
3. W. Hayes and P. H. S. Smith, J. Phys. C: Solid State Phys. **4**, 840 (1971).
4. O. V. Nazarova and T. I. Sanadze, Soobshch. Akad. Nauk SSSR **87** (2), 329 (1977).
5. B. G. Berulava, R. I. Mirianashvili, O. V. Nazarova, and T. I. Sanadze, Fiz. Tverd. Tela (Leningrad) **19** (6), 1771 (1977) [Sov. Phys. Solid State **19** (6), 1033 (1977)].
6. J. M. Baker, E. R. Davies, and J. P. Hurrell, Proc. R. Soc. London, Ser. A **308**, 403 (1968).
7. B. Z. Malkin, Fiz. Tverd. Tela (Leningrad) **11** (5), 1208 (1969) [Sov. Phys. Solid State **11** (5), 981 (1969)].
8. M. P. Davydov, B. Z. Malkin, and A. L. Stolov, in *Spectroscopy of Crystals* (Nauka, Leningrad, 1978) [in Russian].
9. A. E. Nikiforov, A. Yu. Zakharov, and V. A. Chernyshev, Fiz. Tverd. Tela (St. Petersburg) **46** (9), 1588 (2004) [Phys. Solid State **46** (9), 1639 (2004)].

Translated by O. Borovik-Romanova

Physics of the Solid State, Vol. 47, No. 8, 2005, pp. 1443–1445. Translated from Fizika Tverdogo Tela, Vol. 47, No. 8, 2005, pp. 1392–1394.
Original Russian Text Copyright © 2005 by Snigireva, Solomonov.

PROCEEDINGS OF THE XII FEOFILOV WORKSHOP “SPECTROSCOPY OF CRYSTALS ACTIVATED BY RARE-EARTH AND TRANSITION-METAL IONS”

(Yekaterinburg, Russia, September 22–25, 2004)

Role of the Ce^{2+} Ions in Cerium Fluoride Luminescence

O. A. Snigireva and V. I. Solomonov

Institute of Electrophysics, Ural Division, Russian Academy of Sciences,
ul. Komsomol’skaya 34, Yekaterinburg, 620016 Russia
e-mail: snigireva_olga@mail.ru

Abstract—Pulsed cathodoluminescence (PCL) of CeF_3 crystals was studied using a KLAVI-type setup. PCL was excited by bombarding samples in air at room temperature using a 2-ns pulsed electron beam at an electron energy of 170 keV, current density of 160 A/cm^2, and repetition rate of 2.5 Hz. Luminescence and phosphorescence were observed in the UV and visible spectral regions. The phosphorescence is tentatively associated with the Ce^{2+} ion formation. © *2005 Pleiades Publishing, Inc.*

1. INTRODUCTION

The development of fast-response scintillators requires materials with fast luminescence decay kinetics. Among the materials holding most promise in this respect are those producing valence–core luminescence (which derives from radiative transitions between the valence band and the nearest core band of the crystal) and complex compounds activated by the rare-earth ions Ce^{3+}, Nd^{3+}, and Pr^{3+} [1]. Ce^{3+}-activated crystals are also considered promising for the development of fast scintillators whose operation involves $5d \longrightarrow 4f$ interconfiguration transitions in cerium ions [2]. These scintillators can be employed for the detection of events in the physics of elementary particles, nuclear physics, and other areas requiring a fast detector time resolution.

Studies of cerium fluoride–based detectors have been carried out using various methods, more specifically, luminescence, optical methods, and exoelectron emission [1–3]. Along with having such properties as a high density and high mechanical and radiation strength, CeF_3 crystals also exhibit effects that restrict their use as detectors. These include comparatively long luminescence times (~30 ns) [3], a low light yield in the Ce^{3+} band, and hole burning in the luminescence excitation profile [2]. These effects have been attributed to the existence of traps, assumed tentatively to be fluorine vacancies, the O^{2-} ion, impurities, and cerium centers. It was also pointed out in [3] that, since cerium fluoride is a concentrated system, possible interaction between cerium centers and the manifestation of intermediate-valence effects should be taken into account. These conjectures have not been experimentally confirmed.

2. MEASUREMENTS AND RESULTS

2.1. Experimental Technique and Samples

Experiments were conducted on a KLAVI-type setup (pulsed cathodoluminescent analyzer) [4]. The observed pulsed cathodoluminescence (PCL) was excited by bombarding samples in air at room temperature using an electron beam with a pulse length of 2 ns, electron energy of 170 keV, and current density of 160 A/cm^2 at a repetition rate of 2.5 Hz. The error in wavelength measurement was $\Delta\lambda = \pm 0.75$ nm. The spectral resolution was no worse than 2 nm. Additional experiments were carried out in the gated regime to measure afterglow times.

The CeF_3 crystals chosen for the study were of various grades: (i) OSCh, (ii) Ch, and (iii) with low and (iv) a high oxyfluoride contents. The samples were kindly provided by B.P. Sobolev (Institute of Crystallography, Russian Academy of Sciences, Moscow).

2.2. Experimental Results

The PCL spectrum of cerium fluoride in the UV region (Fig. 1a) is typically a set of broad bands: (*1*) an intense asymmetric band peaking at 295 nm and (*2*) a broad band centered at 413 nm, which is most clearly pronounced in crystals containing oxyfluoride. The characteristic decay time of the 295-nm band is $\tau \approx$ 3 ms, which differs markedly from the values given in the literature. In the visible range, all the samples used in this study feature a broad asymmetric luminescence band with a peak near 445 nm. Only Ch-grade samples produce an additional peak at 543 nm (Fig. 1b). The asymmetry of the bands at λ = 295 and 445 nm indicates that they are not elementary. The former band was deconvolved, using the Peakfit code, into three Gaussian bands centered at 285, 305, and 328 nm (Fig. 1a), and the latter band was unfolded into two constituents

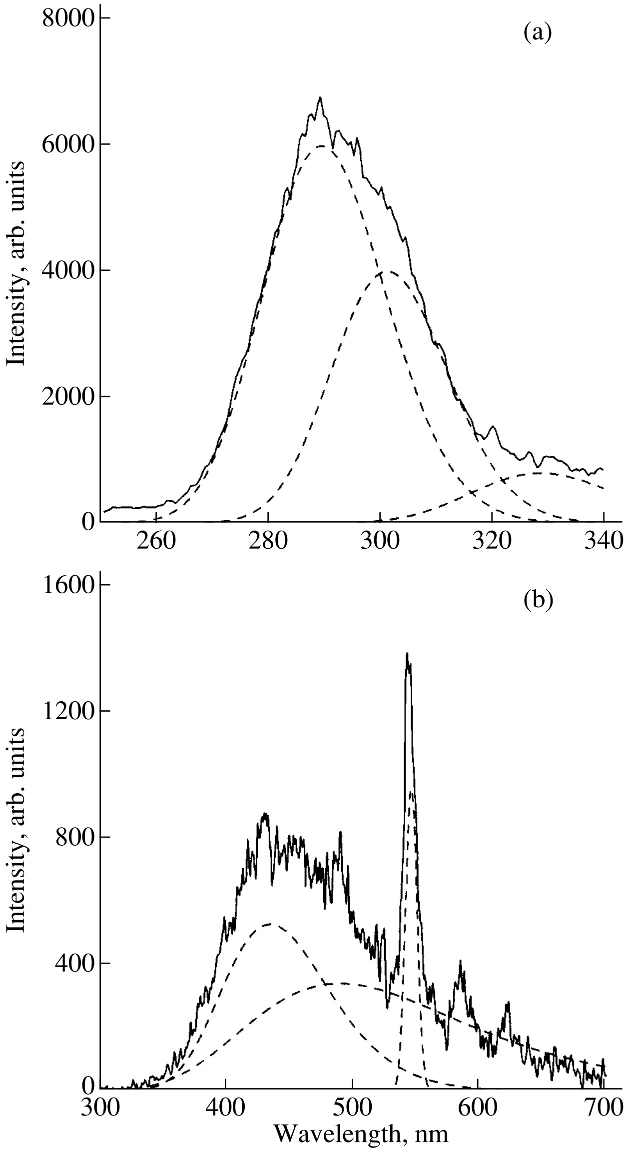

Fig. 1. Typical PCL spectrum of CeF_3 measured in (a) the UV and (b) visible regions.

with wavelengths of 433 and 487 nm (Fig. 1b). The possible deviation of these data from the values given in the literature should be assigned to ambiguities in the unfolding into Gaussians.

2.3. Discussion of the Results

An earlier study of CeF_3 crystals [3] revealed two systems of luminescence bands, namely, fast (at 286 and 305 nm, $\tau \approx 5$ ns) and slow (at 305 and 325 nm, $\tau \approx$ 30 ns) components. The ^2F-level splitting was estimated to be $\Delta E = 2300$ cm^{-1}. The fast luminescence is produced in the $Ce^{3+}(5d) \longrightarrow Ce^{3+}(^2F)$ transition (process *1* in Fig. 2) and is present in the PCL spectrum but cannot be spectrally resolved from the slow components. It is this luminescence that is desirable in designing a scintillator.

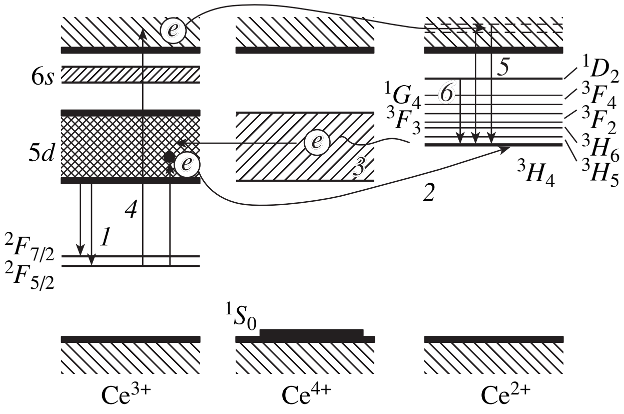

Fig. 2. Energy level diagram of cerium ions in CeF_3 and possible electronic transitions.

The presence of the slow components and the dominant role they play imply, however, the existence of other pathways for excitation energy conversion. We believe that they involve the formation of pairs of Ce^{4+} and Ce^{2+} ions. The latter ion is active in luminescence and, hence, is detectable. The conversion of excitation energy can occur in the following two ways.

(1) A $Ce^{3+}(^2F)$ ion is excited by an electron beam to the $Ce^{3+}(5d)$ state. In this process, the 5*d* electron can transfer resonantly to a neighboring $Ce^{3+}(^2F)$ ion (process *2* in Fig. 2) to form a pair of ions, $Ce^{4+}(^1S_0)$ and $Ce^{2+}(^3H_4)$. This process will be efficient if the energy of the $Ce^{2+}(^3H_4)$ ground state is close to that of the $Ce^{3+}(5d)$ state. Unfortunately, data on the Ce^{2+} energy structure in CeF_3 are lacking. We made an attempt to determine the energy structure from the diagram of Pr^{3+} levels, which have the same electronic configuration $4f^2$ as the Ce^{2+} ion, and to find the position of the energy levels from the dips observed in the luminescence excitation spectrum of CeF_3 crystals [2]. The results are presented in Fig. 2. Electron transfer from the $Ce^{2+}(^3H_4)$ ion back through the 5*d* band of the Ce^{4+} ion (process *3* in Fig. 2) gives rise to the formation of a pair of Ce^{3+} ions, with one of them being in the 5*d* state and the other being in one of the ^2F states. This is followed by a radiative transition from the 5*d* to ^2F levels. The end result is the formation of two Ce^{3+} ions in identical or different ^2F states (process *1* in Fig. 2). In this case, there can be emission at three wavelengths, namely, 285, 305, and 328 nm, which are observed in phosphorescence. The presence of the slow component in the luminescence decay may be ascribed to the Ce^{2+} ion being metastable.

(2) The ground-state Ce^{3+} ion is ionized by an electron beam either directly or via the 6*s* state (process *4* in Fig. 2) to become Ce^{4+}. A conduction band electron

is captured by another $Ce^{3+}(^2F)$ ion to form a Ce^{2+} ion in an excited state, which is then de-excited via a radiative transition to the $Ce^{2+}(^3H_4)$ ground state (process *5* in Fig. 2). As a result, two broad bands centered at 433 and 487 nm appear. The band broadening indicates that the observed transitions originate from radiating levels located in or close to the conduction band. Charge transfer can also occur to the $^1D_2$ level of the Ce^{2+} ion via nonradiative transitions from the conduction band or resonantly from the 6*s* band, which is followed by a radiative transition from the $^1D_2$ to the $^3H_4$ level. This transition produces a narrow band with a wavelength of 543 nm (process *6* in Fig. 2), which is observed only in Ch-grade samples. The narrowness of the band implies an intercombination transition. The process subsequently occurs following the second of the two variants.

The ionization process described above is characteristic of the conditions created by an electron beam in the KLAVI chamber. These conditions are similar to those in which a scintillator operates but are difficult to realize, however, in a photoluminescence study. Photoluminescence is most likely dominated by the first process involving the formation of $Ce^{2+}(^3H_4)$.

3. CONCLUSIONS

The above hypothesis assuming an alternate pathway for the transfer of the $Ce^{3+}(5d)$ excitation energy to the formation of Ce^{2+} and Ce^{4+} ion pairs is corroborated by the results obtained in luminescence studies and accounts for the low scintillation light yield in CeF_3 crystals. It is conceivable that Ce^{2+} forms only in crystals with a high Ce content. Therefore, this hypothesis has to be tested in crystals with a low Ce content (BaF_2 : Ce, CaF_2 : Ce, etc.), where this reaction may not be dominant.

REFERENCES

1. L. P. Benderskaya, A. S. Voloshinovskiĭ, G. N. Novikova, I. P. Pashuk, N. S. Pidzyraĭlo, and P. A. Rodnyĭ, Opt. Spektrosk. **73** (6), 1143 (1992) [Opt. Spectrosc. **73** (6), 679 (1992)].
2. P. A. Rodnyĭ and D. M. Semiverstov, Preprint No. 1886 PIYaF (Peterb. Inst. Yad. Fiz., Gatchina, 1993), SS-17-1993.
3. A. S. Voloshinovskiĭ and P. A. Rodnyĭ, Opt. Spektrosk. **74** (1), 137 (1993) [Opt. Spectrosc. **74** (1), 84 (1993)].
4. V. I. Solomonov and S. G. Mikhaĭlov, *Pulsed Cathodoluminescence and Its Application for Analysis of Condensed Substances* (UrO Ross. Akad. Nauk, Yekaterinburg, 2003).

Translated by G. Skrebtsov

Physics of the Solid State, Vol. 47, No. 8, 2005, pp. 1446–1449. Translated from Fizika Tverdogo Tela, Vol. 47, No. 8, 2005, pp. 1395–1397.
Original Russian Text Copyright © 2005 by Ivanovskikh, Pustovarov, Shul'gin, Kirm.

PROCEEDINGS OF THE XII FEOFILOV WORKSHOP “SPECTROSCOPY OF CRYSTALS ACTIVATED BY RARE-EARTH AND TRANSITION-METAL IONS”

(Yekaterinburg, Russia, September 22–25, 2004)

Low-Temperature Time-Resolved VUV Luminescence Spectroscopy of $SrF_2 : Er^{3+}$ Crystals

K. V. Ivanovskikh*, V. A. Pustovarov*, B. V. Shul'gin*, and M. Kirm**
**Ural State Technical University, ul. Mira 19, Yekaterinburg, 620002 Russia*
e-mail: ikv@dpt.ustu.ru
***Institute of Physics, Tartu University, Riia 142, Tartu, 51014 Estonia*

Abstract—Time-resolved excitation and emission spectra of $SrF_2 : Er^{3+}$ upon selective excitation with synchrotron radiation in the VUV and ultrasoft x-ray ranges at $T = 8$ K were studied. The VUV luminescence of $SrF_2 : Er^{3+}$ derives from high-energy interconfiguration $4f^{10}5d$–$4f^{11}$ transitions in the Er^{3+} ion. The VUV emission spectrum revealed, in addition to the 164.5-nm band (millisecond-range kinetics), a band at 146.4 nm (with a decay time of less than 600 ps). The formation of excitation spectra for the *f–f* and *f–d* transitions in the Er^{3+} ion is discussed. © *2005 Pleiades Publishing, Inc.*

1. INTRODUCTION

SrF_2 crystals doped with rare-earth (RE) elements have long been known to be promising scintillators [1]. Present studies of RE-doped crystals pay particular attention to VUV spectroscopy, primarily because of the growing need to develop a new class of fast VUV scintillators and VUV phosphors for plasma display panels and mercury-free fluorescent lamps, as well as solid-state VUV lasers [2–4].

These considerations have motivated our study of low-temperature time-resolved excitation spectra of Er^{3+} luminescence in $SrF_2 : Er^{3+}$ in the range 4–25 eV (50–309 nm), as well as of VUV luminescence in the 7–9-eV region (138–175 nm). By properly varying the excitation, we succeeded in detecting a new luminescence band at 146 nm with fast decay kinetics in addition to the previously known 164.5-nm band [5, 6].

2. SAMPLES AND EXPERIMENTAL TECHNIQUES

SrF_2 : 1% Er^{3+} single crystals were Stockbarger-grown by K.K. Rivkina and E.G. Morozov at the Pyshma GIREDMET pilot plant.

The excitation and VUV emission spectra were measured under selective excitation by synchrotron radiation (SR) in the VUV and ultrasoft x-ray (USX) regions at the SUPERLUMI station and in the BW3 beamline at HASYLAB (DESY, Hamburg). A 2-m vacuum monochromator with a resolution of 3.2 Å was employed for excitation in the range 4–25 eV. Luminescence in the visible range was detected with a 0.3-m monochromator (ARC Spectra Pro-308i) and an R6358P PM tube (Hamamatsu). Luminescence in the VUV region was measured with an 0.5-m vacuum monochromator and a sun-blind R6836 PM tube. Undulator radiation and a Zeiss SX700 monochromator in the BW3 beamline provided excitation in the USX region. The VUV luminescence was measured with a 0.4-m monochromator (Seya-Namioka arrangement) and a microchannel detector (MCP 1645 U-09, Hamamatsu). The excitation and emission spectra could be obtained both without time resolution (time-integrated) and in time windows Δt_1 (fast component) and Δt_2 (slow component) wide delayed with respect to the SR pulse by δt_1 and δt_2, respectively. The excitation spectra are normalized against an equal number of photons incident on the sample with the use of sodium salicylate. The VUV emission spectra are presented without correction for spectral sensitivity of the optical channel. Measurements were conducted at $T = 8$ K in a cryostat providing an oil-free vacuum of (2–5) × 10^{-10} Torr.

3. EXPERIMENTAL RESULTS AND DISCUSSION

The main features of the excitation spectra of the 551-nm luminescence, which derives from the strongest *f–f* transition ${}^4S_{3/2} \longrightarrow {}^4I_{15/2}$ in the Er^{3+} ion in a SrF_2 : 1% Er^{3+} crystal, are seen in the region of crystal transparency and the long-wavelength fundamental absorption edge (curve *1* in figure). In the range 177–309 nm, the excitation spectrum consists of a number of narrow bands of various intensities. The *f–f* transition bands in the $SrF_2 : Er^{3+}$ excitation spectrum were assigned by us in accordance with calculations and experimental data on the energy levels of the $4f^{11}$ configuration of the Er^{3+} ion in $LiYF_4$ [7, 8]. In the UV

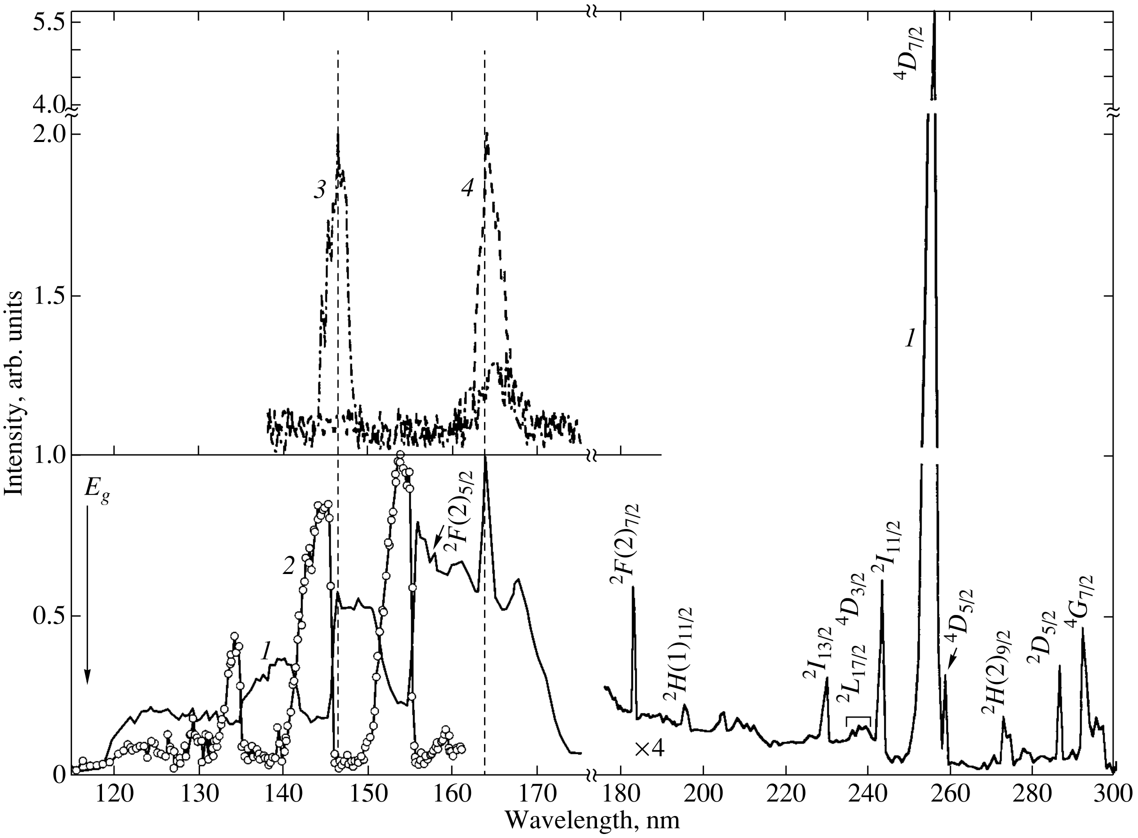

PE spectra (*1*) of the 551-nm *f*–*f* luminescence ($^4S_{3/2} \longrightarrow {}^4I_{15/2}$) and (*2*) of the 164.5-nm *d*–*f* luminescence ($4f^{10}5d$(HS) $\longrightarrow {}^4I_{15/2}$) measured in a slow time window (δt_2 = 0.68 ns, Δt_2 = 103 ns); VUV emission spectra measured in (*3*) a fast time window (δt_1 = 0.6 ns, Δt_1 = 1.8 ns) and (*4*) a slow time window (δt_2 = 12 ns, Δt_2 = 19.3 ns). SrF_2 : 1% Er^{3+}, T = 8 K.

region, transitions are observed to the multiplet levels $^4G_{7/2}$ (292 nm), $^2D_{5/2}$ (287 nm), $^2H(2)_{9/2}$ (273 nm), $^4D_{5/2}$ (259 nm), $^4D_{7/2}$ (256 nm), $^2I_{11/2}$ (243 nm), nonresolvable $^2L_{17/2}$ and $^4D_{3/2}$ (235–241 nm), and $^2I_{13/2}$ (230 nm). In the VUV region, distinct lines are observed corresponding to transitions to the multiplets $^2H(1)_{11/2}$ (195 nm) and $^2F(2)_{7/2}$ (183 nm). The band deriving from the transition to the $^2F(2)_{5/2}$ level and mentioned in [8] is very weakly seen at 158 nm against the background of a strong, broad, structured band extending from 155 to 173 nm. A strong narrow line at 164 nm stands out in this band. As the incident-light wavelength decreases, broad excitation bands appear in the excitation spectrum at 145–153 and 134–142 nm. At the fundamental absorption edge, the excitation intensity falls off with a sharp drop at 119 nm. At higher excitation energies, the luminescence is suppressed.

In addition to the luminescence in the visible range, Er^{3+} ions exhibit luminescence bands in the VUV region, which are due to interconfiguration transitions both from the low-spin (LS) level ($2S + 1 = 4$) (spin-allowed transitions) and from the high-spin (HS) level ($2S + 1 = 6$) (spin-forbidden transitions) to the $4f^{11}$-configuration ground-state levels [5, 6, 9–11]. We measured low-temperature time-resolved VUV emission spectra of SrF_2 : Er^{3+} in the spectral region 135–175 nm under excitation in the USX region with a photon energy of 140 eV (curves *3*, *4* in the figure). In the "slow" time window, the well-known 164.3-nm band is observed; this band is produced by the $4f^{10}5d$(HS) $\longrightarrow {}^4I_{15/2}$ transition [5, 6]. In the fast time window, we succeeded in observing a band at 146.4 nm emitted in the SrF_2 : Er^{3+} system. The decay time constant of this luminescence band, as derived from the convolution integral, does not exceed 600 ps.

In the slow time window, the strongest excitation bands of the *d*–*f* luminescence, $4f^{10}5d$(HS) $\longrightarrow {}^4I_{15/2}$, were observed under excitation near 154, 144, and 134 nm (curve *2* in the figure). One can also see a weak band at 159 nm, which signals the onset of excitation of *d*–*f* luminescence ($4f^{10}5d$(HS) $\longrightarrow {}^4I_{15/2}$). Note also the presence of fairly weak bands at 129 and 139 nm in the spectrum.

An analysis of the VUV luminescence and the excitation spectra of *d*–*f* and *f*–*f* luminescence revealed the following features.

(1) The luminescence bands at 164.3 and 146.4 nm coincide in position with the narrow lines in the 551-nm-luminescence excitation spectra ($^4S_{3/2} \longrightarrow {}^4I_{15/2}$) observed against the background of broad intense bands.

(2) The *d–f* and *f–f* luminescence yield ($4f^{10}5d$(HS) $\longrightarrow {}^4I_{15/2}$ and $^4S_{3/2} \longrightarrow {}^4I_{15/2}$ transitions, respectively) falls off near the long-wavelength fundamental absorption edge and subsequently drops sharply when excited by photons with a wavelength of below 119 nm (this region is not shown in the figure).

(3) The difference in energy position between the maxima of the slow (at 164.3 nm; $4f^{10}5d$(HS) $\longrightarrow {}^4I_{15/2}$) and fast (at 146.4 nm) *d–f* luminescence is fairly large (0.91 eV).

(4) The excitation spectra of the $4f^{10}5d$(HS) $\longrightarrow {}^4I_{15/2}$ and $^4S_{3/2} \longrightarrow {}^4I_{15/2}$ luminescence follow opposite patterns in the range 126–161 nm.

(5) The difference in energy position between the beginning of the strongest broad excitation bands at 155–173 nm in the excitation spectrum of *f–f* luminescence and at 154 nm in the excitation spectrum of *d–f* luminescence in the nearest VUV region is 0.91–0.95 eV.

The opposite patterns of the excitation spectra of the *f–f* and *d–f* luminescence reflect the competitive excitation energy transfer to radiating levels of the $4f^{10}5d$ and $4f^{11}$ configurations, which is characteristic of the Er^{3+} ion in $SrF_2 : Er^{3+}$.

The suppression of impurity luminescence observed to occur under excitation at the onset of interband transitions in SrF_2 (E_g = 11.2 eV [12]) up to 20 eV should be identified with the low efficiency of energy transfer via the electron–hole mechanism, as well as with the low involvement of excitons in energy transfer to the levels of the $4f^{10}$ $5d$ configuration of the Er^{3+} ion in SrF_2.

In terms of its pattern, the 159-nm band in the excitation spectrum of $4f^{10}5d$(HS) $\longrightarrow {}^4I_{15/2}$ luminescence can be assigned to the spin-forbidden *f–d* transition. According to the Hund rule, this suggests that this spectral region corresponds to the lowest energy state in the $4f^{10}5d$ configuration of the Er^{3+} ion in SrF_2 and that the strong 154-nm band indicates the onset of spin-allowed *f–d* transitions. If this is so, then the nature of the 155- to 173-nm structured band in the $^4S_{3/2} \longrightarrow {}^4I_{15/2}$ luminescence excitation spectrum remains unclear.

We estimated the Stokes shift for the low-spin excited state of the $4f^{10}5d$ configuration of the Er^{3+} ion in SrF_2 as 1800 cm^{-1}. Assuming the quartet and sextet excited states to have the same Stokes shifts, one could expect the existence of a *d–f* band with fast decay kinetics in the range 155–158 nm associated with the spin-allowed transition from the lowest LS excited state. However, this band was not observed either in our experiments or in the $SrF_2 : Er^{3+}$ studied in [5, 6]. This may be accounted for by the existence of strong nonradiative cross relaxation between the LS and HS Er^{3+} levels in SrF_2, which are separated by about 2150 cm^{-1}. This value is substantially smaller than, for instance, that in the $LiYF_4$ crystal, where both *d–f* luminescence bands are seen and the difference is about 3300 cm^{-1} [5, 6, 11]. A similar explanation was advanced in [9], where the Er^{3+} *d–f* luminescence in KYF_4 was found to follow the same pattern. This suggests that the observed fast 146.4-nm luminescence in $SrF_2 : Er^{3+}$ should most probably be assigned to a higher lying radiating low-spin $4f^{10}5d$ configuration. As far as we are aware, however, information on the observation of these transitions is presently lacking.

4. CONCLUSIONS

The low-temperature VUV emission spectra of SrF_2 : 1% Er^{3+} have been found to reveal, in addition to the well-known 164.5-nm band associated with the $4f^{10}5d$(HS) $\longrightarrow {}^4I_{15/2}$ transition, a new luminescence band at 146.4 nm ($\tau < 600$ ps), which derives from a transition from one of the high-lying low-spin excited states of the $4f^{10}5d$ configuration. Competitive excited-state relaxation in the $4f^{10}5d$ configuration has been found to occur via the radiative *d–f* and *f–f* transitions. More reliable establishment of the nature of the observed fast 146.4-nm *d–f* luminescence and of the mechanisms governing relaxation of the excited states in the $4f^{10}5d$ configuration of Er^{3+} ions in SrF_2 would require additional studies, in particular, of the excitation spectra of the fast 146.4-nm band, as well as of the emission spectra obtained under selective excitation of the upper excited states of the $4f^{10}5d$ configuration.

Observation of the fast VUV luminescence band in $SrF_2 : Er^{3+}$ crystals is of interest in connection with the development of fast VUV scintillators for detectors with high time resolution .

ACKNOWLEDGMENTS

This study was supported by the Russian Foundation for Basic Research (project no. 02-02-16322); the Ministry of Education, Science, and Technology of the Russian Federation (project no. E02-3.4-362); the program “Universities of Russia” (project no. UR.02.01.023); the Ural Research and Education Center (program “Promising Materials”); and CRDF (project EK-005-XI).

REFERENCES

1. B. V. Shul’gin, Yu. A. Fedorovskikh, E. G. Morozov, F. F. Gavrilov, and B. V. Sinitsyn, in *Proceedings of the II All-Union Symposium on Chemistry of Inorganic Fluorides, Moscow, 1970* (Moscow, 1970).

2. C. R. Ronda, T. Justel, and H. Hikol, J. Alloys Compd. **275–277**, 669 (1998).
3. C. L. Woody and D. F. Anderson, Nucl. Instrum. Methods Phys. Res. A **265**, 291 (1988).
4. V. N. Makhov, J. Y. Gesland, N. M. Khaidukov, N. Yu. Kirikova, M. Kirn, J. C. Krupa, T. V. Ouvarova, and G. Zimmerer, in *Proceedings of the 5th International Conference on Inorganic Scintillators and Their Applications, Russia, Moscow, 1999* (MSU, Moscow, 1999), p. 369.
5. J. Becker, J. Y. Gesland, N. Yu. Kirikova, J. C. Krupa, V. N. Makhov, M. Runne, M. Queffelec, T. V. Uvarova, and G. Zimmerer, J. Lumin. **78**, 91 (1998).
6. J. Becker, J. Y. Gesland, N. Yu. Kirikova, J. C. Krupa, V. N. Makhov, M. Runne, M. Queffelec, T. V. Uvarova, and G. Zimmerer, J. Alloys Compd. **275–277**, 205 (1998).
7. M. A. Couto dos Santos, E. Antic-Fidancev, J. Y. Gesland, J. C. Krupa, M. Lemaite-Blaise, and P. Porcher, J. Alloys Compd. **275–277**, 435 (1998).
8. R. T. Wigh, A. Meijerink, R. -J. Lamminmäki, and J. Hölsä, J. Lumin. **87–89**, 1002 (2000).
9. N. M. Khaidukov, M. Kirm, S. K. Lam, D. Lo, V. N. Makhov, and G. Zimmerer, Opt. Commun. **184**, 183 (2000).
10. V. N. Makhov, N. M. Khaidukov, M. Kirm, E. Negodin, G. Zimmerer, S. K. Lam, D. Lo, and N. V. Suetin, Surf. Rev. Lett. **9** (1), 621 (2002).
11. L. van Pieterson, M. F. Reid, R. T. Wegh, and A. Meijerink, J. Lumin. **94–95**, 79 (2001).
12. L. K. Ermakov, P. A. Rodnyĭ, and N. V. Starostin, Fiz. Tverd. Tela (Leningrad) **33** (9), 2542 (1991) [Sov. Phys. Solid State **33** (9), 1435 (1991)].

Translated by G. Skrebtsov

Physics of the Solid State, Vol. 47, No. 8, 2005, pp. 1450–1453. Translated from Fizika Tverdogo Tela, Vol. 47, No. 8, 2005, pp. 1398–1400.
Original Russian Text Copyright © 2005 by Vazhenin, Potapov, Gorlov, Nikiforov, Kazanskiĭ, Ryskin.

PROCEEDINGS OF THE XII FEOFILOV WORKSHOP “SPECTROSCOPY OF CRYSTALS ACTIVATED BY RARE-EARTH AND TRANSITION-METAL IONS”

(Yekaterinburg, Russia, September 22–25, 2004)

Paramagnetic Resonance of Gd^{3+} Ions in Nonstoichiometric Fluorite $R_xM_{1-x}F_{2+x}$ (R = Y, Gd; M = Ca, Cd)

V. A. Vazhenin*, A. P. Potapov*, A. D. Gorlov*, A. E. Nikiforov*,
S. A. Kazanskiĭ, and A. I. Ryskin****

**Ural State University, pr. Lenina 51, Yekaterinburg, 620083 Russia*
e-mail: vladimir.vazhenin@usu.ru
***Vavilov State Optical Institute, Birzhevaya liniya 14, St. Petersburg, 199034 Russia*

Abstract—EPR studies of $Y_{0.03}Ca_{0.97}F_{2.03} : Gd^{3+}$ and $Y_{0.03}Cd_{0.97}F_{2.03} : Gd^{3+}$ single crystals revealed the presence of Gd^{3+} ions embedded in yttrium clusters. The symmetry of the paramagnetic centers was determined, and the fine-structure parameters were estimated both experimentally and theoretically. *© 2005 Pleiades Publishing, Inc.*

1. Long-standing studies of fluorite structure crystals doped with Group III elements, primarily rare-earth elements and yttrium, have revealed that they contain large clusters of activator ions, which account for the new properties of these materials [1–7]. Three types of rare-earth clusters [3–5], which are essentially the cores of superclusters [6], are currently known: rare-earth octahedral $R_6M_8F_{68,\,69}$, rare-earth tetrahedral $R_4M_{10}F_{67}$, and alkaline-earth octahedral $R_8M_6F_{71}$, where R stands for a rare-earth element or yttrium and M is Ca, Se, Ba, Cd, or Pb. Due to their shape and size, which are practically identical to those of the fluorite building block $M_{14}F_{64}$, superclusters are easily incorporated into a crystal lattice. Coherent matching of superclusters and of their associations to the matrix accounts for the nonstoichiometric phases $R_xM_{1-x}F_{2+x}$ becoming a novel class of nanosized materials that retain their single-crystal character both in outer appearance and as evidenced by electron, neutron, and x-ray diffraction measurements [1]. For certain values of x, these crystals exhibit superstructural lattice ordering.

Studies of optically detected EPR [2, 8, 9] have revealed that the main cluster type in $Y_xCa_{1-x}F_{2+x}$ is Y_6F_{37} (supercluster $Y_6M_8F_{69}$); this is borne out, in particular, by the existence of Tm^{3+}, Er^{3+}, and Yb^{3+} tetragonal centers with anomalously large values of $g_{\parallel}$ and, hence, with an environment structure not typical of a fluorite.

The present paper reports on the use of EPR spectra of high-spin rare-earth Gd^{3+} centers to study the cluster formation in nonstoichiometric fluorites in the absence of an ordered structure.

2. To suppress the spin–spin interaction, the magnetic impurity was diluted, as in [2], by Y^{3+} diamagnetic ions; i.e., we studied CaF_2 and CdF_2 single crystals doped by 3 mol % YF_3 and 0.01 (samples 3, 3') or 0.1 mol % GdF_3 (samples 4, 4'), as well as crystals with the same GdF_3 doping levels but without YF_3 (CaF_2 samples 1, 2; CdF_2 samples 1', 2'). Measurements were conducted on a 3-cm EPR spectrometer at temperatures ranging from 150 to 450 K. No substantial differences were revealed in the EPR spectra of annealed (for 20 h at 600°C) and quenched (cooled from 900°C together with the growth furnace) crystals.

3. All $Y_xCa_{1-x}F_{2+x} : Gd^{3+}$ samples exhibit well-known EPR spectra of cubic centers [10] (a single Gd^{3+} ion occupying the Ca^{2+} position) and simple tetragonal centers (a Gd^{3+} ion in the Ca^{2+} position and a fluorine ion in the nearest neighbor interstice on the C_4 axis) with $S = 7/2$. The only difference is that samples 1 are dominated by tetragonal centers, while in crystals 2 the EPR intensities of the cubic and tetragonal centers are of the same order of magnitude. In yttrium-doped samples 3 and 4, traces of tetragonal centers are barely detectable, whereas the EPR spectra of cubic centers are very strong (although they are noticeably broadened as compared to those of samples 1 and 2).

The spectrum of a cubic center is described by a spin Hamiltonian with the parameters listed in the table. The integrated intensity of the spectrum of cubic centers increases by nearly two orders of magnitude as one goes from samples 1 to samples 2. The concentration of cubic centers in samples 1 and 3 is about the same, while that in samples 4 is higher by a factor of 2 to 3.

Samples 1' and 2' exhibit a strong EPR spectrum of the Gd^{3+} cubic center, which differs only slightly from that of the $CdF_2 : Gd^{3+}$ studied in [11].

As one goes from samples 1' to samples 2' (unlike $Y_xCa_{1-x}F_{2+x}$: Gd^{3+}), the integrated EPR intensity of the Gd^{3+} cubic center grows by more than 20%. Samples 3' and 4' doped by yttrium exhibit a weak spectrum similar to that of the Gd^{3+} cubic center characteristic of samples 1' and 2'. Note that the width of the cubic-center lines in sample 4' is approximately three times larger and their integrated intensity is one order of magnitude weaker than the respective values in sample 2'. In yttrium-doped crystals, the ±7/2 ⟷ ±5/2 transitions (in contrast to other signals) exhibit a pattern (Fig. 1) which could be attributed to a crystal block structure or weak distortions of the cubic environment. This pattern accounts for the sharp increase in the rms deviation (see table).

An analysis of the values of $\Delta B_{res}/\Delta\theta$ and dB_{res}/db_4 for various transitions, as well as the constancy of the structure of signals obtained in different samples, suggests that the observed pattern of ±7/2 ⟷ ±5/2 transitions is due to the existence of a family of quasi-cubic centers. The misorientation of the principal *g*-tensor axes of the low-spin tetragonal centers studied in [2], which becomes manifest in a structure of optically detected EPR lines, is also most likely caused by the specific environment (with a lower than tetragonal symmetry) of the rare-earth ions localized in $Y_6F_{36,\,37}$ clusters (for instance, as a result of the association of several clusters).

Note that our crystals without yttrium reveal an even larger number of weak signals whose pattern varies with gadolinium concentration. These signals can be tentatively assigned to gadolinium ion associates.

4. Crystals with yttrium exhibit, in addition to the spectra of Gd^{3+} cubic centers, new unknown EPR signals. In calcium and cadmium fluorides, these spectra differ substantially in pattern (Figs. 2, 3).

An increase in gadolinium concentration (as one goes from sample 3 to sample 4 or from 3' to 4') does not bring about a change in the intensity ratio between the cubic-center and additional spectra. This argues for the new spectra being due to single Gd^{3+} ions that are in an environment not typical of a stoichiometric fluorite. The assignment of transitions in both crystals is complicated by the large number of signals, their superposition, and, as a result, the impossibility of studying a signal over a large enough range of magnetic field orientations.

Investigation of the angular dependence of the spectrum of $Y_xCa_{1-x}F_{2+x}$: Gd^{3+} showed that the resonance positions of the family of new EPR signals with similar parameters reach an extremum at $\mathbf{B} \parallel C_4$ and that practically all new signals split as one moves away from $\mathbf{B} \parallel C_3$. This behavior of the EPR spectrum suggests the observed centers to have tetragonal symmetry. The averaged axial parameter b_{20} of a group of tetragonal centers is found to be about 600 MHz.

Parameters of the spin Hamiltonian of Gd^{3+} cubic centers (b_n and rms deviation of *f* are given in MHz)

Crystal	*g*	b_4	b_6	*f*
CaF_2 [10]	1.993	–140.08(40)	–0.04(4)	
CaF_2 (nos. 1, 2)	1.992	–139.7	–0.24	2.8
$Y_xCa_{1-x}F_{2+x}$ (nos. 3, 4)	1.991	–139.2	–0.3	3.7
CdF_2 [11]	1.992	–142(1)	0(1)	
CdF_2 (nos. 1', 2')	1.992	–142.4	–0.4	1.7
$Y_xCd_{1-x}F_{2+x}$ (nos. 3', 4')	1.992	–141.7	–0.3	34

In the $Y_xCd_{1-x}F_{2+x}$: Gd^{3+} spectrum, we isolated several signals that passed through an extremal resonance position at $\mathbf{B} \parallel C_3$. The interpretation of these signals as transitions in a trigonal center with $b_{20} \approx$ 300 MHz made it possible to qualitatively explain the observed spectrum, in particular, the strong central group of signals standing out in Fig. 3, whose components split under deviation from the $\mathbf{B} \parallel C_4$ orientation.

5. Summing up the results of a comparison of the intensities of simple cubic and tetragonal centers (see Section 3), we can conclude that doping CaF_2 and CdF_2 crystals with yttrium gives rise to a substantial decrease in the concentration of simple Gd^{3+} centers and, in the

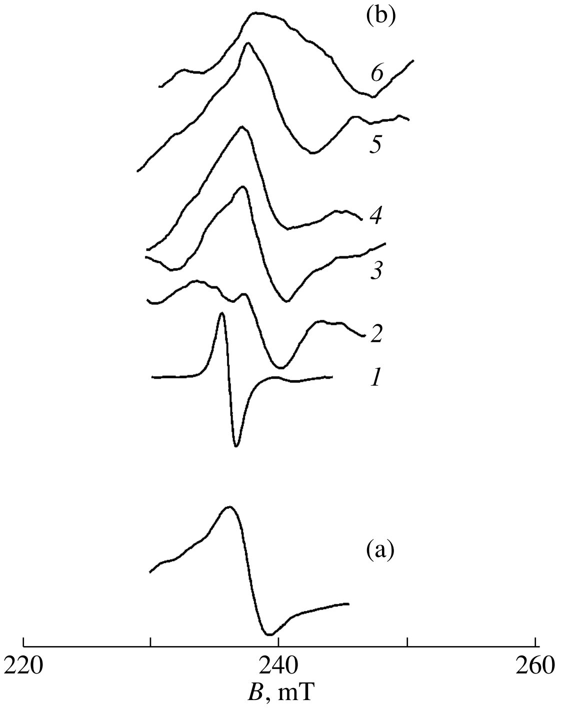

Fig. 1. Pattern of the –5/2 ⟷ –7/2 EPR transition of the Gd^{3+} cubic center. (a) CaF_2, sample 4 at θ = 0 (θ is the angle the magnetic field **B** makes with the C_4 axis). (b) CdF_2 spectra: (*1*) sample 2' for θ = 0, (*2*) sample 4' for θ = 0, (*3*) sample 4' for θ = 2°, (*4*) sample 4' for θ = 4°, (*5*) sample 4' for θ = 6°, and (*6*) sample 4' for θ = 8°.

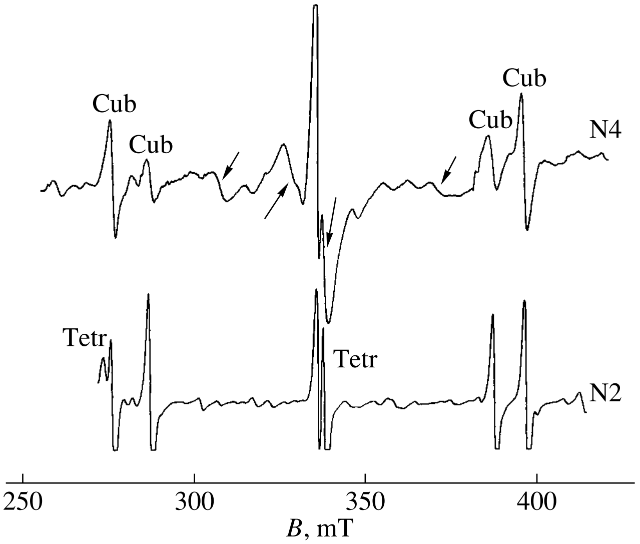

Fig. 2. Fragment of the EPR spectrum of Gd^{3+} (0.1%) in yttrium-doped (sample 4) and undoped CaF_2 (sample 2) obtained with **B** || C_4. Arrows identify signals due to yttrium doping.

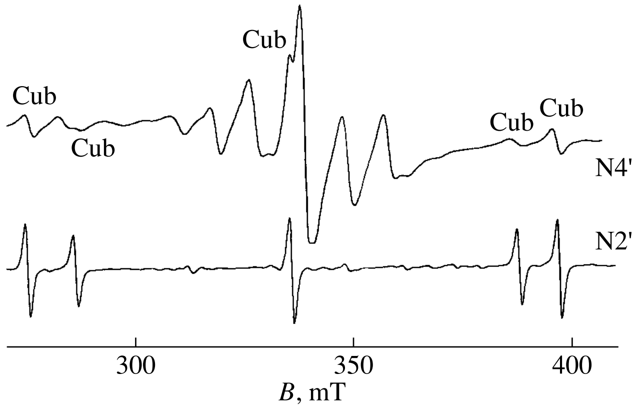

Fig. 3. Central part of the EPR spectrum of Gd^{3+} (0.1%) in yttrium-doped (sample 4') and undoped CdF_2 (sample 2') obtained with **B** || C_4.

case of CaF_2, to a decrease in the concentration of interstitial fluorine ions as well. In view of this, the formation of Gd^{3+} spectra not characteristic of weakly doped materials in yttrium-doped calcium and cadmium fluorides suggests that in both crystals there are yttrium clusters that include interstitial fluorine ions. Under the chosen impurity concentrations, it is most likely that Y^{3+} in only one position is replaced by the Gd^{3+} ion in these clusters and that it is its EPR spectra that are observed. The multiplicity of paramagnetic centers may be due to the fact that various mechanisms of compensation of a charged cluster are operative and that several clusters coalesce.

The observation of tetragonal gadolinium centers in $Y_xCa_{1-x}F_{2+x} : Gd^{3+}$ is in accord with a report [2] suggesting the existence of Y_6F_{37} clusters in this crystal. The trigonal pattern of the EPR spectrum of $Y_xCd_{1-x}F_{2+x} : Gd^{3+}$ indicates the formation of clusters of another type in cadmium fluoride. Note that the symmetry of the rare-earth ion in clusters of the two other known types is trigonal [4, 5].

The structure of the nearest environment of the rare-earth ion in the Gd_6F_{36} cluster was derived in [8] for calcium fluoride by minimizing the energy of a crystal lattice with the embedded cluster. Assuming that the difference in structure between the GdY_5F_{36} and Gd_6F_{36} clusters is inessential, we use the results obtained with a semiempirical superposition model [9, 12], which proves valid for the second-rank fine-structure parameters of rare-earth ions in the *S* state. For the Gd^{3+} ion in this environment, we obtain $b_{20} \approx 2400$ MHz; the inclusion of an interstitial fluorine ion embedded at the cluster center (i.e., the transition to the GdY_5F_{37} cluster) reduces b_{20} by one order of magnitude to bring it close to the experimental value.

In CaF_2 clusters with 3 mol % YF_3, in the case where all yttrium ions reside in isolated Y_6F_{37}-type clusters, the average distance between the centers of the clusters is ~2.4 nm (the clusters are ~0.5 nm in size). According to the superposition model, a fluorine ion localized at the second and third interstices away from the Gd^{3+} ion on the tetragonal axis ($R \approx 0.8$ and 1.4 nm, respectively) brings about an initial splitting $b_{20} \approx -150$ and -35 MHz, respectively (the shift of the $\pm 7/2 \longleftrightarrow \pm 5/2$ transitions in the latter case is $6b_{20}/g\beta \approx 7/5$ mT). Neglecting the cluster strain field, we assume a singly charged cluster Y_6F_{37} to cause about the same Gd^{3+} perturbation as an interstitial fluorine ion. To obtain cubic centers exhibiting a structured spectrum similar to the experimental spectrum of CdF_2 with yttrium (the splitting of the $-7/2 \longleftrightarrow -5/2$ transition in Fig. 1 is ~4 mT), the average cluster separation should be larger than 3 nm, which is possible only when groups of clusters form. The smaller distortion of cubic centers in yttrium-doped CaF_2 crystals (Fig. 1) indicates an even more pronounced cluster association. This conclusion is supported by the observation that the integrated intensity of the spectrum of cubic centers in yttrium-doped CaF_2 crystals is 5 to 10 times higher than that in CdF_2.

ACKNOWLEDGMENTS

This study was supported by the Russian Foundation for Basic Research, project no. 04-02-16427.

REFERENCES

1. B. P. Sobolev, A. M. Golubev, and P. Érrero, Kristallografiya **48** (1), 148 (2003) [Crystallogr. Rep. **48** (1), 141 (2003)].
2. S. A. Kazanskiĭ and A. I. Ryskin, Fiz. Tverd. Tela (St. Petersburg) **44** (8), 1356 (2002) [Phys. Solid State **44** (8), 1415 (2002)].
3. D. J. Bevan, O. Greis, and J. Strahle, Acta Crystallogr. A **36** (6), 889 (1980).
4. L. A. Muradyan, B. A. Maksimov, B. F. Mamin, N. N. Bydanov, V. A. Sarin, B. P. Sobolev, and V. I. Simonov, Kristallografiya **31** (2), 248 (1986) [Sov. Phys. Crystallogr. **31** (2), 145 (1986)].
5. B. P. Sobolev, A. M. Golubev, L. P. Otroshchenko, V. N. Molchanov, R. M. Zakalyukin, E. A. Ryzhova, and P. Herrero, Crystallogr. Rep. **48** (6), 944 (2003).
6. A. M. Golubev and V. I. Simonov, Kristallografiya **31** (3), 478 (1986) [Sov. Phys. Crystallogr. **31** (3), 281 (1986)].
7. S. A. Kazanskiĭ, Pis'ma Zh. Éksp. Teor. Fiz. **38** (9), 430 (1983) [JETP Lett. **38** (9), 521 (1983)].
8. A. E. Nikiforov, A. Yu. Zaharov, M. Yu. Ougrumov, and V. A. Chernyshev, in *Proceedings of the 5th European Conference on Luminescent Detectors, Prague* (Prague, 2003), p. 51.
9. D. J. Newman and W. Urban, Adv. Phys. **24**, 793 (1975).
10. K. Horai, J. Phys. Soc. Jpn. **19**, 2241 (1964).
11. J. M. Baker and F. I. B. Williams, Proc. Phys. Soc. London **78**, 1340 (1961).
12. L. I. Levin, Phys. Status Solidi B **134**, 275 (1986).

Translated by G. Skrebtsov

Physics of the Solid State, Vol. 47, No. 8, 2005, pp. 1454–1456. Translated from Fizika Tverdogo Tela, Vol. 47, No. 8, 2005, pp. 1401–1402.
Original Russian Text Copyright © 2005 by Vazhenin, Guseva, Artemov, Potapov.

PROCEEDINGS OF THE XII FEOFILOV WORKSHOP "SPECTROSCOPY OF CRYSTALS ACTIVATED BY RARE-EARTH AND TRANSITION-METAL IONS"

(Yekaterinburg, Russia, September 22–25, 2004)

Influence of Interacting Resonances on the Electron Paramagnetic Resonance Spectrum of Gd^{3+} Dipole Centers in Fluorites

V. A. Vazhenin, V. B. Guseva, M. Yu. Artemov, and A. P. Potapov
Ural State University, pr. Lenina 51, Yekaterinburg, 620083 Russia
e-mail: vladimir.vazhenin@usu.ru

Abstract—This paper discusses the possibility of detecting the selective averaging of spin packets in the vicinity of coincidence of the electron paramagnetic resonance signals associated with transitions of Gd^{3+} dipole centers due to orientational relaxation. *© 2005 Pleiades Publishing, Inc.*

As was shown earlier in [1–5], an additional EPR signal appears between the initial signals when the orientation of a polarizing magnetic field corresponds to accidental coincidence of the resonance lines associated with two electron paramagnetic resonance (EPR) transitions (the initial signals were attributed either to different transitions of a high-spin center or to hyperfine components of two off-center configurations related through transitions of a low-spin center). In our previous works [2, 6], we demonstrated that the origin of an additional signal both in the EPR spectrum of Gd^{3+} trigonal centers in ferroelectric lead germanate and in the spectrum of Gd^{3+} tetragonal centers in crystals with a $CaWO_4$-type structure is associated with averaging (due to relaxation spin–lattice transitions between resonant doublet states) of the internal part of the spin packets corresponding to the initial signals. A necessary condition for the appearance of a three-component EPR spectrum is a quasi-symmetric structure of the spin packets for a pair of initial lines. This arrangement of the spin packets is determined by the spread of the spin Hamiltonian parameters b_{43} and b_{21} for the $Pb_5Ge_3O_{11} : Gd^{3+}$ compound and by the mosaic structure of crystals for scheelites. Analysis of the observed three-component EPR spectrum allowed us to determine the rate of exchange between accidentally coinciding resonances.

Crystals with a fluorite-type structure contain Gd^{3+} dipole (trigonal and tetragonal) centers in the form of associates with charge-compensating interstitial fluorine ions that undergo thermally stimulated transitions between different orientational configurations (due to fluorine ion hopping) [7–10]. Owing to these features, crystals with a fluorite-type structure are promising model objects for use in analyzing the influence of interacting resonances (reorientation of the dipole centers) on the EPR spectrum in the vicinity of the coincidence of the resonance lines attributed to centers of different orientations.

In a magnetic field $\mathbf{B} \parallel \mathbf{C}_2$, two tetragonal centers become equivalent; in this case, the polar angular dependence of the magnitude $dB_{res}/d\theta$ for the $3 \longleftrightarrow 4$ transition in the CaF_2 compound and the $4 \longleftrightarrow 5$ transition in the SrF_2 compound exhibits a pronounced maximum (Fig. 1). A similar behavior of the linewidth ΔB_{pp} (Fig. 1) indicates that the mosaic structure of the crystal makes a noticeable contribution to the EPR linewidth. It is this mosaicity of the crystal structure that is responsible for the symmetric arrangement of the spin packets corresponding to signals from the aforementioned two centers when the misorientation with respect to $\mathbf{B} \parallel \mathbf{C}_2$ is small.

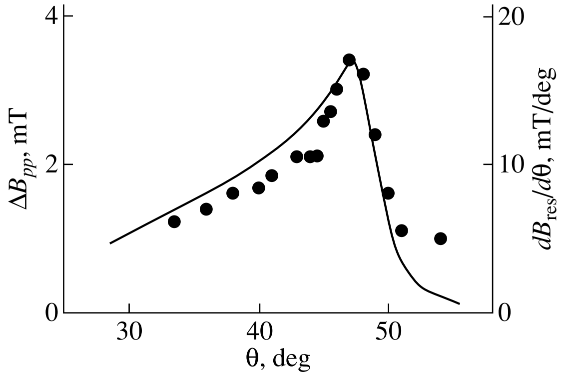

Fig. 1. Polar angular dependence of the linewidth ΔB_{pp} (circles) and the magnitude $dB_{res}/d\theta$ (solid line) for the $3 \longleftrightarrow 4$ transition of the Gd^{3+} tetragonal centers in the CaF_2 compound at T = 300 K.

The spectral measurements in the range close to the intersection of the angular dependences of the positions of the EPR signals attributed to the above transitions were performed at temperatures higher than 370 K for calcium fluoride (0.016 mol % Gd) and above 450 K for strontium fluoride (0.14 mol % Gd). Under these conditions, according to the data obtained in [7, 9], the frequency of reorientations of Gd^{3+} tetragonal dipole centers exceeds 100 MHz and, hence, part of the spin packets should be effectively averaged. For the CaF_2 compound, the measurements were hampered by the fact that the EPR spectrum contained signals associated with cubic centers whose intensity decreased considerably slower than that of the tetragonal centers as the temperature increased. The use of additional angular magnetic modulation made it possible to suppress signals from the cubic centers; however, analysis of the spectrum of Gd^{3+} tetragonal centers, i.e., the second derivatives of the absorption signals with opposite phases, turned out to be inefficient. A better situation occurred with the SrF_2 compound. However, in this case also, no additional signal was observed in the vicinity of the coincidence of the electron paramagnetic resonances. It is worth noting that the intensities of the signals attributed to the two tetragonal centers turned out to be noticeably different from each other, which is most likely caused by the difference in the populations of these configurations [11] due to the different binding energies.

An external electric field **E** aligned with the magnetic field **B** ($\mathbf{E} \parallel \mathbf{B} \parallel \mathbf{C}_4$) leads to splitting of the $5 \longleftrightarrow 7$ transition of the Gd^{3+} tetragonal centers in the CaF_2 compound [12]. In a nonuniform electric field, the split components are broadened with a symmetric arrangement of equifield spin packets. The measurements were carried out using a CaF_2 (0.016 mol % Gd) single crystal 0.54 mm thick with electrodes partially covering the sample at 380 K. (Note that the maximum longitudinal field was 185 kV/cm, and the accompanying transverse fields at even such a field strength did not induce a noticeable pseudo-Stark effect.) No additional signal between the electric-field–split components of the $5 \longleftrightarrow 7$ transition was observed. Furthermore, no features associated with the transitions of Gd^{3+} trigonal centers in the BaF_2 compound were revealed in the spectrum measured in the magnetic field $\mathbf{B} \parallel \mathbf{C}_4$.

In order to understand why an additional signal was not observed in the EPR spectrum, we analyzed the spectral shape as a function of the number of wells in the multiwell potential of the dipole center (the tetragonal center is characterized by a six-well potential). For this purpose, we simulated the EPR spectra in the vicinity of the coincidence of the resonance lines attributed to transitions of a paramagnetic center in two wells of the double-, triple-, and quadruple-well potentials according to the expressions derived in our earlier work [2]. The results of this simulation are compared in Fig. 2. The initial lines correspond to a symmetric spin-packet structure with a Lorentzian packet width of 1.15 mT and a Gaussian intensity distribution of 2.73 mT. In all cases, the lifetime of the relative transition to the neighboring wells is equal to 2×10^{-8} s. The resonance lines of the transitions undergone by the paramagnetic centers in the third and fourth wells were found to be 12 mT away from those of the simulated transitions and, therefore, are not seen in Fig. 2.

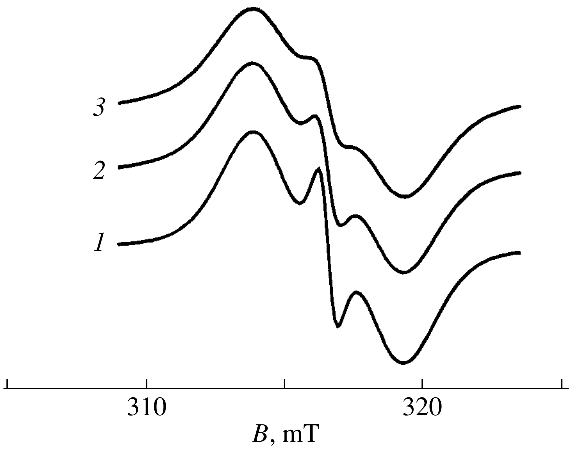

Fig. 2. Comparison of the simulated EPR spectra for (*1*) double-, (*2*) triple-, and (*3*) quadruple-well potentials.

As is clearly seen from Fig. 2, an increase in the number of potential wells leads to a decrease in the rate of exchange between interacting resonances (according to estimates, the effective lifetime increases by a factor of 1.5 upon changing over to the triple-well potential), thus making the additional signal less noticeable. Moreover, the relaxation processes and the reorientation of the dipole center [13] induce transitions of the paramagnetic ion to spin states that do not contribute to the observed resonances, which, in turn, further slows down the exchange between them.

Naturally, an increase in the temperature can accelerate the reorientation of dipole centers. However, the width of the spin packet will also increase accordingly. Since the width of the additional signal is of the same order of magnitude but somewhat exceeds the width of the spin packet, the observation of the additional signal in the EPR spectrum is also unlikely in this case.

ACKNOWLEDGMENTS

This work was supported by the Russian Foundation for Basic Research, project no. 04-02-16427.

REFERENCES

1. V. A. Vazhenin and K. M. Starichenko, Pis'ma Zh. Éksp. Teor. Fiz. **51** (8), 406 (1990) [JETP Lett. **51** (8), 461 (1990)].

2. V. A. Vazhenin, V. B. Guseva, and M. Yu. Artemov, Fiz. Tverd. Tela (St. Petersburg) **44** (6), 1096 (2002) [Phys. Solid State **44** (6), 1145 (2002)].
3. V. K. Voronkova, L. V. Mosina, Yu. V. Yablokob, I. Kovacik, H. Langfelderova, and J. Kozisek, Mol. Phys. **75** (6), 1275 (1992).
4. A. A. Galeev, N. M. Khasanova, A. V. Bykov, G. R. Bulka, V. M. Vinokurov, and N. M. Nizamutdinov, Appl. Magn. Reson. **11**, 61 (1996).
5. G. V. Mamin and V. N. Efimov, Mod. Phys. Lett. B **12** (22), 929 (1998).
6. V. A. Vazhenin, V. B. Guseva, and M. Yu. Artemov, Fiz. Tverd. Tela (St. Petersburg) **45** (12), 2168 (2003) [Phys. Solid State **45** (12), 2271 (2003)].
7. E. L. Kitts, Jr., M. Ikeya, and J. H. Crawford, Jr., Phys. Rev. B **8** (12), 5840 (1973).
8. A. D. Franklin and S. Marzullo, J. Phys. C: Solid State Phys. **3** (9), L171 (1970).
9. V. A. Vazhenin, Yu. A. Sherstkov, N. V. Legkikh, and K. M. Zolotareva, Fiz. Tverd. Tela (Leningrad) **18** (9), 2614 (1976) [Sov. Phys. Solid State **18** (9), 1526 (1976)].
10. V. A. Vazhenin, V. B. Guseva, and M. Yu. Artemov, Fiz. Tverd. Tela (St. Petersburg) **42** (6), 1017 (2000) [Phys. Solid State **42** (6), 1049 (2000)].
11. G. R. Bulka, V. M. Vinokurov, N. M. Nizamutdinov, and N. M. Nasanova, Phys. Chem. Miner. **6**, 283 (1980).
12. Yu. A. Sherstkov, V. A. Vazhenin, and K. M. Zolotareva, Fiz. Tverd. Tela (Leningrad) **17**, 2757 (1975) [Sov. Phys. Solid State **17**, 1830 (1975)].
13. V. S. Vikhnin, Fiz. Tverd. Tela (Leningrad) **20** (5), 1340 (1978) [Sov. Phys. Solid State **20** (5), 771 (1978)].

Translated by V. Artyukhov

Physics of the Solid State, Vol. 47, No. 8, 2005, pp. 1457–1459. Translated from Fizika Tverdogo Tela, Vol. 47, No. 8, 2005, pp. 1403–1405.
Original Russian Text Copyright © 2005 by Nizamutdinov, Semashko, Naumov, Abdulsabirov, Korableva, Marisov.

PROCEEDINGS OF THE XII FEOFILOV WORKSHOP "SPECTROSCOPY OF CRYSTALS ACTIVATED BY RARE-EARTH AND TRANSITION-METAL IONS"

(Yekaterinburg, Russia, September 22–25, 2004)

Photodynamic Processes in CaF_2 Crystals Activated by Ce^{3+} and Yb^{3+} Ions

A. S. Nizamutdinov, V. V. Semashko, A. K. Naumov, R. Yu. Abdulsabirov, S. L. Korableva, and M. A. Marisov
Kazan State University, ul. Kremlevskaya 18, Kazan, 420008 Tatarstan, Russia
e-mail: anizamutdinov@mail.ru, vadim.semashko@ksu.ru

Abstract—The photochemical properties of CaF_2 crystals activated by Ce^{3+} and Yb^{3+} ions are studied. A model of the photodynamic processes induced by pumping UV or VUV radiation in active media is suggested and experimentally verified. This model explains both the presence of color centers of electronic and hole nature in crystals activated by cerium and the mechanism of suppressing of solarization processes after additional activation of the samples by Yb^{3+} ions. The cross sections of the processes of free-carrier capture by various ytterbium impurity centers are estimated. These impurity centers are established to be effective centers of recombination of free carriers of both signs. *© 2005 Pleiades Publishing, Inc.*

The various photodynamic processes induced by exciting UV radiation are the main factors leading to degradation of the optical properties of active and passive crystalline media activated by rare-earth ions; these media are used in UV- and VUV-optical devices. These photodynamic processes involve two-photon absorption at the pumping wavelength and the ionization and deionization of the activating ions resulting in the formation of various color centers (Fig. 1). Recently, we have suggested a crystallochemical method for suppressing the formation of color centers in cerium-containing UV-active media exposed to UV or VUV pumping [1]. However, in spite of successful practical applications of this method, the mechanism of the suppression of solarization is still not sufficiently clear.

The aim of this study is to substantiate the model of suppression of the solarization processes induced by UV pumping in media activated by Ce^{3+} ions. For our investigation, we chose the best studied fluorite CaF_2 matrices. CaF_2 crystals activated by trivalent Ce^{3+} and Yb^{3+} ions were prepared at the Crystal Growth Laboratory, Kazan State University. The concentration of Ce^{3+} ions in the charge components was 0.5 wt %, and the concentration of Yb^{3+} ions varied from 0 to 2 wt %.

It is known that the incorporation of trivalent rare-earth ions into a CaF_2 crystal lattice leads to the formation of tetragonal and cubic impurity centers (with local compensation of the excess positive charge by an interstitial F^- ion and with nonlocal compensation of the charge, respectively) [2, 3]. It is also known that, in $CaF_2 : Ce^{3+}$ crystals, color centers of both electronic and hole types form under UV pumping resonant with the interconfiguration $4f$–$5d$ transitions in Ce^{3+} ions (see references in [1, 4]). In spite of the expected ionization of the activator ions, spectroscopic experiments do not detect any changes in the concentration of Ce^{3+} ions. Within the model proposed here, we assume that, after photoionization, an impurity center quickly restores its valency to 3+ by accepting an electron from the valence band (Fig. 1). Thus, almost simultaneously with photoelectrons, free holes are generated in the valence band. These carriers can be captured by defects of the crystal lattice, forming color centers of both electronic and hole nature.

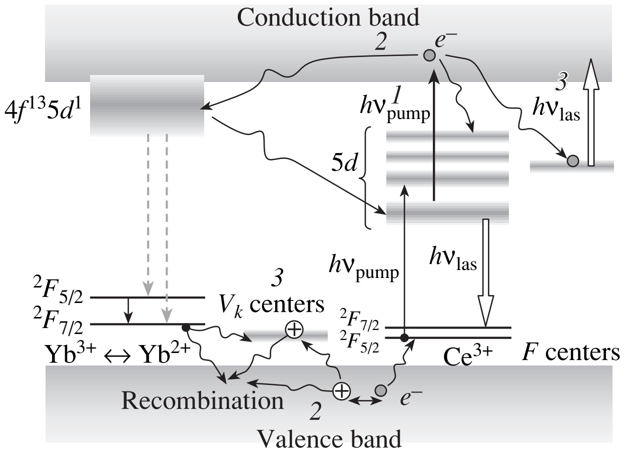

Fig. 1. Model of solarization caused by UV irradiation of a medium activated by Ce^{3+} and Yb^{3+} ions. (*1*) Two-photon pumping absorption, i.e., photoionization of an impurity ion; (*2*) thermalization of free carriers; and (*3*) capture of free carriers by defects and the formation of color centers.

1063-7834/05/4708-1457$26.00 © 2005 Pleiades Publishing, Inc.

Calculated parameters of impurity centers (e is the elementary charge, $a = 5 \times 10^{-10}$ m is the lattice constant)

Parameter	Cubic center		Tetragonal center	
	$Yb^{3+} + e^-$	Yb^{2+} + hole	$Yb^{3+} + e^-$	Yb^{2+} + hole
Effective center charge	$0.65 + 1e$	$-0.51e$	$0.65e$	$-1.51e$
Capture sphere radius	$4.6a$	$19a$	$2a$	?
Capture cross section, 10^{-15} cm^2	192.5	11.9	20	?

The idea behind the crystallochemical method for suppressing solarization processes consists in additional activation of the crystals by ions that, by virtue of their physical and chemical properties, would stimulate the recombination of the majority carriers competing with their capture by the defects of the crystal lattice (Fig. 1) [5]. The Yb^{3+} ion may be one of the ions that inhibit the solarization process, since the states of its mixed $4f5d$ configuration are localized near the bottom of the conduction band or even overlap with it. Moreover, the Yb^{3+} ion has a high electron affinity and, therefore, is a good electron trap (as compared to other rare-earth ions), which decreases the probability of reduction of Ce^{3+} ions to Ce^{2+} ions. However, it follows both from the results obtained earlier [6] and from the results of this study that additional activation of the crystals by Yb^{3+} ions increases the photochemical stability with respect to the formation of color centers not only of electronic but also of hole nature. This can be explained if we assume that, in the case of tetragonal Yb impurity centers, an Yb^{3+} ion is a recombination center for both free electrons and holes. Indeed, after the capture of an electron from the conduction band and reduction to the bivalent state, the ytterbium ion has an excess negative charge and becomes a trap for free holes. The formation of a cubic impurity center with nonlocal charge compensation will, apparently, stabilize the Yb^{2+} ion, since in this case the impurity center is electrically neutral.

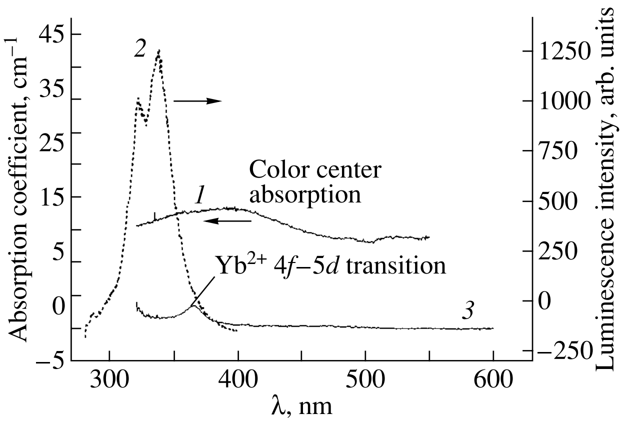

Fig. 2. (*1*, *3*) Absorption and (*2*) luminescence spectra of (*1*, *2*) $CaF_2 : Ce^{3+}$ and (*3*) $CaF_2 : (Yb^{3+} + Ce^{3+})$ crystals. A YAG : Nd laser ($\lambda = 266$ nm) was used for pumping.

The capture cross section can be roughly estimated using the formula [7]

$$\sigma = \frac{4\pi R l}{3} 1.5, \qquad (1)$$

where l is the mean free path of a charge carrier in the matrix and R is the capture radius where the kinetic energy of a free carrier becomes equal to its potential energy in the field of the capture center.

To calculate R, we introduce the concept of the effective charge of a capture center, which takes into account the electron affinity and the type of impurity center involved. The results of the calculations are listed in the table.

The calculations show that the efficiency of electron capture by the cubic Yb^{3+} impurity center is greater than that by the tetragonal Yb center. We also see that the smallest cross section corresponds to the hole capture by the cubic center; therefore, the formation of this center will stabilize the ytterbium ion in the bivalent state. In the model of point charges, it is difficult to estimate the hole capture cross section for the Yb^{2+} ion in a tetragonal environment due to the presence of a compensating ion at the nearest neighbor interstitial site. However, a high efficiency of free-hole capture should be expected in this case.

The above assumptions are fully confirmed experimentally. Figure 2 shows the luminescence spectrum of a $CaF_2 : Ce^{3+}$ crystal; this spectrum is typical of a tetragonal impurity center [2]. In the absorption spectrum of samples exposed to the fourth harmonic of YAG : Nd laser radiation, a wide band is observed in the range 320–470 nm, which overlaps with the band of the radiative $5d$–$4f$ transition of the Ce^{3+} ion and is associated with pumping-induced color centers. However, this band is absent in the spectra of crystals additionally activated by Yb^{3+} ions and exposed to UV radiation under the same conditions. For these crystals, an absorption band with a maximum at 360 nm is observed; according to the data from [3], this band is related to the interconfiguration $4f$–$5d$ transitions in the Yb^{2+} ion. For samples exposed to radiation with wavelengths resonant with the interconfiguration transitions either in the Ce^{3+} ion (in our experiments, 266 nm) or in the Yb^{2+} ion (353 nm), the intensity of this band changes (Fig. 3). This fact indicates that the $Yb^{3+} \longleftrightarrow Yb^{2+}$ recharging processes are reversible. Since the absorption band of the Yb^{2+} ion overlaps with the lumi-

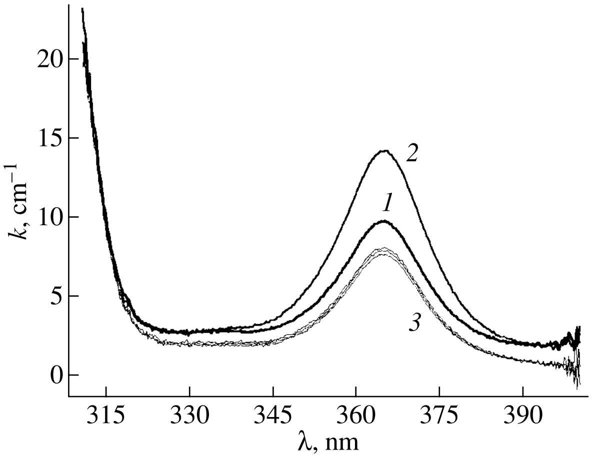

Fig. 3. Change in the equilibrium concentration of Yb^{2+} ions with varying pumping conditions in a CaF_2 : (Yb^{3+} + Ce^{3+}) crystal. A YAG : Nd laser was used for pumping at a wavelength λ equal to (*1*, *2*) 266 and (*3*) 353 nm; (*1*) the initial curve and (*2*) the curve after exposure for 1 h.

nescence band of the Ce^{3+} ion, the concentration of Yb^{2+} ions in the samples is determined by the dynamic equilibrium between these recharging processes.

A straightforward observation of the change in the Yb ion valency ($Yb^{3+} \longleftrightarrow Yb^{2+}$) under resonant UV excitation in the region of the $4f \longleftrightarrow 5d$ transitions in the Ce^{3+} ion confirms the above model for the photodynamic processes in fluorite crystals and the role of Yb^{3+} ions as recombination centers for free carriers. In comparing Figs. 2 and 3, we see that the free-carrier recombination on Yb^{3+} ions competes successfully with the formation of color centers.

ACKNOWLEDGMENTS

This study was supported by CRDF (grant REC-007) and the Russian Foundation for Basic Research (project no. 03-02-17361).

REFERENCES

1. V. V. Semashko, M. A. Dubinskii, R. Yu. Abdulsabirov, S. L. Korableva, A. K. Naumov, A. S. Nizamutdinov, and M. S. Zhuchkov, Proc. SPIE **4766** (17), 119 (2001).
2. I. V. Stepanov and P. P. Feofilov, Dokl. Akad. Nauk SSSR **108**, 615 (1956) [Sov. Phys. Dokl. **1**, 350 (1956)].
3. A. A. Kaplyanskiĭ and P. P. Feofilov, Opt. Spektrosk. **13**, 235 (1962).
4. D. J. Pogashnik and D. S. Hamilton, Phys. Rev. B **36**, 8251 (1987).
5. M. A. Dubinskiĭ, V. V. Semashko, A. K. Naumov, R. Yu. Abdulsabirov, and S. L. Korableva, J. Mod. Opt. **40** (1), 1 (1993).
6. A. S. Nizamutdinov, V. V. Semashko, A. K. Naumov, R. Yu. Abdulsabirov, and S. L. Korableva, in *Proceedings of VI All-Russian Young School "Coherent Optics and Optical Spectroscopy," Kazan, 2002* (Kazan, 2002), p. 197.
7. V. V. Antonov-Romanovskiĭ, *Kinetics of Photoluminescence of Crystal Phosphors* (Nauka, Moscow, 1966) [in Russian].

Translated by I. Zvyagin

Physics of the Solid State, Vol. 47, No. 8, 2005, pp. 1460–1462. Translated from Fizika Tverdogo Tela, Vol. 47, No. 8, 2005, pp. 1406–1408.
Original Russian Text Copyright © 2005 by Nizamutdinov, Marisov, Semashko, Naumov, Abdulsabirov, Korableva.

PROCEEDINGS OF THE XII FEOFILOV WORKSHOP “SPECTROSCOPY OF CRYSTALS ACTIVATED BY RARE-EARTH AND TRANSITION-METAL IONS”

(Yekaterinburg, Russia, September 22–25, 2004)

Spectral Kinetics of Ce^{3+} Ions in Double-Fluoride Crystals with a Scheelite Structure

A. S. Nizamutdinov, M. A. Marisov, V. V. Semashko, A. K. Naumov, R. Yu. Abdulsabirov, and S. L. Korableva
Kazan State University, Kremlevskaya ul. 18, Kazan, 420008 Tatarstan, Russia
e-mail: vadim.semashko@ksu.ru

Abstract—The influence of the cation composition on the spectral kinetics of Ce^{3+} ions in double-fluoride crystals with a scheelite structure is studied. The importance of the photodynamic processes induced in these crystals by the exciting radiation is demonstrated. The difference in luminescence quantum efficiency between Ce^{3+} ions in $LiYF_4$ and $LiLuF_4$ crystals is found to be due to the different lifetimes of color centers produced in the samples by the exciting radiation and to the different efficiency of the free-carrier recombination at cerium impurity centers. It is shown that Yb^{3+} ions can increase the carrier recombination rate in the crystals.

It is well known that the main advantage that makes $LiLuF_4 : Ce^{3+}$ a better material for lasers than its closest chemical relative $LiYF_4 : Ce^{3+}$ is that the luminescence quantum efficiency of Ce^{3+} ions in $LiLuF_4$ crystals is twice as large. However, the positions of the spectral bands of rare-earth ions in $LiYF_4 : Ce^{3+}$ and $LiLuF_4 : Ce^{3+}$ and the widths of their phonon spectra are almost identical [1]. Therefore, there is no obvious reason for such a drastic difference in the luminescence quantum efficiency of these crystals within the model of isolated impurity centers, without taking into account the transitions between the states of the activator ion and crystal lattice. The occurrence of these transitions is beyond doubt by virtue of the mere effect of solarization of the samples by exciting radiation resonant with the internal 4*f*–5*d* transitions in Ce^{3+} ions [1, 2]. However, up to now, manifestation of the former transitions in spectroscopy experiments with low-intensity excitation (as compared to that in laser tests) has been considered unlikely.

In the present paper, the results of investigating the kinetics of the 5*d*–4*f* luminescence of Ce^{3+} ions in a sequence of $LiY_{1-x}Lu_xF_4$ and $LiLu_{1-x}Yb_xF_4$ crystals are reported and the reasons for the difference in the spectral kinetic properties between Ce^{3+} ions in various double-fluoride crystals with a scheelite structure are explained.

In order to study how the cation composition of the matrix influences the spectral kinetic properties of Ce^{3+} ions in scheelite-structure double-fluoride crystals $LiMeF_4 : Ce^{3+}$ (*Me* = Yb, Lu), series of $LiYF_4 : Ce^{3+}$, $LiLuF_4 : Ce^{3+}$, and $LiLu_{1-x}Yb_xF_4 : Ce^{3+}$ crystals were grown in the Crystal Growth Laboratory at Kazan State University. The Ce^{3+} ion content in the samples varies from 0.1 to 1 at. %, and the content of Yb^{3+} ions ranges from 0 to 10 at. %. All samples were grown and processed under identical conditions.

Luminescence was excited by either the fourth harmonic of a YAG : Nd laser working at a wavelength λ_{ex} = 266 nm or the second harmonic of a tunable dye (Rhodamine-6G) laser at λ_{ex} = 297, 300, 301.5, or 303.3 nm. The exciting-pulse duration did not exceed 7 ns. The kinetics of the luminescence was recorded with a BORDO-211 digital oscilloscope and a FÉU-87 fast photomultiplier. Luminescence was observed at the wavelength corresponding to the long-wavelength peak in the luminescence spectrum of Ce^{3+} ions in the crystals under study (λ_{lum} = 325 nm).

According to the experimental data, the Ce^{3+} luminescence kinetics in the samples is nonexponential (Fig. 1) and can be adequately described by the equation

$$I(t) = A_1 e^{-\frac{t}{\tau_{lum}}} + A_2 \frac{\sigma_{rec}\omega}{\sigma_{trap}\nu} \frac{1}{t^2}, \qquad (1)$$

where the short-lifetime exponential component is due to the 5*d*–4*f* transitions in Ce^{3+} ions, τ_{lum} is the lifetime of an excited 5*d* state, and the relatively long-lifetime hyperbolic part of the time-dependent luminescence intensity *I*(*t*) is due to the recombination of free carriers of both signs at Ce^{3+} ions [3]. According to the model of photodynamic processes in cerium-activated crystals [4], free carriers appear in the conduction and valence bands due to the photoionization of impurities by the exciting radiation and as a result of destruction of short-living color centers [4]. The weighting factors A_1 and A_2, according to the same model, are linear and quadratic in the excitation intensity, respectively. In Eq. (1), σ_{rec} is the recombination cross section, σ_{trap} is the capture cross section of free carriers by traps, ω is the thermal-ionization rate of color centers, and ν is the concentration of defect states (traps) in the crystal.

Fitting of the experimental luminescence kinetics curves by Eq. (1) shows that the lifetime of an excited 5*d* state of the Ce^{3+} ion in $LiLuF_4 : Ce^{3+}$ and $LiYF_4 : Ce^{3+}$ crystals is not dependent on either the sample temperature or the exciting radiation wavelength and is 28 ± 2.4 ns rather than 40 ns as reported previously [1]. This new value of the radiative lifetime of the 5*d* states of the Ce^{3+} ion removes the discrepancy between the stimulated-radiation cross-section values for the 5*d*–4*f* transitions calculated using the luminescence spectra and derived from laser tests.

As for the hyperbolic part of the luminescence kinetics, experimental difficulties prevent quantitative determination of the above microscopic parameters of the samples under study. However, for our purpose, it is sufficient to consider the dependence of this component on the experimental conditions qualitatively.

First, the effective decay time of the hyperbolic part of the luminescence kinetics (the time during which the luminescence intensity decrease by *e* times), as expected for recombination processes, is strongly dependent on temperature, activator ion concentration, sample history, and excitation energy. Second, the lifetime of the color centers in $LiLuF_4 : Ce^{3+}$ crystals is much shorter than that in $LiYF_4 : Ce^{3+}$ crystals. This conclusion can be drawn from the slope of the long (recombination) luminescence kinetics components plotted in semilogarithmic coordinates, which characterizes the thermal-ionization rate of short-living color centers. Third, an analysis of the recombination component of the Ce^{3+} luminescence kinetics (weighting factor A_2) of samples with different chemical compositions under equivalent excitation conditions shows that the recombination of free carriers is the most effective in $LiLuF_4 : Ce^{3+}$ crystals. This is the reason for the apparent doubling of the energy yield of Ce^{3+} ion luminescence in $LiLuF_4$ crystals as compared to that in $LiYF_4$ crystals. This conclusion is supported by measurements of the relative quantum yield under various excitation conditions. For example, in the case of high-energy exciting photons (λ_{ex} = 266 nm) or high-power pumping by lower-energy photons (λ_{ex} = 297 or 300 nm), the values of the quantum yield in $LiYF_4 : Ce^{3+}$ and $LiLuF_4 : Ce^{3+}$ differ by a factor of almost 2. However, when the wavelength increases (at $\lambda_{ex} > 301.5$ nm) or the excitation power density decreases, the difference in the luminescence quantum yield between the crystals under study nearly disappears.

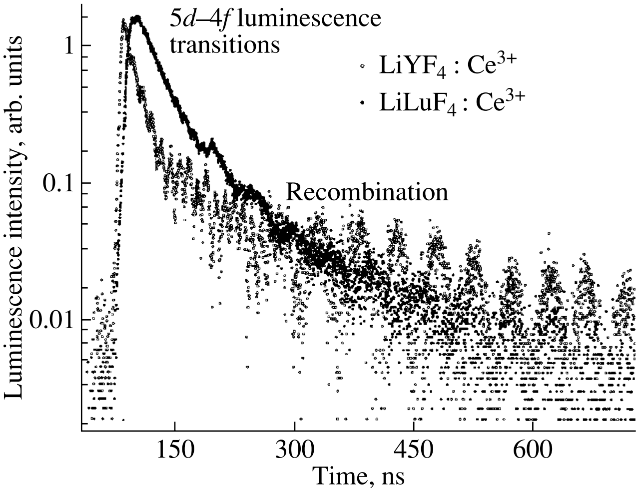

Fig. 1. Typical luminescence kinetics curves of $LiYF_4 : Ce^{3+}$ and $LiLuF_4 : Ce^{3+}$ crystals measured at 300 K at an excitation wavelength of 266 nm. Vertical lines show the time intervals corresponding to the intracenter 5*d*–4*f* transitions in the Ce^{3+} ion in $LiYF_4 : Ce^{3+}$ (dash lines), ~88–125 ns, and in $LiLuF_4 : Ce^{3+}$ (solid lines), ~105–175 ns.

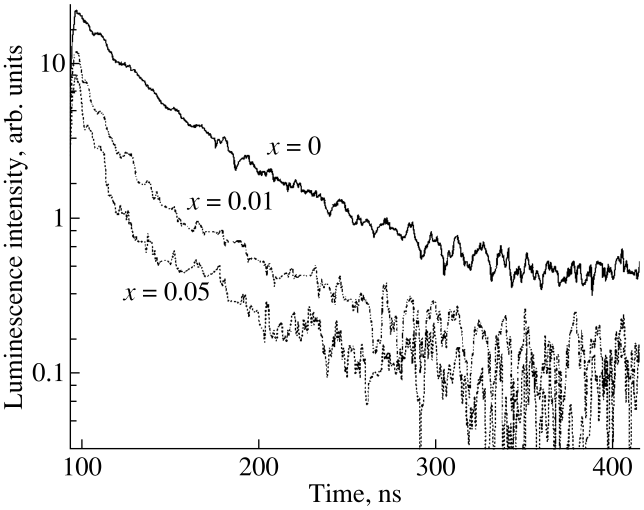

Fig. 2. Luminescence kinetics curves of $LiLu_{1-x}Yb_xF_4 : Ce^{3+}$ (x = 0, 0.01, 0.05) crystals measured at 300 K at an excitation wavelength of 266 nm.

The luminescence kinetics curves of Ce^{3+} ions in crystals additionally activated by Yb^{3+} ions (Fig. 2) do not exhibit the recombination component. This fact confirms the model of suppression of solarization processes proposed earlier in [4]. According to this model, additional activation by Yb^{3+} ions creates a supplementary recombination channel for free carriers, which successfully competes with the capture of carriers by impurities and cerium ions. It is also seen from Fig. 2

that Yb^{3+} ions cause quenching of the 5*d*–4*f* luminescence of Ce^{3+} ions.

ACKNOWLEDGMENTS

This work was supported by the Russian Foundation for Basic Research (project no. 03-02-17361) and BRHE (project REC-007).

REFERENCES

1. M. A. Dubinskiĭ, V. V. Semashko, A. K. Naumov, R. Yu. Abdulsabirov, and S. L. Korableva, Laser Phys. **4** (3), 480 (1994).
2. V. V. Semashko, M. A. Dubinskiĭ, R. Yu. Abdulsabirov, A. K. Naumov, S. L. Korableva, P. Misra, and C. Haridas, in *Proceedings of the International Conference "LASERS 2000"* (STS Press, Varanasi, 2001), p. 675.
3. V. V. Antonov-Romanovskiĭ, *Kinetics of Photoluminescence of Crystal Phosphors* (Nauka, Moscow, 1966) [in Russian].
4. V. V. Semashko, M. A. Dubinskiĭ, R. Yu. Abdulsabirov, S. L. Korableva, A. K. Naumov, A. S. Nizamutdinov, and M. S. Zhuchkov, Proc. SPIE **4766** (17), 119 (2001).

Translated by G. Tsydynzhapov

Physics of the Solid State, Vol. 47, No. 8, 2005, pp. 1463–1466. Translated from Fizika Tverdogo Tela, Vol. 47, No. 8, 2005, pp. 1409–1412.
Original Russian Text Copyright © 2005 by Nurtdinova, Semashko, Naumov, Abdulsabirov, Korableva.

PROCEEDINGS OF THE XII FEOFILOV WORKSHOP “SPECTROSCOPY OF CRYSTALS ACTIVATED BY RARE-EARTH AND TRANSITION-METAL IONS”

(Yekaterinburg, Russia, September 22–25, 2004)

Spectroscopic Indications of the Possible Optical Cooling Effect in Fluoride Crystals Activated by Yb^{3+} and Tm^{3+} Ions

L. A. Nurtdinova, V. V. Semashko, A. K. Naumov,
R. Yu. Abdulsabirov, and S. L. Korableva
Kazan State University, ul. Kremlevskaya 18, Kazan, 420008 Tatarstan, Russia
e-mail: nurlari@yandex.ru

Abstract—The results of spectral kinetic studies of several fluoride crystals activated by Yb^{3+} and Tm^{3+} ions are presented, and their possible application as cooling elements of optical refrigerators is discussed. Optimum excitation conditions for the laser cooling effect in these crystals are found. The cooling efficiency is established to depend on the degree of order in the active medium. © *2005 Pleiades Publishing, Inc.*

1. INTRODUCTION

Optical cooling has a number of advantages over traditional methods for attaining low temperatures due to the possibility of local heat removal and to the fact that optical cooling does not require mechanical contact between a cooled element and a cooling system containing energy sources. The prospects of using the optical cooling effect in the development of various quantum electronic systems (in particular, radiation-balanced self-cooling lasers) are of special interest.

The idea of optical cooling based on anti-Stokes luminescence was first suggested by Pringsheim in 1929 [1, 2]. However, this idea could be implemented only with the appearance of lasers. By 1999, the best achievement in this field had been cooling of optical fibers of metal fluoride glass ZBLANP : Yb^{3+} by 65 K from room temperature [2, 3]. However, the maximum efficiency of laser cooling for this medium (determined by the absorption and luminescence spectra of activating ions) appears to be quite low. The choice of the ZBLANP : Yb^{3+} material for experiments was determined by the development of the preparation technology rather than by the spectroscopic characteristics of the optical fiber. Studies indicate that the maximum cooling efficiency in other activated materials can be much greater [2].

The aim of this study is to estimate the prospects of applying fluoride crystals activated by trivalent ytterbium and thulium ions as cooling elements of optical refrigerators.

2. EXPERIMENTAL RESULTS AND DISCUSSION

According to [1–4], the optical cooling efficiency (OCE) for a sample at a given temperature T is given by

$$\frac{P_{\text{cool}}}{P_{\text{inc}}} = \eta(T)[1-\exp(-\alpha(\lambda, T)L)]\frac{\lambda - \langle\lambda_F\rangle(T)}{\langle\lambda_F\rangle(T)}, \quad (1)$$

where P_{cool} is the cooling power, P_{inc} is the power of the pumping (incident) radiation, η is the quantum yield of luminescence, L is the length of the sample, and $\alpha(\lambda)$ is the absorption coefficient at the wavelength λ of pumping radiation. The quantity $\langle\lambda_F\rangle$ in Eq. (1) is an average luminescence wavelength, which can be estimated from the luminescence spectrum $I_F(\lambda)$ of the sample as

$$\langle\lambda_F\rangle = \frac{\int \lambda I_F(\lambda)d\lambda}{\int I_F(\lambda)d\lambda}. \quad (2)$$

In the case of excitation by radiation with a wavelength greater than $\langle\lambda_F\rangle$, the emitted luminescence photon energy is, on the average, greater than the absorbed pumping photon energy (anti-Stokes luminescence), which can result in cooling of the sample. It follows from Eq. (1) that the OCE is greater for a smaller Stokes shift of the luminescence spectrum with respect to the absorption spectrum (i.e. for a greater area of the anti-Stokes wing of the absorption spectrum bounded on the short-wavelength side by the weighted average luminescence wavelength $\langle\lambda_F\rangle$), for a higher quantum yield, and for a greater fraction of excitation radiation absorbed by the sample. Obviously, the quantum yield varies and the absorption and luminescence spectra transform with decreasing temperature. As a result, the temperature dependence of the OCE will vary from sample to sample. In our experiments, the OCE was estimated at room temperature. Special attention should also be paid to the fact that formula (1) estimates only the maximum possible OCE for a given material, which really can be much smaller because of the presence of foreign impurities causing additional heat gen-

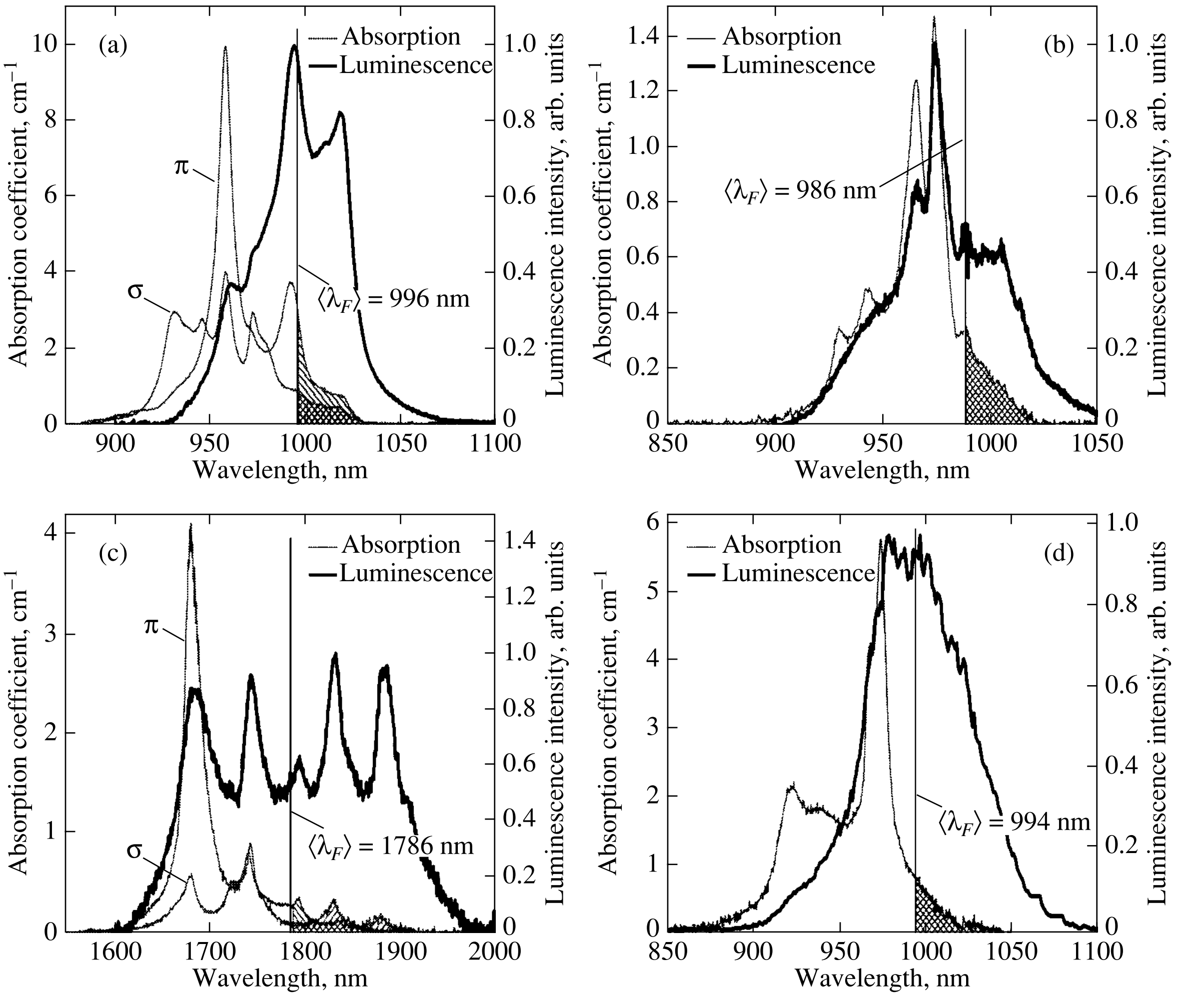

Fig. 1. Absorption and luminescence spectra for the optimum concentrations of active ions in crystals (a) $LiLuF_4 : Yb^{3+}$ (c = 10%), (b) $KY_3F_{10} : Yb^{3+}$ (c = 5%), (c) $LiYF_4 : Tm^{3+}$ (c = 4%), and (d) $N_4Y_6F_{22} : Yb^{3+}$ (c = 5%).

eration in the samples. Since luminescence reabsorption and excitation capture result in additional heat generation, these possible effects should also be eliminated.

As the objects to be studied, with due regard to the above arguments, we chose well-known crystalline laser media with a well-developed preparation technology [5–7]. The samples under study with chemical compositions $KY_3F_{10} : Yb^{3+}$ (KYF : Yb), $N_4Y_6F_{22} : Yb^{3+}$ (NYF : Yb), $LiLuF_4 : Yb^{3+}$ (LLF : Yb), and $LiYF_4 : Tm^{3+}$ (YLF : Tm) were grown at the Crystal Growth Laboratory, Kazan State University. To find the optimum (for attaining a maximum OCE) concentration of activating ions, the content of Yb^{3+} and Tm^{3+} ions in the samples was varied from 0.5 to several tens of atomic percent. The absorption and luminescence spectra of the samples in the region of the $^2F_{7/2}$–$^2F_{5/2}$ transition in the Yb^{3+} ion and the $^3H_6$–$^3F_4$ transition in the Tm^{3+} ion were recorded using a scanning spectrometer on the basis of an MDR-23 monochromator. The luminescence of the samples activated by Yb^{3+} and Tm^{3+} ions was excited by a halogen lamp or by the third harmonic of a YAG : Nd laser. The recorded spectra are shown in Fig. 1. From Figs. 1a and 1c, we see that, in order to obtain the maximum OCE for anisotropic crystals, one must use π-polarized pumping radiation.

Luminescence kinetics at room and liquid-nitrogen temperatures were also studied. Using the results of these studies, we established that, in LLF : Yb and YLF : Tm crystals, the quantum yield falls with increasing Yb^{3+} and Tm^{3+} concentration. On the contrary, the luminescence lifetime of Yb in NYF increases with concentration because of the excitation capture effect. Thus, the optimum (for OCE) concentrations of Yb^{3+} ions were found to be 10 at. % for LLF crystals and 5 at. % for KYF and NYF and the optimum concentration of Tm^{3+} ions for YLF crystals was 4 at. %.

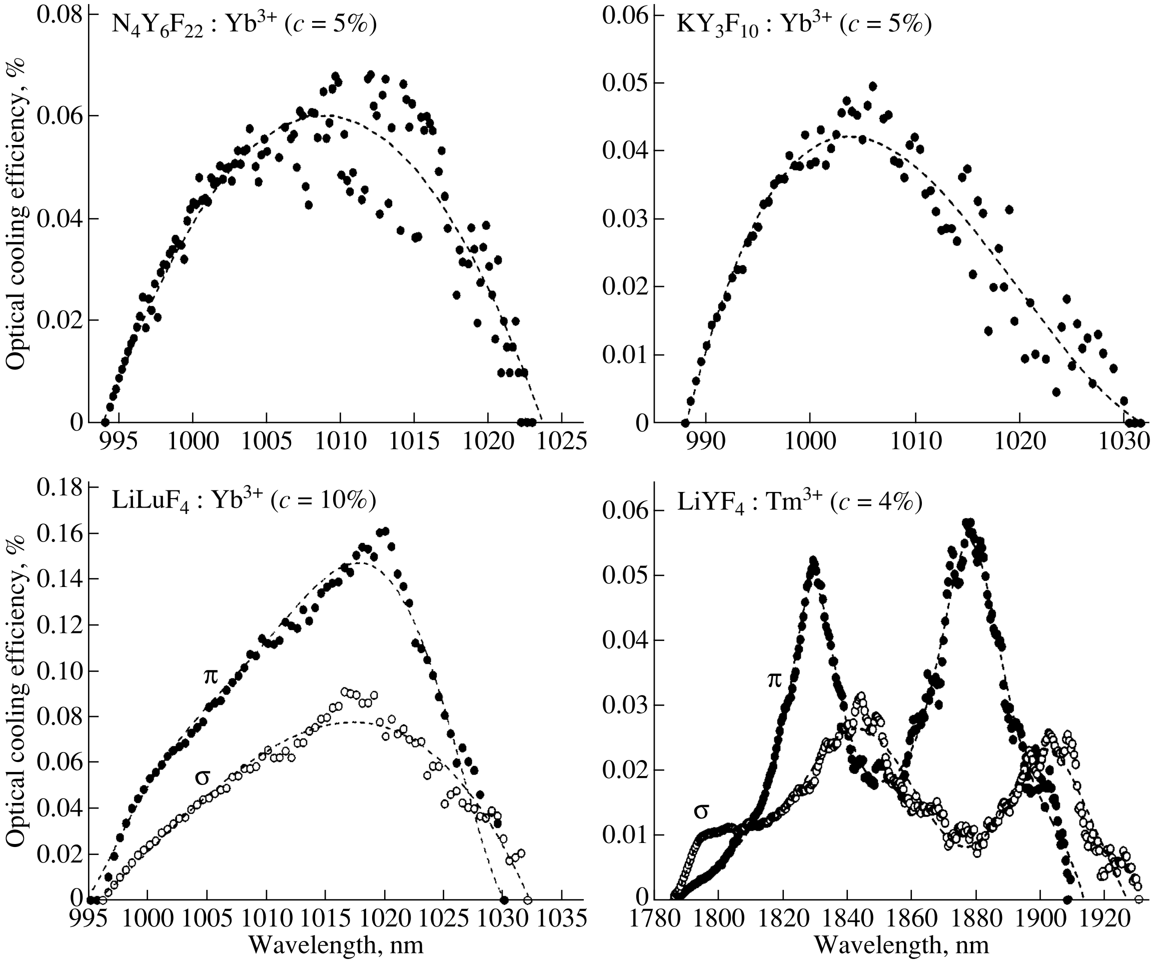

Fig. 2. Optical cooling efficiency for the optimum concentrations of Yb^{3+} and Tm^{3+} ions in the crystals under study.

Numerical estimates of the cooling efficiency for the optimum concentrations of Yb^{3+} and Tm^{3+} ions are shown in Fig. 2. It can be seen that, among the investigated crystalline media activated by Yb^{3+} ions, LLF : Yb^{3+} crystals have the maximum OCE (of about 0.16%) when excited by π-polarized radiation in the wavelength range 1018–1030 nm. For NYF : Yb and KYF : Yb crystals, the cooling efficiency does not exceed 0.05% and reaches a maximum when the samples are excited over the wavelength ranges 1005–1017 and 1002–1008 nm, respectively. A YLF crystal activated by Tm^{3+} ions has a substantially greater OCE efficiency as compared to the ytterbium-containing samples studied earlier. The expected OCE in this crystal is as large as 0.55 and 0.3% when samples are excited with π- and σ-polarized pumping radiation, respectively.

Thus, for our fluoride crystals activated by Yb^{3+} and Tm^{3+} ions, the OCE is more than two times the OCE for the above-mentioned ZBLANP glass [4] calculated using the same method as for our samples. Moreover, we established that the cooling efficiency in crystals with a high degree of order, YLF and LLF, is much higher than that in disordered glassy materials, KYF and NYF (Fig. 3).

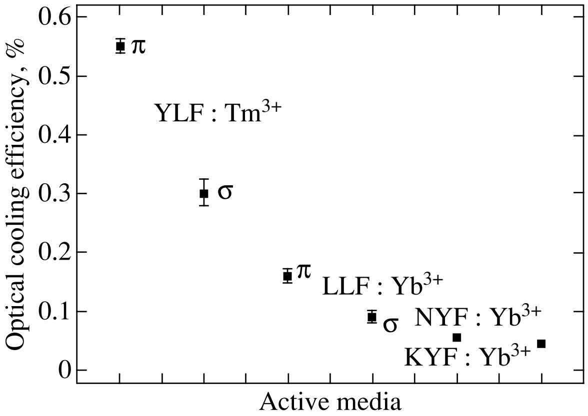

Fig. 3. Optical cooling efficiency in the crystalline media under study.

3. CONCLUSIONS

We have shown experimentally that fluoride crystals activated by Yb^{3+} and Tm^{3+} ions are promising for use as cooling elements of optical refrigerators. It has been shown that the maximum cooling efficiency of these crystals as determined from the absorption and luminescence spectra of the investigated samples exceeds the corresponding efficiency of the known media for which the laser cooling effect has already been demonstrated in practice. We have determined the optimum excitation conditions for the laser cooling effect in the investigated samples and established that the cooling efficiency depends on the degree of order of the active medium.

ACKNOWLEDGMENTS

This study was supported by the International Science and Technology Center (grant no. 2121), CRDF (grant REC-007), and the Russian Foundation for Basic Research (project no. 03-02-17361).

REFERENCES

1. G. Lei, J. E. Anderson, M. I. Buchwald, B. C. Edwards, R. I. Epstein, M. T. Murtagh, and G. H. Sigel, IEEE J. Quantum Electron. **34** (10), 1839 (1998).
2. S. R. Bowman and C. E. Mungan, Appl. Phys. B **71**, 1 (2000).
3. C. W. Hoyt, M. Sheik-Bahae, R. I. Epstein, B. C. Edwards, and J. E. Anderson, Phys. Rev. Lett. **85** (17), 3600 (2000).
4. C. E. Mungan, M. I. Buchwald, B. C. Edwards, R. I. Epstein, and T. R. Gosnell, Math. Sci. Forum **239–241**, 501 (1997).
5. W. F. Krupke, IEEE J. Sel. Top. Quantum Electron. **6** (6), 1287 (2000).
6. V. V. Semashko, M. A. Dubinskiĭ, R. Yu. Abdulsabirov, S. L. Korableva, A. K. Naumov, A. S. Nizamutdinov, and M. S. Zhuchkov, Proc. SPIE **4766** (17), 119 (2001).
7. V. V. Semashko, M. A. Dubinskiĭ, R. Yu. Abdulsabirov, A. K. Naumov, S. L. Korableva, P. Misra, and C. Haridas, in *Proceedings of the International Conference LASERS 2000* (STS, Varanasi, 2001), p. 675.

Translated by I. Zvyagin

Physics of the Solid State, Vol. 47, No. 8, 2005, pp. 1467–1469. Translated from Fizika Tverdogo Tela, Vol. 47, No. 8, 2005, pp. 1413–1414.
Original Russian Text Copyright © 2005 by Aminov, Abdulsabirov, Korableva, Kurkin, Kurzin, Ziganshin, Gromov.

PROCEEDINGS OF THE XII FEOFILOV WORKSHOP "SPECTROSCOPY OF CRYSTALS ACTIVATED BY RARE-EARTH AND TRANSITION-METAL IONS"

(Yekaterinburg, Russia, September 22–25, 2004)

Electron Paramagnetic Resonance in Mixed Crystals $(BaF_2)_{1-x}(LaF_3)_x$ Activated by Ce^{3+} Ions

L. K. Aminov*, R. Yu. Abdulsabirov*, S. L. Korableva*, I. N. Kurkin*, S. P. Kurzin*, A. G. Ziganshin*, and I. A. Gromov**

** Kazan State University, Kremlevskaya ul. 18, Kazan, 420008 Tatarstan, Russia*
e-mail: linar.aminov@ksu.ru, igor.kurkin@ksu.ru
*** Laboratory of Physical Chemistry, ETH-Honggerberg, Zurich, 8093 Switzerland*

Abstract—The electron paramagnetic resonance (EPR) spectra of mixed crystals $(BaF_2)_{1-x-y}(LaF_3)_x(CeF_3)_y$ ($y = 0.001 = 0.1\%$, $x = 0$–0.02) are investigated in a magnetic field $\mathbf{H} \parallel \mathbf{C}_4$ at a frequency of 9.5 GHz. The angular dependence of the EPR spectrum is measured for the sample with $x = 0.02$. The lines attributed to Ce^{3+} impurity centers with tetragonal symmetry and g factors ($g_{\parallel} = 0.75$, $g_{\perp} = 2.4$) close to those measured for the $KY_3F_{10} : Ce^{3+}$ compound are separated in the complex EPR spectrum. The assumption is made that the aforementioned impurity centers are cubooctahedral clusters of the La_6F_{37} type in which one of the La^{3+} ions is replaced by the Ce^{3+} ion. *© 2005 Pleiades Publishing, Inc.*

1. INTRODUCTION

Direct observations of the formation of rare-earth (*RE*) clusters in paramagnetic crystals $(MeF_2)_{1-x}(REF_3)_x$ with the use of electron paramagnetic resonance (EPR) have been practically impossible because of the considerable broadening of the resonance lines at a trifluoride content above $x \approx 0.1\%$. From this standpoint, binary solid solutions $(MeF_2)_{1-x-y}(RF_3)_x(REF_3)_y$ with diamagnetic ions R (R = La, Lu, Y) at a low content y of the paramagnetic rare-earth component seem to be more convenient objects. Kazanskiĭ [1] analyzed optically detected EPR in absorption bands for a series of fluoride compounds and made the inference that the cluster formation is determined by the total trifluoride content $x + y$ and that the EPR spectra of RE^{3+} ions in these compounds at a total content $x + y \geq 0.001$ are associated with the tetragonal positions of diamagnetic ions in the R_6F_{37}-type clusters. In order to clarify the potentials of the EPR method in more detail, it is expedient to analyze the EPR spectra of mixed crystals $(MeF_2)_{1-x-y}(RF_3)_x(REF_3)_y$ with trifluoride contents x and y varying over the widest possible ranges.

In our recent work [2], we studied the EPR spectra of mixed crystals $(BaF_2)_{1-x}(LaF_3)_x$ activated with 0.1% Yb^{3+}. It was found that, even at a low content $x = 0.001$, the EPR spectra exhibit additional resonance lines due to the formation of trigonal clusters involving two trivalent ions in barium positions and two compensating fluorine ions of the La^{3+}–F^-–Yb^{3+}–F^- type. Analysis of these lines was complicated by the fact that the initial EPR spectrum, which was observed even at $x = 0$, had a hyperfine structure caused by ^{171}Yb and ^{173}Yb isotopes. However, we did not reveal indications of the lines associated with tetragonal impurity centers that could be identified with Yb^{3+} ions in the La_6F_{37} clusters.

In the present work, we studied the same mixed crystals $(BaF_2)_{1-x}(LaF_3)_x$ but with Ce^{3+} ions serving as paramagnetic probes. The Ce^{3+} ions do not have magnetic isotopes; consequently, the EPR spectrum of Ce^{3+} does not exhibit a hyperfine structure.

2. SAMPLES AND EXPERIMENTAL TECHNIQUE

In our experiments, we used 0.1% Ce^{3+}-activated samples at trifluoride contents x = 0, 0.001, 0.002, 0.005, 0.01, and 0.02. The EPR spectra were measured by the stationary method on an IRÉS-1003 spectrometer at a frequency of ≈9.5 GHz and at a temperature of ≈15 K. In addition, the samples at trifluoride contents x = 0 and 0.02 were examined using the pulsed method of electron spin echo at a frequency of ≈9.8 GHz and at a temperature of ≈7 K.

3. RESULTS AND DISCUSSION

For pure BaF_2 ($x = 0$), we revealed a single EPR center with tetragonal symmetry ($g_{\parallel} = 2.601$, $g_{\perp} = 1.555$; for comparison, see the results obtained earlier in [3]). In a magnetic field applied parallel to the fourfold symmetry axis ($\mathbf{H} \parallel \mathbf{C}_4$), the characteristic EPR spectrum exhibits a single line at a magnetic field strength of ≈2.603 kG and a double line at a magnetic field strength

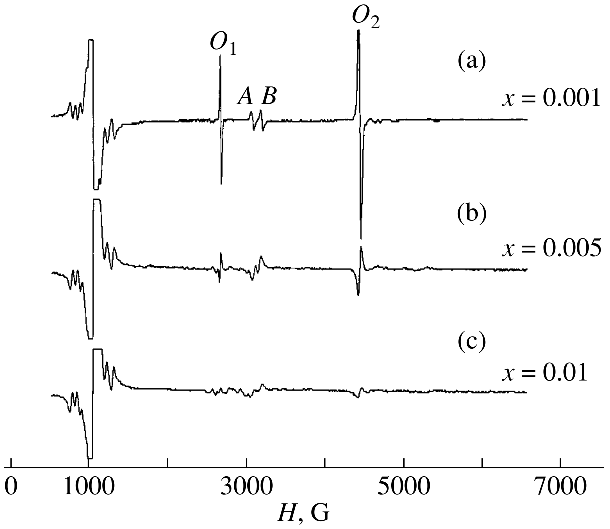

Fig. 1. Ce^{3+} EPR spectrum of mixed crystals $Ba_{1-x}La_xF_{2+x}$ + $0.1\%Ce^{3+}$ at different contents x in the magnetic field $\mathbf{H} \parallel \mathbf{C}_4$. Lines O_1 and O_2 correspond to the Ce^{3+} tetragonal impurity center. Lines A and B are the most intense additional EPR lines at low contents x. The intense line observed in a magnetic field of ~1 kG is the EPR spectrum of the reference sample CaF_2 + 0.8% Er^{3+}.

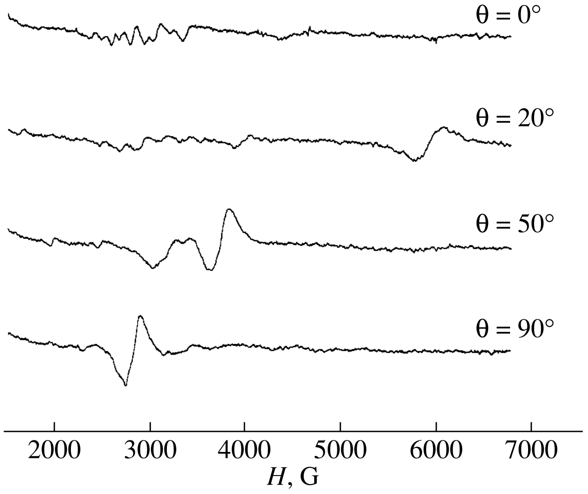

Fig. 2. EPR spectrum of the $Ba_{1-x}La_xF_{2+x}$ + $0.1\%Ce^{3+}$ ($x = 0.02$) sample at different angles θ in the plane C_4–C_3–C_2. The angle θ = 0 corresponds to the magnetic field $\mathbf{H} \parallel \mathbf{C}_4$.

of 4.355 kG (lines O_1 and O_2 in Fig. 1, respectively). It is worth noting that the intensity of the EPR line associated with Ce^{3+} ions in pure BaF_2 ($x = 0$) is several times lower than that of Yb^{3+} ions in pure BaF_2. At $x = 0.001$, the intensity of the line attributed to the initial Ce^{3+} tetragonal center decreases. Moreover, there appear additional lines, among which the two most intense lines are observed at magnetic field strengths $H = 3.070$ and 3.188 kG (lines A and B in Fig. 1a, respectively). A further increase in the LaF_3 content leads to a substantial decrease in the intensity of the initial lines attributed to the tetragonal impurity centers (by approximately one order of magnitude at $x = 0.01$; see Fig. 1c) and to the appearance of new additional lines at magnetic field strengths in the range 2.5–3.2 kG. In order to determine the actual concentration dependence of the intensity of the EPR lines of interest, we measured the EPR spectra of $Ba_{1-x}La_xF_{2+x}$ samples at different contents x and simultaneously recorded the EPR spectrum of the reference sample. As a reference sample, we used a CaF_2 + 0.8% Er single crystal. This crystal is a convenient reference sample, because its EPR spectrum is characterized by only one intense line assigned to the Er^{3+} cubic impurity center (i.e., the isotropic EPR line with $g = 6.78$, $H \sim 1.0$ kG, and a linewidth of ≈40 G, which is close to the linewidth for the Ce^{3+} ions under investigation).

As was noted above, the sample at a trifluoride content $x = 0.02$ was studied in more detail. The electron spin echo measurements demonstrated that the spectrum of this sample does not contain the broad isotropic line, which was previously observed in the spectra of the $(BaF_2)_{1-x}(LaF_3)_x$ + 0.1% Yb^{3+} ($x \geq 0.01$) samples [2]. Thus, there are grounds to believe that no paramagnetic centers whose environment has a disordered structure are formed in the $(BaF_2)_{1-x}(LaF_3)_x$ + 0.1% Ce^{3+} ($x \approx 0.02$) samples studied in the present work.

Analysis of the angular dependence of the EPR spectrum for the sample at $x = 0.02$ (Fig. 2) revealed additional resonance lines that correspond to paramagnetic centers of tetragonal symmetry with $g_\parallel \approx 0.75$ and $g_\perp = 2.4$. The width of the lines attributed to these centers (~200 G) is one order of magnitude larger than that of the O centers, whereas the intensity of these lines is comparable to the intensity of the lines assigned to the O centers in the sample at $x = 0$. The former centers can be associated with the formation of La_6F_{37} clusters. This is confirmed by the fact that the g factors obtained in our case are close to those previously observed for the $KY_3F_{10} : Ce^{3+}$ compound, whose lattice involves Y_6F_{36} cubooctahedral clusters with Ce^{3+} ions occupying Y^{3+} sites ($g_\parallel = 0.77$, $g_\perp = 2.46$ [4]).

4. CONCLUSIONS

Thus, the EPR spectra of mixed crystals $(BaF_2)_{1-x}(LaF_3)_x$ indicate that the structure of these crystals can involve La_6F_{37} cubooctahedral clusters. However, the appearance of additional EPR lines is not necessarily associated with the formation of these clusters in the crystal structure. A more complete identification of the EPR spectra calls for further investigation.

ACKNOWLEDGMENTS

This work was supported by the US Civilian Research and Development Foundation for the Independent States of the Former Soviet Union (grant no. CRDF REC-007) and by the Research and Experimental Development (NIOKR) Foundation of the Tatarstan Republic (project no. 0.6-6.1-192/2004(F)).

REFERENCES

1. S. A. Kazanskiĭ, Zh. Éksp. Teor. Fiz. **89**, 1258 (1985) [Sov. Phys. JETP **62** (4), 727 (1985)]; S. A. Kazanskiĭ and A. I. Ryskin, Fiz. Tverd. Tela (St. Petersburg) **44** (8), 1356 (2002) [Phys. Solid State **44** (8), 1415 (2002)].
2. L. K. Aminov, R. Yu. Abdulasabirov, M. R. Gafurov, S. L. Korableva, I. N. Kurkin, S. P. Kurzin, R. M. Rakhmatullin, and A. G. Ziganshin, in *Specialized Colloque Ampere "NMR and EPR of Broad-Line Solids"* (Portoroz, Slovenia, 2003), p. 114.
3. A. A. Antipin, I. N. Kurkin, G. K. Chirkin, and L. Ya. Shekun, Fiz. Tverd. Tela (Leningrad) **6** (7), 2014 (1964) [Sov. Phys. Solid State **6** (7), 1590 (1964)].
4. V. A. Ivan'shin, I. N. Kurkin, I. Kh. Salikhov, and Sh. I. Yagudin, Fiz. Tverd. Tela (Leningrad) **28** (8), 2580 (1986) [Sov. Phys. Solid State **28** (8), 1448 (1986)].

Translated by N. Korovin

Physics of the Solid State, Vol. 47, No. 8, 2005, pp. 1470–1472. Translated from Fizika Tverdogo Tela, Vol. 47, No. 8, 2005, pp. 1415–1416.
Original Russian Text Copyright © 2005 by Dzholdoshov, Kidibaev, Koroleva, Cherepanov, Raĭkov, Ivanov, Ryabukhin.

PROCEEDINGS OF THE XII FEOFILOV WORKSHOP "SPECTROSCOPY OF CRYSTALS ACTIVATED BY RARE-EARTH AND TRANSITION-METAL IONS"

(Yekaterinburg, Russia, September 22–25, 2004)

Ionoluminescence of Eu^{2+}–Eu^{3+} Clusters in NaF : Eu Single Crystals

B. K. Dzholdoshov*, M. M. Kidibaev*, T. S. Koroleva, A. N. Cherepanov***, D. V. Raĭkov***, V. Yu. Ivanov***, and O. V. Ryabukhin*****

** Issyk-Kul State University, ul. Abdrahmanova 103, Karakol, 722360 Kyrgyzstan*
*** Institute of Physics, National Academy of Sciences of Kyrgyzstan, Chui pr. 265A, Bishkek, 720071 Kyrgyzstan*
**** Ural State Technical University (UPI), ul. Mira 19, Yekaterinburg, 620002 Russia*
e-mail: tch@dpt.ustu.ru

Abstract—The radiation-impurity modification of NaF : Eu crystals results in the formation of optically active planar heterostructures with a complex set of luminescence centers, including, in particular, clusters of the Eu^{2+}–Eu^{3+} type. The luminescence spectra of Eu^{2+}–Eu^{3+} centers exhibit bands at wavelengths of 409 and 442 nm, which are associated with Eu^{2+} ions in nonequivalent crystallographic positions, and a band at a wavelength of 610 nm, which is attributed to Eu^{3+} ions. The luminescence spectra of irradiated NaF : Eu samples contain a broad band with a maximum at 506 nm due to the presence of $F_2 + F_3^+$ color centers in the crystal.

1. INTRODUCTION

In 1955, Ranciman [1] and, a few years later, Kaplyanskiĭ and Feofilov [2] started investigations into the optical and luminescence properties of NaF : U crystals. These investigations were continued by other researchers [3–9], who used new effective *d*- and *f*-element coactivators for impurity uranium ions and revealed a low isomorphic capacity of NaF crystals with respect to rare-earth ions, such as Eu^{3+}, Sm^{3+}, Gd^{3+}, Ce^{3+}, and Tb^{3+} [5, 6, 8]. The photoluminescence and excitation spectra of these crystals were investigated, the electronic structure of the luminescence centers was elucidated, and their spatial models were proposed in [1–8]. In particular, Pisarenko and Potapenko [5, 6] observed the photoluminescence spectrum of NaF : Eu crystals in the wavelength range 500–700 nm. This spectrum exhibits a minimum at a wavelength of 608.7 nm, which corresponds to the transition $^5D_0 \longrightarrow {}^7F_2$ in Eu^{3+} ions, and contains bands at wavelengths of 612.8, 614.9, 624.6, 635.6, 640.6, 649.6, and 654.1 nm. It has been found that NaF activated crystals contain Eu^{3+}–Ce^{3+}, Sm^{3+}–Ce^{3+}, and Ho^{3+}–Ho^{3+} pair centers [8]. In the present work, we studied the NaF : Eu crystals used earlier by Pisarenko [8]. Our investigations were performed using the radiation-impurity modification of these crystals with excitation sources characterized by a higher radiation density (nitrogen ion beams), which allowed us to observe luminescence bands associated with the Eu^{2+}–Eu^{3+} clusters against the background of the intense bands attributed to radiation-induced color centers. This paper reports on the results of these investigations.

2. SAMPLE PREPARATION AND EXPERIMENTAL TECHNIQUE

We studied NaF : Eu single crystals with the europium (Eu_2O_3) content in the batch being as high as 0.01%. The crystals were grown in air in platinum crucibles by the Stockbarger–Bridgman method. These crystals were placed at our disposal by V.F. Pisarenko. The absorption spectra of the samples were recorded on a Helios Alfa spectrophotometer. The samples were irradiated with 10-MeV nitrogen ions at 300 K. The ionoluminescence spectra of NaF : Eu samples were measured using a setup designed on the basis of a cyclotron situated at the Ural State Technical University (Yekaterinburg, Russia). The setup includes a bombardment chamber and a detection system, which consists of an Oriel polychromator and a charged-coupled device (CCD) linear array. Surface layers of the samples were colored during irradiation with fluences of up to 10^{15} cm^{-2}.

3. RESULTS AND DISCUSSION

Figure 1 shows the absorption spectra of the NaF : Eu initial sample and the same sample irradiated with nitrogen ions during recording of the ionoluminescence spectrum. The initial crystals were transparent over the entire visible and near-infrared ranges.

Europium impurities in the NaF crystals were identified from the absorption band located in the range 295–305 nm, which is associated with charge transfer in Eu^{3+}–O^{2-} complexes [6, 8]. The absorption spectrum of the NaF : Eu crystals irradiated with accelerated nitrogen ion beams exhibits dominant bands assigned to radiation-induced color centers. These bands are observed at a wavelength of 340 nm (F centers) and at 506 nm ($F_2 + F_3^+$ centers).

The ionoluminescence spectrum of the NaF : Eu crystals (Fig. 2) includes a series of intrinsic and impurity luminescence bands. A weak ultraviolet luminescence band is observed in the range 275–330 nm with maxima in the vicinity of 300 nm. This band coincides both with the band attributed to charge transfer in the Eu^{3+}–O^{2-} complex, which manifests itself in the absorption spectra (Fig. 1), and with the well-known Fischer band located at a wavelength of 285 nm and assigned to O^{2-} ions. The luminescence band observed at a wavelength of 479 nm is attributed to H centers, which are associated with interstitial halogen atoms [3], whereas the band revealed at 660 nm is due to the luminescence of $F_2 + F_3^+$ centers [3]. Apart from these bands of intrinsic luminescence, the ionoluminescence spectrum contains several bands with maxima in the blue spectral range at wavelengths of 409 and 442 nm, which can be attributed to Eu^{2+} ions located in nonequivalent crystallographic positions, and a band in the red spectral range (at ~610 nm). The latter band is positioned close to the band attributed to Eu^{3+} ions (608.4 nm), which was previously revealed for the same crystals by Pisarenko [8]. The other bands of the Eu^{3+} ions, which were observed by Pisarenko [8], very weakly manifest themselves in the spectrum because of the intense luminescence of color centers. The appearance of the luminescence band attributed to Eu^{2+} ions can be associated with the formation of Eu^{2+} ions due to the reaction $Eu^{3+} + e$ in surface layers of the NaF : Eu crystals. This brings about the formation of heterovalent cluster centers in the form of Eu^{2+}–Eu^{3+} pair centers, which are similar to the Eu^{3+}–Ce^{2+}, Sm^{2+}–Ce^{2+}, and Ho^{3+}–Eu^{3+} pair centers in the NaF crystals [8]. As a model of pair centers in NaF and other alkali halide crystals, Pisarenko proposed to use heterovalent cluster centers consisting of a pair of unlike rare-earth ions, for example, Ho^{3+} and Eu^{2+} in NaBr [8]. By analogy with this model, we can also propose two possible models of a heterovalent cluster center consisting of an Eu^{2+}–Eu^{3+} pair with vacancy–impurity compensation for an excess charge of Eu^{2+} and Eu^{3+} activators (Fig. 3). The excess charge of the cluster (Eu^{2+}, Eu^{3+}) in the NaF lattice is compensated for either through the vacancy mechanism (Fig. 3a) or by the impurity O^{2-} ions (Fig. 3b).

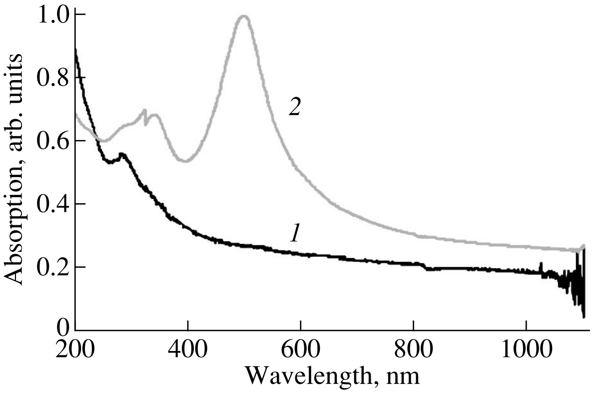

Fig. 1. Absorption spectra of (*1*) unirradiated and (*2*) irradiated NaF : Eu crystals.

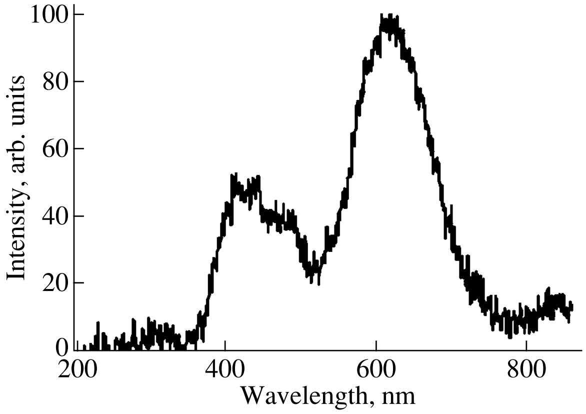

Fig. 2. Ionoluminescence spectrum of the NaF : Eu crystal.

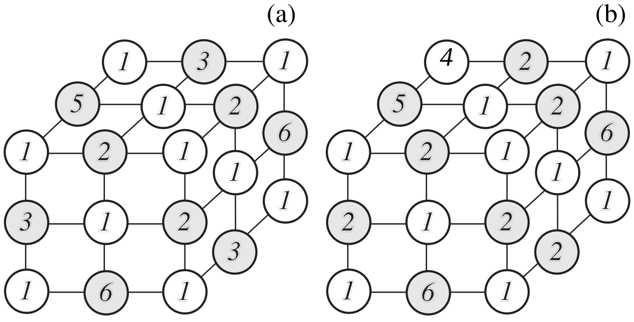

Fig. 3. Models of Eu^{2+}–Eu^{3+} pair centers in NaF crystals with compensation for an excess charge by (a) vacancies of sodium ions and (b) impurity oxygen ions substituting for fluorine ions: (*1*) F^-, (*2*) Na^+, (*3*) Na^+ vacancy, (*4*) O^{2-}, (*5*) Eu^{2+}, and (*6*) Eu^{3+}.

4. CONCLUSIONS

Thus, we investigated the radiation-stimulated effects in NaF : Eu crystals activated by europium ions. The investigations demonstrated that the radiation-impurity modification of these crystals results in the formation of active surface planar heterostructures with a set of effective luminescence centers over a wide spectral range (250–650 nm).

ACKNOWLEDGMENTS

We would like to thank B.V. Shul'gin for proposing the subject of this study and for his participation in discussions of the results and helpful remarks.

This work was performed within the framework of the Kyrgyzstan–Russia program of the International Research and Engineering Center (project MNTTs no. KR-994), the state scientific program "Universities of Russia" (project UR.02.01.023), NATO (grant no. PST.EAP.CLG 980674), and the program "Advanced Materials" of the Ural Research and Educational Center (project no. EK-005-X1).

REFERENCES

1. W. A. Ranciman, Nature (London) **175** (4468), 1082 (1955).
2. A. A. Kaplyanskiĭ and P. P. Feofilov, Opt. Spektrosk. **14**, 664 (1963).
3. M. M. Kidibaev, *Radiation-Stimulated Processes in Crystals (Li,Na)F–U,Me* (Ural. Gos. Tekh. Univ., Yekaterinburg, 1999) [in Russian].
4. B. E. Bron and W. R. Heller, Phys. Rev. A **136**, 1433 (1964).
5. V. F. Pisarenko and G. D. Potapenko, Fiz. Tverd. Tela (Leningrad) **14**, 1361 (1972) [Sov. Phys. Solid State **14**, 1169 (1972)].
6. G. D. Potapenko and V. F. Pisarenko, *Spectroscopy of Crystals* (Nauka, Leningrad, 1972), pp. 193–195 [in Russian].
7. M. Shiber, Solid State Commun. **2**, 261 (1964).
8. V. F. Pisarenko, Doctoral Dissertation in Mathematical Physics (Krasnodar, 1976).
9. M. M. Kidibaev, G. S. Denisov, A. A. Lozovskikh, B. V. Shul'gin, and D. V. Raĭkov, *Problems of Spectroscopy and Spectrometry* (Ural. Gos. Tekh. Univ., Yekaterinburg, 2002), Vol. 9, Part 2, pp. 60–64.

Translated by N. Korovin

Physics of the Solid State, Vol. 47, No. 8, 2005, pp. 1473–1475. Translated from Fizika Tverdogo Tela, Vol. 47, No. 8, 2005, pp. 1417–1419.

PROCEEDINGS OF THE XII FEOFILOV WORKSHOP "SPECTROSCOPY OF CRYSTALS ACTIVATED BY RARE-EARTH AND TRANSITION-METAL IONS"

(Yekaterinburg, Russia, September 22–25, 2004)

Radioluminescence Properties of Bulk, Fiber, and Nanosized NaF–U Crystals

T. S. Koroleva[1], M. M. Kidibaev[2], B. K. Dzholdoshov[2], Ch. Pédrini[3], B. Hautefeuille[3], K. Lebbou[3], O. Tillement[3], J.-M. Fourmigue[4], B. V. Shul'gin[5], A. N. Cherepanov[5], V. I. Solomonov[6], and M. G. Ivanov[6]

[1] *Institute of Physics, National Academy of Sciences of Kyrgyzstan, Chui pr. 265A, Bishkek, 720071 Kyrgyzstan*
[2] *Issyk-Kul State University, ul. Abdrahmanova 103, Karakol, 722360 Kyrgyzstan*
[3] *Université Lyon 1, Campus de la Doua, Villeurbanne, Lyon, 69622 France*
[4] *Fibercryst S.A.S., Lyon, 69001 France*
[5] *Ural State Technical University (UPI), ul. Mira 19, Yekaterinburg, 620002 Russia*
e-mail: tch@dpt.ustu.ru
[6] *Institute of Electrophysics, Ural Division, Russian Academy of Sciences,*
ul. Amundsena 106, Yekaterinburg, 620016 Russia

Abstract—The results of comparative investigations into the scintillation and optical properties of bulk, fiber, and nanosized NaF–U crystals are presented. Fiber and nanosized samples of the NaF–U crystals are prepared for the first time and show considerable promise for practical applications in radiation technology. *© 2005 Pleiades Publishing, Inc.*

1. INTRODUCTION

Sodium fluoride single crystals activated by *d* and *f* elements have been known as promising optical materials for various practical applications. The most research attention has been focused on uranium-activated sodium fluoride crystals. In the late 1950s, Feofilov [1] initiated active research into these materials in Russia. A characteristic feature of NaF–U crystals is a high specific light yield of scintillations, which makes it possible to use these materials for effective detection of ionizing radiation. However, practical implementation of the results of investigations into the properties of NaF–U materials presents considerable difficulties associated with the geometric shape and sizes of the crystals. One method for solving this problem is to design NaF–U materials of known compositions in new geometric configurations, for example, in the form of fibers or nanoobjects. A distinguishing feature of fibers and nanoobjects is an increased ratio of the surface area to the volume of the crystal. Since the surface of the crystal structure is considered a defect, it can be expected that a number of the physical properties of fiber and nanosized crystals will differ from those of bulk samples.

In this work, we compared the main optical and scintillation properties of bulk, fiber, and nanosized NaF–U crystals.

2. OBJECTS OF INVESTIGATION AND EXPERIMENTAL TECHNIQUE

The objects of our investigation were bulk, fiber, and nanosized crystals of uranium-activated sodium fluoride.

Bulk NaF–U single crystals were grown using a modified Kyropoulos method (the step growth method [2]) from a melt (special-purity grade) in a platinum crucible in air at the Institute of Physics of the National Academy of Sciences of Kyrgyzstan (Bishkek, Kyrgyzstan).

Fiber NaF–U single crystals were grown by the micro-pulling-down (MPD) and laser-heated pedestal prepared (LHPG) methods from previously grown bulk NaF–U single crystals at the Physicochemical Laboratory of Luminescent Materials of Lyon University (Lyon, France) for the first time. The MPD method consists in pulling the melt of a raw material through a microorifice with the use of a crystal seed. The pulling speed and the temperature of the melt determine the thickness of the fiber. In essence, the LHPG method is as follows. A previously prepared thin single crystal is subjected to local heating with a laser beam under simultaneous stretching. It is in this region of laser heating that a new crystal structure is formed in the sample and the sample itself lengthens and thins.

1063-7834/05/4708-1473$26.00 © 2005 Pleiades Publishing, Inc.

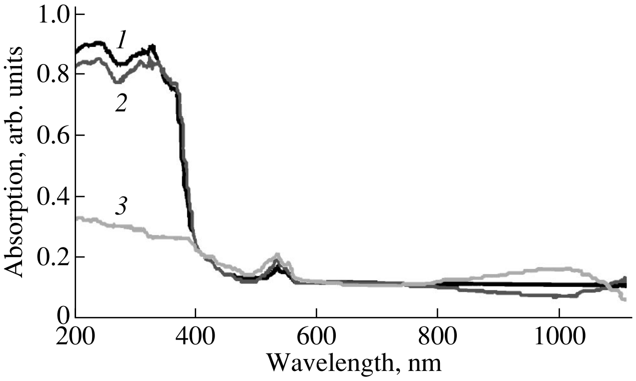

Fig. 1. Optical absorption spectra of NaF–U crystals: (*1*) bulk crystals, (*2*) MPD fibers, and (*3*) LHPG fibers.

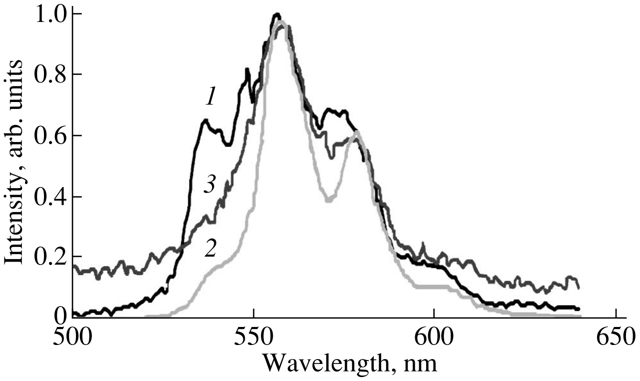

Fig. 2. X-ray luminescence spectra of NaF–U crystals: (*1*) bulk crystals, (*2*) MPD fibers, and (*3*) LHPG fibers.

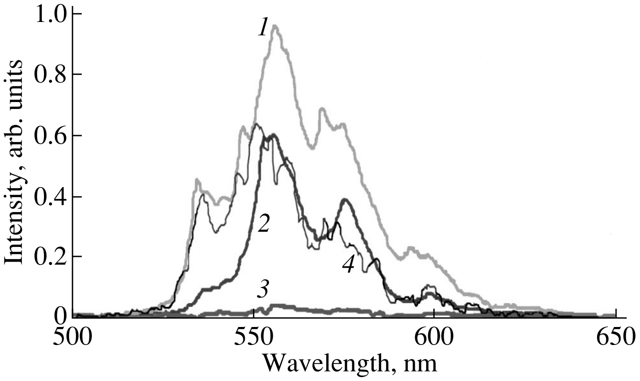

Fig. 3. Pulsed cathodoluminescence spectra of NaF–U crystals: (*1*) bulk crystals, (*2*) MPD fibers, (*3*) LHPG fibers, and (*4*) nanocrystals.

Nanosized NaF–U crystals were prepared by laser sputtering of previously grown bulk NaF–U single crystals at the Institute of Electrophysics (Ural Division, Russian Academy of Sciences, Yekaterinburg, Russia). Nanocrystals were deposited on a molybdenum substrate in the form of a thin layer. The nanocrystals were 20–30 nm in size (estimate).

The luminescence and optical properties of the samples were investigated by measuring and analyzing the optical absorption, x-ray luminescence, pulsed cathodoluminescence, thermally stimulated luminescence, and thermally stimulated exoelectron emission spectra.

3. RESULTS AND DISCUSSION

Figure 1 shows the optical absorption spectra of the bulk and fiber NaF–U crystals. As can be seen from this figure, the spectra contain three absorption bands in the wavelength ranges 200–390, 500–560, and 900–1050 nm. The absorption band observed in the range 200–390 nm can be caused by charge transfer from impurity centers to color centers (*F* centers). This band most clearly manifests itself in the spectra of the bulk crystals and LHPG fibers. The absorption bands of *F* color centers in the MPD fibers are characterized by a considerably lower intensity. The absorption band located in the range 500–560 nm is attributed to the uranium impurities and exhibits identical intensity for different types of samples. In the range 900–1050 nm, the absorption is enhanced in the MPD fibers and is reduced in the LHPG fibers as compared to the bulk crystals, which is most probably associated with the surface effects.

The x-ray luminescence spectra of the bulk and fiber NaF–U crystals are presented in Fig. 2. The major luminescence centers in these samples are uranium ions that exhibit characteristic luminescence in the range 520–600 nm. It is evident from these spectra that the shape and sizes of the samples affect the intensity of the bands attributed to uranium ions. For example, the bands located for the bulk samples at wavelengths of 538, 541, 549, and 571 nm are practically absent in the x-ray luminescence spectra of the fiber crystals. This can be associated with the profound effect of the surface on the energy and charge states of uranium ions and on the conditions providing for compensation of an excess charge of the U^{6+} ions.

The pulsed cathodoluminescence spectra of the NaF–U samples are depicted in Fig. 3. Since the energy density observed upon excitation of pulsed cathodoluminescence was substantially higher than that of x-ray luminescence, it became possible to initiate luminescence even in nanosamples. The higher density of the excitation energy gained by the crystal in the form of pulses favors the manifestation of electron–phonon interactions: the pulsed cathodoluminescence spectra exhibit many additional narrow peaks against the background of the broad luminescence bands. In our experiments, the intensity of the peaks attributed to electron–phonon interactions exceeded the instrumentation noise level by two to three orders of magnitude. The differences in the pulsed cathodoluminescence spectra

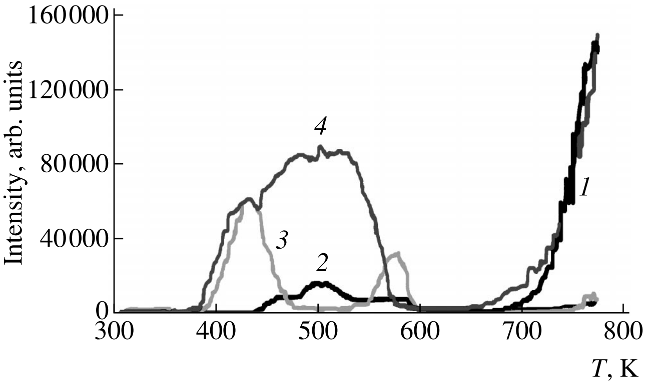

Fig. 4. (*1*) Thermally stimulated luminescence spectra and (*2–4*) thermally stimulated exoelectron emission spectra of NaF–U crystals: (*2*) bulk crystals, (*3*) LHPG fibers, and (*4*) nanocrystals.

of the bulk, fiber, and nanosized crystals can be caused by the mutual influence of radiation-induced impurity centers and the surface of the samples.

Figure 4 shows the thermally stimulated luminescence and exoelectron emission spectra of the NaF–U crystals. These spectra differ significantly for the bulk, fiber, and nanosized samples. This can be explained by the fact that surface traps in samples of different geometric configurations have different structures.

4. CONCLUSIONS

The results of investigations into the scintillation and optical properties of fiber and nanosized crystals indicate possible fields for their application. In particular, scintillation screens of high spatial resolution have been fabricated on the basis of fiber NaF–U crystals and probes for cytological, microbiological, and medical investigations have been designed on the basis of nanocrystals.

ACKNOWLEDGMENTS

This work was carried out within the framework of the program “Universities of Russia” (project no. UR.02.01.023) and was supported by the Ural Research and Educational Center within the program “Advanced Materials” REC-005 (project no. EK-005-X1), NATO (project no. PST.EAP.CLG 980 674), and the Center for Detector Development and Simulation (Yekaterinburg, Russia).

REFERENCES

1. P. P. Feofilov, Opt. Spektrosk. **7**, 842 (1959).
2. M. M. Kidibaev, *Radiation-Simulated Processes in (Li,Na)F–U,Me Crystals* (Ural. Gos. Tekh. Univ., Yekaterinburg, 1999) [in Russian].

Translated by O. Moskalev

Physics of the Solid State, Vol. 47, No. 8, 2005, pp. 1476–1478. Translated from Fizika Tverdogo Tela, Vol. 47, No. 8, 2005, pp. 1420–1422.
Original Russian Text Copyright © 2005 by Chernyshev, Abrosimov, Koroleva, Cherepanov.

PROCEEDINGS OF THE XII FEOFILOV WORKSHOP "SPECTROSCOPY OF CRYSTALS ACTIVATED BY RARE-EARTH AND TRANSITION-METAL IONS"

(Yekaterinburg, Russia, September 22–25, 2004)

Local Structure of Zn^{2+} Impurity Centers in a LiF : U,Zn Crystal

V. A. Chernyshev*, A. V. Abrosimov*, T. S. Koroleva, and A. N. Cherepanov*****
** Ural State University, pr. Lenina 51, Yekaterinburg, 620083 Russia*
*** Institute of Physics, National Academy of Sciences of Kyrgyzstan, Chui pr. 265A, Bishkek, 720071 Kyrgyzstan*
**** Ural State Technical University (UPI), ul. Mira 19, Yekaterinburg, 620002 Russia*
e-mail: tch@dpt.ustu.ru

Abstract—The local structure of Zn^{2+} impurity centers in a uranium-activated lithium fluoride crystal LiF : U,Zn is calculated in the framework of the shell model in the pair potential approximation. © *2005 Pleiades Publishing, Inc.*

1. INTRODUCTION

Uranium-activated lithium fluoride crystals LiF : U,*Me* (*Me* = Zn, Cu, Ti, Sr, Sc, etc.) have been important objects of investigation for many years [1, 2]. These materials are widely used as scintillators and radiation detectors. The main component of luminescence centers in LiF : U,*Me* crystals is the U^{6+} ion in the form of a UO_5F [2] or UO_6 [1] complex. Oxygen is also a necessary component of the uranium-containing luminescence center. The UO_6 complexes can be stabilized and, in some cases, sensibilized by coactivating impurities, such as Zn, Cu, Sr, Ti, etc. This indicates that, in LiF : U,*Me* fluoride crystals, the luminescence center as a whole is a complex cluster.

Hexavalent uranium ions U^{6+} in the crystal lattice of lithium fluoride exhibit intense luminescence in the green spectral range. In this case, the luminescence spectrum consists of several tens of lines associated with the U^{6+} ions. The intensity redistribution of these lines is primarily affected by coactivating impurity ions. However, the luminescence spectra of LiF : U,*Me* do not contain lines characteristic of the majority of the aforementioned coactivating ions. The exception is provided by Ti^{4+} [3], Cu^{+} [3], and Zn^{2+} [4] ions. In the luminescence spectra, the first two types of ions manifest themselves in the form of weak broad lines observed in the wavelength range 460–500 nm, whereas zinc ions are characterized by a single narrow line at a wavelength of 487 nm. This characteristic feature of Zn^{2+} ions distinguishes them from the other coactivating ions in LiF : U,*Me* fluorides and makes it possible to investigate their local structure.

In this paper, we analyze the local structure of a Zn^{2+} impurity center in a uranium-activated lithium fluoride crystal LiF : U,Zn. This ion is considered as a regional center in a complex cluster involving Zn^{2+} and U^{6+} ions with their nearest environment (several hundreds of ions).

2. CALCULATION TECHNIQUE AND RESULTS

The structure of an ionic crystal composed of ions with closed shells can be adequately described in the framework of the shell model in the pair interaction approximation [5]. Within this model, we calculated the local structure of a Zn^{2+} impurity center in a LiF : Zn^{2+} crystal.

The energy of pair interactions can be represented in the form

$$E_{ij} = A\exp(-r_{ij}/\rho) - Cr_{ij}^{-6} + q_iq_j/r_{ij}, \qquad (1)$$

where the two first terms describe a short-range interaction, namely, the short-range repulsion (in the form of the Born–Mayer potential), and the van der Waals interaction, respectively, and the third term characterizes the Coulomb interaction. The quantities A, ρ, and C are parameters of the model.

In our calculations, the Li^+ cations are considered to be rigid and the F^- anions are treated in the shell model. The ion charges correspond to an ionic bond, the charge of the lithium ion is taken as $+e$, and the sum of charges of the core and the shell of the F^- ion is equal to $-e$. Within the shell model, the interaction between the core and the shell of the F^- ion can be written as

$$E_{\text{core–shell}} = \frac{1}{2}kr^2, \qquad (2)$$

where r is the displacement of the shell with respect to the core of the fluorine ion and k is the parameter of the model. The short-range interaction between the cations is disregarded because they are separated by large distances.

The calculation was performed with the GULP program [6] taking into account the interaction parameters and the charges of the core and the shell of the fluorine ions. The numerical values of these parameters are presented in Table 1. The Coulomb interaction included in the GULP program was calculated by the Ewald method. The use of the above parameters for calculating the structure of the pure LiF crystal leads to good results (Table 2).

The Zn^{2+} impurity ion substitutes for the Li^+ cation in the host lattice of the crystal (Fig. 1) with the generation of an excess positive charge. In these calculations, the charge compensation was considered to be nonlocal.

The local structure of an impurity center in the crystal was calculated with the GULP program using the Mott–Littleton method. According to the computational algorithm, region 1 includes an impurity center and its surrounding ions, has a radius of 10 Å, and contains 485 ions. Region 2, in which the relaxation of ions is limited, has a radius of 20 Å. The coordinates of the ions in region 1 are determined by minimizing the energy of the crystal lattice. The calculations demonstrated that the replacement of the Li^+ ion by the Zn^{2+} ion, which has a close value of the radius (0.76 and 0.74 Å [7], respectively) but an excess positive charge, results in a significant distortion of the crystal lattice in the vicinity of the impurity center. Figure 2 presents the radial displacements of the ions in the vicinity of the Zn^{2+} impurity center. Here, it is convenient to use the notion of an orbit, namely, a group of ions capable of transforming into each other through any symmetry operation of the point group of an impure crystal. In this case, each of the first eight coordination shells around the impurity ion is considered an orbit and more distant coordination shells can involve two orbits.

Table 1. Parameters of the model

Ions	Core–core interaction			
	A, eV	ρ, Å	C, eV $Å^6$	Interaction range, Å
$Li^+–F^-$	443.830	0.2714	0.00	10.0
$F^-–F^-$	911.690	0.2707	13.80	10.0
$Zn^{2+}–F^-$	1482.300	0.2664	0.00	10.0
	Core–shell interaction			
	k, eV $Å^{-2}$	Shell charge, e	Core charge, e	
$F_{core}–F_{shell}$	24.36	–1.378	0.378	

Table 2. Lattice parameter a, elastic constants C_{ij}, and permittivities ε of the LiF crystal

	a, Å	C_{11}, GPa	C_{12}, GPa	C_{44}, GPa	ε_∞	ε_0
Calculation	4.024	125	58.9	58.9	8.5	1.9
Experiment	4.028	112	63.2	45.6	8.9	1.9

The first orbit (six fluorine ions) contracts (Fig. 1), whereas the second orbit (12 Li^+ ions) expands. This orbit experiences the maximum displacements (by approximately 0.13 Å) due to the repulsion from the impurity ion with an excess positive charge. After the seventh orbit (Fig. 2), the radial displacements become small and do not exceed 0.02 Å. The coordinates of the ions in the orbits of the pure and distorted lattices are listed in Table 3 (given are the coordinates of one ion from each orbit).

As follows from the calculations, the radial displacements of the orbits in the vicinity of the Zn^{2+}

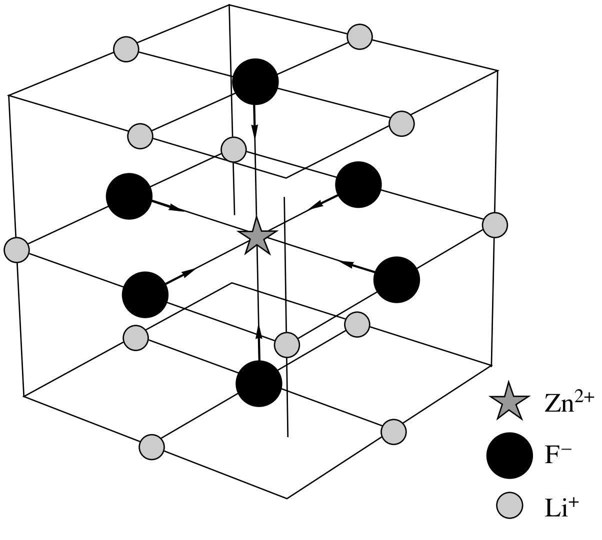

Fig. 1. Zn^{2+} impurity center in the LiF crystal.

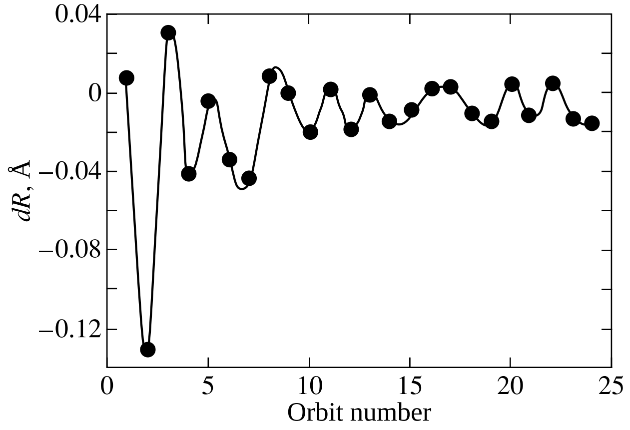

Fig. 2. Radial displacements of the orbits in the vicinity of the impurity center. The positive sign of the quantity dR corresponds to a decrease in the radial coordinate (the displacement toward the impurity center).

Table 3. Coordinates of the ions in the orbits for the pure and distorted LiF lattices (in Å)

Orbit number	Ion type	LiF (pure lattice)			LiF : Zn^{2+} (distorted lattice)			Number of ions in the orbit
		x	*y*	*z*	*x*	*y*	*z*	
	Zn	0	0	0	0	0	0	
1	F	2.0119	0	0	2.0046	0	0	6
2	Li	2.0119	2.0119	0	2.1045	2.1045	0	12
3	F	2.0119	2.0119	2.0119	1.9948	1.9948	1.9948	8
4	Li	4.0238	0	0	4.0658	0	0	6
5	F	4.0238	2.0119	0	4.0295	2.0108	0	24
6	Li	4.0238	2.0119	2.0119	4.0521	2.0257	2.0257	24
7	Li	4.0238	4.0238	0	4.0554	4.0554	0	12
8	F	4.0238	4.0238	2.0119	4.0189	4.0189	2.0086	24
9	F	0	6.0358	0	0	6.0367	0	6
10	Li	6.0358	2.0119	0	6.0546	2.0188	0	24
11	F	6.0358	2.0119	2.0119	6.0347	2.0119	2.0119	24
12	Li	4.0238	4.0238	4.0238	4.0347	4.0347	4.0347	8
13	F	6.0358	4.0238	0	6.0364	4.0253	0	24
14	Li	6.0358	4.0238	2.0119	6.0486	4.0309	2.0181	48
15	Li	0	8.0477	0	0	8.0576	0	6
16	F	6.0358	4.0238	4.0238	6.0342	4.0236	4.0236	24
17	F	2.0119	8.0477	0	2.0115	8.0458	0	24
18	Li	8.0477	2.0119	2.0119	8.0570	2.0153	2.0153	24
19	Li	6.0358	6.0358	0	6.0462	6.0462	0	12
20	F	6.0358	6.0358	2.0119	6.0325	6.0325	2.011	24
21	Li	8.0477	4.0238	0	8.0587	4.0292	0	24
22	F	8.0477	4.0238	2.0119	8.0436	4.0218	2.0113	48
23	Li	6.0358	6.0358	4.0238	6.0439	6.0439	4.0300	24
24	Li	8.0477	4.0238	4.0238	8.0605	4.0304	4.0304	24

impurity ion are stabilized beginning from the eighth or ninth orbit, i.e., beginning at a distance of ~4–6 Å from the central Zn^{2+} ion (Table 3). This suggests that the nucleus of the Zn^{2+} regional impurity center can consist of 116–122 ions involved in its nearest environment and located in these eight or nine orbits. These orbits can be treated as a boundary between the stable Zn^{2+} region and the region around the $(UO_6)^{6-}$ ion responsible for the nonlocal compensation for an excess positive charge of the Zn^{2+} ion.

ACKNOWLEDGMENTS

This work was performed within the framework of the state scientific program “Universities of Russia” (project no. UR.02.01.023) and was supported by the Ural Research and Educational Center within the program “Advanced Materials” REC-005 (project no. EK-005-X1), the Russian Foundation for Basic Research (project no. 04-02-16427), NATO (grant no. PST.EAP.CLG 980 674), and the Center for Detector Development and Simulation (Yekaterinburg, Russia).

REFERENCES

1. W. A. Runciman, Nature (London) **175**, 1082 (1955).
2. A. A. Kaplyanskiĭ, N. A. Moskvin, and P. P. Feofilov, Opt. Spektrosk. **16** (4), 619 (1964).
3. M. M. Kidibaev, *Radiation-Stimulated Processes in Crystals (Li,Na)F–U,Me* (Ural. Gos. Tekh. Univ., Yekaterinburg, 1999) [in Russian].
4. T. S. Koroleva, Candidate’s Dissertation (Karakol, 1996).
5. W. A. Runciman and E. Y. Wong, J. Chem. Phys. **71**, 1838 (1979).
6. C. Catlow and M. Norgett, J. Phys. C: Solid State Phys. **6**, 1325 (1973).
7. C. Catlow, A. Chadwick, and J. Corish, J. Solid State Chem. **48**, 65 (1983).

Translated by I. Volkov

Physics of the Solid State, Vol. 47, No. 8, 2005, pp. 1479–1484. From Fizika Tverdogo Tela, Vol. 47, No. 8, 2005, pp. 1423–1427.
Original English Text Copyright © 2005 by Lezhnina, Kätker, Kynast.

PROCEEDINGS OF THE XII FEOFILOV WORKSHOP “SPECTROSCOPY OF CRYSTALS ACTIVATED BY RARE-EARTH AND TRANSITION-METAL IONS”

(Yekaterinburg, Russia, September 22–25, 2004)

Rare-Earth Ions in Porous Matrices[1]

M. M. Lezhnina[1, 2], Heike Kätker[1], and Ulrich H. Kynast[1]
[1] *University of Applied Sciences Muenster, Steinfurt, 48565 Germany*
[2] *Mart State Technical University, Institute of Physics, Yoshkar-Ola, 424000 Russia*
e-mail: uk@fh-muenster.de; kaetker@fh-muenster.de; marina@fh-muenster.de

Abstract—Initially motivated by the commercial need for cheaper and environmentally friendly luminescent materials for application in fluorescent lamps and cathode ray tubes, the search for new matrices for optically active species has penetrated a scope far beyond “classical” solid-state materials. Porous matrices with voids ranging from the nano- to the microscale have become the subject of recent investigations. Crystalline, amorphous, organomorphous, nanosized matrices and matrices, which are amorphous on the atomic level but have a translational superstructure on the microscale (zeolites, sol–gel materials, polymers, nanoparticles and photonic crystals), are addressed. The optical technologies covered in this research range from mercury free discharge lamps, plasma displays, organic and polymeric light emitting diodes, and novel laser materials to biophotonics and the new generation of white emitting AlGaN solid-state light emitting diodes (LEDs). Due to their specific properties (e.g., high quantum yields, narrow line emission), rare-earth ions are indispensable components of these approaches, be it in the nanoscaling zeolites, sol–gel matrices, or as the active component in optically functional polymers. Optical properties of hybrid materials composed of either rare-earth ions as such, their complexes, or nanoparticles in these matrices, with potential application in the fields mentioned, will form the scope of the present report. *© 2005 Pleiades Publishing, Inc.*

1. INTRODUCTION

The major applications of luminescent materials have traditionally been in lighting, displays, and fluorescent paints. In the last decades, several high-tech and completely new applications have added to this scope, e.g., communication technologies, organic light emitting diodes (OLEDs), biolabels, or the recent white light emitting diodes, of which rare-earth ions, in particular, phosphors, are an essential component. Presently applied phosphors are highly optimized materials, often at the physical boundaries. However, some visions, such as quantum yields in excess of 100% (multiphoton emitters, [1]) or appreciably cheaper material costs, remain to be tackled. In many applications of phosphors, maintenance of high efficiencies on reducing the grain size to the nanoscale is desirable (e.g., in OLEDs [2], in biolabels based on fluorescent nanoparticles [3], or in the production of transparent polymer hybrids for fiber communication [4] and phosphor-converted white LEDs).

Considering the enormous amount of known and documented luminescent materials and phosphors, respectively, it seems worthwhile to assume a somewhat more distant view of the matter when evaluating approaches to surpass “classical” materials in one or another optical property. The view taken in this report, as summarized in Fig. 1, should be considered a guideline for the imagination rather than one of high precision. While the rare-earth ions in the mentioned classical applications are guests in various (micro-) crystalline solids, the *sizes of occupied sites* enter the consideration mostly as a restricting factor. The effects imparted by the size restriction may very well be beneficial, e.g., via the desired crystal field splitting, rigidity, etc. However, a size restriction to a few hundred picometers at best excludes a wide range of highly efficient luminescent entities from the corresponding classical applications. It is worth mentioning dye molecules, molecular ions, and nanoparticles, which cannot be used in many applications due to morphological, chemical, textural, handling, or stability problems.

Nano-, meso-, and microporous matrices (generously including glasses and polymers in this scope) can provide a solution to the size dilemma. We believe that hybrid materials composed of a porous matrix and occluded guests as listed above will open a range of applications in which, on one hand, materials with typical solid-state properties will be desirable but, on the other hand, the molecular or nanoscale properties of the guests will need to be retained. In summary, the goals in investigating the luminescence in microporous hosts are as follows:

(i) to make chemically “impossible” luminescent species possible (isolated ions, complex ions, imbedded and stable nanoparticles);

---

[1] This article was submitted by the authors in English.

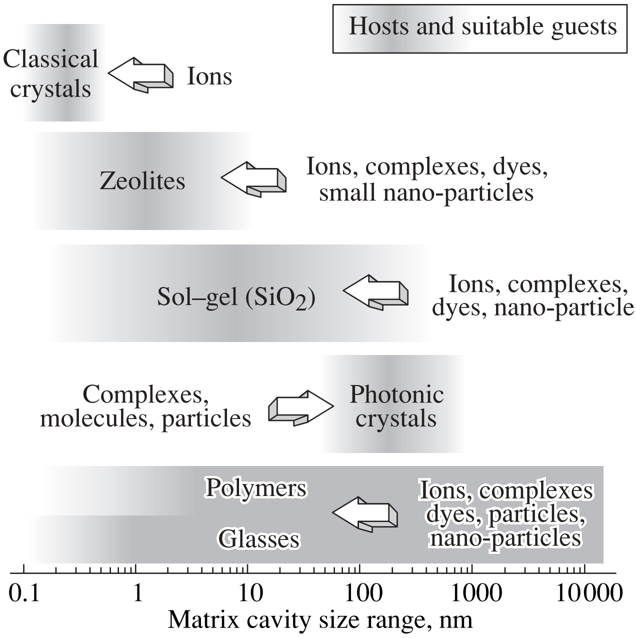

Fig. 1. Range of voids provided for the accommodation of luminescent entities.

(ii) to describe the confinement behavior (cavity and size dependence, influence of matrix);

(iii) to search for possibilities for exploitation, i.e., potential fields of application: new (VUV) phosphors (for plasma display panels, quantum cutters downconverters for lighting), transparent luminescent polymer rare-earth composites from the dissolution/dispersion of complexes and nanophosphors (for OLEDs, signaling, marking, safety, fiber amplifiers, LEDs), and near infrared (NIR) and upconverted emission (for lasers, biolabeling).

As it would be the scope of this report to cover all aspects indicated in Fig. 1 and the goals in the previous list, we will exemplarily focus on the accommodation of metalloorganic complexes and fluoride nanoparticles in zeolites, the sol–gel (SG) matrix, and polymers.

2. METALLOORGANIC ZEOLITE HYBRIDS

Zeolites are microcrystalline solids mainly composed of Si, Al, and O, which form typical cavities and channels of molecular dimensions within the crystals. Certainly the most striking feature of zeolite structures is their unique topology with well-ordered, hospitable cages and channels with diameters in the nanometer regime; in addition to their structural features, they exhibit useful intrinsic chemical and physical properties (e.g., easy accessibility, relatively good stability, and a large band gap). In the area of optical materials, zeolites will be of particular interest when specific distances or a spatial pattern of atomic, ionic, molecular, or nanoscaled quest species are required in order to obtain the desired physical effects.

Free ions can be readily accommodated into the cavities of zeolite X and Y (Fig. 2a, [5]). To this end, very efficient UV emitters based on Ce^{3+} incorporation and green emitters using the pair Ce^{3+}, Tb^{3+} with quantum efficiencies near 100% in the UV and 80% in the visible range have been realized [5, 6]. However, these investigations also reveal the need for alternative sensitization schemes, e.g., for lamp applications.

Rare-earth complexes with ligands rather than Ce^{3+} as sensitizers can be used to improve the absorptivity. As ligands we have investigated aromatic carboxylates and β-diketonates; for completeness, the work on inorganic anions (vanadates, molybdates, tungstates) should also be mentioned, in which the transition metalates possess the $O \longrightarrow M^{+VI}$ charge transfer states in the UV range, which can be exploited for sensitization [7–9]. The organic ligands studied provide high absorptivities due to the allowed π–π^* transitions; the corresponding molecular singlet states after spin–orbit-coupling-mediated intersystem crossing into a molecular triplet state could very efficiently transfer their energy to the rare-earth in [10] and yielded very high quantum efficiencies. Such complexes cover a wide range of excitation wavelengths, both through appropriate choice of the parent ligand itself or appropriate substitution. Metalloorganic inclusion complexes have recently been reviewed [11]. Figures 2b and 2c present an illustrative example of the inclusion of $Eu(ttfa)_2phen$, which exhibits a quantum yield of approximately 80% [12]. Of interest is the overlap of the hatched area, which represents the emission spectrum of a commercial UV–LED with the excitation band: obviously, this rare-earth-complex–zeolite hybrid can be an interesting component in UV–LED driven optical devices, e.g., in phosphor-converted white LEDs, if imbedded in the polymer dome in front of the LED chip.

3. FLUORIDE NANOPARTICLES IN AN SG MATRIX

As opposed to zeolites, SG materials are amorphous hosts with additional degrees of freedom in guest size. While nearly all of the inclusion candidates depicted in Fig. 1 are a subject of ongoing research, we will present here a recent example of fluoride nanoparticle synthesis in the SG matrix. Our studies have thus far been restricted to SiO_2-based matrices.

The use of rare-earth fluorides in optical applications is often hampered by hydrolytic and photochemical instability, but due to their intrinsic properties (low phonon frequencies, wide band gap), the fluoride lattice is often the most efficient or even indispensable, as is the case for rare-earth-based multiphoton emission (MPE), which addresses the desire for quantum yields in excess of 100% [1, 13, 14]. As high energy excitation

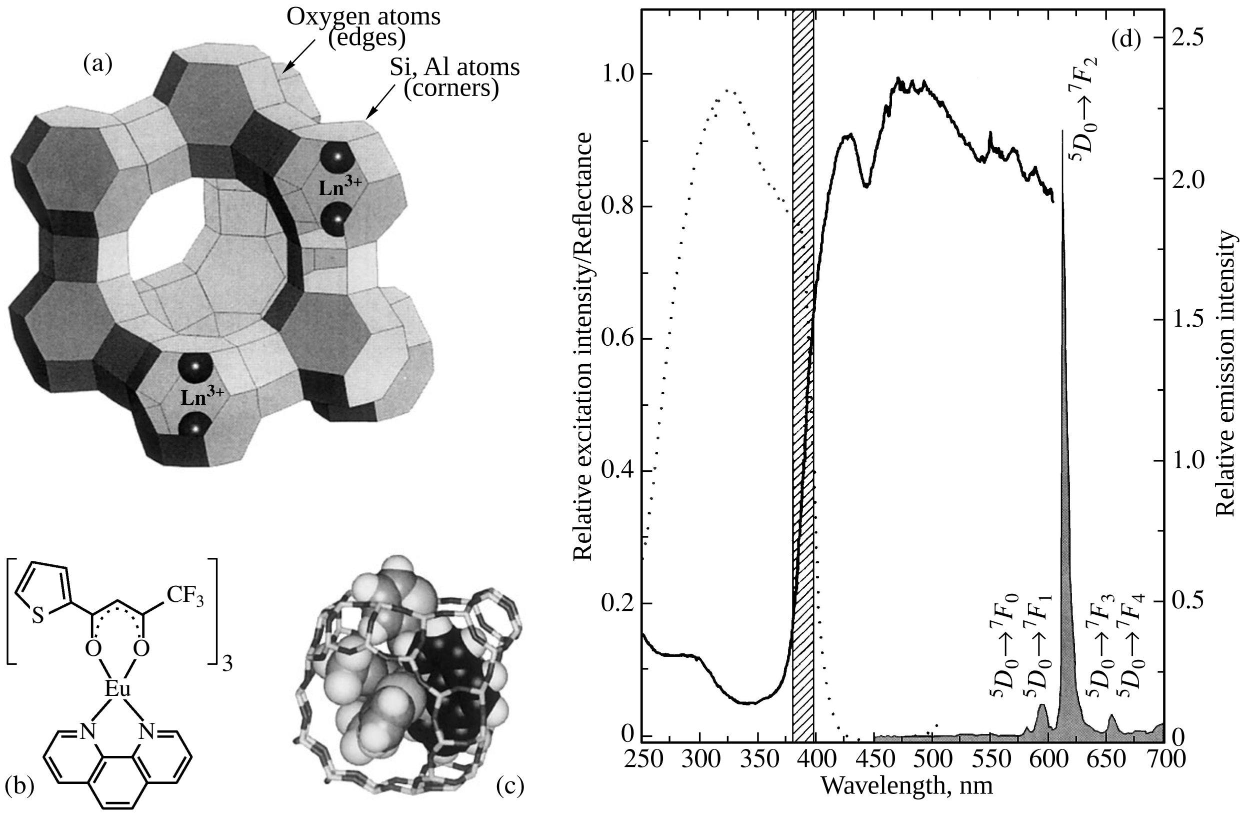

Fig. 2. Intrazeolite luminescence: (a) Tb^{3+}, Ce^{3+} doped and calcined zeolite *X* (up to 16 Ln^{3+}/UC [6]); (b) $Eu(ttfa)_3phen$; (c) model of $Eu(ttfa)_3phen$ occluded in the zeolite *X* supercage, [$Eu(ttfa)_3phen$-*X*]; and (d) optical properties of [$Eu(ttfa)_3phen$-*X*]; the hatched area corresponds to the emission of a commercial UV LED (Nichia).

sources are required for MPE, from the point of view of application, only the Xe_2-excimer emission with a maximum at 172 nm seems feasible. At this wavelength, the absorptivity of most fluorides is unsatisfying. One approach to the problem is to coat the fluoride particles to protect and at the same time sensitize the emission. In order to accomplish energy transfer from the coating to the interior, the coating has to be very thin, which would in turn again be at the cost of absorptivity. To enable short transfer distances but high coating-to-core ratios, the particles have to be very small. Thus, core-shell nanoparticles may offer a conceivable solution. The generation of rare-earth fluoride particles in the SG matrix is particularly promising, because, on one hand, the matrix can be made transparent to the Xe_2 excimer discharge and, on the other hand, secondary chemical manipulation of the particles in this open pore structure should be possible without risk of uncontrolled particle growth.

The synthesis of the (Cd, Eu)F_3 nanoparticles, one promising MPE candidate, was performed by altering a method in the literature describing the preparation of nano-LaF_3 in a SiO_2-based SG matrix [15]. As the aim was not to manufacture glassy monoliths, the use of the inhibiting DMF was refrained from; additionally, trifluoracetic acid (H(tfa)) only yielded oxfluorides after thermal decomposition of the $Ln(tfa)_3$-SG precursor in our experiments. The particles formed are in the range of 20 nm as revealed by XRD and TEM analysis (Fig. 3; obtained on a “Holey–Carbon”-copper net, JEM 3010, 300 kV). Fluorides could only be obtained by replacing acetic acid with HCl and using bis(perfluormethanesulfonimide) $H[(F_3C{-}SO_2)_2N]$ (H(pms)) instead of H(tfa). Coincidentally, $Ln(pms)_3$ converts into LnF_3 at almost the same temperature, 400°C, as $Ln(tfa)_3$. Typically, the rare-earth content was adjusted to 5% of the tetraethyorthosilicate used. The chemical identity of the sample (oxifluoride vs. fluoride) was determined by the analytical Ln : F ratio but could be determined more readily by the emission spectra, which in the case of the Eu-oxifluorides yield an emission pattern characteristic of oxygen-coordinated Eu^{3+} in a glassy matrix dominated by Eu^{3+} $^5D_0 \longrightarrow {}^7F_2$ with a weaker and broad $^5D_0 \longrightarrow {}^7F_2$ emission (compare, e.g., with [16]). As opposed to that, pure fluoride particles are characterized by a $^5D_0 \longrightarrow {}^7F_1/{}^5D_0 \longrightarrow {}^7F_2$ emission ratio near 1 or even larger [17] (see Fig. 3).

Calcined (Gd, Eu)F_3 nanoparticle embeddings in an amorphous, porous SiO_2 matrix were consecutively treated for the generation of a shell in an aqueous sus-

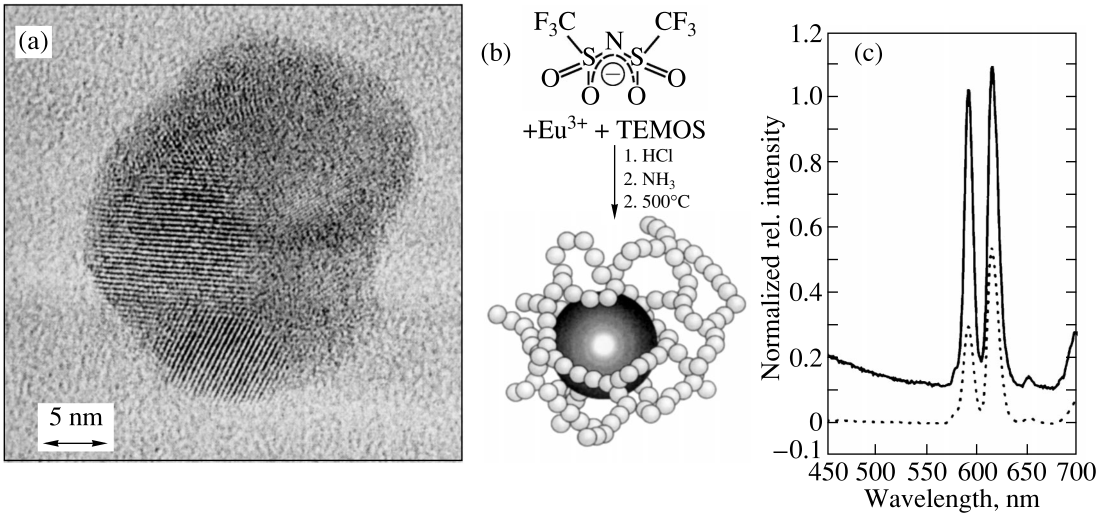

Fig. 3. Fluoride nanoparticles in a SG matrix: (a) HRTEM of an oxifluoride particle in a SG matrix obtained from thermolysis of a $Eu(O_2C–CF_3)_3$ precursor. (b) Preparation of SG-hosted fluorides (see text for details) and (c) emission spectra of fluorides; the dashed line is the $Eu(pms)_3$ precursor, and the solid line is occluded fluoride particles.

pension. We found the following scheme to yield the first acceptable results (S.G. = sol–gel matrix):

$$1.\ (Eu_{0.1}Gd_{0.9}F_3)_{nano}\text{-S.G.} + Gd^{3+}$$

$$\xrightarrow[(N_4CH_2)_6]{\Delta,\ 80–90°C} \{[(Eu_{0.1}Gd_{0.9}F_3)_{nano}]Gd(OH)_3\}\text{-S.G.}$$

$$2.\ (Eu_{0.1}Gd_{0.9}F_3)_{nano}\text{-S.G.} + Gd^{3+}$$

$$\xrightarrow{\Delta,\ 500°C} \{[(Eu_{0.1}Gd_{0.9}F_3)_{nano}]GdO_3\}\text{-S.G.}$$

The calcined gels containing the fluoride particle described in the previous paragraph (300 mg) were suspended in 40 ml of a dilute aqueous solution of Gd^{3+} (3–10 mol/l) and a sevenfold excess of urotropine or urea, respectively. On heating such suspensions (2 h, 80°C), homogeneous precipitation of $Gd(OH)_3$ with urotropine occurs, which is preferably formed on surfaces that can serve as nuclei. In the present case, the nanoparticles adopt the role of the nucleating surface and at least an appreciable amount of the $Gd(OH)_3$ precipitates on the particles. After calcination at 500°C, the resulting product shows a small amount of penetration of oxygen into the core, leading to a slight decrease in the Eu^{3+} ($^5D_0 \longrightarrow {}^7F_1/{}^5D_0 \longrightarrow {}^7F_2$) emission ratio on core excitation at 392 nm, whereas on Gd^{3+} excitation (274 nm, $^8S_{7/2} \longrightarrow {}^6I_J$) the ratio is reversed (Fig. 4). These results show that it is possible to build up shells around the occluded particles on one hand and, furthermore, that energy transfer is observed from the shell to the core on the other hand. The particle efficiency increases by some 30% on deposition of the coating, but we expect that optimally adjusted preparative parameters will allow even further improvements. We would like to mention briefly that, after having taken advantage of the unique possibility of studying these coating effects in the porous matrix under stable conditions, we were also able to transfer some of the results to free standing nanoparticles, whose efficiency now very closely approaches that of their microsized counterparts.

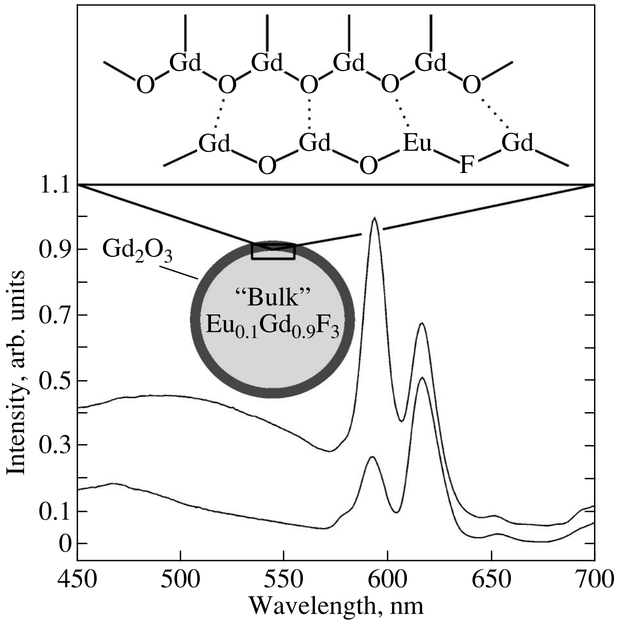

Fig. 4. Core modifications on SG-embedded fluoride particles: $Gd(OH)_3$-coated particles after calcination; Eu^{3+} emission at λ_{exc} = 395 (top) and 274 nm (bottom).

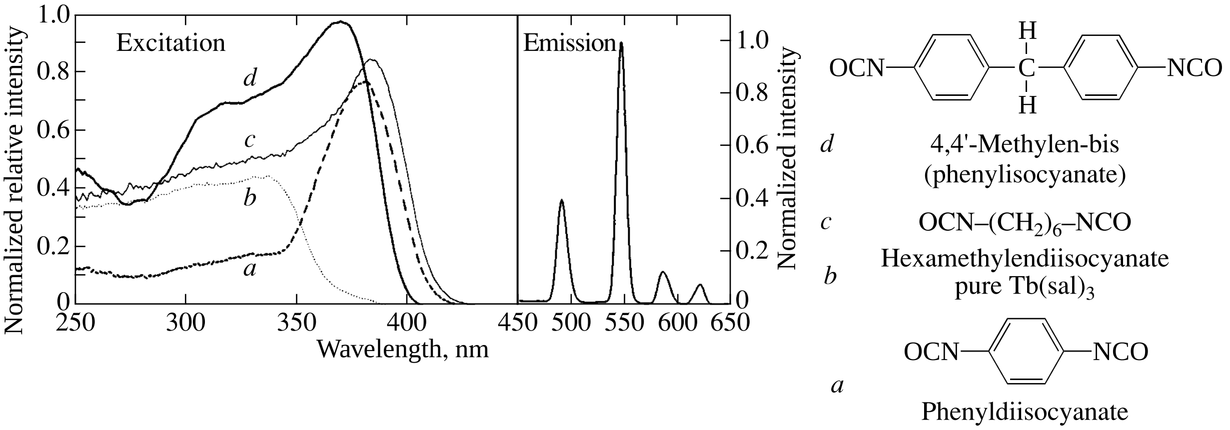

Fig. 5. Polymer (polyurethane)-embedded complexes: $Tb(sal)_3$ coupled to various backbones. Only the emission in HDI polyurethane is given; other emission spectra are practically identical.

4. METALLOORGANIC COMPLEXES IN POLYMERS

Polymers are probably the most flexible host matrix with regard to guest size. To this end, we investigated the insertion of complexes and small phosphor nanoparticles into polyurethanes and silicones. While nanoparticles typically require surface modifications to render them compatible with hydrophobia polymers, complexes with organic ligands can be readily dissolved in the prepolymers. We can distinguish between solid solutions and backbone anchored complexes. Dissolved complexes will preferentially be formed with such systems, which are coordinatively saturated, such as the complex $Eu(ttfa)_3phen$ (see also above, metalloorganic zeolite hybrids). The latter could be successfully incorporated into silicones and polyurethanes. Backbone support may be realized by letting reactive substituents on the ligands react with the prepolymers. Also conceivable would be donor–acceptor interactions by allowing polymer donor atoms to fill the coordination sphere of coordinatively saturated complexes. Examples for backbone support are the reactions of terbium salicylate $Ta(O_2C–C_6H_4–OH)_3$ ($Tb(sal)_3$) and terbium *p*-amino-benzoate $Tb(O_2C–C_6H_4–NH_2)_3$ ($Tb(paba)_3$), e.g., with hexamethylenediisocyanate (HDI): $Ta(O_2C–C_6H_4–\underline{OH})_3$ + $3OCN–[(CH_2)_6]–NCO \longrightarrow Tb(O_2C–C_6H_4–\underline{O}(C{=}O)NH–[(CH_2)_6]–NCO)_3$; $Tb(O_2C–C_6H_4–\overline{NH_2})_3$ + $3OCN–[(CH_2)_6]–NCO \longrightarrow Tb(O_2C–C_6H_4–\underline{NH}(C{=}O)NH–[(CH_2)_6]–NCO)_3$.

Both of the intermediates can react with polyols or amines to form the eventual polymer [18]. The silicone (not plotted) as well as the polyurethane composites show very efficient luminescence (Fig. 5). The spectral features of $Eu(ttfa)_3$ are practically identical to those of the zeolitic complexes above. Worth pointing out in Fig. 5 is the tunable excitation obtained through the reaction with different diisocyanates, which again extends into the spectral range accessible with recent UV LEDs.

5. SUMMARY AND CONCLUSIONS

Generally, classical phosphors or luminescent crystals have not yet been outperformed by host–guest systems, nanoparticles, etc. Exceptions are fields where conventional phosphors are not applicable and thus comparison does not apply (e.g., rare-earth-based biolabels, thin film electroluminescence, (metallo) organic LEDs). However, as we tried to show with the few examples selected, inorganic or polymer host–guest chemistry can provide access to luminescent hybrid materials that are impossible or difficult to employ in conventional applications: the very efficient diketonates or aromatic carboxylates may in inorganic porous matrices or polymers become applicable to, e.g., optical sensors, luminescent paint dispersions, luminescent markers, etc., while matrix-stabilized fluoride particles may eventually be developed into VUV excitable phosphors and applications based on NIR excitation. The evolution of an increasing demand for rare-earth-activated nanophosphors for, e.g., biolabels or transparent, optically functional polymers currently promotes the study of improved surface control and core-shell particles.

REFERENCES

1. R. T. Wegh, H. Donker, K. D. Oskam, and A. Meijerink, Science **283**, 663 (1999).
2. J. Nanda, S. Sapra, and D. Sarma, Chem. Mater. **12**, 1018 (2000).
3. S. Coe, W.-K. Woo, M. Bawendi, and V. Bulovi, Nature **420**, 800 (2002).
4. N. N. Tessler, V. Medvedev, M. Kazes, S. H. Kan, and U. Banin, Science **295**, 1506 (2002).
5. U. Kynast and V. Weiler, Adv. Mater. **6**, 937 (1994).
6. T. Jüstel, D. U. Wiechert, C. Lau, D. Sendor, and U. Kynast, Adv. Funct. Mater. **11**, 105 (2001).

7. C. Borgmann, J. Sauer, T. Jüstel, U. Kynast, and F. Schüth, Adv. Mater. **11**, 45 (1999).
8. C. Lau, H. -J. Mai, and U. Kynast, Microporous Mesopor. Mater. **47**, 339 (2001).
9. M. Lezhnina and U. Kynast, J. Alloys Compd. **380**, 55 (2004).
10. V. L. Ermolaev, Usp. Fiz. Nauk **80**, 3 (1963) [Sov. Phys. Usp. **6**, 333 (1963)].
11. D. Sendor and U. Kynast, in *Host-Guest Systems Based on Nanoporous Crystals*, Ed. by F. Laeri, F. Schüth, U. Simon, and M. Wark (Wiley, Weinheim, 2003), Part 4, Chap. 5, p. 558.
12. D. Sendor and U. Kynast, Adv. Mater. **14**, 1570 (2002).
13. J. L. Sommerdijk, A. Bril, and A. W. de Jager, J. Lumin. **8**, 341 (1974).
14. R. Pappalardo, J. Lumin. **14**, 159 (1974).
15. S. Fujihara, C. Mochizuki, and T. Kimura, J. Non-Cryst. Solids **244**, 267 (1999).
16. R. Van Deun, K. Binnemans, C. Görller-Wallrand, and J. L. Adam, J. Phys.: Condens. Matter **10**, 7231 (1998).
17. J.-L. Adam, in *Advanced Inorganic Fluorides*, Ed. by T. Nakajima, B. Zemva, and A. Tressaud (Elsevier, Amsterdam, 2000), p. 235.
18. U. Kynast, *Paso GmbH. Synthesis of Polymers for Luminescence Effects (Darstellung von Polymeren zur Erzeugung von Lumineszenzeffekten)*, EP Appl. 02025915.6 (2002).

Physics of the Solid State, Vol. 47, No. 8, 2005, pp. 1485–1488. From Fizika Tverdogo Tela, Vol. 47, No. 8, 2005, pp. 1428–1431.
Original English Text Copyright © 2005 by Lezhnina, Kynast.

PROCEEDINGS OF THE XII FEOFILOV WORKSHOP "SPECTROSCOPY OF CRYSTALS ACTIVATED BY RARE-EARTH AND TRANSITION-METAL IONS"

(Yekaterinburg, Russia, September 22–25, 2004)

NIR- and Upconverted Luminescence from Rare-Earth Sodalites[1]

M. M. Lezhnina[1, 2] and U. H. Kynast[1]
[1] *University of Applied Sciences Muenster, Steinfurt, 48565 Germany*
[2] *Mari State Technical University, Institute of Physics, Yoshkar-Ola, 424000 Russia*
e-mail: marina@fh-muenster.de; uk@fh-muenster.de

Abstract—In the recent past, numerous attempts have been made to utilize nano-, meso-, and microporous materials as hosts for luminescent guest species. The accessible spectral range now spreads from the vacuum ultraviolet to the near infrared (NIR), if sodalites are included in this scope. Although borderline materials in this context with respect to pore sizes, examples of the versatility of sodalites in accommodating small but efficient luminescent entities are discussed. In particular, optical materials whose spectral range of operation is allocated in the NIR have recently attracted our attention and will form the focus of this report. *© 2005 Pleiades Publishing, Inc.*

1. INTRODUCTION

Zeolites are crystalline alumosilicates in which tetrahedral SiO_2^- and AlO_2^- are arranged such as to yield a microporous framework. Each negative charge of the lattice brought about by an AlO_2^- building unit is compensated by a cationic species in the voids of the structure (see, e.g., Fig. 1); additionally, most zeolites also readily occlude remarkable amounts of water. One of the most prominent zeolitic materials is synthetic zeolite *X*, which exhibits rather large supercages with a diameter of 1200 pm. These are capable of containing not only a high number of ions but also complexes of these ions. The second representative in this context are the sodalites and their derivatives, which assume a bottom position with respect to the accessible cavity size of approximately 900 pm (the distance from the center of opposite six ring windows; see Fig. 2). Zeolites in general are interesting as matrices for luminescence centers owing to their stability; transparency in the UV and visible spectral ranges; relative simplicity and, therefore, cheapness of synthesis; and, last but not least, ease of accommodation of luminescent components. The simplest way to accomplish optical activation is by means of an aqueous ion exchange in the case of rare-earth ions or via gas phase loading in the case of volatile organic substances.

While the luminescence properties of some lanthanide ions in the zeolite *X* matrix ([Ln–*X*]) have been extensively investigated, only little is known about the potential of rare-earth fictionalized sodalites.

With regard to luminescence efficiency, it has been shown that the quantum output of zeolite-occluded rare-earth ions decreases in the series [Ce–*X*] (100% [1]), [Tb–*X*] (18% [2]), [Eu–*X*] (<5% [3]), and [Nd–*X*] (ca. 0%, own results) with decreasing energy of emission. This tendency is connected to the increase in the

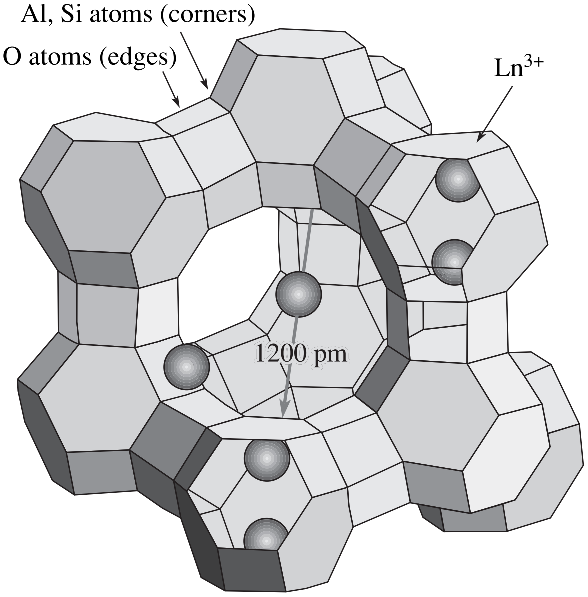

Fig. 1. Sketch of the Faujasite structure (zeolite *X*). Cation sites are indicated by spheres. Positions outside of the cub-octahedral sodalite cages are not occupied in the zeolites *X* discussed in this report.

---

[1] This article was submitted by the authors in English.

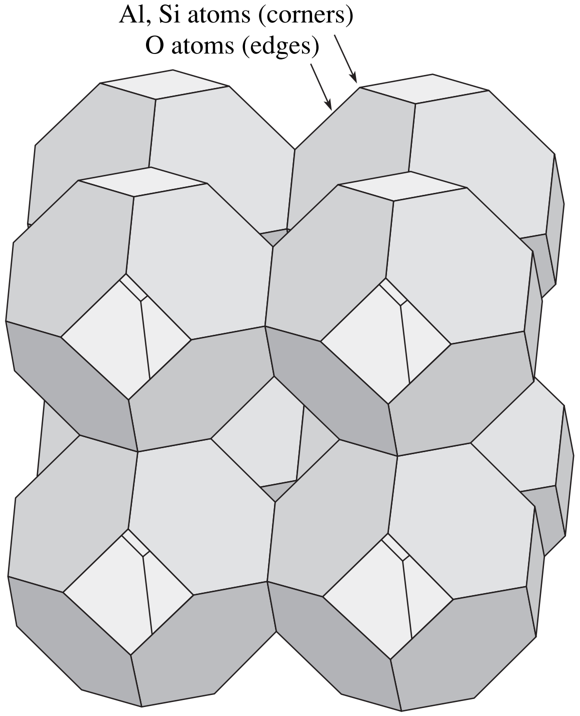

Fig. 2. Simplified sketch of the sodalite structure.

probability of radiationless processes, in particular, vibration relaxation [4]. In the present work, we investigate luminescence processes involving electronic transitions of rare-earth ions in the spectral energy range between 800–1200 nm in the near infrared (NIR), for which the probability of vibrational relaxation will be particularly high.

2. RESULTS AND DISCUSSION

In the zeolite *X* matrix, at room temperature, no emission is observed in the case of neodymium or coupled holmium–ytterbium ions. Within the zeolite, the coordination sphere of rare-earth ions is completed by the coordination of lattice oxygen atoms and, depending on the state of (re)hydration, occluded water. In order to decrease the probability of radiationless processes, it is necessary to introduce ligands with low vibrational energies. Recently, Hasegawa and coworkers observed emission of neodymium ions in the zeolite *X* matrix on complexation of Nd^{3+} with bis-(perfluormethanesulfonimide), $H[(F_3C\text{–}SO_2)_2N]$ [5], a ligand without protons and thus devoid of high-frequency C–H or N–H vibrations. Analogously, the approach chosen in our work is a modification of the rare-earth environment in crystal alumosilicate matrices in such a way as to allow luminescence processes, including electron transitions within low-energy states.

2.1. Fluoride Complexes in Zeolite X

According to the literature, such processes have good intensity in fluorides, or more generally halides, and tungstates [6, 7]. We have thus carried out fluoridation of the pair Ho^{3+}/Yb^{3+} in doped zeolite *X*. This pair is of interest due to upconversion processes, the emission of a high energy photon on excitation with two or three low energy photons; particularly desirable are upconversion materials enabling visible emission on excitation with NIR laser diodes.

The excitation of this system is based on a (spin-allowed) electronic transition of the Yb^{3+} ion ($^2F_{7/2} \longrightarrow {}^2F_{5/2}$), followed by an energy transfer to a nearby electronic level of the Ho^{3+} ion ($^5I_6$). At sufficiently high excitation densities, i.e., with sufficient population of the $^5I_6$ state, a consecutive transition on the same ion can occur ($^5I_6 \longrightarrow {}^5F_4$ or $^5S_2$), followed by an emissive return to the ground state with the yield of a visible 541-nm photon. Alternatively, the Ho^{3+} can undergo an intermediate relaxation to the $^5F_5$ state, which emits a 650-nm photon. Similar processes may also be observed for the pair Er^{3+}/Yb^{3+}. Encaged, pure fluorocomplexes were obtained from excess NH_4F and rare-earth-doped zeolite *X* for a composition of $[Y_8Ho_8\text{–}X]$ loaded with 10 NH_4F (250°C, sealed under vacuum in a glass ampoule, *X* denotes the unit cell of zeolite *X* with composition $Na_{87}Al_{87}Si_{105}O_{384}$; for the preparation of [Ln–*X*], refer to, e.g., [2]). Partially independent of the rare-earth content, analytically ratios of 5 to 6 F^- per rare-earth ion are obtained, while the crystal structure of the zeolite is mostly conserved (XRD). For the example given, this corresponds to an overall composition of the zeolite of $[(NH_4)_{48}(Eu_4Gd_{12})F_{96}\text{–}X]$. Assuming an even distribution of the fluoride species throughout the zeolite, this would yield aggregates of $(NH_4)_6Eu_{0.5}Gd_{1.5}F_{12}$ within each of the eight supercages of the unit cell. Figure 3 depicts the upconverted emission obtained from exciting Yb^{3+} with a 50 mW/980 nm diode laser focussed on an area of approximately 2.5 mm^2 (Acton Monochromator SP 150 with a focal length of 150 mm and a 1200-g/mm grating Acton Photomultiplier tube P2). This green upconverted emission could also clearly be seen in bright daylight; storage under ambient atmosphere did not alter the emission intensities.

One problem with the material is that the ammonium complexes are unstable thermally and it is thus not suitable for further application. Unfortunately, attempts to decompose the complexes to zeolite-encaged fluoride proceed under partial destruction of the zeolite matrix and the formation of rare-earth oxifluoride nanoparticles, which no longer exhibit the upconversion phenomenon.

2.2. Upconversion in Sodalites

Recently, we detected an unexpected access to tungstate-loaded zeolite *X* [8]. In attempts to find low vibrational frequency partners for upconverting and NIR-emitting rare-earth ions, we used the method described in [3] to synthesize the correspondingly modified zeolites *X* [Ln(WO_3)–*X*] (Ln = Yb/Ho; Yb/Er; Nd). However, neither of the materials obtained could be activated to yield the desired upconversion or Nd^{3+} emission. Instead, we were rewarded with upconversion and NIR emission, respectively, after the solid state conversion to sodalite derivatives (Hauyne [$Ln_4(Al_8Si_4O_{24})(WO_4)_2$] and Noseane [$Ln_3(Al_7Si_5O_{24})WO_4$]) [7]. This synthesis may be performed by heating a solid mixture of rare-earth-doped zeolite *X* and WO_3 to 650°C to allow for the penetration of tungsten oxide into the zeolite matrix. Followed by an annealing step at 1000°C, the sodalites crystallize. Rare-earth ions are located in hexagonal windows of the sodalite cage, thus being coordinated by six framework oxygens. Additionally, two oxygen atoms of WO_4 ions in neighboring cages complete the coordination sphere to eight, as represented in Fig. 4. The composition of zeolite *X* slightly differs from the composition required for the sodalite, which leads to small amounts of undesired foreign phases [8] and mediocre crystal quality at best. However, upconversion and efficient neodymium emission can be observed for the first time; for the corresponding upconverted spectra, we refer the reader to [7]. As opposed to that, the direct synthesis of tungstate sodalites in analogy to [3] yields crystalline powders of good quality (crystal sizes of ~20 μm) and purity. The corresponding Nd^{3+} excitation and emission spectra are reproduced in Fig. 5 (emission excited with a pulsed diode laser at a wavelength of 803 nm, detection with a CCD camera, excitation spectra with a 450-W Xe lamp, Acton 300 Monochromators with a focal length of 300 mm, 1200 g/mm (250–700 nm) and 600 g/mm (700–1200 nm) gratings, detection with the Acton Silicon detector SI-440-UV. Labsphere white standards and an optical grade $BaSO_4$ were used as references. Comparison with a commercial Nd^{3+} glass suggests that the novel material, already in this nonoptimized state (see also the remarks below), is an interesting candidate for optical applications in the NIR.

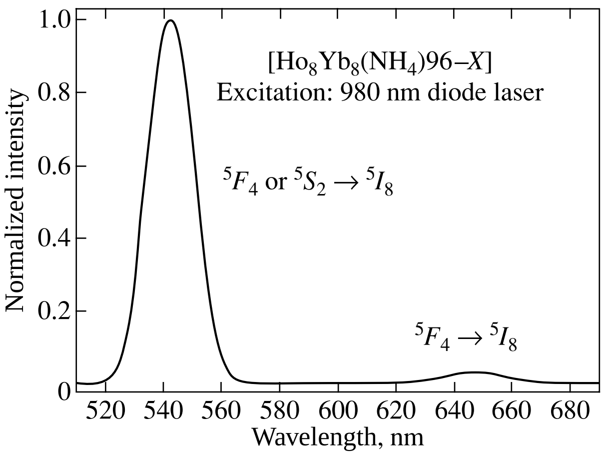

Fig. 3. Upconversion spectra of Yb^{3+}/Ho^{3+} fluorocomplexes obtained in zeolite *X*.

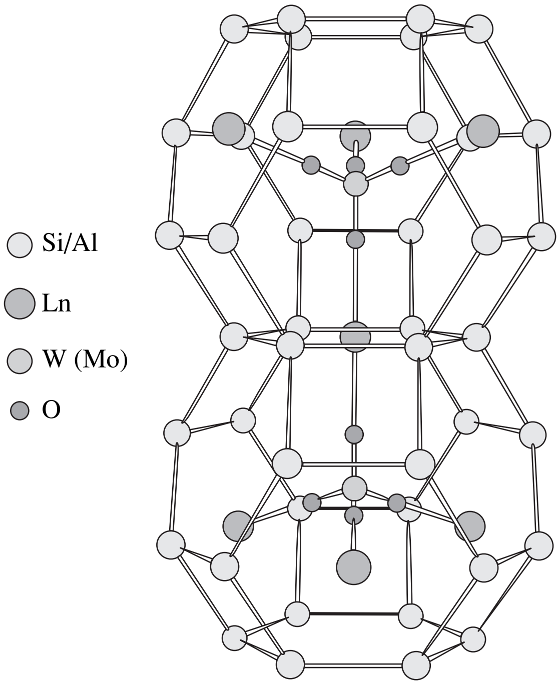

Fig. 4. Structure of sodalite with inclusion of rare-earth tungstates [$Ln_4(Al_8Si_4O_{24})(WO_4)_2$].

In attempts to optimize the efficiency of the sodalites, problems arose with the dilution/substitution of the active ions with La^{3+} or Y^{3+} within the sodalite; correspondingly, pure [$La_4(Al_8Si_4O_{24})(WO_4)_2$] or [$Y_4(Al_8Si_4O_{24})(WO_4)_2$] could not be obtained either; in the case of La^{3+}, the maximum content was restricted to 2.5 ions per unit cell, and Y^{3+} notoriously gave undefined byproducts. We therefore had to fall back on the use of Gd^{3+} as a dilutant, which gave phase pure materials, but at a high cost to crystallinity. Bearing this problem in mind, the concentration dependence of the Nd^{3+} emission intensity as a function of dilution with (Gd^{3+}/La^{3+}), as given in Fig. 6, suggests that dramatic improvements might be possible, if pure and well-crystallized [$La_{3.8}Nd_{0.2}(Al_8Si_{14}O_{24})(WO_4)_2$] were available.

Only recently, we discovered that readily accessible nitrite sodalites [9] can also serve as starting materials for the preparation of [$Ln_4(Al_8Si_4O_{24})(WO_4)_2$], in that at 800°C the thermally labile NO^{2-} can be replaced by WO_4^{2-}. We expect this to be a feasible route to optimize, e.g., the Nd^{3+} content in the sodalite system and thus develop an efficient NIR-emitting material, which we hope to use eventually in the manufacture of a NIR microlaser in analogy to the zeolite microlasers described in combination with organic dyes [10].

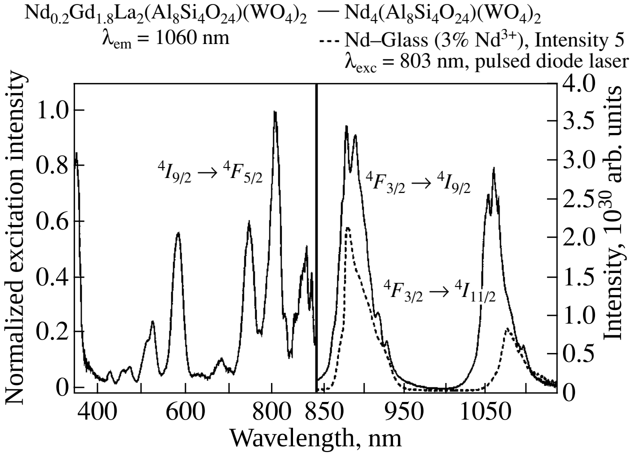

Fig. 5. Excitation (left) and emission (right) spectra of Nd^{3+} activated sodalites $[Ln_4(Al_8Si_4O_{24})(WO_4)_2]$; the dotted line is for comparison with commercial Nd glass (see text for details).

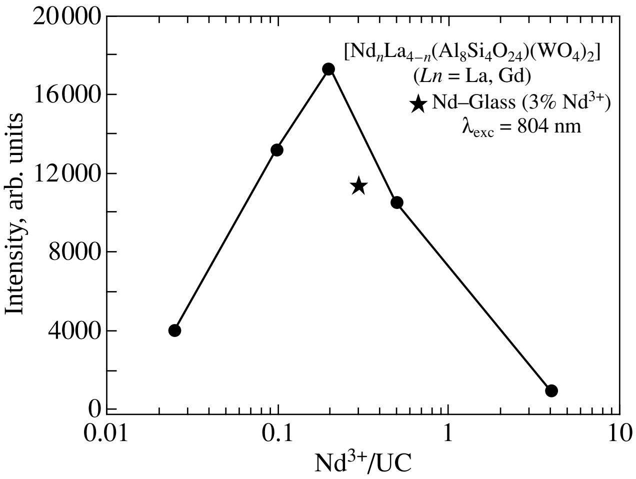

Fig. 6. Nd^{3+} ($^4F_{3/2} \longrightarrow {}^4I_{11/2}$) emission intensity as a function of Nd^{3+} content.

3. SUMMARY AND CONCLUSIONS

Fluoride complexes of rare earths have been synthesized in zeolite X for the first time. Yb^{3+}/Ho^{3+} and Yb^{3+}/Er^{3+} fluorides exhibit comparably efficient upconversion but are unfortunately too labile thermally. Instead, tungstate loaded faujasites, which can subsequently be converted into the sodalite system and also showed the upconversion effect, albeit at lower efficiency, proved to be efficient NIR emitters, despite phase impurities. Phase pure materials were subsequently synthesized directly from individual precursors using a high-temperature route. However, several morphological restrictions have to be overcome and stoichiometric parameters remain to be optimized in striding for the ultimate goal of a sodalite laser. In view of the efficient fluoride complexes in zeolite X, the scope of future experiments will include the synthesis of sodalite-encaged rare-earth fluorides as well.

ACKNOWLEDGMENTS

We owe special thanks to F. Laeri and L. Benmohammadi of the Technical University Darmstadt, Germany, for intense cooperation on the Nd sodalites.

We would like to express our gratitude to the German BMB+F (grant no. 03N8019F) for financial support of part of this research (M.L.).

REFERENCES

1. U. Kynast and V. Weiler, Adv. Mater. **6**, 937 (1994).
2. T. Jüstel, D. U. Wiechert, C. Lau, D. Sendor, and U. Kynast, Adv. Funct. Mater. **11**, 105 (2001).
3. C. Borgmann, J. Sauer, T. Jüstel, U. Kynast, and F. Schüth, Adv. Mater. **11**, 45 (1999).
4. G. Blasse and B. C. Grabmeier, *Luminescent Materials* (Springer, Berlin, 1994), p. 72.
5. M. Ryo, Y. Wada, T. Okubo, T. Nakazawa, Y. Hasegawa, and S. Yanagida, J. Mater. Chem. **12**, 1748 (2002).
6. C. Fouassier, in *Advanced Inorganic Fluorides*, Ed. by T. Nakajima, B. Zemva, and A. Tressaud (Elsevier, Amsterdam, 2000), p. 315.
7. M. Lezhnina and U. Kynast, J. Alloys Compd. **380**, 55 (2004).
8. C. Lau, H. -J. Mai, and U. Kynast, Microporous Mesopor. Mater. **47**, 339 (2001).
9. F. Hund, Z. Anorg. Allg. Chem. **511**, 225 (1984).
10. G. Ihlein, F. Schüth, O. Krauss, U. Vietze, and F. Laeri, Adv. Mater. **10**, 1117 (1998).

Physics of the Solid State, Vol. 47, No. 8, 2005, pp. 1489–1491. Translated from Fizika Tverdogo Tela, Vol. 47, No. 8, 2005, pp. 1432–1434.
Original Russian Text Copyright © 2005 by Rasuleva, Solomonov.

PROCEEDINGS OF THE XII FEOFILOV WORKSHOP “SPECTROSCOPY OF CRYSTALS ACTIVATED BY RARE-EARTH AND TRANSITION-METAL IONS”

(Yekaterinburg, Russia, September 22–25, 2004)

Identification of Luminescence Bands of Nd^{3+} Ions in Yttrium Aluminates $Y_3Al_5O_{12}$ and $YAlO_3$

A. V. Rasuleva and V. I. Solomonov

Institute of Electrophysics, Ural Division, Russian Academy of Sciences,
ul. Amundsena 106, Yekaterinburg, 620016 Russia
e-mail: plasma@iep.uran.ru

Abstract—The pulsed cathodoluminescence spectra of yttrium aluminum garnet and perovskite activated by neodymium are investigated at room temperature in the wavelength range 250–750 nm. The luminescence bands are identified, and all of them are assigned to Nd^{3+} transitions, including those from the doublet levels.

1. Single crystals of yttrium aluminum garnet (YAG) activated by Nd^{3+} ions exhibit a unique combination of luminescence, thermal, and mechanical properties and, consequently, have found wide application in modern science and engineering [1, 2]. Previous investigations into the luminescence properties of these materials [2–4] revealed only intense luminescence in the infrared range due to transitions between the Stark components of the $^{4}F_{3/2}$ and $^{4}I_{9/2–11/2}$ multiplets. In later works [5–7], luminescence was observed in the ultraviolet and visible ranges. Kolomiĭtsev *et al.* [5] assumed that, whatever the type of high-energy excitation, the luminescence is governed by radiative transitions only from the $^{2}F2_{5/2}$ and $^{2}P_{3/2}$ levels.

In this work, we studied the pulsed cathodoluminescence spectra of YAG : Nd^{3+} in the visible and ultraviolet ranges. Pulsed cathodoluminescence combines almost all positive qualities of electro-, x-ray, photo-, and cathodoluminescence [8]. The use of powerful pulsed electron beams makes it possible to excite any energy level in YAG : Nd^{3+}. Therefore, the pulsed cathodoluminescence spectra can exhibit lines corresponding to transitions not only from the $^{4}F_{3/2}$, $^{2}F2_{5/2}$, and $^{2}P_{3/2}$ levels but also from other levels.

2. The luminescence properties of YAG : Nd^{3+} samples were examined on a KLAVI pulsed cathodoluminescent spectrograph [8]. The excitation of luminescence was carried out at room temperature in air with an electron beam (pulse width, 2 ns; maximum electron energy, 150 ± 10 keV). The spectrum was recorded in the form of a dependence of the intensity on the wavelength in the range 250–750 nm. The measured intensity can be represented in the form $I(\lambda) = (\sum_{i=1}^{N}\int_{0}^{T_e} I(\lambda, t)dt)/N$, where N is the number of pulses and T_e is the exposure time (10 ms). The spectral resolution of the instrument was 2 nm. The absolute systematic deviation from the linearity of the scale (the difference between the tabulated wavelengths and the values measured on this scale) was equal to ±0.75 nm.

The measurements were performed with a YAG : Nd^{3+} single crystal grown at Polyus TsNII (Moscow, Russia), YAG : Nd^{3+} nanopowders were prepared using the sol–gel method at the Institute for Low Temperatures and Structural Research (Wroclaw, Poland), and a YAG : Nd^{3+} micropowder was prepared at GIRedMet NII (Moscow, Russia).

3. Figure 1 presents the pulsed cathodoluminescence spectrum of the YAG : Nd^{3+} single crystal in the wavelength range 250–650 nm. Analysis demonstrates that the spectrum contains only bands associated with the Nd^{3+} intracenter luminescence. The multiplets of Nd^{3+} ions in the yttrium aluminum garnet have a well-developed Stark structure. Consequently, the spectrum also has a complex structure with a large number of narrow bands attributed to Nd^{3+} ions. Identical bands at wavelengths coinciding to within the limits of experimental error are also observed in the spectra of YAG : Nd^{3+} nanopowders annealed at temperatures of 900, 1050, and 1200°C.

The kinetic investigations revealed that the spectra contain bands corresponding both to intercombination (forbidden) transitions between the energy levels with different multiplicities and to allowed transitions. The characteristic lifetime of the intercombination transitions is of the order of 1 ms, and the bands assigned to these transitions exhibit two maxima in the luminescence intensity [8]. The system of bands observed in the wavelength range 250–350 nm corresponds to the transitions from the $^{2}F2_{5/2}$ level to the $I_{9/2–15/2}$ levels, which is in good agreement with the data obtained by Kolomiĭtsev *et al.* [5]. The results of the identification are

1063-7834/05/4708-1489$26.00 © 2005 Pleiades Publishing, Inc.

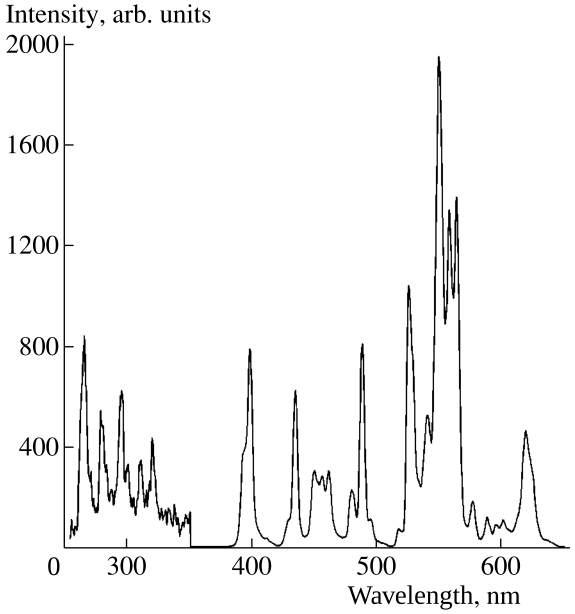

Fig. 1. Pulsed cathodoluminescence spectrum of the YAG : Nd^{3+} single crystal.

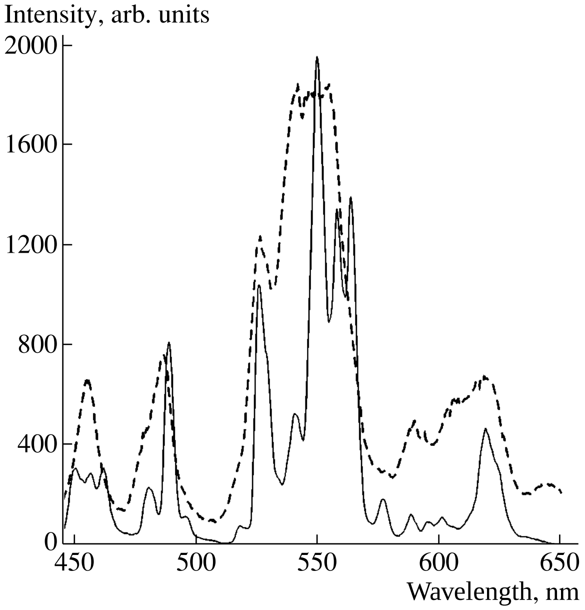

Fig. 2. Pulsed cathodoluminescence spectra of the single crystal (solid line) and the micropowder (dashed line).

given in Table 1. Only one band at a wavelength of 450.2 nm was not identified.

The pulsed cathodoluminescence spectra of the micropowder exhibit new bands that are different from the bands attributed to Nd^{3+} ions in the spectra of the yttrium aluminum garnet. The specific features of the former spectra can be seen in Fig. 2.

With the aim of elucidating the nature of the new luminescence bands, we carried out x-ray diffraction analysis. It was found that the micropowder contains the following three phases: the monoclinic phase ($Y_4Al_2O_9$), perovskite ($YAlO_3$), and garnet ($Y_3Al_5O_{12}$). It was assumed that the aforementioned new bands are associated with the presence of Nd^{3+} ions in the $YAlO_3$ perovskite, because, in our case, the perovskite is the main phase. The multiplets of Nd^{3+} ions in the yttrium aluminum garnet and in the perovskite are virtually identical to each other. Although the energy spectra of the identical multiplets differ only slightly, this difference leads to substantial changes in the pulsed cathodoluminescence spectrum of the perovskite compound (Fig. 2). Table 2 presents the most probable identification of the luminescence bands of Nd^{3+} ions in the perovskite. This identification was carried out taking into

Table 1. Identification of the pulsed cathodoluminescence bands of Nd^{3+} ions in YAG

Wavelength, nm	Transition	Wavelength, nm	Transition
265.6	$^2F2_{5/2}(37850) \longrightarrow {}^4I_{9/2}(199)$	495.3	$^4G_{11/2}(21029) \longrightarrow {}^4I_{9/2}(857)$
278.5	$^2F2_{5/2}(37850) \longrightarrow {}^4I_{11/2}(2002)$	517.8	$^2K_{13/2} + {}^2G_{9/2}(19620) \longrightarrow {}^4I_{9/2}(308)$
295.2	$^2F2_{5/2}(37850) \longrightarrow {}^4I_{13/2}(3930)$	525.7	$^2K_{13/2} + {}^2G_{9/2}(19154) \longrightarrow {}^4I_{9/1}(130)$
300.6	$^2F2_{5/2}(37850) \longrightarrow {}^4I_{13/2}(4507)$	540.4	$^4G_{7/2}(18822) \longrightarrow {}^4I_{9/2}(308)$
310.8	$^2F2_{5/2}(37850) \longrightarrow {}^4I_{15/2}(5757)$	549.8	$^4G_{9/2}(20730) \longrightarrow {}^4I_{11/2}(2521)$
319.4	$^2F2_{5/2}(37850) \longrightarrow {}^4I_{15/2}(6570)$	558.0	$^2D_{5/2}(23674) \longrightarrow {}^4I_{15/2}(5757)$
398.2	$^2P_{3/2}(25994) \longrightarrow {}^4I_{9/2}(857)$	563.8	$^2D_{5/2}(23674) \longrightarrow {}^4I_{15/2}(5933)$
434.5	$^2P_{1/2}(23155) \longrightarrow {}^4I_{9/2}(130)$	577.2	$^2P_{1/2}(23155) \longrightarrow {}^4I_{15/2}(5812)$
456.3	$^4D_{3/2}(27670) \longrightarrow {}^4I_{15/2}(5757)$	588.5	$^4G_{5/2}(16992) \longrightarrow {}^4I_{9/2}(0)$
461.5	$^4D_{3/2}(27670) \longrightarrow {}^4I_{15/2}(5963)$	595.2	$^4G_{5/2}(16992) \longrightarrow {}^4I_{9/2}(199)$
480.1	$^4G_{11/2}(21029) \longrightarrow {}^4I_{9/2}(199)$	601.3	$^4G_{5/2}(16849) \longrightarrow {}^4I_{9/2}(199)$
488.6	$^4G_{9/2}(20773) \longrightarrow {}^4I_{9/2}(308)$	618.9	$^4G_{5/2}(16992) \longrightarrow {}^4I_{9/2}(857)$

Table 2. Identification of the pulsed cathodoluminescence bands of Nd^{3+} ions in perovskite

Wave-length, nm	Transition
455.7	$^2P_{3/2}(25981) \longrightarrow {}^4I_{13/2}(4021)$
478.0	$^4G_{11/2} + {}^2K_{15/2} + {}^2D_{3/2}(21580) \longrightarrow {}^4I_{9/2}(671)$
486.4	$^4G_{11/2} + {}^2K_{15/2} + {}^2D_{3/2}(21231) \longrightarrow {}^4I_{9/2}(671)$
541.9	$^4G_{7/2}(18975) \longrightarrow {}^4I_{9/2}(500)$
545.0	$^4G_{7/2}(18846) \longrightarrow {}^4I_{9/2}(500)$
546.9	$^4G_{7/2}(18975) \longrightarrow {}^4I_{9/2}(671)$
554.7	$^2D_{5/2}(23759) \longrightarrow {}^4I_{15/2}(5757)$
603.3	$^4G_{9/2}(20865) \longrightarrow {}^4I_{13/2}(4291)$
606.1	$^4G_{9/2}(20955) \longrightarrow {}^4I_{13/2}(4446)$
608.0	$^4G_{9/2}(20894) \longrightarrow {}^4I_{13/2}(4446)$
644.3	$^4G_{11/2} + {}^2K_{15/2} + {}^2D_{3/2}(21276) \longrightarrow {}^4I_{15/2}(5757)$

account that the new bands in the spectrum of the perovskite are associated with the same multiplets as in the yttrium aluminum garnet.

Thus, detailed investigation of the pulsed cathodoluminescence spectrum of neodymium ions has demonstrated that these ions exhibit intense luminescence in the ultraviolet and visible ranges. The luminescence spectrum has the form of narrow lines, which can be used to reveal neodymium impurities and to control their content not only in compounds of the garnet type but also in perovskite.

REFERENCES

1. B. I. Minkov, *Influence of Ionizing Radiation on Optical and Laser Properties of Single Crystals* (Nauch. Issl. Inst. Tekh. Éksp. Khim. Mashinostr., Moscow, 1985) [in Russian].
2. A. A. Kaminskii, *Laser Crystals: Their Physics and Properties* (Nauka, Moscow, 1975; Springer, Berlin, 1981).
3. P. P. Feofilov, V. A. Timofeeva, M. N. Tolstoĭ, and L. M. Belyaev, Opt. Spektrosk. **19** (5), 817 (1965).
4. D. T. Sviridov, R. K. Sviridova, and Yu. F. Smirnov, *Optical Spectra of Transition Metal Ions in Crystals* (Nauka, Moscow, 1976) [in Russian].
5. A. I. Kolomiĭtsev, M. L. Meĭl’man, I. S. Volodina, M. V. Chukichev, A. G. Smagin, and Kh. S. Bagdasarov, *Luminescence of Yttrium Aluminum Garnet Crystals Activated by Neodymium in the Ultraviolet and Visible Ranges under High-Energy Excitation* (Vsesoyuzn. Zaochn. Inzhen.-Striot. Inst., Moscow, 1982) [in Russian].
6. Kh. S. Bagdasarov, I. S. Volodina, A. I. Kolomiĭtsev, M. L. Meĭl’man, and A. G. Smagin, Kvantovaya Élektron. (Moscow) **9** (6), 1158 (1982).
7. A. I. Kolomiĭtsev, M. L. Meĭl’man, I. S. Volodina, M. V. Chukichev, A. G. Smagin, and Kh. S. Bagdasarov, Opt. Spektrosk. **56** (2), 365 (1984) [Opt. Spectrosc. **56** (2), 222 (1984)].
8. V. I. Solomonov and S. G. Mikhaĭlov, *Pulsed Cathodoluminescence and Its Application to Analysis of Condensed Materials* (Ural Otd., Ross. Akad. Nauk, Yekaterinburg, 2003) [in Russian].

Translated by O. Moskalev

Physics of the Solid State, Vol. 47, No. 8, 2005, pp. 1492–1496. Translated from Fizika Tverdogo Tela, Vol. 47, No. 8, 2005, pp. 1435–1439.
Original Russian Text Copyright © 2005 by Ivanov, Pustovarov, Kirm, Shlygin, Shirinskiĭ.

PROCEEDINGS OF THE XII FEOFILOV WORKSHOP "SPECTROSCOPY OF CRYSTALS ACTIVATED BY RARE-EARTH AND TRANSITION-METAL IONS"

(Yekaterinburg, Russia, September 22–25, 2004)

Energy Transfer in Gd_2SiO_5–Ce, Y_2SiO_5–Ce, and $Be_2La_2O_5$–Ce Crystals during Selective VUV and Core Excitation

V. Yu. Ivanov*, V. A. Pustovarov*, M. Kirm, E. S. Shlygin*, and K. I. Shirinskiĭ***

** Ural State Technical University, ul. Mira 19, Yekaterinburg, 620002 Russia*
e-mail: ivy@dpt.ustu.ru
*** Institute of Physics, University of Tartu, Tartu, 51014 Estonia*

Abstract—Luminescence vacuum ultraviolet time-resolved spectroscopy is used to study electronic excitations and energy transfer in Ce^{3+}-doped crystals of gadolinium and yttrium oxyorthosilicates excited by synchrotron radiation in the vacuum ultraviolet (4–30 eV) and x-ray (50–200 eV) regions. At $T = 10$ K, both crystals exhibit intrinsic electronic excitations whose radiative relaxation occurs through fast ($\tau = 3$ ns) and slow (microsecond) channels, which correspond to two possible types of self-trapped excitons. A comparison of the relaxation of above-edge and core electronic excitations in the Ce^{3+}-doped crystals of gadolinium oxyorthosilicate and lanthanum beryllate indicates that the nature of the charge carriers involved in the recombination processes of energy transfer to luminescence centers is diverse. © *2005 Pleiades Publishing, Inc.*

1. INTRODUCTION

Energy transfer to luminescence centers by secondary charge carriers is one of the factors that control the efficiency of a scintillator. In [1], the relaxation channels of above-edge secondary electronic excitations were comprehensively analyzed in Gd_2SiO_5–Ce (E_g = 6.2 eV) excited by 30-eV photons at room temperature.

The aim of this work is to compare the relaxation channels of above-edge (E_{exc} = 6–35 eV) and core (E_{exc} = 50–200 and 500–630 eV) electronic excitations in Y_2SiO_5–Ce, Gd_2SiO_5–Ce, and $Be_2La_2O_5$–Ce scintillation crystals at temperatures of 6–10 and 300 K.

2. EXPERIMENTAL

We studied Czochralski-grown Y_2SiO_5–Ce (0.1 mol %) and Gd_2SiO_5–Ce (0.5 mol %) crystals prepared by A. Korovkin at the Vavilov State Optical Institute [2] and $Be_2La_2O_5$–Ce crystals grown by V. Matrosov. The samples to be studied were of optical grade, 10 mm in diameter, and 1-mm thick.

Luminescence excitation spectra (LESs), luminescence spectra (LSs) in the range 2.5–11 eV, and the LS decay kinetics during selective excitation were measured using time-resolved spectroscopy in the VUV region (4–35 eV) at the SUPERLUMI station [3] and in the ultrasoft x-ray region (50–200 and 500–630 eV) in the BW3 channel [4] (HASYLAB, DESY, Hamburg) at temperatures of 6–10 and 295 K. The LSs and LESs were recorded for both time-integrated luminescence and luminescence detected in gated time windows of width Δt delayed by δt with respect to an exciting synchrotron-radiation pulse. The time window parameters for the VUV region were δt_1 = 2.1 ns, Δt_1 = 14.1 ns and δt_2 = 46 ns, and Δt_2 = 155 ns. For excitation in the ranges 50–200 and 500–630 eV, measurements were performed in three time windows with δt = 0.2, 19.5, and 43 ns and Δt = 6.4, 20.5, and 107 ns, respectively.

3. EXPERIMENTAL RESULTS

3.1. Y_2SiO_5–Ce Crystals

At T = 300 K, the LS of the Y_2SiO_5–Ce crystals in all time windows is represented by a structured band irrespective of the energy of exciting photons (Fig. 1a). This band can be resolved into two Gaussians, namely, a dominating component ($E_{max\,1}$ = 2.96 eV) and a weaker component ($E_{max\,2}$ = 3.17 eV). The two-component structure of this LS, formed by the radiative relaxation of the excited state of the Ce^{3+} ion, is due to the splitting of the ^2F ground state of the Ce^{3+} ion [5].

At room temperature, the LES of the Ce^{3+} ions in the VUV region contains narrow excitation bands with maxima at 4.15 and 4.71 eV, a broader 6.82-eV band, and a shoulder near 5.5 eV (Fig. 1b). Moreover, the efficiency of luminescence excitation increases in two ranges, at energies above 15 and 21 eV. The excitation range near 7 eV is much less pronounced as compared to the low-energy bands when recording in the "fast" time window. When exciting the Ce^{3+} ion luminescence in the ultrasoft x-ray region (50–200 eV), we failed to reliably detect the spectral structure corresponding to energy absorption due to transitions from the core levels of the host or impurity ions.

1063-7834/05/4708-1492$26.00 © 2005 Pleiades Publishing, Inc.

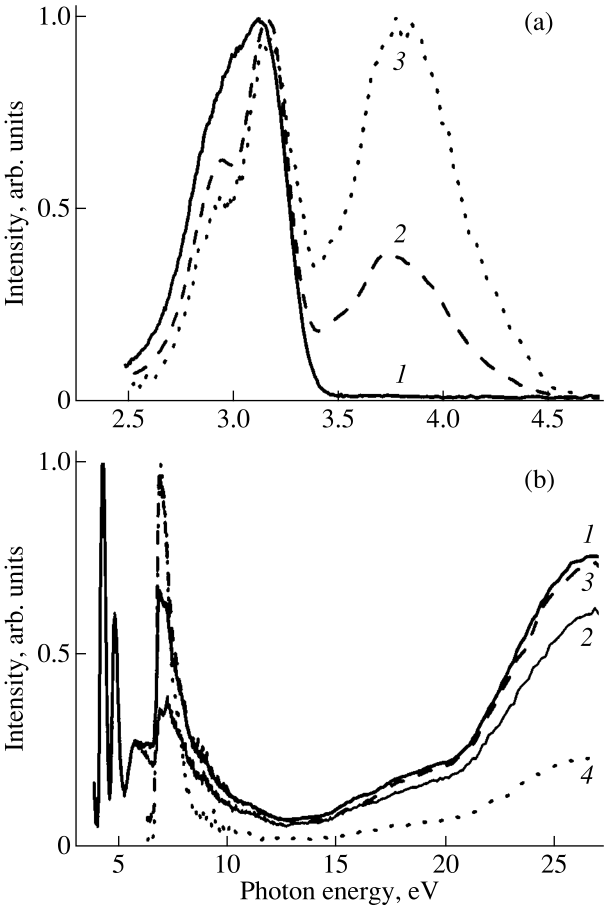

Fig. 1. (a) Luminescence spectra of Y_2SiO_5–Ce crystals excited by photons with an energy of (*1*) 6.9 and (*2, 3*) 24.7 eV at a temperature of (*1, 2*) 5.7 and (*3*) 300 K. Spectrum *1* was measured in the fast time window. (b) Luminescence excitation spectra of Y_2SiO_5–Ce crystals recorded at (*1, 3*) 3.1 and (*2, 4*) 3.75 eV at a temperature T = 5.7 K. Spectra *1* and *2* were measured in the slow window, and spectra *3* and *4*, in the fast window.

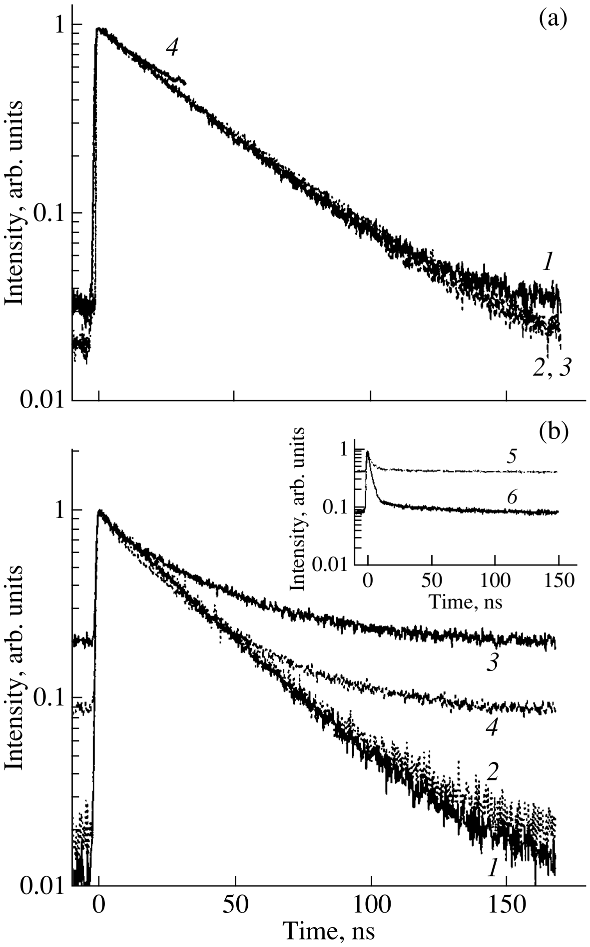

Fig. 2. (a) Decay kinetics of 3.1-eV luminescence of Y_2SiO_5–Ce crystals excited by photons with an energy of (*1*) 4.2, (*2*) 6.9, (*3*) 24.7, and (*4*) 60–200 eV at 300 K. (b) Decay kinetics of 3.1-eV luminescence of Y_2SiO_5–Ce crystals excited by photons with an energy of (*1*) 4.8, (*2*) 5.6, (*3*) 6.9, and (*4*) 24.7 eV at 5.7 K. The inset shows the decay kinetics of luminescence with E_{emis} = 3.75 eV for excitation by photons with an energy of (*5*) 6.9 and (*6*) 24.7 eV.

The luminescence decay kinetics measured for $E_{\max}$ = 3.1 eV at a varied excitation energy E_{exc} can be fitted by two exponential components (Fig. 2a). The decay time of the fast component is τ_1 = 34 ns (at E_{exc} = 4.2 eV), 36 ns (E_{exc} = 6.8 eV), 38 ns (E_{exc} = 24.7 eV), and 34 ns (E_{exc} = 60–200 eV). The slow component has a decay time of longer than 500 ns, and its contribution is insignificant but increases at E_{exc} = 4.2 eV and especially at E_{exc} = 60–200 eV.

At low temperatures, an additional elementary band in the range 3.5–4.5 eV appears in the LSs of the Y_2SiO_5–Ce crystals; this band is more pronounced at E_{exc} = 6.82 eV (Fig. 1a). By resolving the spectrum into Gaussians, we estimated the spectral positions and characteristics of these bands: $E_{\max 3}$ = 3.5 eV and $E_{\max 4}$ = 3.8 eV (FWHM = 0.5 eV for both bands). The 3.5-eV band is more pronounced at E_{exc} > 20 eV, and the 3.8-eV band is more pronounced near the fundamental absorption edge.

The general character of the impurity-luminescence excitation spectrum remains unchanged with decreasing temperature, whereas additional luminescence bands are not excited at energies below 6.5 eV (Fig. 1b). The decay kinetics of the impurity luminescence of the Ce^{3+} ion consists of two components (Fig. 2b). For the fast component, τ = 29 ns (E_{exc} = 4.8 eV), 33 ns (E_{exc} = 6.9 eV), and 35 ns (E_{exc} = 24.7 eV); at excitation energies above 6.9 eV, this component is observed against the background of a microsecond component. The decay kinetics of the additional luminescence bands measured for E_{emis} = 3.7 eV consists of two components (inset to Fig. 2b). The fast component can be fitted by an exponential function (with τ = 3 ns), and the relaxation time of the second

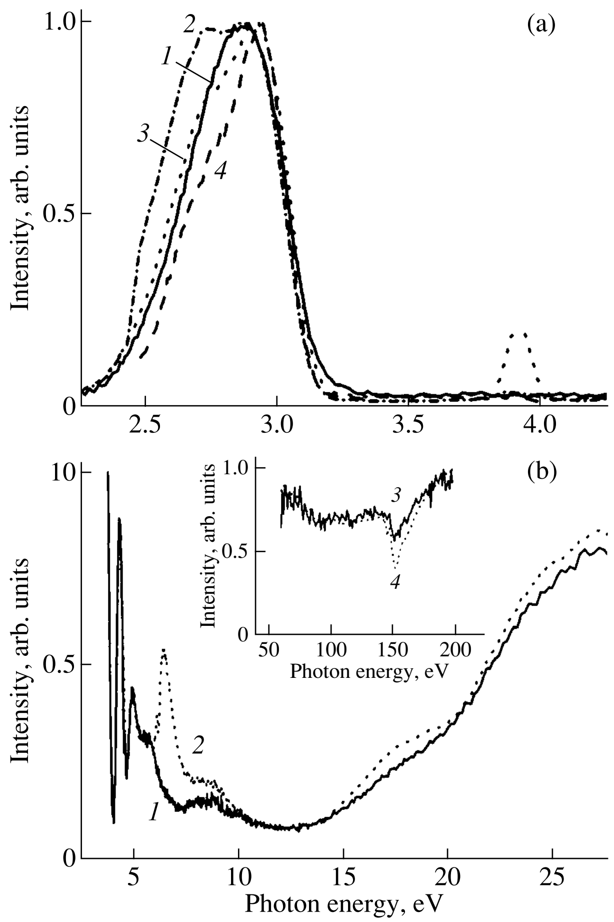

Fig. 3. (a) Luminescence spectra of Gd_2SiO_5–Ce crystals excited by photons with an energy of (*1*, *2*) 6.6, (*3*) 24.7, and (*4*) 140 eV at a temperature of (*2*–*4*) 5.7 and (*1*) 300 K. (b) Luminescence excitation spectra of Gd_2SiO_5–Ce crystals recorded at 2.9 eV at a temperature $T = 5.7$ K. Spectra *1* and *3* were measured in the fast window, and spectra *2* and *4*, in the slow window.

component falls in the microsecond region. Apparently, the overlap of the impurity luminescence bands with the new low-temperature luminescence leads to the appearance of a background (pedestal) in the luminescence kinetics of the Ce^{3+} ion during excitation at $E_{exc} >$ 6.8 eV. Since fast components were not observed in the kinetics of the 3.1-eV luminescence in this case, we can assume that the long (microsecond) decay time characterizes the low-temperature luminescence component with $E_{max\,3} = 3.5$ eV that overlaps with the Ce^{3+} luminescence, whereas the second component of this luminescence with $E_{max\,4} = 3.8$ eV has a decay time of 3 ns.

3.2. Gd_2SiO_5–Ce Crystals

At $T = 300$ K and exciting photon energies $E_{exc\,1} =$ 6.5 eV and $E_{exc\,2} = 24.7$ eV, the photoluminescence spectrum of the Gd_2SiO_5–Ce crystals has a structured band (consisting of two Gaussians with $E_{max\,1} = 2.78$ eV and $E_{max\,2} = 2.93$ eV; Fig. 3a). As the exciting photon energy increases to $E_{exc3} = 140$ eV, both bands are present in the spectrum but the high-energy luminescence is dominant.

Like for the Y_2SiO_5–Ce crystals, the time-integrated 2.81-eV LES contains strong bands at 4.5, 5.1, and 6.5 eV and the luminescence yield increases at $E_{exc} >$ 15 and 21 eV (Fig. 3b). The time-resolved LESs clearly differ: the 6.5-eV band is absent in the fast time window. Unlike the Y_2SiO_5–Ce crystals, the excitation in the range of core transitions results in a deep dip in the range 140–160 eV, which is the range of the L_1 absorption edge of Si (149.7 eV) and the N_5 absorption edge of Gd (142.6 eV) (Fig. 3b).

The most substantial difference in properties between the yttrium and gadolinium silicates manifests itself in the Ce^{3+} luminescence kinetics. When excitation is performed in the region of the low-energy 4.5- and 5.1-eV bands, the decay kinetics is given by one exponential curve ($\tau = 22$ ns). An increase in the photon energy to 6.5 eV leads to the appearance of a rise about 15 ns in length, and the exponential decay time increases to 32 ns (Fig. 4a). At this excitation, the 6.5-eV band is not observed in the impurity LES in the fast time window. At $E_{exc} = 24.7$ eV, the rise stage disappears and the exponential decay time decreases to 25 ns. The most important fact is that the rise stage of impurity luminescence manifests itself during selective excitation in the region of core transitions (Fig. 4a). At energies of 140, 145, and 160 eV, the rise phase lasts ~10 ns and the exponential decay time is ~40 ns. However, upon excitation in the region of the maximum dip in the LES at $E_{exc} = 152$ eV, the rise stage virtually disappears and the exponential decay time decreases to 30 ns.

As the Gd_2SiO_5–Ce crystals are cooled to 5.7 K, the character of the Ce^{3+} LES remains almost unchanged. The LS shape depends substantially on the photon energy (Fig. 3a), which suggests the appearance of new luminescence bands similar to the bands in the low-temperature luminescence spectra of the Y_2SiO_5–Ce crystals. This assumption is supported by the fact that new decay components, namely, fast (4-ns) and slow (microsecond) components, appear in the low-temperature decay curves of the Ce^{3+} luminescence during excitation at above 6.0 eV (Fig. 4b), with the slow component appearing as an increase in the background. By analyzing the time-resolved spectra and the decay kinetics, we established the spectral positions of the low-temperature luminescence bands for Gd_2SiO_5–Ce. They were found to be 2.5 eV for the fast luminescence with a decay time of about 4 ns and 3.05 eV for the microsecond luminescence. Unlike the Y_2SiO_5–Ce crystals, the spectral region of the low-temperature luminescence overlaps substantially with the impurity-luminescence spectrum.

Upon core excitation (at $T = 5.7$ K), the basic difference in the impurity-luminescence kinetics consists in the fact that, at $E_{\mathrm{exc}} = 6.6$ eV, the rise stage increases to 25 ns (Fig. 4b). At $E_{\mathrm{exc}} = 7.5$ eV, the decay kinetics contains a fast 4-ns component. In addition, the luminescence kinetics exhibits a pronounced background (a microsecond component) for any excitation at an energy above 6.6 eV. In contrast to the room-temperature measurements, no rise in luminescence is detected under core excitation and the luminescence decay kinetics has shorter times as compared to the case of $E_{\mathrm{exc}} = 4.4$ eV.

4. DISCUSSION OF THE RESULTS

The band-gap widths of the crystals under study were estimated to be 6.2 eV for Gd_2SiO_5–Ce [6] and 6.4 eV for Y_2SiO_5–Ce. Thus, the photon energy spectrum used allowed us to perform selective excitation in various ranges: (i) in the range of crystal transparency, (ii) at the fundamental absorption edge (FAE), (iii) in the range of creation of separate electron–hole pairs, and (iv) at the core absorption edges of host ions. A combined analysis of the LSs, LESs, and decay kinetics suggests that, at $T = 5.7$ K, the Gd_2SiO_5–Ce and Y_2SiO_5–Ce crystals exhibit two types of intrinsic matrix luminescence. This intrinsic luminescence is excited only above the FAE, and its decay kinetics differs from that of the Ce^{3+} ion. One of these two types of luminescence is characterized by a short exponential decay time (several nanoseconds), and the other has a decay time in the microsecond range. The presence of two types of low-temperature luminescence is typical of complex oxide compounds with low symmetry of the oxygen ions, and they are interpreted as the result of the radiative decomposition of two types of self-trapped excitons (see, e.g., [7]). One type of self-trapped excitons forms via the recombination assembling of charge carriers, and the other type forms via the relaxation of large-radius excitons. The hole components of excitons are genetically different for many oxides [7], which is caused by nonuniformity of the valence band of complex oxides in different directions in the Brillouin zone. In the reflectance spectra of the crystals under study, we did not detect a pronounced exciton structure near the FAE, which can be explained by the substantial exciton–phonon interaction that controls exciton self-trapping. The occurrence of exciton self-trapping can affect the processes of energy transfer to luminescence centers. For example, the Ce^{3+} luminescence excitation spectra measured in the fast time window do not contain the 6.5-eV excitonic excitation band near the FAE. Furthermore, a significant rise stage of impurity luminescence ($\tau_{\mathrm{rise}} = 15$ ns) is observed at $T = 300$ K. We may assume that free excitons transfer energy to luminescence centers very ineffectively; they are likely to decompose with the intermediate capture of the charge carriers by traps, which delays energy transfer. At low temperatures, exciton self-trapping further delays the luminescence rise during excitation in the exciton-absorption band. On the contrary, exciton self-trapping of another type that occurs at a low temperature and favors the recombination assembling of charge carriers can improve energy transfer to luminescence centers via the exciton mechanism proposed, e.g., in [1].

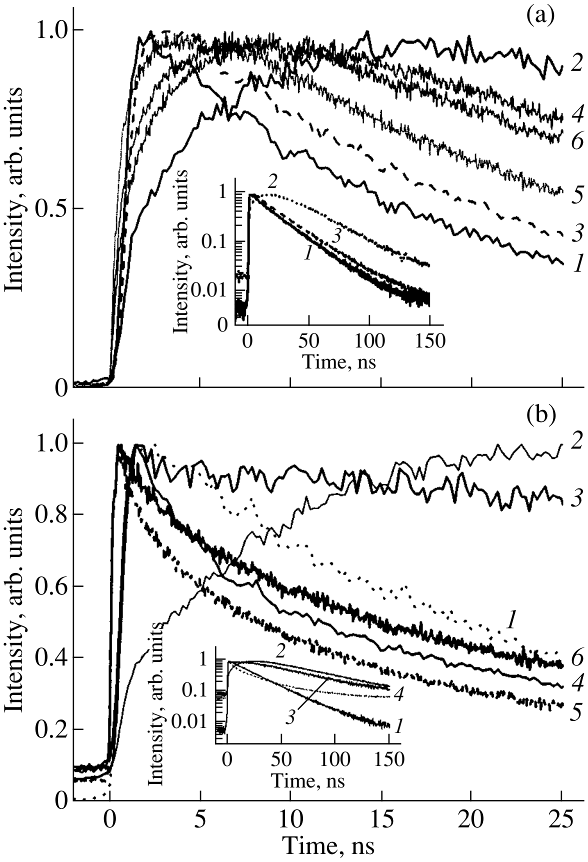

Fig. 4. (a) Decay kinetics of 2.8-eV luminescence of Gd_2SiO_5–Ce crystals excited by photons with an energy of (*1*) 4.4, (*2*) 6.5, (*3*) 24.7, (*4*) 140, (*5*) 152, and (*6*) 160 eV at 300 K. (b) Decay kinetics of 2.9-eV luminescence of Gd_2SiO_5–Ce crystals excited by photons with an energy of (*1*) 4.4, (*2*) 6.6, (*3*) 7.5, (*4*) 24.7, (*5*) 152, and (*6*) 140 or 170 eV at 5.7 K.

We revealed a new pronounced effect of a decrease in the duration of the rise stage and the acceleration of impurity-luminescence decay. This effect was observed during the selective core excitation of the Gd_2SiO_5–Ce crystals in the range 140–160 eV and manifests itself at 5.7 and 300 K. The excitation range mentioned above includes the L_1 absorption edge of Si (149.7 eV) and the N_5 absorption edge of Gd (142.6 eV). However, since this effect was not detected in the Y_2SiO_5–Ce crystals, we have to conclude that it is related to the core absorption of gadolinium. We may assume that the decrease in the duration of the stages of rise and decay of the Ce^{3+} luminescence is caused by an increase in the absorption coefficient upon excitation near the core level and, hence, by an increase in the carrier density in the surface layer of the crystal. However, these effects have not been detected for intrinsic luminescence in oxide crystals but were observed earlier for impurity luminescence in a $Be_2La_2O_5$–Ce crystal [8]. Therefore, the cause can consist in not only the effects of an increase in the secondary-carrier density but also in their different genetic origins. Since the Ce^{3+} luminescence during photoexcitation with $E_{exc} \gg E_g$ is due to recombination, we may assume that the effects observed are caused by the difference in nature between the valence-band holes that form during ordinary interband transitions and the holes that form as a result of Auger processes occurring during the selective excitation of the crystals in the region of core levels. This difference can be related to significant nonuniformity and, as a consequence, different effective hole masses in the valence bands of the oxide crystals.

ACKNOWLEDGMENTS

This work was supported by the Russian Foundation for Basic Research (project no. 02-02-16322), the Ministry of Education and Science of the Russian Federation (project no. E02-3.4-362), and CRDF (Science and Education Center of Promising Materials, grant REC-005 (EK-005-XI)).

REFERENCES

1. S. Shimizu, H. Ishibashi, A. Ejiri, and S. Kubota, Nucl. Instrum. Methods Phys. Res. A **486**, 490 (2002).
2. G. V. Anan’eva, A. I. Korovkin, O. I. Merkulaeva, *et al.*, Izv. Akad. Nauk SSSR, Neorg. Mater. **17**, 442 (1981).
3. S. G. Zimmerer, Nucl. Instrum. Methods Phys. Res. A **308**, 178 (1991).
4. C. U. S. Larsson, A. Beutler, O. Björneholm, F. Federmann, U. Hahn, A. Rieck, S. Verbin, and T. Möller, Nucl. Instrum. Methods Phys. Res. A **337**, 603 (1994).
5. C. L. Melcher, J. C. Schweitzer, C. A. Peterson, R. A. Mamente, and H. Suzuki, in *Proceedings of the International Conference on Inorganic Scintillators and Their Applications, Delft, Netherlands, 1996* (Delft Univ. Press, Delft, Netherlands, 1996), pp. 309–316.
6. Z. A. Racholo, I. A. Tale, V. D. Ryzhikov, J. L. Jansons, and S. F. Burochas, Nucl. Tracks. Radiat. Meas. **21**, 121 (1993).
7. A. I. Kuznetsov, V. N. Abramov, V. V. Myurk, and B. R. Namozov, Fiz. Tverd. Tela (Leningrad) **33** (7), 2000 (1991) [Sov. Phys. Solid State **33** (7), 1126 (1991)].
8. V. A. Pustovarov, M. Kirm, V. Yu. Ivanov, D. B. Puduzov, and A. V. Kruzhalov, Radiat. Meas. **38**, 575 (2004).

Translated by K. Shakhlevich

Physics of the Solid State, Vol. 47, No. 8, 2005, pp. 1497–1503. Translated from Fizika Tverdogo Tela, Vol. 47, No. 8, 2005, pp. 1440–1446.
Original Russian Text Copyright © 2005 by Popova, Romanov, Klimin, Chukalina, Mill, Dhalenne.

PROCEEDINGS OF THE XII FEOFILOV WORKSHOP “SPECTROSCOPY OF CRYSTALS ACTIVATED BY RARE-EARTH AND TRANSITION-METAL IONS”

(Yekaterinburg, Russia, September 22–25, 2004)

Stark Structure and Exchange Splittings of Nd^{3+} Ion Levels in Chain Nickelate Nd_2BaNiO_5

**M. N. Popova*, E. A. Romanov*, S. A. Klimin*, E. P. Chukalina*,
B. V. Mill**, and G. Dhalenne*****

**Institute of Spectroscopy, Russian Academy of Sciences, Troitsk, Moscow oblast, 142190 Russia*
e-mail: popova@isan.troitsk.ru
***Moscow State University, Vorob’evy gory, Moscow, 119899 Russia*
****Laboratoire de Physico-Chimie de l’État Solide, Université Paris-Sud, Orsay, F-91405 France*

Abstract—Diffuse transmittance spectra of polycrystalline samples of chain nickelate Nd_2BaNiO_5 were measured with high resolution (0.1 cm^{-1}) over wide ranges of wavenumbers (1500–20000 cm^{-1}) and temperatures (4.2–300 K). The energies of 54 Stark sublevels of the Nd^{3+} ion and exchange splittings of some of them were determined in the magnetically ordered state of Nd_2BaNiO_5 ($T_N = 47.5 \pm 1$ K). It was shown that the low-temperature magnetic properties of Nd_2BaNiO_5 are determined by exchange splitting (32 cm^{-1}) of the ground state.

1. INTRODUCTION

Due to their structural properties, chain nickelates R_2BaNiO_5 [R is a rare-earth (RE) ion or Y] are interesting model objects for studying one-dimensional magnetism in the system of antiferromagnetic (AFM) chains of atoms with an integer spin ($S = 1$ for Ni^{2+}) and the crossover to three-dimensional magnetic order. As is known, one-dimensional isotropic (Heisenberg) magnets are not ordered even at $T = 0$, because the order is destroyed by fluctuations. In 1983, Haldane showed theoretically that the properties of Heisenberg AFM atomic chains depend strongly on whether the atomic spins are integer or half-integer [1]. In the former case, the ground state is a nonmagnetic singlet and there is a gap in the magnetic excitation spectrum (the Haldane gap). The conclusions reached by Haldane have been confirmed by numerical simulations and experiments with $Ni(C_2H_8N_2)_2NO_2ClO_4$ (NENP) and $CsNiCl_3$ compounds (see, e.g., [2, 3]). Nickelates R_2BaNiO_5 allow smooth variation of the interchain interaction by replacing or partially replacing the rare-earth R^{3+} ion with the nonmagnetic Y^{3+} ion, which offers new opportunities for studying quasi-one-dimensional Haldane magnets.

Nickelates R_2BaNiO_5 (R = Pr–Tm, Y) belong to the orthorhombic crystal system and have space group $Immm$ (D_{2h}^{25}) [4, 5]. The most distinctive feature of the structure is the existence of isolated chains (parallel to each other and to the **a** axis) of compressed NiO_6 octahedra connected together by shared vertices (Fig. 1). The chains are bound to each other via Ba^{2+} and R^{3+} ions. The R^{3+} ions occupy equivalent positions with local symmetry C_{2v} (Fig. 1b). The compound with R = Y (Y_2BaNiO_5) is not ordered at least down to 100 mK [6]. The temperature dependence of its magnetic susceptibility is described by a curve with a wide peak typical of a one-dimensional antiferromagnet (the intrachain interaction was estimated from this curve to be $J \approx$ 25 meV [7]). Neutron inelastic scattering spectra reveal an excitation with energy $\Delta \approx 10$ meV, which is attributed to the Haldane gap [7]. The upper estimate of the interchain interaction J' was found in [8] to be $J'/J \leq 5 \times 10^{-4}$. Thus, Y_2BaNiO_5 is an almost ideal model of the AFM chain of spins $S = 1$. The substitution of a RE element for nonmagnetic yttrium causes an increase in the interchain interaction and the onset of magnetic ordering. The magnetic structure of both the nickel and RE subsystem is characterized by a wave vector $\mathbf{k}$ = (1/2, 0, 1/2) for all compounds with $R \neq$ Y [9]. However, the directions of the magnetic moments are different in compounds with different RE elements. For R = Nd, Tb, Dy, and Ho, the magnetic moments are parallel to the **c** axis of the crystal [9], whereas in the Er_2BaNiO_5 compound they are parallel to the **a** axis [9, 10]. The Néel temperatures T_N vary from 12.5 K for Tm_2BaNiO_5 to 65 K for Tb_2BaNiO_5. For Nd_2BaNiO_5, T_N = 48 K [9, 11, 12]. For the $(R_xY_{1-x})_2BaNiO_5$ systems ($0 \leq x \leq 1$), $T_N(x)$ varies gradually, which makes it possible to study in detail the crossover from a one-dimensional (1D) quantum antiferromagnet to a three-dimensional (3D) classical antiferromagnet and the behavior of Haldane excitations during the 1D–3D crossover.

Such a study was carried out in [13, 14] for $(Nd_xY_{1-x})_2BaNiO_5$ using neutron inelastic scattering.

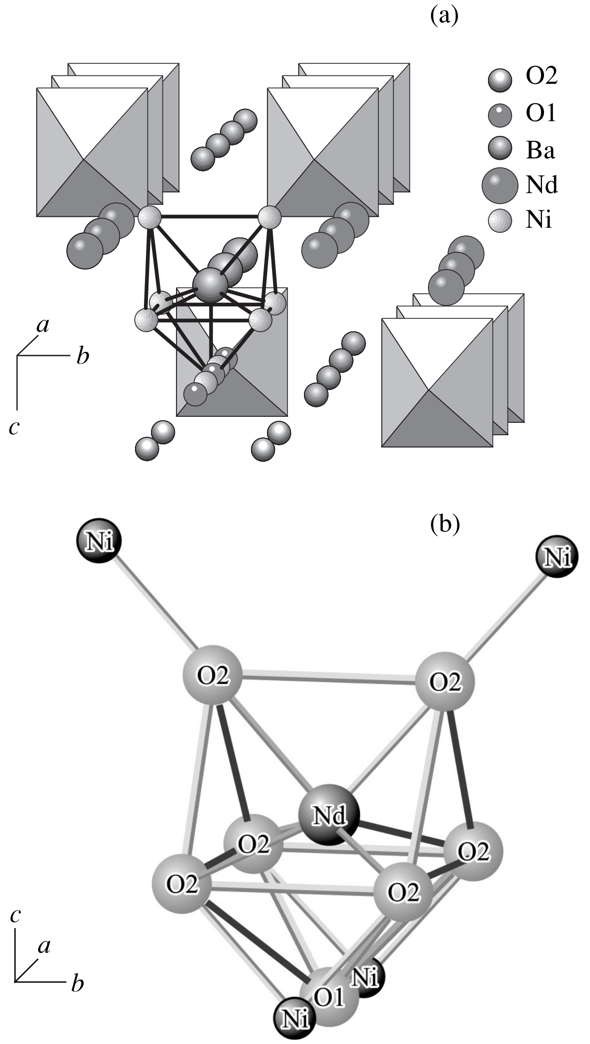

Fig. 1. (a) Structure of Nd_2BaNiO_5 and (b) the nearest neighborhood of the Nd^{3+} ion in Nd_2BaNiO_5. NiO_6 octahedra are bound to each other by shared apical oxygen in chains along the **a** axis. Two octahedra are removed to show the Ni–O–Ni bond in the chains.

Another neutron experiment (for Nd_2BaNiO_5) was performed in [15] with the aim of studying the interaction of 1D magnetic excitations of Ni chains with electronic excitations of the RE subsystem. Interference of these two types of excitation was detected and qualitatively explained. As indicated in [15], the development of a more comprehensive theory of this phenomenon is complicated by the lack of data on the Nd^{3+} electronic states in Nd_2BaNiO_5.

These data are also needed to explain the magnetic properties of Nd_2BaNiO_5. The temperature dependence of the magnetic susceptibility $\chi(T)$ exhibits a very weak feature at the magnetic ordering temperature $T_N = 48$ K [11, 16, 17] and a pronounced peak at a significantly lower temperature, $T_{max} = 26$ K [11, 17], whereas, according to the neutron scattering data, no changes in the magnetic structure are observed. Probably, the peak in the $\chi(T)$ dependence corresponds to depletion of the upper component of the Nd^{3+} Kramers doublet, which is split by exchange interactions in the magnetically ordered state, as is the case in Er_2BaNiO_5 [11, 18]. To test this hypothesis, spectroscopic studies are required.

To our knowledge, the spectroscopic information on the Nd_2BaNiO_5 compound is restricted to the positions of the three lowest Stark sublevels of the ground state (144, 192, 304 cm^{-1}), which were determined using neutron inelastic scattering spectra measured with a resolution of ≈ 2.5 cm^{-1} [15]. This study is devoted to optical high-resolution (0.1 cm^{-1}) spectroscopy of the Nd_2BaNiO_5 compound and, for comparison, $Nd_{0.1}Y_{1.9}BaNiO_5$.

2. EXPERIMENTAL

Polycrystalline Nd_2BaNiO_5 and $Nd_{0.1}Y_{1.9}BaNiO_5$ samples were prepared using solid-phase synthesis from powders of Y_2O_3 (99.99%) and/or Nd_2O_3 (99.99%), NiO (99.99%), and $BaCO_3$ (99.99%), which were mixed and annealed at 900°C in air for 24 h and then pelletized under a pressure of 2500 bar. Particular attention was paid to the volatile components in Nd_2O_3 (~15%). Pellets were sintered at temperatures from 1000 to 1450°C in air for 24–50 h with intermediate grinding. After each treatment, samples were studied using an x-ray diffractometer. After sintering at 1450°C, no impurity phases were detected in the $Nd_{0.1}Y_{1.9}BaNiO_5$ sample and the diffraction pattern corresponded to space group *Immm*. The diffraction pattern of Nd_2BaNiO_5 after treatment at 1350°C also showed the group *Immm*; however, traces of other phases were observed.

High-resolution (to 0.1 cm^{-1}) diffuse transmittance spectra of Nd_2BaNiO_5 samples were measured over wide spectral (1600–20000 cm^{-1}) and temperature (4.2–300 K) ranges using a high-resolution BOMEM DA3.002 Fourier spectrometer. Powder samples were mixed with ethanol and applied onto a BaF_2 substrate. Then, the sample was placed into a cryostat with helium vapor. A silicon detector was used for the spectral range 9000–20000 cm^{-1}. Two InSb detectors were used for the range 5000–10000 cm^{-1}. One of them was conventional; the other, special, detector was positioned in the cryostat immediately behind the sample. The range 1600–5000 cm^{-1} was studied using a mercury cadmium telluride detector.

3. OPTICAL SPECTRA OF $Nd_{0.1}Y_{1.9}BaNiO_5$ AND Nd_2BaNiO_5 IN THE PARAMAGNETIC STATE AND THE STARK STRUCTURE OF THE Nd^{3+} ION LEVELS

Figure 2 shows the general transmittance spectrum of polycrystalline Nd_2BaNiO_5 samples in the paramagnetic state. Narrow lines correspond to the *f–f* transitions in the Nd^{3+} ion from the $^4I_{9/2}$ ground state to excited levels. For comparison, the positions of the Nd^{3+} levels in $LaCl_3$ [19] are shown. The positions of the lower levels $^4I_{11/2}$, $^4I_{13/2}$, and $^4I_{15/2}$ are identical for Nd_2BaNiO_5 and $LaCl_3$, while the higher levels of Nd_2BaNiO_5 are shifted to lower energies in comparison with those of $LaCl_3$. This nephelauxetic shift [20, 21] in Nd_2BaNiO_5 is caused by the strong overlap of the wave functions of the Nd^{3+} excited states with the ligand wave functions.

In the crystal field with C_{2v} local symmetry, each level of the free Nd^{3+} ion with a total angular momentum J is split into $J + 1/2$ Kramers doublets (see the diagram in Fig. 3). All spectra can be interpreted in terms of a single neodymium center. To facilitate analysis of the Stark splittings, we used the diluted $Nd_{0.1}Y_{1.9}BaNiO_5$ compound, which is not ordered at least down to 10 K and whose spectrum is not complicated by exchange splittings. The transmittance spectra of both compounds are compared in Fig. 4. The Stark sublevel energies of the Nd^{3+} ion multiplets as determined from the spectra are listed in the table. The Stark sublevels of the $^4I_{9/2}$ ground state were determined from transmittance spectra at elevated temperatures (Fig. 5). The intensities of the lines that become stronger as the temperature increases correlate with the population of the excited Stark sublevels of the ground state (Fig. 6). The energies of the lowest levels thus determined (140, 190, 302 cm^{-1}) agree well with the neutron scattering data (144, 192, 304 cm^{-1}) [15].

The experimentally determined positions of 54 Stark levels of the Nd^{3+} ion in Nd_2BaNiO_5 can be used for performing an analysis in terms of crystal field theory.

4. EXCHANGE SPLITTINGS IN Nd_2BaNiO_5 SPECTRA: MOLECULAR-FIELD MODEL

In the magnetically ordered state, magnetic interactions remove the Kramers degeneracy of Nd^{3+} levels, which results in a splitting of spectral lines (Fig. 3). Figure 7 shows the variation of one of the lines as the temperature is lowered. The splitting arising at ~50 K increases and the lines narrow. At $T \leq 35$ K, all four components of the split line are clearly visible, with the low-frequency components being “frozen out.” By analyzing the spectra, we can determine the exchange splittings (due to magnetic ordering) of the Kramers doublets corresponding to the initial and final levels of an optical transition. The splittings as determined from the spectra at $T = 5$ K are listed in the table.

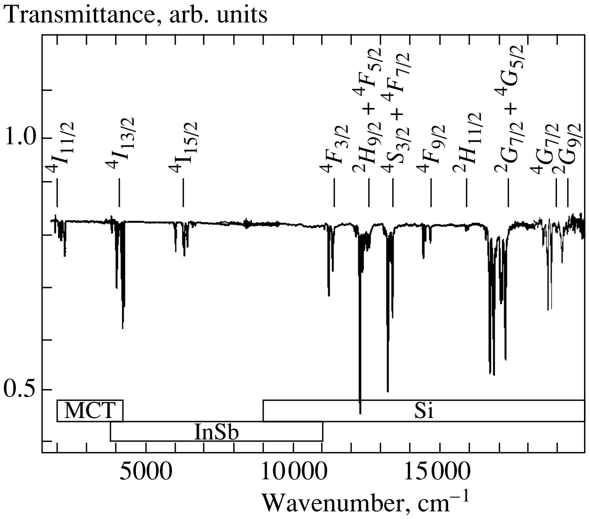

Fig. 2. Transmittance spectrum of Nd_2BaNiO_5 at ~100 K. The operational spectral ranges of the radiation detectors employed are indicated at the bottom (MCT stands for mercury–cadmium–tellurium). The positions of the Nd^{3+} ion multiplets in the $LaCl_3 : Nd^{3+}$ compound are shown at the top [19].

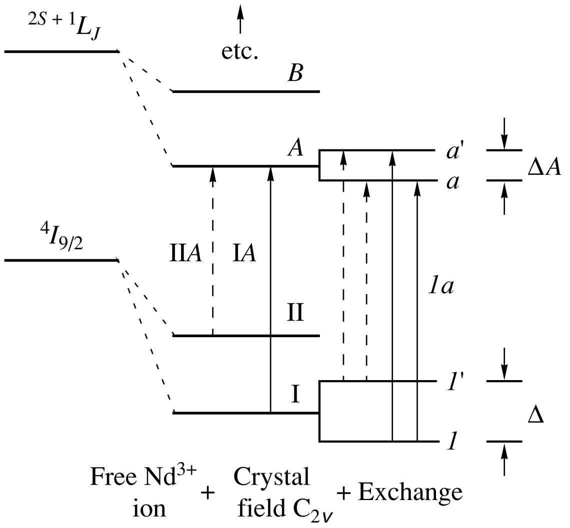

Fig. 3. Schematic diagram of the Nd^{3+} level splitting in the crystal field and of the Kramers doublet splitting in the magnetically ordered state. The optical transitions frozen out at low temperatures are indicated by dashed lines.

Figure 8 shows the temperature dependences of the ground-state splitting $\Delta(T)$, of the energy of the 4-meV mode detected in the neutron scattering spectrum [14], and of the magnetic moment of the nickel subsystem

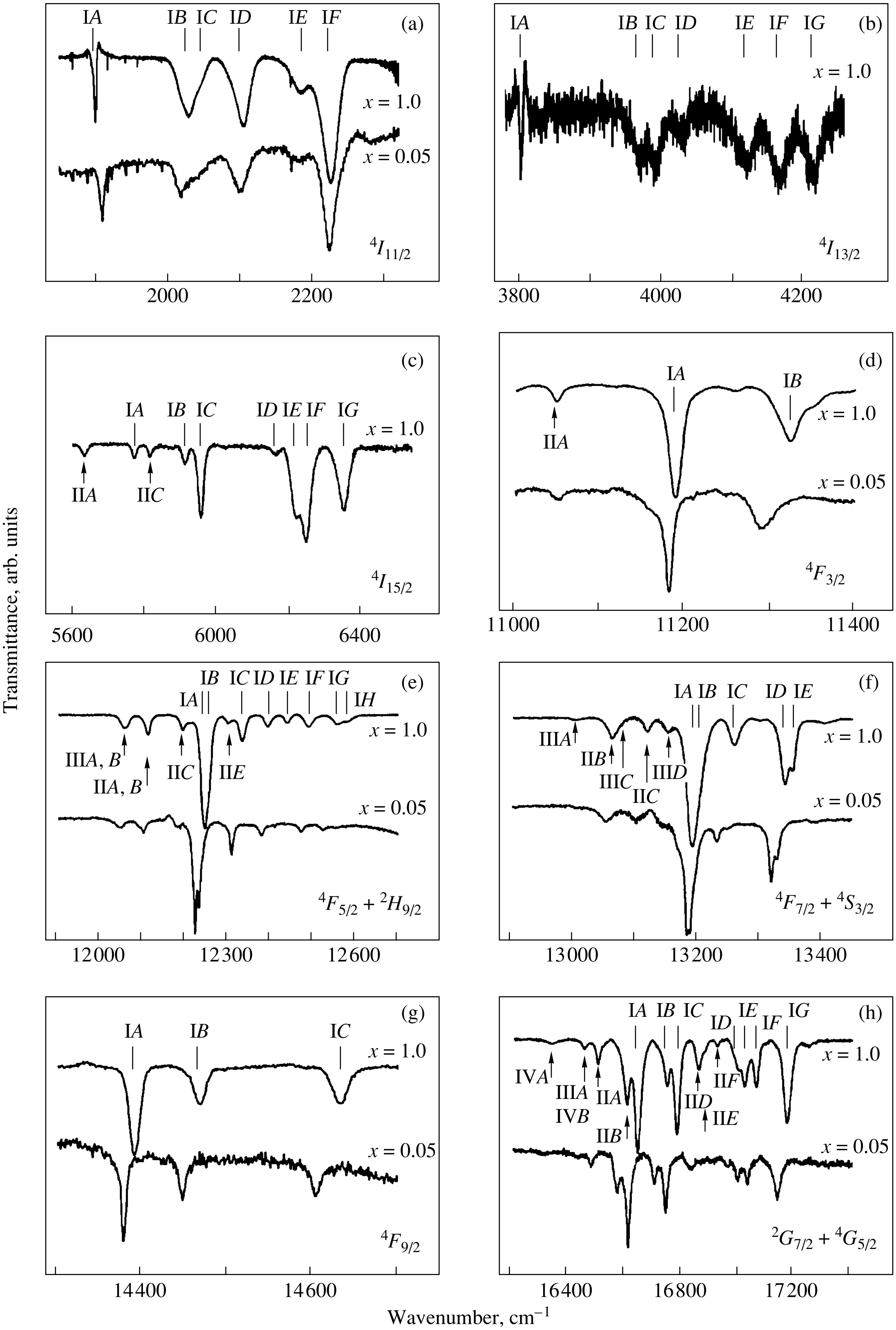

Fig. 4. Transmittance spectra of $(Nd_xY_{1-x})_2BaNiO_5$ at 100 K in the range of transitions from the $^4I_{9/2}$ ground state of the Nd^{3+} ion to excited states (indicated in the right bottom of each panel). Spectral lines are denoted according to the notation in Fig. 3.

Stark level energies of the Nd^{3+} ion in chain nickelates $(Nd_xY_{1-x})_2BaNiO_5$ determined from the transmittance spectra at $T = 90$ K; the exchange splittings (cm^{-1}) for Nd_2BaNiO_5 at $T = 5$ K are given in parentheses

Multiplet	E, cm^{-1}		Multiplet	E, cm^{-1}	
	$x = 1$	$x = 0.05$		$x = 1$	$x = 0.05$
$^4I_{9/2}$	0 (32)	0	$^4F_{5/2}$	12241 (<2)	12222
	140	130		12251 (<2)	12231
	190	180		12330 (3.7)	12306
	302	290	$^2H2_{9/2}$	12390	12377
	~440	440		12438	12410
$^4I_{11/2}$	1901	1909		12490	12470
	2029	2018		12552	12521
	2046			12580	12551
	2104	2100	$^4F_{7/2}$	13190 (5.3)	13183
	2183	2178		13200 (5.3)	13187
	2224	2222		13258 (4)	13229
$^4I_{13/2}$	3807		$^4S_{3/2}$	13340 (14.5)	13318
	3970	3956		13352 (22)	13327
	3992 (11)	3978	$^4F_{9/2}$	14390 (2)	14379
	4029	4022		14468 (7)	14447
	4119	4117		14631 (14)	14603
	4169	4160	$^4G_{5/2}$	16640 (6)	16608
	4217	4212		16743 (10)	16699
$^4I_{15/2}$	5772			16779 (7)	16738
	5912 (16)		$^2G_{7/2}$	16996	16992
	5956 (<4)			17015	17026
	6163			17057	
	6220			17168	17132
	6248		$^4G_{7/2}$	18585	18600
	6353			18625	18704
$^4F_{3/2}$	11188 (11.4)	11182		18748	
	11323	11290	$^2G_{9/2}$	19114	

$m_{Ni}(T)$ determined from the neutron scattering data [14]. The 4-meV mode in Nd_2BaNiO_5 observed in neutron scattering experiments was initially assigned to the Stark level of the Nd^{3+} ion [22]. However, it is clearly seen from Fig. 8 that, in actual fact, this mode corresponds to the transition between the components of the Nd^{3+} ground-state Kramers doublet split by the magnetic interaction in the magnetically ordered state, i.e., to the neodymium magnetic moment being flipped, as expected in [14].

For $T < 0.9T_N$, the splitting of the RE-ion ground state in Nd_2BaNiO_5 is proportional to the magnetic moment of the nickel subsystem (Fig. 8), as in the case of Er_2BaNiO_5 [11, 18]. Therefore, the molecular-field model is applicable to this system, according to which the RE ions are subject to the effective magnetic field B_{eff} induced by the ordered nickel subsystem [11, 17, 18]. Within this approximation, we can write

$$\Delta(T) = 2m_{Nd}^{(0)}B_{eff}(T), \tag{1}$$

$$B_{eff}(T) = \lambda m_{Ni}(T), \tag{2}$$

where $m_{Nd}^{(0)}$ is the magnetic moment of the Nd^{3+} ion in the ground state and λ is the molecular-field constant. Using the experimental values $m_{Nd}^{(0)} = 2.65\mu_B$ and $m_{Ni}^{(0)} = 1.6\mu_B$ (derived from the neutron scattering data [9]) and fitting the experimental $\Delta(T)$ dependence with Eqs. (1) and (2), we obtain $\lambda = 7.61\mu_B$. This value agrees well with the value $\lambda = 7.51\mu_B$ obtained in [17] by analyzing the Nd_2BaNiO_5 magnetic susceptibility.

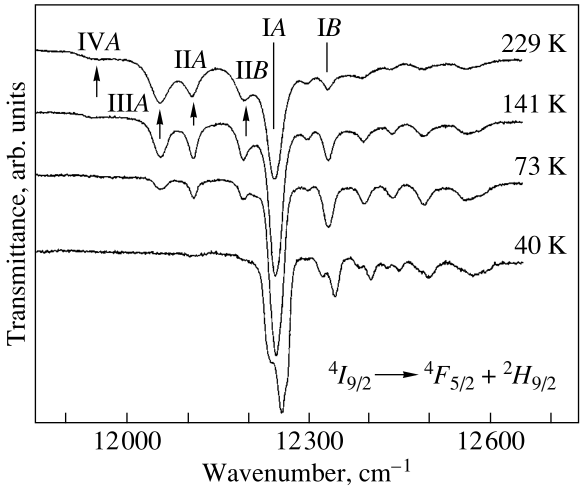

Fig. 5. Transmittance spectrum of Nd_2BaNiO_5 at various temperatures. The lines corresponding to transitions from the excited sublevels of the $^4I_{9/2}$ multiplet disappear as the temperature decreases. At 40 K, one can see exchange splittings of the I*A* and I*B* lines.

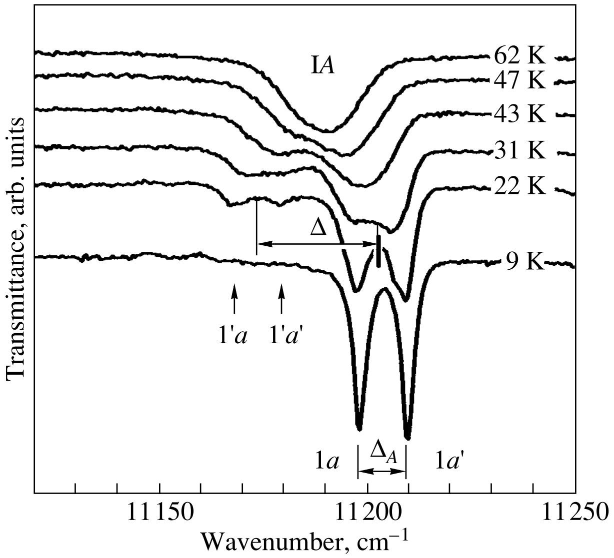

Fig. 7. Line I*A* (Fig. 4d) at various temperatures. The notation corresponds to that in Fig. 3.

At $T > T_N$, the spectral line splitting does not disappear completely. The remaining splitting is associated with the short-range order. Previously, we assumed that the magnetic ordering temperature could be determined from the position of the inflection point in the $\Delta(T)$ dependence [23, 24]. A comparison of the optical and neutron scattering data for Nd_2BaNiO_5 (Fig. 8) confirms this assumption. Based on the spectroscopic data, we obtained $T_N = 47.5 \pm 1$ K, which agrees with $T_N = 48$ K determined from neutron diffraction studies [9, 16].

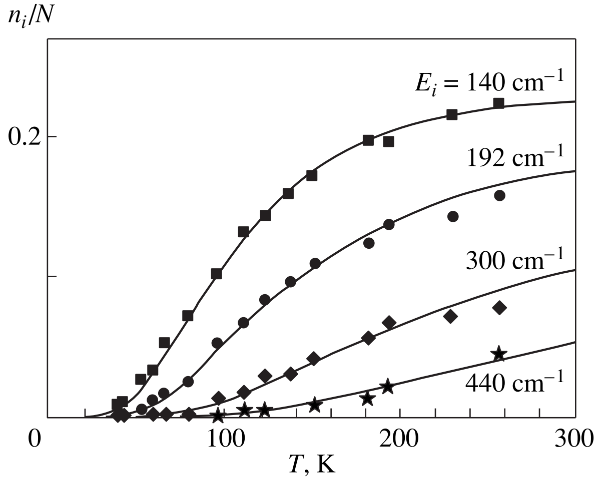

Fig. 6. Populations of excited levels with energy E_i as calculated using the formula $n_i/N = \exp(-E_i/kT)/\sum_{j=1}^{5}\exp(-E_j/kT)$ (solid curves) and experimentally measured intensities of spectral lines (dots).

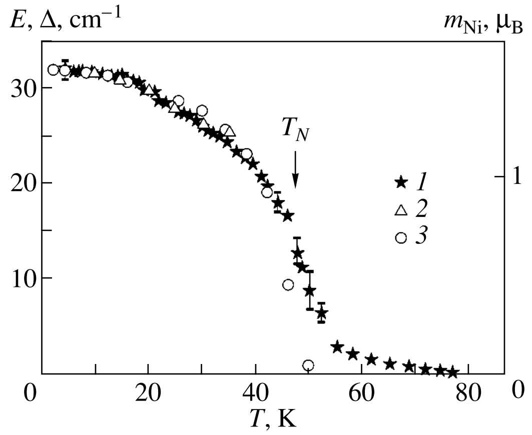

Fig. 8. Temperature dependences of (*1*) the splitting Δ of the Nd^{3+} ion ground state, (*2*) the energy *E* of the 4-meV mode observed in the neutron scattering spectrum, and (*3*) the magnetic moment m_{Ni}. The $\Delta(T)$ dependence was obtained from the spectroscopic measurements in this study, and $E(T)$ and $m_{Ni}(T)$ were plotted using the experimental data on neutron scattering [14].

5. MAGNETIC MOMENT OF THE NEODYMIUM SUBSYSTEM IN MAGNETICALLY ORDERED Nd_2BaNiO_5

The excited Stark sublevels of the ground-state multiplet (140, 190 cm^{-1}, etc.; see table) are almost empty at $T < T_N$. Therefore, only the ground-state Kramers doublet contributes to the magnetic moment m_{Nd} of the neodymium subsystem and we can write

$$m_{Nd}(T) = m_{Nd}^{(0)}\frac{n_1 - n_2}{n_1 + n_2} = m_{Nd}^{(0)}\tanh\frac{\Delta(T)}{2kT}, \qquad (3)$$

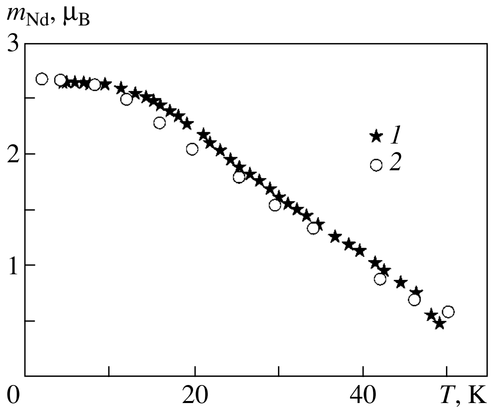

Fig. 9. Temperature dependences of the Nd^{3+} magnetic moment in the magnetically ordered state of Nd_2BaNiO_5 as obtained (*1*) from the spectroscopic data using Eq. (3) and (*2*) from neutron scattering data.

where $m_{Nd}(T)$is the magnetic moment per Nd^{3+} ion and n_1 and $n_2 = n_1\exp(\Delta/kT)$ are the populations of the lower and upper sublevels of the ground-state Kramers doublet.

Figure 9 shows the $m_{Nd}(T)$ dependences calculated from Eq. (3) using the spectroscopic data on the ground-state splitting $\Delta(T)$ and found from the neutron scattering data [14]. The good agreement confirms the applicability of the spectroscopic technique for studying the magnetic properties of chain nickelates.

The data obtained in this study also directly substantiate the approach (proposed for the first time in [11]) applied in [17] to calculate the magnetic susceptibility $\chi(T)$ of Nd_2BaNiO_5. Moreover, these data show that the peak in the $\chi(T)$ dependence at a temperature $T_{max} \sim$ 26 K (or at 30 K, according to [11]), which is significantly lower than the magnetic ordering temperature $T_N = 47.5$ K, is caused by depletion of the upper component of the Nd^{3+} ion ground-state Kramers doublet split by Nd–Ni interactions in magnetically ordered Nd_2BaNiO_5. Using this approach, the temperature of this peak can be estimated from the formula $kT_{max} = 0.65\Delta(0)$ without calculating the entire $\chi(T)$ dependence [23]. By substituting $\Delta(0) = 32$ cm^{-1} determined from the spectra, we obtain an estimate $T_{max} = 30$ K that is close to the observed value.

ACKNOWLEDGMENTS

This study was supported by the Russian Foundation for Basic Research (project no. 04-02-17346) and the Russian Academy of Sciences (fundamental research programs).

REFERENCES

1. F. D. M. Haldane, Phys. Rev. Lett. **50** (15), 1153 (1983).
2. W. J. L. Buyers, R. M. Morra, R. L. Armstrong, M. J. Hogan, P. Gerlach, and K. Hirakawa, Phys. Rev. Lett. **56** (4), 371 (1986).
3. Z. Tun, W. J. L. Buyers, A. Harrison, and J. A. Rayne, Phys. Rev. B **43** (16), 13 331 (1991).
4. S. Schiffler and H. Müller-Buschbaum, Z. Anorg. Allg. Chem. **532**, 10 (1986).
5. E. García-Matres, J. L. Martínez, and J. Rodríguez-Carvajal, J. Solid State Chem. **103**, 322 (1993).
6. K. Kojima, A. Keren, L. P. Le, G. M. Luke, B. Nachumi, W. D. Wu, Y. J. Uemura, K. Kiyono, S. Miyasaka, H. Takagi, and S. Uchida, Phys. Rev. Lett. **74** (17), 3471 (1995).
7. J. Darriet and L. P. Regnault, Solid State Commun. **86** (7), 409 (1993).
8. Guangyong Xu, J. F. Ditusa, T. Ito, K. Oka, H. Takagi, C. Broholm, and G. Aeppli, Phys. Rev. B **54** (10), 6827 (1996).
9. E. García-Matres, J. L. Martínez, and J. Rodríguez-Carvajal, Eur. Phys. J. B **24**, 59 (2001).
10. K. A. Alonso, J. Amador, J. L. Martinez, I. Rasines, J. Rodríguez-Carvajal, and R. Saez-Puche, Solid State Commun. **76** (4), 467 (1990).
11. G. G. Chepurko, Z. A. Kazei, D. A. Kudrjavtsev, R. Z. Levitin, B. V. Mill, M. N. Popova, and V. V. Snegirev, Phys. Lett. A **157** (1), 81 (1991).
12. A. Zheludev, J. M. Tranquada, T. Vogt, and D. J. Buttrey, Phys. Rev. B **54** (9), 6437 (1996).
13. T. Yokoo, A. Zheludev, M. Nakamura, and J. Akimitsu, Phys. Rev. B **55** (17), 11 516 (1997).
14. T. Yokoo, S. A. Raymond, A. Zheludev, S. Maslov, E. Ressouche, I. Zaliznyak, R. Erwin, M. Nakamura, and J. Akimitsu, Phys. Rev. B **58** (21), 14 424 (1998).
15. A. Zheludev, S. Maslov, T. Yokoo, J. Akimitsu, S. Raymond, S. E. Nagler, and K. Hirota, Phys. Rev. B **61** (17), 11 601 (2000).
16. A. Zheludev, J. P. Hill, and D. J. Buttrey, Phys. Rev. B **54** (10), 7216 (1996).
17. E. García-Matres, J. L. García-Munos, J. L. Martínez, and J. Rodríguez-Carvajal, J. Magn. Magn. Mater. **149**, 363 (1995).
18. M. N. Popova, S. A. Klimin, E. P. Chukalina, B. Z. Malkin, R. Z. Levitin, B. V. Mill, and E. Antic-Fidancev, Phys. Rev. B **68** (15), 155103 (2003).
19. G. H. Dieke, *Spectra and Energy Levels of Rare Earth Ions in Crystals* (Interscience, New York, 1968), p. 142.
20. P. Caro, O. Beaury, and E. Antic, J. Phys. (France) **37**, 671 (1976).
21. E. Antic-Fidancev, M. Lemaitre-Blaise, and P. Caro, New J. Chem. **11** (6), 467 (1987).
22. A. Zheludev, J. M. Tranquada, T. Vogt, and D. J. Buttrey, Phys. Rev. B **54** (10), 7210 (1996).
23. M. N. Popova, Proc. SPIE **2706**, 182 (1996).
24. M. N. Popova, J. Alloys Compd. **275–277**, 142 (1998).

Translated by A. Kazantsev

Physics of the Solid State, Vol. 47, No. 8, 2005, pp. 1504–1506. Translated from Fizika Tverdogo Tela, Vol. 47, No. 8, 2005, pp. 1447–1449.
Original Russian Text Copyright © 2005 by Lebedev, Ryabov, Gaister, Podstavkin, Zharikov, Shestakov.

PROCEEDINGS OF THE XII FEOFILOV WORKSHOP “SPECTROSCOPY OF CRYSTALS ACTIVATED BY RARE-EARTH AND TRANSITION-METAL IONS”

(Yekaterinburg, Russia, September 22–25, 2004)

Spectral and Generation Properties of a New Laser Crystal $(Cr^{3+},Li) : Mg_2SiO_4$

V. F. Lebedev*, I. D. Ryabov, A. V. Gaister***, A. S. Podstavkin****,**
E. V. Zharikov*, and A. V. Shestakov******

**Fiber Optics Research Center, Prokhorov General Physics Institute, Russian Academy of Sciences,*
ul. Vavilova 38, Moscow, 119991 Russia
e-mail: vfleb@fo.gpi.ru
***Geological Institute, Russian Academy of Sciences, Pyzhevskiĭ per. 7, Moscow, 119017 Russia*
****Laser Materials and Technology Research Center, Prokhorov General Physics Institute,*
Russian Academy of Sciences, ul. Vavilova 38, Moscow, 119991 Russia
*****Research and Development Center of Elements of Laser Systems (ÉLS-94),*
ul. Vvedenskogo 3, Moscow, 117342 Russia

Abstract—Based on the results of a comparative analysis of luminescence spectroscopy and EPR spectroscopy data, it was found for the first time that the wide-band luminescence of Cr^{3+} ions in a forsterite crystal is due to the Cr^{3+}–V_{Mg} center or, in a crystal additionally doped with lithium, to a Cr^{3+}–Li^+ center. For the first time, tunable laser action was obtained with Cr^{3+}–Li^+ centers responsible for the wide-band luminescence. *© 2005 Pleiades Publishing, Inc.*

1. It is well known that, in the forsterite structure, Cr^{3+} ions substitute for Mg^{2+} ions in two nonequivalent crystallographic positions, *M*1 and *M*2, and form $Cr^{3+}(M1)$ and $Cr^{3+}(M2)$ isolated centers with different spectral luminescent properties [1]. It is generally agreed that, both in $Cr^{3+} : Mg_2SiO_4$ and in $(Cr^{3+}, Li) : Mg_2SiO_4$ crystals, the wide-band luminescence of Cr^{3+} ions in the spectral range 850–1000 nm is caused by isolated chromium ions located in the mirror-symmetry magnesium positions *M*2 [2, 3].

It was established in [4] that the wide-band luminescence of Cr^{3+} ions in forsterite crystals doped with chromium and lithium ions, $(Cr^{3+}, Li) : Mg_2SiO_4$, is a superposition of two bands peaked at wavelengths λ_{max} of approximately 890 and 950 nm (with polarization **E || c** for space group *Pbnm*). When the lithium concentration reaches a value C_{Li}^{min}, the luminescence intensity in the band at λ_{max} ~ 890 nm decays to zero.

Non-isovalent substitution of Cr^{3+} for Mg^{2+} ions in the forsterite structure should be accompanied by the formation of point defects serving as charge compensators. In $Cr^{3+} : Mg_2SiO_4$ crystals, these defects are negatively charged magnesium vacancies V_{Mg}. However, the results of computer modeling show that lithium ions can be more effective charge compensators. Thus, it is expected that Cr^{3+}–V_{Mg} centers will form in $Cr^{3+} : Mg_2SiO_4$ crystals and Cr^{3+}–Li^+ centers will form in $(Cr^{3+},Li) : Mg_2SiO_4$ crystals [5].

2. Crystals doped either with chromium alone or with both lithium and chromium were studied. The crystals were grown using the Czochralski technique in an atmosphere of highly pure argon ($\log f_{O_2}$ ~ –4). The chromium concentration in a melt was 0.06 ± 0.01 wt %. The lithium concentration in a melt varied from 0.01 to 0.42 wt %. In order to study laser action, crystals were grown from a melt containing approximately 0.25 ± 0.01 wt % chromium.

A description of the technique used to measure polarized luminescence spectra can be found in [4]. The structure and relative concentrations of various Cr^{3+} centers were determined using EPR spectroscopy data and a technique described in [6]. To study the possible laser action, a *Q*-switched single-mode alexandrite $(Cr^{3+} : BeAl_2O_4)$ laser operating at a wavelength λ_p = 750 nm was used for pumping.

3. The wide-band luminescence of Cr^{3+} ions in $Cr : Mg_2SiO_4$ crystals is polarized predominantly along the **c** axis. At $C_{Li} = 0$, the Cr^{3+} ion luminescence with polarization along the **c**, **b**, and **a** axes has a maximum at λ ~ 890, 860, and 850 nm, respectively [7]. It can be seen from Figs. 1a and 1b that, in $Cr^{3+} : Mg_2SiO_4$ crystals additionally doped with Li^+ ions, the luminescence with polarization along the **c** and **b** axes in the initial

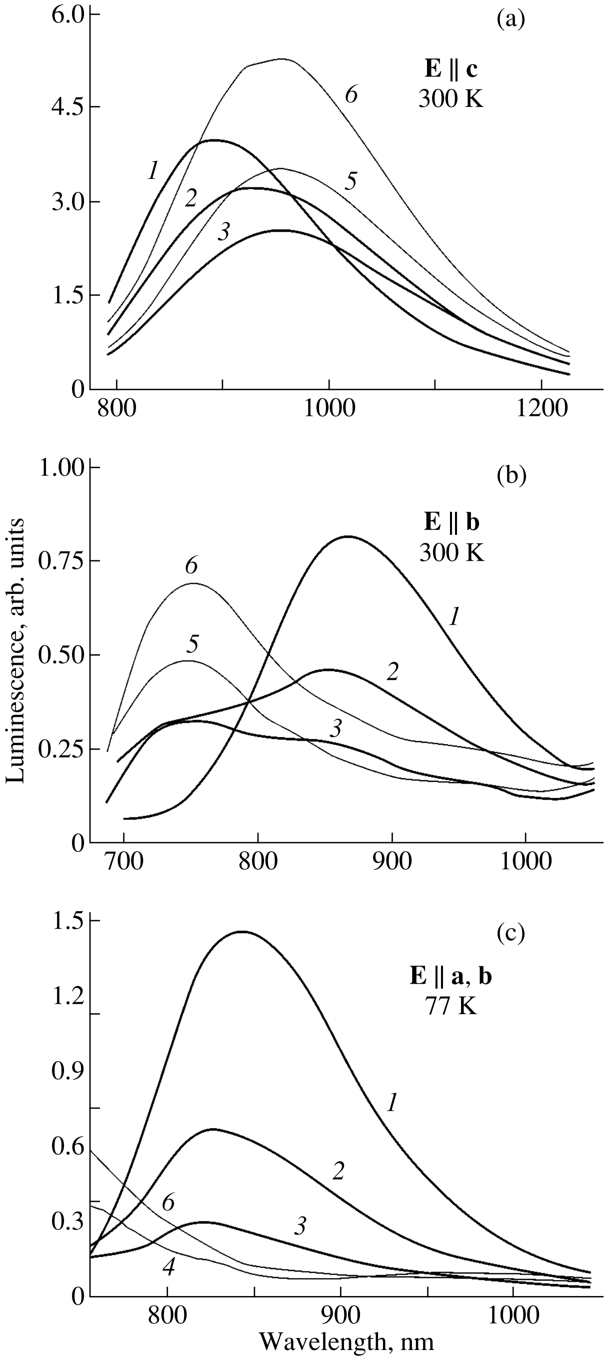

Fig. 1. Transformation of wide-band luminescence spectra of Cr^{3+} ions in forsterite crystals grown from a melt with various lithium concentrations: (*1*) 0, (*2*) 0.02, (*3*) 0.03, (*4*) 0.05, (*5*) 0.10, and (*6*) 0.32 wt %.

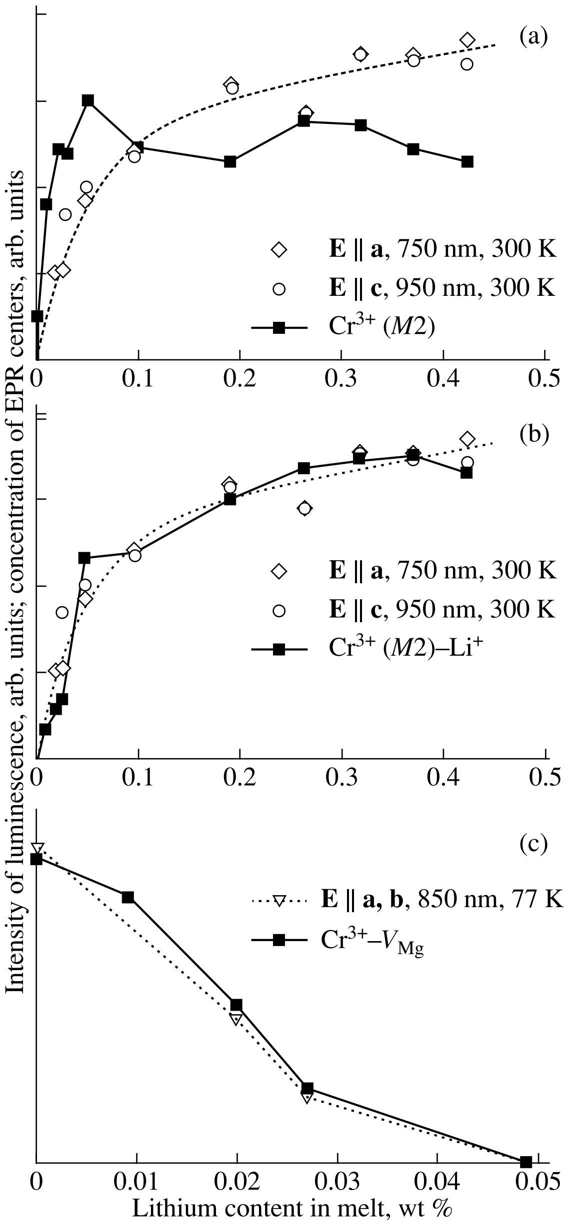

Fig. 2. Variations in the intensity of Cr^{3+} wide-band luminescence (open symbols) and in the concentration of Cr^{3+} EPR centers having different structure (solid symbols) in $(Cr^{3+},Li) : Mg_2SiO_4$ crystals with the lithium concentration in the melt from which the crystals were grown. The normalization factors for the curves are determined by minimizing the sum of the squares of the relative deviations. The dotted lines are fits to the normalized dependence of the luminescence intensity on the lithium concentration in the melt.

bands with maxima at approximately 850–890 nm weakens rapidly and finally disappears completely for samples grown from a melt with a lithium concentration higher than $C_{\mathrm{Li}}^{\mathrm{min}}$ = 0.05 wt %. In place of this luminescence, there appear bands with maxima at 750 nm (for **E** || **b**) and 950 nm (for **E** || **c**). Therefore, a forsterite crystal contains Cr^{3+} luminescence centers whose concentration reduces to zero at a certain concentration of Li^+ ions. The disappearance of the band corresponding to the initial Cr^{3+} center is most clearly observed in a sample cooled to a temperature of 77 K (Fig. 1c). In this case, the band belonging to the initial Cr^{3+} center and the new band at $\lambda_{max} \sim 750$ nm overlap only weakly.

The EPR spectra of the crystals under study exhibit signals from seven different Cr^{3+} paramagnetic centers. Two of them are well-known isolated Cr^{3+} centers in the structurally nonequivalent magnesium positions $M1$ and $M2$ with C_i and C_s local symmetry, respectively [1]. Two other centers are typical only of $(Cr^{3+},Li) : Mg_2SiO_4$ crystals. These were assumed in [6] to be the $Cr^{3+}(M1)$–$Li^+(M2)$ and $Cr^{3+}(M2)$–$Li^+(M1)$ centers. This conclusion was based on a comparative analysis of the angular dependences of the EPR lines and the spin Hamiltonian parameters of these centers and the $Cr^{3+}(M1)$ and $Cr^{3+}(M2)$ centers. Three more centers exist both in $Cr^{3+} : Mg_2SiO_4$ and in $(Cr^{3+},Li) : Mg_2SiO_4$ crystals [8]. The concentration of these three centers decreases rapidly to zero for samples grown from a melt with a Li^+ ion concentration $C_{Li} > 0.05$ wt %.

A comparative analysis of the luminescence and EPR spectroscopy data demonstrates that the variations in the intensity of the luminescence bands at 750 and 950 nm with concentration C_{Li} correlate most closely with the variations in the concentration of Cr^{3+}–Li^+ centers (Fig. 2b) rather than the concentration of isolated Cr^{3+} centers (Fig. 2a). Moreover, in the range of C_{Li} values covered, the concentration of the isolated centers increases approximately fivefold, whereas the luminescence intensity increases by a factor of about 1.3 [4]. The initial luminescence centers that disappear with increasing C_{Li} can be identified with one of the detected chromium–vacancy centers (Fig. 2c).

Thus, the data shown in Fig. 2 give grounds to believe that the wide-band luminescence observed in the range 900–950 nm can be assigned to the Cr^{3+}–V_{Mg} center in $Cr^{3+} : Mg_2SiO_4$ crystals and to the Cr^{3+}–Li^+ center in $(Cr^{3+},Li) : Mg_2SiO_4$ crystals. Contrary to a wide-spread belief, the isolated $Cr^{3+}(M2)$ centers do not have a significant effect on the formation of the wide-band luminescence spectrum.

The results of the analysis of the spectral properties of the $(Cr^{3+},Li) : Mg_2SiO_4$ crystals studied were confirmed directly by laser action studies. The absorption associated with the $^4A_2$–$^4T_2$ transition in a crystal at the pumping wavelength was ~2.5 cm^{-1} (for **E || c**). Laser radiation with polarization **E || c**, tunable in the wavelength range 1030–1180 nm, was observed in a three-mirror dispersive resonator with plane mirrors. The transmittance of the exit mirror varied gradually from 1.4% at a wavelength of 1000 nm to 4% at 1200 nm. More detailed data on the laser efficiency and its possible tuning wavelength range (in particular, under the conditions of continuous wave generation) can be obtained by optimizing the properties of the crystal and laser cavity and the pumping conditions.

4. It has been established that an additional lithium doping of $Cr^{3+} : Mg_2SiO_4$ crystals changes the mechanism of charge compensation. Based on a comparative analysis of the data obtained, the wide-band luminescence has been attributed to the Cr^{3+}–V_{Mg} centers in crystals with $C_{Li} = 0$ and to the Cr^{3+}–Li^+ centers in crystals with $C_{Li} > C_{Li}^{min} = 0.05$ wt %. Tunable laser action has been obtained for the first time for Cr^{3+}–Li^+ centers in forsterite crystals.

REFERENCES

1. H. Rager, Phys. Chem. Miner. **1**, 371 (1977).
2. R. Moncorge, G. Cormier, D. J. Simkin, and J. A. Capobianco, IEEE J. Quantum Electron. **27**, 114 (1991).
3. A. Sugimoto, Y. Nobe, T. Yamazaki, Y. Yamaguchi, K. Yamagishi, Y. Segava, and H. Takei, Phys. Chem. Miner. **24**, 333 (1997).
4. V. F. Lebedev, A. V. Gaister, S. Yu. Tenyakov, and E. V. Zharikov, Proc. SPIE **5478**, 37 (2004).
5. V. B. Dudnikova, A. V. Gaister, E. V. Zharikov, N. I. Gul'ko, V. G. Senin, and V. S. Urusov, Neorg. Mater. **39** (8), 985 (2003) [Inorg. Mater. **39** (8), 845 (2003)].
6. I. D. Ryabov, A. V. Gaister, and E. V. Zharikov, Fiz. Tverd. Tela (St. Petersburg) **45** (1), 51 (2003) [Phys. Solid State **45** (1), 51 (2003)].
7. V. F. Lebedev, A. V. Gaister, S. Yu. Tenyakov, E. M. Dianov, and E. V. Zharikov, Kvantovaya Elektron. **33** (3), 197 (2003) [Quantum Electron. **33** (3), 192 (2003)].
8. I. D. Ryabov, A. V. Gaister, and E. V. Zharikov, in *Abstracts of the Int. Conference "Modern Development of Magnetic Resonance," Kazan, 2004* (Kazan, 2004), p. 157.

Translated by E. Borisenko

Physics of the Solid State, Vol. 47, No. 8, 2005, pp. 1507–1511. Translated from Fizika Tverdogo Tela, Vol. 47, No. 8, 2005, pp. 1450–1454.
Original Russian Text Copyright © 2005 by Semashko.

PROCEEDINGS OF THE XII FEOFILOV WORKSHOP “SPECTROSCOPY OF CRYSTALS ACTIVATED BY RARE-EARTH AND TRANSITION-METAL IONS”

(Yekaterinburg, Russia, September 22–25, 2004)

Problems in Searching for New Solid-State UV- and VUV-Active Media: The Role of Photodynamic Processes

V. V. Semashko
Kazan State University, ul. Kremlevskaya 18, Kazan, 420008 Tatarstan, Russia
e-mail: vadim.semashko@ksu.ru

Abstract—The impact of photodynamic processes induced by pump radiation in crystals doped with rare-earth (RE) ions on the possibility of generating stimulated radiation in the UV and VUV spectral ranges is analyzed. It is shown that, in addition to objective factors, one of the main causes preventing the lasing effect from being obtained using the interconfigurational $4f^{n-1}5d$–$4f^n$ transitions of RE ions is insufficient consideration of the photodynamic processes involved in experiments. It is proposed to correct laser test techniques and “pump-probe” experiments aimed at investigating active media appropriate for lasing in the UV and VUV ranges. Extended criteria oriented to search for new solid-state UV and VUV active media are formulated. *© 2005 Pleiades Publishing, Inc.*

1. INTRODUCTION

One of the most attractive methods for generating tunable radiation in the UV and VUV spectral ranges is the use of parity-allowed interconfigurational $4f^{n-1}5d^1$–$4f^n$ (5*d*–4*f*) transitions of rare-earth (RE) ions in wide-band-gap dielectric crystals. However, to date, UV and VUV stimulated emission has been achieved only in few crystalline matrices doped with trivalent cerium and neodymium ions (see table) [1–13]. Other numerous attempts to obtain UV and VUV lasing due to 5*d*–4*f* transitions in other ions and in other crystals have failed. Moreover, it is not always possible to reproduce the laser test results even in the UV- and VUV-active media already discovered. Currently, it is well established that the efficiency of UV and VUV lasing and even its possible excitation depend on many, often poorly controlled factors, including the micro-

Summary table of known crystalline UV- and VUV-active media based on the interconfigurational $4f^{n-1}5d^1 - 4f^n$ transitions in trivalent RE ions

Active medium	Detection date	Date of reproduction of the laser test results	Note
$LiYF_4 : Ce^{3+}$	Ehrlich *et al.*, 1979 [1]	Dubinskii *et al.*, 1994 [4]	Solarization of samples, short lasing
$LaF_3 : Ce^{3+}$*	Ehrlich *et al.*, 1980 [2]	Not reproduced	Strong solarization of samples
$LaF_3 : Nd^{3+}$*	Waynant *et al.*, 1985 [3]	Dubinskii *et al.*, 1992 [9]	Photorefractive effect; not reproduced in several laboratories
$LiLuF_4 : Ce^{3+}$	Dubinskii *et al.*, 1994 [4]	Sarukura *et al.*, 1995 [10] Rambaldi *et al.*, 1998 [11]	Solarization; differential efficiency of up to 55%
$LiCaAlF_6 : Ce^{3+}$	Dubinskii *et al.*, 1993 [5]	Marshall *et al.*, 1994 [12]	Solarization has not been observed; differential efficiency of up to 46%. The single UV-active medium used for producing commercial UV lasers
$LiSrAlF_6 : Ce^{3+}$	Pinto *et al.*, 1994 [6]	Marshall *et al.*, 1994 [12]	Solarization; differential efficiency of up to 47%
$LiLu_{0.99}Y_{0.01}F_4 : Ce^{3+}$	Semashko *et al.*, 2000 [7]	Laroche *et al.*, 2003 [13]	Improved photochemical stability in comparison with $LiLuF_4 : Ce^{3+}$; differential efficiency of up to 62%
$KY_3F_{10} : Ce^{3+}$*	Semashko *et al.*, 2001 [8]	No data	Solarization of samples, short lasing

* The laser test results depend on the crystal-growth technology and experimental technique.

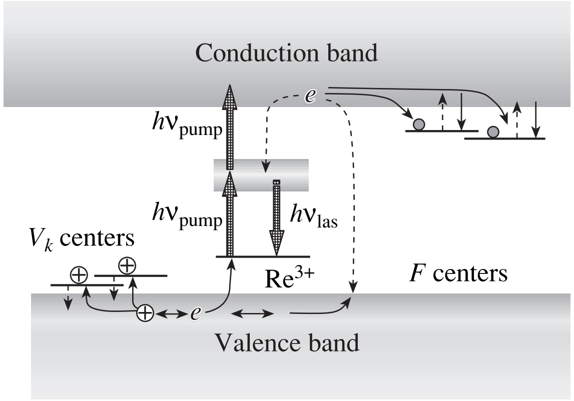

Fig. 1. Simplified schematic diagram for photodynamic processes induced by pump radiation in UV- and VUV-active media in which the laser transitions are the interconfigurational 5*d*–4*f* transitions in trivalent RE ions.

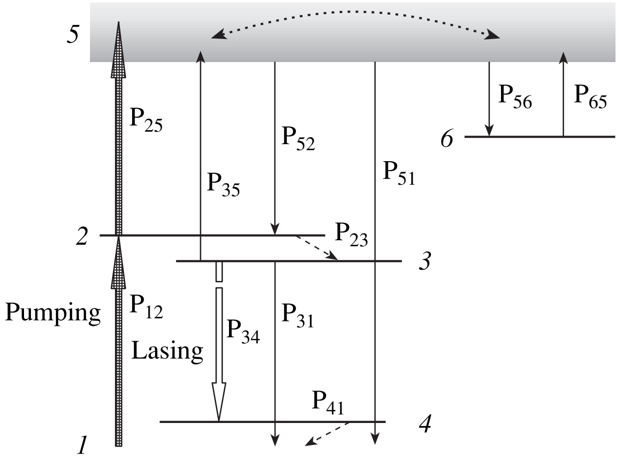

Fig. 2. Probabilistic model of photodynamic processes in UV-active crystals doped with RE ions.

scopic quality of crystalline samples, their prehistory, and even their origin.

In this study, we analyze the major factors determining the results of laser and pump-probe tests of solid-state active media for which the operating electron transitions are the interconfigurational 5*d*–4*f* transitions in RE ions.

2. RESULTS AND DISCUSSION

The nonreproducibility of the results of studies aimed at obtaining the UV or VUV lasing excitation is mainly due to the photodynamic processes (PDPs) induced by intense pump radiation in UV-active media based on crystals doped with RE ions. Among these processes are (see Fig. 1) nonlinear two-step absorption of pump radiation, absorption from the excited $4f^{n-1}5d$ states at lasing frequencies, multiphoton photoionization, reduction of activator ions, the migration of free carriers of both signs, their trapping by lattice defects [the formation of color centers (CCs)], and various types of carrier recombination. The CCs that are generated in crystals by UV pumping resonant with the 4*f*–5*d* interconfigurational transitions of RE ions feature various lifetimes. They can accumulate in the sample and also be bleached by either the exciting or laser radiation. The dynamic equilibrium between the processes indicated above controls losses induced by pumping in active media. These losses, in turn, decrease the UV and VUV lasing efficiency or even make lasing impossible. Moreover, laser test techniques and our understanding of the PDP mechanisms operative in active materials under conditions of pumping and lasing become extremely important in basic research aimed at evaluating the suitability of RE-doped crystals as UV- or VUV-active media. In particular, due to the accumulation of CCs induced by pump radiation in active media, it becomes important to consider the experiment prehistory and the sequence of experimenter operations [8].

We analyzed the influence of PDPs on the laser test results using a probabilistic method and the model shown in Fig. 2. The model is based on the conventional four-level scheme of a laser oscillator (energy levels *1*–*4*) in which the above-mentioned PDPs in active media are additionally taken into account. States *5* and *6* are the matrix conduction band and the CC ground state, respectively. For a pulse-pumped active medium placed in a high-Q laser cavity, the population of each energy level at the instant t and the stimulated-emission photon density $U_{\rm las}$ is determined by the balance kinetic equations

$$\frac{d}{dt}n_1 = -R(t)\sigma_{\rm pump}n_1 + P_{31}n_3 + P_{41}n_4 + P_{51}n_5,$$

$$\frac{d}{dt}n_2 = R(t)\sigma_{\rm pump}n_1 - (P_{23} + \sigma_{\rm ion}R(t))n_2 + P_{52}n_5,$$

$$\frac{d}{dt}n_3 = P_{23}n_2 - \Big[P_{31} + \sigma_{\rm ion}R(t)$$

$$+\left(\frac{1}{\tau_{\rm rad}} + (\sigma_{\rm las} - \sigma_{\rm las}^{ESA})cU_{\rm las}\right)\Big]n_3 + \sigma_{\rm las}cU_{\rm las}n_4,$$

$$\frac{d}{dt}n_4 = \left(\frac{1}{\tau_{\rm rad}} + \sigma_{\rm las}cU_{\rm las}\right)n_3 - (P_{41} + \sigma_{\rm las}cU_{\rm las})n_4, \quad (1)$$

$$\frac{d}{dt}n_5 = R(t)\sigma_{\rm ion}n_2 + (R(t)\sigma_{\rm ion} + \sigma_{\rm las}^{ESA}cU_{\rm las})n_3$$

$$-(P_{51} + P_{52} + P_{56})n_5$$

$$+\left(\sigma_{\rm pump}^{cc}R(t) + \sigma_{\rm las}^{cc}cU_{\rm las} + \frac{1}{\tau_{cc}}\right)n_6,$$

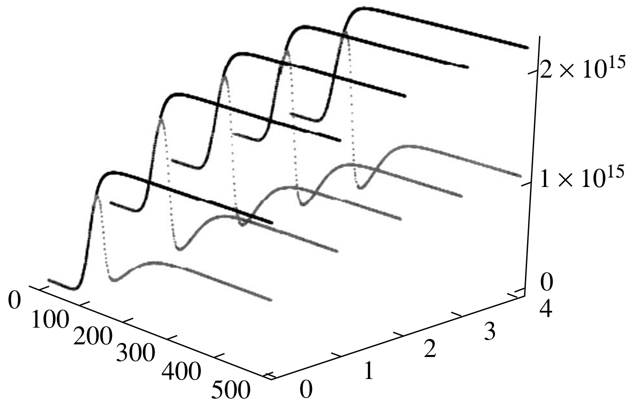

Fig. 3. Typical evolution of pump-induced losses in UV-active media without (dark curves) and with laser action (gray curves). The *X*, *Y*, and *Z* axes show the time (ns), the pump pulse number, and the defect (color center) concentration (cm^{-3}), respectively.

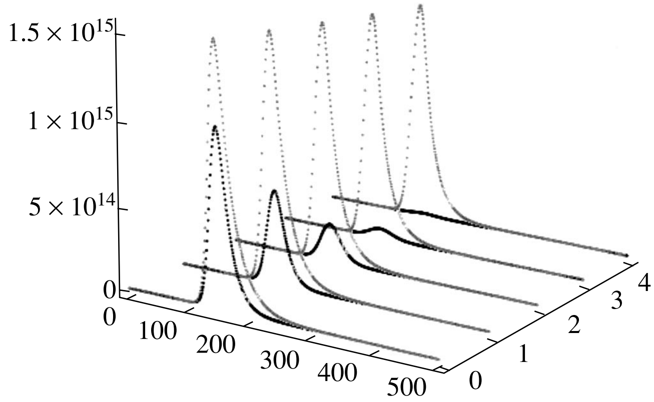

Fig. 4. Typical evolution of the laser UV radiation energy at a fixed pump energy for two values of the defect concentration, 10^{16} and 10^{17} cm^{-3} (gray and dark curves, respectively). The *X*, *Y*, and *Z* axes show the time (ns), pump pulse number, and the lasing photon flux density (cm^{-3}), respectively.

$$\frac{d}{dt}n_6 = P_{56}\frac{N_{\mathrm{def}} - n_6}{N_{\mathrm{def}}}n_5$$

$$-\left(\sigma_{\mathrm{pump}}^{cc}R(t) + \sigma_{\mathrm{las}}^{cc}cU_{\mathrm{las}} + \frac{1}{\tau_{cc}}\right)n_6,$$

$$\frac{d}{dt}U_{\mathrm{las}} = (U_{\mathrm{las}} + 1)[\sigma_{\mathrm{las}}(n_3 - n_4) - \sigma_{\mathrm{las}}^{ESA}n_3$$

$$-\left(\rho_0 + \sigma_{\mathrm{las}}^{cc}n_6 + \frac{1}{2L}\ln\left(\frac{1}{R}\right)\right)\Bigg]c,$$

where n_1–n_6 are the instantaneous populations of the corresponding states; $R(t)$ is the pump photon density (the time profile of the pump pulse); σ_{pump} and σ_{ion} are the absorption and ionization cross sections of the activator ion at the pump radiation frequency, respectively; σ_{las} and $\sigma_{\mathrm{las}}^{ESA}$ are the cross sections of the laser transition and absorption from the upper laser level at the stimulated-radiation frequency, respectively; $\sigma_{\mathrm{pump}}^{cc}$ and $\sigma_{\mathrm{las}}^{cc}$ are the CC absorption cross sections at the pump radiation and lasing frequencies, respectively; τ_{rad} and τ_{cc} are the lifetimes of the upper laser level and CC, respectively; P_{ij} are the corresponding transition probabilities; c is the speed of light; L is the active-medium length; R is the reflectance of the cavity output mirror; ρ_0 is the passive cavity loss factor; and N_{def} is the number of defect states responsible for the CC formation in the crystal.

To solve Eqs. (1) numerically, we used the experimental values of σ_{pump}, σ_{las}, $\sigma_{\mathrm{las}}^{ESA}$, τ_{rad}, τ_{cc}, P_{23}, and P_{41} available for crystals of fluoride scheelite [7, 8, 10, 11, 13] and colquirite [8, 10, 12]. The other parameters were tabulated to within two orders of magnitude using typical published values for other crystalline matrices (see, e.g., references in [14]). Calculations were carried out for 30-ns Gaussian pump pulses.

Above all, it is clear that lasing is impossible only in the case where the cross section of absorption from the excited $4f5d$ state (the upper laser level) exceeds the stimulated-emission cross section. In the opposite case, stimulated UV emission can be achieved even in the case of strong solarization of an active medium under pump radiation. However, it is unclear whether this emission will remain stable for a long time or the pump-induced loss will exceed the optical gain in the course of time and lasing will cease.

Analysis shows that the answer depends on the number N_{def} of crystal matrix microdefects (causing the formation of CCs), on the pumping rate, and on whether or not the excitation threshold for stimulated emission is reached at once at the first pump pulse. If lasing occurs, then the pump-induced CCs will be partly bleached by laser radiation and the induced-loss factor in the active medium will depend on the dynamic equilibrium between the generation and destruction of CCs. Figure 3 shows the evolution of the CC concentration in a sample. We can see that, as the stimulated emission arises, the pump-induced losses decrease abruptly and the time profile of the “dip” in the gray curves reproduces the UV lasing profile. If lasing does not occur, losses will increase from pulse to pulse until all of the defect states responsible for the formation of CCs that absorb in the frequency range of stimulated UV emission are filled (dark curves in Fig. 3).

Figure 4 shows the calculated lasing evolution at a fixed pump pulse energy for two values of the lattice defect concentration, 10^{16} and 10^{17} cm^{-3} (gray and dark curves, respectively). We can see that, at a high defect concentration, lasing is observed only during the first few pump pulses. If the laser cavity has a low Q factor

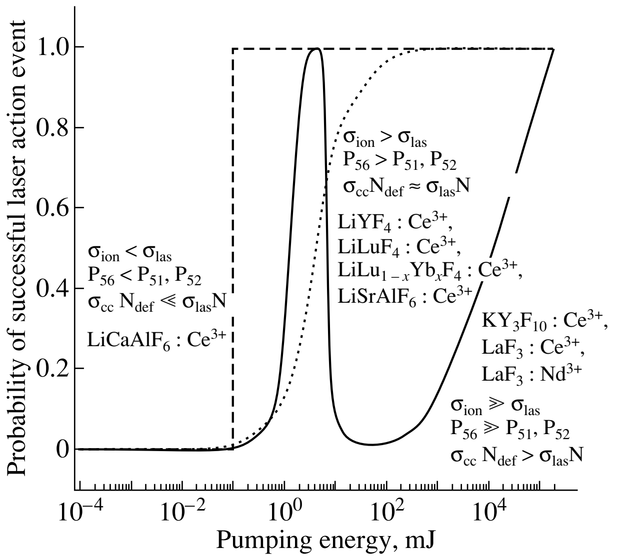

Fig. 5. Pump-energy dependence of the lasing-excitation probability at various values of the microscopic parameters of photodynamic processes in active media.

or is inaccurately aligned or an experimenter slowly increases the pump energy from pulse to pulse in order to determine the excitation threshold for stimulated emission, then it is likely that the lasing excitation will not occur at all at any reasonable pump energies due to CC accumulation. In this case, it would be incorrect to conclude that the sample is unsuitable as an active medium. The same incorrect conclusion might be drawn from the results of pump-probe experiments in which a low-intensity probe beam is used. It was for these reasons that the application prospects of solid-state UV and VUV tunable lasers based on interconfigurational 5*d*–4*f* transitions of RE ions had been doubted for a long time and that previous results had been considered incorrect. In particular, attempts to reproduce the laser test results for $LiLuF_4 : Ce^{3+}$ crystals, (which are currently the most efficient UV-active medium [7, 11]) had failed for several years.

The influence of PDPs on the laser test results obtained in the UV range becomes clear from Fig. 5, which shows the dependence of the probability of successful lasing excitation on the pump energy at various values of the microscopic parameters of PDPs in active media. This probability is determined as the number of lasing events divided by the number of pumping events.

If the excited-state absorption cross section from the 5*d* states into the host conduction band is small in comparison with the laser transition cross section ($\sigma_{ion} < \sigma_{las}$), the free-carrier recombination rate is high (P_{51}, $P_{52} > P_{56}$), and the number of lattice defects N_{def} is small, then the pump-energy dependence of the lasing event probability has the classical form plotted in Fig. 5 (dashed curve). In this case, there exists a threshold energy for stimulated emission excitation and each pump pulse with an energy higher than the threshold causes a lasing event. However, this classical dependence is not typical of most UV-active crystalline media. The sole exception to this is provided by UV-active $LiCaAlF_6 : Ce^{3+}$ crystals, which is explained by the extraordinarily wide band gap (~100000 cm^{-1}) of the matrix and the low probability of multiphoton ionization of the Ce^{3+} ion [15].

When the lattice defect density N_{def} is comparable to the activator ion concentration N, the threshold energy becomes dependent on the pumping rate, stimulated radiation intensity, and the prehistory of the active medium. For this reason, the dependence of the stimulated-emission excitation probability on the pump energy does not have the classical form. For example, if the activator ion ionization cross section is equal to or higher than the cross section of the laser transition ($\sigma_{ion} \geq \sigma_{las}$) and, simultaneously, the recombination rate of free carriers is lower than the CC generation probability (P_{51}, $P_{52} > P_{56}$), then there exists a pump energy range in which lasing will be observed for only a short time during the first few pump pulses (see, e.g., Fig. 4). At high pump energies, stimulated radiation can be observed for an infinitely long time. This situation is typical of UV-active $LiYF_4 : Ce^{3+}$, $LiLuF_4 : Ce^{3+}$, and $LiSrAlF_6 : Ce^{3+}$ crystals.

Finally, if the CC generation probability significantly exceeds the free-carrier recombination rate (P_{51}, $P_{52} \ll P_{56}$) and $\sigma_{ion} \gg \sigma_{las}$, then there exists a narrow pump energy range in which stable lasing becomes possible (solid curve in Fig. 5). In this case, experimenters are especially likely to draw incorrect conclusions, since stimulated radiation outside this range will be observed for only a short time and CC accumulation will make it impossible to overcome the lasing excitation threshold, because the next “stability range” corresponds to very high pumping rates, which are often unacceptable in practice. This case is typical of the majority of known crystalline UV- or VUV-active media, apparently including those in which the lasing effect has not been observed.

3. CONCLUSIONS

We have explained the results of laser tests of known solid-state UV- and VUV-active media, including failed attempts to excite lasing in several of them. It has been shown that in general the pump-energy dependence of the probability of generation of UV-stimulated radiation does not have the classical form and is determined by both objective and subjective factors, depending on the active-medium prehistory and experimenter operations. It has been proposed to correct the laser test techniques and “pump-probe” experiments by taking into account the pump-induced PDPs in active media. In particular, it was proposed to test new promising active media beginning from the maximum allowed pumping rates to overcome the excitation energy range in which lasing can be unstable.

When searching for new UV- and VUV-active media, one should prefer crystals with low cross sections of multiphoton ionization of impurity ions, with a small number of lattice defects, and with high free-carrier recombination rates, all other things being equal.

ACKNOWLEDGMENTS

This study was supported by the Russian Foundation for Basic Research (project no. 03-02-17361) and CRDF (grant BRHE REC-007).

REFERENCES

1. D. J. Ehrlich, P. F. Moulton, and R. M. Osgood, Jr., Opt. Lett. **4** (6), 184 (1979).
2. D. J. Ehrlich, P. F. Moulton, and R. M. Osgood, Jr., Opt. Lett. **5**, 10 (1980); **5**, 339 (1980).
3. R. W. Waynant and P. H. Klein, Appl. Phys. Lett. **46** (1), 14 (1985).
4. M. A. Dubinskiĭ, V. V. Semashko, A. K. Naumov, R. Yu. Abdulsabirov, and S. L. Korableva, Laser Phys. **4** (3), 480 (1994).
5. M. A. Dubinskiĭ, V. V. Semashko, A. K. Naumov, R. Yu. Abdulsabirov, and S. L. Korableva, J. Mod. Opt. **40** (1), 1 (1993).
6. J. F. Pinto, G. H. Rosenblatt, L. Esterowitz, and G. J. Quarles, Electron. Lett. **30**, 240 (1994).
7. V. V. Semashko, M. A. Dubinskiĭ, R. Yu. Abdulsabirov, A. K. Naumov, S. L. Korableva, P. Misra, and C. Haridas, in *Proceedings of the International Conference “LASERS 2000”* (STS, McLean, 2001), p. 675.
8. V. V. Semashko, M. A. Dubinskiĭ, R. Yu. Abdulsabirov, S. L. Korableva, A. K. Naumov, A. S. Nizamutdinov, and M. S. Zhuchkov, Proc. SPIE **4766**, 17 (2001); **4766**, 119 (2001).
9. M. A. Dubinskiĭ, A. C. Cefalas, E. Sarantopoulou, S. M. Spirou, C. F. Nikolaides, R. Y. Abdulsabirov, S. L. Korableva, and V. V. Semashko, J. Opt. Soc. Am. B **9** (7), 1148 (1992).
10. N. Sarukura, M. A. Dubinskiĭ, Z. Liu, V. V. Semashko, A. K. Naumov, S. L. Korableva, R. Yu. Abdulsabirov, K. Edamatsu, Y. Suzuki, T. Itoh, and Y. Segawa, IEEE J. Sel. Top. Quantum Electron. **1** (3), 792 (1995).
11. P. Rambaldi, R. Moncorge, S. Girard, J. P. Wolf, C. Pedrini, and J. Y. Gesland, OSA Trends Opt. Photonics Ser. **19**, 10 (1998).
12. C. D. Marshall, S. A. Payne, J. A. Speth, W. F. Krupke, G. J. Quarles, V. Castillo, and B. H. T. Chai, J. Opt. Soc. Am. B **11** (10), 2054 (1994).
13. M. Laroche, S. Girard, R. Moncorge, M. Bettinelli, R. Abdulsabirov, and V. Semashko, Opt. Mater. **22** (2), 147 (2003).
14. Z. Liu, N. Sarukura, and M. A. Dubinskiĭ, *Ultraviolet Spectroscopy and Ultraviolet Lasers* (Marcel-Dekker Inc., New York, 2002), p. 397.
15. V. V. Semashko, R. Yu. Abdulsabirov, S. L. Korableva, A. K. Naumov, B. M. Galjautdinov, A. C. Cefalas, Z. Kollia, and E. Sarantopoulou, Proc. SPIE **3239**, 240 (1997).

Translated by A. Kazantsev

Physics of the Solid State, Vol. 47, No. 8, 2005, pp. 1512–1515. From Fizika Tverdogo Tela, Vol. 47, No. 8, 2005, pp. 1455–1458.
Original English Text Copyright © 2005 by Gontchar, Mozhegorov.

PROCEEDINGS OF THE XII FEOFILOV WORKSHOP “SPECTROSCOPY OF CRYSTALS ACTIVATED BY RARE-EARTH AND TRANSITION-METAL IONS”

(Yekaterinburg, Russia, September 22–25, 2004)

Magnetic Structure and Antiferromagnetic Resonance Spectrum in Manganites: The Effect of Orbital Structure[1]

L. E. Gontchar* and A. A. Mozhegorov
Ural State University, pr. Lenina 51, Yekaterinburg, 620083 Russia
**e-mail: lyudmila.gonchar@usu.ru*

Abstract—This paper presents an investigation into the temperature dependence of magnetic structure and antiferromagnetic resonance frequencies. Taking into account the crystal and orbital structures of pure lanthanum manganite, it is shown that the orbital structure plays a crucial role in forming the magnetic structure. The *H*–*T* phase diagrams for the magnetic structure are drawn. *© 2005 Pleiades Publishing, Inc.*

1. INTRODUCTION

The interest in pure rare-earth orthorhombic manganites and manganite compounds doped by alkaline-earth ions has increased, because many unusual effects have been studied in experiments and theoretically predicted. We turn our attention to the interrelation between crystal, charge, orbital, and magnetic subsystems of pure rare-earth manganite.

The present work is aimed at theoretical study of the magnetic resonance spectra of manganite. The external magnetic field dependence of the magnetic structure and AFMR frequencies show the presence of a spin–flop transition [1]. Because of the strong effect of the orbital structure on the magnetic structure, the field behavior of the magnetic subsystem is more complicated than that of a usual antiferromagnet. The temperature dependences of the magnetic structure and AFMR frequencies show critical behavior [1–3]. The experimentally determined Néel temperature is 138 K [1–3]. At this temperature, the magnetization and the AFMR frequencies go to zero.

For description of the external magnetic field and temperature effects on the magnetic structure and AFMR frequencies, we use a recently developed model [4] which includes orbitally dependent interactions: superexchange interaction and single-ion anisotropy. The temperature dependence is described in the mean-field approximation. The field dependence and value of the spin–flop transition field are in excellent agreement with experiment [1]. Taking into account the overestimation of the Néel temperature due to approximation, the temperature dependences are also in good agreement with experiment [1–3] and explain the splitting of AFMR frequencies without an external magnetic field and the disappearance of this splitting near the Néel temperature [3].

Using the described calculations, the *H*–*T* phase diagrams in the main field directions (*a*, *b*, *c*) are drawn, which show antiferromagnetic, ferromagnetic, and paramagnetic regions of the magnetic structure of pure manganite.

2. CRYSTAL AND ORBITAL STRUCTURES OF $LaMnO_3$

Manganite crystal (Fig. 1) has a distorted perovskite structure (space group *Pnma*). The distortions are of two kinds: rotational distortions of oxygen octahedra and shifts of the lanthanum ion similar to those in orthoferrite crystals and Jahn–Teller distortions of oxygen octahedra of the *e* type [5]. The strong electron–lattice interaction causes the presence of *e*-type distortions due to the degenerate trivalent manganese-ion ground state and helps the orbital structures to be established.

The wave function of the ground state of each manganese ion in the distorted perovskite crystal is [4]

$$\psi_n = \sin(\phi_n/2)\varphi_{n\theta} + \cos(\phi_n/2)\varphi_{n\varepsilon}, \qquad (1)$$

where $\varphi_{n\theta}$ and $\varphi_{n\varepsilon}$ are the eigenfunctions of the degenerated ^5E term. The values of ϕ_n can be derived from experimental data using the parameters of the lattice distortions [5] within the framework of strong electron–lattice coupling. The orbital structure is described by a correlation of orbital angles,

$$\phi_1 = -\phi_2 = -\phi_3 = \phi_4 = \phi, \qquad (2)$$

where ϕ characterize the orbital state of the Mn^{3+} sublattice according to Eq. (2).

---

[1] This article was submitted by the authors in English.

3. ORBITAL-DEPENDENT MAGNETIC INTERACTIONS

In order to predict the magnetic properties, we use the following spin -Hamiltonian:

$$\hat{H} = \sum_{n>m} J_{n,m}(\mathbf{S}_n \cdot \mathbf{S}_m) + \hat{H}_n^{\text{anis}} + g\mu_{\text{B}}\sum_n(\mathbf{H}\cdot\mathbf{S}_n), \quad (3)$$

where

$$J_b = J_0\frac{\cos^2\varphi_b}{r_b^{10}}[1 + 2\alpha\cos\phi + \beta\cos^2\phi], \quad (4)$$

$$J_{ac} = J_0\frac{\cos^2\varphi_{ac}}{r_{ac}^{10}}[1 - \alpha\cos\phi + \beta(\cos^2\phi - 3/4)], \quad (5)$$

the parameters of dependences are [4] $J_0 = 1.69 \times 10^4$ K Å^{10}, $\alpha = 1.0$, and $\beta = 4.5$; and the experimental structural parameters are $\varphi_b = 155.1°$ and $\varphi_{ac} = 154.8°$ (Mn–O–Mn bond angles), $r_b = 1.97$ Å and $r_{ac} = 2.05$ Å (mean Mn–O distances), and $\phi = 107.8°$ (angle of orbital mixing without ambient pressure [5]). The single-ion anisotropy of manganese ions in the octahedral oxygen environment is given by

$$\begin{aligned} \hat{H}_n^{\text{anis}} &= D_n S_{nzl}^2 + E_n(S_{nxl}^2 - S_{nyl}^2), \\ D_n &= 3P\cos\phi, \quad E_n = \sqrt{3}P\sin\phi, \end{aligned} \quad (6)$$

where $P = -1.15$ K [4], n enumerates manganese ions, and the index l denotes local axes of octahedra nearly corresponding to cubic axes. In order to take into account the rotational distortions, we have to transform Hamiltonian (6) to the *Pnma* axes.

The temperature dependence can be taken into account within the framework of the molecular field approximation:

$$\langle S_i\rangle = S_i B_{S_i}\left(\frac{g\mu_B\langle H_i^{\text{eff}}\rangle S_i}{kT}\right), \quad (7)$$

where $B_{S_i}(x)$ is the Brillouin function and

$$\mathbf{H}_i^{\text{eff}} = \sum_j J_{ij}\mathbf{S}_j + \partial H_i^{\text{anis}}/\partial\mathbf{S}_i + g\mu_{\text{B}}\mathbf{H} \quad (8)$$

is the effective magnetic field acting on the ith sublattice.

4. RESULTS AND DISCUSSION

These parameters describe a magnetic structure of the *A* type. The single-ion anisotropy (or the Dzyaloshinsky–Moria interaction, as in paper [3]) establishes the magnetic structure to be of $A_xF_yG_z$ type (in *Pnma* notation) [4]. The molecular field theory gives overestimated critical temperatures for magnetic transitions. For LaMnO$_3$, we obtained $T_{\text{N}} = 216$ K, while experimentally $T_{\text{N}} \approx 140$ K is observed [2, 3]. However, qualitatively, our results are in good agreement with experiment (see Figs. 2, 3). The temperature dependence of total magnetization is given in Fig. 3.

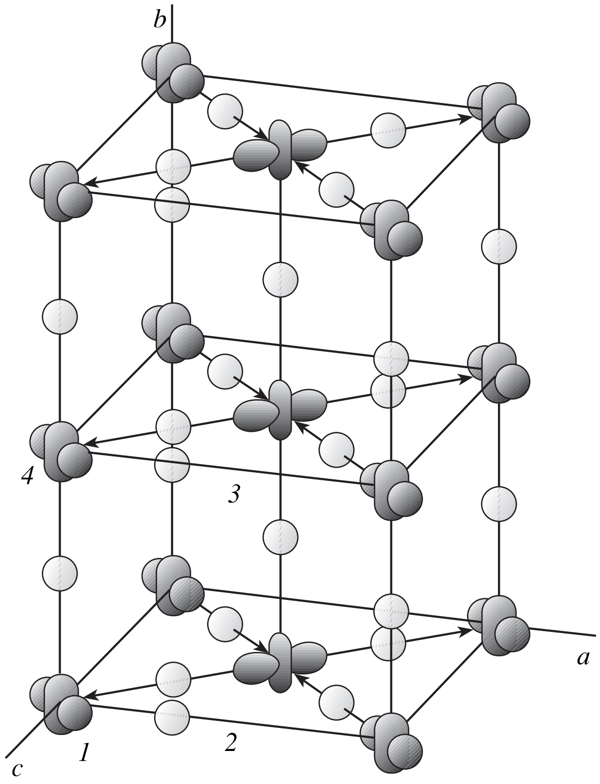

Fig. 1. Crystal and orbital structures. Lanthanum ions are omitted. Manganese ions are drawn as *e* orbitals. Arrows show *e*-type distortions of oxygen octahedral. Numbers enumerate orbital and magnetic sublattices.

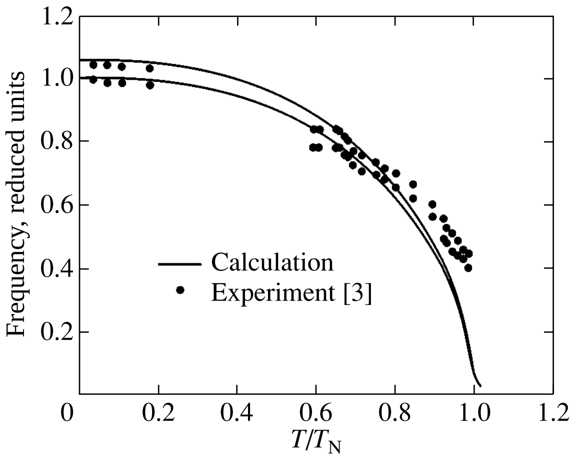

Fig. 2. Temperature dependence of AFMR frequencies.

The slight discrepancy for the AFMR frequencies temperature dependence is reasoned to be caused by an

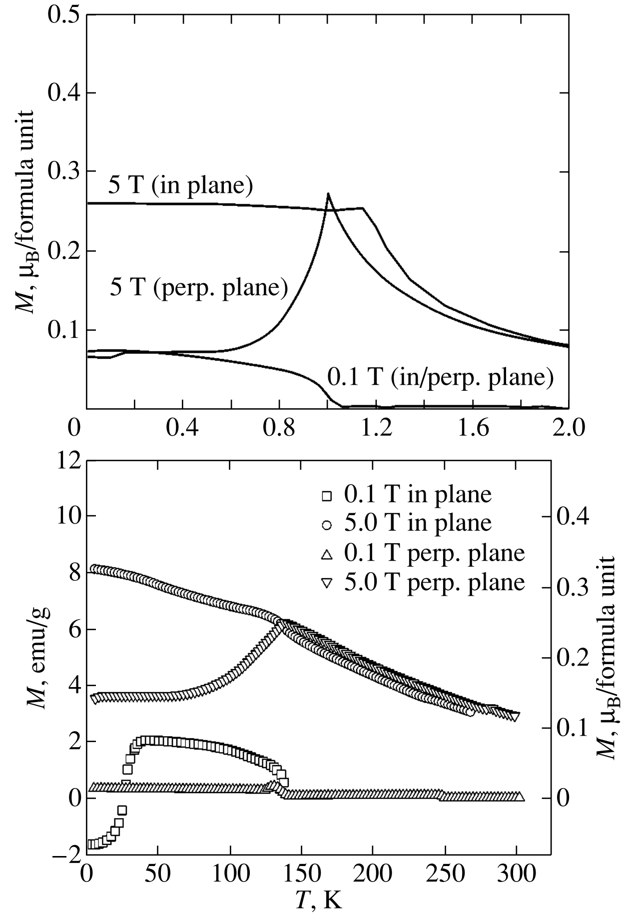

Fig. 3. Temperature dependence of total magnetization. Experimental data are taken from paper [6].

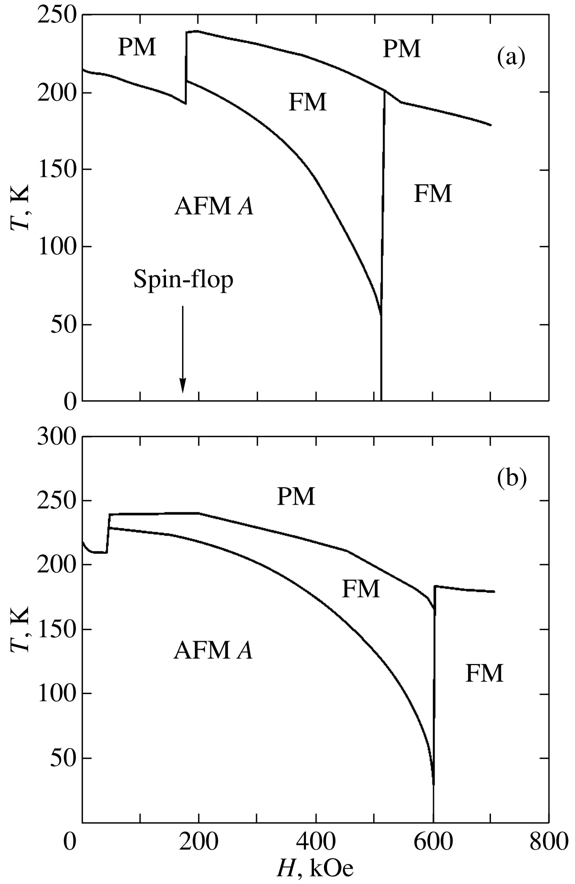

Fig. 4. H–T phase diagram. (a) $H \parallel x$; (b) $H \parallel y$. AFM A is the A-type antiferromagnet.

inaccuracy in the measurements near the edge of the receptive band at low temperatures. As for Fig. 3, the divergence between the theoretical and experimental [6] data (which almost coincide even quantitatively) is also caused by a twinning of the $LaMnO_3$ crystal and magnetic domains (which could be treated by field cooling of the sample [7]). Magnetic domains are the reason for the presence of negative magnetization at low temperatures and low in-plane fields (see Fig. 3).

In order to determine and explain the different magnetic structures of pure lanthanum manganite, magnetic field–temperature phase diagrams (H–T) in different directions of the magnetic field were obtained (Fig. 4). As is known, pure lanthanum manganite is a canted antiferromagnet. Its magnetic structure, therefore, is characterized by a mixture of basic magnetic structures (A, C, G—AFM structures and an F—FM structure). With increasing temperature, the antiferromagnetic A component decreases but the ferromagnetic F component remains almost constant. That is why the model predicts an A-antiferromagnetic to F-ferromagnetic transition (AFM A to FM). While the temperature of this transition is close to that of the ferromagnetic–paramagnetic transition (FM to PM), one can observe a direct switch from the AFM A to PM phase (for fields up to 45 kOe for H perpendicular to the easy axis and up to 190 kOe for H parallel to the easy axis) and the gap between the AFM A–FM and FM–PM (FM gap on the diagrams) transition temperatures widens with increasing magnetic field. This effect is stimulated by strong damping of the A component by the magnetic field.

Due to a spin–flop transition in the external magnetic field directed along the easy axis x near H = 190 kOe [1, 4], there is a slight step in the corresponding diagram. The point is that there are two structures that are close energetically ($A_xF_yG_z$ and $G_xC_yA_z$) and a switch in the energy minimum takes place in the spin–flop field when the magnetic structure is changed rapidly.

5. CONCLUSIONS

A theoretical investigation of the temperature dependences of the magnetic properties of $LaMnO_3$ was performed within the framework of the spin Hamiltonian including three parts: isotropic exchange, single-ion anisotropy, and Zeeman interaction. Mean field approximation was used to obtain the macroscopic parameters.

Experimental temperature dependences for the total magnetizations in low (0.1 T) and high (5 T) magnetic fields were reproduced. *H*–*T* phase diagrams were obtained and qualitatively discussed. A rich phase diagram originates from the nontrivial character of the magnetic interactions caused by the orbital structure in the compound. Different magnetic parameters were varied to determine their influence on the behavior of the system in a magnetic field. It was found that single-ion anisotropy plays a crucial role in the reaction of the magnetic system with the external magnetic field along the easy axis of magnetization (where a spin–flop transition is observed). Thus, this factor does not seem to be as important as antiferromagnetic exchange when we investigate the perpendicular direction (hard direction) of the external magnetic field. Thereby, it is evident that $LaMnO_3$ possesses a nontrivial, strongly anisotropic magnetic structure caused by its orbital and crystal structures.

ACKNOWLEDGMENTS

This work was partially supported by CRDF REC-005 and the Russian Foundation for Basic Research, project nos. 04-02-16204 and 04-02-96078.

REFERENCES

1. Y. Endoh and K. Hirota, J. Phys. Soc. Jpn. **66**, 2264 (1997).
2. F. Moussa, M. Hennion, J. Rodriguez-Carvajal, H. Moudden, L. Pinsard, and A. Revcolevschi, Phys. Rev. B **54**, 15149 (1996).
3. V. Yu. Ivanov, V. D. Travkin, A. A. Mukhin, S. P. Lebedev, A. A. Volkov, A. Pimenov, A. Loidl, A. M. Balbashov, and A. V. Mozhaev, J. Appl. Phys. **83**, 7180 (1998).
4. L. E. Gonchar, A. E. Nikiforov, and S. E. Popov, JETP **91**, 1221 (2000).
5. Q. Huang, A. Santoro, J. W. Lynn, R. W. Erwin, J. A. Borchers, J. L. Peng, and R. L. Greene, Phys. Rev. B **55**, 14987 (1997).
6. L. Mihaly, D. Talbayev, L. F. Kiss, J. Feher, and A. Janossy, Phys. Rev. B **69**, 024414 (2004).
7. V. Markovich, I. Fita, A. I. Shames, R. Puzniak, E. Rozenberg, Ya. Yuzhelevski, D. Mogilyansky, A. Wisniewski, Ya. M. Mukovskiĭ, and G. Gorodetsky, J. Phys.: Condens. Matter **15**, 3985 (2003).

Physics of the Solid State, Vol. 47, No. 8, 2005, pp. 1516–1522. From Fizika Tverdogo Tela, Vol. 47, No. 8, 2005, pp. 1459–1464.
Original English Text Copyright © 2005 by Mironova-Ulmane, Skvortsova, Kuzmin, Ulmanis, Sildos, Cazzanelli, Mariotto.

PROCEEDINGS OF THE XII FEOFILOV WORKSHOP “SPECTROSCOPY OF CRYSTALS ACTIVATED BY RARE-EARTH AND TRANSITION-METAL IONS”

(Yekaterinburg, Russia, September 22–25, 2004)

Magnetic Ion Exchange Interactions in NiO–MgO Solid Solutions[1]

N. Mironova-Ulmane*, V. Skvortsova*, A. Kuzmin*, U. Ulmanis*, I. Sildos,**
E. Cazzanelli*, and G. Mariotto******
** Institute of Solid State Physics, University of Latvia, Riga, LV-1063 Latvia*
e-mail: ulman@latnet.lv
*** Institute of Physics, University of Tartu, Tartu, EE-2400 Estonia*
**** INFM and Dipartimento di Fisica, Universitá della Calabria, Arcavacata di Rende (Cosenza), I-87036 Italy*
***** INFM and Dipartimento di Fisica, Universitá di Trento, Povo (TN), I-38050 Italy*

Abstract—In this work, a review of recent experimental data and their interpretation for $Ni_cMg_{1-c}O$ solid solutions is given. In particular, the influence of exchange interactions between Ni^{2+} ions on the structural, optical, magnetic, and vibrational properties is discussed. *© 2005 Pleiades Publishing, Inc.*

1. INTRODUCTION

Solid solutions in which magnetic ions occupy sites in a face-centered-cubic (fcc) lattice have been of continued interest over recent decades [1]. Magnetic ordering in these compounds depends on the concentration and site distribution of magnetic ions, as well as on the signs and strengths of the nearest neighbor (NN) J_{NN} and next-to-nearest-neighbor (NNN) J_{NNN} superexchange interactions [2]. Since superexchange interactions depend on the values of the cation–anion distance and of the cation–anion–cation angle [2], precise knowledge of the relationship between the crystallographic and magnetic structure is important for a deep understanding of the exchange phenomenon in these materials. In this paper, we will review the available experimental data and their interpretation for the case of exchange interactions between Ni^{2+} ions in $Ni_cMg_{1-c}O$ solid solutions.

Pure nickel oxide (NiO) is a classical example of a type-II antiferromagnet having a high Néel temperature $T_N = 523$ K [3]. Below T_N, the spins of the Ni^{2+} ions are ordered ferromagnetically in the {111} planes, where they lie along the $\langle 11\bar{2}\rangle$ axes [4, 5]. In the paramagnetic phase, pure NiO has a rock-salt-type crystal structure with nickel ions located at the center of the NiO_6 octahedra. In the antiferromagnetic (AF) phase, the structure of NiO undergoes a week cubic-to-rhombohedral distortion due to the magnetostriction effect. The AF structure of NiO is determined by dominating superexchange interactions in linear Ni^{2+}–O^{2-}–Ni^{2+} atom chains ($J_{NNN} \approx 150\ cm^{-1}$) and weak 90° superexchange Ni^{2+}–O^{2-}–Ni^{2+} interactions ($J_{NN} \approx 11\ cm^{-1}$) [4, 6, 7]. Second harmonic generation was recently observed in NiO below the Néel temperature; it is due to the combined magnetic-dipole and electric-dipole transitions between the $3d^8$ levels of the Ni^{2+} ion subject to the crystal field [8].

Substitution of nickel ions by magnesium ions leads to the formation of a continuous series of $Ni_cMg_{1-c}O$ solid solutions and stabilizes the cubic structure [9, 10].

A magnetic phase diagram of the $Ni_cMg_{1-c}O$ system has been established by elastic magnetic neutron scattering [11] and SQUID magnetometry [11, 12]. There are four domains (Fig. 1): (1) a homogeneous antiferromagnet ($0.63 \le c \le 1$), (2) a tricritical region or a frustrated antiferromagnet ($0.04 \le c \le 0.63$), (3) a spin-glass state ($0.25 \le c < 0.4$), and (4) a diamagnet ($c \le 0.2$) [11]. Complementary information on the magnetic ordering in $Ni_cMg_{1-c}O$ single crystals has been obtained from microscopic investigations of the composition and temperature dependence of the domain structure [13]. It was found that the regular domain structure is more sensitive to the concentration of magnesium ions than T_N and appears upon cooling at temperatures well below T_N (dashed line in Fig. 1) [13]. The aforementioned techniques provide a rather macroscopic view on the magnetic structure of solid solutions. In what follows, we discuss experimental results which shed light on the magnetic interactions in $Ni_cMg_{1-c}O$ at the microscopic level.

---

[1] This article was submitted by the authors in English.

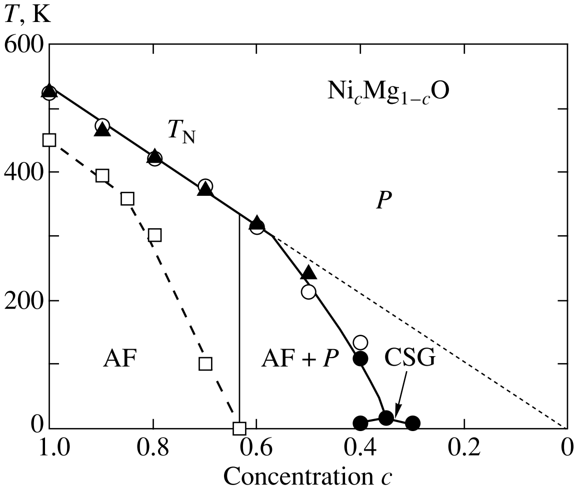

Fig. 1. Magnetic phase diagram of the $Ni_cMg_{1-c}O$ system according the elastic magnetic neutron scattering [11] and SQUID magnetometry [11, 12]. The region of the infinite antiferromagnetic cluster [13] is indicated by open squares. *P* is paramagnetic region, AF is antiferromagnetic region, and CSG is cluster spin glass.

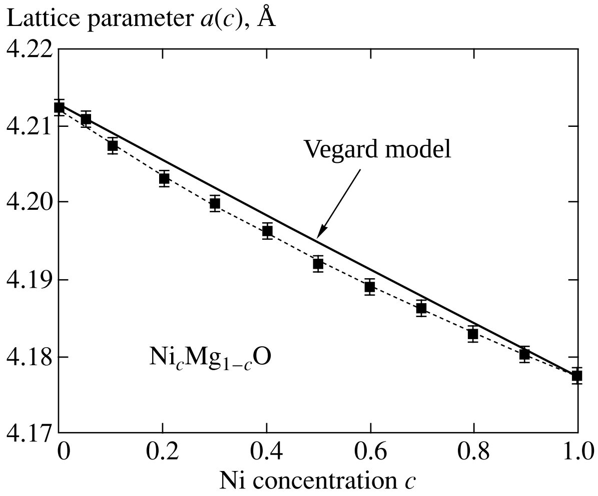

Fig. 2. Variation of the lattice parameter $a(c)$ (shown by points) in $Ni_cMg_{1-c}O$ [25]. The solid line shows the linear Vegard model. The dashed line corresponds to the model $a(c) = c^2a_{NiO} + 2c(1-c)(b_1 + b_2c) + (1-c)^2(ca_{NiO} + (1-c)a_{MgO})$ with $b_1 = 4.206$ Å and $b_2 = -0.014$ Å, taking into account a displacement of nickel atoms upon dilution by magnesium [25].

2. SAMPLE PREPARATION AND EXPERIMENTAL TECHNIQUES

The $Ni_cMg_{1-c}O$ samples used in the present work were green-colored polycrystalline powders or single crystals [9, 10]. Polycrystalline solid solutions were prepared using ceramic technology from the appropriate amounts of aqueous solutions of $Mg(NO_3)_2 \cdot 6H_2O$ and $Ni(NO_3)_2 \cdot 6H_2O$ salts, which were mixed and slowly evaporated. The remaining dry “flakes” were heated up to 500–600°C to remove NO_2 completely. The obtained polycrystalline solid solutions were pressed and annealed for 100 h at 1200°C in air and then rapidly cooled to room temperature. $Ni_cMg_{1-c}O$ single crystals were grown by the method of chemical transport reactions (the sandwich technique) on the (100) face of MgO single crystals. The chemical composition of samples was controlled by instrumental neutron-activated analysis [14]; the content of nickel was in agreement with the stoichiometric content to within ±0.01%. The obtained $Ni_cMg_{1-c}O$ solid solutions were studied by several experimental techniques: IR–VIS optical absorption [15–17], photoluminescence [18–22] and Raman spectroscopy [23, 24], x-ray [25] and neutron [11] diffraction, and x-ray absorption spectroscopy (XAS) [26–28]. The details of the experiments are available from the corresponding references.

3. RESULTS AND DISCUSSION

First, let us discuss the influence of magnetic interaction on the crystallographic structure of $Ni_cMg_{1-c}O$ solid solutions, whose continuous series can be prepared due to the small difference (about 0.02 Å) of the ionic radii of Ni^{2+} and Mg^{2+} ions [9, 10]. It was believed for a long time that the lattice parameter of the $Ni_cMg_{1-c}O$ system depends linearly on the composition and follows the Vegard rule: $a(c) = ca_{NiO} + (1-c)a_{MgO}$ [9, 12, 29, 30]. However, the results of Ni *K*-edge XAS studies [26, 27] suggested a deviation of the local environment around Ni^{2+} ions from the Vegard model. It was observed that, while the nearest interatomic Ni–O and Ni–Mg distances change linearly, according to the Vegard model, the nearest Ni–Ni distance remains nearly constant at all compositions [26, 27]. These results stimulated more accurate x-ray diffraction (XRD) study [25], which confirmed the XAS findings. It was determined that the values of the lattice parameter $a(c)$ in the $Ni_cMg_{1-c}O$ series differ from those predicted by the Vegard model and that the maximum deviation is about –0.002 Å for $c \sim 0.4$ (Fig. 2) [25]. Note that this $a(c)$ dependence can be well fitted by the model assuming constant nearest Ni–Ni distance [25]. Thus, both XRD and XAS experiments suggest a distortion of the local environment around the nickel ion, which progressively increases upon dilution with magnesium ions. The origin of this distortion is attributed to the exchange interaction between neighboring nickel ions, causing them to displace to an off-center position. We correlate a symmetry lowering at nickel ion sites with the observed splitting of the zero-phonon line in the low-temperature optical absorption and photoluminescence spectra of $Ni_cMg_{1-c}O$ for $c \leq 0.2$ in the energy range 7800–8300 cm^{-1} of the $^3A_{2g} \longleftrightarrow {}^2T_{2g}$ band [21]. The existence of the two sharp zero-phonon

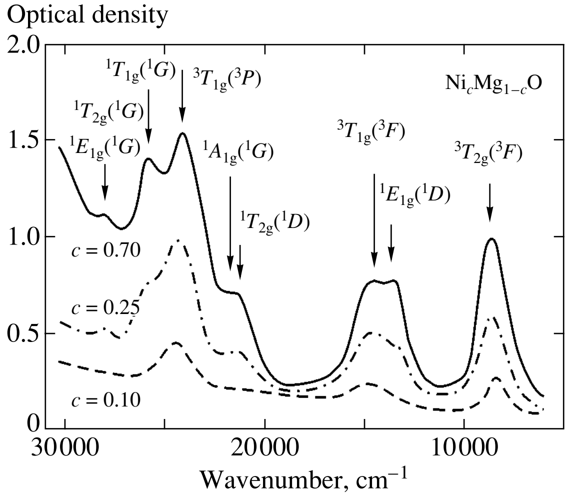

Fig. 3. Room-temperature optical absorption in Ni$_c$Mg$_{1-c}$O single crystals [10].

lines (E and T) in the $^3A_{2g} \longleftrightarrow {}^3T_{2g}$ band at 8005 and 8182 cm^{-1} has been traditionally explained by the spin-orbit splitting [18–20, 31]. However, according to calculations [31], four zero-phonon lines are expected with relative intensities of 0.677, 1.000, 0.790, and 0.235, while only two lines with relative intensities equal to 0.645 and 1.000 are observed in the experiment [18–21]. Moreover, it is known that at nickel concentrations $0.01 < c < 0.2$, additional zero-phonon lines appears at 7822, 7888, 7921, and 7937 cm^{-1}, which are attributed to the exchange-coupled Ni^{2+}–Ni^{2+} pairs formed due to the 90° superexchange Ni^{2+}–O^{2-}–Ni^{2+} interactions [19–21]. The maximum number of isolated pairs is observed at $c = 0.05$, and they aggregate into clusters at higher nickel concentrations [20, 21].

The optical properties of the Ni$_c$Mg$_{1-c}$O solid solutions with a small concentration of nickel ions has been studied in detail previously [18–21, 32–34]. Therefore, we will further discuss the case of high nickel content ($c > 0.05$). The optical absorption spectra of Ni$_c$Mg$_{1-c}$O solid solutions can be interpreted using the energy level diagram of a free nickel ion Ni^{2+}(3d^8) in a cubic crystal field. The observed absorption bands (Fig. 3) are related to the parity-forbidden d–d transitions, three of which, $^3A_{2g}(F) \longrightarrow {}^3T_{2g}(F)$, $^3A_{2g}(F) \longrightarrow {}^3T_{1g}(F)$, and $^3A_{2g}(F) \longrightarrow {}^3T_{1g}(P)$, are spin-allowed ($\Delta S = 0$), whereas the others are forbidden. We will consider the two lowest bands, which correspond to the magnetic-dipole transition $^3A_{2g}(F) \longrightarrow {}^3T_{2g}(F)$ at ~8800 cm^{-1} and the electric-dipole transition $^3A_{2g}(F) \longrightarrow {}^1E_g(D)$ at ~13800 cm^{-1}. Note that both bands are sensitive to the magnetic ordering.

At low temperature, the magnetic-dipole band $^3A_{2g}(F) \longrightarrow {}^3T_{2g}(F)$ consists of two sharp zero-phonon lines (peaks A and B in Fig. 4), phonon satellite peaks, and a broad sideband [16, 19]. The peak A at ~7800 cm^{-1} is assigned to the pure exciton transition, whereas the peak B at ~7840 cm^{-1} is assigned to the exciton–one-magnon excitation [16, 19]. Here, the one-magnon excitation occurs at the Brillouin zone center (BZC) and its energy is defined by the difference between peaks A and B. Upon a change in temperature or substitution of nickel ions with magnesium ions, the band experiences homogeneous and inhomogeneous broadening, which influences the intensity and the position of both peaks and of the phonon sideband [35]. An introduction of less than 10% magnesium ions ($c > 0.9$) results in a strong damping of the peak B intensity already at $T = 6$ K, which is very far below the Néel temperature (Fig. 1). Within the accuracy of our experimental data, the one-magnon energy in Ni$_c$Mg$_{1-c}$O for $c > 0.95$ is nearly unchanged and equals that of pure NiO $\omega_{1M} \approx 41$ cm^{-1}. There is also some evidence of a decrease in ω_{1M} by ~8 cm^{-1} for $c = 0.95$ (Fig. 4). Note that a similar variation of ω_{1M} with composition has been observed recently in one-magnon Raman scattering [24]. For $c \le 0.9$, the one-magnon contribution cannot be detected as a distinct peak at 6 K; however, a shoulder on peaks A and B is visible in Ni$_{0.90}$Mg$_{0.10}$O (Fig. 4). According to the magnetic phase diagram (Fig. 1), the antiferromagnetic ordering in Ni$_c$Mg$_{1-c}$O exists [11, 12] at $T = 6$ K for $c \ge {\sim}0.4$ and, moreover, an infinite antiferromagnetic domain structure is observable for $c > {\sim}0.6$ [13]. In pure or lightly doped NiO, an infinite antiferromagnetic domain structure is present up to ~450 K [13] and the antiferromagnetic ordering remains up to 523 K. However, these results reflect the macroscopic magnetic properties of NiO and Ni$_c$Mg$_{1-c}$O, whereas optical spectroscopy provides a microscopic point of view. Our results indicate that long-wavelength BZC magnons are very sensitive to a disturbance of long-range spin–spin correlations due to a temperature increase or dilution by nonmagnetic ions.

The temperature dependence of the electric-dipole transition $^3A_{2g}(F) \longrightarrow {}^1E_g(D)$ in Ni$_{0.60}$Mg$_{0.40}$O is shown in Fig. 5, and a variation of the band with composition is shown in Fig. 3. Note that the $^1E_g(D)$ band partially overlaps with the $^3T_{1g}(F)$ band located at ~15700 cm^{-1}. The intensity of the $^1E_g(D)$ band for $c = 0.60$ experiences an abrupt decrease in the temperature interval 200–275 K, just below the Néel temperature $T_{\rm N}$ ~ 320 K (Fig. 5). At room temperature, an abrupt change occurs between $c = 0.25$ and 0.7 (Fig. 3). Our previous study [36] of this band in KNiF$_3$ single crystals suggests that the $^1E_g(D)$ band has a complex structure, consisting of the exciton–photon background and the exciton–two-magnon contribution sitting on it. The pure exciton transition is parity- and spin-forbidden, so it is not visible in the experimental data but is expected to be at ~12500 cm^{-1}. The two magnons are excited at the Brillouin zone boundary (BZB), so they are short-

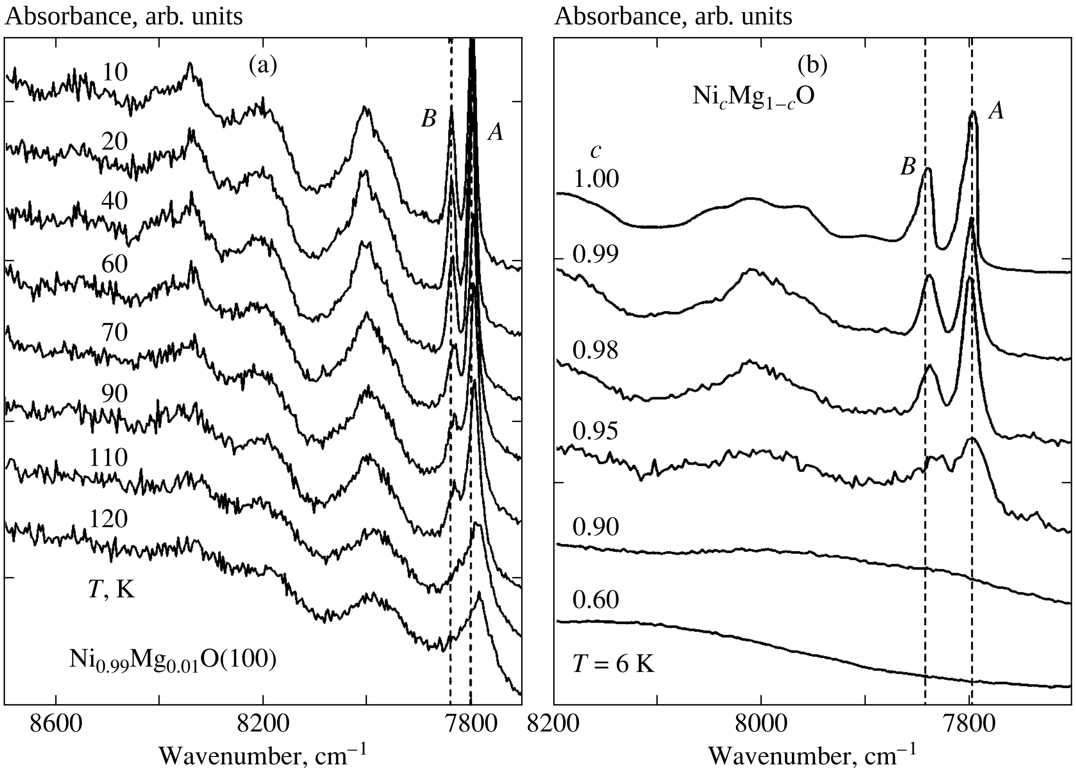

Fig. 4. (a) Temperature and (b) concentration dependences of the low-energy part of the $^3A_{2g}(F) \longrightarrow {}^3T_{2g}(F)$ absorption band in $Ni_cMg_{1-c}O$ single crystals [16]. The peaks due to the pure excition transition and exciton–one-magnon excitation are indicated by the letters *A* and *B*, respectively.

wavelength magnons and, thus, are sensitive to the short-range magnetic ordering. As a result, the two-magnon contribution remains visible up to T_N (Fig. 5). Similar behavior of the two-magnon contribution has also been found in the Raman spectra of NiO [37] and $KNiF_3$ [38]. The two-magnon energy ω_{2M} can be roughly estimated to be ~1400 cm^{-1}, which is much larger than in $KNiF_3$ (ω_{2M} = 813 cm^{-1}) due to the stronger superexchange interactions between Ni^{2+} ions.

Contrary to the optical absorption spectra (Fig. 3), where several bands due to intra Ni^{2+} ion transitions are observed (Fig. 3), the photoluminescence spectra [22] in the range 11000–22000 cm^{-1} at high nickel concentrations consist of only two broad bands (Fig. 6): a red band at 12500 cm^{-1} and a green band at 18500 cm^{-1}. The intensity of both bands decreases with increasing temperature but is still detectable at room temperature. Moreover, we found that the intensity ratio for the two bands depends strongly on the sample composition and the excitation laser wavelength [22]. We attribute the two bands to the impurity- or defect-perturbed Ni^{2+} states, similar to that observed [39, 40] in MnO and MnS. The band at 12500 cm^{-1} is related to the transitions from some defect levels located in the gap between the $^3T_{1g}(F)$ and $^1T_{2g}(D)$ Ni^{2+} levels. Similarly, the position of the red band is attributed to the defect levels located in the gap between the $^3T_{2g}(F)$ and $^1E_g(D)$ Ni^{2+} levels. The observed luminescence bands experience inhomogeneous and homogeneous broadening due to compositional disorder, exciton–phonon and exciton–magnon interactions. The intensity of the bands is also determined by an off-center displacement of nickel ions due to substitution by magnesium.

The room temperature Raman spectrum of pure NiO consists of several bands (Fig. 7): a one-magnon (1*M*) band [41] at 34 cm^{-1}, five vibrational bands [6]—one-phonon (1*P*) *TO* (at 440 cm^{-1}, peak *A*) and *LO* (at 560 cm^{-1}, peak *B*) modes, two-phonon (2*P*) 2*TO* modes (at 740 cm^{-1}, peak *C*), *TO* + *LO* (at 925 cm^{-1}, peak *D*) and 2*LO* (at 1100 cm^{-1}, peak *E*) modes, and a two-magnon (2*M*) band *F* at ~1500 cm^{-1}. The frequency and shape of the phonon bands do not vary with temperature, whereas the magnon scattering intensities are strongly temperature-dependent and shift to lower frequencies and decrease in intensity with increasing temperature, to disappear completely close to the Néel point [6, 41].

The one-magnon Raman scattering measured for $c \geq 0.6$ is shown in Fig. 7a for a $Ni_{0.8}Mg_{0.2}O$ solid solution [24]. Here it can be detected up to about 270 K, and the one-magnon frequency extrapolated to $T = 0$ K is about 26 ± 1 cm^{-1}. As expected, the one-magnon frequency

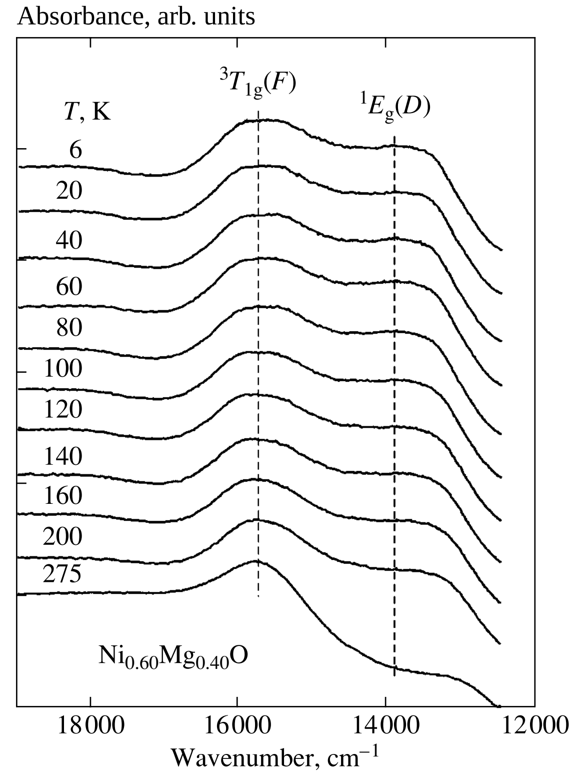

Fig. 5. Temperature dependences of $^3A_{2g}(F) \longrightarrow {}^3T_{1g}(F)$, $^1E_g(D)$ absorption bands in $Ni_{0.60}Mg_{0.40}O$ single crystals [16].

decreases and the peak progressively broadens with increasing temperature. The extrapolation of the temperature dependence of the one-magnon frequency to $\omega_{1M} = 0$ gives a critical temperature $T_C \approx 300$ K, which is much smaller than the Néel temperature [11] T_N (c = 0.8) ≈ 420 K. The analysis of one-magnon Raman scattering for other compositions allowed us to conclude that (a) the one-magnon frequency extrapolated to T = 0 K experiences an abrupt change between c = 0.99 and 0.9 and (b) the one-magnon energy for highly diluted nickel oxide vanishes significantly below the Néel temperature. The abrupt change of the one-magnon frequency at T = 0 K with composition is unexpected and requires further study. Also, the behavior of the one-magnon frequency close to the Néel temperature requires clarification.

Room-temperature Raman spectra of polycrystalline $Ni_cMg_{1-c}O$ solid solutions are shown in Fig. 7b [24]. The most exciting result is concerned with the strong decrease of the two-phonon band intensity relative to the one-phonon contribution for small nickel concentrations. As one can see, upon dilution with magnesium ions, the one-phonon bands *A* and *B* change slightly in shape: mainly, the band *A* becomes more pronounced. At the same time, the two-phonon bands *C*, *D*, and *E* broaden for $0.5 \le c < 0.9$ and disappear completely for $c \le 0.4$. Since the crystalline structure of $Ni_cMg_{1-c}O$ solid solutions follows that of NiO and MgO, no significant changes in the phonon density of states are expected [24]. Therefore, we suggest that for increasing magnesium concentration the first-order Raman scattering becomes more and more allowed due to a lowering of local symmetry at Ni^{2+} sites caused by two effects: composition disorder and off-center displacement of nickel ions. The intensity of the two-magnon band *F* decreases with increasing magnesium concentration, and its position shifts to the lower frequencies as expected. In fact, the two-magnon band *F* becomes located under the phonon bands and could be partially responsible for the background contribution for $c < 0.7$.

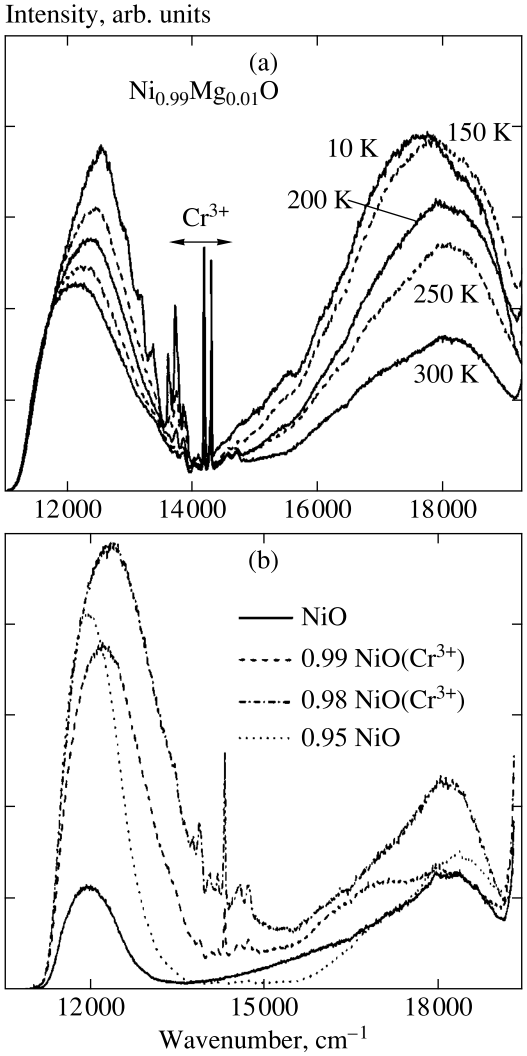

Fig. 6. (a) Temperature and (b) composition (at room temperature) dependences of the photoluminescence in $Ni_cMg_{1-c}O$ solid solutions under a 514-nm excitation laser wavelength [22]. The luminescence due to Cr^{3+} ions comes from the MgO substrate.

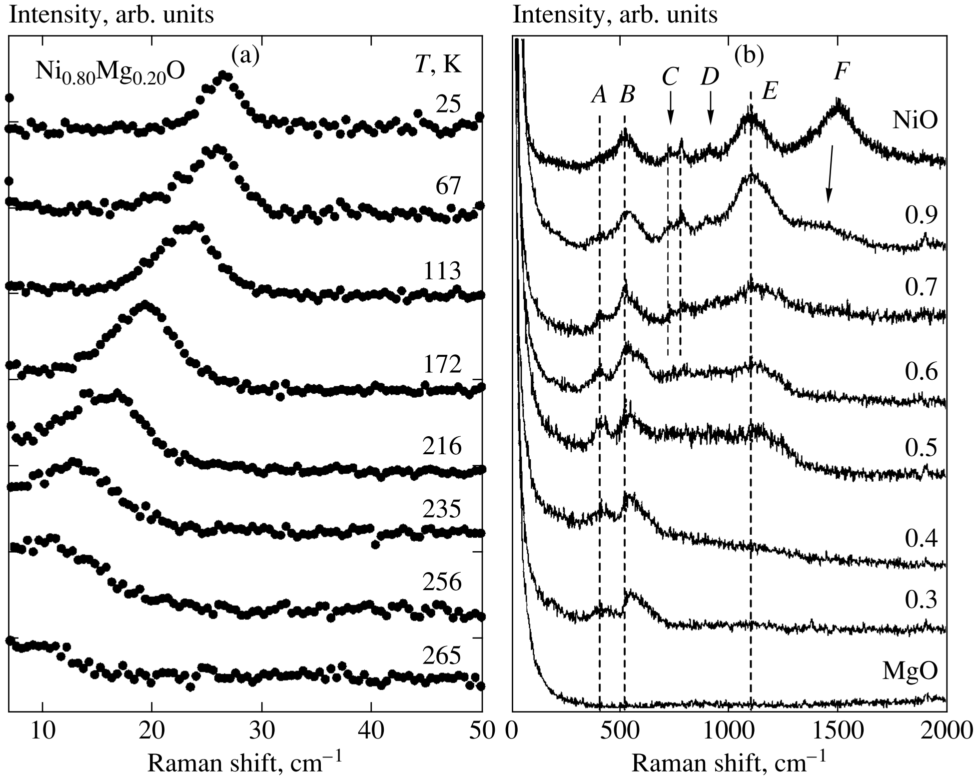

Fig. 7. (a) Temperature dependence of the one-magnon Raman scattering in a $Ni_{0.80}Mg_{0.20}O$ solid solution [24]. (b) Composition dependence of the room-temperature Raman spectra of polycrystalline $Ni_cMg_{1-c}O$ solid solutions [23]. The origin of peaks *A*–*F* is explained in the text. The spectral intensities are scaled so that one-phonon scattering in different spectra is roughly comparable.

4. SUMMARY AND CONCLUSIONS

We have reviewed the recent experimental data together with their interpretation for $Ni_cMg_{1-c}O$ solid solutions with an emphasis on the exchange interactions between Ni^{2+} ions. We have shown that different experimental methods provide complementary information and allow a deeper understanding of the $Ni_cMg_{1-c}O$ system. It was found that dilution of nickel oxide with magnesium ions strongly affects the atomic structure and optical, magnetic, and vibrational properties. Opposite to the conventional point of view, the local symmetry at Ni^{2+} ions sites does lower upon dilution due to magnetic interactions between neighboring nickel ions. The magnetic interactions can be accessed through the study of optical and Raman spectroscopy, since both one-magnon and two-magnon excitations contribute strongly to optical and Raman spectra. We found that the one-magnon energy, depending on the composition, shows an unexpected trend that can be explained by a strong decrease in the spin–spin correlation length upon dilution. However, further studies are required to fully understand this behavior.

ACKNOWLEDGMENTS

This work was partially supported by grants from the Latvian government (nos. 01.0806 and 01.0821) and the Estonian Science Foundation (no. 3453).

REFERENCES

1. W. Giriat and J. K. Furdyna, in *Semiconductors and Semimetals*, Ed. by J. K. Furdyna and J. Kossut (Academic, New York, 1988), Vol. 25.
2. J. B. Goodenough, *Magnetism and Chemical Bond* (Interscience, New York, 1963; Metallurgiya, Moscow, 1968).
3. W. L. Roth, Phys. Rev. **110**, 1333 (1958).
4. M. T. Hutchings and E. J. Samuelsen, Phys. Rev. B **6**, 3447 (1972).
5. F. U. Hillebrecht, H. Ohldag, N. B. Weber, C. Bethke, U. Mick, M. Weiss, and J. Bahrdt, Phys. Rev. Lett. **86**, 3419 (2001).
6. R. E. Dietz, W. F. Brinkman, A. E. Meixner, and H. J. Guggenheim, Phys. Rev. Lett. **27**, 814 (1971).
7. M. J Massey, N. H. Chen, J. W. Allen, and R. Merlin, Phys. Rev. B **42**, 8776 (1990).

8. M. Fiebig, D. Fröhlich, Th. Lottermoser, V. V. Pavlov, R. V. Pisarev, and H.-J. Weber, Phys. Rev. Lett. **87**, 137 202 (2001).
9. N. A. Mironova and G. V. Bandurkina, Izv. Akad. Nauk LatvSSR, Ser. Fiz. Tekh. Nauk **4**, 14 (1975).
10. N. A. Mironova and U. A. Ulmanis, *Radiation Defects and Metal Ions of Iron Group in Oxides* (Zinatne, Riga, 1988).
11. A. Z. Menshikov, Yu. A. Dorofeev, A. G. Klimenko, and N. A. Mironova, Phys. Status Solidi B **164**, 275 (1991).
12. Z. Feng and M. S. Seehra, Phys. Rev. B **45**, 2184 (1992).
13. N. A. Mironova, A. I. Belyaeva, O. V. Miloslavskaya, and G. V. Bandurkina, Ukr. Fiz. Zh. **34**, 848 (1981).
14. D. V. Riekstina, I. E. Cirkunova, and G. J. Eglite, Izv. Akad. Nauk LatvSSR, Ser. Fiz. Tekh. Nauk **1**, 3 (1975).
15. N. A. Mironova, G. A. Grinvald, V. N. Skvortsova, and U. A. Ulmanis, Fiz. Tverd. Tela (Leningrad) **23**, 1498 (1981) [Sov. Phys. Solid State **23**, 874 (1981)].
16. N. Mironova-Ulmane, V. Skvortsova, A. Kuzmin, and I. Sildos, Phys. Solid State **44**, 1403 (2002).
17. N. Mironova-Ulmane, A. Kuzmin, M. Cestelli Guidi, M. Piccinini, and A. Marcelli, Phys. Status Solidi C (2005) (in press).
18. G. A. Grinvald and N. A. Mironova, Izv. Akad. Nauk LatvSSR, Ser. Fiz. Tekh. Nauk **4**, 79 (1978).
19. G. A. Grinvald and N. A. Mironova, Izv. Akad. Nauk LatvSSR, Ser. Fiz. Tekh. Nauk **1**, 28 (1983).
20. G. A. Grinvald and N. A. Mironova, Phys. Status Solidi B **99**, K101 (1980).
21. N. Mironova, V. Skvortsova, A. Kuzmin, and J. Porans, J. Lumin. **72–74**, 231 (1997).
22. A. Kuzmin, N. Mironova-Ulmane, and S. Ronchin, Proc. SPIE **5122**, 61 (2003).
23. E. Cazzanelli, A. Kuzmin, G. Mariotto, and N. Mironova-Ulmane, J. Phys.: Condens. Matter **15**, 2045 (2003).
24. E. Cazzanelli, A. Kuzmin, G. Mariotto, and N. Mironova-Ulmane, Phys. Status Solidi (2005) (in press).
25. A. Kuzmin and N. Mironova, J. Phys.: Condens. Matter **10**, 7937 (1998).
26. A. Kuzmin, N. Mironova, J. Purans, and A. Rodionov, J. Phys.: Condens. Matter **7**, 9357 (1995).
27. A. Kuzmin, N. Mironova, and J. Purans, J. Phys.: Condens. Matter **9**, 5277 (1997).
28. A. Kuzmin, J. Purans, and R. Kalendarev, Phys. Status Solidi C (2005) (in press).
29. W. C. Hahn and J. A. Muan, J. Phys. Chem. Solids **19**, 338 (1961).
30. T. Yoshida, T. Tanaka, H. Yoshida, T. Funabiki, and S. Yoshida, J. Phys. Chem. **100**, 2302 (1996).
31. K. Y. Wong, D. Sengupta, and E. R. Krausz, Chem. Phys. Lett. **21**, 137 (1973).
32. R. Pappalardo, D. L. Wood, and R. C. Linares, Jr., J. Chem. Phys. **35**, 1460 (1961).
33. J. E. Ralph and M. G. Townsend, J. Chem. Phys. **48**, 149 (1968).
34. J. E. Ralph and M. G. Townsend, J. Phys. C: Solid State Phys. **3**, 8 (1970).
35. K. K. Rebane, in *Zero-Photon Lines and Spectral Hole Burning in Spectroscopy and Photochemistry*, Ed. by O. Sild and K. Haller (Springer, Berlin, 1988), pp. 1–18.
36. N. Mironova-Ulmane, V. Skvortsova, A. Kuzmin, and I. Sildos, Ferroelectrics **258**, 177 (2001).
37. R. E. Dietz, G. I. Parisot, and A. E. Meixner, Phys. Rev. B **4**, 2302 (1971).
38. S. R. Chinn, H. J. Zeiger, and J. R. O. Connor, Phys. Rev. B **3**, 1709 (1971).
39. S. Mochizuki, B. Piriou, and J. Dexpert-Ghys, J. Phys.: Condens. Matter **2**, 5225 (1990).
40. S. Mochizuki, J. Phys.: Condens. Matter **2**, 7225 (1990).
41. D. J. Lockwood, M. G. Cottam, and J. H. Baskey, J. Magn. Magn. Mater. **104–107**, 1053 (1992).

Physics of the Solid State, Vol. 47, No. 8, 2005, pp. 1523–1525. Translated from Fizika Tverdogo Tela, Vol. 47, No. 8, 2005, pp. 1465–1467.
Original Russian Text Copyright © 2005 by Leskova, Gonchar’, Popov, Agzamova.

PROCEEDINGS OF THE XII FEOFILOV WORKSHOP “SPECTROSCOPY OF CRYSTALS ACTIVATED BY RARE-EARTH AND TRANSITION-METAL IONS”

(Yekaterinburg, Russia, September 22–25, 2004)

Hyperfine Interaction in Charge-Ordered Manganites

Yu. V. Leskova, L. É. Gonchar’, S. É. Popov, and P. A. Agzamova
Gorkiĭ Ural State University, pr. Lenina 51, Yekaterinburg, 620083 Russia
e-mail: Julia.Leskova@usu.ru

Abstract—Nonempirical calculations of the unpaired-spin density and NMR frequencies for charge-ordered compounds $La_{0.333}Ca_{0.667}MnO_3$ and $La_{0.5}Ca_{0.5}MnO_3$ are carried out. The effect of the local-structure parameters on the resonance frequencies is shown to be dominant. © *2005 Pleiades Publishing, Inc.*

1. INTRODUCTION

The interest demonstrated initially in undoped lanthanum manganite and other manganites can be traced to the discovery of colossal magnetoresistance [1]. Subsequent studies have also revealed other features intimately connected with the physics of manganites. No less attention is being paid to the properties of the charge-ordered phases observed in these compounds. Numerous studies have dealt with the crystal structure, magnetic properties, and orbital ordering in crystals residing in a charge-ordered state [2–6]. There are several commonly accepted models of the crystal structure, among them the Wigner model [7] and the paired JT stripe model [8]. Choosing an ordering model for some charge-ordered compounds remains, however, an unsolved problem.

Some uncertain aspects can be partially clarified using NMR. The sensitivity of this method to changes in the local structure is high enough to test whether ordering can exist in a crystal. Regrettably, the resonance lines observed in a sample are strongly broadened, precluding a more detailed investigation of the crystal structure. Because the charge orbital and lattice degrees of freedom are coupled, charge ordering affects the formation of crystalline, magnetic, and orbital structures. Therefore, based on calculations, one can derive the actual type of ordering involved from analyzing the frequency shifts in an NMR spectrum. Another problem is correct assignment of the observed NMR lines. Nonempirical calculations offer the possibility of predicting the position of the line related to a charge state of manganese. In this paper, we report on a nonempirical calculation of the NMR frequencies for manganese ions incorporated into charge-ordered $La_{0.5}Ca_{0.5}MnO_3$ and $La_{0.333}Ca_{0.667}MnO_3$ crystals.

2. MODEL

NMR lines are determined by the hyperfine magnetic interaction between the electron and nuclear magnetic moments. In crystals, a significant part is also played by chemical bonding, which is governed primarily by the interaction with the nearest neighbors. Therefore, it is appropriate to use the molecular-orbital formalism, which permits adequate estimation of the effects associated with chemical bonding. In our model, we take into account only the isotropic hyperfine interaction, because it is this interaction that determines the position of spectral lines.

The isotropic hyperfine interaction constant is given by

$$A_S = \frac{8\pi}{3} g\beta g_N \beta_N \rho, \qquad (1)$$

where g and g_N are the electronic and nuclear g factors, respectively; β and β_N are the electronic and nuclear Bohr magnetons; and ρ is the unpaired-spin density at the nucleus site. By substituting the wave function expressed through molecular orbitals, we find the magnetic resonance frequency to be

$$h\nu = \frac{8\pi}{3} g\beta g_N \beta_N \frac{1}{2}\left[\sum_i (|\varphi\alpha_i|^2 - |\varphi\beta_i|^2)\right], \qquad (2)$$

where summation is performed over all spin-polarized wave functions of the ion and $\varphi\alpha$ and $\varphi\beta$ are the spin-polarized wave functions with spin up and down, respectively.

Calculations were performed with the GAMESS code [9, 10]. The bases used for the manganese ions were taken from [11], and the basis for the oxygen ion was taken from [12].

We used the SCF approximation of the unrestricted Hartree–Fock method, which allows one to obtain the value of the unpaired-spin density at the nucleus site. Optimization was applied to the complete set of molecular orbitals describing the cluster.

NMR line positions for the Mn^{3+} and Mn^{4+} ions

Compound	Mn^{3+}, MHz	Mn^{4+}, MHz
$LaMnO_3$ (expt.) [13, 14]	350	
$LaMnO_3$ (calc.)	427	
$La_{0.5}Ca_{0.5}MnO_3$ (expt.) [3]	380	310
$La_{0.5}Ca_{0.5}MnO_3$ (calc.)	473	369
$La_{0.35}Ca_{0.65}MnO_3$ (expt.) [5]	375	290
$La_{0.333}Ca_{0.667}MnO_3$ (calc.)	478	361

3. RESULTS AND DISCUSSION

The $La_{0.5}Ca_{0.5}MnO_3$ and $La_{0.333}Ca_{0.667}MnO_3$ compounds studied here are dielectrics possessing a charge-ordered structure at temperatures below T_{CO}. For the $La_{0.333}Ca_{0.667}MnO_3$ crystal, the temperature of transition to the charge-ordered state is T_{CO} = 260 K [4]. The NMR spectra of both compounds contain two clearly pronounced lines [3, 5]. The parameters of $La_{0.5}Ca_{0.5}MnO_3$ can be found in [2], and the parameters of $La_{0.333}Ca_{0.667}MnO_3$, in [4]. The crystal structure of both compounds contains ordered tri- and quadrivalent manganese ions. Note that the ground state of the trivalent manganese ion is degenerate; therefore, this ion is involved in the formation of the orbital structure of the compound. The actual type of orbital structure is closely connected with the crystal structure; therefore, selection of the ground state of the trivalent manganese ion needed to calculate the hyperfine interaction constant is uniquely specified by the type of local distortions of the oxygen environment.

In the case of half-doping, the crystal structure of lanthanum manganite is described by space group $P2_1/m$ and is essentially orthorhombic with a double unit cell. Thus, the trivalent manganese ion occupies two structurally inequivalent positions that differ in terms of the orientation of local distortions. Jahn–Teller distortion is the dominant type of distortion of the oxygen octahedron located near the Mn^{3+} ion. The Mn–O bond lengths are chosen, in accordance with [2], to be 2.068 and 1.929 Å for the first center and 2.056 and 1.919 Å for the second center in the case where the in-plane bond connects the axial oxygen ions and the manganese ion for both centers. We calculated the unpaired spin density for both Mn^{3+} positions and determined the NMR signal frequency. The unpaired spin density was calculated for a cluster made up of a manganese ion and its nearest environment, with due account of the effect of all other ions in the crystal. The ions outside the cluster were taken into account in the point-charge approximation. The frequencies thus obtained are listed in the table. It can be seen that the values calculated in the nonempirical model are higher than those observed experimentally. The inclusion of point charges lowers the calculated NMR frequency. Moreover, a decrease of the distortions arising in the crystal structure entails a lowering of the NMR frequency. The NMR frequencies related to the manganese ions occupying inequivalent lattice positions turned out to be similar in magnitude and cannot be isolated from the strongly broadened line. This effect should be assigned to the small difference in bond length between the two inequivalent manganese ion positions.

There is only one position for quadrivalent manganese in the crystal. Its nearest environment is only slightly distorted; therefore, the state of the cluster approaches that of an undistorted octahedron. The quadrivalent manganese ions together with the oxygen octahedra are shifted in the plane with respect to the complexes containing trivalent ions. The manganese–oxygen bond length is 1.915 Å [2].

$La_{0.333}Ca_{0.667}MnO_3$ belongs to space group *Pnma* and can be described by a triple-content orthorhombic unit cell in one direction and a double-content unit cell in another, both being in-plane directions [4]. Thus, this compound has only one Mn^{3+} center and one center related to Mn^{4+}. The local distortions of the trivalent ion environment are close in amplitude to those of the cluster for $La_{0.5}Ca_{0.5}MnO_3$ and can be characterized by the following bond lengths: 2.024 and 1.916 Å for the in-plane bonds and 1.902 Å for the oxygen ions on the orthorhombic axis. A small change in local distortions of the oxygen octahedron gives rise to a slight shift of NMR frequencies relative to the NMR frequencies observed in the $La_{0.5}Ca_{0.5}MnO$ compound. The quadrivalent ion in $La_{0.333}Ca_{0.667}MnO_3$ occupies an off-center position. Therefore, the Mn^{4+} bond lengths are 1.87, 1.89, 1.90, and 2.01 Å for the in-plane oxygen ions and 1.904 and 1.907 Å for the axial oxygen ions. However, despite the local structures being substantially different, the corresponding isotropic hyperfine constants are similar.

The calculated NMR frequencies for both Mn^{3+} and Mn^{4+} are given in the table.

We performed first-principles calculations of the unpaired spin density and NMR frequencies for $LaMnO_3$ [15]. The results are listed in the table. The NMR frequency calculation conducted in terms of the empirical model is described in [16]. As is evident from the table, the frequency for the trivalent manganese ion in $LaMnO_3$ is lower than the Mn^{3+} frequency in charge-ordered compounds. This effect should be assigned to the magnitude of local distortions in the nearest environment of the manganese ion.

4. CONCLUSIONS

To sum up, our calculations make it possible to find the positions of NMR lines, to compare the NMR frequencies observed experimentally with those of the tri- and quadrivalent manganese ions, and to qualitatively reconstruct the pattern of NMR frequency variations as a function of the extent of local distortions of the oxygen octahedron.

ACKNOWLEDGMENTS

This study was supported by the Russian Foundation for Basic Research (project nos. 04-02-16204, 04-02-96078) and CRDF (project REC-005).

REFERENCES

1. S. Jin, T. H. Tiefel, M. McCormack, R. A. Fastnacht, R. Ramesh, and L. H. Chen, Science **264**, 413 (1994).
2. P. G. Radaelli, D. E. Cox, M. Marezio, and S.-W. Cheong, Phys. Rev. B **55** (5), 3015 (1997).
3. G. Allodi, R. De Renzi, F. Licci, and M. W. Pieper, Phys. Rev. Lett. **81** (21), 4736 (1998).
4. P. G. Radaelli, D. E. Cox, L. Capogna, S.-W. Cheong, and M. Marezio, Phys. Rev. B **59** (22), 14440 (1999).
5. Cz. Kapusta, P. C. Riedi, M. Sikora, and M. R. Ibarra, Phys. Rev. Lett. **84** (18), 4216 (2000).
6. M. Pissas and G. Kallias, Phys. Rev. B **68** (13), 134414 (2003).
7. E. P. Wigner, Phys. Rev. **46**, 1002 (1934).
8. S. Mori, C. H. Chen, and S.-W. Cheong, Nature **392**, 473 (1998).
9. A. A. Granovsky, http://classic.chem.msu.su/gran/gamess/index.html.
10. M. W. Schmidt, K. K. Baldridge, J. A. Boatz, S. T. Elbert, M. S. Gordon, J. J. Jensen, S. Koseki, N. Matsunaga, K. A. Nguyen, S. Su, T. L. Windus, M. Dupuis, and J. A. Montgomery, J. Comput. Chem. **14**, 1347 (1993).
11. H. Partridge, J. Chem. Phys. **90**, 1043 (1989).
12. T. H. Dunning, J. Chem. Phys. **90**, 1007 (1989).
13. A. Sidorenko, G. Allodi, M. C. Guidi, and R. De Renzi, J. Magn. Magn. Mater. **272–276**, 108 (2004).
14. K. N. Mikhalev, A. P. Gerashchenko, V. E. Arkhipov, A. V. Korolev, Ya. M. Mukovskiĭ, and A. A. Arsenov, Pis'ma Zh. Éksp. Teor. Fiz. **72** (12), 599 (2000) [JETP Lett. **72** (12), 599 (2000)].
15. Yu. V. Leskova, P. A. Agzamova, L. É. Gonchar', S. É. Popov, and A. E. Nikiforov, in *Proceedings of XIX International School–Seminar "New Magnetic Materials of Microelectronics," 2004* (2004), p. 331.
16. S. Yu. Prosvirnin, M. V. Eremin, and S. I. Nikitin, in *Proceedings of XIX International School–Seminar "New Magnetic Materials of Microelectronics," 2004* (2004), p. 570.

Translated by G. Skrebtsov

Physics of the Solid State, Vol. 47, No. 8, 2005, pp. 1526–1527. Translated from Fizika Tverdogo Tela, Vol. 47, No. 8, 2005, pp. 1468–1469.
Original Russian Text Copyright © 2005 by Druzhinin, Varenkov, Kochedykov, Akashev.

PROCEEDINGS OF THE XII FEOFILOV WORKSHOP “SPECTROSCOPY OF CRYSTALS ACTIVATED BY RARE-EARTH AND TRANSITION-METAL IONS”

(Yekaterinburg, Russia, September 22–25, 2004)

Mechanism of Optical Absorption in Ferromagnetic Materials

A. V. Druzhinin*, V. I. Varenkov*, V. A. Kochedykov, and L. A. Akashev*****

** Institute of Metal Physics, Ural Division, Russian Academy of Sciences,*
ul. S. Kovalevskoĭ 18, Yekaterinburg, 620219 Russia
*** Institute of High-Temperature Electrochemistry, Ural Division, Russian Academy of Sciences,*
ul. S. Kovalevskoĭ 20, Yekaterinburg, 620219 Russia
e-mail: V.Kochedykov@ihte.uran.ru
**** Institute of Solid-State Chemistry, Ural Division, Russian Academy of Sciences,*
ul. Pervomaiskaya 91, Yekaterinburg, 620219 Russia

Abstract—The optical spectrum is calculated for the nondiagonal component of the permittivity tensor of a ferromagnet. *© 2005 Pleiades Publishing, Inc.*

When analyzing the mechanisms of optical absorption in solids, it is necessary to choose an appropriate set of macroscopic frequency-dependent functions, which, then, can be used to compare the experimental and calculated spectra.

These functions are the complex permittivity $\varepsilon(\omega)$ and the complex permeability $\mu(\omega)$. However, the bilinear relation between these quantities and the complex refractive index $N = n - ik$ does not allow one to separate their partial spectra from the experimentally observed spectrum even in a simple isotropic case.

Since the general form of the expression relating the quantities ε, μ, and N (for an anisotropic absorbing medium) remains unknown, the permeability has been completely eliminated from the phenomenological description of optical phenomena.

The immaturity of the phenomenology and, as a consequence, the inadequate interpretation of the experimental spectra, in turn, have impeded the development of unambiguous procedures for microscopic calculations of the complex permittivity $\varepsilon(\omega)$ and the complex permeability $\mu(\omega)$.

In this paper, we will demonstrate one possible way out of this impasse.

It is known that, in the equatorial geometry (with the magnetization **M** parallel to the **z** axis and perpendicular to the plane of light incidence), the effects linear with respect to the vector **M** allow one to measure the nondiagonal components of the permittivity ($\varepsilon_{xy}(\omega)$) [1] and permeability ($\mu_{xy}(\omega)$) [2] tensors separately (in the latter case, the diagonal components are taken equal to unity). When comparing the experimental and theoretical spectra of the nondiagonal components of the tensors, the main difficulties arise in the microscopic calculation of the components. First, the functions $\varepsilon_{xy}(\omega)$ and $\mu_{xy}(\omega)$ are determined by the electronic states with spin projections that are transverse with respect to the magnetization direction (an arbitrary direction in the *xy* plane). However, calculations have provided information about electronic states with spin projections that are aligned with or opposite to the magnetization direction (the **z** axis). The most serious attempt to calculate the magneto-optical spectra within this discordance does not show convincing agreement with experiment [3].

The results of measuring the real part of the quantity $\omega^2\varepsilon_{xy}(\omega)$ [1] for iron (dotted line), the calculation hitherto reputed to be best [3] (dashed line), and the results obtained in this work (solid line) are compared in the figure.

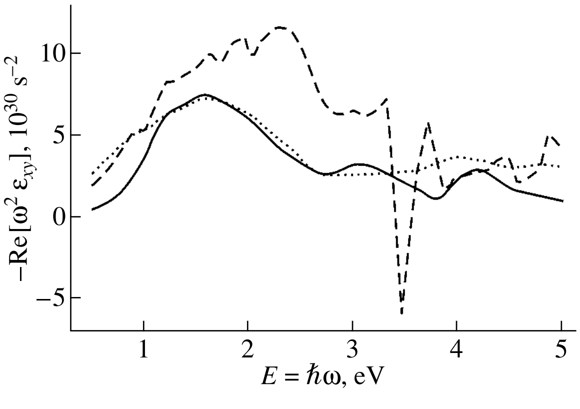

Real part of the quantity $\omega^2\varepsilon_{xy}(\omega)$ for iron according to the measurements made in [1] (dotted line), the calculation performed in [3] (dashed line), and the results obtained in this work (solid line).

1063-7834/05/4708-1526$26.00 © 2005 Pleiades Publishing, Inc.

The spectrum we have calculated is in good agreement with the experimental curve in terms of its main features and was obtained without any fitting.

In our calculations, we used the energy densities of states for iron [4] (which are longitudinal in terms of spin projections with respect to the magnetization) to obtain new functions that correspond to the energy densities of transversal electric dipole states: $g_{\Rightarrow}$, $g_{\Leftarrow}$, $G_{\Rightarrow}$, and $G_{\Leftarrow}$.

The real and imaginary parts of the nondiagonal component of the permittivity tensor can be found from the formula

$$\int_{E_r}^{E_r + h\omega} G_{\Rightarrow}(E - h\omega)G'_{\Rightarrow}(E)dE$$

$$- \int_{E_r}^{E_r + h\omega} G_{\Leftarrow}(E - h\omega)G'_{\Leftarrow}(E)dE,$$

where the integrals relating the occupied and unoccupied (denoted by prime) states are defined in the same way as in [5].

REFERENCES

1. G. S. Krinchik and V. A. Artem’ev, Zh. Éksp. Teor. Fiz. **53** (6), 1901 (1967) [Sov. Phys. JETP **26** (6), 1080 (1967)].
2. I. D. Lobov, A. V. Druzhinin, and V. M. Maevskiĭ, Fiz. Met. Metalloved. **83** (4), 81 (1997).
3. Yu. A. Uspenskiĭ and S. V. Khalilov, Zh. Éksp. Teor. Fiz. **95** (3), 1022 (1989) [Sov. Phys. JETP **68** (3), 588 (1989)].
4. L. M. Sandratskii and P. G. Guletskii, Phys. Status Solidi B **154**, 623 (1989).
5. C. N. Berglund and W. E. Spicer, Phys. Rev. **136** (4A), A1030 (1964).

Translated by V. Artyukhov

Physics of the Solid State, Vol. 47, No. 8, 2005, pp. 1528–1531. Translated from Fizika Tverdogo Tela, Vol. 47, No. 8, 2005, pp. 1470–1473.
Original Russian Text Copyright © 2005 by Chukalina, Bezmaternykh.

PROCEEDINGS OF THE XII FEOFILOV WORKSHOP "SPECTROSCOPY OF CRYSTALS ACTIVATED BY RARE-EARTH AND TRANSITION-METAL IONS"

(Yekaterinburg, Russia, September 22–25, 2004)

Spectroscopic Study of Magnetic Phase Transitions in $Nd_xGd_{1-x}Fe_3(BO_3)_4$

E. P. Chukalina* and L. N. Bezmaternykh**
**Institute of Spectroscopy, Russian Academy of Sciences, Troitsk, Moscow oblast, 142190 Russia*
e-mail: echukalina@isan.troitsk.ru
***Kirensky Institute of Physics, Siberian Division, Russian Academy of Sciences,*
Akademgorodok, Krasnoyarsk, 660036 Russia

Abstract—Magnetic ordering and spin reorientation in iron borates $Nd_xGd_{1-x}Fe_3(BO_3)_4$ ($x = 0.01, 0.04, 0.25, 1.0$) are studied using a rare-earth spectroscopic probe. © *2005 Pleiades Publishing, Inc.*

1. INTRODUCTION

Owing to their physical properties and their mechanical and chemical resistance, rare-earth (RE) borates $RM_3(BO_3)_4$ (R = Y, Ln; M = Al, Ga, Cr, Fe, Sc) are promising materials for quantum- and optoelectronics. $YAl_3(BO_3)_4$ and $GdAl_3(BO_3)_4$ crystals are employed in frequency-doubled and frequency-mixed lasers, while $NdAl_3(BO_3)_4$ is a highly effective concentrated material for miniature medium-power lasers [1–3]. The compound obtained by replacing Al^{3+} with Fe^{3+} ions (which have a magnetic moment) is an interesting magnetic material containing two magnetic subsystems, namely, the RE subsystem and the iron subsystem, the latter being quasi-one-dimensional.

The compounds mentioned above crystallize in the trigonal system and belong to trigonal space group $R32$ (D_3^7) [4]. $RFe_3(BO_3)_4$ crystals are shaped like a hexagonal prism and consist of layers perpendicular to the c axis, which, in turn, consist of RO_6 trigonal prisms and FeO_6 octahedra (smaller in size). The RO_6 polyhedra are linked to BO_3 groups of two types and to FeO_6 octahedra by shared vertices in such a way that each FeO_6 octahedron shares two faces, one with each of the two adjacent layers. The FeO_6 octahedra share a common face with each other in such a way that they form isolated helical chains, which are parallel to the c axis and are independent of each other. The R^{3+} ions occupy equivalent positions with trigonal symmetry (point group D_3).

The magnetic properties of iron borates were measured in [4–6]. The temperature dependence of the magnetic susceptibility exhibits an anomaly at 32 K for $NdFe_3(BO_3)_4$ [4] and at 10 and 40 K for $GdFe_3(BO_3)_4$ [5, 6]. From the temperature dependence of the transmission spectra, it follows that $NdFe_3(BO_3)_4$ undergoes magnetic ordering at 33 ± 1 K [7]. Studies of the heat capacity and Raman scattering in $GdFe_3(BO_3)_4$ and of the absorption spectra of a Nd^{3+} probe in $GdFe_3(BO_3)_4$, in combination with measurements of the magnetic properties of $GdFe_3(BO_3)_4$ [8], show that gadolinium iron borate undergoes three phase transitions: a first-order structural transition at 156 K, magnetic ordering (a second-order transition) at 37 K, and spin reorientation (a first-order transition) at 9 K [8]. In [6], the temperature dependences of the heat capacity and magnetic susceptibility of several RE iron borates were measured and the temperatures of the structural phase transition and magnetic ordering in $RM_3(BO_3)_4$ were found as a function of the R^{3+} ionic radius. In this paper, we report on the results of spectroscopic studies on magnetic phase transitions in the mixed system $Nd_xGd_{1-x}Fe_3(BO_3)_4$.

2. EXPERIMENTAL

Transparent dark-green $Nd_xGd_{1-x}Fe_3(BO_3)_4$ (x = 0.01, 0.04, 0.25, 1.0) single crystals of high optical quality were grown using the flux-melt method [9]. From these prism-shaped crystals with x = 0.01, 0.04, 0.25, and 1.0, plates were cut with thicknesses of 0.2, 0.2, 1.0, and 0.15 mm, respectively. The samples were not oriented, and all subsequent measurements were performed in unpolarized light.

A sample was mounted on a special insert inside an optical helium-vapor cryostat. A thermocouple was located in the immediate vicinity of the sample. The temperature control system used made it possible to stabilize the temperature to within ±0.05 K and perform measurements over the range from 4.2 to 300 K to within ±0.05 K. The low-temperature transmission spectra of the borate single crystals under study were measured over the spectral range 5000–14000 cm^{-1}

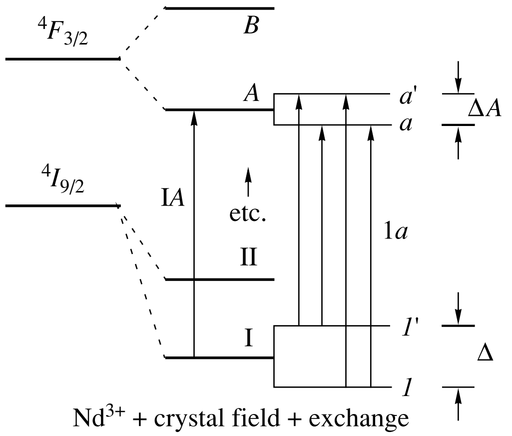

Fig. 1. Splitting of the Nd^{3+} ion levels in a D_3-symmetry crystal field (schematic).

with a resolution of 1 to 0.15 cm^{-1} on a BOMEM DA3.002 high-resolution Fourier spectrometer equipped with a liquid-nitrogen-cooled InSb detector.

3. RESULTS AND DISCUSSION

As indicated above, the local symmetry of the RE center in iron borates is described by the D_3 point group. The Nd^{3+} ion has an odd number of electrons and is a Kramers ion. A D_3-symmetry crystal field lifts the degeneracy of the levels of a free ion except the Kramers degeneracy. The number of levels is dictated by the value of the total angular momentum J; a $(2J + 1)$-fold degenerate level is split into $(J + 1/2)$ Kramers doublets. The crystal-field splitting of the Nd^{3+} ion levels is shown schematically in Fig. 1.

Figure 2 shows the transmission spectra of $Nd_xGd_{1-x}Fe_3(BO_3)_4$ at 50 K (in the paramagnetic phase) in the region of the transitions $^4I_{9/2} \longrightarrow {}^4I_{15/2}$ (for $x = 0.25$, 1.0) and $^4I_{9/2} \longrightarrow {}^4F_{3/2}$ (for $x = 0.01$, 0.04). With our samples, we could not study one spectral region for all values of x, because the $^4I_{9/2} \longrightarrow {}^4I_{15/2}$ transition is not observed in samples with small values of x, whereas the $^4I_{9/2} \longrightarrow {}^4F_{3/2}$ transition is saturated in samples with large values of x.

In the case where there is magnetic ordering in a sample, the RE ion is subjected to an effective magnetic field, which splits the Kramers doublets and thereby causes splitting of the spectral lines. Therefore, the optical spectra contain information on magnetic phase transitions. In iron borates, the RE ions are isolated; therefore, their interaction with one another is much weaker than the RE ion–Fe interaction and the variations in the RE spectrum are associated, for the most part, with changes in the magnetic system of Fe ions. Figure 3 shows in more detail the low-frequency lines of the transitions $^4I_{9/2} \longrightarrow {}^4I_{15/2}$ (for $x = 0.25$, 1.0) and $^4I_{9/2} \longrightarrow {}^4F_{3/2}$ (for $x = 0.01$, 0.04) at various temperatures. At $T > 40$ K, the spectra are seen to have one broad line. As the temperature decreases, this line splits, because the Kramers degeneracy of the Stark levels of the Nd^{3+} ion is lifted when magnetic ordering occurs in $Nd_xGd_{1-x}Fe_3(BO_3)_4$. The designations of the components of split lines in Fig. 3 correspond to those of the energy levels in Fig. 1. In the case of $NdFe_3(BO_3)_4$, splitting of the two closely spaced lines IA and IB in the spectral range 5850–5910 cm^{-1} is seen to occur, as can also be clearly seen from a comparison with the spectrum of the compound with $x = 0.25$ in this spectral range (Fig. 2a). The components of these split lines corresponding to transitions from the upper sublevel of the Kramers doublet split by the magnetic interaction in the magnetically ordered state are “frozen out” at low temperatures. For the $Nd_xGd_{1-x}Fe_3(BO_3)_4$ compounds with $x = 0.01$, 0.04, and 0.25, a sharp change in the relative intensity of lines is also seen to occur within a narrow temperature range (less than 1-K wide). For the earlier studied compound $GdFe_3(BO_3)_4$: Nd (1 at. %), this change in the relative intensities in the

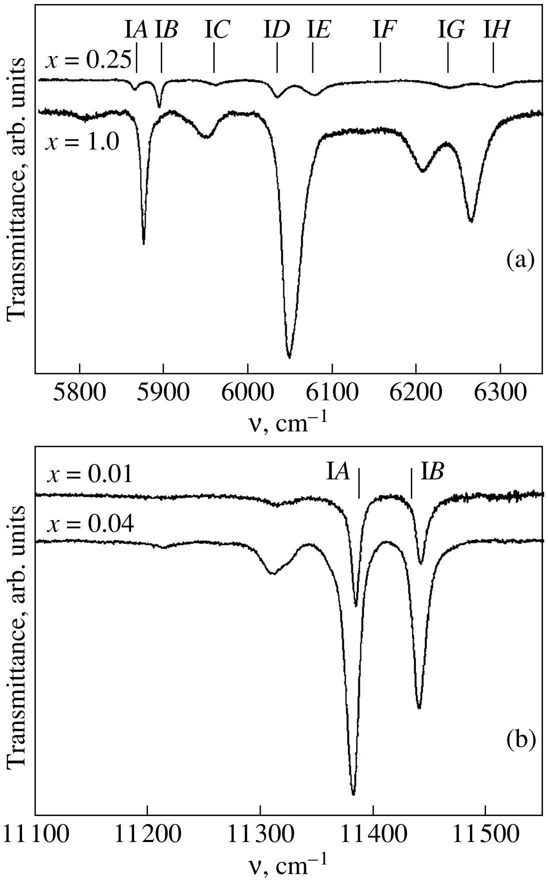

Fig. 2. Transmission spectra of $Nd_xGd_{1-x}Fe_3(BO_3)_4$ in the region of the transitions (a) $^4I_{9/2} \longrightarrow {}^4I_{15/2}$ (for $x = 0.25$, 1.0) and (b) $^4I_{9/2} \longrightarrow {}^4F_{3/2}$ (for $x = 0.01$, 0.04). $T = 50$ K. The designations of the spectral lines correspond to those of the energy levels in Fig. 1.

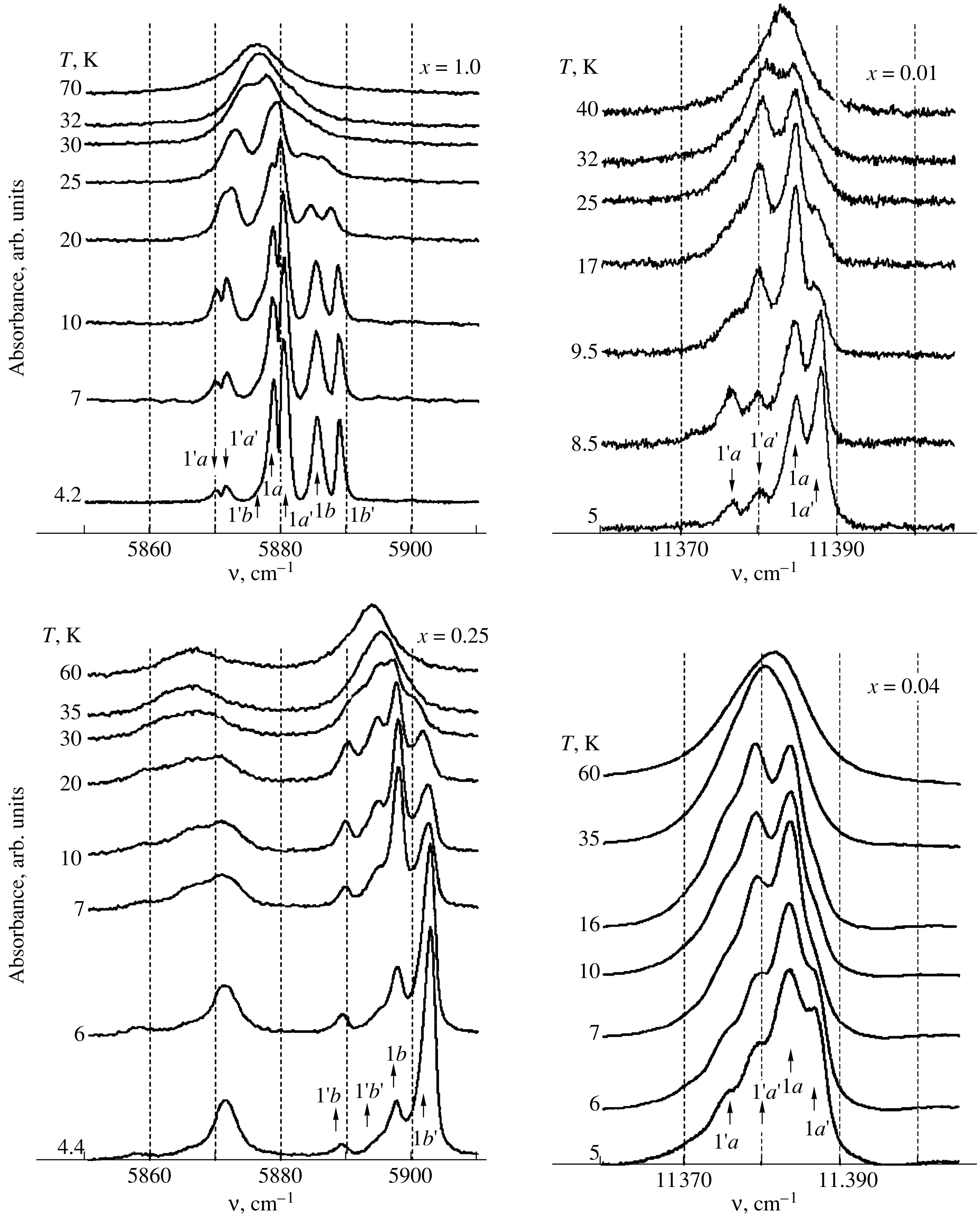

Fig. 3. Absorption spectra in the region of low-frequency lines of the transitions $^4I_{9/2} \longrightarrow {}^4I_{15/2}$ (for $x = 0.25$, 1.0) and $^4I_{9/2} \longrightarrow {}^4F_{3/2}$ (for $x = 0.01$, 0.04) at various temperatures.

RE spectrum (observed at $T_R = 9$ K) was assigned to the spin reorientation first-order phase transition, during which the magnetic moments of the Fe ions change their orientation from the *ab* plane (at temperatures $T_R < T < T_N$) to the *c* axis (at $T < T_R$) [8]. The temperatures of the magnetic ordering and the spin-reorientation transition as determined from the temperature dependences of the splittings and relative intensities of the

Temperatures of magnetic ordering (T_N) and the spin-reorientation transition (T_R) in $Nd_xGd_{1-x}Fe_3(BO_3)_4$ as a function of x

x	T_N, K	T_R, K
0.01	37.0 ± 0.5 [8]	9.00 ± 0.25
0.04	37.0 ± 1.0	7.0 ± 0.5
0.25	36.5 ± 1.0	6.5 ± 0.5
1.0	33 ± 1 [7]	–

spectral lines are given in the table. In $NdFe_3(BO_3)_4$, the spin-reorientation transition is not observed above 3 K. The decrease in the magnetic-ordering temperature with an increase in the Nd^{3+} ion concentration in $Nd_xGd_{1-x}Fe_3(BO_3)_4$ is due to the fact that the replacement of Gd^{3+} by Nd^{3+} (which has a larger ionic radius) increases the interatomic distances and the lattice parameters. This behavior is consistent with the variations in T_N of iron borates $RFe_3(BO_3)_4$ along the row of RE elements [6] and indicates that the links between the Fe chains are mainly due to BO_3 groups rather than to RE ions. As for the spin-reorientation transition, which is associated with temperature variations in the anisotropy of magnetic interactions [10], the available data are insufficient to explain the tendency of T_R to decrease as the neodymium content increases.

ACKNOWLEDGMENTS

This study was supported by the Russian Foundation for Basic Research (project no. 04-02-17346) and the Department of Physical Sciences of the Russian Academy of Sciences (program “Optical Spectroscopy and Frequency Standards”).

REFERENCES

1. D. Jaque, J. Alloys Compd. **323–324**, 204 (2001).
2. M. Huang, Y. Chen, X. Chen, Y. Huang, and Z. Luo, Opt. Commun. **208**, 163 (2002).
3. X. Chen, Z. Luo, D. Jaque, J. J. Romero, J. G. Sole, Y. Huang, A. Jiang, and C. Tu, J. Phys.: Condens. Matter **13**, 1171 (2001).
4. J. A. Campá, C. Cascales, E. Gutierrez-Puebla, M. A. Monge, I. Rasines, and C. Ruíz-Valero, Chem. Mater. **9** (9), 237 (1997).
5. D. Balaev, L. N. Bezmaternyh, I. A. Gudim, V. L. Temerov, S. G. Ovchinnikov, and S. A. Kharlamova, J. Magn. Magn. Mater. **258–259**, 532 (2003).
6. Y. Hinatsu, Y. Doi, K. Ito, M. Wakeshima, and A. Alemi, J. Solid State Chem. **172**, 438 (2003).
7. E. P. Chukalina, D. Yu. Kuritsin, and M. N. Popova, Phys. Lett. A **322**, 239 (2004).
8. R. Z. Levitin, E. A. Popova, R. M. Chtsherbov, A. N. Vasil’ev, M. N. Popova, E. P. Chukalina, S. A. Klimin, P. H. M. van Loosdretch, D. Fausti, and L. N. Bezmaternykh, Pis’ma Zh. Éksp. Teor. Fiz. **79** (9), 531 (2004) [JETP Lett. **79** (9), 423 (2004)].
9. L. N. Bezmaternykh, V. G. Mashchenko, N. A. Sokolova, and V. L. Temerov, J. Cryst. Growth **69**, 407 (1984).
10. K. P. Belov, A. K. Zvezdin, A. M. Kadomtseva, and R. Z. Levitin, *Orientational Transitions in Rare-Earth Magnets* (Nauka, Moscow, 1979) [in Russian].

Translated by Yu. Epifanov

Physics of the Solid State, Vol. 47, No. 8, 2005, pp. 1532–1534. Translated from Fizika Tverdogo Tela, Vol. 47, No. 8, 2005, pp. 1474–1476.
Original Russian Text Copyright © 2005 by Bannikov, Mitrofanov.

PROCEEDINGS OF THE XII FEOFILOV WORKSHOP "SPECTROSCOPY OF CRYSTALS ACTIVATED BY RARE-EARTH AND TRANSITION-METAL IONS"

(Yekaterinburg, Russia, September 22–25, 2004)

Double Exchange in Cubic Crystals with Pairs of Exchange-Coupled Mixed-Valence $3d^3$ –$3d^4$ Ions

V. V. Bannikov and V. Ya. Mitrofanov
Institute of Metallurgy, Ural Division, Russian Academy of Sciences, Yekaterinburg, 620016 Russia
e-mail: luda@imet.mplik.ru

Abstract—Specifics of the exchange interaction in mixed-valence Cr^{2+}–Cr^{3+} 3*d*-ion pairs in $KZnF_3$ crystals are studied. It is shown that the double-exchange interaction can be significantly reduced by the low-symmetry crystal field created by a compensator. The features of the exchange interaction and optical absorption spectra are qualitatively analyzed. © *2005 Pleiades Publishing, Inc.*

1. Isolated complexes of exchange-coupled mixed-valence 3*d* ions, which are created in crystals due to non-isovalent substitution or nonstoichiometry with respect to either cations or anions, are important for understanding the part the double exchange plays in various properties of these centers [1, 2]. Experimental and theoretical studies of the optical absorption spectra of $KZnF_3$: Cr crystals [3, 4] have shown that these crystals contain (Cr^{2+}–Cr^{3+}) centers composed of mixed-valence chromium ions. Observations of the pseudo-Stark effect for the optical absorption lines of this center [3, 4] indicate that an excess electron is mainly localized on one member of the ion pair; i.e. the pair has no inversion center. The experimental data from [3, 4] have been explained in terms of the small-radius polaron [5] and the strong electron–phonon interaction, which completely reduces the double-exchange interaction in first-order perturbation theory. It was assumed that local compensation of the excess charge does not occur and that the symmetry of the Cr^{2+}–Cr^{3+} center in $KZnF_3$ is tetragonal.

It seems that the model of the Cr^{2+}–Cr^{3+} center in $KZnF_3$ crystal proposed in [6] is closer to reality. In this model, the charge is compensated mainly by a K^+ vacancy located in the first or second coordination shell of one of the chromium ions. Possible versions of the Cr^{2+}–Cr^{3+} complex with a vacancy in $KZnF_3$ are shown in the figure. Because the positions of the chromium ions relative to the nearest neighbor vacancy are not equivalent, the low-symmetry crystal field at the different centers of the mixed-valence ion pair is substantially inhomogeneous. It has been shown that the crystal field can significantly reduce the double exchange and complicates the energy spectrum and exchange interaction in the mixed-valence 3*d*-ion pair. Allowance for this field makes it possible to explain the pseudo-Stark effect observed in $KZnF_3$: Cr [3].

2. In an O_h-symmetry crystal field, the $3d^3$ (Cr^{3+}) ground state is a $^4A_2$ orbital singlet and the $3d^4$ (Cr^{2+}) ground state is a ^5E doubly degenerate term. Let us choose the states $|^5E_\mu(a) \times {}^4A_2(b)SM\rangle$ and $|^4A_2(a) \times {}^5E_\mu(b)SM\rangle$ ($\mu = u, v$) as a basis to describe the localization of an excess electron on one of the two ions (*a* or *b*). The Hamiltonian of the exchange-coupled mixed-valence ion pair is given by

$$H = H(a^*b) + H(ab^*) + V_{\text{de}}, \qquad (1)$$

where $H(a^*b)$ and $H(ab^*)$ are the Hamiltonians corresponding to the case where the excess electron is localized on the ions *a* and *b*, respectively, and V_{de} is the double-exchange interaction Hamiltonian of the ion pair. The Hamiltonian $H(a^*b)$ has the form

$$H(a^*b) = H_{\text{lsf}}(a^*b) + H_{\text{Cr}}(a^*b) + H_{\text{ex}}(a^*b), \qquad (2)$$

where the first term describes the low-symmetry crystal field produced by the vacancy, the second term corresponds to the low-symmetry tetragonal field exerted on the Cr^{2+} ion by the Cr^{3+} ion (h_{Cr}), and the third term is the superexchange interaction of the mixed-valence ions of the pair. The Hamiltonian $H(ab^*)$ is similar in structure to Eq. (2). The terms $H_{\text{lsf}}(a^*b)$ and $H_{\text{Cr}}(a^*b)$ are given by

$$\begin{aligned} H_{\text{lsf}}(a^*b) + H_{\text{Cr}}(a^*b) &= \Delta c[I(b) - I(a)] \\ &+ [h_1(a) + h_{\text{Cr}}]X_u(a) + h_2(a)X_v(a), \end{aligned} \qquad (3)$$

where *I* is the unit operator and X_μ ($\mu = u, v$) is an orbital operator acting in the space of the *E*-term wave functions. The terms containing $h_1(a)$ and $h_2(a)$ describe the tetragonal and orthorhombic components of the crystal field produced by the vacancy at the Cr^{2+} ion site, respectively, and Δc is a parameter characterizing the degree of inhomogeneity of the crystal field at the centers *a* and *b*. The term $H_{\text{ex}}(a^*b)$ describes the superexchange interaction between the mixed-valence ions modified by orbital effects:

$$H_{\text{ex}}(a^*b) = [J_0 I(a) + J_1 X_u(a)](S_a S_b), \qquad (4)$$

where J_0 and J_1 are the superexchange interaction constants and S_a and S_b are the spins of the centers a and b, respectively. The Hamiltonian V_{de} has the traditional form

$$V_{\text{res}} = \sum_{\substack{i \neq j = a, b \\ \mu, \nu, \sigma}} b_{\mu\nu} \hat{c}^{+}_{i\mu\sigma} \hat{c}_{j\nu\sigma}, \qquad (5)$$

where indices μ and ν denote summation over $e_g(u, v)$ and $t_{2g}(\xi, \eta, \zeta)$ orbitals and $\sigma = \pm 1/2$. The nonzero transfer integrals $b_{\mu\nu}$ satisfy the relations $b_{uu} = b_e$, $|b_{uu}| \gg |b_{vv}|$, $b_{\xi\xi} = b_{\eta\eta} = b_t$, and $|b_t| \gg |b_{\zeta\zeta}|$. All these interactions are assumed to be weaker than the interatomic exchange J_H.

The constants contained in H_{lsf} can be estimated using the crystal-field approximation, because the Zn^{2+}–K^+ and $\text{Cr}^{2(3)+}$–K^+ distances in a KZnF_3 crystal are significantly larger than the sums of the corresponding ionic radii (see table). The value of h_{Cr} is about $-240\ \text{cm}^{-1}$. Neglecting the orthorhombic component of the crystal field in comparison with the tetragonal component $(h_1 + h_{\text{Cr}})$ for the sake of simplicity, the eigenenergies of the mixed-valence ion pair can be found to be

$$E_1 = -\Delta c - h_1(a) - h_{\text{Cr}} + (J_0 - J_1) f_s(S),$$

$$E_2 = \Delta c - h_1(b) - h_{\text{Cr}} + (J_0 - J_1) f_s(S),$$

$$E_{3,4} = h_{\text{Cr}} + (J_0 + J_1) f_s(S) + \frac{h_1(a) + h_1(b)}{2} \qquad (6)$$

$$\pm\sqrt{(2\Delta c + h_1(a) - h_1(b))^2 + 4t^2},$$

where $t = t(S) = b_e(S + 1/2)/(2S_0 + 1)$, $f_s(S) = [S(S + 1) - S_a(S_a + 1) - S_b(S_b + 1)]/2$, S is the total spin of the pair, and $S_0 = 3/2$ is the spin of the ion core. It can be seen that there is strong resonant coupling between the $\text{Cr}^{3+}(a)$–$\text{Cr}^{2+}(b)$ and $\text{Cr}^{2+}(a)$–$\text{Cr}^{3+}(b)$ configurations in the case of $|t/\Delta c| \gg 1$. In the opposite limiting case $|t/\Delta c| \ll 1$, the orientation degeneracy is lifted and the excess electron is localized predominantly on one ion of the pair.

The sign and magnitude of the exchange interaction constants in Hamiltonian (4) depend on two different factors. One of them is the potential and Anderson kinetic exchanges [4]. In our case, the Anderson kinetic exchange appears in second-order perturbation theory due to virtual transitions of t_{2g} electrons from the center b to the center a. In zero approximation, the excited state $a^*(t_{2g}^4 e_g)b(t_{2g}^2)$ is separated from the ground state $a(t_{2g}^3 e_g)b(t_{2g}^3)$ by $U_{\text{de}} \sim 2U$ instead of U, as in the case of a pair of identical $3d$ ions (here, $U \sim 5$–10 eV is the Coulomb repulsion energy of two electrons located on one center). The second factor is the double-exchange interaction, which arises in the second order of perturbation theory when the virtual transition of an e_g or t_{2g} electron from the center a to the center b with an excitation energy of about $\Delta \approx J_H$ is taken into account. For example, the transition of a t_{2g} electron $(t_2^3 e^1 \times t_2^3 \xrightarrow{t_2} t_2^2 e^1 \times t_2^4)$ leads to mixing of the ground state $(^5E \times {}^4A_2)$ and excited states $(^4T_2 \times {}^3T_1, {}^4T_1 \times {}^3T_1)$ of the mixed-valence ion pair due to the resonance interaction (5). Obviously, the second factor, for which the electron excitation energy is $\Delta \sim J_H < U$, can make a significant contribution to the constants J_0 and J_1 in Eq. (4). Notice that the importance of the double exchange increases significantly for the excited states of the mixed-valence $3d$ ion pair due to the relative proximity of the other excited states.

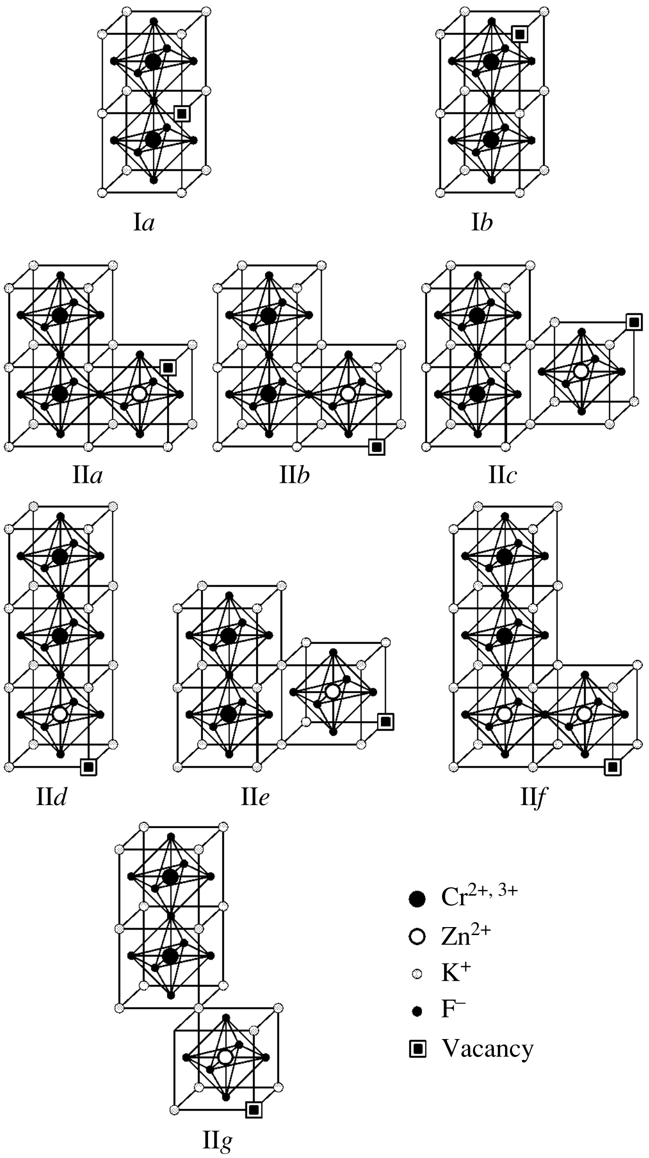

Schematic structures of various types of Cr^{2+}–Cr^{3+} ion pair centers in the KZnF_3 crystal for the (I) first and (II) second coordination shells

Parameters of the low-symmetry crystal fields for various types of Cr^{2+}–Cr^{3+} ion pair centers in $KZnF_3$

Center type	Δc, cm^{-1}	$h_1(a)$, cm^{-1}	$h_1(b)$, cm^{-1}	$h_2(a)$, cm^{-1}	$h_2(b)$, cm^{-1}
I*a*	0	0	0	0	0
I*b*	7900	0	–40	0	0
II*a*	0	20	20	34	34
II*b*	2060	–5	20	9	34
II*c*	0	11	11	0	0
II*d*	3130	–12	–40	0	0
II*e*	1060	0	11	0	0
II*f*	1740	–5	–5	2	9
II*g*	1150	3	0	0	0

3. According to experimental data, the optical absorption spectra of the Cr^{2+}–Cr^{3+} pair in $KZnF_3$ have intense lines at 16720 and 19880 cm^{-1}, which were attributed in [3, 4] to the $^5E \times {}^4A_2 \longrightarrow {}^3E_a \times {}^4A_2$ and $^5E \times {}^4A_2 \longrightarrow {}^3E_b \times {}^4A_2$ transitions, respectively. When interpreting the optical absorption lines of the Cr^{2+}–Cr^{3+} pair at frequencies of 16720 and 19880 cm^{-1}, one should taken into account not only the excitation of the Cr^{3+} ion ($^4A_2 \longrightarrow {}^4T_2$, ^2E) but also the excitation of the Cr^{2+} ion ($^5E \longrightarrow {}^3E_{a,\,b}$). In the case under study, the lowest state of the pair from which these transitions are possible is the state with $S = 5/2$. At low temperatures, the main contribution to the spectral distribution of optical transition frequencies should come from mixed-valence ion pairs with local compensation of the excess charge, because the double exchange is significantly reduced by the vacancy crystal field and the $S = 5/2$ state is populated. The distinguishing feature of this case is that this field lifts the forbiddenness of transitions between states of a certain parity, thereby causing the appearance of additional lines in the optical absorption spectrum of the mixed-valence ion pairs.

Spectroscopy studies of the mixed-valence Cr^{2+}–Cr^{3+} ion pair in $KZnF_3$ subjected to axial strain and electric fields [3, 6] show unambiguous manifestations of the pseudo-Stark effect (for an external field $E \parallel C_4$) and tetragonal symmetry of the ion pair center. The linear character of the pseudo-Stark effect indicates the absence of an inversion center in the pair; that is, it indicates predominant localization of the excess electron on one ion of the pair. These results can be naturally explained in terms of the proposed model of the mixed-valence ion pair in $KZnF_3$.

Indeed, the tetragonal field H_{Cr} and the resonant interaction stabilize the excess electron in the *u* orbital of the Cr^{2+} ion and the low-symmetry field (Δc) causes its predominant localization on one of the 3*d* ions of the pair. The low-symmetry orthorhombic fields h_2, which arise from the various paths of excess-charge compensation, are much smaller than the axial component of the crystal field h_{Cr} and do not manifest themselves in the polarization of the absorption lines of the ion pair center.

The interaction Hamiltonian of the mixed-valence 3*d*-ion pair oriented along the *z* axis in an external electric field can be written as

$$\begin{aligned} H_E &= \alpha\tau_z \mathbf{p}\mathbf{E}_z + \beta(X_u(a) - X_u(b))E_z, \\ \mathbf{p} &= \mathbf{n}p, \end{aligned} \qquad (7)$$

where E_z is the external electric field ($E_z \parallel C_4$), p is the electric dipole moment of the impurity center in which the excess charge is localized on one of the ions of the pair, τ_z is the orbital operator responsible for the localization of the excess charge on one ion (*a* or *b*), and $\mathbf{n}$ is the unit vector along the pair axis. In Eq. (7), the first term is self-evident and the second is related to the different displacements of the intermediate F^- ion for the states *u* and *v* of the Cr^{2+} ion when the excess electron is localized on one ion of the pair. Obviously, the linear Stark effect in the optical absorption spectrum of the mixed-valence ion pair becomes possible only if the excess electron is predominantly localized on one ion of the pair and if the effective dipole moments of the pair in the ground and excited states are different. Since the first term in Eq. (7) is dominant, a noticeable linear pseudo-Stark effect in the optical spectrum of the mixed-valence chromium ion pair is possible only when the given state is relatively close to other excited states of the pair.

ACKNOWLEDGMENTS

The authors are grateful to M.V. Eremin and C.I. Nikitin for helpful discussions.

This work was supported by the Russian Foundation for Basic Research, project nos. 05-02-16236 and NSh-468.2003.3.

REFERENCES

1. P. W. Anderson, in *Magnetism* (Academic, New York, 1963).
2. P. W. Anderson and H. Hasegawa, Phys. Rev. **100**, 675 (1955).
3. M. V. Eremin, S. I. Nikitin, N. I. Silkin, S. Yu. Prosvirnin, and R. V. Yusupov, Zh. Éksp. Teor. Fiz. **114**, 1421 (1998) [JETP **87** (4), 771 (1998)].
4. M. V. Eremin, C. I. Silkin, S. Yu. Prosvirnin, N. I. Silkin, and R. V. Yusupov, Solid State Commun. **117**, 297 (2001).
5. Yu. A. Firsov and E. K. Kudinov, Fiz. Tverd. Tela (St. Petersburg) **39** (12), 2159 (1997) [Phys. Solid State **39** (12), 1930 (1997)]; Fiz. Tverd. Tela (St. Petersburg) **43** (3), 431 (2001) [Phys. Solid State **43** (3), 447 (2001)].
6. M. I. Mityagin, S. I. Nikitin, A. I. Pominov, N. I. Silkin, and A. L. Stolov, Fiz. Tverd. Tela (St. Petersburg) **35** (9), 2578 (1993) [Phys. Solid State **35** (9), 1278 (1993)].

Translated by G. Tsydynzhapov

Physics of the Solid State, Vol. 47, No. 8, 2005, pp. 1535–1539. From Fizika Tverdogo Tela, Vol. 47, No. 8, 2005, pp. 1477–1481.
Original English Text Copyright © 2005 by Vikhnin, Asatryan, Zakharchenya, Kutsenko, Kapphan.

PROCEEDINGS OF THE XII FEOFILOV WORKSHOP “SPECTROSCOPY OF CRYSTALS ACTIVATED BY RARE-EARTH AND TRANSITION-METAL IONS”

(Yekaterinburg, Russia, September 22–25, 2004)

Magnetic Resonance in $Pb_xNb_yO_z$ Ceramics as a System Containing Chemical Fluctuation Regions[1]

V. S. Vikhnin*, H. R. Asatryan*, R. I. Zakharchenya*, A. B. Kutsenko*, and S. E. Kapphan**

** Ioffe Physicotechnical Institute, Russian Academy of Sciences, St. Petersburg, 194021 Russia*
e-mail: hike.asatryan@mail.ioffe.ru
*** FB Physik, Universität Osnabrück, Osnabrück, 49069 Germany*

Abstract—Simulation of the chemical fluctuation regions in PMN-like relaxors through growth of the $Pb_xNb_yO_z$ ceramics was performed. Different $Pb_xNb_yO_z$ clusters (chemically and structurally) coexist in such ceramics. Hole polaron and bipolaron (Cr^{3+}–two polaronic-hole) paramagnetic complexes were considered for explanation of the EPR spectra in $Pb_xNb_yO_z$ ceramics. Dynamical averaging, light-induced effects, and significant effects of reduction treatment giving the coexistence of Nb^{5+} and Nb^{3+} ions, as well as of a strong internal magnetic field, were discovered in this ceramics. The latter could be related to antiferromagnetic phase realization in $Pb_xNb_yO_z$ clusters containing a sufficiently high concentration of magnetic Nb^{3+} host lattice ions. Such a situation leads to antiferromagnetic resonance on Nb^{3+} ions, as well as to EPR of Cr^{3+}-related paramagnetic complexes in a Nb^{3+}-induced internal magnetic field. Charge transfer vibronic excitons (CTVE) in free and in CTVE phase states were detected in $Pb_xNb_yO_z$ ceramics by photoluminescence studies. *© 2005 Pleiades Publishing, Inc.*

1. INTRODUCTION

It is known that the ordering in ferroelectric relaxors is controlled mainly by the cooperative behavior of polar clusters [1, 2]. One of the polar cluster models is the cluster of ferro-ordered localized charge transfers corresponding to bipolaronic electron–hole pairs [3, 4]. This is the cluster of localized charge transfer vibronic excitons (CTVE) (see [3–5] and references therein). Another source of polar cluster formation could be chemical fluctuation regions with ferro ordering (for example, some kinds of Nb-rich regions with different Pb–Nb–O compositions in the ferroelectric relaxor PMN). To study this situation, we will investigate in this paper the limiting case of $Pb_xNb_yO_z$ ceramics consisting only of different-type $Pb_xNb_yO_z$ clusters.

The chemical analysis study showed that the average normalized concentration of the oxygen ion for as-grown $Pb_xNb_yO_z$ ceramics is approximately 3.5. That is, the Nb^{3+} ions have here a relatively low concentration with respect to the Nb^{5+} ion contribution. Nevertheless, the situation becomes principally different for the samples after reduction treatment. Indeed, the average oxygen ion concentration becomes approximately 3 after essential sample reduction in a hydrogen atmosphere. This reflects the coexistence of different $Pb_xNb_yO_z$ clusters with chemical compositions inclusive on average of Nb^{5+} as well as Nb^{3+} ions with approximately the same concentration. Note that the corresponding significant Nb^{3+} ion contribution could be responsible for the appearance of magnetic behavior for such a $Pb_xNb_yO_z$ ceramics. The latter is related to the paramagnetic properties of the Nb^{3+} ion ($S = 1$). As a result, antiferromagnetic ordering of Nb^{3+} ion spins will be predicted here due to the antiferromagnetic exchange interaction between these ions.

The coexistence of $Pb_xNb_yO_z$ clusters with different chemical compositions inclusive of Nb^{5+} as well as Nb^{3+} ions in the reduced ceramic Pb–Nb–O samples (Fig. 1) will be the main supposition of our model. We assume that $Pb_xNb_yO_z$ ceramics consists of nonmagnetic $Pb^{2+}Nb_2^{5+}O_6^{2-}$, $Pb_5^{2+}Nb_4^{5+}O_{15}^{2-}$, and $Pb_2^{2+}Nb_2^{5+}O_7^{2-}$ clusters on the one hand and of antiferromagnetic $Pb_2^{2+}Nb_2^{3+}O_5^{2-}$, $Pb^{2+}Nb_2^{3+}O_4^{2-}$, and $Pb^{2+}Nb_{1/2}^{3+}Nb_{1/2}^{5+}O_3^{2-}$ clusters on the other.

2. EXPERIMENTAL RESULTS AND INTERPRETATION

Let us consider some new effects detected by EPR and by photoluminescence in $Pb_xNb_yO_z$.

---

[1] This article was submitted by the authors in English.

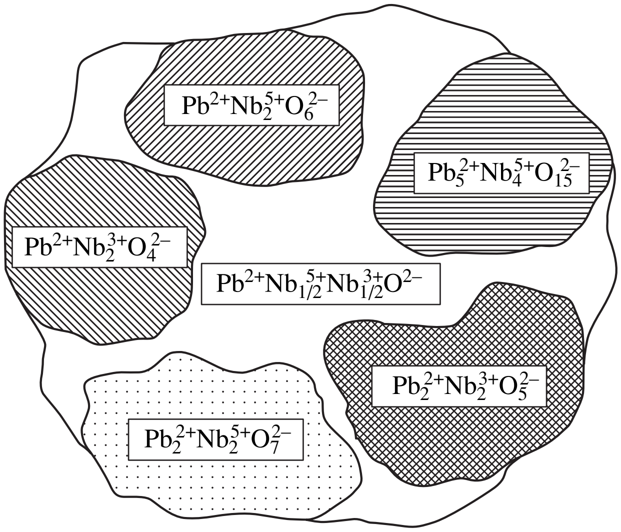

Fig. 1. Coexistence of different Pb–Nb–O clusters with different chemical compositions and different structure in $Pb_xNb_yO_z$ ceramics.

2.1. *Light-Induced Effects in EPR*

A significant increase in definite EPR lines due to illumination (for instance, by a mercury lamp for 0.5 h) takes place for as-grown $Pb_xNb_yO_z$ ceramic samples. Indeed, the *b* and *b*' doublet is essentially increased by such illumination (Fig. 2). In contrast with this, the central *a* line (with respect to doublet *b* and *b*') at least is not increased by the same illumination (or is slightly decreased by light) (Fig. 2). We assume that this behavior could be related to the EPR manifestation of polaronic and bipolaronic states in $Pb_xNb_yO_z$ ceramic samples. Indeed, the *b* and *b*' doublet lines could be considered to result from the $|0\rangle \longrightarrow |\pm1\rangle$ transitions of triplet spin state ($S = 1$). Here, splitting between the $|0\rangle \longrightarrow |+1\rangle$ and $|0\rangle \longrightarrow |-1\rangle$ lines formation could be explained as a result of uniaxial in-cluster field action. It is natural to assume that the photoinduced triplet could be related to pairs of self-localized carriers. These self-localized pairs of carriers in ferroelectric oxides become polaronic pairs. This conclusion seems quite natural because small polaron states are responsible for the well-defined carrier ground state in ferroelectric oxides in accordance with conductivity investigations on the one hand and calculations of the positions of polaronic levels in many ferroelectric oxides (for instance, on the basis of the semiempirical Hartree–Fock approach in the INDO approximation) on the other. So, the here active $|0\rangle$, $|+1\rangle$, and $|-1\rangle$ triplet spin states could be treated as the states of a photoinduced triplet hole bipolaron (*b* and *b*').

The central *a*-line (with respect to doublet *b* and *b*') could be interpreted as a free polaronic hole effect. Its *g*-factor value ($g = 3.015$) is high enough and could be explained as resulting from the direct contribution to the *g* factor of the orbital Zeeman effect for the ground double degenerate state for an oxygen-related hole, $2p_x$ and $2p_y$. Such a ground state decreases its energy due to an interaction with the $4d_{xy}$-type ground states of two neighboring Nb ions. The a-line intensity will decrease with illumination due to transfer of the free hole state occupation to the hole bipolaronic state (the appearance of a two-hole strong correlation with bipolaron formation) on the one hand and will increase with the same illumination due to the direct generation of a free hole polaron by light on the other. We have to deal here with competition between these two opposite tendencies, which lead finally to a rather weak change in the experiment in the intensity of the *a* line induced by light under discussion.

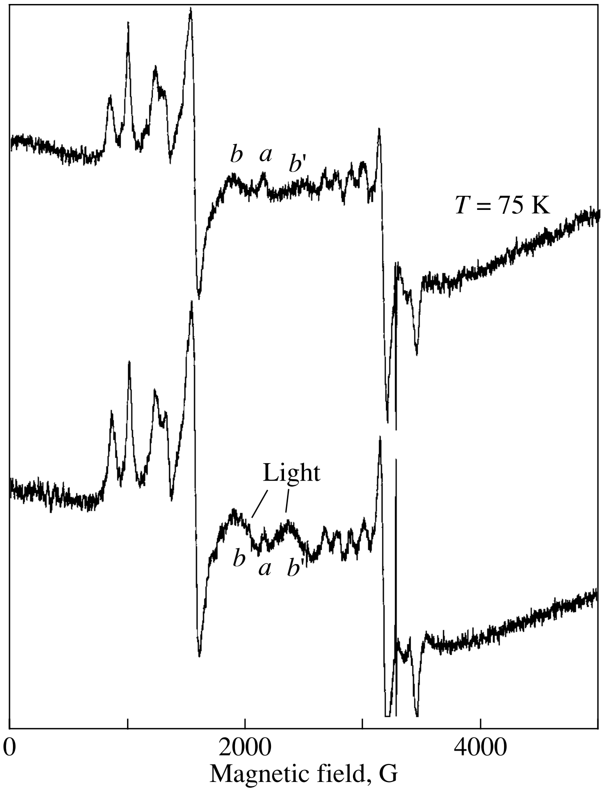

Fig. 2. EPR spectra of $Pb_xNb_yO_z$ ceramics registered at T = 75 K without and with simultaneous light irradiation in the microwave cavity and manifestation of a light-induced center.

2.2. *Cr^{3+}-Related Polaron Complexes*

In accordance with photoluminescence studies of the $Pb_xNb_yO_z$ ceramics under discussion, these samples contain an unwanted Cr^{3+} impurity [6]. Its existence was confirmed by the detection of very narrow *R*-lines of luminescence that are characteristic of the $3d^3$ shell of a Cr^{3+} ion [6]. Note that some specific charge compensation for the Cr^{3+} impurity on the Nb^{5+} site is typical for the case of $Pb_xNb_yO_z$ clusters with a Nb^{5+} ion state (for $PbNb_2O_6$, $Pb_5Nb_4O_{15}$, and $Pb_2Nb_2O_7$ clusters). Indeed, an extra (–2) charge on the Cr^{3+} site here requires the corresponding charge compensation. This is realized due to two oxygen hole trapping on the Cr^{3+} ion of the Nb^{3+} site. In reality, we deal with Cr^{3+}-ion extra-charge compensation under the conditions of hole–hole correlation, as well as of essential hole–lattice polarization and lattice deformation interactions. As a result, hole bipolaron trapping to the first coordination sphere of the Cr^{3+} impurity ion takes place. We suppose in the present work that charge compensation of a Cr^{3+} ion located on a Nb^{5+} site is realized namely due to the trapping of two oxygen-related holes to the first coordination sphere of this Cr^{3+} ion. As a result, a neutral impurity–two-hole complex with the related three-particle negative-U effect appears. The corresponding holes can be in small polaron states, as well as in large (intermediate) polaron states. These aspects were also discussed in [6, 7]. In the present work, we will extend this model to a real case of coexistence of low and high total spin states on the one hand and establish links between the magnetic states of such a Cr^{3+}–two-polaronic-hole paramagnetic complex and its structure with important consequences for this complex spin-orientation relaxation and the related dynamical averaging effects on the other.

Let us discuss this aspect in more detail. Here, a paramagnetic complex with a corelike Cr^{3+} ion (S = 3/2) and with a definite internal magnetic structure due to the exchange interaction between holes with $S = 1/2$ within a bipolaron, as well as between the same holes and the corelike Cr^{3+} ion, occurs. We have the case of the formation of three types of states with total spin values S = 5/2, 3/2, and 1/2, respectively. The ferromagnetic-type state with $S = 5/2$ is the ground state of our system for the case of a weak vibronic interaction for polaronic holes and of a corresponding weak negative-U effect, which could not compensate for the Coulomb hole–hole repulsion in this case. This situation is characterized by a complex linear chain geometry h^+–Cr^{3+}–h^+ and by ferromagnetic ordering of all three spins for the three centers forming the complex under discussion. That is, the geometry corresponds to a total spin $S = 5/2$. On the contrary, the $S = 3/2$ complex state is characterized by antiferro-ordering for trapped h^+–h^+ holes. This $S = 3/2$ state becomes a ground complex state due to the strong negative-U effect for the h^+–h^+ pair in the framework of strong vibronic coupling for holes accompanied by an essential decrease in the distance h^+–h^+. This situation is characterized by near right angle geometry for the complex, ${}^{h^+}_{h^+}Cr^{3+}$. At last, the S = 1/2 state of the complex is the excited state with respect to both limiting situations discussed above. Now let us treat the EPR-related aspects.

2.3. *Dynamical Averaging Effect and the Origin of the Main EPR Spectrum*

As is seen, the linear chain and near right angle geometries are related to different types of hole–hole exchange interaction and to the corresponding different spin structures. As a result, a spin-lattice relaxation transition with a change in the spin value, $|S = 5/2\rangle \rightleftarrows |S = 3/2\rangle$, is accompanied by a spin-flip process for a single hole. The latter means that the linear chain geometry—near right angle geometry relaxation transition in reality is the spin-flip transition, which influences the EPR. For instance, such a transition could directly take part in the formation of the EPR-line dynamical averaging phenomenon and of spin-lattice relaxation.

The next significant aspect here is related to the sufficiently strong vibronic reduction of the corresponding exchange interaction due to a strong enough difference between the contribution of the vibronic effect to the $S = 5/2$ linear chain and to the $S = 3/2$ near right angle states under discussion. The latter leads to an important decrease in the corresponding exchange splitting between the $|S = 5/2\rangle$ and $|S = 3/2\rangle$ state energies up to the values of the same order as the room-temperature equivalent value. As a result, we have to deal with a strong acceleration with the temperature of this spin-flip relaxation accompanied by linear chain geometry—near right angle geometry reorientation transitions in the room-temperature region. The latter allows to use the $|S = 5/2\rangle \rightleftarrows |S = 3/2\rangle$ relaxation transitions as an origin for the dynamical averaging phenomenon within our experiments. Indeed, as shown in Fig. 3, the *d* group of EPR lines manifests a transformation with temperature, which can be treated as the dynamical averaging effect in the range 75–230 K. It is important for this explanation that both types of active states, $|S = 5/2\rangle$ and $|S = 3/2\rangle$, could be realized in the framework of the EPR experiment. Moreover, we have to deal here with not only a simple coexistence of $|S = 5/2\rangle$ and $|S = 3/2\rangle$ states but with their multiple coexistence, taking into account the realization of Cr^{3+}–two-polaronic-hole paramagnetic complexes within three different Pb–Nb–O clusters containing Nb^{5+} ions (Fig. 1). Namely, this model has explained the main EPR line spectrum structure (Figs. 2, 3). The latter was accomplished using the WINEPR SimFonia Program for powder spectra treatment. It is important to underline that EPR lines connected both with the $|S = 5/2\rangle$ state and with the $|S = 3/2\rangle$ state take part in the *d*-line group (Fig. 3) formation but are responsible for different EPR lines in this group, as follows from a computer analysis of the powder spectra mentioned above. We conclude that the $|S = 5/2\rangle \rightleftarrows |S = 3/2\rangle$ fluctuation mechanism could be effective here for explaining the dynamical averaging effect. Last but not least, such a model could also explain not only the averaging effect but also the strong increase in intensity with temperature of the averaged spectra. The latter could be due to a direct contribution from the spin-flip

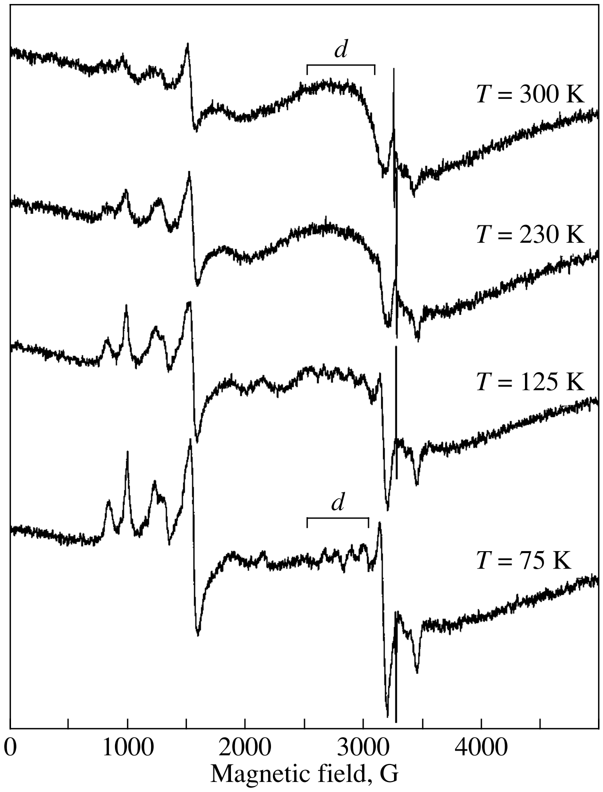

Fig. 3. Temperature dependences of EPR spectra of $Pb_xNb_yO_z$ ceramics at ν = 9.35 GHz in the range 300–75 K. Manifestation of a broad and intense EPR line (spectrum denoted by bracket "*d*") appearing with temperature for magnetic fields in the $2150 \le H \le 3100$ G region.

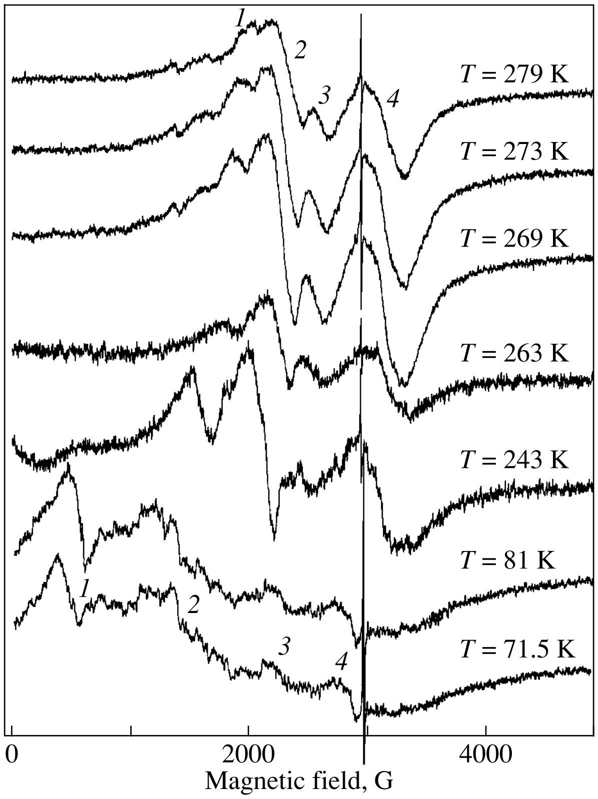

Fig. 4. Temperature dependence of antiferromagnetic resonance lines (two doublets, *1* and *2*, *3* and *4*) accompanied by EPR lines of defects in an internal magnetic field for strongly reduced $Pb_xNb_yO_z$ ceramics. Essential line shifts, line broadenings, decreases in intensity, and the appearance of multiline structure with decreasing temperature are presented.

relaxation transition $|S = 5/2\rangle \rightleftarrows |S = 3/2\rangle$ to microwave absorption as a result of mixed absorption transitions. Here, the usual external microwave magnetic field and the resonance microwave component of the spectrum of internal magnetic-field fluctuations related to the $|S = 5/2\rangle \rightleftarrows |S = 3/2\rangle$ relaxation transitions together form the cross-type absorption effect. As a result, we have a pronounced enhancement of the microwave absorption, which could be related to the experiment (Fig. 3).

In concluding this section it should be noted that another type of unwanted paramagnetic impurity center in the $Pb_xNb_yO_z$ ceramics, namely, that related to Cu^{2+} ions, should not be disregarded. The possibility of there being different types of unwanted paramagnetic centers in the $Pb_xNb_xO_z$ ceramics considered was discussed previously in [7].

2.4. Antiferromagnetic $Pb_xNb_yO_z$ Clusters, Antiferromagnetic Resonance, and EPR in an Internal Magnetic Field

Strong reduction treatment of the $Pb_xNb_yO_z$ ceramics under consideration leads to a entirely new situation for the relative contribution of Nb^{5+} and Nb^{3+} charge states of the Nb ion to this ceramics. Namely, the contribution of Nb^{3+} ions is significantly increased and reaches the contribution of Nb^{5+} ions. Antiferromagnetic clusters appear here namely on the basis of the above-mentioned (see Section 1 and Fig. 1) three types of microregions containing Nb^{3+} paramagnetic ions with the $3d^2$ shell and $S = 1$. The antiferromagnetic ordering is created there due to Nb^{3+}–O–Nb^{3+} superexchange interaction via intermediate oxygen ions. Such clusters were detected in the present work by antiferromagnetic resonance [8, 9], AFMR (Fig. 4). Note that the magnetic ordering mentioned above is accompanied by the appearance of an internal local magnetic field with a characteristic temperature dependence. Characteristic antiferromagnetic ordering features, namely, strong AFMR line shifts with a decrease in temperature up to the appearance of near-zero-field AFMR lines on the one hand and a decrease in the resonance line intensity and an increase in the linewidth with the same decease in temperature on the other (Fig. 4), support this interpretation. Moreover, as follows from Fig. 4, we have to deal with AFMR induced by two different Nb^{3+} rich antiferromagnetic clusters (for example, by $Pb_2^{2+}Nb_2^{3+}O_5^{2-}$ and $Pb^{2+}Nb_2^{3+}O_4^{2-}$ clusters), because there are two basic doublets (AFMR lines *1*, *2* and *3*, *4* in Fig. 3) in the experiment.

The internal local magnetic field in the ferromagnetic clusters discussed above also leads to a significant EPR-line shift for impurity-related paramagnetic centers located in the intercluster interface regions. We assume that EPR-active impurity centers Cr^{3+}, Cr^{3+} with two oxygen-related holes and Cr^{3+}–V_O^{2+} on the one hand and Cu^{2+}, Cu^{2+}–V_O^{2+}, and V_O^{2+}–Cu^{2+}–V_O^{2+} on the other are realized in intercluster interfaces for the antiferromagnetic clusters under discussion. So, the AFMR and EPR signals coexist in the super-high-frequency response and are both under the action of the internal magnetic field of the Nb^{3+} ion system. Taking into account the increase in these internal magnetic fields with decreasing temperature and its random behavior in the framework of a random interface structure, we have to deal here with an extended distribution for the resonance magnetic field shifts of the AFMR and EPR lines under discussion. This type of multiline phenomenon induced with a decrease in temperature was detected experimentally, namely, in reduced samples containing Nb^{3+}.

2.5. *CTVE Manifestation in Pb_xNb_yO Ceramics. Free CTVE and CTVE Phase States*

Charge transfer vibronic excitons (CTVEs) are a characteristic long-living dipole excitation in ferroelectric oxides (see [3–5] and references therein). They are polaronic electron–hole pairs or triads. In this work, we detected CTVEs in $Pb_xNb_yO_z$ ceramics (Fig. 5). Here, CTVEs with $O \longrightarrow Nb^{5+}$ charge transfer were directly manifested in photoluminescence studies. Band–band excitation by a pulse N_2 laser was used. We detected a photoluminescence line related to the recombination of $O \longrightarrow Nb^{5+}$ CTVE at ~500 nm. This line coincides to good approximation with the corresponding photoluminescence line of $O \longrightarrow Nb^{5+}$ CTVE in Nb_2O_5 ceramics. Note that $O \longrightarrow Nb^{3+}$ CTVEs were not obtained in the experiment. This is an indication that $O \longrightarrow Nb^{3+}$ CTVEs are characterized by a higher excitation energy than in the $O \longrightarrow Nb^{5+}$ case.

Special interest is aroused by the detection of two red luminescence lines (at approximately 740, 760 nm), which can be connected with the recombination of $O \longrightarrow Nb^{5+}$ CTVEs in the CTVE phase state. This phase is related to the appearance of a system of strongly correlated CTVEs when the CTVE appears in each cell [3–5]. Note that recombination of free CTVEs explains the origin of the green luminescence, which is a general enough phenomenon for ferroelectric oxides. As has been shown recently [5], the red luminescence phenomenon is also related to CTVE recombination but in the CTVE phase state. Here, a strong red luminescence signal corresponding to a lower luminescence quantum is related to CTVE recombination in the lowest ferroelectric CTVE phase. Vice versa, a weak red luminescence signal corresponding to a higher luminescence quantum is related to CTVE recombination in the excited, antiferroelectric CTVE phase.

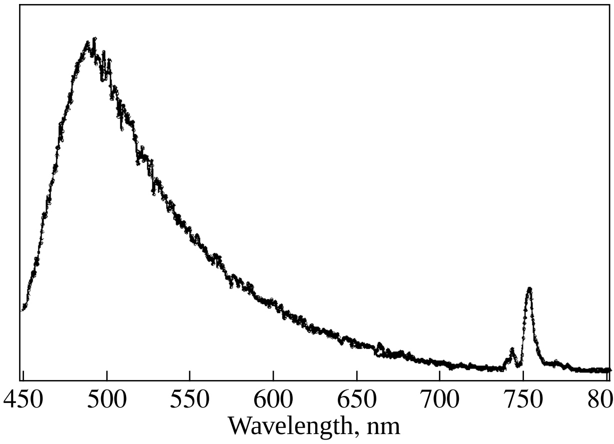

Fig. 5. Photoluminescence intensity spectral dependence for ceramics powders of $PbNb_{x1}O_{y1}$. Photoluminescence was excited by a N_2 laser (λ = 337 nm); T = 293 K.

ACKNOWLEDGMENTS

The authors are grateful to L.S. Sochava, P.G. Baranov, and A.A. Kaplyanskii for useful discussions and their consideration and to Yu.P. Stepanov and H. Eickmeier for performing chemical and diffractional phase analyses.

Supported in part by the Russian Foundatin for Basic Research (project no. 03-02-17589) and by the programs “Low-Dimension Quantum Structures” and “Spin-Dependent Effects in Solids and Spintronics.”

REFERENCES

1. L. E. Cross, Ferroelectrics **76**, 241 (1987); **151**, 305 (1994).
2. Y. Yan, S. J. Pennycook, Z. Xu, and D. Viehland, Appl. Phys. Lett. **72**, 3145 (1998).
3. V. S. Vikhnin, R. I. Eglitis, S. Kapphan, E. A. Kotomin, and G. Borstel, Europhys. Lett. **56** (5), 702 (2001).
4. V. S. Vikhnin, R. I. Eglitis, S. E. Kapphan, G. Borstel, and E. A. Kotomin, Phys. Rev. B **65**, 104 304 (2002).
5. V. S. Vikhnin, S. E. Kapphan, R. I. Eglitis, and R. Pirc, Phys. Status Solidi C **2** (1), 120 (2004).
6. V. S. Vikhnin, R. I. Zakharchenya, H. R. Asatryan, A. B. Kutsenko, and S. E. Kapphan, Appl. Magn. Reson. **28** (1), 1 (2005).
7. V. S. Vikhnin, R. I. Zakharchenya, H. R. Asatryan, A. B. Kutsenko, S. E. Kapphan, and H. Eickmeyer, Ferroelectrics **307**, 67 (2004).
8. T. Okamura, Y. Torizuka, and Y. Kojima, Phys. Rev. **82**, 285 (1951).
9. C. Kittel, Phys. Rev. **82**, 565 (1951).

Physics of the Solid State, Vol. 47, No. 8, 2005, pp. 1540–1543. Translated from Fizika Tverdogo Tela, Vol. 47, No. 8, 2005, pp. 1482–1485.

PROCEEDINGS OF THE XII FEOFILOV WORKSHOP "SPECTROSCOPY OF CRYSTALS ACTIVATED BY RARE-EARTH AND TRANSITION-METAL IONS"

(Yekaterinburg, Russia, September 22–25, 2004)

Electron Spin Resonance of Localized Copper States in $Sr_{1-x}A_xCuO_2$ Ceramics ($A = Li^+, K^+, La^{3+}; x \leq 0.15$)

T. A. Ivanova*, I. Jacyna-Onyszkiewicz, M. A. Augustyniak-Yablokova***, Yu. V. Yablokov***, and V. A. Shustov***

**Zavoiskiĭ Physicotechnical Institute, Kazan Scientific Center, Russian Academy of Sciences,*
Sibirskiĭ trakt 10/7, Kazan 29, 420029 Tatarstan, Russia
e-mail: alex@kfti.knc.ru
***Adam Mickiewicz University, Umultowska 85, Poznan, 61-614 Poland*
****Institute of Molecular Physics, Polish Academy of Sciences,*
ul. Mariana Smoluchowskiego 17, Poznan, 60-179 Poland

Abstract—The orthorhombic modification of $SrCuO_2$ ceramics and its derivatives $Sr_{1-x}A_xCuO_2$ ($A = Li^+$, K^+, La^{3+}) were studied using the ESR and x-ray diffraction methods. Orthorhombic and axial-symmetry paramagnetic centers caused by oxygen defects in samples were detected. From comparing the ESR and x-ray phase data, it follows that the oxygen distribution in ceramics is inhomogeneous. © *2005 Pleiades Publishing, Inc.*

1. INTRODUCTION

Depending on the synthesis conditions, the $SrCuO_2$ compound can exist in two modifications. At high pressures, a tetragonal structure with infinite copper–oxygen layers is stabilized which exhibits HTSC properties when doped with rare-earth elements [1, 2]. When synthesized under standard conditions, the compound has an orthorhombic structure and consists of double zigzag Cu–O chains and SrO layers [3]. At high pressures and high temperatures, one modification can transform into the other [2, 4]. The orthorhombic $SrCuO_2$ modification features a very low (~10^{-4} emu/mol) magnetic susceptibility that is weakly dependent on temperature [5, 6], which allows one to ascribe this material to strongly correlated antiferromagnets. The electron spin resonance (ESR) is not observed in strongly correlated two- and one-dimensional magnets. Described facts of ESR signal observation in these systems are generally explained by various structural defects. In 1D systems, such as $SrCuO_2$, Sr_2CuO_3, and Li_2CuO_2, the ESR is observed much more often than in 2D magnets containing CuO_2 layers [7–9]. In this work, the destruction of spin correlations and the formation of Cu^{2+} localized states are studied using the orthorhombic $SrCuO_2$ modification as an example.

2. EXPERIMENTAL

$Sr_{1-x}A_xCuO_2$ ceramic samples with $x \leq 0.15$ were synthesized at standard pressure in air and studied using the ESR and x-ray diffraction methods. The A ions were Li^+, K^+, or La^{3+}, which produce either a deficiency or excess of positive charges in the material. The description of the synthesis technique can be found in [10]. Samples (prepared about one year ago) were annealed in an oxygen atmosphere at 450°C for 10 h (annealing I) and then annealed in an argon atmosphere at 870°C for 10 h (annealing II). The x-ray diffraction patterns of the synthesized samples were measured using a DRON-2 diffractometer (FeK_α radiation with a beta filter in the 30-kV/15-mA mode) and were processed using the full-profile Rietveld method with the MAUD 1.9992 code [11].

Figure 1 shows the x-ray diffraction patterns of several of the compositions studied and a theoretical x-ray diffraction pattern of the orthorhombic $SrCuO_2$ modification calculated using the data from [3]. The results of fitting of the structural parameters for the samples under study are shown by a solid line. Possible impurity of the accompanying Sr_2CuO_3 and $Sr_{14}Cu_{24}O_{41}$ phases was taken into account according to [12]. The structural parameters thus obtained and the relative contents of the accompanying phases are listed in the table.

ESR measurements were carried out in the X and Q ranges at temperatures of 10–300 K on samples synthesized previously and also one day after annealings I and II. Repeated measurements were carried out over one - and a half years. For an initial $SrCuO_2$ sample, the ESR signal is a superposition of two spectra corresponding to orthorhombic and axial-symmetry centers. In the Q range, the peaks belonging to these centers are partly separated in weak magnetic fields and coincide in strong fields (Fig. 2a). In the X range, the axial centers manifest themselves only in the increased intensity of the strong-field peak in comparison with the spectrum of purely orthorhombic centers. The hyperfine structure arising due to the interaction of an unpaired electron with the copper nucleus is not resolved in the observed spectra. The spectral parameters were determined from model calculations to be $g_1 = 2.045$, $g_2 = 2.110$, and $g_3 = 2.242$ for orthorhombic centers and $g_\perp = 2.047$ and $g_\parallel = 2.260$ for axial centers. The ratio between the numbers of orthorhombic and axial centers is approximately 2 : 1. Measurements of the absolute intensity of the observed signals showed that the amount of paramagnetic centers in samples varies from 0.5 to ~4% of all copper ions. A single-crystal $BaMnF_4$ sample was used as a reference.

Partial substitution of monovalent Li^+ or K^+ ions for the Sr^{2+} ions does not change the signal parameters. The ratio between the intensities of the orthorhombic- and axial-center spectra is also retained in most cases. The deviations observed in certain cases do not depend directly on the monovalent cation content. For example, the relative content of axial centers in $Sr_{0.95}Li_{0.05}CuO_2$ was somewhat higher (~1 : 1) than that in $SrCuO_2$. In $Sr_{0.90}Li_{0.10}CuO_2$, axial centers are almost absent. In $Sr_{0.85}Li_{0.15}CuO_2$, the ratio again approaches 2 : 1 and the observed spectrum is identical to that for $SrCuO_2$. Apparently, these deviations are caused by uncontrollable features of the redox conditions during synthesis. In $SrCuO_2$ doped with La^{3+} ions, only axial centers with the same parameters were observed (Fig. 2b).

$SrCuO_2$, $Sr_{0.95}Li_{0.05}CuO_2$, $Sr_{0.95}K_{0.05}CuO_2$, and $Sr_{0.90}La_{0.10}CuO_2$ samples were subjected to sequential annealings I and II. Annealing I results in the disappearance of previously detected signals and the formation of a broad single line (ΔB ~ 300 Oe; Fig. 2c). After annealing II, instead of a broad line, a weak anisotropic signal appears, which is similar to the initial signal in the corresponding samples. After exposure of the samples to standard conditions (room temperature, atmospheric pressure), the signals measured before annealing were gradually restored. In this case, if the anisotropic spectrum observed immediately after annealing II contains signals from both orthorhombic and axial centers, then, over the course of time, the axial centers gradually disappear and only orthorhombic centers remain (Fig. 2d). The same signal transformation occurs in the $SrCuO_2$ sample, which was filled with paraffin after annealings I and II and was not exposed to air during storage. The signal transformation time is different for samples of different composition and varies from 3.5 weeks to approximately one year. In the $Sr_{0.90}La_{0.10}CuO_2$ sample, which initially featured only axial-center spectra, no ESR signals arose even after long-term storage.

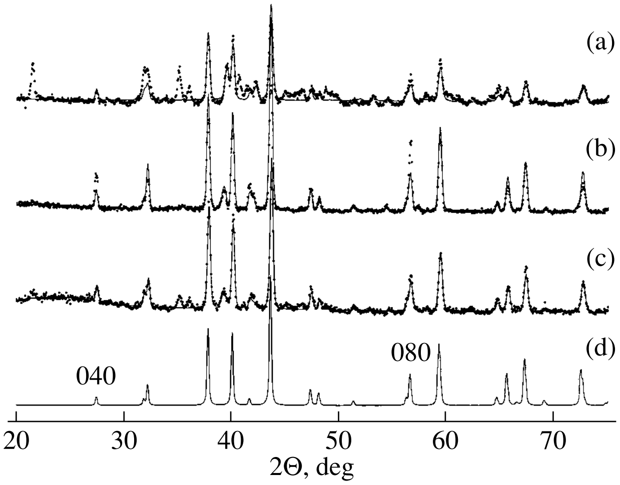

Fig. 1. X-ray diffraction patterns of $Sr_{1-x}A_xCuO_2$ samples for (a) A = La, $x = 0.10$; (b) A = Li, $x = 0.10$; and (c) $x = 0$. (d) A calculated x-ray diffraction pattern of $SrCuO_2$.

Structural parameters of $Sr_{1-x}A_xCuO_2$ and the Cu^{2+} paramagnetic center content (according to the ESR data)

	$SrCuO_2$	$Sr_{0.95}Li_{0.05}CuO_2$	$Sr_{0.90}Li_{0.10}CuO_2$	$Sr_{0.85}Li_{0.15}CuO_2$	$Sr_{0.90}La_{0.10}CuO_2$
a, Å	3.5712	3.5697	3.5711	3.5687	3.5765
b, Å	16.3247	16.3153	16.3241	16.3105	16.3242
c, Å	3.9113	3.9098	3.9093	3.9076	3.9101
$K1$	0.894	0.721	0.865	0.843	0.746
$K2$	0.0996	0.279	0.060	0.154	0.206
$K3$	0.006	0	0.075	0.002	0.048
N	0.027	0.016	0.004	0.045	0.04
N_{ax}	0.009	0.008	~0	0.015	0.04

Note: a, b, and c are the unit cell parameters; $K1$, $K2$, and $K3$ are the relative contents of the $Sr_{1-x}A_xCuO_2$, $Sr_{14}Cu_{24}O_{41}$, and Sr_2CuO_3 phases, respectively; N is the total content of Cu^{2+} paramagnetic centers according to the ESR data; and N_{ax} is the content of Cu^{2+} axial centers according to the ESR data.

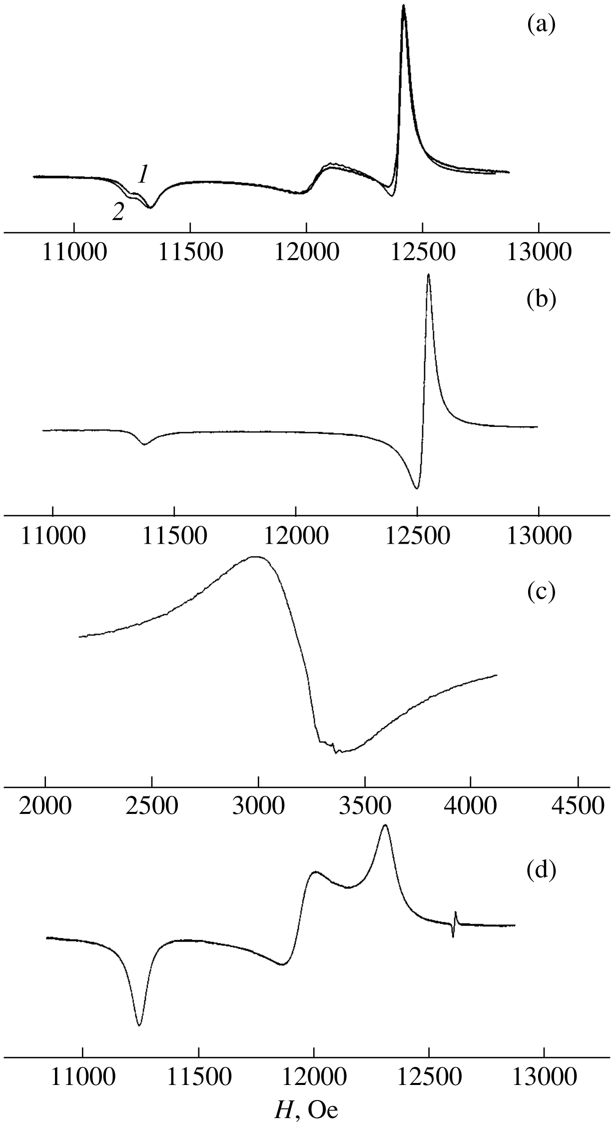

Fig. 2. ESR spectra of $Sr_{1-x}A_xCuO_2$ samples at $T = 293$ K. (a) $SrCuO_2$, $\nu = 35.5$ GHz: (*1*) an experimental spectrum and (*2*) a theoretical spectrum calculated for $g_1 = 2.045$, $g_2 = 2.110$, and $g_3 = 2.242$ for orthorhombic centers and $g_\perp = 2.047$ and $g_\parallel = 2.260$ for axial centers; $N_{\text{rhomb}} : N_{\text{ax}} = 68:32$. (b) $Sr_{0.90}La_{0.10}CuO_2$, $\nu = 35.5$ GHz. (c) $SrCuO_2$, $\nu = 9.4$ GHz; after annealing I. (d) $SrCuO_2$, $\nu = 35.2$ GHz; two months after annealings I and II.

3. DISCUSSION

An analysis of the x-ray diffraction patterns shown in Fig. 1 shows that the synthesized compounds belong to space group *Cmcm*. However, the experimental x-ray diffraction patterns slightly differ from the calculated ones; namely, they include additional low-intensity peaks which do not belong to the $SrCuO_2$ structure. Moreover, the intensities of certain peaks differ significantly. According to the phase diagram of the SrO–CuO_x system obtained in [12], Sr_2CuO_3 and $Sr_{14}Cu_{24}O_{41}$ can be accompanying phases during the $SrCuO_2$ synthesis. Taking into account this fact improves the agreement with experiment in the range $2\Theta \sim 39°$. We failed to explain the peaks in the range $2\Theta \sim 35°–36°$ in $SrCuO_2$ and $Sr_{0.90}La_{0.10}CuO_2$ samples by the presence of known structures. According to the data from [13], these features in the x-ray diffraction pattern are typical of samples synthesized in air and disappear in the case of synthesis in vacuum. Apparently, they are associated with excess oxygen and with the formation of a modulated structure having a larger unit cell. We also failed to explain the significant increase in the (040) and (080) reflection intensity in samples containing Li^+ by the presence of additional impurity phases. A comparison of the x-ray phase analysis data with the results of the ESR concentration measurements (see table) shows that the ESR signal intensity does not correlate with the impurity phase contents. Therefore, the observed paramagnetic centers form in the main phase.

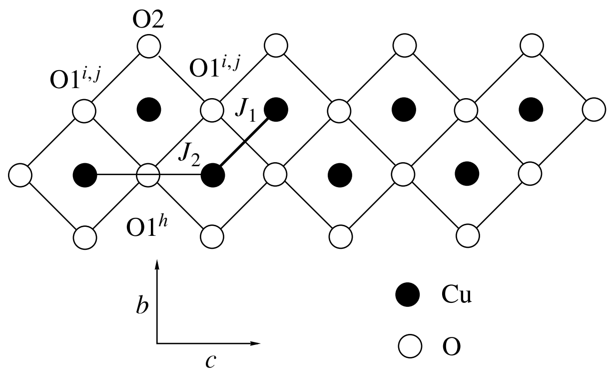

Fig. 3. Double zigzag chain along the *c* axis in $SrCuO_2$.

Since the ESR signal intensity corresponds to only a small fraction (from 0.5 to 4%) of the total introduced amount of copper, it can be concluded that these signals do not belong to the basic mass of copper ions but rather are associated with certain defects that produce localized copper states. The absence of a hyperfine structure in the measured ESR spectra suggests that the detected copper centers are not isolated but rather are coupled by exchange interactions in microscopic regions in which the correlation of Cu^{2+} ions is destroyed and the ESR signal can be observed.

The structure of $SrCuO_2$ contains double binary zigzag CuO_2 chains (Fig. 3). Magnetic susceptibility measurements [5] showed that the antiferromagnetic exchange J_2 between the copper ions in Cu–O–Cu with the 180° interaction in chains is ~ 660 cm^{-1} and that the exchange J_1 between copper ions of different chains with the 90° interaction is smaller by one to three orders of magnitude. Thus, the double zigzag chain can be represented as two linear chains with antiferromagnetically correlated spins coupled by fairly weak exchange interactions. The ESR is not observed in such chains.

The possible existence of Sr and Cu ion vacancies was confirmed in [3] even for single crystals. It is reasonable to assume that the necessity of charge stoichiometry retention requires an accompanying oxygen vacancy. According to [3], vacancies of nonbridge O2 oxygen ions are most probable. Copper vacancies break chains, and the correlation of the spins of the end Cu^{2+} ions with the spins of other copper ions can be destroyed. These defects were considered in [14]. According to the x-ray diffraction data from [3], the interatomic distances and angles between corresponding bond axes in the CuO_4 polyhedron are $R(Cu–O1^h) = 1.910$ Å, $R(Cu–O2) = 1.930$ Å, $R(Cu–O1^{i,j}) = 1.961$ Å $\cdot$ 2, $O1^h–Cu–O1^{i,j} = 87.5° \cdot 2$, and $O2–Cu–O1^{i,j} = 92.5° \cdot 2$ (Fig. 3). We can see that a Cu vacancy in combination with an O2 vacancy could result in an ESR signal of orthorhombic symmetry even in the case of nonlocal charge compensation.

Oxygen migration during annealings and after them will be considered in a later paper. We only note here that the gradual disappearance of axial-center signals after annealing II seems to be caused by partial removal of excess oxygen and its migration within the sample. This suggests that excess oxygen is involved in the formation of axial centers. Excess oxygen should also exist in samples doped with La^{3+}, in which only axial-center ESR signals are observed. The excess of oxygen is associated with the charge stoichiometry violation caused by trivalent ions. If excess oxygen is not distributed uniformly over the sample but rather is localized in microscopic regions enriched with oxygen, then the most probable position of excess oxygen ions seems to be between two copper atoms along the *c* axis. This will increase the coordination number of CuO_4 polyhedra to five or six. In copper–oxygen CuO_6 octahedra, the axial-center signal should be observed, since the positions of oxygen ions in the *ac* plane become equivalent. The observation of ESR axial-center signals in other samples (not containing La^{3+} ions) can apparently be considered an indication of an inhomogeneous oxygen distribution with the formation of microscopic regions enriched with oxygen.

The observed ESR signal transformation during long-term storage after annealing is caused by oxygen migration. The fact that the processes proceeding in samples coated with paraffin and in air are identical allows one to conclude that oxygen migration takes place inside a sample rather than between a sample and the ambient air.

Thus, the possible observation of orthorhombic- and axial-center ESR signals can be due to the specific features in the oxygen distribution over the samples under study (the existence of microscopic regions depleted or enriched with oxygen). The oxygen distribution over a sample depends on many fine synthesis features, which are difficult to control and poorly reproduced. This explains the fact that the published data on observed ESR signals do not always agree. For example, only axial centers were detected in $SrCuO_2$ in [7]. In our experiments, it was also impossible to trace a regular dependence of the observed signal intensity on the doping ion concentration.

REFERENCES

1. T. Siegrist, S. M. Zahurak, D. W. Murphy, and R. S. Roth, Nature **334**, 231 (1988).
2. A. Podlesnyak, A. Mirmelstein, V. Bobrovskiĭ, V. Voronin, A. Karkin, I. Zhdakhin, B. Goshitskiĭ, E. Midberg, V. Zubov, T. D’yachkova, E. Khlybov, J.-Y. Genoud, S. Rosenkranz, F. Fauth, W. Henggeler, and A. Furrer, Physica C **258**, 159 (1996).
3. Y. Matsushita, Y. Oyama, M. Hasegawa, and H. Takei, J. Solid State Chem. **114**, 289 (1994).
4. X. Zhou, C. Dong, F. Wu, H. Chen, G. Che, Yu. Yao, and Zh. Zhao, Physica C **235–240**, 995 (1994).
5. M. Matsuda and K. Katsumata, J. Magn. Magn. Mater. **140–145**, 1671 (1995).
6. N. Motoyama, H. Eisaki, and S. Uchida, Phys. Rev. Lett. **76**, 3212 (1996).
7. H. Ohta, N. Yamauchi, M. Motokawa, M. Azuma, and M. Takano, J. Phys. Soc. Jpn. **61**, 3370 (1992).
8. H. Ohta, N. Yamauchi, T. Nanba, M. Motokawa, S. Kawamata, and K. Okuda, J. Phys. Soc. Jpn. **62**, 785 (1993).
9. C. Oliva, L. Forni, and A. Vishniakov, *Mendeleev Commun*. (1992), p. 88.
10. I. Jacyna-Onyszkiewicz, M. Sidowski, and A. Porebska, Mol. Phys. Rep. **12**, 109 (1995).
11. *The Rietveld Method*, Ed. by R. A. Young (Oxford Univ. Press, New York, 1993).
12. D. Risold, B. Hallstedt, and L. J. Gauckler, J. Am. Ceram. Soc. **80** (3), 527 (1997).
13. L. Forni, C. Oliva, F. Vatti, N. Sinitsina, S. V. Sorochkin, A. V. Moev, and A. V. Vishniakov, J. Chem. Soc., Faraday Trans. **88** (7), 1041 (1992).
14. A. I. Smirnov, V. N. Glazkov, L. I. Leonyuk, A. G. Vetkin, and R. M. Eremina, Zh. Éksp. Teor. Fiz. **114** (11), 1876 (1998) [JETP **87** (11), 1019 (1998)].

Translated by A. Kazantsev

Physics of the Solid State, Vol. 47, No. 8, 2005, pp. 1544–1547. Translated from Fizika Tverdogo Tela, Vol. 47, No. 8, 2005, pp. 1486–1489.
Original Russian Text Copyright © 2005 by Gaĭdideĭ, Gomenyuk, Nedelko, Sleptsov, Antraptseva, Boĭko, Tkachova.

PROCEEDINGS OF THE XII FEOFILOV WORKSHOP "SPECTROSCOPY OF CRYSTALS ACTIVATED BY RARE-EARTH AND TRANSITION-METAL IONS"

(Yekaterinburg, Russia, September 22–25, 2004)

Luminescence and Vibration Spectra of Zinc Manganese Diphosphates

G. I. Gaĭdideĭ*, O. V. Gomenyuk*, S. G. Nedelko*, A. A. Sleptsov*, N. M. Antraptseva, V. V. Boĭko**, and N. V. Tkachova****

**Shevchenko National University, Vladimirskaya ul. 64, Kiev, 03680 Ukraine*
e-mail: SNedilko@univ.kiev.ua
***National Agricultural University, Kiev, 03041 Ukraine*

Abstract—The synthesis conditions for new luminescent materials, zinc manganese diphosphates $Zn_{2-x}Mn_xP_2O_7 \cdot 5H_2O$) ($0 \leq x \leq 2.0$), are considered. The photoluminescence and its excitation spectra, IR absorption, and Raman spectra of these materials are studied. The red luminescence band with a peak at about 700 nm is shown to be due to the radiative transitions in Mn^{2+} ions, which are set in an octahedral oxygen environment. The range of concentration quenching of Mn^{2+} ion radiation is determined. Correlation of the luminescent and vibration properties of these compounds is discussed. *© 2005 Pleiades Publishing, Inc.*

1. INTRODUCTION

Zinc and manganese diphosphates, $Zn_2P_2O_7$ and $Mn_2P_2O_7$, are quite different in terms of their mechanical and optical properties. These compounds are well known as heat-resistant coloring agents, catalysts, solid-state electrolytes, anticorrosive liquids, etc. [1, 2]. Diphosphates containing simultaneously zinc and manganese have different physical and chemical properties (and, accordingly, different performance) as compared to single-element diphosphates. Their properties can be tailored to need by adjusting the relative content of the transitional elements, zinc and manganese. Preliminary studies have shown that compounds containing manganese exhibit red-orange photoluminescence (PL). In the present work, we study the nature of this luminescence and analyze the synthesis conditions for diphosphates with a continuously variable ratio of the zinc and manganese contents.

2. SAMPLE SYNTHESIS AND EXPERIMENTAL TECHNIQUE

We used the residual-concentration method to study the synthesis conditions of the diphosphates [3]. Water solutions of ChDA-grade $ZnSO_4 \cdot 7H_2O$, $MnSO_4 \cdot 5H_2O$, and $K_4P_2O_7$ were used for synthesis. The optimal proportion was found to be $P_2O_7^{4-}/(Zn^{2+} + Mn^{2+}) = 0.2$; the k = Zn/Mn ratio was varied in the range 5.67–0.18.

The obtained solid-phase sediment was separated and rinsed with cool water (until the reaction for sulfate ions became negative) and then was recrystallized from slightly acid solutions. The phosphorus content was measured using the gravimetric quinoline molybdate method with an accuracy of 0.2%; the Zn^{2+} and Mn^{2+} cation contents were determined using the complexometric method, and the anion composition was determined by paper chromatography [4].

In order to identify the phase composition of the solid sediment, we analyzed x-ray diffraction patterns (obtained using a DRON-4M x-ray diffractometer), IR absorption spectra (taken with a Nexus-470 spectrometer in the frequency range 400–4000 cm^{-1}), and Raman spectra (measured on a DFS-52 spectrometer in the frequency range 20–1700 cm^{-1}). For the PL and Raman scattering studies, we used molded tablets of the synthesized compounds. The IR absorption spectra were measured, using a conventional technique, on a fine powder embedded in a KBr matrix. The PL was studied at 4.2, 77, and 300 K, and the IR absorption and Raman spectra were studied at 300 K. Luminescence was excited by an ILGI-501 laser at a wavelength λ_{exc} = 337.1 nm and by a DKsEl-1000 xenon lamp. The lamp radiation was monochromatized by a DMR-4 monochromator, and the PL spectra were measured using DMR-4 and DFC-12 spectrometers.

3. EXPERIMENTAL RESULTS

According to the x-ray analysis, all compounds obtained are single-phase with either a zinc or manganese diphosphate pentahydrate structure [5]. The analysis shows that the synthesized crystals are a continuous sequence of substitutional solid solutions $Zn_{2-x}Mn_xP_2O_7 \cdot 5H_2O$, where x varies from 0 to 2 and

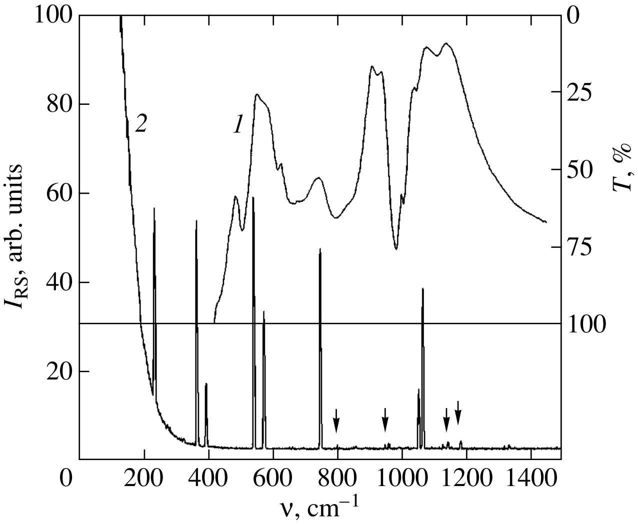

Fig. 1. (*1*) Part of the IR absorption spectrum and (*2*) the Raman scattering spectrum of the $ZnMnP_2O_7 \cdot 5H_2O$ compound at room temperature.

zinc and manganese are distributed randomly over the crystal lattice.

Additional data about the features of the crystal structure of $Zn_{2-x}Mn_xP_2O_7 \cdot 5H_2O$ compounds are obtained from the IR absorption (Fig. 1) and Raman scattering spectra. The IR absorption spectra exhibit wide bands in the range 1500–4000 cm^{-1} associated with water absorption (which are not analyzed here) and, irrespective of the x value, 12 peaks with different intensity and resolution in the range 400–1200 cm^{-1} (curve *1* in Fig.1). The same number of lines (having a different intensity distribution and, for several of them, other frequencies) are observed in the Raman spectra in the same frequency range. Also, under certain conditions, up to 7 Raman lines can be observed in the low-frequency range 100–400 cm^{-1}. It can be seen in Fig. 1 that the strongest Raman peaks in the frequency range 400–1200 cm^{-1} coincide in position with the IR absorption lines (curve *2* in Fig.1).

As for luminescence, the PL spectrum of zinc diphosphate $Zn_2P_2O_7 \cdot 5H_2O$ at T = 300 K contains a wide blue-orange radiation band with an envelope maximum at about 500 nm. When manganese is added, the PL intensity decreases and the band shape changes (the relative intensity of its long-wavelength part grows). Obviously, for $Zn_{2-x}Mn_xP_2O_7 \cdot 5H_2O$, this PL band consists of 2 or 3 components. Simultaneously, as the manganese content grows, the red PL band appears with a maximum at about 700 nm (Fig. 2a). The red-band intensity maximum I_{red} and the ratio of the intensity maxima of the blue-green and red bands I_{green}/I_{red} are shown in Fig. 2b as a function of the manganese content x.

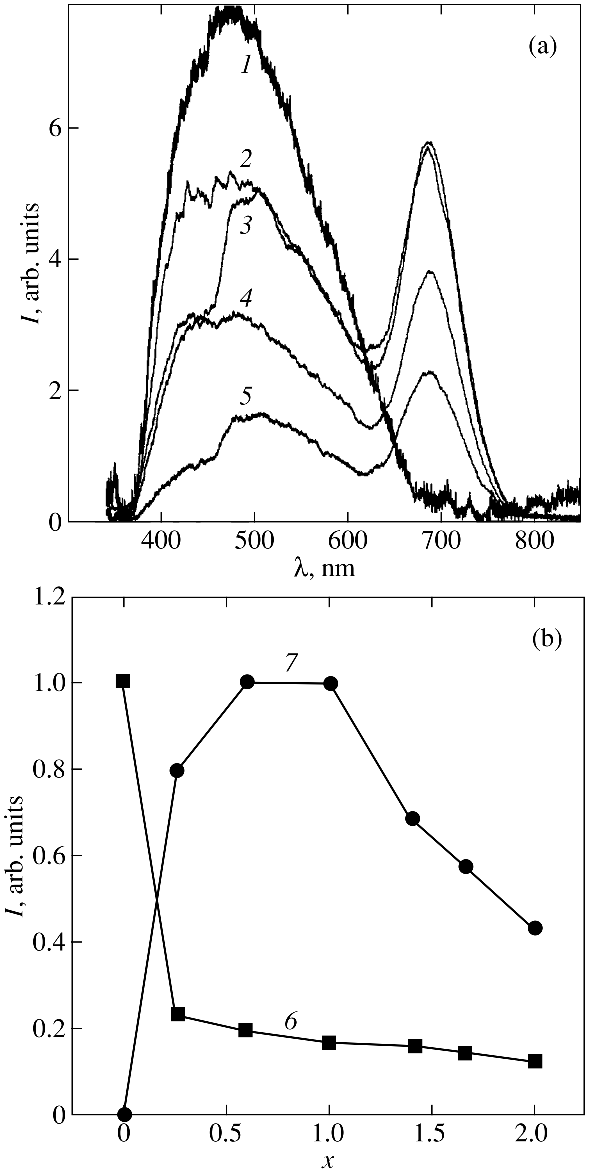

Fig. 2. (a) Luminescence spectra of $Zn_{2-x}Mn_xP_2O_7 \cdot 5H_2O$ at room temperature excited at a wavelength λ_{exc} = 337.1 nm for various values of x: (*1*) 0, (*2*) 0.7, (*3*) 1.0, (*4*) 1.3, and (*5*) 2. (b) Dependences of (*6*) the ratio of the maximum intensities of the blue-green and red PL bands I_{green}/I_{red} and (*7*) the maximum intensity of the red PL band I_{red} on the manganese content x for $Zn_{2-x}Mn_xP_2O_7 \cdot 5H_2O$ measured at room temperature.

When the sample temperature decreases to 4.2 K, the long-wavelength components begin to dominate the blue-orange PL and the relative intensity of the red PL band decreases (Fig. 3). Evidently, the changes are related to the specifics of the relative positions of the blue-orange PL band and the strongest bands in the red PL excitation spectrum (Fig. 3). Indeed, two of the three strongest bands in the spectrum (namely, the bands in the ranges 480–580 and 580–630 nm) overlap

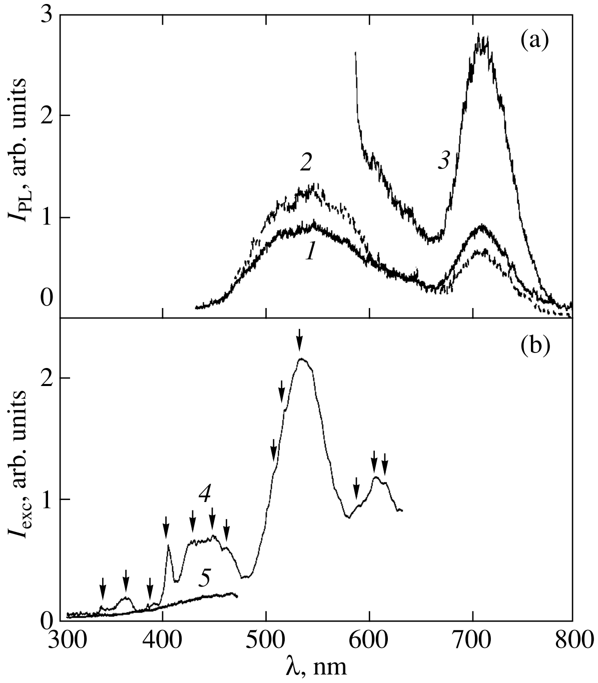

Fig. 3. (a) Luminescence and (b) luminescence excitation spectra of $ZnMnP_2O_7 \cdot 5H_2O$ measured at (*1*) 77 and (*2*–*5*) 4.2 K. The PL spectrum was excited at λ_{exc} equal to (*1, 2*) 355 and (*3*) 545 nm, and the PL excitation spectrum was recorded at (*4*) 710 and (*5*) 500 nm.

with the blue-orange PL band. Within these bands, there are at least three structural peaks in each band (at 506, 517, 535 nm and at 590, 604, 618 nm, respectively). Moreover, the red PL is excited in the shortest wavelength range of the PL excitation spectrum (in peaks at 320, 338, 361, 386 nm) and also in the medium range at 390–480 nm, where there is a sharp peak at 403 nm and three weak peaks at 428, 446, and 462 nm (curve *4* in Fig.3). Unlike the excitation spectra described above, the excitation spectrum of the blue-orange PL does not exhibit any features (curve *5* in Fig. 3).

4. DISCUSSION

We do not yet have precise data about the structure and spatial geometry of the compounds we synthesized. Therefore, in order to analyze the data obtained, it is instructive to consider the structure of an analogous compound, a $Mn_2P_2O_7 \cdot 2H_2O$ crystal [6]. In its lattice, each manganese atom is coordinated to six oxygen atoms, one of which belongs to a water molecule. The octahedra are linked together by common edges and form infinite chains. The anion sublattice consists of $P_2O_7^{4-}$ ions, which can be thought of as two PO_4 tetrahedra linked by a common oxygen, with the P–O–O bond deviating significantly from a straight line. The mean P–O distance is 1.520 Å for terminal P–O bonds and 1.613 Å for bridge oxygen atoms.

IR absorption and Raman spectra we obtained indicate that the structure of the $Zn_{2-x}Mn_xP_2O_7 \cdot 5H_2O$ compounds is similar to that described above. This fact can be used to explain the luminescent properties of the compounds, in particular, the red PL. Indeed, in the vibration spectrum, it is simple to distinguish high frequencies related to fixed crystallization water and hydrogen bonds: there are IR absorption lines at 1640 and 1657 cm^{-1}, at 2125 and 2380 cm^{-1}, and at 3200 and 3365 cm^{-1}.

The low-frequency lines in the Raman spectra (in the range below 300 cm^{-1}) correspond to interstitial vibrations. As follows from comparing with the available data, the IR absorption and Raman lines in the range 400–1500 cm^{-1} are related to intramolecular vibrations of the $P_2O_7^{4-}$ anion [7, 8]. In interpreting the luminescence data, it is important to know whether the bond between the two PO_4 tetrahedra within the $P_2O_7^{4-}$ group is bent or not. In the former case, the $P_2O_7^{4-}$ group has the D_{3d} symmetry; otherwise, its symmetry is C_{2v} or lower, depending on the particular crystal structure. In the first case, the vibration spectrum can have up to 12 lines (with allowance for the degeneracy) and the mutual exclusion rule should be obeyed, because the group has an inversion center. According to our data, this rule is not obeyed and the total number of distinct lines observed in the two types of IR absorption and Raman scattering spectra within the intramolecular vibration range of $P_2O_7^{4-}$ is as large as 18. Therefore, the $P_2O_7^{4-}$ molecular anion has low symmetry or no symmetry at all. We notice that this can be the case not only when the P–O–P bond angle is not right but also when one or a few oxygen atoms are shared by this group and water molecules.

Based on this conclusion regarding the $P_2O_7^{4-}$ group, we can deduce that the oxygen octahedra surrounding the zinc and manganese ions are seriously distorted, which manifests itself in the luminescence spectra. Indeed, the red PL band observed in the presence of manganese in $Zn_{2-x}Mn_xP_2O_7 \cdot 5H_2O$ ($x \neq 0$) should be related to radiative transitions in Mn^{2+} ions that are in a near-octahedral oxygen environment [9, 10]. The red PL excitation spectra are also typical of Mn^{2+} ions located in a crystal field with this symmetry and can be associated with transitions to the $^4F_2$ (320- to 390-nm range), $^4A + {}^4E + {}^4F_2$ (390–480 nm), and $^4F_1$ levels (480–580 nm). However, the fact that each of the spectral bands has three or more structure components indicates that the degeneracy is lifted and, therefore, confirms the conclusion concerning a strong deformation of the oxygen octahedra.

Another possible indication of the presence of certain structural defects in our samples is the fact that the PL associated with manganese ions is also observed in the blue spectral range. It is known that the Mn^{2+} ion luminescence can be observed in this range when the ions are in a near-tetrahedral oxygen environment [11, 12]. Probably, in the fairly loose $Zn_{2-x}Mn_xP_2O_7 \cdot 5H_2O$ structure, some manganese ions can have less then six oxygen ions in their nearest neighborhood and, therefore, are in near-tetrahedral coordination.

5. CONCLUSIONS

Diphosphates $Zn_{2-x}Mn_xP_2O_7 \cdot 5H_2O$ with $x = 0–2$ have been synthesized, and their luminescence and vibration spectra have been studied. The red luminescence band was found to be due to radiative transitions in the Mn^{2+} ion. The concentration range of Mn^{2+} radiation quenching was determined. The optimal compositions for effective Mn^{2+} radiation correspond to values of x less than 0.5.

The ability of the $Zn_{2-x}Mn_xP_2O_7 \cdot 5H_2O$ system to form a continuous sequence of solid solutions is an important feature for its potential application as a phosphor. However, it is necessary to find a way to deal with the crystallization water, which is most likely a strong quencher for the luminescence of these compounds.

REFERENCES

1. T. Kanazawa, *Inorganic Phosphate Materials* (Nauk. Dumka, Kiev, 1998) [in Russian].
2. Y. Takita, H. Yamashita, and K. Morstaka, Chem. Lett. **10**, 1733 (1989).
3. É. N. Beresnev, *Method of Residual Concentrations* (Nauka, Moscow, 1992) [in Russian].
4. T. Rossel and H. Kiesslich, Z. Anal. Chem. **225** (3), 391 (1967).
5. *Powder Diffraction Fill. JCPDS, International Center Diffraction Data* (Swarhmere, USA, 1986).
6. S. Schneider and R. Collin, Acta Crystallogr. B **21**, 13 (1968).
7. A. N. Lazarev and V. S. Aksel'rod, Opt. Spektrosk. **9** (3), 326 (1960).
8. A. N. Lazarev and T. F. Tenishcheva, Neorg. Mater. **5** (1), 82 (1969).
9. D. T. Palumbo and J. J. Brown, J. Electrochem. Soc. **118** (7), 1159 (1971).
10. K. Petermann and G. Huber, J. Lumin. **31–32**, 71 (1994).
11. M. Kaplanova, M. Trojan, D. Brandova, and J. Navratil, J. Lumin. **29**, 199 (1984).
12. M. A. Scott, T. P. J. Han, H. G. Gallagher, and B. Henderson, J. Lumin. **72–74**, 260 (1997).

Translated by G. Tsydynzhapov

Physics of the Solid State, Vol. 47, No. 8, 2005, pp. 1548–1551. From Fizika Tverdogo Tela, Vol. 47, No. 8, 2005, pp. 1490–1493.
Original English Text Copyright © 2005 by Vikhnin.

PROCEEDINGS OF THE XII FEOFILOV WORKSHOP "SPECTROSCOPY OF CRYSTALS ACTIVATED BY RARE-EARTH AND TRANSITION-METAL IONS"

(Yekaterinburg, Russia, September 22–25, 2004)

Charge Transfer Vibronic Excitons: Charge-Transfer Lattice-Instability Effects[1]

V. S. Vikhnin

Ioffe Physicotechnical Institute, Russian Academy of Sciences, St. Petersburg, 194021 Russia
e-mail: valentin.vikhnin@mail.ioffe.ru

Abstract—Two aspects for investigating bipolaronic excitons [charge transfer vibronic exciton (CTVE)] in ionic-covalent solids are considered. These aspects are predictions of the charge-transfer lattice instability corresponding to charge transfer and lattice anharmonicity, as well as to repulsion between different types of CTVEs in the order parameter field. Oxide crystals ($SrTiO_3$, $BaTiO_3$, $K_3Na(CrO_4)_2$) are considered as an example. *© 2005 Pleiades Publishing, Inc.*

1. INTRODUCTION

Bipolaronic excitons (charge transfer vibronic exciton (CTVE); see, for example, [1–5] and references therein) are a topic of recent importance for ferroelectric oxides. CTVEs are correlated polaronic electron–hole pairs or triads. Our first phenomenological models of CTVEs [1] were based on the validity of the strong vibronic coupling limit (including charge-transfer lattice coupling). This was confirmed in [2, 3] in the framework of semiempirical Hartree–Fock calculations of the CTVE in the INDO approach. These first CTVE calculations confirmed the realization of CTVE self-localization with the formation of a well-defined CTVE dipole moment, as well as its triad structure in model ferroelectric oxides. Another step was taken in [5], where CTVE dipole reorientations due to CTVE–CTVE cross relaxation were considered and manifested in the experiments. As a result, CTVEs have an electric dipole moment (evaluated, for instance, in [6, 7]) which can reorient due to CTVE–CTVE cross relaxation. Hence, CTVEs manifest themselves as dipole reorienting centers which can directly interact with the soft polarization mode. It is due to this reason that the CTVEs in ferroelectric oxides can shift (or induce) ferroelectric phase transitions [6, 7]. The main topics of this paper will be the following.

(i) Local (Fig. 1a) and cluster-type (Fig. 1b) transitions connected with first order charge-transfer lattice instability [4] in the low-lying excited state of the ionic-covalent crystal due to charge transfer and lattice anharmonicity will be considered. This phenomenon could be a candidate for explaining the recently detected [8] strong order-disorder-type fluctuations in the soft dynamic temperature regions in nominally pure $SrTiO_3$ and in $BaTiO_3$ crystals. (ii) Another mechanism of charge-transfer lattice instability could be related to the order parameter induced by the mixing of different types of CTVEs. Namely, it will be a ferroelastic order parameter that mixes CTVE-I, which exists even in the linear approximation, and pure anharmonic CTVE-III (in accordance with the classification in [4]). We do connect this behavior with the recently detected anomalous EPR-spectrum transformation in the oxide ferroelastic $K_3Na(CrO_4)_2$ at low temperature [9].

2. LOCAL AND MACROSCOPIC CHARGE-TRANSFER LATTICE INSTABILITY CORRESPONDING TO ANHARMONIC CHARGE TRANSFER EXCITATIONS

The considerations in this section will be based on a dynamical model with an on-center single-well potential for an active vibration in each cell of the crystal. Nevertheless, a multiwell potential with off-center behavior occurs here for low-lying excited anharmonic state. Such a potential could be induced by charge-transfer lattice interaction relating to a specific anharmonic CTVE due to the ground-state potential anharmonicity (so-called CTVE-III; see [4]).

Let us consider the free energy of such a CTVE-III system interacting with a soft TO polarization for the typical case of a soft direction of polarization, namely, along the [001]-type direction. Here, only two of six possible CTVE orientations (which are parallel and antiparallel to **P** orientation) interact with **P**. As a result, the CTVE-related free energy has the following form:

---

[1] This article was submitted by the author in English.

$$\begin{aligned}\delta F_{\mathrm{CTVE}} &= -N_{\mathrm{CTVE}}kT\\ &\times \ln[1+\exp\{[(4\pi/3)d_i^{\mathrm{CTVE}}P_i-\Delta_0+\Delta_1(T)]/kT\}\\ &\quad + 4\exp\{[-\Delta_0+\Delta_1(T)]/kT\}\\ &\quad + \exp\{[-(4\pi/3)d_i^{\mathrm{CTVE}}P_i-\Delta_0+\Delta_1(T)]/kT\}]\\ &\quad + \frac{\alpha_0(T-T_C)}{2}P_i^2+\frac{\beta}{4}P_i^4+\dots,\end{aligned} \tag{1}$$

T_C is the initial ferroelectric phase transition temperature, and N_{CTVE} is the CTVE concentration. Here, the CTVE activation energies that are related to the CTVE-induced lattice polarization for noncritical, Δ_0, and for soft lattice, $\Delta_1(T)$, degrees of freedom of the ferroelectric, as well as the CTVE effective dipole moment soft polarization d_i^{CTVE}–P_i interaction, all form as a result of the CTVE-III excitation energy. Related splitting appears between the lowest CTVE-III-type excitation in the off-center potential well located along the total internal field on the one hand and the on-center ground state on the other $[\Delta_0-(4\pi/3)d_i^{\mathrm{CTVE}}P_{i0}-\Delta_1(T)]$. Note also that the temperature dependence for $\Delta_1(T)$ could be evaluated here in the framework of minimization of the soft mode polarization field induced by the CTVE-III total electric dipole moment bilinearly interacting with the soft polarization, $\sim d_i^{\mathrm{CTVE}}P_i$. Taking into account the contribution of the soft polarization mode, $\omega_0^2(T) = \lambda(T-T_C)$, we get a rather smooth $\Delta_1(T)$ dependence for the parabolic dispersion law for the soft mode and for fulfilling the inequality $a \ll R_C(T)$, where $R_C(T)$ is the soft polarization correlation radius and a is a lattice constant: $\Delta_1(T) \propto [1-(a/2R_C)]$.

In general, we could get here the phase transition of the second order due to sufficiently fast CTVE-III reorientations and the possibility of their alignment with the mean field effect formation. This phenomenon is similar to a phase transition induced by reorientable CTVE-I pumped by irradiation [4]. Here, we have thermal population of the off-center potential minima. As a result, the approximate equation for the free energy at high CTVE-III activation energies, temperatures that are not very low, and at sufficiently low magnitudes of soft polarization, when the inequalities $(\Delta_0-\Delta_1(T)) \gg kT \gg (4\pi/3)d_i^{\mathrm{CTVE}}P_i$ are fulfilled, becomes

$$\begin{aligned}\delta F_{\mathrm{CTVE}} &= \Bigg(\frac{\alpha_0(T-T_C)}{2}\\ &- \frac{N_0\exp\{(-\Delta_0+\Delta_1(T))/kT\}\{(4\pi/3)d_i^{\mathrm{CTVE}}\}^2}{6kT}\Bigg)P_i^2\\ &+\frac{\beta}{4}P_i^4+\dots\end{aligned} \tag{2}$$

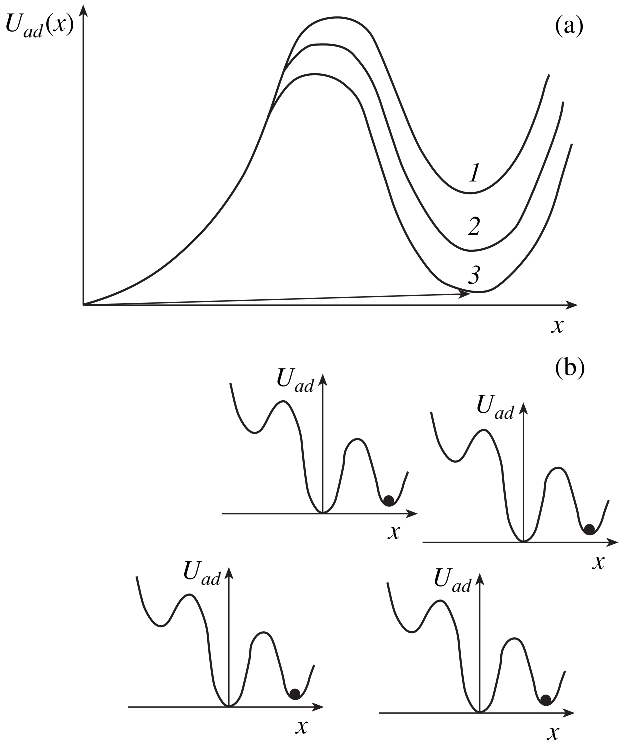

Fig. 1. (a) Local charge-transfer lattice transition with occupation of the anharmonic-charge-transfer-related minimum of the adiabatic potential. Potential curves *1*–*3* correspond to the following inequalities: $T_1 > T_2 > T_3 \geq T_{\mathrm{loc}}\dots$, where T_{loc} is the local transition temperature. (b) Precursor polar cluster formation due to preferable occupation of low-lying excited anharmonic charge-transfer states in the neighboring cells in the vicinity of local charge-transfer lattice transitions.

and leads to the following transcendental equation for the CTVE-III-induced second-order ferroelectric phase transition:

$$\begin{aligned}&(T-T_C)T\\ &= \frac{N_0\exp\{(-\Delta_0+\Delta_1(T))/kT\}\{(4\pi/3)d_i^{\mathrm{CTVE}}\}^2}{3k\alpha_0}.\end{aligned} \tag{3}$$

The above equation could be solved numerically.

Now we will discuss the CTVE clustering effects (see also Fig. 1b). First, we have to consider the additional CTVE energy lowering due to the cooperative negative-U effect. As a result, clustering becomes advantageous. Second, let us now take into account that CTVEs are mobile excitations due to cross-relaxation processes [5]. Together, these two circumstances lead to the possibility of clustering for the CTVE-III under consideration. The necessary condition for its effective realization is t the requirement that the average CTVE–CTVE distance, $\langle R_{\mathrm{CTVE-CTVE}}\rangle$, be less or at least have the same order as the distance which the CTVE can pass in the framework of random cross-relaxation hopping before its recombination. This condition can be expressed in the following form:

$$\langle R_{\mathrm{CTVE/CTVE}} \rangle \le a \sqrt{\frac{1/\tau_{\mathrm{cross}}}{1/\tau_{\mathrm{recomb}}}}, \quad (4)$$

where a is a lattice constant and $(1/\tau_{\mathrm{cross}})$ and $(1/\tau_{\mathrm{recomb}})$ are the rates of CTVE–CTVE cross relaxation and of CTVE recombination, respectively. It should be noted that the latter rate has a tunneling-related nature for the case of CTVE-III and is rather slow. This aspect is favorable for the fulfillment of inequality (4). So, let us consider now the CTVE-III clustering. For instance, the free energy of the system with the density of the CTVE-III clusters (N_{cluster}) and with the number of CTVE-III in each cluster (n_{CTVE}) has the following form:

$$\begin{aligned} \delta F_{\mathrm{CTVE}} &= -N_{\mathrm{cluster}} kT \\ &\times \ln[1 + \exp\{[(4\pi/3) n_{\mathrm{CTVE}} d_i^{\mathrm{CTVE}} P_i \\ &- \Delta_0 n_{\mathrm{CTVE}} + \Delta_1(T) n_{\mathrm{CTVE}} + \Delta_2 n_{\mathrm{CTVE}}^2]/kT\} \\ &+ 4\exp\{[-\Delta_0 n_{\mathrm{CTVE}} + \Delta_1(T) n_{\mathrm{CTVE}} + \Delta_2 n_{\mathrm{CTVE}}^2]/kT\} \\ &+ \exp\{[-(4\pi/3) n_{\mathrm{CTVE}} d_i^{\mathrm{CTVE}} P_i - \Delta_0 n_{\mathrm{CTVE}} \\ &+ \Delta_1(T) n_{\mathrm{CTVE}} + \Delta_2 n_{\mathrm{CTVE}}^2]/kT\} \\ &+ \frac{\alpha_0 (T - T_C)}{2} P_i^2 + \frac{\beta}{4} P_i^4 + \ldots . \end{aligned} \quad (5)$$

Here, the $\Delta_2 n_{\mathrm{CTVE}}^2$ term is related to the cooperative negative-U effect and leads to an essential decrease in the off-center CTVE-III minima energies. Under similar approximations as above, $(\Delta_0 n_{\mathrm{CTVE}} - \Delta_1(T) n_{\mathrm{CTVE}} - \Delta_2 n_{\mathrm{CTVE}}^2) \gg kT \gg (4\pi/3) n_{\mathrm{CTVE}} d_i^{\mathrm{CTVE}} P_i$, we obtain the following approximate free energy equation for its harmonic part:

$$\begin{aligned} \delta F_{\mathrm{CTVE}} &= \left(\frac{\alpha_0 (T - T_C)}{2} - \frac{N_{\mathrm{cluster}}}{6kT}\right. \\ &\times \exp\{(-\Delta_0 n_{\mathrm{CTVE}} + \Delta_1(T) n_{\mathrm{CTVE}} + \Delta_2 n_{\mathrm{CTVE}}^2)/kT\} \\ &\times \left.\{(4\pi/3) n_{\mathrm{CTVE}} d_i^{\mathrm{CTVE}}\}^2\right) P_i^2 + \ldots . \end{aligned} \quad (6)$$

The latter leads to an equation for the second-order ferroelectric phase transition temperature induced by CTVE-III-related reorienting polar clusters:

$$\begin{aligned} (T - T_c)T &= \frac{N_{\mathrm{cluster}}}{3k\alpha_0} \\ &\times \exp\{(-\Delta_0 n_{\mathrm{CTVE}} + \Delta_1(T) n_{\mathrm{CTVE}} + \Delta_2 n_{\mathrm{CTVE}}^2)/kT\} \\ &\times \{(4\pi/3) n_{\mathrm{CTVE}} d_i^{\mathrm{CTVE}}\}^2. \end{aligned} \quad (7)$$

The solution of Eq. (7) corresponds to the soft-mode condensation point. It is seen from this equation that the new critical temperature induced by thermally occupied CTVE-III states increases with the concentration-dependent factors $\exp\{(-\Delta_0 n_{\mathrm{CTVE}} + \Delta_1(T) n_{\mathrm{CTVE}} + \Delta_2 n_{\mathrm{CTVE}}^2)/kT\}$ and $N_{\mathrm{cluster}} n_{\mathrm{CTVE}}^2$. On the other hand, it is namely these factors that increase with clustering together with a decrease in free energy.

Note also that the total number of CTVEs could increase if the CTVE-III excitation energy becomes not so high. This occurs, for instance, in the vicinity of the second-type phase transition in the framework of our model. This is the first-order ferroelectric phase transition. The corresponding critical temperature for this phase transition will be the solution of the following equation:

$$[(4\pi/3) d_i^{\mathrm{CTVE}} P_i(T) - \Delta_0 + \Delta_1(T) + \Delta_2 n_{\mathrm{CTVE}}] = 0. \quad (8)$$

Here, the equilibrium soft polarization $P_i(T)$ could be evaluated by minimizing the free energy from Eq. (5).

Note in the conclusion that the distinguishing feature of the model is the natural coexistence of order–disorder and displacive-type degrees of freedom. This coexistence strengthening appears namely in the vicinity of the first-order phase transition mentioned above. It does not disregard that order–disorder dynamics and related CTVE fluctuations within such a model could be a possible explanation for the order–disorder behavior discovered recently by Zalar *et al.* [8] in $BaTiO_3$ and $SrTiO_3$ ferroelectric oxides.

3. CHARGE-TRANSFER LATTICE INSTABILITY INDUCED BY INTERACTION BETWEEN CHARGE TRANSFER VIBRONIC EXCITONS OF DIFFERENT NATURE DUE TO THE ORDER PARAMETER FIELD

Let us consider now another mechanism of charge-transfer lattice instability of the first order that is likewise related to the CTVE-III state discussed in the previous section. This state is characterized by an additional anharmonic potential well for the potential branch of the ground state (in accordance with the classification in [4]). We will consider the coexistence of CTVE-III with the CTVE-I type state [4] (Fig. 2) for the case of a proper ferroelastic. For simplicity, we will discuss the case of a one-component order parameter η_1. Nevertheless, the proper ferroelastic $K_3Na(CrO_4)_2$ [9], which very probably manifests local instability of the same type as discussed here, belongs to the two-component order-parameter case. The required generalization of the model will be published later. We will also consider the situation where the CTVE-III and CTVE-I states have minima for the adiabatic potential that are close to one another. As a result, the overlap of related vibrational wave functions for CTVE-III and CTVE-I will be sufficiently high. The latter corresponds to effective mixing of these states under the action of internal or external fields. For instance, the

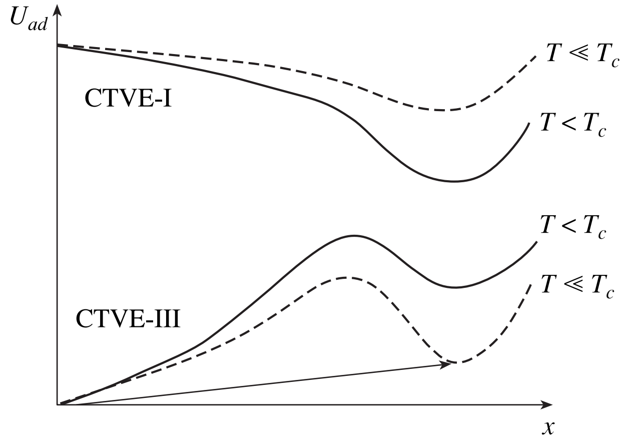

Fig. 2. Order-parameter-induced repulsion of CTVE-I and CTVE-III states as a mechanism of local charge-transfer lattice transition. The arrow corresponds to realization of a local transition with lowering of the anharmonic state energy.

ferroelastic order parameter η_1 can mix the CTVE-III and CTVE-I states mentioned above due to linear vibronic interaction. Such a field can also form diagonal matrix elements of the vibronic interaction on the basis of both of the CTVE states discussed. These vibronic interactions can be presented in the following form:

$$H_{\text{III–I}} = W\eta_1\sigma_x, \tag{9}$$

$$H_- = V_1\eta_1\sigma_z, \tag{10}$$

$$H_+ = V_2\eta_1 I, \tag{11}$$

where W, V_1, are V_2 are vibronic constants and the operators σ_x, σ_z, and I have the form $\sigma_x = |a\rangle\langle b| + |b\rangle\langle a|$, $\sigma_z = |a\rangle\langle a| - |b\rangle\langle b|$, and $I = |a\rangle\langle a| + |b\rangle\langle b|$; states a and b correspond to the CTVE-I and CTVE-II vibrational states, respectively. Taking into account Eqs. (9)–(11) and the initial energy splitting between the CTVE-I and CTVE-III vibrational states Δ, the final equation for the CTVE-III energy in the order parameter field will be presented as

$$E_{\text{CTVE-III}} = V_2\eta_1 + \sqrt{\frac{(\Delta + V_1\eta_1)^2}{4} + (W\eta_1)^2}. \tag{12}$$

It is important to underline that the $E_{\text{CTVE-III}}$ energy can be equal to zero (at the first-order local transition point). This important point could be reached taking into account the temperature dependence of the order parameter in Eq. (12), $\eta_1(T)$. The corresponding equation for the temperature of the first-order local transition point could be derived from Eq. (12):

$$(V_2\eta_1(T))^2 = \frac{(\Delta + V_1\eta_1(T))^2}{4} + (W\eta_1(T))^2. \tag{13}$$

This is the type of local transition related to charge-transfer lattice instability of the first order that was probably detected by EPR at low temperatures for the proper ferroelastic $K_3Na(CrO_4)_2$ [9].

ACKNOWLEDGMENTS

The work was supported by NATO (CLG 980378), the Russian Foundation for Basic Research (project no. 03-02-17589), and by the programs "Low-Dimension Quantum Structures" and "Spin-Dependent Effects in Solids and Spintronics."

REFERENCES

1. V. S. Vikhnin, Ferroelectrics **199**, 25 (1997); Z. Phys. Chem. **201**, 201 (1997); Ferroelectr. Lett. Sect. **25**, 27 (1999).
2. V. S. Vikhnin, R. Eglitis, S. Kapphan, E. A. Kotomin, and G. Borstel, Europhys. Lett. **56** (5), 702 (2001).
3. V. S. Vikhnin, R. Eglitis, S. Kapphan, G. Borstel, and E. A. Kotomin, Phys. Rev. B **65**, 104304 (2002).
4. V. S. Vikhnin, Solid State Commun. **127**, 283 (2003).
5. V. Vikhnin, H. Liu, and W. Jia, Phys. Lett. A **245**, 307 (1998).
6. V. S. Vikhnin, S. E. Kapphan, R. Pirc, and A. S. Sigov, Phys. Status Solidi C **1** (11), 2820 (2004).
7. V. S. Vikhnin, S. E. Kapphan, R. I. Eglitis, and R. Pirc, Phys. Status Solidi C **2** (1), 120 (2004).
8. B. Zalar, V. V. Laguta, and R. Blinc, Phys. Rev. Lett. **90**, 037601 (2003).
9. H. R. Asatryan, V. S. Vikhnin, T. I. Maksimova, M. Maczka, and J. Hanusa, in *Proceedings of the XII Feofilov Symposium on Spectroscopy of Crystals Activated by Rare Earth and Transition Ions, Yekaterinburg-Zarechniy, 2004* (Yekaterinburg, 2004), p. 75.

Physics of the Solid State, Vol. 47, No. 8, 2005, pp. 1552–1555. Translated from Fizika Tverdogo Tela, Vol. 47, No. 8, 2005, pp. 1494–1497.
Original Russian Text Copyright © 2005 by Sokolov, Dubinin, Teploukhov, Parkhomenko, Gruzdev.

PROCEEDINGS OF THE XII FEOFILOV WORKSHOP "SPECTROSCOPY OF CRYSTALS ACTIVATED BY RARE-EARTH AND TRANSITION-METAL IONS"

(Yekaterinburg, Russia, September 22–25, 2004)

Lattice Instability Induced by 3*d* Impurities in II–VI Compound Semiconductors

V. I. Sokolov, S. F. Dubinin, S. G. Teploukhov, V. D. Parkhomenko, and N. B. Gruzdev

Institute of Metal Physics, Ural Division, Russian Academy of Sciences,
ul. S. Kovalevskoĭ 18, Yekaterinburg, 620219 Russia
e-mail: visokolov@imp.uran.ru

Abstract—Nickel-impurity-induced transverse displacements of ions in a $Zn_{1-x}Ni_xSe$ lattice ($x = 0.0025$) were detected. This type of displacement correlates with macroscopic distortions of a crystal associated with transverse ultrasonic waves that are propagated along the ⟨110⟩ direction. The shear instability is assumed to be due to the hybridization of the sp^3 bonds with the 3*d* states of the impurity centers. *© 2005 Pleiades Publishing, Inc.*

Semiconductors with ionic–covalent bonding are attracting interest both for fundamental research and for practical application. The interest in wideband semiconductors of this class (GaN, ZnO, SiC) containing 3*d* transition metal impurities (Cr, Mn, Fe, Co, Ni) has increased rapidly over the past few years, because these materials undergo ferromagnetic ordering with the Curie point lying near or above room temperature [1].

It has been believed that 3*d* impurities in semiconductors can cause only local deformation of the lattice near isolated impurity centers due to a change in the interaction between the 3*d* center and its nearest neighbors. However, it has recently been discovered that $Zn_{1-x}Ni_xSe$ ($x = 0.0025$) undergoes a nickel-induced structural phase transition at a temperature $T_S = 14.5$ K [2]. This transition indicates that a nickel impurity can cause significant long-range correlated displacements of ions in the lattice, which is a surprise because the Ni concentration is low. The temperature dependence of the changes in the ultrasound velocity suggests that, as the temperature decreases, the lattice elastic modulus c_{44} begins to decrease at ~120 K, which is significantly above T_S [3]. It is of interest to elucidate the structural changes in $Zn_{1-x}Ni_xSe$ at high temperatures that cause the $c_{44}(T)$ anomaly to occur with a decrease in temperature.

In this paper, we report on the results of a study into the fine details of the structure of a $Zn_{1-x}Ni_xSe$ solid solution ($x = 0.0025$) using thermal-neutron elastic scattering, which is very sensitive to weak structural imperfections of crystals. A neutron beam with a wavelength of 1.568 Å was prepared with a double-crystal monochromator based on pyrolitic graphite and strained germanium. Using a highly monochromatized beam and the optimal neutron wavelength made it possible to suppress higher harmonics. In order to increase the sensitivity of measurements to weak distortions of the crystal lattice, rocking curves were recorded near diffraction peaks with high indices: (220), (022), and (400). Measurements were performed at 300 and 120 K.

Figure 1a shows the neutron diffraction pattern taken from the (001) plane of the reciprocal lattice of a doped single crystal. The (220) Bragg reflection is a Gaussian with a half-width of $\Delta_{1/2} = 0.014$ Å^{-1} in momentum-transfer space. The high resolution attained in the wave-vector range covered is due to the weak misorientations (less than 15′) of mosaic blocks in the crystal under study. The diffuse maximum was determined by subtracting the calculated Bragg peak intensity from the experimentally measured scattering intensity. The accuracy of the profile analysis of the diffraction pattern in Fig. 1 is better than 2%. Note that the diffraction pattern taken from an undoped ZnSe crystal does not have a characteristic diffuse maximum.

The presence of diffuse scattering in $Zn_{1-x}Ni_xSe$ ($x = 0.0025$) suggests that the nickel impurity produces weak distortions of the crystal structure. In order to examine the topology of diffuse scattering in the reciprocal lattice of the doped crystal more thoroughly, we also performed measurements near the (022) and (400) reflections (Figs. 1b and 2a, respectively). Note that the diffuse scattering near the (022) and (400) reflections is more intense and less extended in wave-vector space than that shown in Fig. 1a. It is clearly seen that the diffuse scattering peak narrows and becomes stronger as the temperature decreases (Fig. 2).

In our opinion, the occurrence of diffuse scattering in the region of the main Bragg reflections indicates that microscopic regions with displaced ions arise in the $Zn_{1-x}Ni_xSe$ crystal ($x = 0.0025$). Therefore, the intensities and widths of the diffuse maxima carry

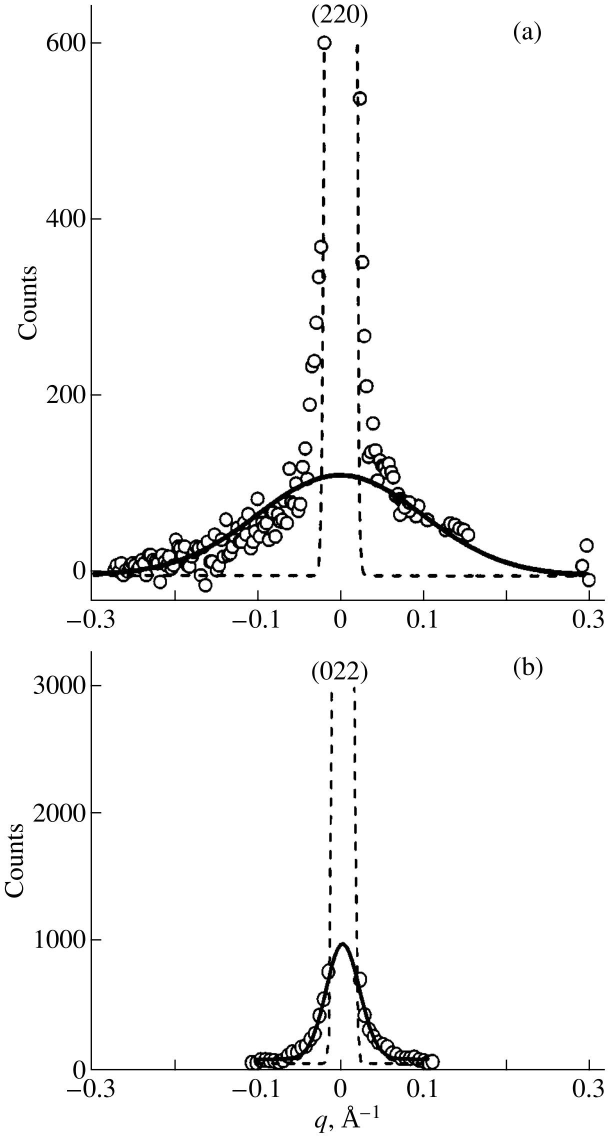

Fig. 1. Rocking curves for a $Zn_{1-x}Ni_xSe$ single crystal (x = 0.0025) near Bragg reflections (a) (220) (along the $\langle 1\bar{1}0\rangle$ direction) and (b) (022) (along the $\langle 100\rangle$ direction) obtained at T = 300 K. Points are experimental data, and the dashed and solid lines are the profiles of the Bragg reflections and diffuse maxima, respectively.

information on the number of regions with certain amplitudes of ionic displacements and on the average dimensions of these regions along different crystallographic directions, respectively.

Thus, within our model, the intensity of diffuse scattering from a distorted crystal can be written as [4]

$$J_d \sim b^2 c(\boldsymbol{\kappa}\cdot\mathbf{u})^2, \tag{1}$$

where b is the average nuclear scattering amplitude, c is the concentration of displaced ions, $\boldsymbol{\kappa} = (\mathbf{B}_{hkl} + \mathbf{q})$ is the scattering vector, $\mathbf{B}_{hkl}$ is a reciprocal lattice vector, $\mathbf{q}$ is the wave vector, and $\mathbf{u}$ is the displacement of an atom.

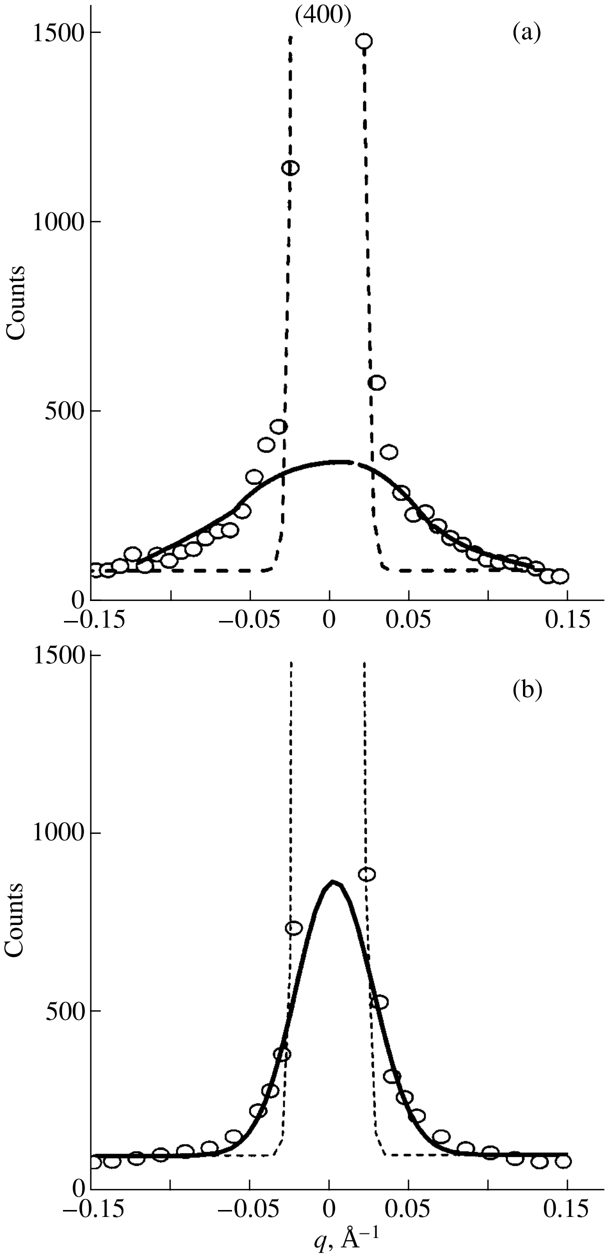

Fig. 2. Rocking curves for a $Zn_{1-x}Ni_xSe$ single crystal (x = 0.0025) near the (400) Bragg reflection taken along the $\langle 011\rangle$ direction at temperatures of (a) 300 and (b) 120 K. Points are experimental data, and the dashed and solid lines are profiles of the Bragg reflections and diffuse maxima, respectively.

Note that the geometry of the diffraction experiments is chosen such that the vector $\mathbf{u}$ is parallel to the scattering vector $\boldsymbol{\kappa}$ and the wave vector $\mathbf{q}$ is always perpendicular to $\boldsymbol{\kappa}$. In this geometry, static displacements of the atoms in a crystal manifest themselves if they are perpendicular to the wave vector (i.e., if they are transverse). In principle, there can be regions with two types of transverse static displacements with respect to the wave vec-

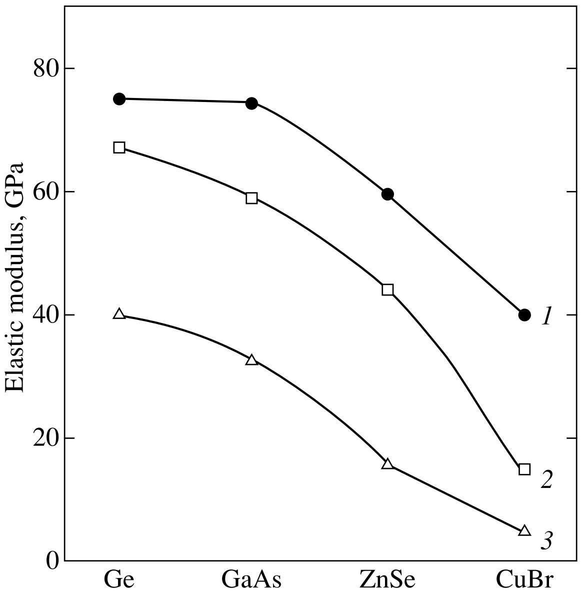

Fig. 3. Elastic moduli of Ge, GaAs, ZnSe, and CuBr crystals: (*1*) the bulk modulus $(c_{11} + 2c_{12})/3$, (*2*) the shear modulus c_{44}, and (*3*) the effective shear modulus $(c_{11} - c_{12})/2$.

tor. Therefore, regions with transverse ionic displacements are characterized by the scanning vector **q** and the ionic displacement vector **u**. Experimentally, it is easiest to determine the dimensions of distorted regions along crystallographic directions:

$$L = 2\pi/\Delta q_{\text{calc}}, \qquad (2)$$

where $\Delta q_{\text{calc}} = (\Delta q^2_{\text{obs}} - \Delta q^2_{\text{inst}})^{1/2}$, Δq_{obs} is the half-width of the observed diffuse maximum, and Δq_{inst} is the instrumental half-width. The linear dimensions of distorted regions in a crystal at room temperature are found to be

$$\begin{aligned} L_1 &= 25\ \text{Å}\ (\langle 1\bar{1}0\rangle[110]), \\ L_2 &= 50\ \text{Å}\ (\langle 011\rangle[100]), \\ L_3 &= 120\ \text{Å}\ (\langle 100\rangle[011]). \end{aligned} \qquad (3)$$

Here, the directions of the vector **q** and of ionic displacements **u** perpendicular to **q** are indicated in angular and square brackets, respectively. It follows from Eqs. (3) that the linear dimensions of a distorted region along different crystallographic directions differ significantly. The correlation length L depends not only on the scanning direction but also on the orientation of the ionic displacement vector relative to a wave vector of one type [L_1, L_2 in Eqs. (3)].

This result agrees with the data obtained in [3] on the propagation of transverse ultrasonic waves along the ⟨110⟩ direction. The velocities of these waves polarized along $[1\bar{1}0]$ and [001] are $v^2[1\bar{1}0] = \boldsymbol{\rho}^{-1}(c_{11} - c_{12})/2$ and $v^2[001] = \boldsymbol{\rho}^{-1}c_{44}$, respectively. According to the experimental data from [3], the temperature dependence of $v[1\bar{1}0]$ in ZnSe and $Zn_{1-x}Ni_xSe$ ($x = 0.0025$) crystals differs from that of $v[001]$. Indeed, $v[1\bar{1}0]$ in a pure and a doped crystal varies with temperature only weakly, whereas the temperature dependence of $v[001]$ over the range 15–120 K indicates that the doping causes the elastic modulus c_{44} of the crystal to decrease noticeably. In our opinion, ionic displacements of the ⟨011⟩[100] type observed in diffuse neutron scattering are directly related to the elastic modulus c_{44}. In a doped crystal, the linear dimension L_2 of regions with ⟨011⟩[100] ionic displacements increases from 50 Å at 300 K to 120 Å at 120 K (Fig. 2). Therefore, there is an apparent correlation between transverse shear ionic displacements in nanosized regions of a crystal that manifest themselves in diffuse neutron scattering and macroscopic shear displacements of ions produced by transverse ultrasonic waves.

This correlation allows us to use extensive experimental data on the shear properties of lattices with a zinc-blende structure in studying the mechanism of the variation in the stability of these lattices and, in particular, the mechanism through which nickel doping lowers the shear stability of the ZnSe lattice. The ionic–covalent crystal lattices are characterized by the spatial orientation of sp^3 bonds, their length, and the electron-density distribution along a bond, all of which influence the properties of crystals with a zinc-blende structure [5].

It should be noted that the agreement between the calculated frequencies of transverse acoustic phonons at the Brillouin zone boundary of Ge and GaAs with experiment becomes better when one takes into account the long-range interaction that originates in an ionic–covalent lattice from the sp^3 bond charges interacting with one another and from charge displacement from the center of a bond to the anion in the case of GaAs [6].

Figure 3 presents the elastic moduli at 300 K for Ge, GaAs, ZnSe, and CuBr crystals [5], in which the ionic–covalent sp^3 bond lengths are approximately equal. It can be seen that the shear moduli c_{44} and $(c_{11} - c_{12})/2$ decrease significantly as one goes along this row of materials. This decrease is related to the magnitude and position of the charge on a bond or, more exactly, to a redistribution of electron density over the sp^3 bond as one goes along this row from Ge to CuBr.

The thermal expansion coefficient of ionic–covalent crystals is negative at temperatures below 100 K [7]. Therefore, as the temperature decreases, these crystals expand rather than contract beginning at a certain temperature (about 70 K for ZnSe). The maximum magnitude of the negative thermal expansion coefficient increases as one goes along the row Ge, GaAs, and ZnSe [7]. Therefore, the properties of crystal lattices with ionic–covalent bonding, including ZnSe, are highly sensitive to a change in the sp^3 bond parameters.

The influence of Ni impurities on the stability of the ZnSe lattice with respect to shear can be explained as follows. A Ni atom substituting for a Zn atom donates two electrons to form an sp^3 bond. The d^8 orbitals are hybridized with sp^3 bonds and thereby distort them, changing the direction and length of the bonds between the impurity atom and its nearest neighbors and causing a redistribution of electron density along these bonds. As a result, the nearest neighbors of the impurity center are displaced. In terms of the $NiSe_4$ cluster model, these displacements are tetragonal and/or trigonal shear shifts of Se ions. Due to the effective long-range interaction mechanism, local Se ion shear shifts also occur in the adjacent unit cells, thereby causing the formation of regions of transverse ionic displacements, which manifest themselves in diffuse neutron scattering at room temperature. As the temperature decreases, the regions of ionic shear shifts expand and coalesce, which brings about the gradual formation of macroscopic regions of lattice shear strains associated with the shear modulus c_{44}. Thus, a multielectron 3*d*-impurity center in an ionic–covalent crystal causes nonlocal, large-scale shear strains in the crystal lattice. Determining these strains is a very complicated problem; its solution necessitates both detailed studies into structural lattice distortions in II–VI compounds doped with 3*d*-metal impurities and *ab initio* calculations of distortions of MSe$_4$-type clusters.

In summary, large-scale transverse ionic displacements induced by nickel impurity have been detected for the first time in a $Zn_{1-x}Ni_xSe$ crystal ($x = 0.0025$) over a wide temperature range by studying diffuse neutron scattering. It has been shown that the ionic shear displacements in the $Zn_{1-x}Ni_xSe$ lattice are due to a hybridization of sp^3 bonds with the d^8 orbitals of the Ni impurity. The results obtained indicate that multielectron 3*d* impurities cause nonlocal distortions of the ionic–covalent crystal lattice, which is a fundamentally new problem.

ACKNOWLEDGMENTS

This study was supported by the Russian Foundation for Basic Research (project no. 04-02-96094-r2004ural_a), the Ministry of Industry, Science, and Technology of the Russian Federation (contract no. 40.012.1.1.1150), the Department of Physical Sciences of the Russian Academy of Sciences (program “Neutron Studies on Material Structure and the Fundamental Properties of Matter”), and a grant from the president of the Russian Federation for the support of leading scientific schools of the Russian Federation (no. NSh-639.2003.2).

REFERENCES

1. S. J. Pearton, C. R. Abernathy, G. T. Thaler, R. Frazier, F. Ren, A. F. Hebard, Y. D. Park, D. N. Norton, W. Tang, M. Stavola, J. M. Zavada, and R. G. Wilson, Physica B **340–342**, 39 (2003).
2. V. I. Sokolov, S. F. Dubinin, S. G. Teploukhov, V. D. Parkhomenko, A. T. Lonchakov, V. V. Gudkov, A. V. Tkach, I. V. Zhevstovskikh, and N. B. Gruzdev, Solid State Commun. **129** (8), 507 (2004).
3. V. V. Gudkov, A. T. Lonchakov, A. V. Tkach, I. V. Zhevstovskikh, V. I. Sokolov, and N. B. Gruzdev, J. Electron. Mater. **33** (7), 815 (2004).
4. Yu. A. Izyumov, V. E. Naĭsh, and R. P. Ozerov, *Neutronography of Magnets* (Atomizdat, Moscow, 1981), p. 194 [in Russian].
5. W. A. Harrison, *Electronic Structure and the Properties of Solids: The Physics of the Chemical Bond* (Freeman, San Francisco, 1980; Mir, Moscow, 1983), Vol. 1.
6. W. Weber, Phys. Rev. B **15** (10), 4789 (1977).
7. D. N. Talwor, M. Vandevyver, K. Kunc, and M. Zigone, Phys. Rev. B **24** (2), 741 (1981).

Translated by Yu. Epifanov

Physics of the Solid State, Vol. 47, No. 8, 2005, pp. 1556–1559. Translated from Fizika Tverdogo Tela, Vol. 47, No. 8, 2005, pp. 1498–1500.
Original Russian Text Copyright © 2005 by Gudkov, Lonchakov, Sokolov, Zhevstovskikh, Gruzdev.

PROCEEDINGS OF THE XII FEOFILOV WORKSHOP "SPECTROSCOPY OF CRYSTALS ACTIVATED BY RARE-EARTH AND TRANSITION-METAL IONS"

(Yekaterinburg, Russia, September 22–25, 2004)

Specific Features of the Absorption and Phase Velocity of Ultrasound near the Low-Temperature Phase Transition Induced by 3*d* Impurities in a ZnSe Crystal

V. V. Gudkov[1, 2], A. T. Lonchakov[1], V. I. Sokolov[1], I. V. Zhevstovskikh[1], and N. B. Gruzdev[1]

[1] *Institute of Metal Physics, Ural Division, Russian Academy of Sciences,*
ul. S. Kovalevskoĭ 18, Yekaterinburg, 620219 Russia
e-mail: gudkov@imp.uran.ru
[2] *Russian State Vocational Pedagogical University,*
ul. Mashinostroiteleĭ 11, Yekaterinburg, 620012 Russia

Abstract—This paper reports on the results of temperature investigations into the absorption and velocity of ultrasound in ZnSe : Ni and ZnSe : Cr crystals in the frequency range 33–268 MHz. The frequency dependence of the absorption at the maximum is analyzed, and the energy of the excited state of the Ni^{2+} ions is calculated. The dynamic contribution to the effective elastic modulus is determined, and the results obtained are used to construct the temperature dependences of the relaxed and unrelaxed elastic moduli. *© 2005 Pleiades Publishing, Inc.*

1. INTRODUCTION

Earlier [1], we carried out neutron diffraction investigations of ZnSe crystals and revealed a low-temperature phase transition induced by nickel impurities. Subsequently, this phase transition was examined using ultrasonic methods. In our recent work [2], it was established that the maximum in the absorption and the minimum in the phase velocity of ultrasound are observed at a temperature $T \approx 14$ K. At the same time [3], we found that the C_{44} elastic modulus decreases with decreasing temperature. As a rule, structural phase transitions bring about considerable changes in the complex elastic moduli in the immediate vicinity of the phase transition temperature T_c. However, since changes in the elastic moduli of ZnSe : Ni crystals were observed over a rather wide temperature range and the temperatures of the observed anomalies were found to be dependent on the frequency, we undertook further investigations into the lattice instability effect. In order to reveal the specific features of the observed phenomenon, we measured the ultrasonic characteristics of ZnSe crystals containing ions of another 3*d* element, namely, chromium. This paper reports on the results of these investigations.

2. SAMPLE PREPARATION AND EXPERIMENTAL TECHNIQUE

Single crystals of the ZnSe : 3*d* compound doped with Ni (5.5×10^{19} cm^{-3}) and Cr (1×10^{21} cm^{-3}) were grown by the Bridgman method from a melt under an excess pressure of a noble gas. For measurements, samples were prepared in the form of a parallelepiped with sides a few millimeters in size. The phase velocity and absorption of longitudinal ultrasonic waves were measured on an ultrasonic setup operating on the principle of a frequency-tunable ultrasonic bridge in the frequency range 33–268 MHz at temperatures $T = 4.2$–160 K. Ultrasonic waves were excited and recorded using $LiNbO_3$ piezoelectric transducers. The experimental technique, the assumptions made, and their justification were described earlier in [2]. In the experiments, we used longitudinal waves propagating along the [110] crystallographic axis. As is known, the effective elastic modulus is a complex quantity. Knowing this quantity, we can determine the velocity v and the absorption Γ of ultrasound according to the formulas

$$v = \sqrt{\frac{\mathrm{Re}\{C_{\mathrm{eff}}\}}{\rho}},$$
$$\Gamma = \frac{\omega}{2v}\frac{\mathrm{Im}\{C_{\mathrm{eff}}\}}{\mathrm{Re}\{C_{\mathrm{eff}}\}} = \frac{\omega}{2\rho v^3}\mathrm{Im}\{C_{\mathrm{eff}}\}, \qquad (1)$$

where ρ is the density of the material and ω is the circular frequency of the wave. In this case, the effective elastic modulus is a linear combination of all independent components of the elastic modulus tensor for a cubic crystal: $C_{\mathrm{eff}} = \frac{1}{2}(C_{11} + C_{12} + 2C_{44})$.

1063-7834/05/4708-1556$26.00 © 2005 Pleiades Publishing, Inc.

3. RESULTS AND DISCUSSION

The study of ZnSe : Ni crystals revealed that, as the frequency increases, the maximum in the absorption (Fig. 1) and the minimum in the velocity of ultrasound considerably shift toward the high-temperature range. In our earlier work [2], the phase transition temperature T_c was determined from the temperature corresponding to the ultrasonic velocity at the minimum. A minimum or a kink in the curve $v(T)$ and a maximum in the curve $\Gamma(T)$ have been frequently observed upon phase transitions. The possible origin of the absorption peak has been analyzed in a number of works. In particular, Zherlitsyn *et al.* [4] assumed that the absorption peak is attributed to the order parameter fluctuations in the vicinity of the critical temperature; i.e., it is closely related to the phase transition. However, in this situation, the position of the absorption peak should not depend strongly on the frequency. In doped crystals, the maximum in the dependence $\Gamma(T)$ can be associated with the relaxation occurring in the system of electron levels of impurity centers [5]. In this case, the ultrasonic absorption can be written in the form

$$\Gamma = \frac{A}{kT}\frac{\omega^2\tau}{1+\omega^2\tau^2}, \qquad (2)$$

where A is a parameter that depends only slightly on the temperature T, k is the Boltzmann constant, and τ is the relaxation time. The maximum in the dependence $\Gamma(T)$ corresponds to the condition $\omega\tau = 1$. Therefore, the measurements performed at different frequencies provide a means for determining the temperature dependence of the relaxation time τ. Inset (b) to Fig. 1 shows the dependence of the relaxation time on the reciprocal of the temperature on the logarithmic scale. It can be seen from this dependence that the experimental points fit a straight line fairly well. This means that, in our case, as in [5], the relaxation occurs through excited states of impurity centers and the relaxation time can be adequately described by the relationship $\tau(T) \propto \exp(\Delta/kT)$. Here, the energy of the excited state of Ni^{2+} ions with respect to the ground level $\Delta = 3.5$ meV is determined from the slope of the straight line in inset (b) to Fig. 1. This level can result from the Jahn–Teller effect for the ground state $^3T_1$ of the Ni^{2+} ion in the tetrahedral environment. The manifestation of this effect was recently revealed when analyzing the thermal conductivity in II–VI semiconductors doped with 3*d* metals [6].

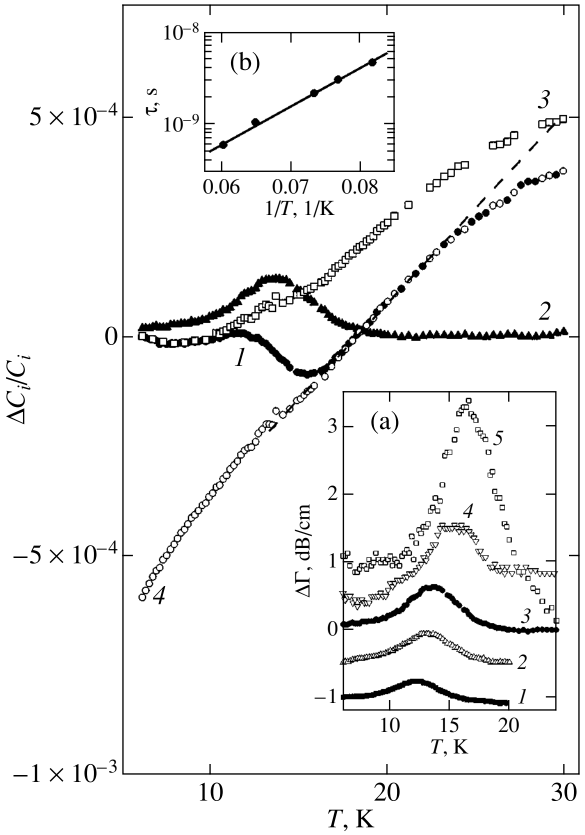

Fig. 1. Temperature dependences of the elastic moduli for the ZnSe : Ni crystal at a frequency of 74 MHz. $\Delta C_i = C_i(T) - C_i(0)$, where $C_i(0)$ is the modulus C_i extrapolated to 0 K. C_i = (*1*) Re$\{C_{\text{eff}}\}$, (*2*) Im$\{C_{\text{eff}}\}$, (*3*) C_U, and (*4*) C_R. Inset (a) shows the temperature dependences of the absorption $\Delta\Gamma = \Gamma(T) - \Gamma(5\text{ K})$ at frequencies of (*1*) 33, (*2*) 53, (*3*) 74, (*4*) 156, and (*5*) 268 MHz (the curves are shifted along the vertical axis with respect to curve *3*). Inset (b) shows the dependence of the relaxation time on the reciprocal of the temperature on the logarithmic scale.

Since the ultrasonic absorption is a dynamic effect, we investigated the possibility of determining the dynamic contribution to the real part of the elastic modulus. According to Pomerantz [7], the effective elastic modulus, with due regard for the dynamic contribution, can be described in terms of the relaxation time τ, the relaxed elastic modulus C_R, and the “instantaneous” (unrelaxed) elastic modulus C_U as follows:

$$\begin{aligned} C_{\text{eff}} &= C_U - \frac{\Delta C}{1+\omega^2\tau^2}(1 - i\omega\tau) \\ &= C_R + \frac{\Delta C}{1+\omega^2\tau^2}(\omega^2\tau^2 + i\omega\tau), \end{aligned} \qquad (3)$$

where $\Delta C = C_U - C_R \ll C_U$, C_R, and Re$\{C_{\text{eff}}\}$. It is evident that C_U and C_R are real quantities corresponding to the limiting values of the effective elastic modulus C_{eff} as a function of the parameter $\omega\tau$: $C_U = C_{\text{eff}}(\infty)$ and $C_R = C_{\text{eff}}(0)$. Then, the relationship for the absorption takes the form

$$\Gamma = \frac{1}{2}\frac{\Delta C}{Cv}\frac{\omega^2\tau}{1+\omega^2\tau^2} + \frac{1}{2}\frac{\Delta C}{C}\text{Re}\,k\frac{\omega\tau}{1+\omega^2\tau^2}, \qquad (4)$$

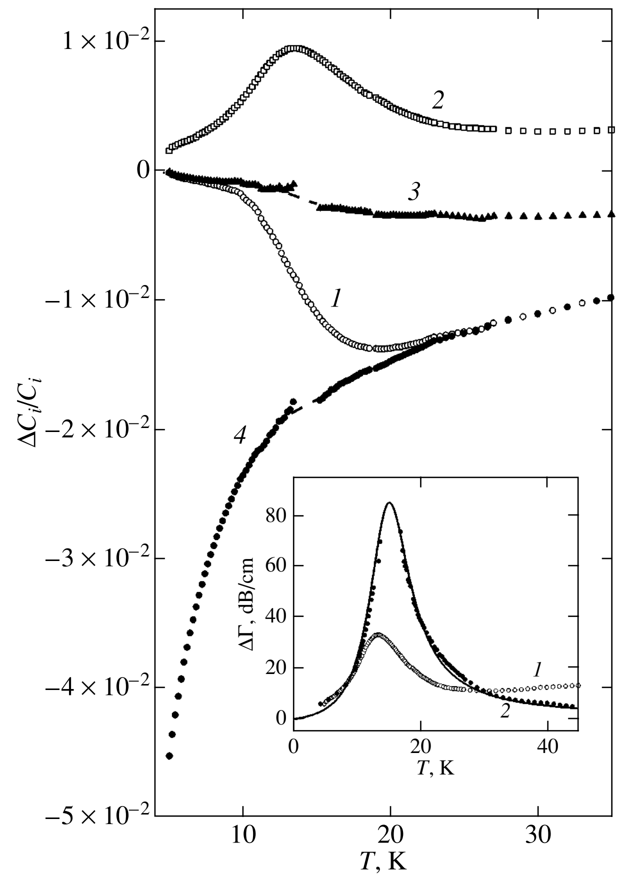

Fig. 2. Temperature dependences of the elastic moduli for the ZnSe : Cr crystal at a frequency of 56 MHz. $\Delta C_i = C_i(T) - C_i(0)$, where $C_i(0)$ is the modulus C_i extrapolated to 0 K. C_i = (*1*) Re$\{C_{\text{eff}}\}$, (*2*) Im$\{C_{\text{eff}}\}$, (*3*) C_U, and (*4*) C_R. The inset shows the temperature dependences of the absorption $\Delta\Gamma = \Gamma(T) - \Gamma(0\text{ K})$ at frequencies of (*1*) 56 and (*2*) 157 MHz. Symbols are the experimental data, and solid lines indicate the results of fitting according to the formula $\Gamma = 0.4T/[(1 - T/14.75)^2 + 0.07]$. Curve *1* is shifted along the vertical axis with respect to curve *2*.

where $k = \omega/v - i\Gamma$ is the complex wavenumber and C can be given by the moduli C_U, C_R, or Re$\{C_{\text{eff}}\}$ because of the smallness of the difference $C_U - C_R$. This relationship, with allowance made for formula (2), permits us to express the relaxation time τ as a function of the quantities T, Γ, and ω. Moreover, since the maximum of the absorption Γ is observed at $\omega\tau = 1$, the relaxation time τ can be expressed through the experimentally measurable parameters; that is,

$$\tau(T) = \frac{1}{\omega}\left(\frac{\Gamma_m T_m}{\Gamma T} \pm \sqrt{\frac{\Gamma_m^2 T_m^2}{\Gamma^2 T^2} - 1}\right), \tag{5}$$

where Γ_m is the absorption $\Gamma(T)$ at the maximum and T_m is the temperature corresponding to the absorption at the maximum. Equations (3) and (4) enable us to write the elastic moduli $C_U(T)$ and $C_R(T)$ as functions of the measurable quantities; that is,

$$\begin{aligned} C_U &= \operatorname{Re} C_{\text{eff}} + 2\frac{\Gamma}{\operatorname{Re} k}\frac{C}{\omega\tau}, \\ C_R &= \operatorname{Re} C_{\text{eff}} - 2\frac{\Gamma}{\operatorname{Re} k} C\omega\tau. \end{aligned} \tag{6}$$

The experimental data and the results of their processing according to formulas (5) and (6) are presented in Fig. 1. As can be seen from this figure, the minimum observed in the temperature dependence of the real part of the effective elastic modulus C_{eff} is absent in the curves $C_U(T)$ and $C_R(T)$. Consequently, the minimum in the dependence $C_{\text{eff}}(T)$ has a dynamic nature and is not related to the phase transition. Most likely, the critical temperature corresponds to a change in the behavior of the curve $C_R(T)$, namely, to a deviation from the linear dependence at temperatures somewhat higher than 20 K.

The data obtained for the ZnSe : Cr crystal indicate that the dependence $\Gamma(T)$ also exhibits a maximum at low temperatures (see inset to Fig. 2); however, the dependences $v(T)$ for this crystal and the ZnSe : Ni crystal differ in behavior. The temperature dependences of the elastic moduli calculated from relationships (2)–(6) are plotted in Fig. 2. It can be seen from Fig. 2 that, with a decrease in the temperature, the elastic modulus C_U for the ZnSe : Cr crystal increases. At the same time, this modulus for the ZnSe : Ni crystal initially decreases and, at temperatures below 10 K, becomes only slightly dependent on temperature (Fig. 1). Upon cooling, the modulus C_R for the ZnSe : Cr crystal, as for the ZnSe : Ni crystal, decreases significantly. In our opinion, this situation can be associated with the fact that different 3*d* ions bring about Jahn–Teller distortions of different types, namely, tetragonal distortions in the ZnSe : Cr crystal [8] and, most likely, trigonal distortions in the ZnSe : Ni crystal.

4. CONCLUSIONS

Thus, the frequency dependence of the maximum in the curve $\Gamma(T)$ was analyzed and the energy of the excited state of Ni^{2+} ions with respect to the ground level was determined to be 3.5 meV. It was assumed that this excited state has a Jahn–Teller nature. The temperature dependences of the relaxed and unrelaxed elastic moduli were obtained for ZnSe : Ni and ZnSe : Cr crystals. It was demonstrated that these dependences do not have the minimum observed in the curves $v(T)$. The inference was made that this anomaly is determined by the dynamic contribution to the elastic modulus and is not related to the phase transition.

ACKNOWLEDGMENTS

This work was supported by the Russian Foundation for Basic Research, project no. 04-02-96094-r2004 ural_a.

REFERENCES

1. V. I. Sokolov, A. V. Lukoyanov, I. A. Nekrasov, N. B. Gruzdev, E. A. Shirokov, S. F. Dubinin, S. G. Teploukhov, V. D. Parkhomenko, A. T. Lonchakov, A. V. Sokolov, and V. I. Anisimov, in *Proceedings of XXXIII Meeting on Physics of Low Temperatures, Yekaterinburg, Russia, 2003* (Yekaterinburg, 2003), p. 278.
2. V. I. Sokolov, S. F. Dubinin, S. G. Teploukhov, V. D. Parkhomenko, A. T. Lonchakov, V. V. Gudkov, A. V. Tkach, I. V. Zhevstovskikh, and N. B. Gruzdev, Solid State Commun. **129** (8), 507 (2004).
3. V. V. Gudkov, A. T. Lonchakov, A. V. Tkach, I. V. Zhevstovskikh, V. I. Sokolov, and N. B. Gruzdev, J. Eng. Math. **33** (7), 815 (2004).
4. S. Zherlitsyn, G. Bruls, A. Goltsev, B. Alavi, and M. Dressel, Phys. Rev. B **59** (21), 13 861 (1999).
5. K. Lassmann and Hp. Schad, Solid State Commun. **18** **(**4), 449 (1976).
6. A. T. Lonchakov, V. I. Sokolov, and N. B. Gruzdev, in *Proceedings of the 11th International Conference on Phonon Scattering in Condensed Matter, St. Petersburg, Russia, 2004* (St. Petersburg, 2004), p. 222.
7. M. Pomerantz, Proc. IEEE **53** (10), 1438 (1965).
8. T. L. Estle and W. C. Holton, Phys. Rev. **150** (1), 159 (1966).

Translated by O. Borovik-Romanova

Physics of the Solid State, Vol. 47, No. 8, 2005, pp. 1560–1562. Translated from Fizika Tverdogo Tela, Vol. 47, No. 8, 2005, pp. 1501–1503.

PROCEEDINGS OF THE XII FEOFILOV WORKSHOP “SPECTROSCOPY OF CRYSTALS ACTIVATED BY RARE-EARTH AND TRANSITION-METAL IONS”

(Yekaterinburg, Russia, September 22–25, 2004)

Charge State of a Transition Metal Impurity in II–VI Semiconductors

A. V. Lukoyanov[1, 2], I. A. Nekrasov[1], V. I. Sokolov[1], and V. I. Anisimov[1]

[1] *Institute of Metal Physics, Ural Division, Russian Academy of Sciences,*
ul. S. Kovalevskoĭ 18, Yekaterinburg, 620219 Russia
[2] *Ural State Technical University (UPI), ul. Mira 19, Yekaterinburg, 620002 Russia*
e-mail: lukoyanov@optics.imp.uran.ru

Abstract—The results of calculating the electronic structure of semiconductor compounds $A^{II}B^{VI}$: 3d (A = Zn; B = S, Se, Te; 3d = Sc–Cu) at a low content of 3d impurities are discussed. The excess charge of an impurity ion with respect to the charge of the zinc ion is determined for the whole series of 3d impurities. It is found that the excess charge gradually varies from $+0.6|e|$ for the scandium impurity to $-0.2|e|$ for the copper impurity. Photoionization of an impurity ion is simulated by adding a hole or an electron to the impurity center. The added charge is redistributed between the impurity ion and its nearest neighbors, thus decreasing or increasing the total excess charge of the impurity center by a magnitude of $\sim 0.2|e|$. *© 2005 Pleiades Publishing, Inc.*

1. INTRODUCTION

Over the past several decades, II–VI semiconductors doped with 3d metals have been studied intensively [1]. These materials hold considerable promise for use in spintronics [2].

The introduction of substitutional 3d impurities into II–VI wide-band-gap semiconductors leads to the formation of additional donor or acceptor impurity levels in the energy gap. The transition of a carrier between these levels is referred to as an intracenter transition. It is worth nothing that the state of the impurity center in these transitions remains unchanged. The excitation energy can be high enough to provide photoionization of impurity centers, which is accompanied either by a transition of the 3d electron to the conduction band or by a transition of the 3d hole to the valence band. The Coulomb field of the impurity center can capture an electron or a hole into a hydrogen-like orbit. This excited state of the 3d impurity center is referred to as an impurity exciton [3–5]. Upon substituting the 3d impurity for the A component in the $A^{II}B^{VI}$ crystal, the impurity acquires an uncompensated excess charge relative to the lattice of the semiconductor. Charged impurity centers can initiate displacements of the neighboring ions and, as a consequence, induce new local vibrations, as has been shown both in the model calculations and in the experiments performed for ZnSe : Ni and ZnO : Ni semiconductors in an earlier work by Sokolov *et al.* [5]. It has also been found that the ZnSe : Ni semiconductor exhibits an anomalous temperature dependence of the phonon heat conductivity and undergoes a structural phase transition with a deep minimum at a temperature $T = 14.5$ K [6, 7].

The excess charge of a 3d impurity center can be estimated from the results of calculating the electronic structure of these compounds. In the framework of the density functional theory (DFT) [8], it was demonstrated that semiconductors are adequately described in the most universal, local density approximation (LDA) [9]. However, the strong covalency of semiconductor crystals leads to a minor underestimation of the energy gap [10].

2. COMPUTATIONAL TECHNIQUE

As is known, ZnS, ZnSe, and ZnTe semiconductors crystallize in the structure of zinc blende (space group $F\bar{4}3m$). The electronic structure of these compounds was calculated within the local density approximation in the orthogonal representation using the tight-binding (TB) linear muffin-tin orbital (LMTO) method in the atomic sphere approximation (ASA) (the TB–LMTO–ASA program package [11]). For pure compounds ZnS, ZnSe, and ZnTe, the calculated energy gaps (3.19, 2.70, and 1.71 eV, respectively) turned out to be close to the experimental values (3.80, 2.80, and 2.34 eV at $T = 4.2$ K, respectively).

3. RESULTS AND DISCUSSION

The total and partial densities of states for pure ZnS are presented in Fig. 1a (similar results were obtained by Oshikiri and Aryasetiawan [12] with a different calculation technique). In order to simulate the situation with a single impurity center, a 3d impurity ion was placed in a supercell of a semiconductor with 32 atoms.

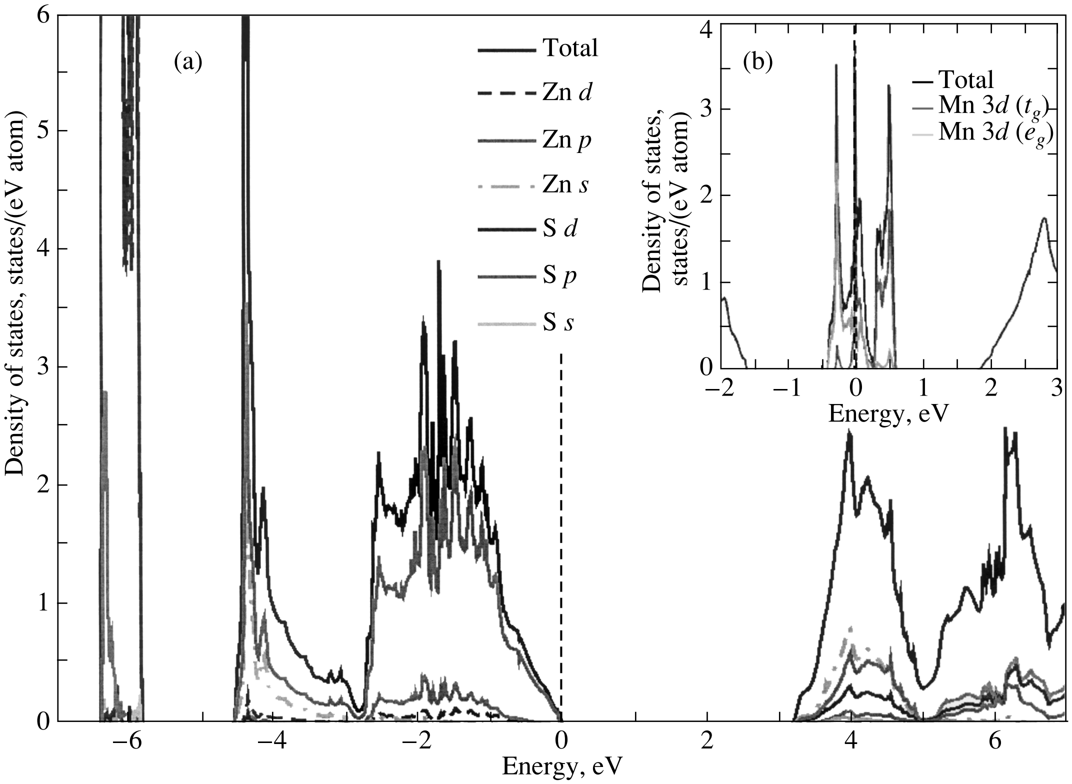

Fig. 1. (a) Total and partial densities of states for ZnS and (b) total and Mn $3d$ partial densities of states for ZnSe : Mn near the Fermi level.

Figure 2a presents the density of states in the impurity band near the Fermi level. It should be noted that, as was shown by Ueda *et al.* [13], the inclusion of the magnetic ordering in these compounds can lead to a change in the location of the impurity levels.

The integrated charge density at the atomic sphere was obtained from the results of calculating the electronic structure in the atomic sphere approximation. This quantity can be considered a difference characteristic with respect to the charge of the zinc ion substituting for the impurity center in the semiconductor. The dependence of this characteristic on the impurity type is shown in Fig. 2a. The maximum and minimum values of the excess charge, namely, $+0.6|e|$ and $-0.2|e|$, are obtained for the scandium and copper impurities, respectively.

We also considered the situations in which a charge equal to the elementary charge was either added to the impurity center or eliminated from it (Fig. 2b). Experimentally, these variations in the electron configuration of the impurity ion correspond to photoionization of the impurity center. For an excess charge of the impurity center, this leads to a complex redistribution of the electron density between the impurity center and the nearest neighbor ions; consequently, the excess charge of the impurity ion either decreases or increases by a magnitude of ~$0.2|e|$, respectively. Such a small change in the excess charge upon photoionization should lead to a situation where the frequencies of local vibrations

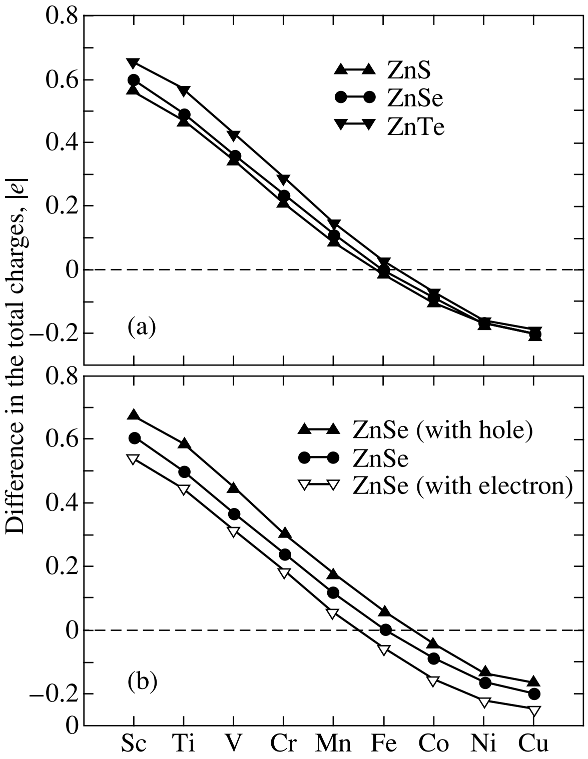

Fig. 2. (a) Difference between the total charges of the impurity ion and the zinc ion (excess charge) for ZnS : $3d$, ZnSe : $3d$, and ZnTe : $3d$. (b) Difference between the total charges of the impurity ion and the zinc ion (excess charge) for ZnSe and the variation in this quantity due to the addition of an electron or a hole to the impurity center.

only slightly change in comparison with the phonon frequencies, i.e., where resonance vibrations occur. This phenomenon was actually observed in the experiments conducted in [3–5], and it is precisely this situation that is unusual considering the assumption that the charge changes by an integral number of charges of electrons or holes upon photoionization of the impurity center.

4. CONCLUSIONS

Thus, in this work, the charge state of a 3*d* impurity center in semiconductors $A^{II}B^{VI} : 3d$ (A = Zn; B = S, Se, Te; $3d$ = Sc–Cu) was estimated from the results of calculating the electronic structure within the local density approximation in the orthogonal representation with the TB–LMTO–ASA program package. The spontaneous excess charge of the impurity center depends strongly on the atomic number of the impurity ion and gradually increases from $-0.6|e|$ for the scandium impurity to $+0.2|e|$ for the copper impurity. The addition of an electron or a hole to the electron system of the impurity center, which corresponds to photoemission excitation of the impurity ion, leads to a redistribution of the charge between the impurity ion and its nearest neighbors. The electron density at the impurity ion changes by a magnitude of the order of $0.2|e|$. Therefore, the photoinduced local vibrations in the lattice are resonant in nature.

ACKNOWLEDGMENTS

This work was supported in part by the Russian Foundation for Basic Research (projects nos. 04-02-96094-R2004ural_a, 04-02-16096), the National Natural Science Foundation (project no. RFFI-GFEN-03-02-39024a), the Council on Grants from the President of the Russian Federation for Young Scientists (grant no. MK-95.2003.02), the Dinasty Foundation and the International Center for Fundamental Physics in Moscow "Young Scientists 2004," and the Russian Science Support Foundation for Young Candidates of Sciences of the Russian Academy of Sciences 2004.

REFERENCES

1. L. A. Kikoin and V. N. Fleurov, *Transition Metal Impurities in Semiconductors (Electronic Structure and Physical Properties)* (World Scientific, Singapore, 1994).
2. I. Žutic, J. Fabian, and S. D. Sarma, Rev. Mod. Phys. **76**, 323 (2004).
3. V. I. Sokolov, Fiz. Tekh. Poluprovodn. (St. Petersburg) **28**, 545 (1994) [Semiconductors **28**, 329 (1994)].
4. V. I. Sokolov, N. B. Gruzdev, and I. A. Farina, Fiz. Tverd. Tela (St. Petersburg) **45** (9), 1560 (2003) [Phys. Solid State **45** (9), 1638 (2003)].
5. V. I. Sokolov, N. B. Gruzdev, E. A. Shirokov, and A. I. Kislov, Fiz. Tverd. Tela (St. Petersburg) **44** (1), 33 (2002) [Phys. Solid State **44** (1), 34 (2002)].
6. V. I. Sokolov and A. T. Lonchakov, Pis'ma Zh. Éksp. Teor. Fiz. **73** (11), 708 (2001) [JETP Lett. **73** (11), 626 (2001)].
7. V. I. Sokolov, S. E. Dubinin, S. G. Teploukhov, V. D. Parkhomenko, A. T. Lonchakov, V. V. Gudkov, A. V. Tkach, I. V. Zhevstovskikh, and N. B. Gruzdev, Solid State Commun. **129** (8), 507 (2004).
8. P. Hohenberg and W. Kohn, Phys. Rev. **136** (3B), B864 (1964).
9. R. O. Jones and O. Gunnarsson, Rev. Mod. Phys. **61**, 689 (1989).
10. O. Gunnarsson and K. Schönhammer, Phys. Rev. Lett. **56** (18), 1968 (1986).
11. O. K. Andersen, Phys. Rev. B **12** (8), 3060 (1975).
12. M. Oshikiri and F. Aryasetiawan, Phys. Rev. B **60** (15), 10 754 (1999).
13. K. Ueda, H. Tabata, and T. Kawai, Appl. Phys. Lett. **79** (7), 988 (2001).

Translated by O. Moskalev

Physics of the Solid State, Vol. 47, No. 8, 2005, pp. 1563–1566. Translated from Fizika Tverdogo Tela, Vol. 47, No. 8, 2005, pp. 1504–1506.
Original Russian Text Copyright © 2005 by Lonchakov, Sokolov, Gruzdev.

PROCEEDINGS OF THE XII FEOFILOV WORKSHOP “SPECTROSCOPY OF CRYSTALS ACTIVATED BY RARE-EARTH AND TRANSITION-METAL IONS”

(Yekaterinburg, Russia, September 22–25, 2004)

Specific Features of the Phonon Thermal Conductivity of II–VI Compound Semiconductors Doped with 3*d* Transition Metal Ions

A. T. Lonchakov, V. I. Sokolov, and N. B. Gruzdev
Institute of Metal Physics, Ural Division, Russian Academy of Sciences,
ul. S. Kovalevskoĭ 18, Yekaterinburg, 620219 Russia
e-mail: lonchakov@imp.uran.ru

Abstract—The phonon thermal conductivity of II–VI compound semiconductors doped with 3*d* transition metal ions is studied. The observed temperature anomalies are analyzed in terms of the dynamic Jahn–Teller effect. © *2005 Pleiades Publishing, Inc.*

1. INTRODUCTION

Practical application of II–VI compound semiconductors doped with 3*d* transition metal ions requires comprehensive study of their physical properties, among which the phonon thermal conductivity is of great importance as a fundamental characteristic of the relaxation of lattice vibrations. Recently, it has been discovered that the phonon thermal conductivity of ZnX : Ni^{2+} crystals (X = Se, S) undergoes a dramatic (resonance-like) change at low temperatures [1]. The nature of this anomaly and the ZnSe : Ni^{2+} lattice instability associated with it [2, 3] are not clearly understood. In this work, in order to gain a better understanding of the mechanisms of resonance scattering of acoustic phonons in ZnX : Ni^{2+} and the reason for the instability of the ZnSe : Ni^{2+} lattice, we measured the phonon thermal conductivity of ZnX single crystals doped with various 3*d* transition metal ions (Ni^{2+}, Cr^{2+}, Fe^{2+}, Co^{2+}, Ti^{2+}, and V^{2+}).

2. EXPERIMENTAL

Single crystals were grown from a melt using the Bridgman method under conditions of an excess inert-gas pressure [4]. The impurity concentration in samples was determined using optical emission spectroscopy of an inductively coupled plasma and x-ray microanalysis.

The thermal conductivity was measured over the temperature range 1.8–200 K using the steady-state heat flow method. The temperature gradient and the average temperature of a sample were measured at $T \geq 10$ K with two (Au + 0.012% Fe)–Cu thermocouples and at $T \leq 10$ K with two germanium thermometers. The average size of the samples was $1.5 \times 2.5 \times 10$ mm.

3. EXPERIMENTAL RESULTS AND DISCUSSION

First, let us discuss the low-temperature data (1.8–80 K). Figure 1a shows the temperature dependence of the thermal conductivity κ measured on ZnSe crystals containing Ni^{2+}, Co^{2+}, and Fe^{2+} ions. It can be seen that the $\kappa(T)$ curves for ZnSe : Ni^{2+} samples have a deep, resonance-like minimum at $T_{\min} \cong 15$ K, with the position of this minimum being independent of the Ni^{2+} ion concentration. A minimum in $\kappa(T)$ was also observed for a ZnSe : Fe^{2+} sample at $T_{\min} \cong 13$ K. Figure 2a shows the $\kappa(T)$ dependence for ZnSe : Cr^{2+} crystals and undoped ZnSe [5]. It can be seen that the $\kappa(T)$ curves for doped crystals have a minimum at $T_{\min} \cong 27$ K. In contrast to Ni^{2+}, Fe^{2+}, and Cr^{2+} dopants, doping of ZnSe with cobalt does not cause a resonance-like anomaly in $\kappa(T)$ at temperatures of up to $T_{\min} \cong 100$ K. Note that, among the ions for which the data are presented in Figs. 1 and 2a, Co^{2+} is the only ion whose ground state is orbitally nondegenerate in a T_d-symmetry crystal field (singlet $^4A_2$). The ground terms of the Ni^{2+}, Cr^{2+}, and Fe^{2+} ions are orbital triplets $^3T_1$ and $^5T_2$ and a doublet ^5E, respectively. Another 3*d* ion whose ground state is orbitally nondegenerate in a tetrahedral environment is Ti^{2+} (a singlet $^3A_2$). It can be seen from Fig. 2b that the $\kappa(T)$ dependence for a ZnS : Ti^{2+} sample, as well as that for ZnS : Co^{2+}, does not exhibit any pronounced, resonance-like anomalies. The $\kappa(T)$ curves for ZnS : Ni^{2+} and ZnS : Fe^{2+} crystals have minima at $T_{\min} \cong 22$ and 10 K, respectively. The $\kappa(T)$ dependence for a ZnS sample doped with V^{2+} ions (the ground state is a triplet $^4T_1$) is likewise unusual: doping with vanadium to a

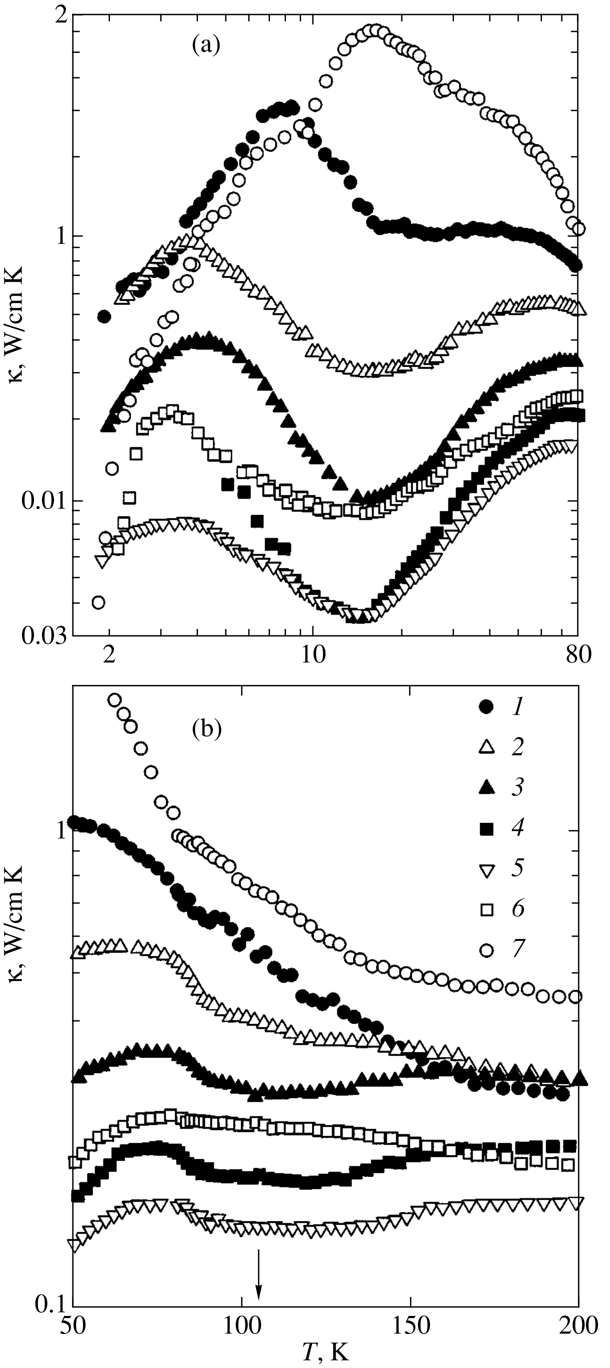

Fig. 1. Temperature dependence of the thermal conductivity κ at (a) low and (b) higher temperatures for ZnSe samples doped with various 3*d* transition metal ions (the doping concentration is given in cm^{-3} in parentheses): (*1*) Ni^{2+} (1×10^{19}), (*2*) Ni^{2+} (2×10^{19}), (*3*) Ni^{2+} (5.5×10^{19}), (*4*) Ni^{2+} (1×10^{20}), (*5*) Ni^{2+} (2×10^{20}), (*6*) Fe^{2+} (3.8×10^{20}), and (*7*) Co^{2+} (5×10^{19}). The arrow indicates the Debye temperature (104 K) for transverse acoustic phonons in ZnSe [10].

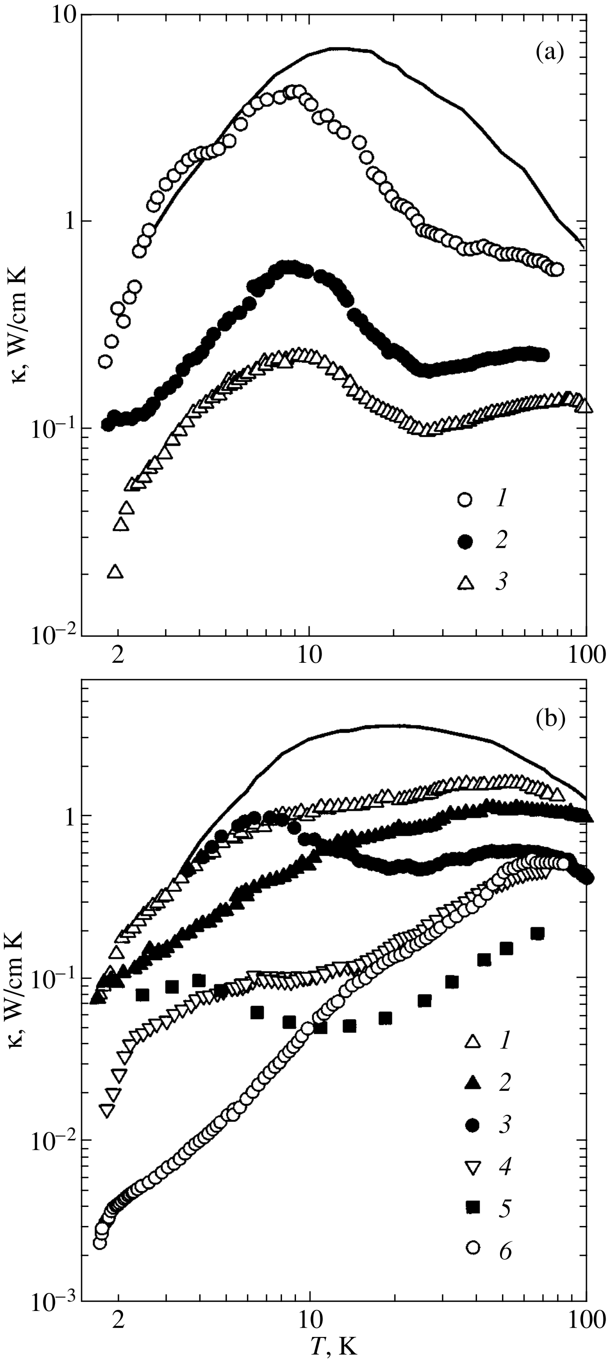

Fig. 2. Temperature dependence of the thermal conductivity κ (a) for ZnSe : Cr^{2+} samples with various Cr^{2+} concentrations: (*1*) 1×10^{19}, (*2*) 6.5×10^{19}, and (*3*) 1×10^{21} cm^{-3} and (b) for ZnS samples doped with various 3*d* transition metal ions (the doping concentration is given in cm^{-3} in parentheses): (*1*) Ti^{2+} (3.8×10^{19}), (*2*) Co^{2+} (5×10^{19}), (*3*) Ni^{2+} (2.6×10^{19}), (*4*) Fe^{2+} (6×10^{19}), (*5*) Fe^{2+} (3.5×10^{20}) [5], and (*6*) V^{2+} (5×10^{19}). Solid curves are the data on the thermal conductivity of undoped ZnSe and ZnS taken from [5].

concentration of 5×10^{19} cm^{-3} decreases κ at $T \approx 4$ K by approximately two orders of magnitude relative to that of undoped ZnS.

The κ(*T*) dependences at high temperatures ($T >$ 80 K) for ZnSe crystals doped with 3*d* transition metal ions are shown in Fig. 1b. It can be seen that the κ(*T*) curves for ZnSe : Ni^{2+} samples have a minimum at $T_{min} \cong 115$ K, with its position being independent of the impurity concentration. From comparing Figs. 1a and 1b, it follows that the high-temperature minimum in $\kappa(T)$ appears at a higher Ni^{2+} concentration than the low-temperature minimum. It can be seen from Fig. 1b that the high-temperature minimum in $\kappa(T)$ is absent for ZnSe : Fe^{2+} and ZnSe : Co^{2+} crystals and for ZnSe samples with a relatively low Ni^{2+} concentration of about $(1–2) \times 10^{19}$ $cm^{–3}$.

Thus, the experimental data indicate that the Co^{2+} and Ti^{2+} ions do not cause resonance phonon scattering in Zn*X* semiconductors and that 3*d* ions whose ground state in a tetrahedral environment is orbitally degenerate (Ni^{2+}, Cr^{2+}, Fe^{2+}, V^{2+}) have an unusually strong effect on the phonon thermal conductivity. In the latter case, the interaction of the electronic state of an impurity ion with lattice vibrations removes the degeneracy of the ground state of the ion. This dynamic Jahn–Teller (JT) effect can cause additional acoustic phonon scattering (which is resonance in nature) and thereby significantly influence the $\kappa(T)$ of semiconductors [6].

If the minimum in $\kappa(T)$ of Zn*X* crystals doped with 3*d* transition metal ions is caused by resonance phonon scattering, then the electrons of impurity ions in the ground state have to transfer to an excited state. As an example, let us consider ZnSe : Ni^{2+}. It is well known that the spin–orbit interaction (SOI) splits the ground state of the Ni^{2+} ion in a T_d-symmetry crystal field into four sublevels [7]. To first order in SOI, the spacing δ between the ground state A_1 (or Γ_1) and the next upper sublevel T_1 (Γ_4) is equal to $\approx(3/2)\lambda$, where λ is the SOI constant. Unfortunately, the value of this parameter for Ni^{2+} in cubic II–VI compounds is unknown. Taking $\lambda \approx$ 100–150 $cm^{–1}$ (which is likely to be close to the value of λ for the free Ni^{2+} ion [8]), we obtain $\delta \approx$ 20–30 meV, which is far greater than the expected value of the resonance energy, 4 meV [3]. The situation can change radically if the JT effect is taken into account. In the case where the JT effect is strong and, therefore, the JT interaction energy is greater than the SOI energy, the spin–orbit splitting decreases, as shown in [9], and the resonance energy in ZnSe : Ni^{2+} can become as low as several millielectronvolts.

Thus, the deep low-temperature minimum in $\kappa(T)$ (at $T_{min} \approx 15$ K) observed for ZnSe : Ni^{2+} crystals can be associated with resonance phonon scattering in a system with a strong JT coupling.

In interpreting the high-temperature minimum in $\kappa(T)$, we take into account that $T_{min} \cong 115$ K is close to the Debye temperature $\Theta = 104$ K for transverse acoustic phonons, which make a dominant contribution to the phonon thermal conductivity [10]. According to [6], the resonance phonon energy for scattering from a two-level system is at least two to three times greater than T_{min}. Therefore, in contrast to the low-temperature minimum, the high-temperature minimum in ZnSe : Ni^{2+} cannot be of a resonance nature. In our opinion, this minimum is due to specific scattering of JT phonons in crystals with a high Ni^{2+} concentration. This type of scattering involves the dynamic JT effect, which causes a reorientation of JT distortions [11]. Based on the phonon spectra of ZnSe [12], we can assume that the JT phonons in ZnSe : Ni^{2+} are either TA(*L*) or TA(*X*) phonons. The interaction of the Ni^{2+} ion with the former and latter phonons produces tetragonal [13] and presumably trigonal lattice distortions, respectively. The JT interaction is known to be weak for the ground state ^5E of the Fe^{2+} ion in II–VI compounds [14]. Probably, this is the reason why the high-temperature minimum is absent in $\kappa(T)$ of ZnSe : Fe^{2+}.

4. CONCLUSIONS

The phonon thermal conductivity of ZnSe and ZnS crystals doped with various 3*d* transition metal ions has been studied over the temperature range 1.8–200 K. Two main features of $\kappa(T)$ have been detected: (i) strong resonance phonon scattering from 3*d* ions whose ground state is orbitally degenerate and (ii) a high-temperature minimum in $\kappa(T)$ for ZnSe : Ni^{2+} crystals at $T_{min} \cong 115$ K, which is close to the Debye temperature Θ of transverse acoustic phonons. The observed anomalies in $\kappa(T)$ of II–VI compounds have been interpreted as a manifestation of the dynamic Jahn–Teller effect in deep impurity centers.

ACKNOWLEDGMENTS

This study was supported by the Russian Foundation for Basic Research, project no. 04-02-96094-r2004ural_a.

REFERENCES

1. V. I. Sokolov and A. T. Lonchakov, Pis'ma Zh. Éksp. Teor. Fiz. **73** (11), 708 (2001) [JETP Lett. **73** (11), 626 (2001)]; A. T. Lonchakov, N. B. Gruzdev, and V. I. Sokolov, Fiz. Tverd. Tela (St. Petersburg) **44** (8), 1462 (2002) [Phys. Solid State **44** (8), 1529 (2002)].
2. V. I. Sokolov, S. F. Dubinin, S. G. Teploukhov, V. D. Parkhomenko, A. T. Lonchakov, V. V. Gudkov, A. V. Tkach, I. V. Zhevstovskikh, and N. B. Gruzdev, Solid State Commun. **129** (8), 507 (2004).
3. V. V. Gudkov, A. T. Lonchakov, A. V. Tkach, I. V. Zhevstovskikh, V. I. Sokolov, and N. B. Gruzdev, J. Electr. Mater. **33** (7), 815 (2004).
4. M. P. Kulakov and A. V. Fadeev, Izv. Akad. Nauk SSSR, Neorg. Mater. **22** (3), 392 (1986).
5. G. A. Slack, Phys. Rev. B **6** (10), 3791 (1972).

6. E. Sigmund and K. Lassmann, Phys. Status Solidi B **111** (2), 631 (1982); J. Maier and E. Sigmund, J. Phys. C: Solid State Phys. **17** (23), 4141 (1984); A. Puhl, E. Sigmund, and J. Maier, Phys. Rev. B **32** (12), 8234 (1985).
7. H. A. Weakliem, J. Chem. Phys. **36** (8), 2117 (1962).
8. G. Goetz, G. Roussos, and H.-J. Schulz, Solid State Commun. **57** (5), 343 (1986).
9. F. S. Ham, Phys. Rev. **138** (6A), A1727 (1965).
10. R. D. Bijalwan, P. N. Ram, and M. D. Tiwari, J. Phys. C: Solid State Phys. A **16** (13), 2537 (1983).
11. M. D. Sturge, *The Jahn–Teller Effect in Solids. Solid State Physics* (Academic, London, 1967), Vol. 20, pp. 126–127.
12. K. Kunc, M. Balkanski, and M. A. Nusimovich, Phys. Status Solidi B **72** (1), 229 (1975).
13. J. T. Vallin, G. A. Slack, and S. Roberts, Phys. Rev. B **2** (11), 4313 (1970).
14. G. A. Slack, F. S. Ham, and R. M. Chrenko, Phys. Rev. **152** (1), 376 (1966); F. S. Ham and G. A. Slack, Phys. Rev. B **4** (3), 777 (1971).

Translated by Yu. Epifanov

Physics of the Solid State, Vol. 47, No. 8, 2005, pp. 1567–1569. Translated from Fizika Tverdogo Tela, Vol. 47, No. 8, 2005, pp. 1507–1509.
Original Russian Text Copyright © 2005 by Sokolov, Fillaux, Romain, Lemmens, Gruzdev.

PROCEEDINGS OF THE XII FEOFILOV WORKSHOP “SPECTROSCOPY OF CRYSTALS ACTIVATED BY RARE-EARTH AND TRANSITION-METAL IONS”

(Yekaterinburg, Russia, September 22–25, 2004)

A Raman Study of Lattice Vibrations in II–VI Semiconductors Doped with 3*d* Elements

V. I. Sokolov*, F. Fillaux, F. Romain**, P. Lemmens***, and N. B. Gruzdev***

**Institute of Metal Physics, Ural Division, Russian Academy of Sciences,*
ul. S. Kovalevskoĭ 18, Yekaterinburg, 620219 Russia
e-mail: visokolov@imp.uran.ru
***Université P. et M. Curie, LADIR–CNRS, UMR 7075, 2 rue Henry Dunant 94320, Thiais, France*
****MPI for Solid State Research, Heisenberg Str. 1, MPI–FKF Stuttgart, D-70569 Germany*

Abstract—Room-temperature Raman spectra were obtained for powder samples of $\mathrm{Zn}_{1-x}\mathrm{Ni}_x\mathrm{Se}$ and $\mathrm{Zn}_{1-y}\mathrm{Cr}_y\mathrm{Se}$ compounds and for a single-crystal $\mathrm{Zn}_{1-x}\mathrm{Ni}_x\mathrm{Se}$ ($x = 0.0025$) sample in the temperature range 5–140 K. The results obtained are interpreted in terms of large-scale lattice shear strains induced by 3*d* elements in these solid solutions. *© 2005 Pleiades Publishing, Inc.*

The effect of 3*d* impurities on the structure of II–VI semiconductors was earlier treated as the merely local lattice strain around an impurity center caused by the 3*d*-center interaction with its nearest neighbors. The Raman spectra of $A^{\mathrm{II}}_{1-x}M_xB^{\mathrm{VI}}$ solid solutions were interpreted in terms of local vibrations or as a change in the TO and LO optical vibration frequencies in the single- or two-mode model [1–3].

Recently, a nickel-induced structural phase transition was observed in the $\mathrm{Zn}_{1-x}\mathrm{Ni}_x\mathrm{Se}$ ($x = 0.0025$) system at 14.5 K [4].This transition indicates the existence of appreciable long-range correlated displacements of the lattice ions induced by the nickel impurity. It thus appeared of interest to study the vibrational states of the $\mathrm{Zn}_{1-x}\mathrm{Ni}_x\mathrm{Se}$ ($x = 0.0025$) system and related compounds, because lattice vibrations are very sensitive to structural lattice distortions. We report here on a Raman spectroscopy study of the vibrational lattice states in $\mathrm{Zn}_{1-x}\mathrm{Ni}_x\mathrm{Se}$ and $\mathrm{Zn}_{1-y}\mathrm{Cr}_y\mathrm{Se}$ solid solutions. Raman spectra were obtained from powder samples of the $\mathrm{Zn}_{1-x}\mathrm{Ni}_x\mathrm{Se}$ and $\mathrm{Zn}_{1-y}\mathrm{Cr}_y\mathrm{Se}$ systems. The atomic fraction of the 3*d* elements was measured using inductively coupled plasma atomic-emission spectroscopy [4] and was found to vary in the samples under study in the ranges $0 \le x \le 0.026$ and $0 \le y \le 0.046$. The measurements were conducted with a Spex Jvon-Dilor spectrometer and lasers operating at 632.8, 514, and 488 nm. One of the samples of the $\mathrm{Zn}_{1-x}\mathrm{Ni}_x\mathrm{Se}$ system ($x = 0.0025$) was a (110) single crystal; its Raman spectra were taken with a laser operating at a wavelength of 514 nm.

Figure 1 presents the Raman spectra of powder samples. The spectrum of a ZnSe powder contains the well-known TO, LO, 2TA(X), and 2LO peaks [5]. The Raman spectrum of $\mathrm{Zn}_{1-x}\mathrm{Ni}_x\mathrm{Se}$ powders undergoes a number of changes. The TO and LO peaks broaden; this effect is particularly pronounced for the LO peak. While the second-order 2LO peaks persist, their widths

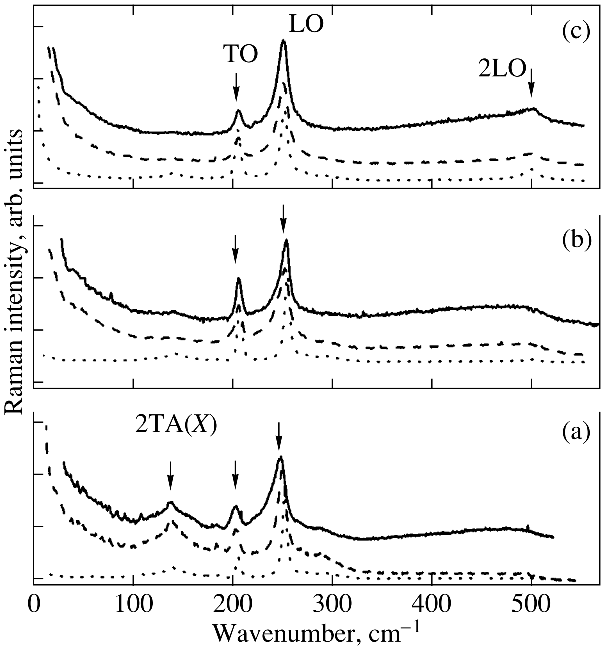

Fig. 1. Raman spectra of powder samples of ZnSe (dotted lines), $\mathrm{Zn}_{1-y}\mathrm{Cr}_y\mathrm{Se}$ ($y = 0.046$; dashed lines), and $\mathrm{Zn}_{1-x}\mathrm{Ni}_x\mathrm{Se}$ ($x = 0.026$; solid lines) observed in the backscattering geometry at $T = 300$ K. The laser excitation wavelength is (a) 632.8, (b) 514, and (c) 488 nm. All peaks are normalized against the LO-peak intensity.

1063-7834/05/4708-1567$26.00 © 2005 Pleiades Publishing, Inc.

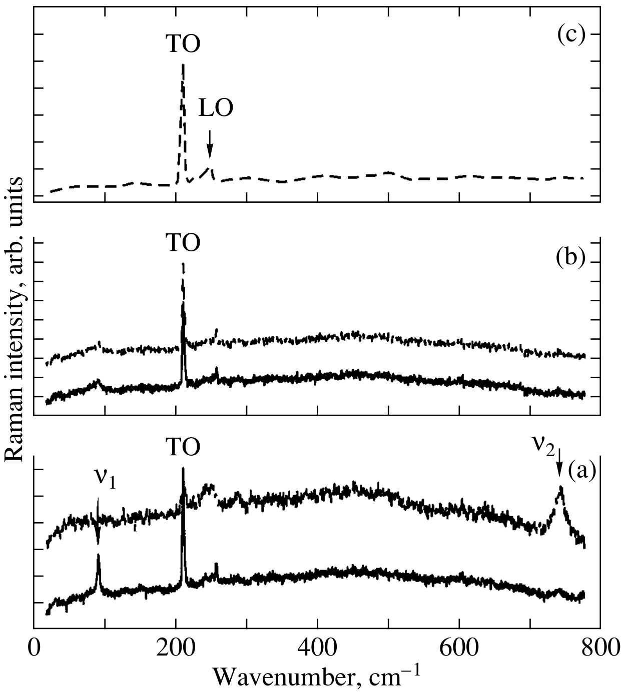

Fig. 2. Raman spectra of a single-crystal $Zn_{1-x}Ni_xSe$ sample ($x = 0.0025$) observed in the backscattering geometry from the (110) plane at temperatures of (a) 5, (b) 20, and (c) 140 K. Solid curves correspond to the x polarization (along $[1\bar{1}0]$) of the incident beam and the y polarization (along [001]) of the reflected beam; dashed curves relate to the y polarization (along [001]) of both beams.

also broaden as compared to their initial values. The 2TA(X) peak intensity grows with increasing doping level, which becomes particularly manifest in the spectra obtained at a wavelength of 633 nm (Fig. 1a). Similar changes are seen to occur in $Zn_{1-y}Cr_ySe$ crystalline powders.

We also observed new, heretofore undetected changes in the spectra of doped compounds, because we used powder samples, in which all vibration modes are manifested simultaneously. $Zn_{1-x}Ni_xSe$ and $Zn_{1-y}Cr_ySe$ crystals reveal two intense Raman bands. One of them is seen in the low-frequency part of the spectrum, where the Raman scattering intensity increases strongly with a decrease in the frequency of scattered light. At low frequencies, the scattered light intensity becomes comparable to or exceeds that of the most intense LO peaks. The low-frequency scattering grows with increasing concentration of the nickel and chromium impurities and with decreasing laser photon energy. The other band appears at higher frequencies, between the LO and 2LO peaks. Its intensity increases as the frequency of scattered light, the nickel impurity concentration, or the laser photon energy increases. This implies the onset of additional Raman scattering in the $Zn_{1-x}Ni_xSe$ and $Zn_{1-y}Cr_ySe$ semiconductors as compared to undoped ZnSe, which is due to the presence of the Ni and Cr impurities. In what follows, we discuss only these bands.

We start with the $Zn_{1-x}Ni_xSe$ system for which diffuse neutron scattering was recently observed [6]. An analysis of those results led to the understanding that the $Zn_{1-x}Ni_xSe$ system ($x = 0.0025$) has regions with transversely displaced lattice ions, which measure 3 to 15 nm in different crystallographic directions.

The presence of these regions in a crystal indicates the onset of a large-scale disorder capable of distorting the phonon modes and producing first-order Raman peaks activated by lattice disorder [7–9]. The first-order Raman peak intensity is proportional to the phonon density in the lattice. The broad band starts from low frequencies; therefore, the dominant contribution to it comes from, primarily transverse, acoustic phonons because they produce the first phonon density maximum near 70 cm^{-1} [10]. The Raman scattering intensity is also proportional to the Bose–Einstein factor, which increases sharply with decreasing energy, and this is why no maximum is seen in the Raman scattering spectrum. The second broad band in the LO–2LO interval can be interpreted as resulting from a third-order process at a frequency equal to the difference between the two-phonon 2LO vibration frequency and the frequency of a disorder-induced single-phonon vibration mode.

The increase in the intensity of the broad low-frequency band with increasing laser wavelength implies that there is resonance at an energy less than the 632.8-nm-laser photon energy. This resonance energy may be the energy of the nickel impurity ionization, $d^8 + \omega \longrightarrow d^9 + h$, which is approximately 1.85 eV [11]. The Raman spectrum of $Zn_{1-y}Cr_ySe$ also features a broad band whose intensity grows with decreasing laser photon energy. The energy of chromium ionization in ZnSe, $d^4 + \omega \longrightarrow d^5 + h$, is 2.26 eV [12]. This energy slightly exceeds the laser photon energy at 632.8 nm. This is probably why the resonance character is not so distinct here. To verify this conjecture, it would be desirable to measure the Raman spectrum with a laser emitting photon of an energy substantially lower than the resonance energy. In view of the obvious similarity between the broad low-frequency Raman bands, the broad bands in the Raman spectra of $Zn_{1-x}Ni_xSe$ and $Zn_{1-y}Cr_ySe$ can be considered to be of common origin. In other words, we believe that the chromium impurity in $Zn_{1-y}Cr_ySe$ also induces large-scale transverse displacements of lattice ions.

The Raman spectra of single-crystal $Zn_{1-x}Ni_xSe$ ($x = 0.0025$) are displayed in Fig. 2. The (110) plane was chosen because backscattering from this plane in zinc blende crystals produces transverse vibrations only [13]. The spectra measured above the phase transition temperature ($T_c = 14.5$ K) clearly exhibit TO-phonon lines. The LO-phonon lines are very weak and appeared most probably as a result of crystal misorientation and disorder in the $Zn_{1-x}Ni_xSe$ ($x = 0.0025$) crystal. At 20 K, two comparatively broad weak peaks are seen in the (xy) and (yy) geometries at a frequency of about 90 cm^{-1}. However, the spectra taken at 5 K exhibit noticeable changes. While the energy of the TO-phonon line remains practically unchanged, this line is observed only in the (xy) geometry. Two new lines became clearly visible. One line with a frequency $\nu_1 =$ 91 cm^{-1} is observed in the (yy) geometry only and is comparable in width to the TO line observed in the high- and low-frequency phases. The other new line, at $\nu_2 = 740$ cm^{-1}, appears only in the (xy) geometry. Its width is seen to be a few times that of the first line. We do not know anything on the low-temperature phase symmetry. It thus appears impossible to identify the Raman spectrum peak reliably. One can, however, safely maintain that the difference between the Raman spectra obtained at 20 and 5 K is very substantial.

We note in conclusion that the difference between the Raman spectra of $Zn_{1-x}Ni_xSe$ ($x = 0.0025$) obtained at 5 and 20 K is yet another convincing argument for the existence of a phase transition in this compound at 14.5 K. The similarity between the broad low-frequency Raman bands in $Zn_{1-x}Ni_xSe$ and $Zn_{1-y}Cr_ySe$ suggests that at room temperature $Zn_{1-y}Cr_ySe$ suffers Cr-induced structural lattice strains, which are possibly similar to those observed earlier in $Zn_{1-x}Ni_xSe$.

ACKNOWLEDGMENTS

One of the authors (V.I.S.) is grateful to the French Ministry of Youth, Education, and Science for financially supporting his visit to France and to the personnel of LADIR CNRS for their warm reception. The authors are grateful to J.-C. Rouchaud for performing the measurements of the 3*d*-element concentration in the samples under study.

This study was supported by the Russian Foundation for Basic Research, project no. 04-02-96094-r2004ural_a.

REFERENCES

1. A. V. Krol’, N. V. Levichev, A. L. Natadze, and A. I. Ryskin, Fiz. Tverd. Tela (Leningrad) **20**, 154 (1978) [Sov. Phys. Solid State **20**, 85 (1978)].
2. D. L. Peterson, A. Petrou, A. K. Ramdas, and S. Rodriguez, Phys. Rev. B **33**, 1160 (1986).
3. A. K. Arora, E. K. Suh, U. Debska, and A. K. Ramdas, Phys. Rev. B **37**, 2927 (1988).
4. V. I. Sokolov, S. F. Dubinin, S. G. Teploukhov, V. D. Parkhomenko, A. T. Lonchakov, V. V. Gudkov, A. V. Tkach, I. V. Zhevstovskikh, and N. B. Gruzdev, Solid State Commun. **129**, 507 (2004).
5. N. N. Mel’nik and E. A. Vinogradov, Fiz. Tverd. Tela (Leningrad) **18** (11), 3259 (1976) [Sov. Phys. Solid State **18** (11), 1900 (1976)].
6. V. I. Sokolov, S. F. Dubinin, S. G. Teploukhov, V. D. Parkhomenko, and N. B. Gruzdev, Fiz. Tverd. Tela (St. Petersburg) **47** (8), 1494 (2005).
7. R. Shuker and R. W. Gammon, Phys. Rev. Lett. **25**, 222 (1970).
8. J. E. Smith, Jr., M. H. Brodsky, B. L. Crowder, M. I. Nathan, and A. Pinczuk, Phys. Rev. Lett. **26**, 642 (1971).
9. M. H. Brodsky, in *Light Scattering of Solids*, Ed. by M. Cardona, (Springer, Berlin, 1975), Chap. 5.
10. Landolt-Börnstein, *Numerical Data and Functional Relationships in Science and Technology*, Vol. 17: *Semiconductors, Physics of II–VI Compounds*, Ed. by O. Madelung (Springer, Berlin, 1982).
11. V. I. Sokolov, Fiz. Tekh. Poluprovodn. (St. Petersburg) **28** (4), 545 (1994) [Semiconductors **28** (4), 329 (1994)].
12. G. Grebe, G. Rousos, and H.-J. Schulz, J. Lumin. **12**, 701 (1976).
13. *Light Scattering in Solids*, Ed. by M. Cardona and G. Güntherodt (Springer, Berlin, 1982; Mir, Moscow, 1984), Vol. 2.

Translated by G. Skrebtsov

Physics of the Solid State, Vol. 47, No. 8, 2005, pp. 1570–1572. Translated from Fizika Tverdogo Tela, Vol. 47, No. 8, 2005, pp. 1510–1511.
Original Russian Text Copyright © 2005 by Pustovarov, Ogorodnikov, Kuz'mina, Smirnov, Yelisseyev.

PROCEEDINGS OF THE XII FEOFILOV WORKSHOP "SPECTROSCOPY OF CRYSTALS ACTIVATED BY RARE-EARTH AND TRANSITION-METAL IONS"

(Yekaterinburg, Russia, September 22–25, 2004)

Excitons and Energy Transfer in KPb_2Cl_5 and $RbPb_2Br_5$ Laser Crystals

V. A. Pustovarov*, I. N. Ogorodnikov*, N. S. Kuz'mina*,
A. A. Smirnov*, and A. P. Yelisseyev**
**Ural State Technical University (UPI), ul. Mira 19, Yekaterinburg, 620002 Russia*
e-mail: ogo@dpt.ustu.ru
***Branch of the Institute of Mineralogy and Petrography, Siberian Division, Russian Academy of Sciences,*
Novosibirsk, 630058 Russia

Abstract—Excitonic states, radiative relaxation of electronic excitations, and energy transfer to luminescence centers in both undoped and rare-earth activated (Pr, Er, Nd, Ho, Tb, Tm) KPb_2Cl_5 and $RbPb_2Br_5$ crystals were studied using low-temperature (8 K) time-resolved VUV spectroscopy under selective photoexcitation by synchrotron radiation. *© 2005 Pleiades Publishing, Inc.*

The use of laser diodes based on rare-earth-doped crystals for selective pumping of active media stimulates the search for new crystal matrices with narrow phonon spectra, in which thermal losses would be minimal and radiative processes would occur with a high quantum yield. Such crystals have application potential as active media for lasers operating in the medium IR and visible ranges, for telecommunication amplifiers, and for optical communication lines. KPb_2Cl_5 (KPC) and $RbPb_2Br_5$ (RPB) optical crystals belong to a class of new laser matrices appropriate for rare-earth (RE) doping. These crystals are not hygroscopic, exhibit a high resistance to corrosion, have a narrow phonon spectrum, and possess satisfactory mechanical properties [1].

In this paper, we report on a study of the excitonic states, radiative relaxation of electronic excitations, and energy transfer in both undoped and RE-activated KPC and RPB crystals.

The KPC and RPB crystals were grown using the Stockbarger method at a branch of the Institute of Mineralogy and Petrography (Novosibirsk, Siberian Division, Russian Academy of Sciences) [2]. The time-resolved VUV spectroscopy of low-temperature (8 K) optical luminescence under selective excitation by synchrotron radiation was conducted at HASYLAB, DESY (Hamburg, Germany). The description of the experimental techniques employed and the data obtained in our preliminary measurements can be found in [3, 4]. Steady-state photoluminescence (PL) and reflectance spectra in the temperature range 80–300 K were measured with a DMR-4 monochromator and a DDS-400 deuterium lamp.

The measured reflectance spectra (a fragment of which is shown in Fig. 1) exhibit a number of features in the ranges 4.3–4.7 eV (KPC) and 4.9–4.2 eV (RPB). The shape and temperature dependence of these features suggest that they are connected with cation excitonic states. The electronic transitions in the KPC and RPB crystals at the lowest temperatures derive from the $6s \longrightarrow 6p$ transitions in the Pb^{2+} ion between the states that, as in lead chloride [5], form the valence band top and conduction band bottom in these crystals. By analyzing these features in the reflectance spectra of KPC and RPB crystals, we determined the bandgap width E_g and exciton binding energy R in these crystals within the hydrogen-like model; namely, at 8 K, E_g = 4.79 and

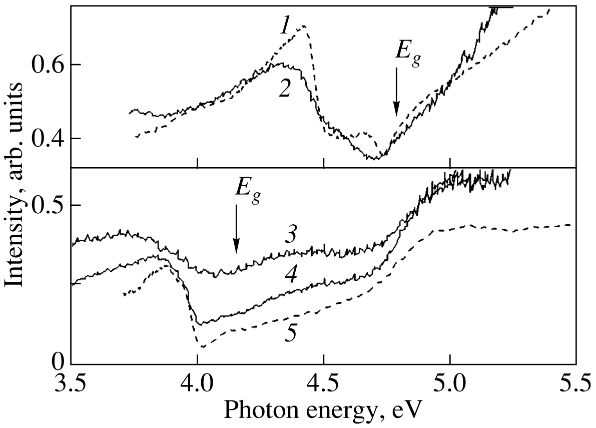

Fig. 1. Fragment of the reflectance spectra of (*1*, *2*) KPb_2Cl_5 and (*3*–*5*) $RbPb_2Br_5$ crystals measured at various temperatures T: (*1*, *5*) 8, (*4*) 80, and (*2*, *3*) 300 K.

1063-7834/05/4708-1570$26.00 © 2005 Pleiades Publishing, Inc.

4.15 eV and $R = 0.34$ and 0.37 eV for the KPC and RPB crystals, respectively. The replacement of the cation, K ⟶ Rb, and of the anion, Cl ⟶ Br, brings about a long-wavelength shift of the exciton peaks and, hence, a decrease in E_g. In a higher energy region, at 21–23 eV, the reflectance spectra exhibit clearly pronounced peaks corresponding to the excitation of Pb^{2+} cation core excitons (E_{c1}, E_{c2} in Fig. 2). Note that analogous peaks were observed earlier in the reflectance spectra of $PbCl_2$ and $PbBr_2$ [5].

Doping with RE elements (Pr, Er, Nd, Ho, Tb, Tm) gives rise to a characteristic activator luminescence, which depends on the RE element. The impurity luminescence has a fairly high yield both under selective intracenter excitation with photons of energy $E_{exc} < E_g$ (the bands in the excitation spectrum in this case refer to the position of excited impurity-center levels) and under excitation in the regions of the selective creation of excitons or electron–hole pair generation by photons of energy $E_{exc} > E_g$ (Figs. 2, 3). An analysis of the spectra shows that there is efficient energy transfer in these crystals both via the excitonic mechanism and via electron and hole migration followed by their recombination at the activator.

The energy transfer efficiency is temperature-dependent. At low temperatures ($T = 8$ K), as the excitation energy $E_{exc} > E_g$ is increased, the energy transfer efficiency decreases; this is usually associated with the increased kinetic energy of the created electrons and holes and their nonradiative annihilation at the crystal surface. The efficiency of this channel in the doped crystals under study is also indicated by the absence of multiplication of the electronic excitations at energies $E_{exc} > (2–3)E_g$. At 8 K, the thermal ionization of excitons in KPC crystals is unlikely; therefore, the energy transfer mechanisms involving excitons are quite efficient. This scenario is consistent with the excitation spectra of activator luminescence. Figure 2 exemplifies these spectra obtained on KPC : Ho and KPC : Er. A possible excitonic energy transfer to luminescence centers at low temperatures could be the nonradiative resonance energy transfer from self-trapped excitons (STEs) to an impurity center through dipole–dipole interaction. Indeed, low-temperature PL spectra of undoped KPC crystals contain several bands, namely, broad overlapping bands peaking at 2.4 and 1.9 eV and exhibiting microsecond-range decay kinetics and fast 3.75-eV luminescence ($\tau_1 = 0.8$ ns, $\tau_2 = 3.5$ ns) [4]. The luminescence at 1.9 eV is excited both in the crystal transparency region and in the fundamental absorption region. The PL bands at 2.4 and 3.75 eV are excited solely near the fundamental absorption edge by photons of energy $E_{exc} > E_g$. Therefore, we believe that the 1.9-eV PL band in KPC crystals originates from lattice defects and that the bands at 2.4 and 3.75 eV are due to radiative annihilation of triplet and singlet STEs, respectively. Another mechanism of energy transfer at low temperatures can be associated with bound excitons, which are produced as a result of the migration of unrelaxed excitons and their capture by an impurity center. This is certainly an interesting problem; however, as with other RE-doped crystals, it would require additional study.

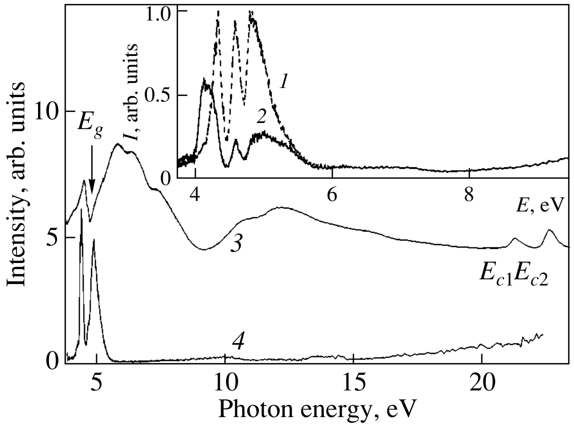

Fig. 2. (*1*, *2*) Excitation spectra of PL at (*1*) 548 and (*2*) 665 nm for KPb_2Cl_5 : Ho crystals and (*3*) the reflectance spectrum and (*4*) excitation spectrum of PL at 550 nm ($^4S_{3/2} \longrightarrow {}^4I_{15/2}$ transition) for KPb_2Cl_5 : Er crystals measured at 8 K. The E_{c1} and E_{c2} peaks are due to excitation of Pb^{2+} cation core excitons.

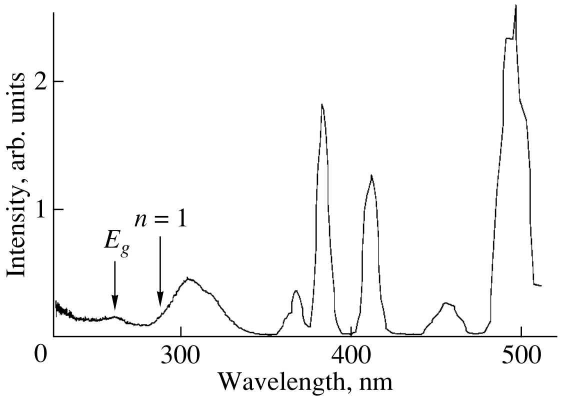

Fig. 3. Excitation spectrum of PL at $E_m = 2.25$ eV for a KPb_2Cl_5 : Er crystal measured at $T = 300$ K.

At room temperature, STE luminescence in KPC crystals is thermally quenched and, in addition, unrelaxed excitons can undergo thermal dissociation. In these conditions, the electron–hole mechanism of energy transfer dominates and the recombination luminescence of impurity centers is observed.

ACKNOWLEDGMENTS

The authors are indebted to A.M. Tkachuk for helpful discussions and to L.I. Isaenko for providing the crystals and performing their characterization.

This study was supported by the Russian Foundation for Basic Research (project no. 02-02-16322), the Ural Science and Education Center (program “Promising Materials”), and CRDF (project no. EK-005-XI).

REFERENCES

1. A. M. Tkachuk, S. E. Ivanova, L. I. Isaenko, A. P. Eliseev, S. Payne, R. Solarz, R. Page, and M. Nostrand, Opt. Spektrosk. **92** (1), 89 (2002) [Opt. Spectrosc. **92** (1), 83 (2002)].
2. L. Isaenko, A. Yelisseyev, A. Tkachuk, S. Ivanova, S. Vatnik, A. Merkulov, S. Payne, R. Page, and M. Nostrand, Mater. Sci. Eng. B **81**, 188 (2001).
3. I. N. Ogorodnikov, V. A. Pustovarov, M. Kirm, A. V. Kruzhalov, L. I. Isaenko, and A. P. Yelisseyev, HASYLAB Annu. Rep. (2001), p. 233.
4. I. N. Ogorodnikov, V. A. Pustovarov, M. Kirm, A. V. Kruzhalov, L. I. Isaenko, and A. P. Yelisseyev, HASYLAB Annu. Rep. (2002), p. 247.
5. R. Kink, T. Avramaa, V. Kisand, A. Lohmus, I. Kink, and I. Martinson, J. Phys. C **10**, 693 (1998).

Translated by G. Skrebtsov

Physics of the Solid State, Vol. 47, No. 8, 2005, pp. 1573–1575. Translated from Fizika Tverdogo Tela, Vol. 47, No. 8, 2005, pp. 1512–1514.
Original Russian Text Copyright © 2005 by Pilipenko.

PROCEEDINGS OF THE XII FEOFILOV WORKSHOP “SPECTROSCOPY OF CRYSTALS ACTIVATED BY RARE-EARTH AND TRANSITION-METAL IONS”

(Yekaterinburg, Russia, September 22–25, 2004)

Donor Excitons in LiH and LiD Single Crystals

G. I. Pilipenko
Ural State Technical University, ul. Mira 19, Yekaterinburg, 620002 Russia
e-mail: gip@dpt.ustu.ru

Abstract—The formation of bound excitons of the donor type was observed in LiH and LiD single crystals activated by 4*d* or 5*d* transition elements (Rh, Ru, Ir). The bound excitons were found to form under direct optical excitation of impurity ions. © *2005 Pleiades Publishing, Inc.*

The presence of transition-metal (*d*-element) impurities in semiconductor and dielectric crystals can cause various optical phenomena due to the rich energy spectrum of the partially occupied *d* shells in these materials. In some studies, exciton binding by 3*d* impurities in II–VI semiconductors has been observed [1, 2]. By studying the spectra of bound excitons, one can determine the energy positions of impurity levels and identify the structure of the impurity energy states.

In this paper, we describe the experimental data on the formation of donor excitons in LiH and LiD single crystals activated by 4*d* elements (Rh, Ru) and 5*d* elements (Ir).

Figure 1 shows the optical absorption spectrum of LiH–Rh single crystals. The rhodium content in these crystals is 0.05 wt %. The high-intensity absorption band has a maximum with a half-width of 3000 cm^{-1} in the region of 24000 cm^{-1}. The intensity of the band is practically the same at 80 and 300 K. This band is related to charge-transfer transitions of the impurity–band type. At 80 K, a vibrational structure appears in the low-energy part of the charge-transfer band. This structure consists of four lines separated by equal intervals of 76–80 cm^{-1}; these intervals do not depend on the isotope composition of the crystal matrix. The relative line intensities are the same in all samples, thus making it possible to associate the entire group of lines with the same center. The half-widths of the lines as determined without taking their overlap into account increase from 20 cm^{-1} for the first line (corresponding to the lowest energy) to 40 cm^{-1} for the third line. The low intensity of the fourth line did not allow us to determine its half-width.

The first line does not involve phonons, and the three others are phonon replicas involving a local vibration mode with an energy quantum of 78 cm^{-1}. In Table 1, the wavenumbers and the interpretation of the peaks in the absorption spectra of LiH–Rh and LiD–Rh crystals are listed. In LiH(D)–Ir crystals with an iridium concentration of 0.08 wt %, the charge-transfer absorption band is observed in the region of 24500 cm^{-1}. At 80 K, a structure consisting of a zero-phonon line and a vibrational wing is also observed on the low-energy edge of the absorption band. However, in contrast to LiH(D)–Rh crystals, the structure of the vibrational wing in LiH(D)–Ir can be explained by the one-phonon contribution to the electron–phonon interaction in the iridium impurity center; this follows from comparing the density of one-phonon states in LiH and LiD crystals with the features of the vibrational wing (Fig. 2). This conclusion agrees with the weaker electron–phonon coupling for a more extended orbital of the 5*d* shell of an iridium ion.

The positions of the peaks in the vibrational structure of the optical absorption of LiH(D)–Ir crystals are given in Table 2.

The analysis of the experimental data on optical absorption spectra shows that 4*d* and 5*d* transition elements create one or several deep energy levels in the band gap of LiH and LiD crystals, which is indicated by the occurrence of charge-transfer (impurity–band or

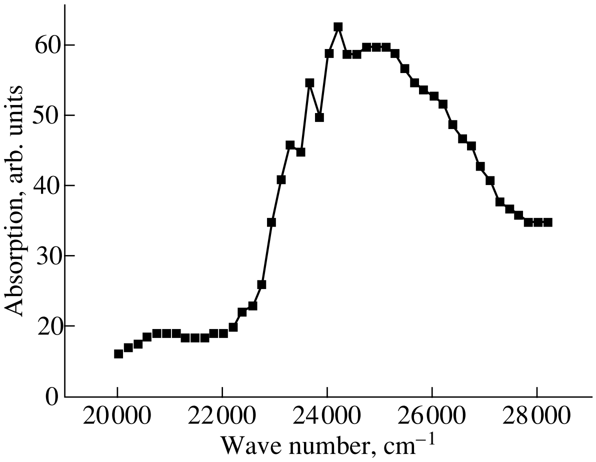

Fig. 1. Absorption spectrum of LiH–Rh crystals at 80 K.

Table 1. Positions of the peaks in the donor-excitonic absorption spectrum of LiH–Rh and LiD–Rh crystals and their interpretation

LiH		LiD		$\Delta\nu_H/\Delta\nu_D$	$\nu_D - \nu_H$, cm^{-1}	Interpretation
ν_H, cm^{-1}	peak position with respect to the zero-phonon line $\Delta\nu_H$, cm^{-1}	ν_D, cm^{-1}	peak position with respect to the zero-phonon line $\Delta\nu_D$, cm^{-1}			
22700 ± 4		22972 ± 4			272	Zero-phonon line
	78 ± 4		78 ± 4	1.00		Local vibration
	1240 ± 4		905 ± 4	1.37		Local vibration

Table 2. Position of the peaks in the donor-excitonic absorption spectrum of LiH(D)–Ir crystals and their interpretation

LiH		LiD		$\Delta\nu_H/\Delta\nu_D$	$\nu_D - \nu_H$, cm^{-1}	Interpretation
ν_H, cm^{-1}	peak position with respect to the zero-phonon line $\Delta\nu_H$, cm^{-1}	ν_D, cm^{-1}	peak position with respect to the zero-phonon line $\Delta\nu_D$, cm^{-1}			
22800 ± 4		23064 ± 4			264	Zero-phonon line
	310 ± 10		310 ± 10	1.00		TA(X)
	410 ± 10		410 ± 10	1.00		LA(X)
	710 ± 10					TO(L)
	800 ± 10		580 ± 10	1.38		TO(X)
	950 ± 10		710 ± 10	1.34		LO(X)
	1380 ± 10		1000 ± 10	1.38		Local vibration
	1520 ± 10		1110 ± 4	1.37		Local vibration

band–impurity) transitions [3]. These transitions can form electron and hole bound states or excitons bound to an acceptor or a donor.

The Rh$^+$ ions in lithium hydride and deuteride are isoelectronic impurities. An isoelectronic impurity can create bound states depending on the ratio of the bandwidth to the magnitude of the attractive potential [4]. Transitions of an electron from the ground state of the impurity ion to an excited state usually result in a line absorption spectrum. It should be noted that, for impurities having several excited states, the absorption spectrum is similar to an excitonic spectrum. Therefore, it is difficult to separate the spectra attributed to bound excitons and to hydrogenic impurities. In the case considered, the terms “bound exciton” and “excited impurity state” have the same meaning, since an excited state of an impurity is directly created by light in our experiments [5].

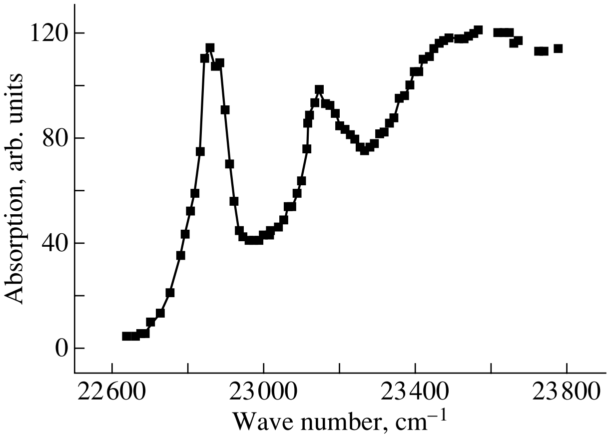

Fig. 2. Donor-excitonic absorption spectrum of LiH–Ir crystals.

Optical measurements showed that univalent Rh$^+$ ($4d^8$ shell) and Ir$^+$ ($5d^8$ shell) impurity ions have characteristic line absorption spectra indicating the formation of donor excitons. A photoinduced transition of an electron into a bound hydrogenic state is described by the reaction

$$d^8 + h\nu \longrightarrow [d^7e],$$

where the square brackets symbolize the Coulomb interaction between an electron and a hole on the donor.

The energy levels of univalent Rh$^+$ and Ir$^+$ ions lie far from the edge of the conduction band of lithium hydride (deuteride); therefore, the absorption involving these levels corresponds to the visible part of the spectrum. The absorption spectra of LiH(D)–Rh(Ir) crystals have several lines due to the excitation of an electron from the ground level and there is also a continuous absorption band related to the photoionization of the impurity center.

The first absorption line corresponds to the transition of the donor from the ground state to the first excited state. The other absorption peaks correspond to the phonon replicas caused by interaction with local impurity vibrations [in LiH(D)–Rh] or with crystal vibrations [in LiH(D)–Ir]. The high-energy absorption lines merge with the band corresponding to full donor ionization. The decrease in absorption with increasing energy is due to the decrease in the probability of transitions to the states located far from the bottom of the conduction band.

The irradiation in the region corresponding to full ionization of Rh^+ or Ir^+ impurities results in the formation of Rh^{2+} or Ir^{2+} ions, whose presence can be detected using the ESR method [6, 7]. The excitation spectrum of the paramagnetic Rh^{2+} (Ir^{2+}) ion state coincides with the full-ionization band of the Rh^+ (Ir^+) ion.

Analogous features are observed in the absorption spectra of LiH(D)–Ru crystals in the case where excitons bound to Ru^+ ions ($4d^7$ configuration) form after the reduction of Ru^{2+} ions arising under irradiation with ultraviolet light. In this case, the hole component of the donor exciton is localized on the Ru^+ ion; therefore, the Ru^+ ion is charged positively with respect to the lattice and the electron is captured by the Coulomb field of this charge. The electron transition responsible for the band induced by ultraviolet light is described by the reaction

$$d^7 = h\nu \longrightarrow [d^6 e].$$

The energy of this transition is equal to 20110 cm^{-1} for LiH–Ru crystals and 20440 cm^{-1} for LiD–Ru crystals.

Thus, 4*d* and 5*d* transition metals (Ru, Rh, Ir) create deep levels in the band gap of lithium hydride and deuteride; bound excitons are produced directly by light during the excitation of these ions.

REFERENCES

1. P. Dean and D. Herbert, Top. Curr. Phys. **14**, 55 (1979).
2. K. A. Kikoin, V. I. Sokolov, and T. P. Surkova, *Spectroscopy of Crystals* (Nauka, Leningrad, 1989), pp. 148–161 [in Russian].
3. G. I. Pilipenko, A. A. Sabirzynov, D. V. Oparin, V. G. Stepanov, and F. F. Gavrilov, J. Phys.: Condens. Matter **4**, 4055 (1992).
4. F. Bassani and G. Pastori Parravicini, *Electronic States and Optical Transitions in Solids* (Pergamon, New York, 1975; Nauka, Moscow, 1982).
5. R. S. Knox, *Theory of Excitons* (Academic, New York, 1963; Mir, Moscow, 1966).
6. G. I. Pilipenko, A. A. Sabirzyanov, D. V. Oparin, and V. G. Stepanov, in *Proceedings of XXVII Congress Ampere on Magnetic Resonance and Related Phenomena, Kazan, 1994* (Kazan, 1994), Vol. 1, pp. 488–489.
7. G. I. Pilipenko, A. A. Sabirzyanov, V. G. Stepanov, D. V. Oparin, V. V. Izotov, and F. F. Gavrilov, J. Phys.: Condens. Matter **4**, 4047 (1992).

Translated by I. Zvyagin

Physics of the Solid State, Vol. 47, No. 8, 2005, pp. 1576–1578. Translated from Fizika Tverdogo Tela, Vol. 47, No. 8, 2005, pp. 1515–1517.
Original Russian Text Copyright © 2005 by Nedelko, Gomenyuk, Slobodyanik, Stus’.

PROCEEDINGS OF THE XII FEOFILOV WORKSHOP “SPECTROSCOPY OF CRYSTALS ACTIVATED BY RARE-EARTH AND TRANSITION-METAL IONS”

(Yekaterinburg, Russia, September 22–25, 2004)

Luminescence Centers Generated by Chromium Ions in Potassium–Aluminum (Indium) Diphosphates

S. Nedelko, O. Gomenyuk, N. Slobodyanik, and N. Stus’
Shevchenko National University, Vladimirskaya ul. 64, Kiev, 03680 Ukraine
e-mail: SNedilko@univ.kiev.ua

Abstract—Crystals of potassium–aluminum (indium) diphosphates K*Me*P_2O_7 (*Me* = Al, In) doped by chromium ions are synthesized for the first time, and their main spectral luminescence properties are described. The luminescence of these crystals is studied in the temperature range 4.2–300 K under excitation by light with a wavelength of 270–650 nm. The luminescence spectrum has two wide bands in the ranges 450–650 nm (“green” photoluminescence) and 700–800 nm (“red” photoluminescence). The green photoluminescence band is assumed to be a superposition of the intrinsic radiation of the matrix and the radiation of molecular centers generated by chromium ions that are surrounded by four oxygen atoms. At low temperatures, the red photoluminescence band consists of a wide unstructured band and narrow lines on its short-wavelength wing and is associated with the radiation of Cr^{3+} ions that replace Al^{3+} matrix ions and are in an octahedral oxygen environment. Parameters of the electron energy level diagram of the Cr^{3+} ion in the matrices of the investigated crystals are determined. © *2005 Pleiades Publishing, Inc.*

1. INTRODUCTION

When developing new laser materials on the basis of oxide crystals and glasses, chromium ions are often chosen as impurities [1–3]. In spite of the fact that there are numerous data on the physical and chemical properties and quite a good understanding of the physics of absorption and emission of light and energy dissipation in these systems, certain physical problems remain unsolved. Among them is the problem of the simultaneous existence of chromium ions in different charge states Cr^{n+} ($n = 3, 4, 5$) occupying different positions in the matrix. This problem is especially important in the case of a complicated oxide matrix where the cationic sublattice is formed by cations of different types and where oxygen molecular groups occupy anionic sites. In such matrices, the bonding is mainly ionic between the cations and anions and covalent inside the molecular groups. The presence of the two types of bonding gives rise to specific features of the centers of intrinsic photoluminescence (PL); to a variety of charge states of impurity ions; and, as a consequence, to a variety of spectral luminescence properties of such compounds [4, 5].

This study deals with the luminescence spectral properties of aluminum or indium diphosphates with the general formula K*Me*P_2O_7 (*Me* = Al or In) doped by chromium ions, which are new promising compounds for quantum electronics. The lattice of these crystals admits an isovalent replacement of aluminum or indium ions by Cr^{3+} ions; however, in principle, chromium ions (possibly, having a different charge) can also be located at the Na^+ or P^{5+} ion positions.

2. EXPERIMENTAL

K*Me*P_2O_7 crystals $3 \times 3 \times 3$ mm in size were synthesized from a melt solution using K_2O–Me_2O_3–P_2O_5–Cr_2O_3 oxide mixtures. The concentration of chromium oxides in the melt did not exceed 1 wt %. A description of the structure of K*Me*P_2O_7 crystals can be found in [6]. Photoluminescence was investigated at 4.2, 77, and 300 K. Photoluminescence was excited using ILGI-501 lasers (with radiation wavelength λ_{ex} = 337.1 nm), LGN-503 lasers (λ_{ex} = 476.5, 488.4, 514.0 nm), and DKSL-1000 xenon lamp radiation filtered by a DMR-4 double monochromator and was recorded using a DFS-12 spectrometer. The spectrometers, signal recording, and data processing were computer-controlled.

3. EXPERIMENTAL RESULTS

At room temperature, the PL spectrum of chromium-doped $KAlP_2O_7$: Cr crystals consists of two (green and red) wide bands in the wavelength regions 450–650 and 700–800 nm, respectively. The green band is undoubtedly structured; what more, its short wavelength components are also observed under the same excitation and temperature conditions for crystals not doped with chromium (Fig. 1). For $KInP_2O_7$: Cr crystals, the PL spectra are basically the same; however, in the long-wavelength range mentioned above, we failed to resolve the structure of the red band, probably because of the insufficient resolution of the spectral equipment used (Fig. 1). With increasing chromium content, the maximum of the envelope curve of the green band shifts to longer wavelengths, since the intensity of the long-wavelength component increases. Simultaneously, the red PL band increases in intensity.

The excitation spectra of these PL bands are different. The short-wavelength part of the green PL band is excited in a wide smeared band in the range 270–350 nm, whereas in the excitation spectra of red PL there are three distinct bands in the regions 270–345 (band I), 400–500 (band II), and 530–680 nm (band III). In bands II and III, structural peaks are observed (curve *5* in Fig. 1). Thus, band I of the red-PL excitation spectrum and the green-PL excitation band overlap strongly. We also note that band II of the red-PL excitation spectrum in crystals $KAlP_2O_7$: Cr overlaps with the green PL band of undoped crystals (curves *1*, *5* in Fig. 1).

As the temperature decreases from 300 to 77 and further to 4.2 K, the shapes and intensities of both PL bands change; more specifically, under short-wavelength excitation (λ_{ex} = 310–350 and 375–500 nm), the intensities of the long-wavelength components of the green band decrease and the intensity of the red band increases (Fig. 1) and, under excitation in band III, the red PL band narrows and there appear narrow fine-structure lines at its short-wavelength edge with maxima at λ_{max} = 708, 712, and 725 nm (Fig. 2).

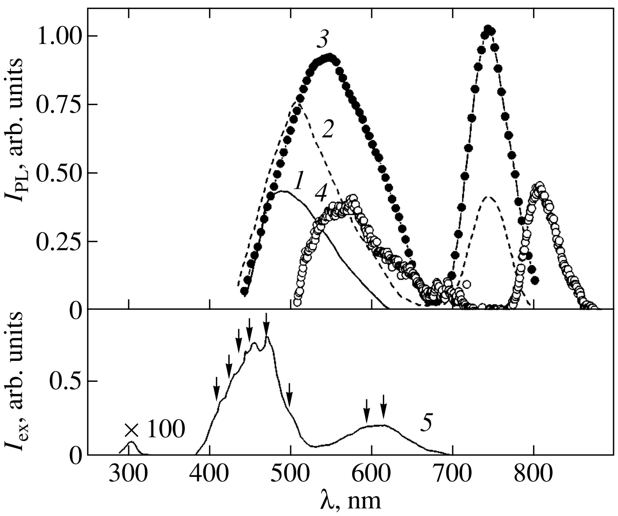

Fig. 1. (*1*–*4*) PL spectra and (*5*) the PL excitation spectrum of (*1*–*3*, *5*) $KAlP_2O_7$ and (*4*) $KInP_2O_7$ crystals at temperatures of (*3*) 300, (*1*, *4*) 77, and (*2*) 4.2 K. The excitation wavelength λ_{ex} is (*1*–*3*) 337.1 and (*4*) 488 nm; excitation spectrum *5* is recorded at a luminescence wavelength λ = 740 nm. The Cr_2O_3 concentration *C*(Cr) in the melt was (*1*) 0, (*2*, *3*, *5*) 0.08, and (*4*) 1 wt %. Curve *4* does not include the correction for the spectral sensitivity of the spectrometer.

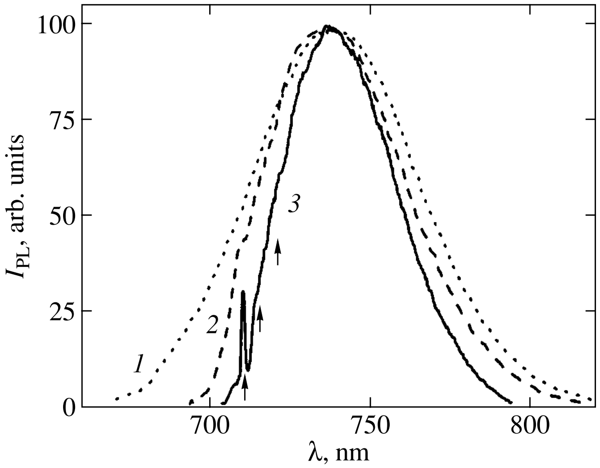

Fig. 2. Luminescence spectra of $KAlP_2O_7$: Cr crystals recorded at λ_{ex} = 632.8 nm at temperatures of (*1*) 300, (*2*) 77, and (*3*) 4.2 K. *C*(Cr) = 0.08 wt %.

4. DISCUSSION

The experimental data obtained allow us to conclude that the PL of the K*Me*P_2O_7 : Cr crystals is a superposition of the intrinsic luminescence of the undoped matrix (the short-wavelength components of the green PL band) and the PL of the centers related to chromium ions (long-wavelength components of the green band, the wide red unstructured band, and the fine-structure lines). The red PL can be excited both directly in bands II and III and via the matrix by light in the range 270–350 nm. With increasing temperature, the excitation energy is likely to transfer more effectively from the centers of intrinsic PL to the red-PL centers.

As to the nature of the intrinsic PL of the matrix, this luminescence (typical of the systems in question) is commonly accepted to be related to various intrinsic defects of the matrix and uncontrollable impurities. Therefore, we do not analyze it here. The impurity long-wavelength components of the green band can be due to radiation of molecular groups of the form $[CrO_3–O–PO_3]^+$ created when one of the P^{5+} ions in the P_2O_7 group is replaced by a Cr^{6+} ion. It was shown in [7, 8] that deformed CrO_4^{2-} tetrahedra in various matrices are characterized by PL emitted in this spectral region.

The intense red PL of $KAlP_2O_7$: Cr crystals is likely due to Cr^{3+} ions occupying the Al^{3+} ion positions with octahedral oxygen surroundings. This conclusion follows from the fact that the spectral characteristics of the red PL are similar to those of the experimental and theoretical spectra of Cr^{3+} ions in solids, according to which the unstructured band is due to $^4T_2 \longrightarrow {}^4A_2$ transitions and the fine-structure lines (*R* lines) correspond to the $^2E \longrightarrow {}^4A_2$ transitions in the 3*d* shell of the Cr^{3+} ion [1–3, 9]. From the positions of the bands and lines in the PL spectra and PL excitation spectra, we can estimate parameters describing the positions of the Cr^{3+} energy levels in $KAlP_2O_7$: Cr crystals using the Tanabe–Sugano model [9]: the crystal-field parameter $D_q = 1342$ cm^{-1}, the ^2E level splitting $\Delta(^2E) = 80$ cm^{-1}, and the energy spacing between the $^4T_2$ and ^2E levels $\Delta(^4T, {}^2E) = 530$ cm^{-1}.

The differences between the PL spectra of $KAlP_2O_7$: Cr crystals and $KInP_2O_7$: Cr crystals (Fig. 1) agree with the assumption that the observed red PL is related to Cr^{3+} ions. Indeed, according to the crystal-field theory, the parameter D_q (determining the transition energies for the Cr^{3+} ion), can be written as $D_q \sim qr^4/R^5$, where q is the charge of the ligand (O^2 ion), R is the distance from the impurity ion to the ligand, and r is the average radius of the 3*d* orbital of the Cr^{3+} ion [9]. The energy of the $^4T_2 \longrightarrow {}^4A_2$ transition (which determines the position of the red PL band) is proportional to the parameter D_q. Therefore, knowing the position of this band for $KAlP_2O_7$: Cr crystals ($\lambda_{max} = 735$ nm) and the quantities R(Al–O) and R(In–O), we can estimate the position of the red band for $KInP_2O_7$: Cr crystals. The result is $\lambda_{max} \sim 1300$ nm. This value is approximate but nevertheless explains the strong shift of the red PL band towards the near IR region.

5. CONCLUSIONS

We have synthesized for the first time chromium-doped $KAlP_2O_7$ and $KInP_2O_7$ crystals and studied their main luminescence spectral properties over wide temperature and spectral intervals. We have also estimated the energy parameters describing the Cr^{3+} impurity luminescence of these crystals.

ACKNOWLEDGMENTS

This study was performed in the framework of the projects supported by the Shevchenko National University (Kiev, Ukraine).

REFERENCES

1. S. Heer, M. Wermuth, K. Kramer, D. Ehrentraut, and H. U. Gudel, J. Lumin. **94–95**, 341 (2001).
2. Weiyi Jia, Huimin Liu, Yanyun Wang, U. Hommerich, H. Eilers, K. R. Hoffman, and W. M. Yen, J. Lumin. **60–61**, 158 (1994).
3. J. Dong and P. Deng, J. Lumin. **104** (3), 161 (2003).
4. S. G. Nedelko, Opt. Spektrosk. **87** (1), 61 (1999) [Opt. Spectrosc. **87** (1), 61 (1999)].
5. S. G. Nedilko, Funct. Mater. **9** (2), 336 (2002).
6. E. A. Genkina, Zh. Strukt. Khim. **15** (6), 92 (1990).
7. M. U. Belyĭ, S. G. Nedelko, and O. V. Chukova, Zh. Prikl. Spektrosk. **63** (3), 241 (1995).
8. M. U. Belyĭ, O. V. Chukova, S. G. Nedelko, and V. P. Scherbatskyi, J. Appl. Spectrosc. **67** (2), 182 (2000).
9. D. T. Sviridov, R. K. Sviridova, and Yu. F. Smirnov, *Optical Spectra of Transition-Metal Ions in Crystals* (Nauka, Moscow, 1976) [in Russian].

Translated by I. Zvyagin

Physics of the Solid State, Vol. 47, No. 8, 2005, pp. 1579–1583. Translated from Fizika Tverdogo Tela, Vol. 47, No. 8, 2005, pp. 1518–1521.
Original Russian Text Copyright © 2005 by Zhuravlev, Yakovlev.

PROCEEDINGS OF THE XII FEOFILOV WORKSHOP "SPECTROSCOPY OF CRYSTALS ACTIVATED BY RARE-EARTH AND TRANSITION-METAL IONS"

(Yekaterinburg, Russia, September 22–25, 2004)

Properties of a Thin-Film Electroluminescent Diode Based on Poly(*N*-vinylcarbazole) Doped by the Tris Complex of Europium with Dibenzoylmethane and 1,10-Phenanthroline

K. P. Zhuravlev and Yu. O. Yakovlev

Institute of Radio Engineering and Electronics (Fryazino Branch), Russian Academy of Sciences,
pl. Vvedenskogo 1, Fryazino, Moscow oblast, 141190 Russia
e-mail: kpz225@ire216.msk.su, e-mail: yoy225@ire216.msk.su

Abstract—The electroluminescence spectra of thin-film organic diodes with light-emitting layers that consist of poly(*N*-vinylcarbazole) (*PVK*) doped by the tris complex of europium with dibenzoylmethane and 1,10-phenanthroline [Eu(*DBM*)$_3$*phen*] are investigated. It is revealed that an increase in the Eu(*DBM*)$_3$*phen* concentration in the light-emitting layer leads to an increase in the decay rate of electroluminescence of the cell. A decrease in the contribution from the intensity of the luminescence lines associated with the Eu(*DBM*)$_3$*phen* complex to the total electroluminescence spectrum of the cell with time is explained by the degradation of Eu(*DBM*)$_3$*phen* molecules upon excitation. *© 2005 Pleiades Publishing, Inc.*

1. INTRODUCTION

Electroluminescence in structures consisting of thin organic films has been extensively investigated since the pioneering work by Tang and VanSlyke [1].

Luminescence in thin-film organic structures is caused by radiative recombination of electrons and holes injected from a cathode and an anode, respectively. At present, a large number of works have been devoted to the study of structures in which a light-emitting layer consists of a mixture of two or more compounds. The use of mixtures for fabricating light-emitting layers makes it possible to combine individual properties of different compounds (such as a high conductivity provided by charge carriers, a high quantum yield of electroluminescence, and necessary spectral characteristics) in a single layer. Moreover, mixtures are characterized by a weaker concentration quenching. Matrices for light-emitting layers can be prepared from polymers and low-molecular organic compounds. When fabricating electroluminescent cells, polymer layers, as a rule, have been produced using spin coating. For a mixture of compounds, this method allows one to control simply and very accurately the concentrations of components in the mixture by adding a required amount of each compound to the solution. Furthermore, unlike thermal evaporation, the low-temperature preparation of layers by spin coating makes possible the use of compounds that decompose upon heating. The disadvantages of the spin coating method are unavoidable contamination of the prepared films with solvents and also complication of the technology for fabricating electroluminescent cells due to the employment of an additional process that differs substantially from the processes of vacuum thermal evaporation used for producing other layers of the cell. Ouro Djobo *et al.* [2] compared the electroluminescence properties of poly(*N*-vinylcarbazole) (*PVK*) layers prepared by thermal evaporation and spin coating and revealed that the turn-on voltage in the former case is considerably lower than the turn-on voltage in the latter case.

In this work, we investigated the electroluminescence of poly(*N*-vinylcarbazole) doped by the tris complex of europium with dibenzoylmethane and 1,10-phenanthroline [Eu(*DBM*)$_3$*phen*] in electroluminescent diodes entirely fabricated using thermal evaporation.

2. SAMPLE PREPARATION AND EXPERIMENTAL TECHNIQUE

The design of an organic electroluminescent diode is shown in Fig. 1. The lithium fluoride (LiF) layer located under an aluminum cathode is used to decrease the energy barrier to injection of electrons. The tris(8-hydroxyquinoline) aluminum (Alq_3) layer serves as a conductor of electrons. The layer consisting of a *PVK* : Eu(*DBM*)$_3$*phen* mixture is a light-emitting layer. The *N*,*N*'-bis(3-methylphenyl)-*N*,*N*'-diphenylbenzylidene (*TPD*) layer acts as a conductor of holes. The copper phthalocyanine (Cu*Pc*) layer is used as a buffer layer that prevents diffusion of oxygen from the transparent

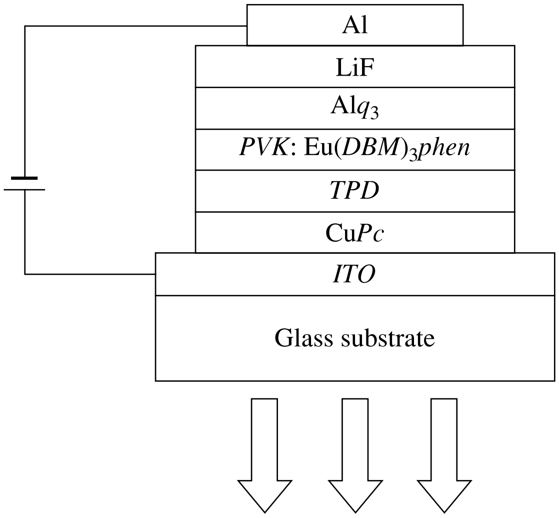

Fig. 1. Design of the electroluminescent diode under investigation.

anode based on an indium–tin oxide (*ITO*) solid solution and decreases the energy barrier to injection of holes from the anode into the *TPD* layer. This leads to an increase in the luminance and the lifetime of light-emitting diodes [3, 4].

The molecular structures of the compounds used are shown in Fig. 2. The Cu*Pc* and *TPD* compounds were purchased from the Aldrich Chemical Co. The *PVK* polymer was synthesized at the NPO Organic Intermediaries and Dyes, and the Alq_3 and Eu(*DBM*)$_3$*phen* compounds were prepared at our laboratory according to standard procedures.

A glass plate that was preliminarily coated on one side by an *ITO* layer with a specified topology served as a substrate. The surface resistivity of the *ITO* layer was of the order of 50 Ω per square. Substrate washing involved three stages. At the first stage, the substrate was wiped using a cloth moistened with ethanol. At the second stage, the wiped substrate was treated in an ultrasonic bath in isopropanol. At the third stage, the substrate was washed in a stream of distilled water. Thereafter, the substrate was dried initially in a centrifuge and then in a desiccator cabinet at a temperature of 70°C for 1 h.

The layers were deposited through thermal evaporation in a vacuum chamber at a pressure of 5×10^{-5} Torr. The deposition rate was approximately equal to 0.5 Å/s

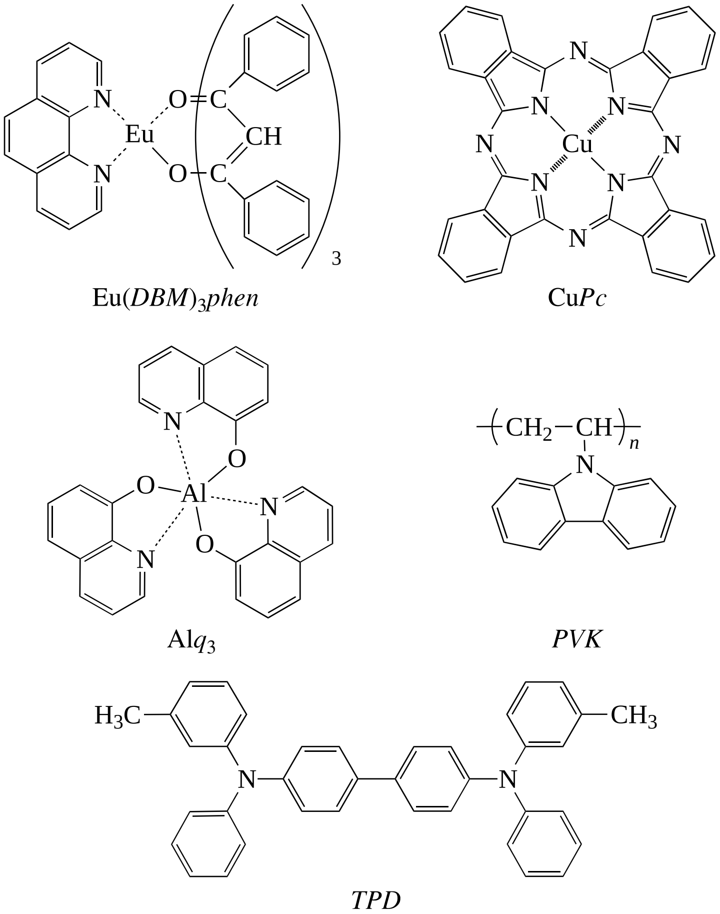

Fig. 2. Molecular structures of the organic compounds.

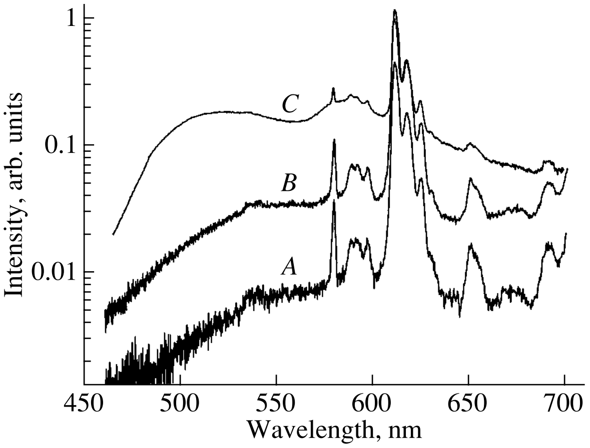

Fig. 3. Electroluminescence spectra of Cu*Pc*/*TPD*/*PVK* : Eu(*DBM*)$_3$*phen*/Alq_3/LiF/Al cells. The mass ratios *PVK* : Eu(*DBM*)$_3$*phen* for cells *A*, *B*, and *C* are equal to 2 : 1, 10 : 1, and (> 10) : 1, respectively.

for the LiF layers, 7.0 Å/s for the Al layers, and 2.0–2.5 Å/s for the organic films. The layer thicknesses were as follows: Al, ~100 nm; LiF, 0.9 nm; Alq_3, 15 nm; *PVK* : Eu(*DBM*)$_3$*phen*, 54 nm; *TPD*, 36 nm; and Cu*Pc*, 15 nm.

All the compounds, except for the *PVK* polymer, were used without preliminary purification and treatment. Poly(*N*-vinylcarbazole) evaporated at a rate suitable for deposition of layers over a wide range of temperatures. It is evident that this polymer contained oligomers with different masses and lengths of polymer chains. Preliminary sublimation of the initial *PVK* polymer under vacuum allowed us to obtain a fraction for which deposition rate in the temperature range 250–300°C was equal to 2.0–2.5 Å/s. In this temperature range, the Eu(*DBM*)$_3$*phen* complex had approximately the same deposition rate. Codeposition of the Eu(*DBM*)$_3$*phen* compound and the obtained fraction of the *PVK* polymer was performed from the same evaporator. In this case, we assumed that, at identical deposition rates, the concentration ratio of the compounds in the deposited film is equal to the concentration ratio of the compounds placed in the evaporator.

The light-emitting diode thus fabricated was placed in a hermetic chamber, which was filled with an inert medium (dried nitrogen). The electroluminescence spectra were recorded in this chamber. All the measurements were carried out at room temperature.

3. RESULTS AND DISCUSSION

We prepared *ITO*/Cu*Pc*/*TPD*/*PVK*:Eu(*DBM*)$_3$*phen*/Alq_3/LiF/Al electroluminescent cells in which the light-emitting layers contained the *PVK* and Eu(*DBM*)$_3$*phen* compounds at three different concentrations (cells *A*, *B*, *C*).

The mass ratio of the *PVK* and Eu(*DBM*)$_3$*phen* compounds is equal to 2 : 1 for cell *A* and 10 : 1 for cell *B*. Cell *C* was prepared using the *PVK* polymer without preliminary separation into fractions. For cell *C*, the mass ratio of the *PVK* and Eu(*DBM*)$_3$*phen* compounds placed in the evaporator was equal to 10 : 1, as is the case with cell *B*. However, the *PVK* polymer contained fractions that evaporate at temperatures lower and higher than the evaporation temperature of the Eu(*DBM*)$_3$*phen* complex. Since, after the sample preparation, a portion of the material remains in the evaporator, we assume that, for the most part, light fractions

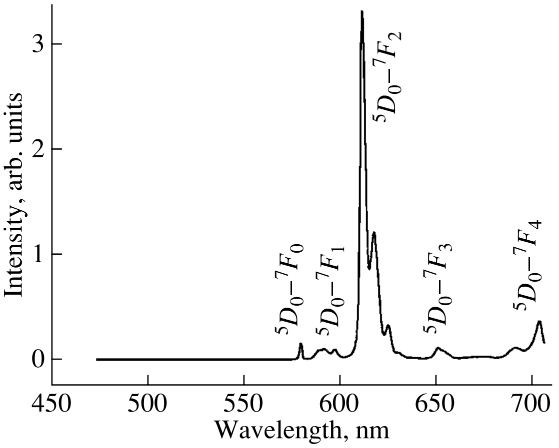

Fig. 4. Photoluminescence spectrum of the Eu(*DBM*)$_3$*phen* powder.

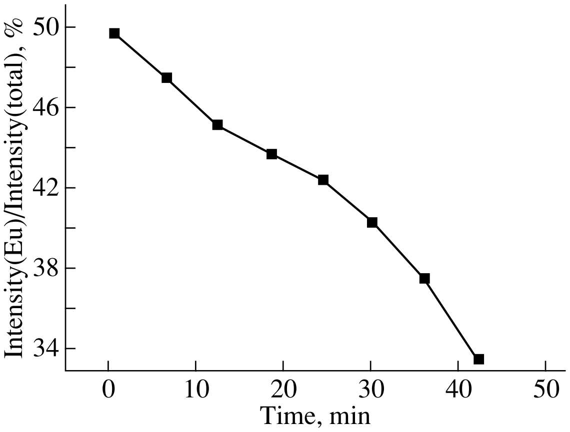

Fig. 5. Dependence of the ratio between the integrated intensity of the luminescence of the Eu(*DBM*)$_3$*phen* complex and the total intensity of the luminescence of the cell on the operation time at the mass ratio *PVK* : Eu(*DBM*)$_3$*phen* = 10 : 1 in the light-emitting layer.

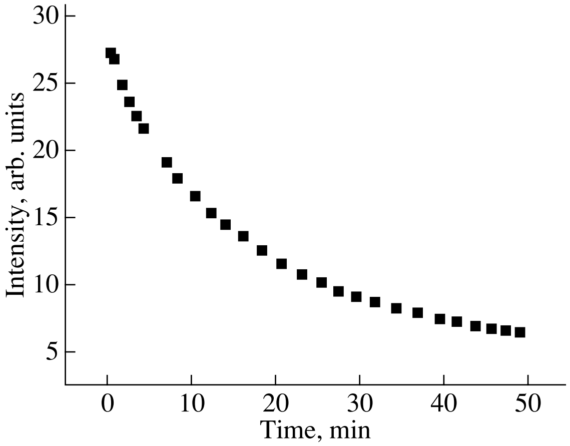

Fig. 6. Dependence of the photoluminescence intensity on the exposure time for the *PVK* : Eu(*DBM*)$_3$*phen* (10 : 1) film at a wavelength of 612 nm.

of the *PVK* polymer evaporate during deposition of the light-emitting layer and the mass fraction of the europium complex deposited on the substrate appears to be considerably lower than that in the initial mixture.

The electroluminescence spectra of the prepared samples (Fig. 3) involve narrow emission lines that correspond to the Eu(*DBM*)$_3$*phen* compound and follow the shape of its photoluminescence spectrum (Fig. 4). Moreover, the electroluminescence spectra contain broad bands attributed both to impurities in the *PVK* polymer and to the adjacent layer consisting of the Al*q*$_3$ compound. This compound is a good luminescent material characterized by a broad luminescence band in the green spectral range. However, the Al*q*$_3$ compound in the cells under investigation is used as a conductor of electrons and makes an insignificant contribution to the luminescence. This was confirmed by comparing the electroluminescence spectra of the given cells and the cells in which the Al*q*$_3$ layer was replaced by another conductor of electrons.

As the Eu(*DBM*)$_3$*phen* concentration in the light-emitting layer decreases, the total intensity of the luminescence of the cell increases but the fraction of the luminescence corresponding to the europium complex decreases. In particular, the contribution from the luminescence of the Eu(*DBM*)$_3$*phen* compound in cell *A* is equal to 80% of the integrated intensity. When the Eu(*DBM*)$_3$*phen* concentration decreases to 10 : 1 (cell *B*), the contribution from the luminescence of the europium complex amounts to 60%. With a further decrease in the concentration (cell *C*), the luminescence of the Eu(*DBM*)$_3$*phen* complex in the cell accounts for only 10% of the integrated intensity of the electroluminescence, which becomes yellowish green.

The degradation rate of the cell upon electrical excitation depends on the Eu(*DBM*)$_3$*phen* concentration in the light-emitting layer. The cell with a high Eu(*DBM*)$_3$*phen* concentration degrades at a higher rate. For example, the luminescence intensity of cells *C*, *B*, and *A* at a supply voltage of 20 V is halved for 40, 8, and approximately 3 min, respectively.

Furthermore, the intensity of the luminescence lines attributed to the europium complex decreases more rapidly than the intensity of the broad-band emission of the cell. The dependence of the ratio between the integrated intensity of the luminescence attributed to the Eu(*DBM*)$_3$*phen* compound and the total intensity of the luminescence of the cell on the operation time for cell *B* at a supply voltage of 20 V is plotted in Fig. 5. A decrease in the contribution of the europium luminescence to the total spectrum suggests that, in the light-emitting layer, Eu(*DBM*)$_3$*phen* molecules undergo degradation to the greatest extent.

Karasev *et al.* [5] investigated the photodestruction of europium chelate complexes, including the Eu(*DBM*)$_3$*phen* complex, in poly(methyl methacrylate) films. It was demonstrated [5] that the photoexcitation results in the dissociation of coordinated β-diketones, diimine, or phosphine oxide. Note that, for a series of similar compounds, the photodestruction is enhanced when the lifetime of the excited state of molecules increases.

In order to examine the degradation of luminescence of the Eu(*DBM*)$_3$*phen* complex upon photoexcitation, a film similar to the light-emitting layer in cell *B*, i.e., with the mass ratio *PVK* : Eu(*DBM*)$_3$*phen* = 10 : 1, was deposited on a quartz plate through vacuum thermal evaporation. The photoexcitation was produced by radiation of a mercury lamp. The photoluminescence intensity was measured at the maximum of the line corresponding to the $^5D_0$–$^7F_2$ transition of europium ions (at 612 nm) in the luminescence spectrum of the Eu(*DBM*)$_3$*phen* complex.

The luminescence intensity of the film under investigation decreases almost exponentially with an increase in the time of exposure to light (Fig. 6). An increase in the power of exciting radiation leads to a shortening of the decay time of photoluminescence.

Taking into account the dominant decay of the luminescence associated with the Eu(*DBM*)$_3$*phen* complex upon electrical excitation and the quenching of luminescence of this compound upon photoexcitation due to the dissociation of molecules, we make the inference that the Eu(*DBM*)$_3$*phen* molecules undergo degradation irrespective of the type of luminescence excitation.

Thus, the results obtained in this work allowed us to draw the conclusion that the use of the Eu(*DBM*)$_3$*phen* compound as a light-emitting material in electroluminescent devices for commercial applications does not hold promise, because the excitation of this luminophor is accompanied by partial degradation of the molecules.

REFERENCES

1. C. W. Tang and S. A. VanSlyke, Appl. Phys. Lett. **51**, 913 (1987).
2. S. Ouro Djobo, J. C. Bernéde, K. Napo, and Y. Guellil, Math. Chem. Phys. **77**, 476 (2002).
3. Sang Keol Kim, Taek Gyun Chung, Dong Hoe Chung, Ho Sik Lee, Min Jong Song, Jong Wook Park, Joon Ung Lee, and Tae Wan Kim, Opt. Mater. **21**, 159 (2003).
4. D. Hohnholz, S. Steinbrecher, and M. Hanack, J. Mol. Struct. **521**, 231 (2000).
5. V. E. Karasev, A. G. Mirochnik, and I. V. Vovna, Zh. Neorg. Khim. **33** (9), 2234 (1988).

Translated by O. Borovik-Romanova

Physics of the Solid State, Vol. 47, No. 8, 2005, pp. 1584–1589. Translated from Fizika Tverdogo Tela, Vol. 47, No. 8, 2005, pp. 1522–1527.
Original Russian Text Copyright © 2005 by Dzhioev, Zakharchenya, Lazarev, Tkachuk.

SEMICONDUCTORS AND DIELECTRICS

Electron Spin Filtering in the GaAs/AlGaAs Interface Space Charge Field

R. I. Dzhioev, B. P. Zakharchenya,† M. V. Lazarev, and M. N. Tkachuk
Ioffe Physicotechnical Institute, Russian Academy of Sciences, Politekhnicheskaya ul. 26, St. Petersburg, 194021 Russia
e-mail: dzhioev@orient.ioffe.ru

Received November 3, 2004

Abstract—The circularly polarized recombination radiation produced by optically oriented electrons in GaAs and viewed in the direction of and opposite to the pump light propagation was found to have opposite signs of polarization. The excitation was effected by photons of energy $E_{h\nu} \approx E_g + \Delta$ through a transparent AlGaAs window. The opposite signs of circular polarization and its complex dependence on the luminescence wavelength are accounted for by the influence of the space charge field created by the depleted layer near the interface. *© 2005 Pleiades Publishing, Inc.*

1. Investigation of spin transport has proved to be of considerable interest for spin electronics (spintronics) [1] and has been ongoing practically from the very outset of studies of the optical orientation in semiconductors. The effect of diffusive electron spin transport on the shape of the magnetic depolarization curve was studied theoretically in [2] and observed experimentally in [3]. A study of the drift of optically oriented carriers and of its manifestation in the polarization of recombination radiation in variband structures was reported in [4].

A substantial part of present research in this area deals with the spatial separation of carriers with oppositely directed spins. Most of the devices proposed for spin filtering make use of magnetic materials [5] or of a magnetic field (which lifts the spin degeneracy of carriers) in order to pass the carriers that are predominantly in one spin state while creating a barrier for the carriers in the other spin states. Efficient operation of such a system is possible only at liquid-helium temperatures [6].

As far back as the 1980s, experiments were carried out [7] in which spin filtering was actually demonstrated in gallium arsenide (a nonmagnetic semiconductor) at 77 K through asymmetric scattering of electrons with respect to the plane containing the spin and the initial angular momentum. This effect was predicted in [8].

In this paper, we report on our observation of spatial separation (filtering) of electrons in spin in the space charge field near the interface in AlGaAs/GaAs at 77 K, with the electrons in GaAs excited simultaneously from both valence subbands by circularly polarized light. It is this effect that accounts for the seemingly paradoxical observation that, in such an experiment, the circular polarization of recombination radiation observed in transmission (i.e., in the direction of pump beam propagation) has a positive sign and in reflection (i.e., opposite to the pump beam) has a negative sign.[1]

In what follows, we present the results of measurements performed in both the transmission and reflection geometries, where we succeeded in showing that the luminescence propagating along and opposite to the pump beam can (under certain conditions) have opposite signs of circular polarization. This effect is accounted for by the difference in the transport of hot generated electrons and of electrons that are created in a nearly thermalized state at the conduction band bottom. In the concluding part of this paper, the complicated dependence of the degree of polarization on the luminescence wavelength is explained as being due to the existence of a depleted layer in GaAs near the interface.

2. The sample under study was a 0.4-mm-thick plane-parallel plate cut from a Czochralski-grown gallium arsenide crystal. Doping was effected by zinc diffusion from both sides [10]. The near-surface dopant concentration was determined to be 3×10^{18} cm^{-3}. After this, a layer of an Al$_x$Ga$_{1-x}$As solid solution ($x \approx 0.5$) was LPE grown on one of the plate surfaces. This layer is practically transparent for photons with an energy $E_{h\nu} \leq 2.1$ eV pumping GaAs through the interface.

Photoluminescence (PL) was excited by circularly polarized light using a grating monochromator, a krypton laser (lines at $E_{h\nu}$ = 1.65, 1.92, 2.18 eV), the 1.96-eV line of a He–Ne laser, or a tunable Ti–sapphire laser. The photon energy $E_{h\nu}$ was varied from 1.52 to 2.2 eV, i.e., up to levels in excess of $E_g + \Delta$ (Δ is the

---

† Deceased.

[1] Following [9], we assume the sign of circular polarization of luminescence to be positive if it coincides with the sign of pump light polarization.

1063-7834/05/4708-1584$26.00 © 2005 Pleiades Publishing, Inc.

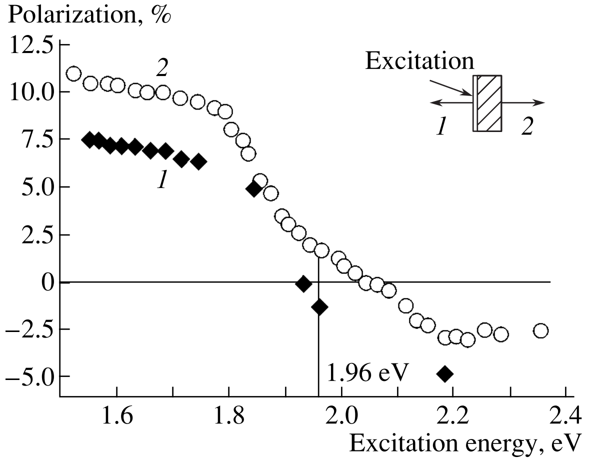

Fig. 1. Degree of circular polarization of photoluminescence measured (*1*) in reflection and (*2*) in transmission (see inset) as a function of exciting photon energy for the case where excitation is performed from the side of the interface.

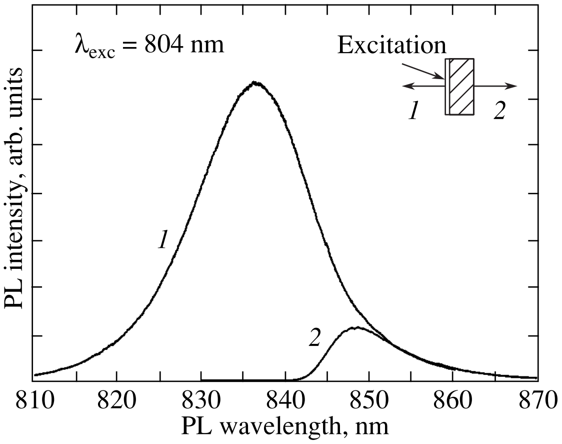

Fig. 2. Photoluminescence spectra under excitation from the interface side measured (*1*) in reflection and (*2*) in transmission (see inset).

spin–orbit splitting of the valence band). The degree of circular polarization of the luminescence ρ was measured using an analyzer consisting of a photoelastic quartz modulator and a linear polarizer [11]. For *p*-GaAs under quasi-resonant excitation and with a uniform average spin distribution in the region where nonequilibrium electrons undergo recombination, this quantity is

$$\rho = 0.25\frac{T_s}{\tau}.$$

Here, τ is the nonequilibrium electron lifetime and T_s is the spin orientation lifetime, which is defined as $T_s^{-1} = \tau^{-1} + \tau_s^{-1}$, where τ_s is the spin relaxation time [12].

In this work, we compare the dependences of the degree of luminescence circular polarization ρ on pump light energy $E_{h\nu}$ as obtained in transmission and reflection. The inset to Fig. 1 illustrates the measurement geometries used in optical carrier pumping through the AlGaAs layer.

The luminescence band peaking at 838 nm derives from transitions from the conduction band to the zinc acceptor level [13]. When observed in transmission, the recombination radiation is partially absorbed, thus shifting the luminescence maximum toward longer wavelengths. Figure 2 shows the luminescence bands measured in reflection (curve *1*) and transmission (curve *2*). With respect to band *1*, band *2* is shifted 12 nm toward longer wavelengths.

The spectral response of absorbance $\alpha(\lambda)$ for *p*-GaAs samples in which the acceptor concentration was close to the value measured for doped surface layers of the given crystal can be found in [14]. For $\lambda = 850$ nm, α is approximately 400 cm^{-1}. Because the thickness of our GaAs sample is $d = 0.04$ cm, nothing would have been left from the recombination radiation in transmission but one ten-millionth part if the dopant had been uniformly distributed over the crystal volume.

Rough estimates suggest that the total thickness of the doped gallium arsenide layer near both surfaces does not exceed 5 μm. The remainder of the crystal inside the plate is practically undoped [10]. The bulk of the crystal absorbs the short-wavelength part of the recombination radiation and is practically transparent to it in the long-wavelength region [15].

3. Figure 1 shows the $\rho(E_{h\nu})$ dependences measured in reflection (curve *1*) and in transmission (curve *2*) at liquid-nitrogen temperature. While these dependences do have common features, they also exhibit noticeable differences. A common feature of curves *1* and *2* is that, for energies higher than $E_{h\nu} = E_g + \Delta$, the degree of circular polarization ρ starts to decrease rapidly and reverses sign as $E_{h\nu}$ increases further. Both the decrease in ρ and the reversal of the sign of polarization with increasing pump photon energy are well known and are due to the onset of optical transitions from the valence band split off due to spin–orbit coupling [16].

Reversal of the sign of electron spin orientation at $E_{h\nu} > E_g + \Delta$ was observed in [17]. The essence of the effect consists in that, in crystals lacking inversion center, the efficiency of spin relaxation due to spin–orbit interaction in the conduction band grows strongly with increasing electron energy [16]. As a result, the electrons excited by photons with energies $E_{h\nu} > E_g + \Delta$ from the heavy- and light-hole band Γ_8 can forget their spin orientation almost completely during thermalization, whereas the electrons from the valence band Γ_7 split off due to spin–orbit coupling retain their opposite orientation. The net result is that the overall spin orientation reverses sign to become negative.

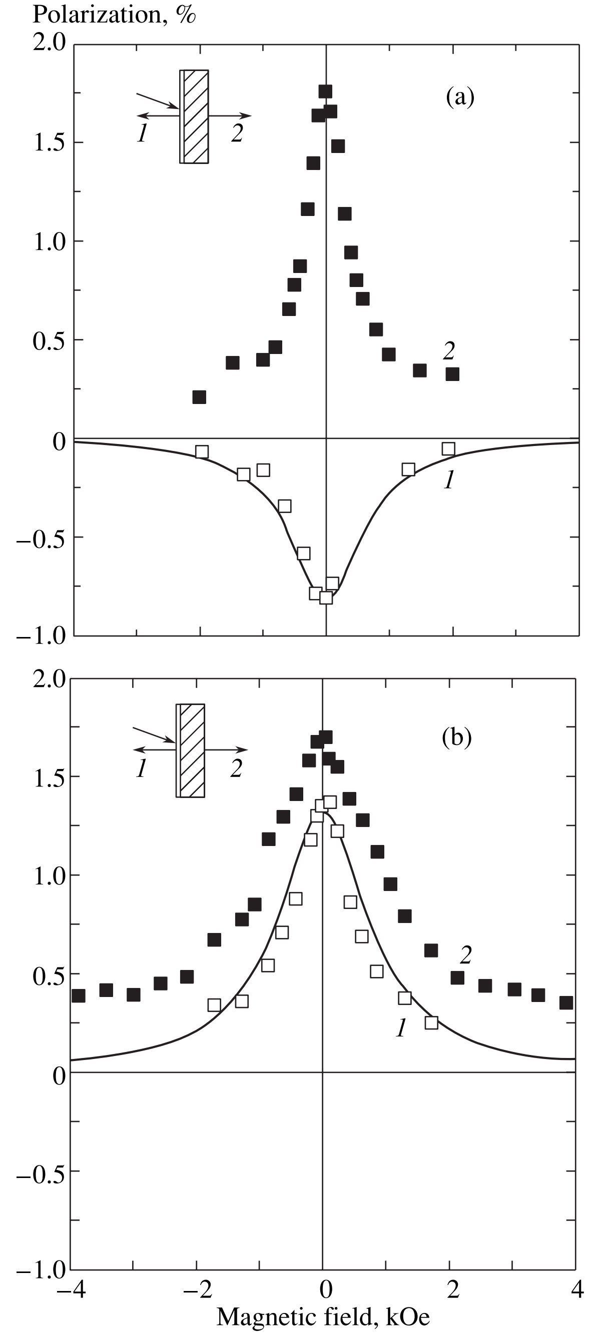

Fig. 3. Photoluminescence depolarization in a transverse magnetic field (the Hanle effect) measured (*1*) in reflection and (*2*) in transmission (see insets) under pumping (a) from the interface side and (b) from the side of the free surface.

Curves *1* and *2* in Fig. 1 differ in that, first, for energies $E_g < E_{h\nu} < E_g + \Delta$, the degree of luminescence polarization observed in reflection is smaller than that in transmission and, second, the circular polarization observed in transmission reverses sign at energy $E_{h\nu}$ = 2.06 eV, which is larger than $E_{h\nu}$ = 1.92 eV in reflection. Thus, in the region 1.92 < $E_{h\nu}$ < 2.06 eV, the signs of luminescence circular polarization measured in reflection and transmission for the same pump photon energy (e.g., at $E_{h\nu}$ = 1.96 eV) are opposite.

The fact that the signs of polarization are indeed opposite also follows from measurements of the degree of luminescence polarization as a function of transverse magnetic field under He–Ne laser excitation ($E_{h\nu}$ = 1.96 eV). Figure 3a presents luminescence depolarization curves obtained in a transverse magnetic field. Filled squares show experimental results obtained in transmission. Curve *1* describes magnetic depolarization studied in reflection and is essentially a Lorentzian,

$$\rho(H) = \frac{\rho(0)}{1 + \omega_L^2 T_s^2},$$

where ω_L is the frequency of spin Larmor precession in a magnetic field [12]. Both the positive and negative circular polarizations decrease almost to zero in a sufficiently strong magnetic field.

Similar experiments were carried out in the same two geometries by pumping the rear surface, which was free of the GaAlAs solid solution. In both cases, a positive sign of circular polarization was observed; the corresponding curves of depolarization in a magnetic field are displayed in Fig. 3b. On the side of the free surface, there is no depleted layer and no near-surface localization of thermalized electrons. The near-surface zinc concentration on this side is fairly high ($p \sim 3 \times 10^{18}$ cm^{-3}). The $\rho(E_{h\nu})$ dependences in heavily doped samples were measured earlier in [18] in reflection and in [19] in transmission (on the sample under study here with the free surface pumped). It was established that frequent electron collisions give rise to a dynamic averaging of the effect caused by the effective spin–orbit interaction fields. For this reason, the D'yakonov–Perel' (DP) spin relaxation slows down and we have $\rho > 0$ at $E_{h\nu}$ = 1.96 eV in both geometries. Thus, in three cases out of four, the circular polarization at $E_{h\nu}$ = 1.96 eV is positive and, only in one case, namely, in the reflection geometry with pumping done through the AlGaAs layer, it is negative and tends to zero with increasing field.

4. The above experimental results can be explained if one considers that, in both reflection and transmission geometries, recombination is actually detected from different regions of the crystal. In reflection, the recombination radiation is emitted primarily from the pocket formed at the interface by the layer depleted in equilibrium holes, while in transmission measurements it exits from under this layer, a region that is accessible for electrons with a higher initial energy.

A study of photoreflectance spectra has shown that, if a layer depleted in equilibrium carriers (in particular, by holes) forms near the surface of gallium arsenide doped by an acceptor impurity, then an energy barrier arises for electrons; the height of this barrier can be estimated as about 0.3 eV [20]. It appears that we have a similar situation near the interface. Estimates showed that the gallium arsenide doping level in the interface region is approximately 10^{16} cm^{-3} [14]. The deeper lying doped layer should have an acceptor concentration that decreases away from the interface [10]. Thus, near the surface, there is a potential well and the electrons with energies lower than the barrier height become confined at the interface surface. The smaller polarization observed in reflection at energies $E_g < E_{h\nu} < E_g + \Delta$ (Fig. 1) likewise suggests the presence of a space charge field drawing electrons and holes in opposite directions. The recombination probability decreases, thus bringing about an increase in the nonequilibrium carrier lifetime.

As the excitation energy increases, electrons with an initial energy in excess of the barrier height appear in the conduction band and a sizable part of them overcome the barrier. Recombination with these electrons provides the dominant contribution to the luminescence analyzed in transmission, whereas in reflection these electrons do not manifest themselves. Starting from the energy $E_{h\nu} = E_g + \Delta$, the electrons excited from the spin–orbit-split-off valence band turn out to be confined at the interface and it is these electrons that now contribute heavily to the luminescence intensity in reflection. The electrons that have succeeded in moving from the pumped surface (at the interface) toward the opposite surface free of the solid solution account for the dominant contribution to the luminescence in transmission. Most of them are electrons excited from the fourfold-degenerate Γ_8 band, because they are created with an excess energy. The polarization of these electrons is low, because the DP spin relaxation for hot electrons is a more efficient mechanism [16]. The electrons excited from the split-off valence band with energies within a certain interval cannot overcome the barrier. Only starting with an energy $E_{h\nu} = 2.06$ eV do they begin to surmount the barrier and move toward the opposite surface. Recombination with their participation is also detected in transmission. According to [16], this results in an inversion of the direction of predominant orientation of thermalized electrons and, therefore, in the reversal of the sign of the luminescence circular polarization observed in transmission.

5. Figure 4a shows the dependence of the degree of polarization on luminescence wavelength obtained in reflection under pumping through a transparent window. Figure 4b displays an analogous dependence measured under excitation of the surface free of the solid solution. Both relations reveal an increase in polarization with decreasing wavelength. The difference between these curves is greatest in the short-wavelength region. As seen in Fig. 4a, after reaching a maximum, the polarization decreases again with decreasing wavelength.

One can derive a straightforward analytical expression for the dependence of the degree of polarization on luminescence wavelength in reflection. The luminescence is emitted from a surface layer with a thickness of the order of the reciprocal absorbance of the recombination radiation, α_λ^{-1}. For $\lambda = 838$ nm (maximum of the luminescence line), we have $\alpha_\lambda^{-1} \approx 5$–6 μm [14]. Assuming reflection geometry and excitation from the side of the AlGaAs coating, the reradiation of the edge luminescence can be neglected, because the solid solution reduces the reflection from the gallium arsenide surface; as a result, there is almost no backscattering of the recombination radiation from the interface [21]. The surface recombination can likewise be disregarded. Indeed, the surface recombination rate at the interface is negligible even at room temperature and at liquid-

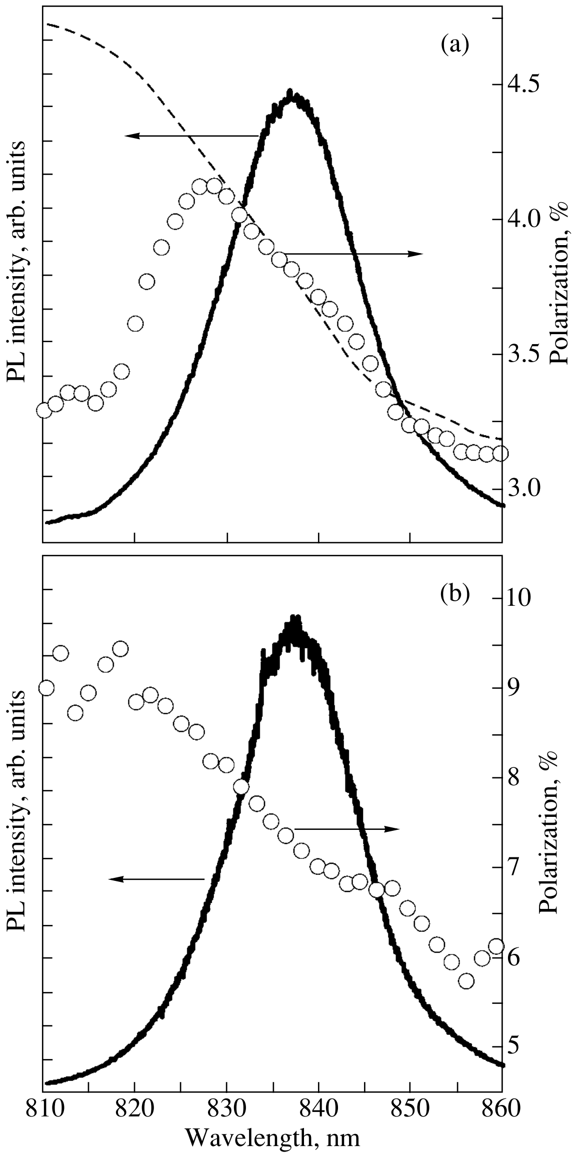

Fig. 4. Photoluminescence and circular polarization spectra measured in reflection when pumped (a) from the side of the interface and (b) from the side of the free surface (the exciting photon energy is 1.65 eV). The dashed line is a plot of Eq. (2) for $L_e = 4.3$ μm and $L_s = 2.4$ μm.

nitrogen temperature it should be still lower [21]. The diffusion lengths L_e and L_s are much smaller than the crystal thickness, so the sample may be treated as semi-infinite.

In reflection, the degree of circular polarization as a function of radiation wavelength is defined as

$$\rho(\lambda) = \frac{\int_0^\infty dz S(z) e^{-\alpha_\lambda z}}{\int_0^\infty dz N(z) e^{-\alpha_\lambda z}}, \qquad (1)$$

where $S(z)$ is the spin density and $N(z)$ is the electron concentration. The functions $S(z)$ and $N(z)$ are solutions of a system of rate equations [21],

$$D\frac{d^2N}{dz^2} - \frac{N}{\tau} = 0, \quad -D\frac{dN}{dz}\bigg|_{z=0} = J, \quad N|_{z\to\infty} \longrightarrow 0,$$

$$D\frac{d^2S}{dz^2} - \frac{S}{T_s} = 0, \quad -D\frac{dS}{dz}\bigg|_{z=0} = \frac{J}{4}, \quad S|_{z\to\infty} \longrightarrow 0,$$

where D is the diffusion coefficient and J is the surface electron-generation rate. Substituting the solution to this system into Eq. (1), we find the spectral response of the degree of polarization of the recombination radiation for optically oriented electrons to be

$$\rho(\lambda) = 0.25\frac{\tau_s}{\tau + \tau_s}\frac{(1 + \alpha_\lambda L_e)}{(1 + \alpha_\lambda L_s)}. \qquad (2)$$

Because the absorbance α_λ varies within the PL line profile by more than three orders of magnitude, the degree of polarization ρ should depend on wavelength in accordance with Eq. (2).

Our earlier study of the Hanle effect performed on the same sample revealed that, near the interface at 77 K, we have $\tau_s = 0.6$ ns and that the DP mechanism dominates in electron spin relaxation [14]. In this case, the electron momentum relaxation time can be estimated to be $\tau_p = 0.5$ ps.[2] With this value of τ_p, we find the electron mobility $\mu_e = e\tau_p/m_e = 19\,500$ cm^2/V s and the diffusion lengths of electrons $L_e = 4.3$ μm and of the electron spins $L_s = 2.4$ μm (the diffusion coefficient is derived from the Einstein relation to be $D = 130$ cm^2/s). In Fig. 4a, the dashed line is calculated from Eq. (2) using the spectral response of absorbance and the above values of L_e and L_s. It is seen that this line fits the experimental data well everywhere except in the short-wavelength region of the spectrum.

When luminescence is excited from the side of the interface, the experiment is seen to disagree noticeably with the calculated $\rho(\lambda)$ graph in the short-wavelength region. Here, the measured degree of luminescence polarization is substantially lower than follows from the calculations (Fig. 4a). The disagreement between the theoretical and experimental relations is a result of the existence of a built-in electric field at the interface; this field separates the electrons from holes in space, thus bringing about an increase in the lifetime and, hence, a decrease in the degree of polarization of the recombination radiation. The thickness of the depleted layer is approximately equal to the reciprocal absorbance at the wavelength $\lambda = 820$ nm, i.e., about 1 μm.

The $\rho(\lambda)$ graph obtained under excitation of the free surface does not have such a region at the short-wavelength edge (Fig. 4b). Here, the polarization grows monotonically with decreasing luminescence wavelength, because the electrons diffuse away from the surface into the bulk of the crystal.

Thus, the electric field created by the space charge field of the depleted GaAs layer near the AlGaAs/GaAs interface gives rise to spatial separation of the electrons excited from the spin–orbit-split valence subbands into the conduction band. By slightly varying the pump energy, one can control the direction and mutual orientation of the spins of electrons located in different regions of the crystal.

ACKNOWLEDGMENTS

The authors are grateful to A.V. Kudinov and K.V. Kavokin for helpful discussions and to I.G. Aksyanov and O.A. Ninua for their assistance in the experiment.

This study was supported by the Russian Foundation for Basic Research, CRDF, the Department of Physical Sciences, and the Presidium of the Russian Academy of Sciences.

REFERENCES

1. S. A. Wolf, D. D. Awschalom, R. A. Buhrman, J. M. Daughton, S. von Molnar, M. L. Roukes, A. Y. Chtchelkanova, and D. M. Trager, Science **294**, 1488 (2001).
2. M. I. D’yakonov and V. I. Perel’, Fiz. Tekh. Poluprovodn. (Leningrad) **10**, 350 (1976) [Sov. Phys. Semicond. **10**, 208 (1976)].
3. V. L. Vekua, R. I. Dzhioev, B. P. Zakharchenya, and V. G. Fleĭsher, Fiz. Tekh. Poluprovodn. (Leningrad) **10**, 354 (1976) [Sov. Phys. Semicond. **10**, 210 (1976)].
4. A. S. Volkov, I. K. Volkova, A. L. Lipko, S. M. Meretlev, and B. V. Tzarenkov, Fiz. Tekh. Poluprovodn. (Leningrad) **21**, 1146 (1987) [Sov. Phys. Semicond. **21**, 1146 (1987)].
5. C. A. Dartora and G. G. Cabrera, J. Appl. Phys. **95**, 6058 (2004).

---

[2] In the DP mechanism, $\tau_s^{-1} = A\tau_p$, where the coefficient A depends on temperature and the electron scattering mechanism. At $T = 77$K and for scattering from ionized impurities, we have $A = 3.3$ ns^{-1} ps^{-1}. Therefore, for $\tau_s = 0.6$ ns, we obtain $\tau_p = 0.5$ ps.

6. M. J. Gilbert, J. P. Bird, T. Sugaya, and R. Akis, Physica B **314**, 230 (2002).
7. A. A. Bakun, B. P. Zakharchenya, A. A. Rogachev, M. N. Tkachuk, and V. G. Fleĭsher, Pis'ma Zh. Éksp. Teor. Fiz. **40**, 464 (1984) [JETP Lett. **40**, 1293 (1984)].
8. N. S. Averkiev and M. I. D'yakonov, Fiz. Tekh. Poluprovodn. (Leningrad) **17**, 629 (1983) [Sov. Phys. Semicond. **17**, 393 (1983)].
9. A. Bennot, R. Planel, and C. Benoit a la Guillaume, Phys. Rev. B **9**, 690 (1974).
10. S. Tiwari, J. Hintzman, and A. Callegari, Appl. Phys. Lett. **51**, 2118 (1987); K. B. Kahen, Appl. Phys. Lett. **55**, 2117 (1989).
11. S. N. Jasperson and S. E. Schnatterly, Rev. Sci. Instrum. **40**, 761 (1969).
12. *Optical Orientation*, Ed. by F. Meier and B. P. Zakharchenya (North-Holland, Amsterdam, 1984; Nauka, Leningrad, 1989).
13. Marshall I. Nathan, Gerald Durns, Samuel E. Blum, and John C. Marinace, Phys. Rev. **132**, 1482 (1963).
14. R. I. Dzhioev, B. P. Zakharchenya, K. V. Kavokin, and M. V. Lazarev, Fiz. Tverd. Tela (St. Petersburg) **45** (12), 2153 (2003) [Phys. Solid State **45** (12), 2255 (2003)].
15. H. C. Casey, Jr., D. D. Sell, and K. W. Wecht, J. Appl. Phys. **46**, 250 (1975).
16. M. I. D'yakonov and V. I. Perel', Zh. Eksp. Teor. Fiz. **60**, 1954 (1971) [Sov. Phys. JETP **33**, 1053 (1971)].
17. A. I. Ekimov and V. I. Safarov, Pis'ma Zh. Éksp. Teor. Fiz. **13**, 700 (1971) [JETP Lett. **13**, 495 (1971)].
18. B. P. Zakharchenya, V. G. Fleĭsher, R. I. Dzhioev, Yu. P. Veshchunov, and I. B. Rusanov, Pis'ma Zh. Eksp. Teor. Fiz. **13**, 195 (1971) [JETP Lett. **13**, 137 (1971)].
19. D. Z. Garbuzov, R. I. Dzhioev, L. M. Kanskaya, and V. G. Fleĭsher, Fiz. Tverd. Tela (Leningrad) **14**, 1720 (1972) [Sov. Phys. Solid State **14**, 1481 (1972)].
20. C. Van Hoof, K. Deneffe, J. De Boek, D. J. Arent, and G. Borghs, Appl. Phys. Lett. **54**, 608 (1989).
21. R. I. Dzhioev, B. P. Zakharchenya, K. V. Kavokin, and P. E. Pak, Fiz. Tverd. Tela (St. Petersburg) **36** (9), 2752 (1994) [Phys. Solid State **36** (9), 1501 (1994)].

Translated by G. Skrebtsov

Physics of the Solid State, Vol. 47, No. 8, 2005, pp. 1590–1594. Translated from Fizika Tverdogo Tela, Vol. 47, No. 8, 2005, pp. 1528–1532.
Original Russian Text Copyright © 2005 by Geĭvandov, Yudin, Fridkin, Ducharme.

MAGNETISM AND FERROELECTRICITY

Manifestation of a Ferroelectric Phase Transition in Ultrathin Films of Polyvinylidene Fluoride

A. R. Geĭvandov*, S. G. Yudin*, V. M. Fridkin*, and S. Ducharme**
**Shubnikov Institute of Crystallography, Russian Academy of Sciences, Leninskiĭ pr. 59, Moscow, 119333 Russia*
e-mail: LBF@ns.crys.ras.ru
***University of Nebraska, Lincoln, USA*

Received October 5, 2004

Abstract—Temperature dependences of the dielectric properties of ultrathin polyvinylidene fluoride films prepared using the Langmuir–Blodgett method were studied by linear and nonlinear dielectric spectroscopy. It is shown that ultrathin Langmuir films of polyvinylidene fluoride exhibit a manifestation of a first-order ferroelectric phase transition, which can be assigned to the interaction between the spontaneous polarization and the surfaces bounding the film. As the film thickness increases, the effect of the surfaces decreases and the ferroelectric phase transition shifts to high temperatures to vanish altogether when the temperature region of the transition rises above the melting point. © *2005 Pleiades Publishing, Inc.*

1. INTRODUCTION

Numerous experimental studies seem to suggest that observation of the ferroelectric phase transition in polyvinylidene fluoride (PVDF) is impossible because bulk samples (films with a thickness of above 100 nm) undergo melting before the onset of the hypothetical transition to the ferroelectric phase [1–3]. It was shown in [4] that, as one crosses over to ultrathin (less than 5-nm-thick) Langmuir–Blodgett (LB) films [5] of 70/30 vinylidene fluoride copolymer with trifluoroethylene (VDF/TrFE), the ferroelectric phase transition region shifts toward lower temperatures. It is known [3, 4] that films of pure PVDF have a lower spontaneous polarization than copolymer films (such as VDF/TrFE). This can be accounted for by the low crystallinity of PVDF films (the content of the ferroelectric β phase is approximately 50%). We believe that the effect of the bounding surfaces on the sample properties increases with decreasing PVDF film thickness. The fact is that surface layers of a ferroelectric behave differently from the bulk of the material. Because boundary layers of thin films contribute more to the sample characteristics under study than those of thick films, the properties of the sample on the whole change. Thus, it is thin films that offer the possibility of studying the ferroelectric phase transition in films prepared of pure PVDF. Note that the ferroelectric phase transition has been observed previously only in copolymers (such as VDF/TrFE) of different compositions (from 37/63 to 73/27) [2–4].

The present paper reports on a study of the temperature dependences of the dielectric properties of PVDF ferroelectric films prepared using the LB method by linear and nonlinear dielectric spectroscopy (NDS).

2. SAMPLE PREPARATION AND EXPERIMENT

The PVDF molecule consists of (–CH_2–CF_2–) monomer chain links. The total molecular mass of the polymer chain is approximately 10^5. LB films of PVDF were obtained in a setup described in [6]. First, a solution of 0.01–0.02 wt % PVDF in acetone was prepared. PVDF monolayers were transported from the water surface, using the Langmuir–Schaffer method [5] (horizontal lifting), onto glass substrates with 1-mm-wide aluminum electrodes evaporated in vacuum. The PVDF films were deposited under a surface pressure $\pi = 1.5$–3 mN/m at a temperature of 17–19°C. The number of layers (from 5 to 36) was varied depending on the desired total film thickness. The thickness of one monolayer as estimated from the size of the PVDF molecule is 0.5 nm [4]. It is known, however, that the thickness of a film after its deposition on the substrate turns out to be larger. Indeed, as follows from capacitance measurements, the thickness of one transported layer exceeds the calculated value by two to three times [7]. After the layer deposition, a top aluminum electrode was evaporated such that the electrode overlap area was 1 ± 0.0025 mm^2.

The electric properties of LB PVDF films were measured on an automated setup. A computer audio card was used to generate and detect electric signals. The measurement system consisted of a set of virtual instruments (a generator, a lock-in detector, a digital oscilloscope, etc.) realized with the PhysLab computer code [6]. The setup included a thermostat, whose temperature was monitored by means of a Peltier element and measured with a platinum resistance thermometer. The sample temperature was varied from 30 to 185°C.

The dielectric properties of LB PVDF films were studied by NDS, the principles of which are explained in detail in [8, 9].

The NDS method is based on phase-sensitive measurements of the fundamental and higher harmonics of the current flowing through a sample to which a harmonic voltage is applied. Therefore, lock-in detection was employed for current measurement [8]. In this method, the sample, which can generally be considered a capacitance and a resistance connected in parallel, is inserted in series with a load resistor and the voltage drop across it (which is proportional to current) is measured by the detector. The reference signal for lock-in detection is supplied from a second generator channel.

When a sine voltage $U(t) = U_0\sin(\omega t)$ is applied to a sample, the total current in the measuring electric circuit is given by

$$I = \frac{U_0\sin\omega t}{R} + \omega U_0 C_0\cos(\omega t) + \omega U_0^2\sin(2\omega t)\frac{dC}{dU}, \tag{1}$$

where $\omega = 2\pi f$ is the circular frequency, U_0 is the amplitude of the voltage U applied to the sample, t is the time, and f is the frequency of the sine voltage. The first term is inversely proportional to the Ohmic resistance of the sample R. The second term is proportional to the sample capacitance $C_0 = C(U = 0)$. These terms are easily separated in lock-in detection, because they are shifted in phase by 90°. The third term is the nonlinear contribution connected with the ferroelectric properties of the sample under study.

Ferroelectricity can be conveniently studied by introducing quantities that are defined through the ratios of the Fourier components [8] measured by the lock-in detector. In the case where the fourth and the fifth current harmonics are negligible (at the noise level), the intermodulation contributions to the first three harmonics are small and we can write

$$A_2 = \frac{-\sqrt{2}\Phi_{2x}}{2\left(\sqrt{2}\Phi_{1y} - \omega\varepsilon_0\frac{U_0S}{d}\right)^3}\frac{U_0}{d}(\omega S)^2, \tag{2}$$

$$A_3 = \frac{\sqrt{2}\Phi_{3y}}{3\left(\sqrt{2}\Phi_{1y} - \omega\varepsilon_0\frac{U_0S}{d}\right)^4}\frac{U_0}{d}(\omega S)^3, \tag{3}$$

$$A_4 = \frac{\sqrt{2}\Phi_{4x}}{15\left(\sqrt{2}\Phi_{1y} - \omega\varepsilon_0\frac{U_0S}{d}\right)^5}\frac{U_0}{d}(\omega S)^4, \tag{4}$$

$$A_5 = \frac{-2\sqrt{2}\Phi_{5y}}{5\left(\sqrt{2}\Phi_{1y} - \omega\varepsilon_0\frac{U_0S}{d}\right)^6}\frac{U_0}{d}(\omega S)^5, \tag{5}$$

where S is the electrode overlap area; d is the film thickness; $\varepsilon_0 \cong 8.85 \times 10^{-12}$ F/m; and Φ_{1y}, Φ_{2x}, Φ_{3y}, Φ_{4x}, and Φ_{5y} are the effective values of the Fourier x and y components detected by the lock-in detector, from the first to the fifth harmonic. Recall that the x component should be identified with the signal that is in phase with the reference (which, in turn, is proportional to $\sin(k\omega t)$, where k is the harmonic number), whereas the y component is proportional to $\cos(k\omega t)$ and, hence, is shifted with respect to the reference signal by 90°. The quantities A_k (k = 2, 3, 4, 5) were obtained in the approximation of infinite sample resistances.

The convenience of using the above quantities becomes obvious when one learns their relation to the Landau–Ginzburg coefficients in the equation for the free energy of the ferroelectric [10]:

$$F_{LG} = \frac{1}{2}\alpha P^2 + \frac{1}{4}\beta P^4 + \frac{1}{6}\gamma P^6 - EP, \quad \alpha = \alpha_0(T - T_0), \tag{6}$$

where α_0, β, and γ are temperature-independent coefficients; T_0 is the Curie temperature; E is the electric field amplitude; and P is the polarization. As shown in [8], quantities (2)–(5) for a uniformly polarized ferroelectric can be expressed as

$$A_2 = P_s(3\beta + 10\gamma P_s^2), \tag{7}$$

$$A_3 = \beta + 10\gamma P_s^2, \tag{8}$$

$$A_4 = \gamma P_s, \tag{9}$$

$$A_5 = \gamma, \tag{10}$$

where P_s is the spontaneous polarization.

We readily see that the quantity A_3 is connected with the coefficient β, which, together with the coefficient γ, determines the order of the phase transition. It is known that, for $\beta > 0$ and $\gamma \geq 0$, Eq. (6) describes a second-order phase transition and, for $\beta < 0$ and $\gamma > 0$, the first-order transformation. Thus, in the case of a first-order phase transition, there is a temperature at which A_3 can vanish and reverse sign.

In addition to NDS, polarization switching in films was probed using the classical Merz method [11], in which triangular voltage pulses are applied to a sample and the current response is measured as the voltage drop across the load resistor connected in series with the sample. In addition to the capacitive and resistive current contributions, the current response contains characteristic nonlinear contributions originating from switching of the spontaneous polarization (Fig. 1).

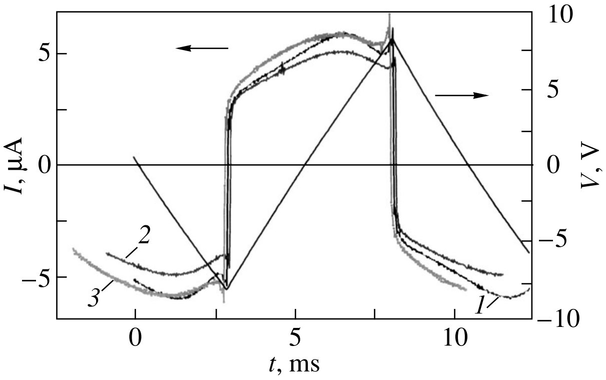

Fig. 1. Oscilloscopic traces of current (left) obtained with triangular voltage pulses of amplitude U_0 = 14 V and frequency f = 96 Hz applied to the sample at various temperatures *T*: (*1*) 35, (*2*) 57, and (*3*) 88°C.

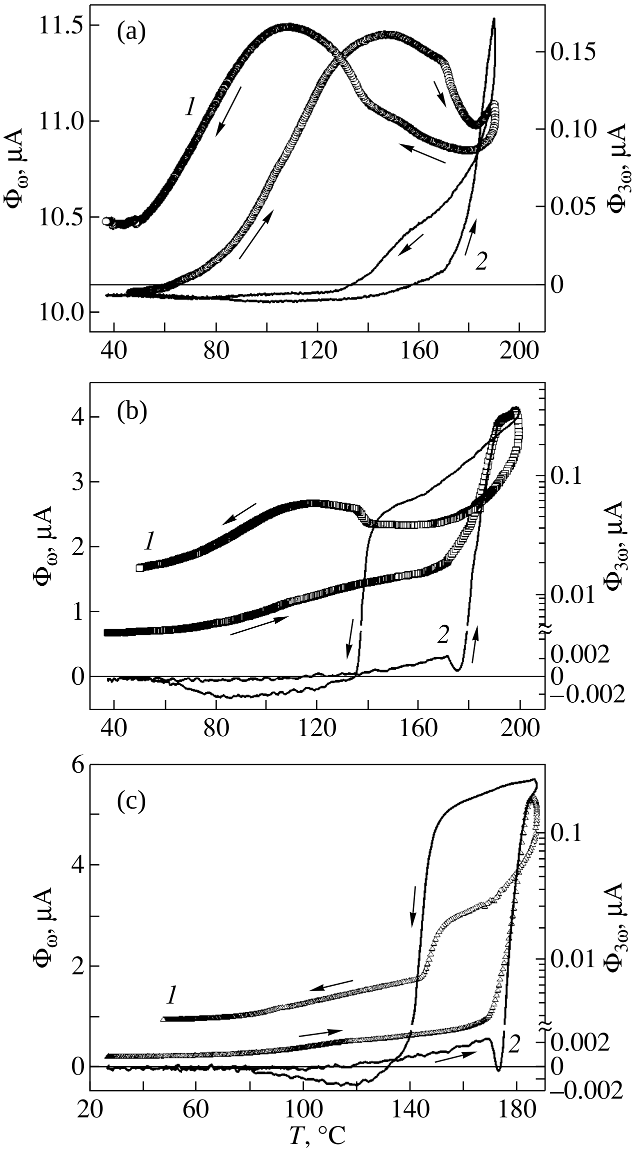

Fig. 2. Temperature dependences of (*1*) the fundamental and (*2*) third harmonics in the current for PVDF films with various thicknesses: (a) 5, (b) 10, and (c) 36 layers. U = 0.5 V and f = 1 kHz. Arrows refer to sample heating and cooling. The right-hand scale in panels (b, c) is linear near zero and logarithmic otherwise.

3. DISCUSSION OF THE RESULTS

The LB PVDF films exhibit ferroelectric properties. This is borne out by observation of the characteristic current responses obtained using the Merz technique [11] (Fig. 1).

Figure 2 shows the temperature dependences of the first and third current harmonics. The thermal hysteresis seen in the permittivity of the 5-layer LB PVDF film (curve *1* in Fig. 2a) indicates a first-order phase transition similar to the one observed in LB films of a VDF/TrFE 70/30 copolymer [12]. However, the amplitude of the first current harmonic in the VDF/TrFE 70/30 copolymer films varied within a factor of 1.5 to 2 during heating and cooling runs, whereas the variation in this quantity in the 5-layer PVDF film does not exceed 10%. As the LB PVDF film thickness increases to 10 layers (curve *1* in Fig. 2b), the thermal hysteresis becomes less pronounced, with the maxima shifting toward higher temperatures. For instance, the maximum at 147°C (Fig. 2a, heating run) shifts to 160°C (Fig. 2b, heating) and the maximum at 108°C (Fig. 2a, cooling run) shifts to 119°C (Fig. 2b, cooling). A further increase in the LB PVDF film thickness to 36 layers entails a shift of the ferroelectric phase transition to high temperatures, where melting occurs and the transition becomes virtual. We explain these experimental data as due to the fact that the free-energy contribution generated by surface interaction becomes progressively more significant with decreasing film thickness than that due to the bulk of the sample. The low-temperature shift of the phase transition is caused by the polarization interacting with the surface. Because the surface interaction is localized, there occurs a surface-induced phase transition in thin surface layers. Thus, ultrathin films of pure PVDF exhibit a superposition of two ferroelectric phase transitions, more specifically, of a surface-induced and a bulk transition. The surface-induced phase transition is characterized by a Curie temperature lying below the melting point ($T_m \approx$ 168–170°C), while in bulk samples a ferroelectric phase transition cannot be observed, because it is expected to occur in the melting-temperature region, as indicated in a number of papers [1, 3].

The existence of a first-order phase transition is also corroborated by the clearly pronounced sign reversal of the third harmonic in the current response (curve *2* in Fig. 2a) observed at 156°C on heating and at 132°C on cooling, because, as follows from Eqs. (3) and (8), sign reversal is possible only for $\beta < 0$. In 10- and 36-layer-thick LB films, however, it becomes difficult to reliably detect sign reversal of the third harmonic (Figs. 2b, 2c) during heating. At temperatures below 100°C, the signal is very low. Note that the right-hand scale in Figs. 2b and 2c is divided into a linear (near the zero signal) and a logarithmic (region of positive response) part. A distinct sign reversal in the vicinity of $T = 132$°C in 10- and 36-layer films could be identified only in the cooling run. Thus, measurement of the third harmonic in the current response again reveals the above-mentioned interplay between the surface-induced and bulk ferroelectric phase transitions with increasing film thickness.

Figures 3a and 3b display the temperature dependences of A_3 for 5- and 10-layer PVDF films, respectively. The quantity A_3 is expressed through the first and third current harmonics and is a more revealing characteristic for describing the ferroelectric properties of a uniform sample [see Eqs. (3), (8)]. The condition $A_3 = 0$ for a 5-layer film is met at 156°C (under heating) and at 132°C (under cooling). In the paraelectric phase, where $P_s = 0$, the quantity A_3 is negative and temperature-independent, according to Eq. (8) for the uniform model. It has indeed been found that, in LB films of the VDF/TrFE 70/30 copolymer above the transition temperature $T \cong 110$°C, the value of A_3 in the paraelectric phase is negative and that the $A_3(T)$ dependence is weak (the curve is parallel to the horizontal axis) and switches sign only on cooling to 70°C [8]. In our case, the 5-layer LB PVDF film (Fig. 3a) exhibits a weak $A_3(T)$ dependence in the temperature regions 120–150°C (under heating) and 130–90°C (under cooling). Although $A_3 > 0$, we attribute these temperature regions to the paraelectric state of the surface layer of the film (surface-induced ferroelectric phase transition). The fact that $A_3 > 0$ in these regions may be explained as being due to the positive background produced by the bulk of the film, which resides in the ferroelectric state. It is because of the dominant background due to the bulk of the film that analysis of the surface-induced ferroelectric phase transition is hampered (Fig. 3b). Thus, only in the 5-layer LB PVDF film does the $A_3(T)$ dependence exhibit features characteristic of the surface-induced ferroelectric phase transition; these features are not manifest in thicker films.

The experimental data can be qualitatively treated in terms of the quasi-uniform model with inclusion of the nonpolar part of the surface energy. Using the approach explicated in [9], the nonpolar contribution to the surface energy can be found to be

$$W_2 = \frac{1}{2}W_{2m}(P_i n_{e,i})^2, \qquad (11)$$

where W_{2m} is the surface energy amplitude, P_i are the components of the spontaneous polarization vector (the index i labels the spatial directions x, y, z), and $n_{e,i}$ are the components of the unit vector $\mathbf{n}_e$ oriented along the specific ("easy") direction on the surface. The concept of specific direction (easy axis) is introduced here by analogy with the description of surface interaction (cohesion) in the theory of liquid crystals [13]. The easy axis corresponds to extremal values of surface interaction. For instance, in the particular case of an isotropic substrate surface, the only preferred direction is the surface normal $\mathbf{n}_s$, so $\mathbf{n}_e = \mathbf{n}_s$. Near the surface, there is always an electric field, and its spatial distribution is dependent on the symmetry properties of this surface. The surface energy quadratic in polarization reflects the nonpolar interaction of this field with the polarization.

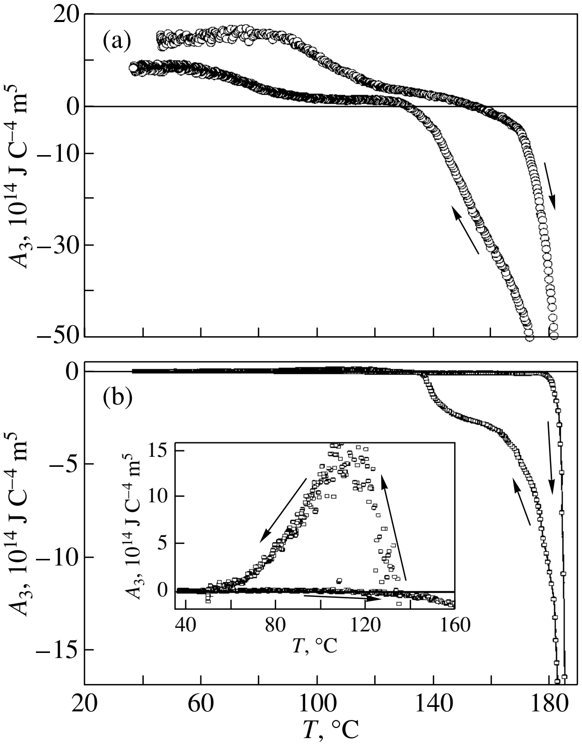

Fig. 3. Temperature dependences of the coefficient A_3 for PVDF films (a) 5- and (b) 10-layers thick. $U = 0.5$ V and $f = 1$ kHz. Arrows refer to sample heating and cooling. In the inset, the coefficient A_3 is shown in an enlarged scale.

Let us consider the free energy of a planar uniform ferroelectric domain, with the easy axis vector $\mathbf{n}_e$ aligned with the surface normal $\mathbf{n}_s$. With inclusion of the nonpolar surface interaction, the free-energy density of a uniform ferroelectric can be written in the form

$$F = \frac{1}{2}\alpha P_z^2 + \frac{1}{4}\beta P_z^4 + \frac{1}{6}\gamma P_z^6 - E_z P_z - [W_{2m,s1}P_z^2\delta(0) + W_{2m,s2}P_z^2\delta(z-d)], \qquad (12)$$

where P_z and E_z are the z components of the spontaneous polarization and electric field, respectively (the z axis is directed along the surface normal); $\delta(z)$ is a delta function characterizing the localization of the surface interaction; and $W_{2m,s1}P_z^2\delta(0) + W_{2m,s2}P_z^2\delta(z-d)$ is the sum of the quadratic surface energies localized near the two surfaces of the *d*-thick film. Obviously enough, the sum of quadratic surface energies describing the nonpolar interaction between the surface and the polarization vector P_z modifies the coefficient α. The sign of this sum in Eq. (12) can be either positive or negative, depending on which (normal or planar) orientation of the polarization vector is preferred for a given surface. We chose the minus sign in order for the polarization orientation along the surface normal to be favorable at positive values of W_{2m}. Accordingly, the temperature of the surface-induced phase transition can either increase or decrease, depending on the sign of W_{2m}. Measurement of the dependence of the first Landau coefficient α on film thickness in more uniform LB films of the VDF/TrFE 70/30 copolymer would make it possible to quantify the quadratic surface interaction.

4. CONCLUSIONS

Using nonlinear dielectric spectroscopy, we have shown that, as the film thickness is reduced, a ferroelectric phase transition (which is absent in bulk samples) begins to appear. A qualitative theoretical model based on the Landau–Ginzburg theory with inclusion of surface interaction has been proposed for describing this surface-induced phase transition.

ACKNOWLEDGMENTS

The authors are indebted to S.P. Palto for his assistance in the study and helpful discussions.

This study was supported by the Russian Foundation for Basic Research (project nos. 03-02-17288, 04-02-16466), the International Association of European Communities (project no. 03-51-39-67), and the Department of Physical Sciences of the Russian Academy of Sciences (program "Novel Materials and Structures").

REFERENCES

1. *The Applications of Ferroelectric Polymers*, Ed. by T. T. Wang, J. M. Herbert, and A. M. Glass (Chapman and Hall, New York, 1988).
2. K. Koga and H. Ohigashi, J. Appl. Phys. **59**, 2142 (1986).
3. T. Furukawa, M. Date, and E. Fukada, Ferroelectrics **57**, 63 (1980).
4. A. V. Bune, V. M. Fridkin, S. Ducharme, L. M. Blinov, S. P. Palto, A. V. Sorokin, S. G. Yudin, and A. T. Zlatkin, Nature **391**, 274 (1998).
5. J. Langmuir and V. Schaffer, J. Chem. Soc. **59**, 2400 (1937).
6. S. P. Palto, Doctoral Dissertation (Inst. Kristallogr. Ros. Akad. Nauk, Moscow, 1998).
7. L. M. Blinov, V. M. Fridkin, S. P. Palto, A. V. Bune, P. A. Dauben, and S. Dyusharm, Usp. Fiz. Nauk **170** (3), 247 (2000) [Phys. Usp. **43** (3), 243 (2000)].
8. S. P. Palto, G. N. Andreev, N. N. Petukhova, S. G. Yudin, and L. M. Blinov, Zh. Éksp. Teor. Fiz. **117** (5), 1003 (2000) [JETP **90** (5), 872 (2000)].
9. A. R. Geĭvandov, S. P. Palto, S. G. Yudin, and L. M. Blinov, Zh. Éksp. Teor. Fiz. **126** (1), 99 (2004) [JETP **99** (1), 83 (2004)].
10. V. L. Ginzburg, Zh. Éksp. Teor. Fiz. **19**, 36 (1949).
11. W. J. Merz, J. Appl. Phys. **27**, 938 (1956).
12. S. P. Palto, A. M. Lotonov, K. A. Verkhovskaya, G. N. Andreev, and N. D. Gavrilova, Zh. Éksp. Teor. Fiz. **117** (2), 342 (2000) [JETP **90** (2), 301 (2000)].
13. R. Barberi, I. Dozov, M. Giocondo, M. Iovane, Ph. Martinot-Lagarde, D. Stoenescu, S. Tonchev, and L. V. Tsonev, Eur. Phys. J. B **6**, 83 (1998).

Translated by G. Skrebtsov